Mechanical Behaviour of Ultra fine grain aluminium alloy. Analysis and modelling of the enhanced role of grain boundaries

Anchal Goyal

NNT : 2018SACLX091

Comportement mécanique d'un alliage d'aluminium à grains ultrafins. Analyse et modélisation du rôle exacerbé des joints de grains.

Thèse de doctorat de l'Université Paris-Saclay
préparée à l'Ecole Polytechnique

Ecole doctorale n°579 Sciences mécaniques et énergétiques, matériaux et géosciences (SMEMAG)
Spécialité de doctorat: Mécanique des matériaux

Thèse présentée et soutenue à Palaiseau, le 29th November 2018, par

ANCHAL GOYAL

Composition du Jury :

Edgar Rauch Directeur de Recherche, Université Grenoble Alpes (SIMAP)	Rapporteur
Xavier Sauvage Directeur de Recherche, Université de Rouen (GPM)	Rapporteur
Ilchat Sabirov Senior Researcher, IMDEA Materials	Examinateur
Jean-Jacques Fundenberger Maître de Conférences, Université de Lorraine (LEM3)	Examinateur
Eric Charkaluk Directeur de Recherche, Ecole Polytechnique (LMS)	President
Véronique Doquet Directeur de Recherche, Ecole Polytechnique (LMS)	Directeur de thèse

Thèse de doctorat

Abstract (English)

Mechanical behaviour of ultra-fine grain Al 5083 alloy: Analysis and modelling of the role of grain boundaries to overall plastic deformation.

Ultrafine grained (UFG) alloys seem promising, based on their high tensile properties and the possibility of superplastic forming at relatively low temperature. However, their deformation mechanisms are not fully understood, and their performance in fatigue has not been thoroughly investigated. This work compares the viscoplastic behaviour, and the deformation and damage mechanisms in tension and fatigue of a UFG Al-Mg alloy (600 nm mean grain size) obtained by severe plastic deformation (ECAP process) with that of its coarse-grained (CG) counter- part. The strain rate sensitivity (SRS) of both materials has been measured during creep, relaxation and tensile tests run at various strain rates and temperature. Microstructural refinement is shown to increase the SRS, which rises as the strain rate decreases, and controls the ductility. The UFG material becomes softer and more ductile than the CG material at high temperature. The temperature and strain rate domain for which the UFG alloy is stronger or softer has been determined.

Tensile tests run in a SEM, with DIC measurements of strain fields at meso/micro scales (using gold microgrids printed by electron beam lithography) and at sub-micron scale (using a superfine speckle obtained by film remodelling) have shown that grain boundary sliding is more and more active in both materials as the temperature rises and as the strain rate decreases. Grain boundary sliding is cooperative and occurs mostly at high-angle grain boundaries in the UFG alloy, where the strain field is more heterogeneous, and where very high strain levels (>100%) are often observed in localized bands. A 2D finite element model taking into account the viscoplastic behaviour inside the grains, and viscous sliding at the grain boundaries has been identified other the whole temperature range investigated. It captures well the observed behaviours and the much larger contribution of grain boundary sliding in the UFG alloy. It also provides the evolution of this contribution during strain hardening. Plastic strain-controlled push-pull tests and stress- controlled push-pull tests were run to investigate the cyclic behaviour and damage mechanisms of the two materials in low and high-cycle fatigue. The tests were followed by fractographic observations, statistical analysis of surface damage, as well as TEM observations of dislocations arrangements. Both materials exhibit cyclic hardening, although it is more modest in the UFG alloy, in which grain growth occurs at high amplitude. While isotropic hardening predominates in the CG alloy where the density of dislocation strongly increases during cyclic tests, kinematic hardening predominates in the UFG alloy, because of its limited capacity to store dislocations and its more heterogeneous plastic deformation. For a given plastic strain range, the UFG alloy has a shorter fatigue life than its CG counterpart, because of a much easier crack initiation, mostly from intermetallic particles. For a given stress range, it has a slightly higher life, due to a slower development of microcracks, which have a transgranular path in the largest grains, with some intergranular growth within the smallest grains.

Abstract (French)

Comportement mécanique d'un alliage d'aluminium à grains ultrafins : Analyse et modélisation du rôle exacerbé des joints de grains.

Les alliages à grains ultrafins semblent prometteurs, au vu de leur forte résistance en traction et de la possibilité d'une mise en forme superplastique à basse température. Toutefois, leurs mécanismes de déformation, qui comportent une part plus ou moins forte de glissement aux joints de grains restent mal connus, et leurs performances en fatigue ont été peu étudiées. Ce travail vise à comparer et analyser le comportement viscoplastique et les mécanismes de déformation et d'endommagement en traction et en fatigue d'un alliage d'aluminium-magnésium "classique" et à grains ultrafins (600nm en moyenne) obtenu par déformation plastique sévère, selon le procédé ECAP.

Des essais de relaxation, fluage et traction à diverses vitesses et températures ont permis de mesurer les évolutions des sensibilités à la vitesse en fonction de ces deux paramètres et de montrer: 1) que le raffinement microstructural accroît sensiblement la sensibilité à la vitesse 2) que ce paramètre augmente avec la vitesse de déformation 3) qu'il contrôle la ductilité du matériau à grains ultrafins, qui s'accroît donc à faible vitesse 4) que cette ductilité devient supérieure à celle du matériau classique lorsque la température s'élève. Les domaines de vitesse et température dans lesquels le raffinement microstructural accroît ou diminue la résistance en traction ont été délimités.

Les mécanismes de déformation et d'endommagement des deux matériaux ont été étudiés au moyen d'essais de traction sous MEB accompagnés de mesures des champs de déformation par corrélation d'images à plusieurs échelles: méso et microscopique, grâce à des microgrilles d'or et sub-micrométrique, grâce à un mouchetis très fin obtenu par démouillage d'un film d'or. Le glissement aux joints est d'autant plus actif, dans les deux matériaux, que la température augmente et que la vitesse de déformation diminue. Dans l'alliage à grains ultrafins, il a un caractère coopératif et survient préférentiellement aux joints de forte désorientation. Les champs de déformation sont plus hétérogènes dans le matériau à grains ultrafins, où le taux de déformation dépasse 100% dans des bandes localisées.

Un modèle éléments finis 2D intégrant, outre la viscoplasticité au sein des grains, un glissement visqueux des joints, a été identifié dans toute la gamme de température explorée et rend assez bien compte du comportement viscoplastique des deux matériaux et de la contribution beaucoup plus forte du glissement aux joints dans l'alliage à grains ultrafins. Il permet également de préciser comment évolue cette contribution au cours de l'écrouissage.

Des essais de traction-compression à déformation plastique imposée ont permis d'étudier la plasticité cyclique et les mécanismes d'endommagement en fatigue oligocyclique et des essais à contrainte imposée, d'explorer la fatigue à grand nombre de cycles. Les essais ont été suivis d'observations des surfaces de rupture et d'une analyse statistique de l'endommagement en surface, ainsi que d'observations au MET des arrangements de dislocations. Les deux matériaux manifestent un durcissement cyclique, plus modeste dans

l'alliage à grains ultrafins, qui présente, à forte amplitude, une croissance de ses grains. L'écrouissage isotrope prédomine dans l'alliage classique, où la densité de dislocations augmente fortement avec la plasticité cyclique, alors que l'écrouissage cinématique prédomine dans l'alliage à grains ultrafins, en raison de sa moindre aptitude à stocker des dislocations et de la plus grande hétérogénéité de sa déformation plastique. A même amplitude plastique, ce dernier a une durée de vie plus faible, en raison d'un amorçage bien plus rapide des fissures, à partir de particules intermétalliques. A contrainte imposée, le matériau a grain ultrafins a une durée de vie légèrement supérieure, grâce à une propagation plus lente des microfissures, dont le trajet est transgranulaire dans les plus gros grains et intergranulaire dans les plus petits.

Contents

Introduction

The ability of a metal to deform plastically depends of the ability of its dislocations to move. When their motions are hindered by microstructural obstacles, like solute atoms, dispersoids, precipitates, twin boundaries or grain boundaries (GBs), it increases the strength of the metal at the expense of its ductility, while unhindered motions render the material soft and ductile.

Several strategies can be employed to increase the strength of metals:

Alloying is a long known method, however the alloying elements are often quite expensive and a change in chemical composition can alter some functional properties: it leads to a loss of electrical conductivity for Cu alloys, a loss of bio-compatibility for Ti alloys or a decrease in resistance to intergranular corrosion for Al alloys.

Strain hardening, which is also a long known method, is quite effective. However, a pre-strain induces some anisotropy and leads to a reduction in ductility. In addition it is less effective to treat components for high temperature applications, because of temperature-induced recovery.

Finally, grain refinement, which was probably the most intensively investigated strategy during the last two decades, increases the strength of metals at least at room temperature (RT) according to Hall & Petch equation:

$$\sigma = \sigma_0 + \frac{k}{\sqrt{d}} \tag{1}$$

Here, σ is the tensile yield strength, d is the mean grain size and σ_0 and k are material constants. The coefficient k is generally higher in planar slip materials in which larger dislocations pileups can form on the GBs. However this relationship was found invalid for grain size below 20 nm approximately (Figure 1).

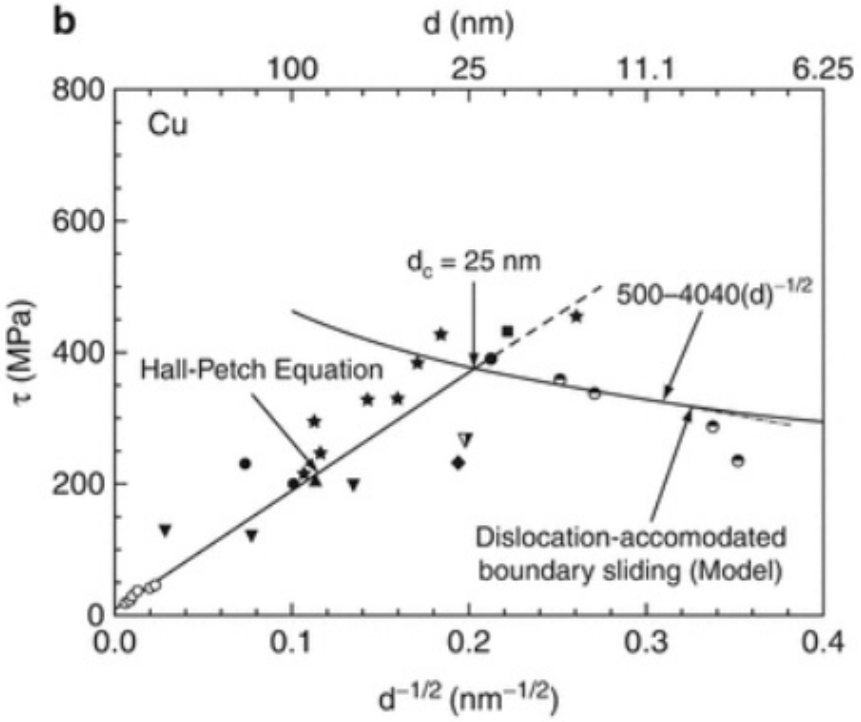

Figure 1: Yield strength as a function of the inverse square root of the grain size for copper [1]

Metallic materials having grain size less that 1 μm can be divided into two categories: "nanocrystalline materials", with grain size less than 100 nm and "ultrafine-grain (UFG) materials", with grain size in the range of 100-1000 nm. While UFG materials fall in the range of validity of Hall-Petch relation, this is not always the case for nanocrystalline materials. In addition, the latter exhibit a low hardening capacity and poor ductility. That is why in a chapter of Techniques de l'Ingénieur devoted to these materials, D. François wrote in 2010: "On constate donc que du point de vue des propriétés mécaniques, les matériaux nanostructurés ne présentent pas d'avantages marquants, au contraire. Se limiter aux matériaux à grains ultrafins (de l'ordre de la centaine de nanométres) est la solution qui semble s'imposer": which means that nanocrystalline materials are disappointing in terms of mechanical properties, and that UFG seem more promising. He added that UFG materials deserve sufficient research regarding the effect of strain rate and temperature on deformation mechanisms, fatigue, creep and fracture [2].

Materials with grain size less than 1 μm can be produced in two ways [3], [4]. First is the "bottom-up" approach, where polycrystalline metal is assembled from individual atoms using deposition techniques, or by compaction of ultrafine or nano-crystalline powder obtained by cryomilling. However, the quantity of nanocrystalline or UFG material produced that way is very small and sometimes with a poor ductility due to high impurity contents and some residual porosity.

The second strategy is a "top-down" approach where coarse-grained (CG) metal is processed by severe plastic deformation (SPD) to introduce a high dislocation density leading to grain refinement by dynamic recrystallisation [5]. It was considered one of the most effective grain refinement procedure by Zhu et al. [4] because the processed metals can be produced relatively in bulk and are free from contamination and porosity, if the stress triaxiality ratio is sufficiently low, or -even better- negative during SPD [6].

Among the various SPD processes that currently exist (Equal Channel Angular Pressing (ECAP) [7], High Pressure Torsion [8], Accumulative Roll Bonding [9], Constrained Groove Pressing [10], Accumulative Back Extrusion [11], Tubular Channel Angular Pressing [12], etc), one of the most attractive is ECAP because of the relatively large volume of uniformly deformed -and thus ultrafine grained material- that it can provide. This process was thus chosen to produce the UFG Al-Mg alloy of this study.

In CG materials, the flow processes are mostly intragranular in nature, but for UFG, and even more so, for nanocrystalline materials, "grain boundary-mediated plasticity"(GBMP, described in more details in the next chapter) becomes more important and would be responsible for the breakdown of Hall-Petch equation below a given grain size in nanocrystalline materials (Figure 1). At RT, GB strengthening results in an excellent yield stress for UFG materials, but at elevated temperature, GBs can slide, and eventually lead to softening.

While a lot of research was devoted to the analysis and prediction of GBMP-induced breakdown of Hall-Petch equation at RT, as the grain size is refined into the nanometer range, the temperature and strain rate-controlled transition from GB-induced reinforcement to GB-induced softening of UFG materials has been much less investigated and modelled. However, this transition has to be understood, in order to provide a safe maximum temperature for structural applications of UFG materials. That is one of the objectives of this study, in the case of Al 5083 alloy.

Besides, literature on UFG materials insists on their tendency for strain localization, which limits their ductility, but until now, this conclusion was based mostly on post-fracture observations of surface roughness and shear bands, without any insight into the progression of localization during plastic flow and limited quantitative data due to the high spatial resolution needed for an accurate measurement of strain distribution in UFG materials. This study aims at providing such elements, thanks to *in situ* tensile tests and fine-scale measurements of strain fields by Digital Image Correlation (DIC).

Finally, since the resistance to fatigue is a key factor for the choice of structural materials, the effect of microstructural refinement on cyclic plasticity and fatigue resistance needs to be investigated and analysed in terms of damage mechanisms.

Structure of the thesis

The structure of the manuscript is as follows:

Chapter 1 first presents a general literature survey regarding the deformation mechanisms and mechanical properties of UFG materials, and later, a more specific review on CG and UFG Al 5083.

Chapter 2 focusses on the microstructural characterisation of the CG and UFG materials of the study.

Chapter 3 presents a comparative analysis of the viscoplastic behaviour of CG and UFG Al 5083 from room temperature to 200°C. The focus is mostly on the effect of temperature and strain rate on the macroscopic properties, depending on grain size.

Chapter 4 analyses the deformation and damage mechanisms of the two materials during the tests described in previous chapter, and suggests possible explanations for the observed differences in the mechanical behaviour.

After a literature survey on the introduction of grain boundary sliding in constitutive models, chapter 5 presents an attempt to capture its contrasted effects in CG and UFG materials, through a phenomenological viscoplastic model, with sliding interfaces.

Chapter 6 presents a compared experimental study of the cyclic behaviour and fatigue resistance of the two materials at room temperature.

Finally, a concluding chapter summarizes the results, lists questions that remain open and proposes some perspectives.

References

[1] B. Bhushan and F. A. Mohamed, “Mechanical Properties of Nanocrystalline Metals,” *Encyclopedia of Nanotechnology*, 2012.

[2] D. François, “Propriétés mécaniques des matériaux nanostructurés,” *Techniques de l’Ingenieur*, p. m4029, 2010.

[3] Y. Huang and T. G. Langdon, “Advances in ultrafine-grained materials,” *Materials Today*, vol. 16, pp. 85–93, 2013.

[4] Y. T. Zhu, T. C. Lowe, and T. G. Langdon, “Performance and applications of nanostructured materials produced by severe plastic deformation,” *Scripta Materialia*, vol. 51, pp. 825–830, 2004.

[5] V. M. Segal, “Materials processing by simple shear,” *Materials Science and Engineering: A*, vol. 197, pp. 157–164, 1995.

[6] R. Lapovok, “Damage evolution under severe plastic deformation,” *International Journal of Fracture*, vol. 115, pp. 159–172, 2002.

[7] Y. Iwahashi, J. Wang, Z. Horita, M. Nemoto, and T. G. Langdon, “Principle of equal-channel angular pressing for the processing of ultra-fine grained materials,” *Scripta Materialia*, vol. 35, pp. 143–146, 1996.

[8] A. P. Zhilyaev and T. G. Langdon, “Using high-pressure torsion for metal processing: Fundamentals and applications,” *Progress in Materials Science*, vol. 53, pp. 893–979, 2008.

[9] N. Tsuji, Y. Saito, H. Utsunomiya, and S. Tanigawa, “Ultra-fine grained bulk steel produced by accumulative roll-bonding (ARB) process,” *Scripta Materialia*, vol. 40, pp. 795–800, 1999.

[10] D. H. Shin, J. J. Park, Y. S. Kim, and K. T. Park, “Constrained groove pressing and its application to grain refinement of aluminum,” *Materials Science and Engineering A*, vol. 328, pp. 98–103, 2002.

[11] S. Fatemi-Varzaneh and A. Zarei-Hanzaki, “Accumulative back extrusion (ABE) processing as a novel bulk deformation method,” *Materials Science and Engineering: A*, vol. 504, pp. 104–106, 2009.

[12] G. Faraji, M. M. Mashhadi, and H. S. Kim, “Tubular channel angular pressing (TCAP) as a novel severe plastic deformation method for cylindrical tubes,” *Materials Letters*, vol. 65, pp. 3009–3012, 2011.

Chapter 1

Literature survey

1.1 Basic notions about grain refinement by ECAP

Equal channel angular pressing (ECAP) developed in 1973 in the Soviet Union by Segal [1] is an extrusion method for accumulating high plastic strains. It is a highly effective method with respect to grain size refinement, since the extrusion happens without any change in billet shape and thus the process can be repeated several times, so that a very high plastic strain can be accumulated, if the material is ductile enough. Ultra-fine grained (UFG) materials of grain size ranging from 100 to 1000 nm can be produced using this method. Historically, it started with processing of pure metals, (UFG Ti, for example, is used in dentistry) but due to the lack of thermo-mechanical stability of pure metals, this process was later extended to alloys. So far, ECAP has been successfully applied for Al alloys, Cu alloys, Ti alloys, Pb alloys, Mg alloys and a few steels.

In ECAP, a billet with a circular or rectangular cross-section is forced through a die with intersecting channels of similar width, at a die channel angle ϕ and the outer corner angle ψ, as shown in figure 1.1 [2].

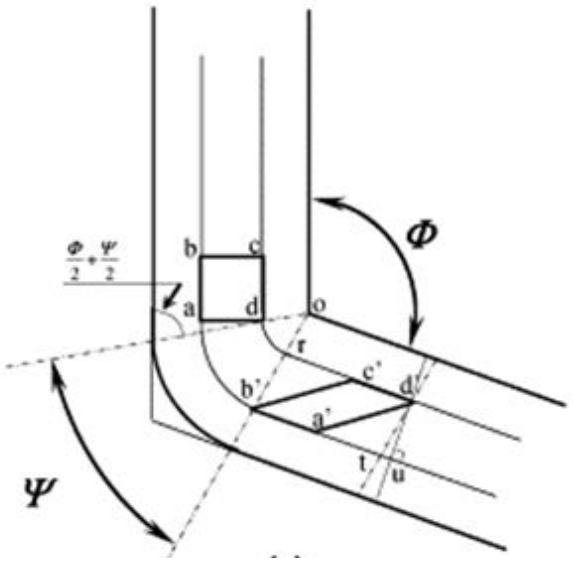

Figure 1.1: Schematics of ECAP [2].

The billet gets sheared sharply on crossing the line of intersection between the 2 channels. The Von Mises equivalent plastic strain after N passes is given by [3]:

$$\varepsilon_{eq} = N/\sqrt{3}\left[2cot\left(\frac{\phi+\psi}{2}\right) + \psi cosec\left(\frac{\phi+\psi}{2}\right)\right] \tag{1.1}$$

The equivalent strain obtained for ϕ=90° and ψ=0° is $\sim$1 per pass, but it varies significantly depending on the die angle, outer corner angle, and friction conditions.

The maximum length and the aspect ratio of the billets are constrained by the required pressing load (which depends both on the sample length and its diameter); and the risk of buckling of the punch, whose cross-section is the same as that of the billet. The maximum pressure required to extrude the specimen through the channel can be calculated as [4].

$$P = \tau_0(1+m)\left[2cot\left(\frac{\phi+\psi}{2}\right) + \psi\right] + 4m\tau_0\left(\frac{l_i + l_o}{a}\right) \tag{1.2}$$

Here, τ_0 and m are the shear strength of the sample and friction coefficient, l_i and l_o are the instant length of the specimen at entry and exit channels, and a is the width of the channel, nearly equal to the billet diameter or side length. The length to diameter (or side length) ratio is generally less than 10.

Unrefined zones (also called "dead zones") are observed at both ends of the ECAPed rod [5]–[7] and have to be removed to machine test samples, leading to a wastage of matter (Figure 1.2).

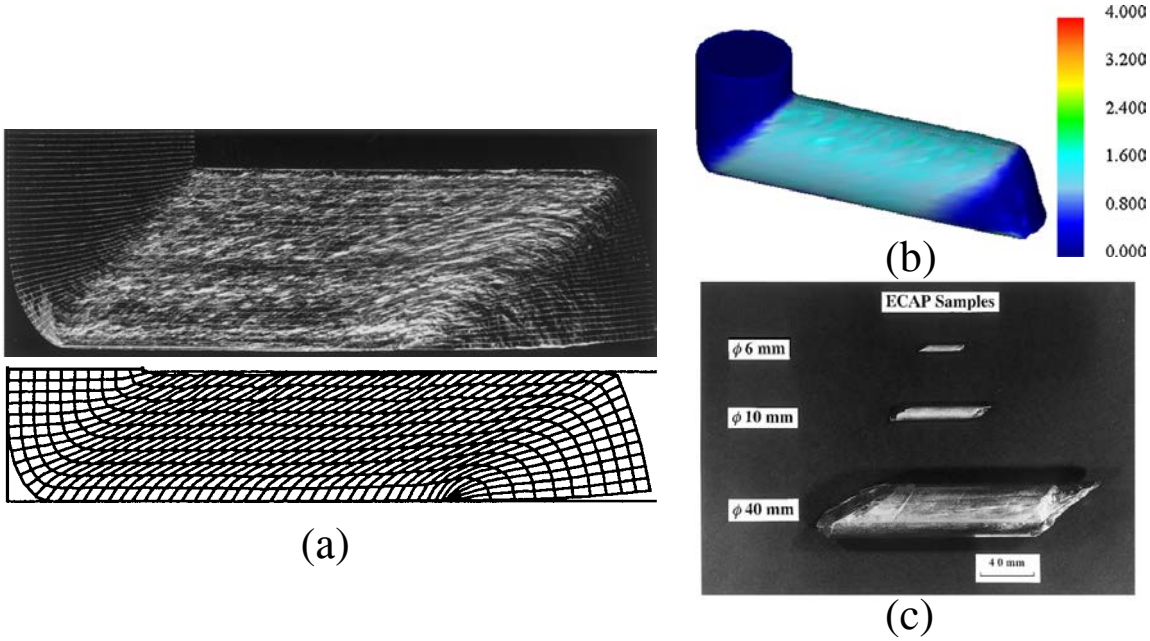

Figure 1.2: (a) Plastic flow during ECAP emphasized by engraved grids [6], (b) Computed effective strain contour after one ECAP pass [8], (c) ECAPed rods [9].

It can be minimised by the application of a back pressure during ECAP. An additional advantage of back pressure is to raise the hydrostatic compression, leading to enhanced ductility of the material (see Figure 1.3) and preventing the formation of nano-cavities and surface cracks [10]. Back pressure can be applied, ideally, using a secondary actuator [11], or by a slight reduction in diameter of the exit channel [12], however the latter solution is only effective for the first ECAP pass, while the diameter of the extruded sample is still higher than that of the exit channel.

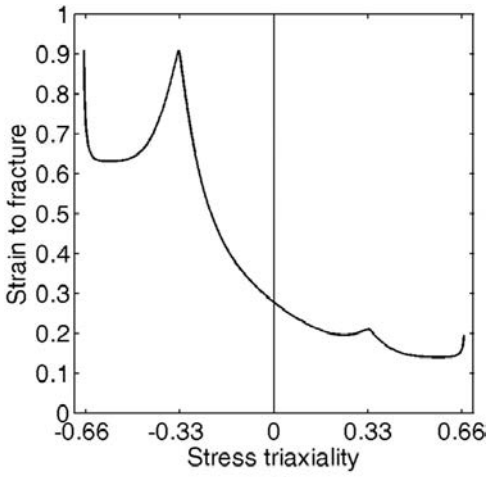

Figure 1.3: Equivalent strain at fracture versus stress triaxiality for Al2024-T351 [13].

The mean grain size generally decreases in a non-linear way with the number of ECAP passes and reaches a steady-state value after a few passes. Mohamed proposed a model to predict the minimum grain size as a function of material parameters, such as the hardness, melting temperature, and stacking fault energy [14]. Although, it was developed for ball milling, it has been successfully applied to other SPD processes. If all other factors remain constant, the minimum achievable grain size is proportional to the amount of alloying element as inversely proportional to the stacking fault energy (SFE) as shown in figure 1.4. For Al-4.6%Mg, this value was predicted to be 0.27 μm [15].

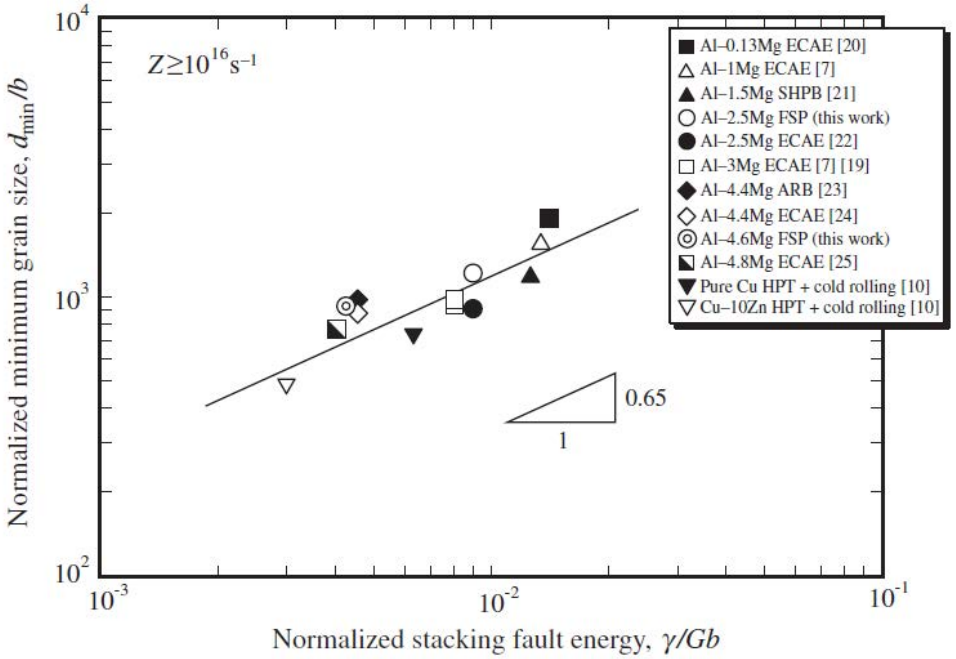

Figure 1.4: Relationship between the normalised stacking fault energy and the normalised minimum grain size [15].

This relation between minimum mean grain size and SFE was proven false by Edalati et al. [16]. Moreover, he showed that the the dominant factor for extra grain refinement by alloying is the effect of atomic-size and modulus mismatch on the mobility of edge dislocations. Thus, the minimum grain size decreases with the increase in the amount of alloying elements.

The evolution of hardness and yield stress is also observed to be non-linear with a tendency to reach steady state values after 2-3 passes only (Figure 1.5).

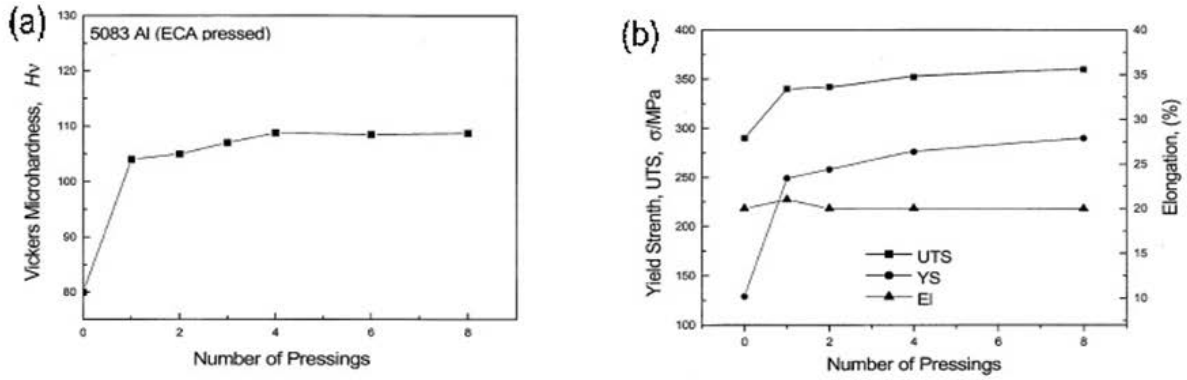

Figure 1.5: Effect of the number of pressings on (a) Vickers hardness, and (b) tensile properties of 5083 Al alloy after ECAP using Route C [17].

However, even when the grain size and tensile properties reach steady-state values, the microstructure still continues to evolve, as shown by Chowdhury et al. for Al 6xxx

series alloy [18]. The fraction of high angle grain boundaries (HAGBs, with misorientations higher than 15°) was found to reach its maximum after only 4 passes, but the grain orientation distribution continued its evolution towards a random texture until 8 passes (Figure 1.6).

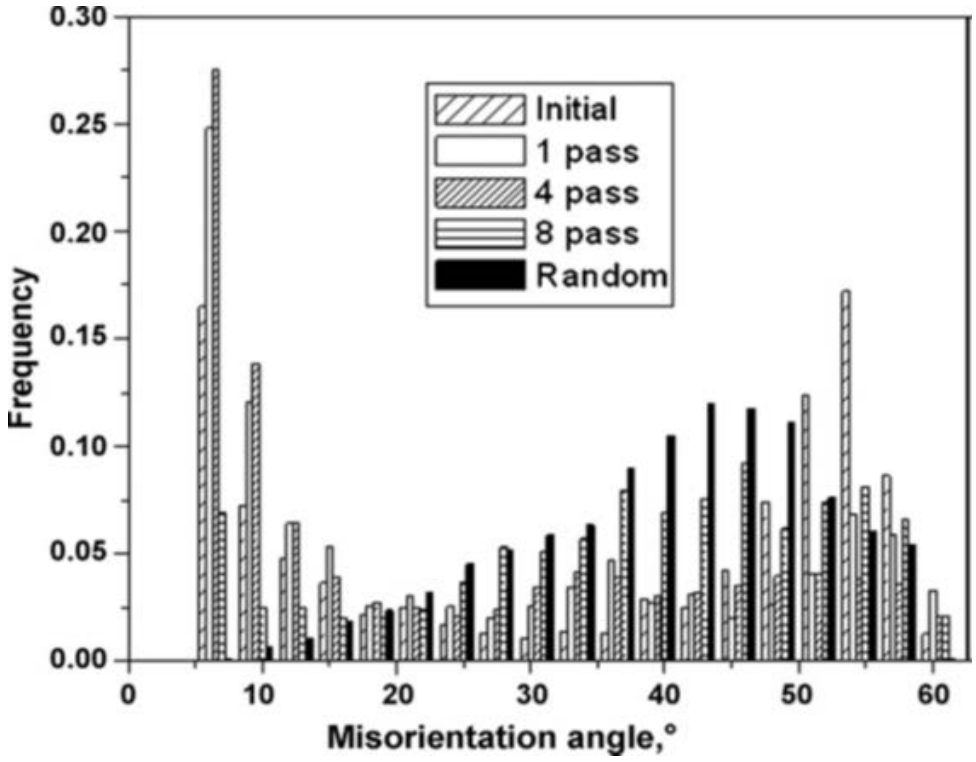

Figure 1.6: Evolution of grain misorientation distribution with increasing number of ECAP passes for Al6082 alloy [18].

The maximum number of ECAP passes achievable without damage of the sample depends on the ductility of the material, and hence can be increased by increasing the processing temperature. However, since the SFE rises with temperature, the efficiency of the process in terms of grain size reduction decreases, because of the enhanced dynamic recovery. Increasing temperature also slows down the formation of HAGBs [19]. A decrease in pressing speed may increase the ductility (as explained below for UFG materials) and thus allow more passes. It also has a positive influence on microstructure: an increased fraction of HAGBs [20], more equiaxed grains [21], and on the mechanical properties: reduced flow localisation [22].

It has been shown that the efficiency of ECAP process -i.e. microstructural refinement, fragmentation and redistribution of second phase particles- depends largely on the processing "route" [23]–[26]. Initially, there were four basic processing routes defined by the rotation scheme of the sample between successive passes, as shown in figure 1.7 [2], [27]. In this figure, as well as in the whole manuscript, the entrance and exit directions are denoted by y and z, respectively, while x corresponds to the width of the sample.

In route A, the billet is re-inserted without any rotation. In route B_A, it is rotated alternatively by $\pm$90 degrees around its axis between each pass, while in B_C, it is rotated by 90 degrees, always in the same direction. In route C, it is rotated by 180 degrees.

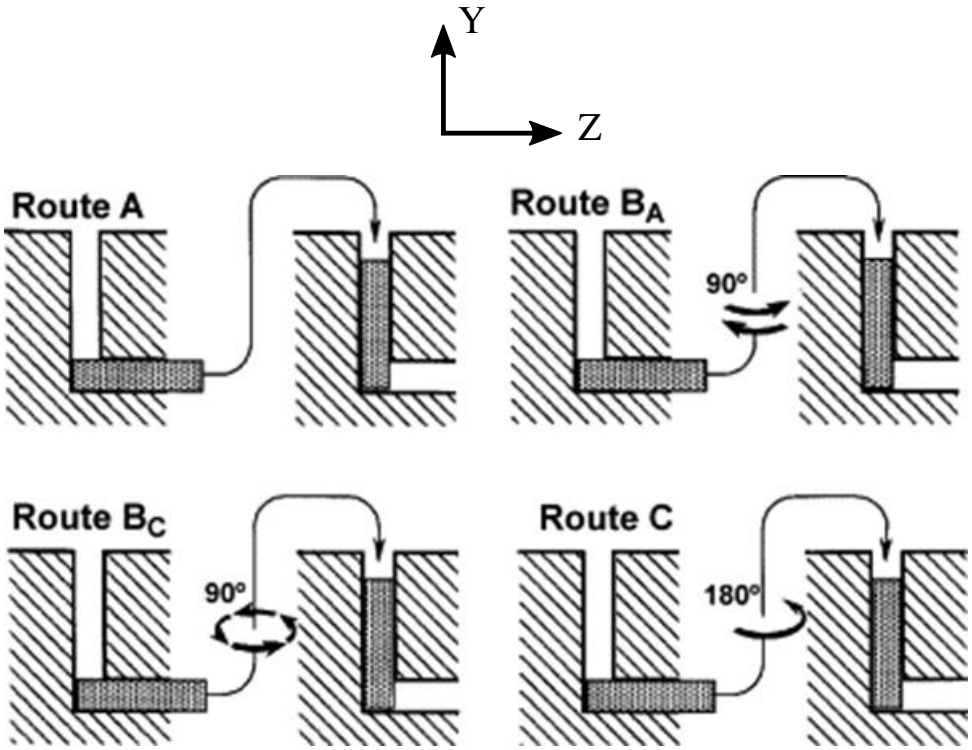

Figure 1.7: Four processing routes in ECAP [27].

Figure 1.8 compares the orientation of the maximum shear stress plane in the reference frame of the sample during consecutive passes, for each route. It appears that all routes, except route C (which corresponds to reversed loading) lead to non-proportional loading [5], with transient latent hardening when the activated slip systems change, at the beginning of each pass, followed by softening, when the "memory" of the previous pass fades away. This can lead to strain localization and fracture. Some researchers thus prefer route C with proportional loading [28].

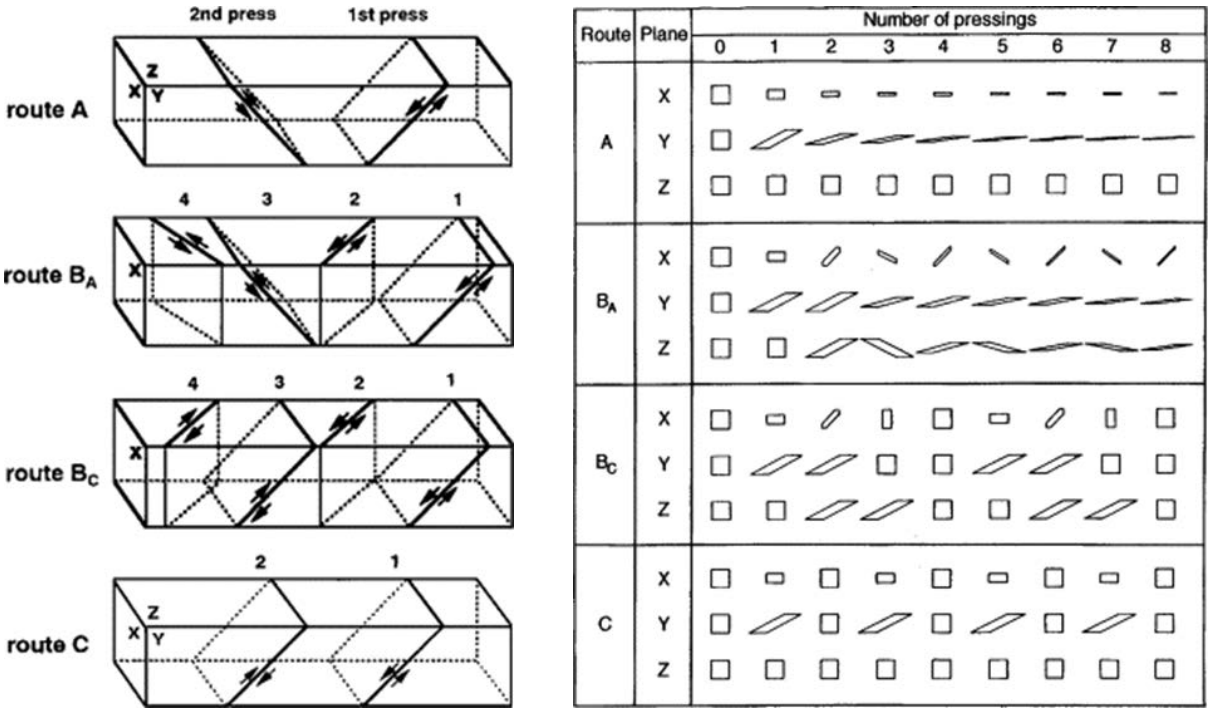

Figure 1.8: Maximum shear stress planes for each route [2].

However, route B_C is recognised as the most effective in yielding equiaxed grains, while very elongated grains are observed for Route B_A, with route C as an intermediate case (Figure 1.9a) [24], [26], [29]. The evolution towards HAGBs is also the fastest for route B_C, followed by route C and route A, making route B_C the most popular choice. The resulting texture and mechanical properties of an ECAPed material vary significantly with the chosen route, as illustrated by the work of Soliman et al on aluminum (Figure 1.9b, c).

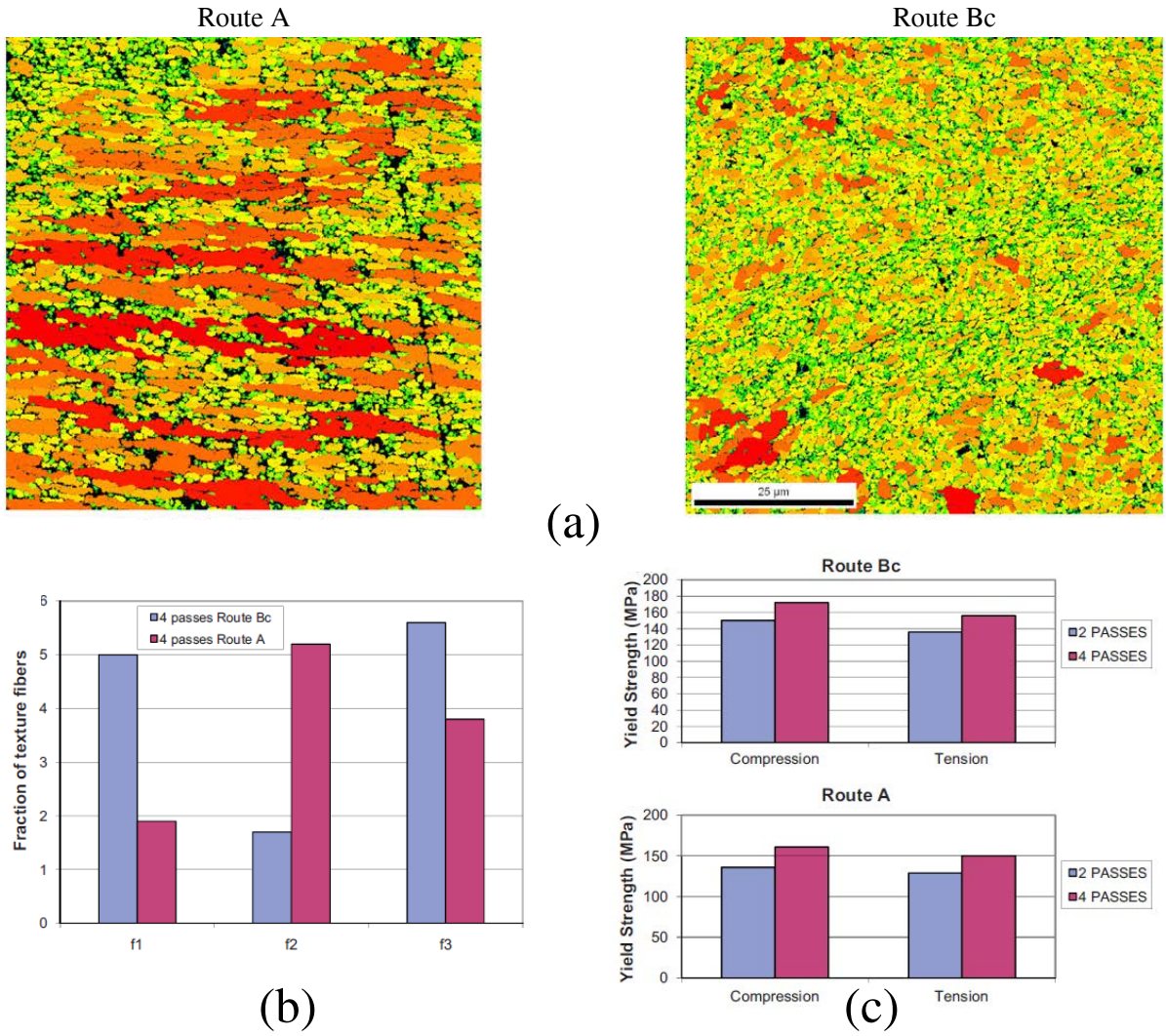

Figure 1.9: (a) Colour coded map of grain size b) compared fraction of texture fibres and c) compared yield stress for CP Al after 4 passes [29].

In most cases, a drop in ductility is observed after ECAP, due to a high dislocation density which decreases the hardening capacity [5], [30]. Well chosen annealing treatments that do not change the UFG microstructure, but promote recovery are often performed after ECAP, to regain ductility, at the price of a slight drop in yield stress. The processing route has a great influence on the ductility, especially in alloys which contain second phase particles and precipitates that get fragmented and redistributed during ECAP, as shown in figure 1.10 for Al-Si alloy [23], [31].

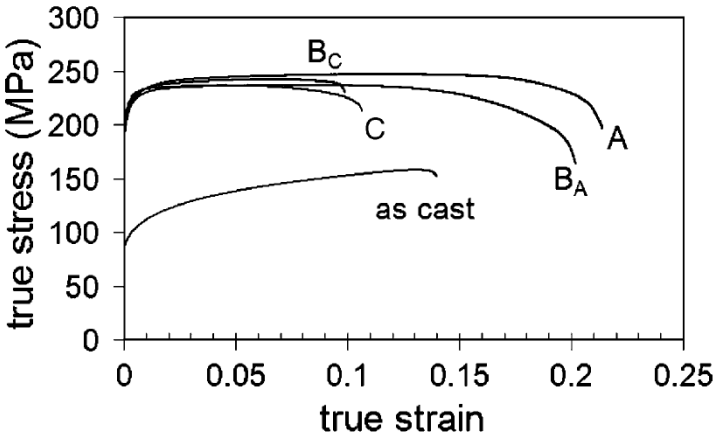

Figure 1.10: Stress-strain curves for as-cast and ECAPed Al-Si alloy [23].

The structure of the grains and grain boundaries (GBs) after ECAP or any other SPD process is modified and out of equilibrium. HRTEM observations by Horita et al. [32] revealed wavy, corrugated and faceted GBs. Such a high energy state promotes GB motion, to reach a more stable state. Danilenko et al. measured by TEM grain rotations of several degrees during 120s in situ annealing at 200°C on SPD- processed UFG Al, which is a direct evidence of a relaxation phenomenon [33].

The grain size distribution after ECAP is often heterogeneous with a mixed grain-subgrain structure and a high dislocation density [34]. The distribution of solute atoms and vacancies in alloys is also affected by SPD. Clusters and segregations of Mg atoms was observed at GBs and triple junctions in an HPT processed Al-Mg alloy [35]. SPD-induced vacancies were observed to annihilate at GBs leading to a vacancy gradient in grains and a vacancy flux towards GBs.

Finally, the diffusivity of UFG material is enhanced, as compared to CG materials, due to an increase in point defects concentration and an increased surface of GBs that constitute fast diffusion circuits. The diffusivity increases with increasing fraction of HAGBs [36].

1.2 General trends in the mechanical behaviour of UFG materials

1.2.1 Tensile or compressive behaviour at room temperature

High values of yield and ultimate tensile stress, modest strain hardening, and thus low uniform elongation and relatively low fracture strain are characteristic features of the tensile behaviour of UFG materials. This tendency for early necking is consistent with Considere's criterion, according to which failure should occur when the hardening rate, θ becomes equal to the flow stress σ:

$$\frac{\theta(\epsilon)}{\sigma(\epsilon)} < 1, \qquad \theta = \frac{d\sigma}{d\epsilon} \tag{1.3}$$

However, the room temperature (RT) ductility of UFG materials often increases substantially as the strain rate decreases, as reported by Sabirov et al. (Figure 1.11a), or Ivanov & Naydenkin [20]. This dramatic effect is consistent with the strain rate dependence of the strain rate sensitivity (Figure 1.11b), considering Hart's (Equation 1.4) criterion for necking in viscous materials.

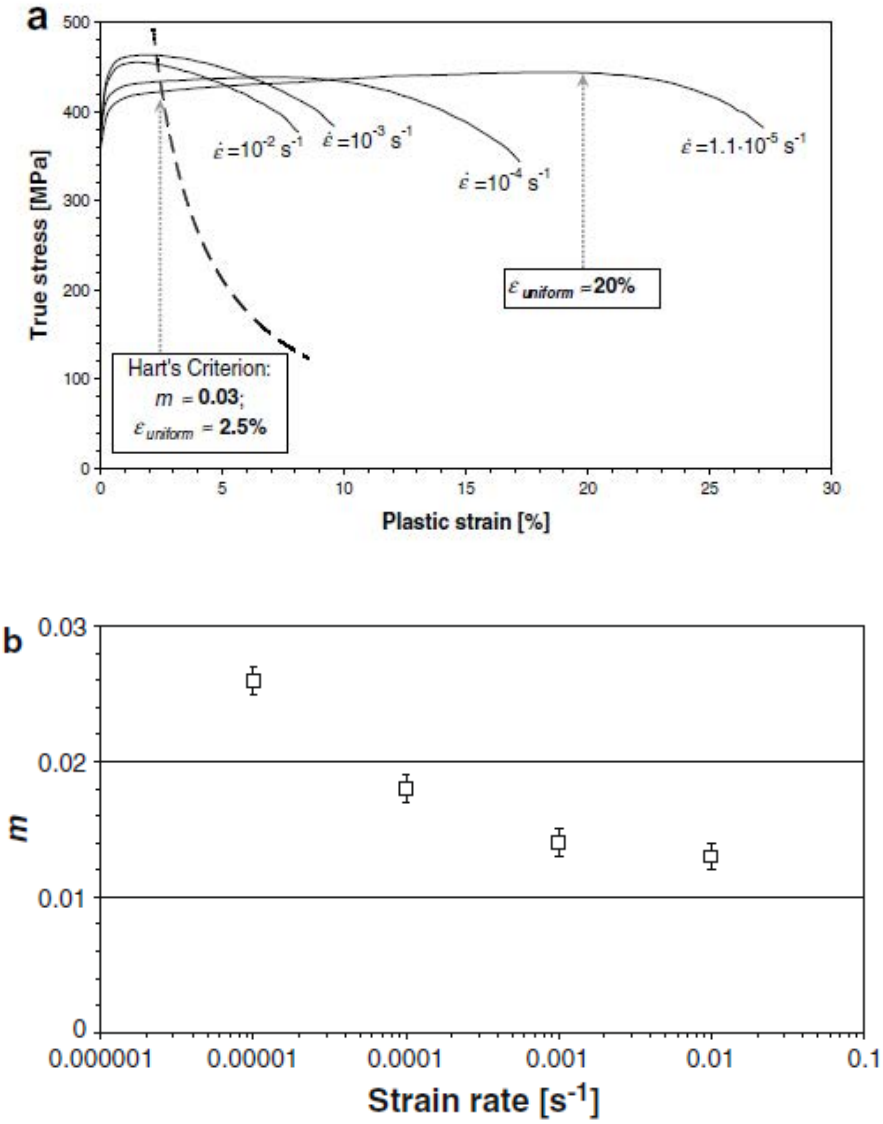

Figure 1.11: True stress-strain curves for the ECAPed AA6082 alloy (a) at different strain rates [37], (b) SRS evolution with the strain rate [38].

According to Hart [39], plastic instability is predicted by:

$$\frac{\theta(\varepsilon)}{\sigma(\varepsilon)} < 1 - m \tag{1.4}$$

where the strain rate sensitivity (SRS), m is defined as:

$$m = \frac{d\sigma}{d\dot{\varepsilon}} \tag{1.5}$$

When m is positive, the domain of plastic stability increases and the higher SRS found at low strain rates can explain the rise in ductility.

In FCC metals, grain refinement down to the UFG and nano-crystalline regimes leads to an increase in strain rate sensitivity (SRS), illustrated by figure 1.12 for Cu and Ni, while the opposite trend appears in BCC metal [40]. For FCC UFG metals, this somewhat mitigates the detrimental effect of a reduced strain hardening.

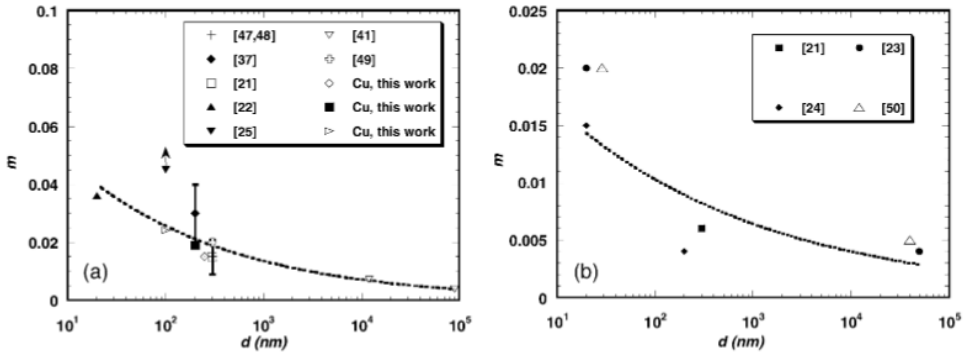

Figure 1.12: Variation of SRS, m vs. grain size, d for (a) Cu and (b) Ni [40].

Many reports of tension-compression asymmetry, in nanocrystalline and UFG materials can be found in the literature [41]–[45] and models based on the pressure dependence of dislocations self energy [41] or on molecular dynamics [46]–[48] were proposed to explain it, while the introduction of the first invariant in the yield criterion was proposed to capture it in constitutive equations.

However, many reports are based on questionable experimental data (different sample geometries and experimental set-ups in tension and compression, absence of extensometer so that the machine stiffness may bias the results, no lubrication in compression, reproducibility not documented...) and are conflicting (some report a higher yield stress in compression [41], [42], [44] or in tension [45], [49] or no difference [43], suggesting that this might not be an intrinsic effect of a small grain size. For ECAPed copper, the flow stress anisotropy was clearly related by Haouaoui et al. [49] to the anisotropic pre-strain induced by ECAP and to the Bauschinger effect responsible for a tension-compression asymmetry which changes its sign, depending on the loading direction, relative to the extrusion axes (Figure 1.13).

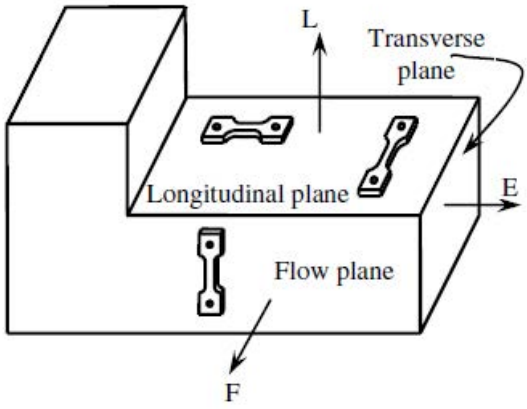

ECAE route	Number of passes	Stress differential (SD), Δ(%)		
		L direction	E direction	F direction
A	1	12.9	−13	19.3
	2	26.1	−25.7	6.9
	4	21.4	−26.6	10
		Inclined shear direction: SD = −33.5		
	8	–	−29.1	–
B	2	31.2	−22.9	7.3
	4	24.3	−29.6	11
C	2	−10.1	−15.1	22.5
	4	14.7	−19.4	4.3
C′	4	11.8	−26.2	5.7
E	4	38.4	−20.9	11.8
	8	–	−24.4	–
	16	–	−7.8	–

Figure 1.13: Yield stress differential (S.D.) in tension and compression along different loading directions of ECAPed Cu [49].

Residual stresses, if any, may also play a role in the tension-compression asymmetry of ECAPed materials. The number of available measurements of these stresses is quite limited: Reyes-Ruiz et al. [50] used X-ray diffraction to measure it near the surface (Figure 1.14a-b) or along a radial section (Figure 1.14c-d) after a single ECAP pass on 6061-T6 Al alloy at RT. They emphasized the effect of friction against the die, that makes residual stresses at the surface different from those in the bulk.

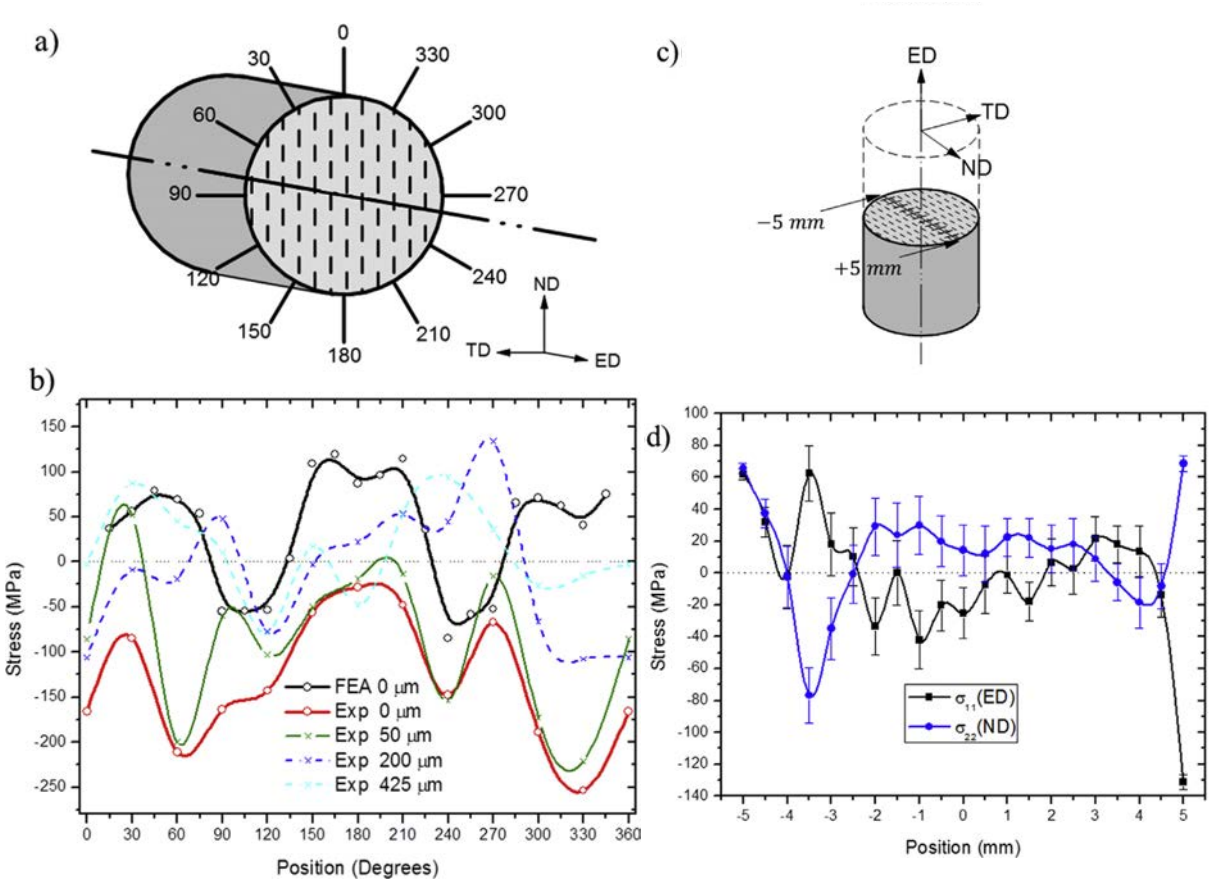

Figure 1.14: Residual stress measurements (a),(b) at the surface and (c), (d) along a radial section after a single ECAP pass on 6061-T6 Al alloy at RT [50].

Lee et al. [51] used neutron diffraction to measure it along a radial section, from the bottom to the top of the billet, after a single pass at RT in copper (Figure 1.15). In both cases, significant but heterogeneous residual stresses were measured. Subsequent annealing treatments may reduce it, but to an unknown extent.

Region	Distance from the bottom (mm)	Axial residual stress, σ_{xx} (MPa)	Radial residual stress, σ_{yy} (MPa)	Hoop residual stress, σ_{zz} (MPa)
Bottom	2	1.5 ± 13.9	161.5 ± 8.5	171.3 ± 8.5
Middle	4.5	41.5 ± 18.4	3.6 ± 11.2	−37.9 ± 10.8
	9	48.8 ± 18.3	13.7 ± 14.6	32.7 ± 14.3
	13.5	35.4 ± 14.1	18.1 ± 13.3	8.1 ± 13.6
Top	16	126.3 ± 10.4	−21.8 ± 9.7	−32.6 ± 10.8

Figure 1.15: Residual stress distribution along a radial section after a single ECAP pass on Cu measured by neutron diffraction [51].

1.2.2 Effect of temperature on the flow stress of UFG materials

At low temperatures, GBs act as barriers for mobile dislocations leading to an increase of dislocation density inside the grains, which in turn leads to a high flow stress. With increasing temperature and decreasing strain rate, their efficiency decreases as they behave as sinks for lattice dislocations, reducing their density inside the grain, and themselves become able to glide. Both effects contribute to softening. A transition from GB-induced hardening to GB-induced softening was observed with decrease in strain rate and increase temperature in UFG copper by Li et al. [52] and in Al-1.5Mg alloy by Kapoor et al.[53], as shown in figure 1.16. The data points, on the top figure, represent the strain rate for which the flow stress of UFG alloy is the same as that of CG alloy at a given temperature and the bottom figure shows the corresponding flow stress. This softening effect is not a consequence of the lack of thermal stability in UFG microstructure, as observed from the post deformation TEM micrographs by Kapoor et al. [53].

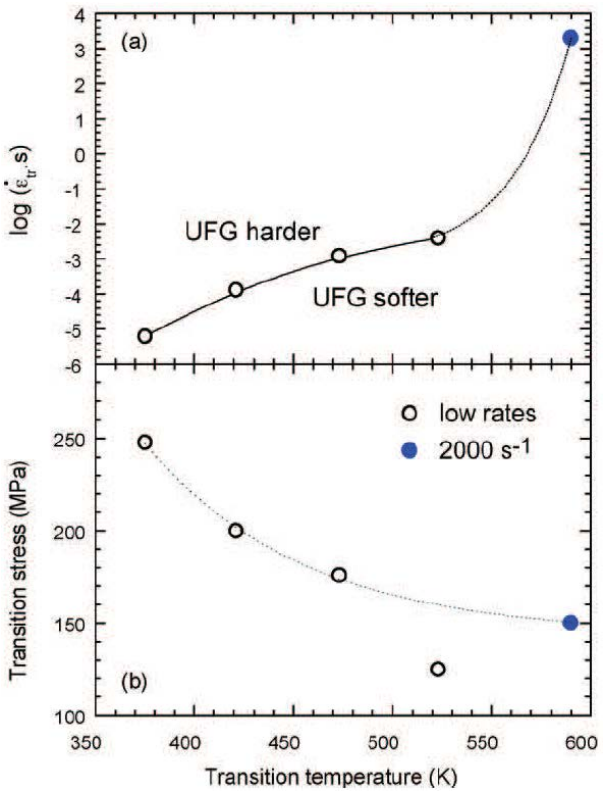

Figure 1.16: Transition from strengthening to softening of UFG compared with CG Al-1.5%Mg alloy [53].

Their data were consistent with one of the two conditions proposed by Li et al. for GB-induced softening: that the mean grain size becomes smaller than the expected (stress-dependent) sub-grain size, so that dislocations are able to reach the neighbouring grain boundaries without storage at intragranular obstacles. The second condition, according to Li et al., is that "temperature is high and strain rate low enough to allow grain boundaries to act as effective sinks which would quickly annihilate intruding

dislocations" [52]. They estimated the rate-dependent transition temperature (which depends on the diffusivity of the GBs) for copper, but, as it can be seen on figure 1.17, these predictions did not capture well the experimental data. To date a predictive model of this transition, quite important for engineering applications of UFG materials, seems to be missing.

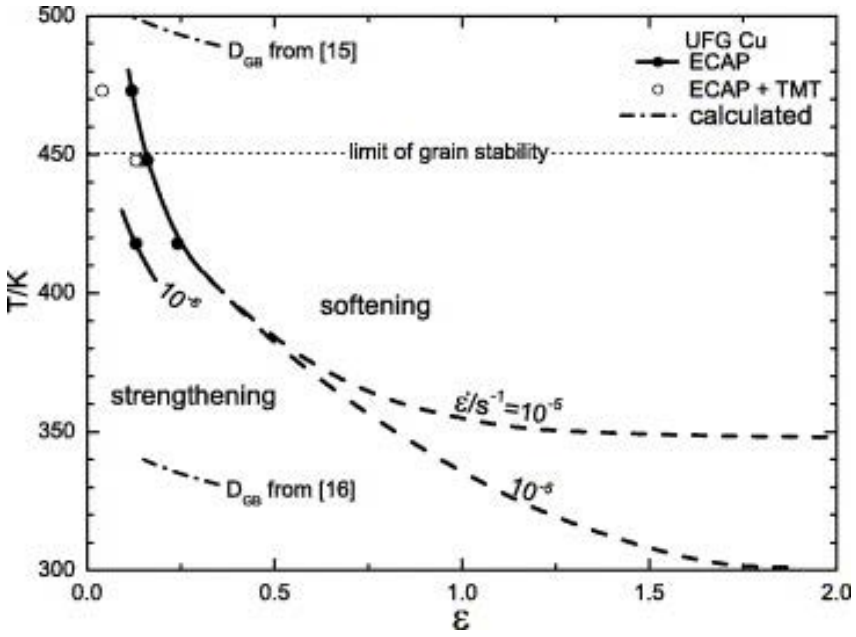

Figure 1.17: Transition from strengthening to softening of UFG Cu [52].

Furthermore, even though many experimental studies on the high temperature plastic behaviour of UFG materials were run, the interpretation of macro-scale effects in terms of deformation and damage mechanisms are often rather speculative, because of the combined experimental difficulties related to 1) the required spatial resolution of observation techniques and 2) high temperature. An effort to document these mechanisms at fine scale and high temperature is thus done in the present work.

Cyclic plasticity and fatigue of UFG materials

In pure UFG metals, cyclic softening is generally observed, above a certain amplitude, during plastic strain controlled fatigue tests, due to plasticity-induced grain growth (Figure 1.18) [54].

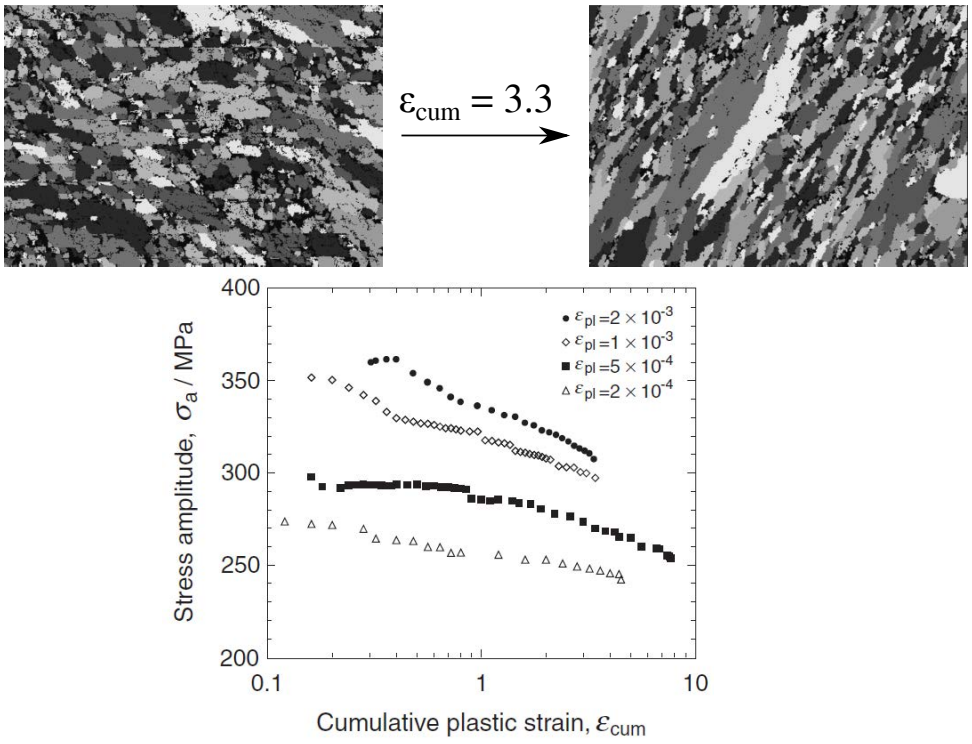

Figure 1.18: Evolution of the stress range in UFG Copper during strain-controlled fatigue tests and evidence of plasticity-induced grain growth [54].

Even without grain growth, which is the case for most of the UFG alloys and some pure UFG metals, like Ti, cyclic hardening is generally limited, which reflects a poor dislocation storage capacity and the absence of dislocation structures formation in UFG materials.

Due to the high yield strength of UFG and NC materials, an increase in fatigue lives is expected for stress-controlled, high cycle fatigue (HCF) tests. However, since CG materials are more ductile than their UFG and NC counterparts, common wisdom predicts a reduction in low cycle fatigue (LCF) lives for UFG materials. These trends are reflected by the expected strain-life diagram plotted by Mughrabi and Höppel [55], presented in figure 1.19.

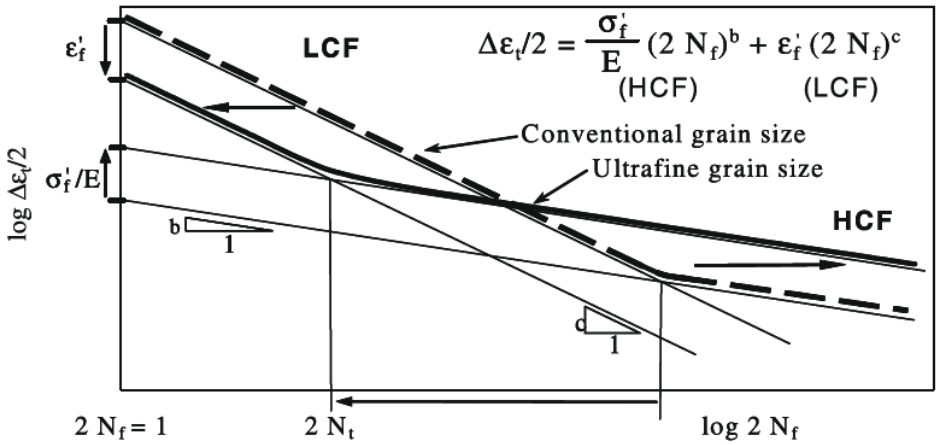

Figure 1.19: Expected trend for the fatigue lives of strong UFG and more ductile CG materials [55].

LCF and HCF lives were compared for different CG and UFG materials by Mughrabi and Höppel (Figures 1.20 and 1.21). Although the S-N curve of UFG materials lies above that of CG material in LCF regime, there is actually no gain in life at equal plastic strain range (Figure 1.20b) and in some cases, a reduction in the resistance to LCF can be observed (Figure 1.21). A substantial gain in LCF and HCF lives was however observed by Cavaliere [56] and Estrin [57] in pure UFG metals (Ti, Al, Cu and Ni) for stress-controlled tests.

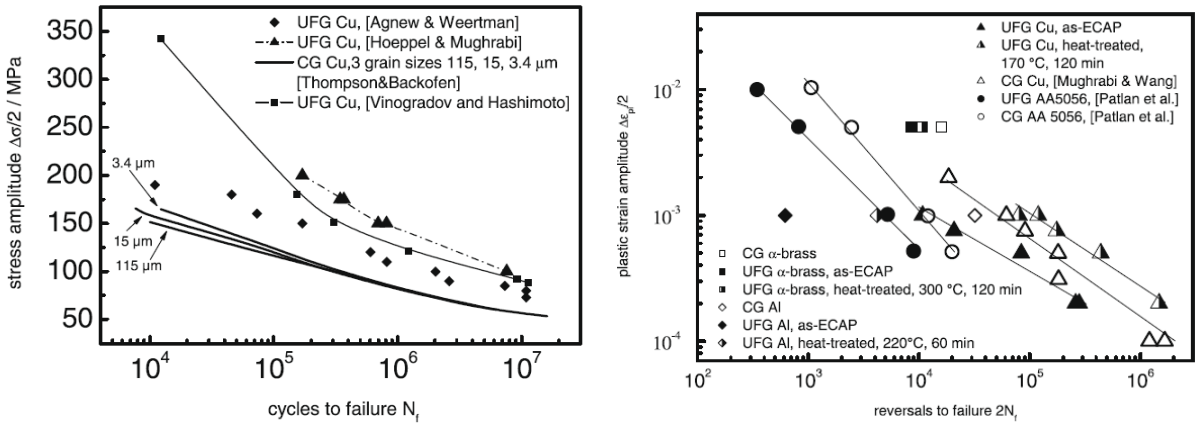

Figure 1.20: Wöhler (S-N) curve (left) and Coffin-Mason curve (right) for various CG and UFG materials [55].

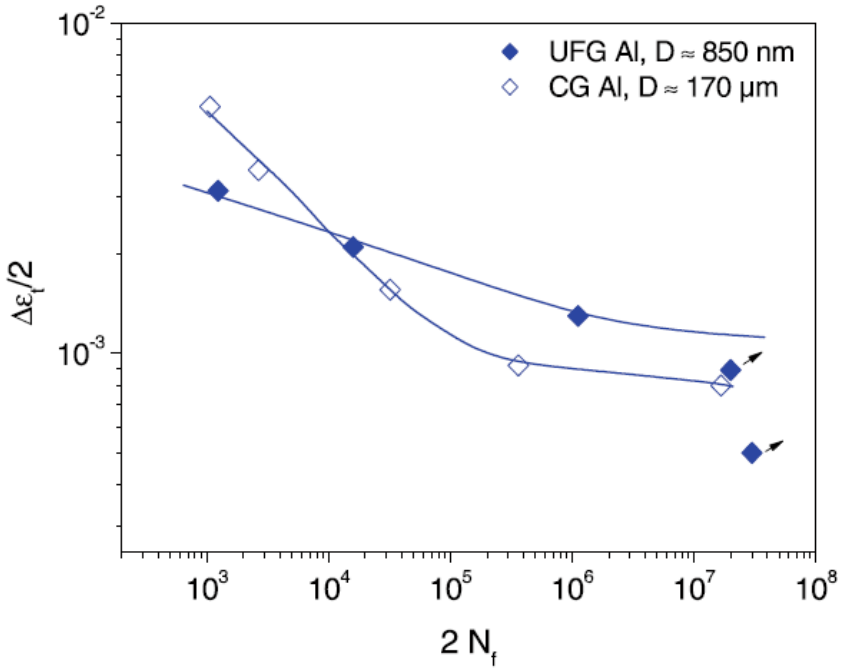

Figure 1.21: Total-strain fatigue life diagram of CG and UFG Al, showing the crossing of the curves [55].

In high and very-high cycle fatigue, the largest grains and the largest defects (e.g. inclusions or pores) are more important than the average grain size, so that crack initiation and incipient growth are determined by heterogeneities in the microstructure and the "statistics of extremes".

In UFG pure metals, a higher near-threshold crack growth rate and a lower threshold $\triangle K$ for crack growth values were observed, as compared to their CG counterpart, as shown in figure 1.22 [56]. Similar observation was made by Neindorf et al. for UFG steels [58].

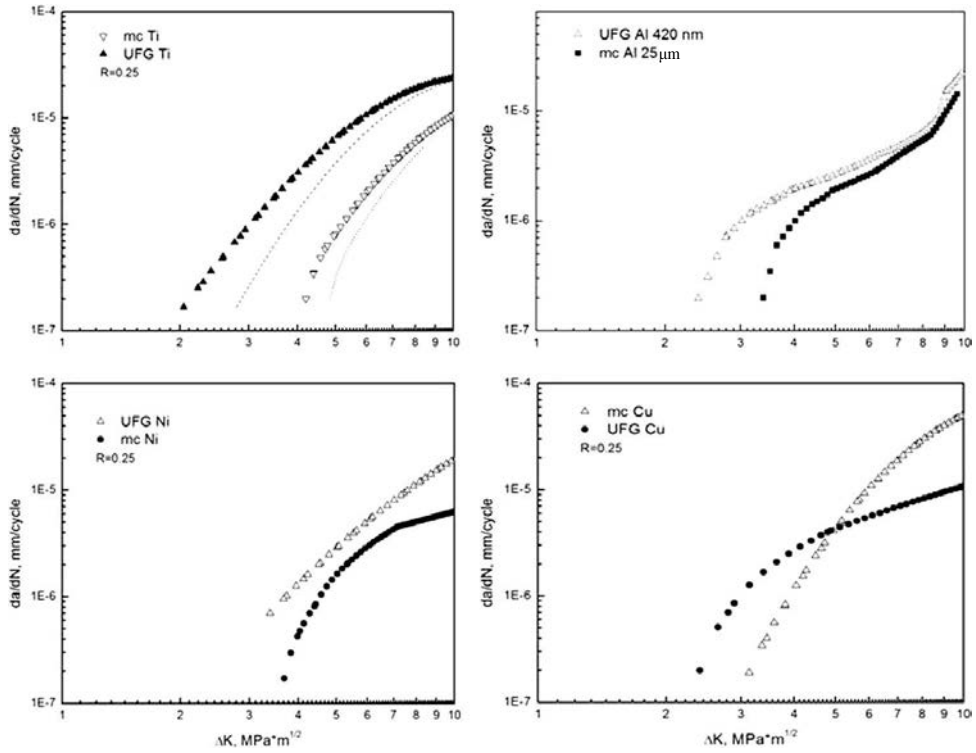

Figure 1.22: Mode I crack growth kinetics in various CG (denoted by "mc" as micro-crystalline) and UFG metals [56].

This decreased resistance to crack propagation in UFG material is usually blamed on smoother fracture paths and a reduction in roughness-induced crack closure with decrease in grain size. On the other hand, according to Irwin's model, the plastic zone size at the crack tip, r_y is inversely proportional to the square of the tensile yield stress, σ_Y:

$$r_y = \frac{1}{2\pi}\left(\frac{K_I}{\sigma_Y}\right)^2 \tag{1.6}$$

Here, K_I is the stress intensity factor.

Since UFG materials have a higher yield stress, a reduction in plastic zone size and thus of plasticity-induced crack closure is also expected, which might at the contrary induce an acceleration in crack propagation.

GBs can be expected to slow down transgranular crack growth or even arrest transgranular microcracks in HCF, as they do in CG metals (Figure 1.23), but might, at the contrary, accelerate intergranular crack growth. Furthermore, the efficiency of GBs in blocking the propagation of fatigue microcracks depends on the relative misorientation between neighbouring grains, and more specifically the tilt and twist angles between their slip planes [59]. Since ECAPed UFG materials usually have a strong texture, the probability of highly misoriented grains might be lower than in non textured materials, so that the barrier effect of GBs might be lower than expected. Thus, in UFG materials, the role of GBs in fatigue is not so clear, and deserves an investigation.

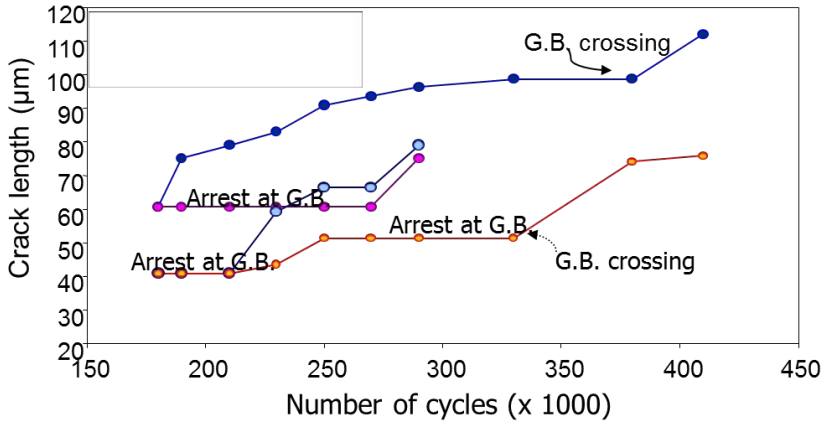

Figure 1.23: Crack length as a function of the number of push-pull cycles in the HCF regime for CG 316L Steel [60].

1.3 Effect of microstructural refinement on plastic deformation mechanisms

Below sub-micron level (< 1 μm), a transition from dislocation mediated to grain boundary mediated plasticity (grain boundary sliding (GBS), grain boundary migration and grain rotation) is observed. A few elements about these phenomena are thus given below.

1.3.1 Grain boundary sliding and its quantification methods

Grain boundary sliding (GBS) is a thermally activated process, normally expected in polycrystalline metals, at temperatures above 0.4Tm (where Tm is the melting temperature). It is responsible for superplasticity and was thoroughly investigated in the 60s and 70s [61]–[63]. The constitutive equation below was proposed to describe it:

$$\dot{\varepsilon}_{GBS} = A\left(\frac{Gb}{kT}\right)\left(\frac{b}{d}\right)^{p}\left(\frac{\sigma}{G}\right)^{n} exp\left(-\frac{Q}{RT}\right) \tag{1.7}$$

Here, G is the shear modulus; d the mean grain size; b the Burger's vector; Q an activation energy, and A, p and n the constants. A typical value of n = 2 was identified for various metals, which corresponds to a SRS of 0.5 observed in most cases for superplasticity and is typically used as a representation of GBS [64]. An increasing contribution of GBS is predicted as the grain size decreases. GBS indeed seems to be quite active at RT in UFG metals, although direct and convincing observations at the appropriate scale are not numerous. Yang et al provided such evidence (Figure 1.24 [65]).

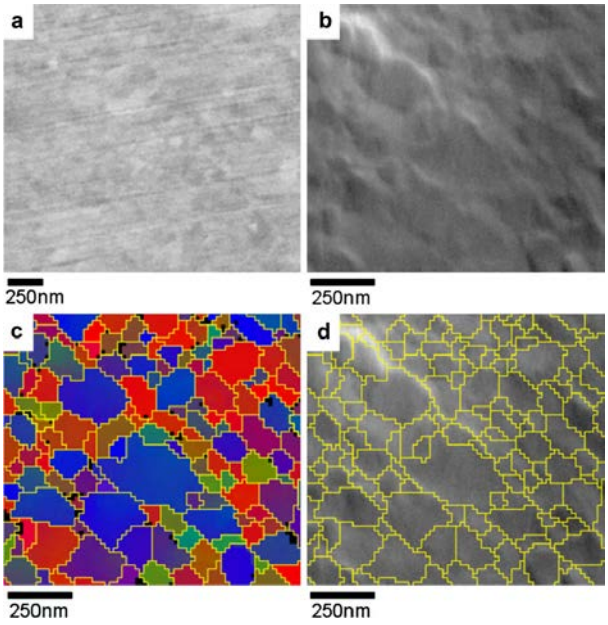

Figure 1.24: Direct evidence of GBS using SEM+EBSD after 17% strain in UFG Pd [65]

Raj & Ashby [63] predicted that grain boundary roughness and the presence of second-phase particles along the boundaries would slow down GBS. Experimental observations by Matsunaga et al. [66] or Soula et al. [67] suggest that special GBs (Σ3, Σ5... Σ< 29 according to the CSL nomenclature) tend to slide less than "random" GBs (Σ>29), which was attributed to the greater ability of lattice dislocations to dissociate into random GBs, producing a glissile component responsible for GBS (Figure 1.25).

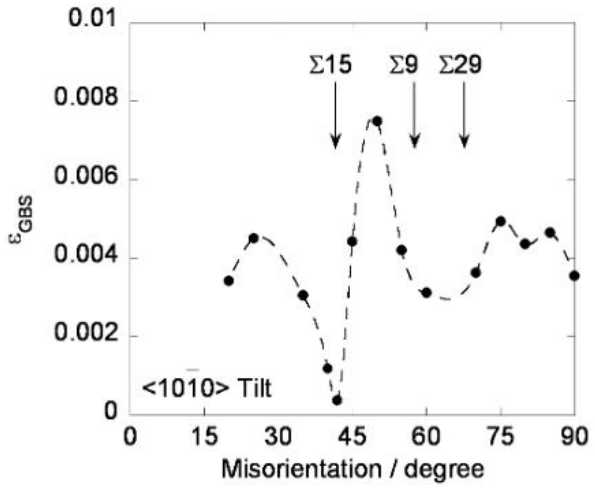

Figure 1.25: Grain boundary structure dependency of GBS in pure Zn [66]

Various micromechanical models of GBS have been developed [61]–[63] and will be reviewed in chapter 5.

Different intercept methods and averaging techniques were provided by Bell, Langdon & Gifkins [68]–[70] to estimate the contribution of GBS to overall deformation,

based on a simple geometrical representation. For a planar GB with a 3D orientation characterized by two angles θ and ψ, the sliding displacement can be decomposed in three components u, v, w (Figure 1.26), including an out-of-plane component v (Figures 1.26 and 1.27) related by

$$u = \frac{v}{tan\psi} + \frac{w}{tan\theta} \tag{1.8}$$

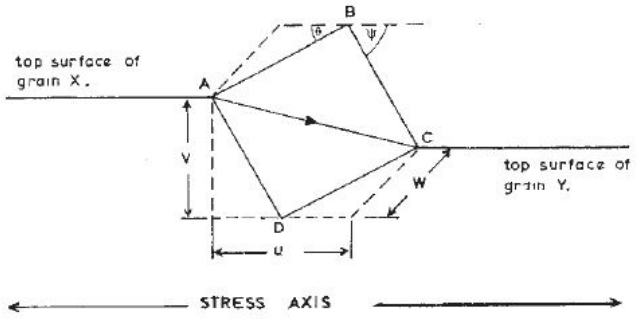

Figure 1.26: Schematic representation of grain boundary sliding [68]

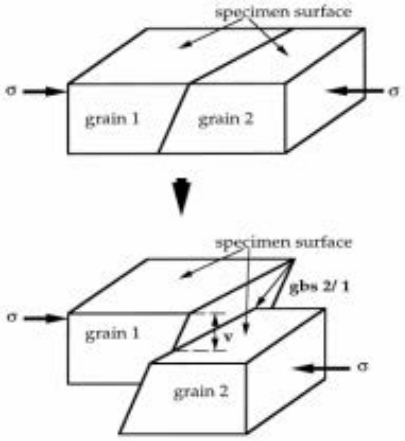

Figure 1.27: Out-of-plane component of GBS [71]

Bell et al. [68] proposed 3 ways to estimate the contribution of grain boundary sliding to the overall strain $\gamma = \varepsilon_{GBS}/\varepsilon_T$, based on measurements of the average value of u, v or w over a large number of grain boundaries intercepted by series of lines of total length l parallel to the tensile axis,

$$\varepsilon_{GBS} = \frac{1}{l}\sum_{0}^{l} u = \frac{1}{l}\sum_{0}^{l}\left(\frac{v}{tan\psi} + \frac{w}{tan\theta}\right) = \frac{k}{xd}\sum_{0}^{x} v \tag{1.9}$$

where, k is an averaging factor, issued from a statistics of grain boundaries emergence angle on the surface. Note that the appropriate value of k (1.4 for annealed samples,

and 1.1 for polished sample, according to Bell & Langdon) is generally unknown (especially after SPD), and this constitutes a major source of error, which most often is not even discussed in papers that use this technique.

Most researchers measure in-plane horizontal grid shifts, u to estimate the contribution of GBS. However, since it is difficult to measure a reliable value of u from the longitudinal lines, the most popular approach is to use a series of transverse lines, t (perpendicular to the tensile axis). Since a transverse line tends to intersect boundaries that are parallel to stress axis whereas a longitudinal one more frequently cuts transverse boundaries, equation 1.9 cannot be used directly and is modified by Bell & Langdon as follows:

$$\varepsilon_{GBS} = \frac{1}{t}\sum_{0}^{t} u \cdot tan(\theta) \tag{1.10}$$

Gifkins et al. [69] measured all 3 components on four different materials to validate the estimates of GBS contribution based on their measurement. Based on the inclination of sliding GBs relative to the tensile axis, they also concluded that GBS was controlled by the resolved shear stress on the grain boundary.

This technique became quite popular and many applications to CG materials were made, for example, by Koike et al. [64]) who performed scanning laser microscopy measurements of the out-of-plane displacements of FIB-engraved lines (Figure 1.28), or by Soula et al. [67], who used SEM measurements of in-plane GBS-induced shift of microgrids with a 5 μm pitch to estimate GBS in a Ni based superalloy after creep.

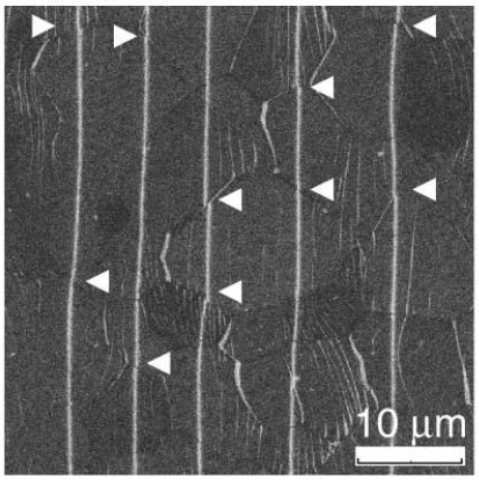

Figure 1.28: Measurement of offsets on FIB-engraved lines to derive the contribution of GB sliding by Bell & Langdon's method in AZ31 Mg alloy at 523K [64]

However, these techniques become somewhat questionable (Equation 1.8 assumes a fixed orientation of the GB during deformation, which is no more correct in case of grain rotation, or just of large deformation with a substantial change in grain shape) and more difficult to use for UFG materials, because 1) the exact position of the GBs may be difficult to detect and 2) a high spatial resolution measurement technique is

needed, but over a statistically representative area.
Clarisse [71] applied this technique, using AFM measurements of ledges heights formed at the grain boundaries (revealed by thermal etching), in a very fine grained alumina (grain size 0.98 μm) during high temperature compression tests.
Han and Mohamed also used AFM to measure out-of-plane GB displacements in UFG (cyromilled) Al5083 alloy in which the GBs had been revealed by ion etching before tensile tests at 10^{-4} s^{-1} at 200°C (Figure 1.29). They reported a contribution of GBS to total strain in the range of 17 and 30% [72]. Their observations seem statistically representative, as they observed 4 different area containing approximately 200 grains each.

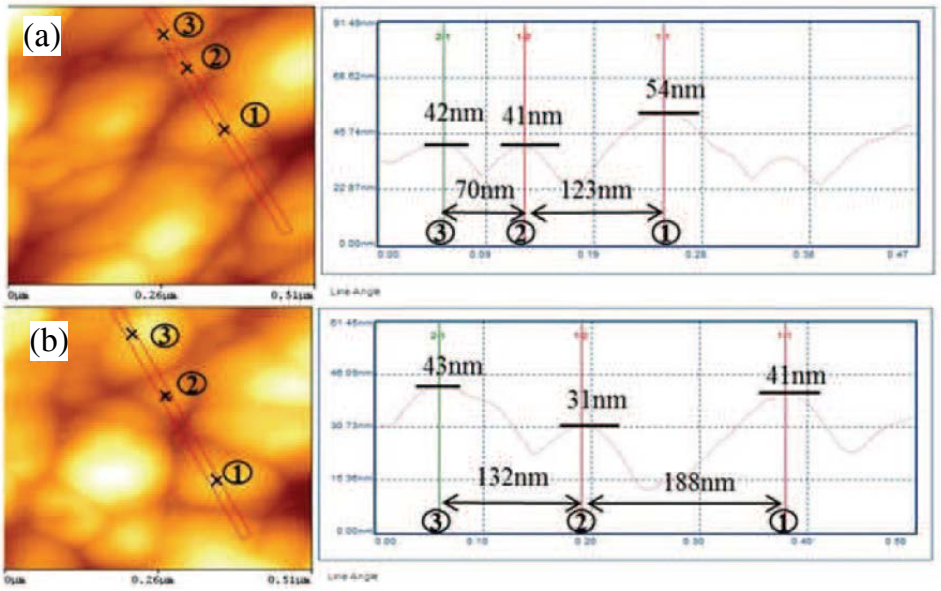

Table Contribution of Grain Boundary Sliding to Total Strain in Areas A, B, C, and D

Area	A	B	C	D
Grain boundary contribution pct	30 ± 4	17 ± 2	26 ± 3	30 ± 3

Figure 1.29: 2-D AFM images and corresponding height profiles in the same area before and after deformation. The table shows the contribution of GBS measured in different areas in Al 5083 alloy [72].

Ivanov et al. used FIB sectioning to measure the vertical surface offsets produced by GBS in pure UFG Al produced by ECAP, as shown in figure 1.30 [73]. They reported a contribution of GBS to overall deformation as high as 70% in some areas, which decreased with increasing strain (Figure 1.31). This technique however has several limitations. First, it is a destructive method, hence the thin foil analysed at every strain increment was different and second, the analysed volume was quite limited (8-10 measurements of vertical offsets at each step) so that it is difficult to get statistically meaningful quantitative information.

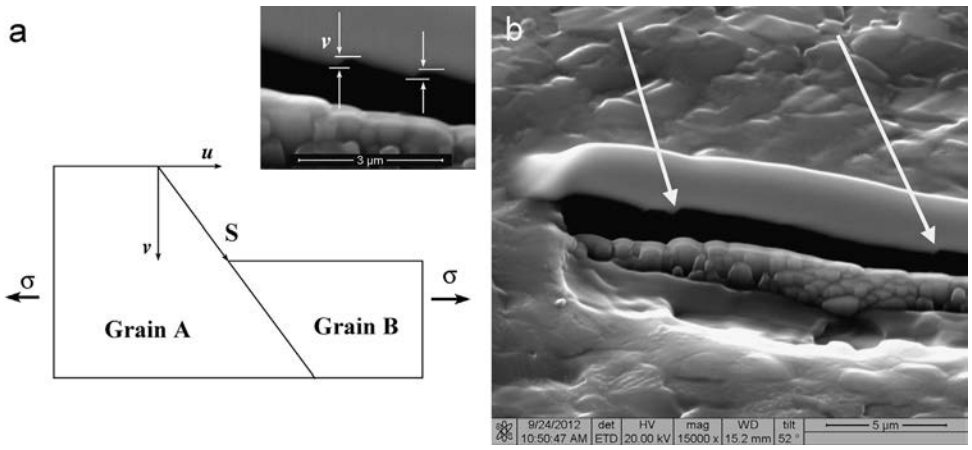

Figure 1.30: Vertical offsets (steps) on grain boundaries produced by GBS on a FIB cross section in UFG Al after tension [73].

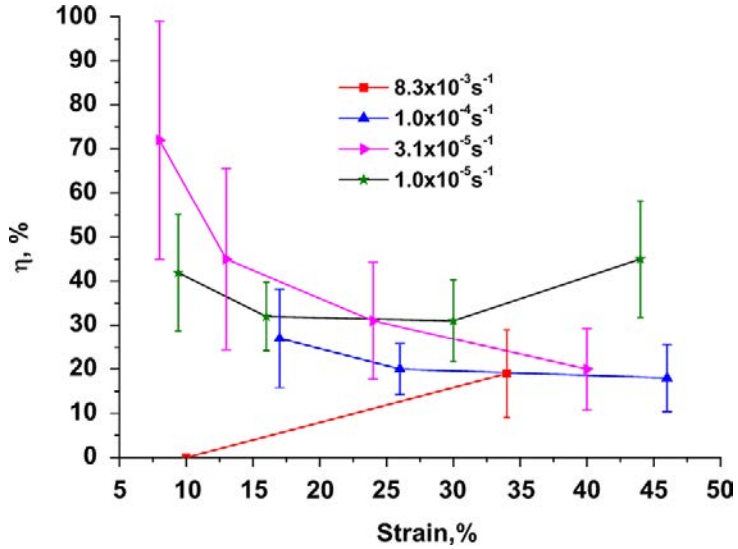

Figure 1.31: Estimated contribution of GBS to the overall deformation in the local area versus the strain in this area for UFG Al [73].

It is a popular concept, although not based on very reliable elements, apart from relatively large offsets of scratches compared to the mean grain size, that in UFG materials, a group of favourably oriented grains slide together as a unit until they get blocked by an unfavourably oriented grain, where sliding is accommodated by dislocation motion [74].

A more direct experimental characterization and a more elaborate mechanical analysis of GBS in UFG materials are still needed at this stage.

1.3.2 Grain rotation

Grain rotation, different from the change in crystal orientation induced by large slip deformation, is a plastic deformation mode observed mostly in NC and to some extent in UFG materials. According to Bobylev et al. [75] the rotation is mediated by diffusion-assisted climb of grain boundary dislocations (Figure 1.32).

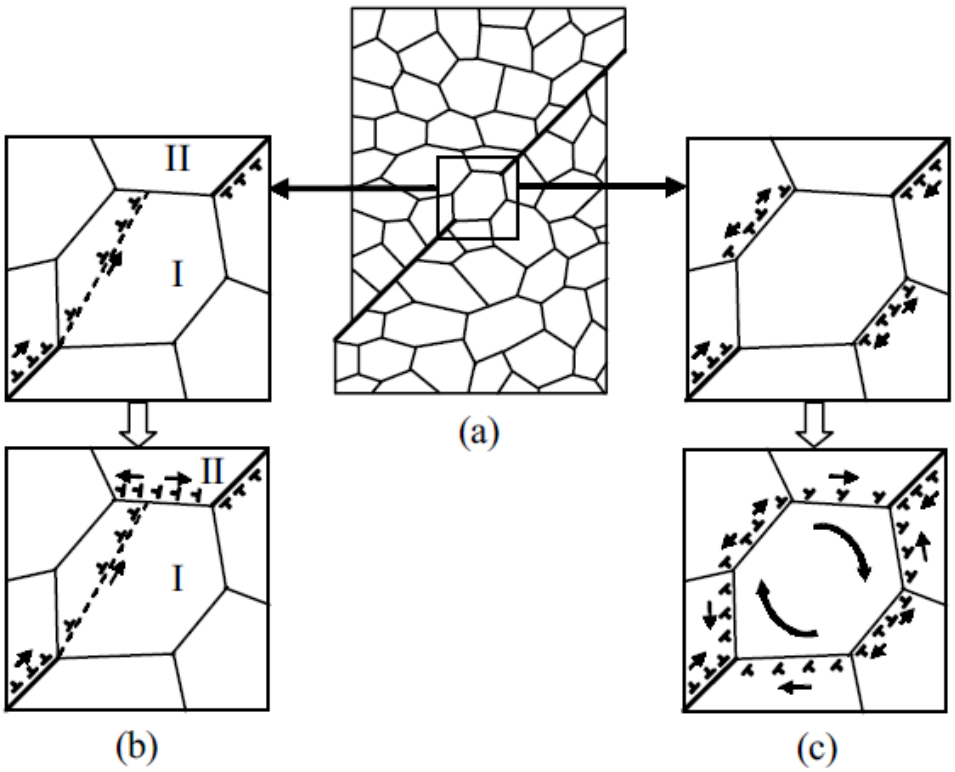

Figure 1.32: Shear and rotation deformation modes in NC material containing a mesoscopic sliding surface. (a) Enhanced GBS along the mesoscopic sliding surfaces stops at a grain whose geometry prevents such sliding. (b) Lattice dislocations are emitted from a triple junction into the grain. They transform into GB dislocations whose slow climb controls the rate of both dislocation emission from the triple junction and thereby GBS. (c) Shear deformation mode transforms into rotation deformation occurring in the grain. The rotation deformation involves slow climb of GB dislocations, and the climb rate controls the rate of GBS [75].

After grain rotation, the aligned GBs form "smooth mesoscale sliding surfaces" which enhance cooperative GBS over distances larger than one grain size.

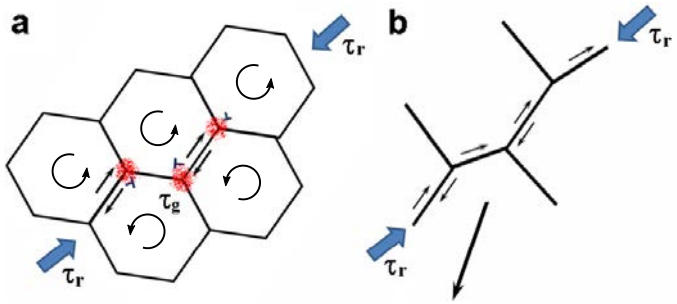

Figure 1.33: Schematic diagram explaining the cooperative GBS facilitated by grain rotation in NC Pd10Au alloy [76].

Quantification of grain rotation is even more complicated than the quantification of GBS for UFG/nano materials because of the high resolution required to measure small rotations. Izadi et al. [77], Noskova et al. [78], Milligan et al. [79] and Mompiou & Legros [80] performed *in-situ* tensile tests in a TEM to measure the changes in grain orientations in nanocrystalline or UFG Al or Fe thin films. Rotations by several degrees were reported within a few percent strain. According to Mompiou et al: " Grain growth and rotation are limited to areas where the stress is concentrated, and occur as a collective process, involving several neighbouring grains. These mechanisms are carried out by the nucleation and propagation of GB dislocations" [80].

Ivanisenko et al. took this method a step forward, using crystal plasticity to predict and later subtract from the measured rotation, crystallographic orientation changes related to dislocation glide on UFG Pd specimens [76]. It was shown that the smallest grains have a pronounced tendency for non-crystallographic rotations.

1.3.3 Shear bands and strain distribution

The way plastic strain is distributed in the volume plays an essential role in the resistance to ductile fracture of a metal.
Sabirov et al., observed that, in Al 6082 UFG alloy, the rise in ductility when the strain rate decreases (Figure 1.11) correlates with profuse micro shear banding and signs of cooperative GBS. Based on measurements of shear-induced offsets of scratches at their intersection with the bands (relatively large compared with the mean grain size), they report that these short (< 20 μm) and relatively wide micro-bands, homogeneously distributed on the surface, locally accommodate 12 to 20% plastic strain without damage, at 1.1×10^{-5} s^{-1}, but that their width and surface fraction drop with increasing strain rate, leading to a detrimental transition towards a few macro-shear bands spanning over the whole gage width (Figure 1.34) [81].

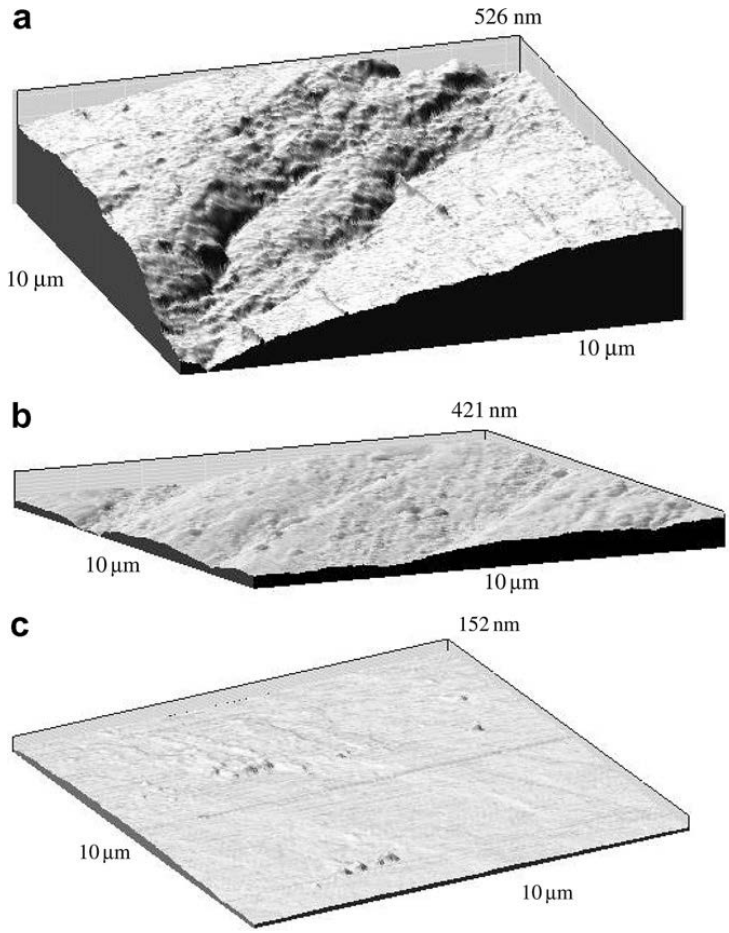

Figure 1.34: 3D AFM images of deformation relief for UFG Al6082 alloy tested at: (a) 1.1$\times 10^{-5}$ s^{-1}, (b) 10^{-4} s^{-1} and (c) 10^{-3} s^{-1} [81].

Note that the broadening of strain localization bands depends on the hardening exponent and on the SRS: the higher the SRS, the stronger the local increase in viscous stress following a local increase in strain rate, and the higher the hardening exponent, the stronger the local increase in flow stress following a local increase in strain. Both effects hinder further localization, and favour band broadening, this leading to more diffused bands.

Several researchers used high resolution digital image correlation (HR-DIC) during *in-situ* tensile tests in a SEM to visualise the effect of microstructural heterogeneity, which is inevitable after SPD, on the strain fields [82]–[84]. Strain localisation primarily occurred within large grains due to higher dislocation-mediated plasticity, and then extended across neighbouring grains though HAGBs or along the interfaces between large and small grains via GB-mediated plasticity.

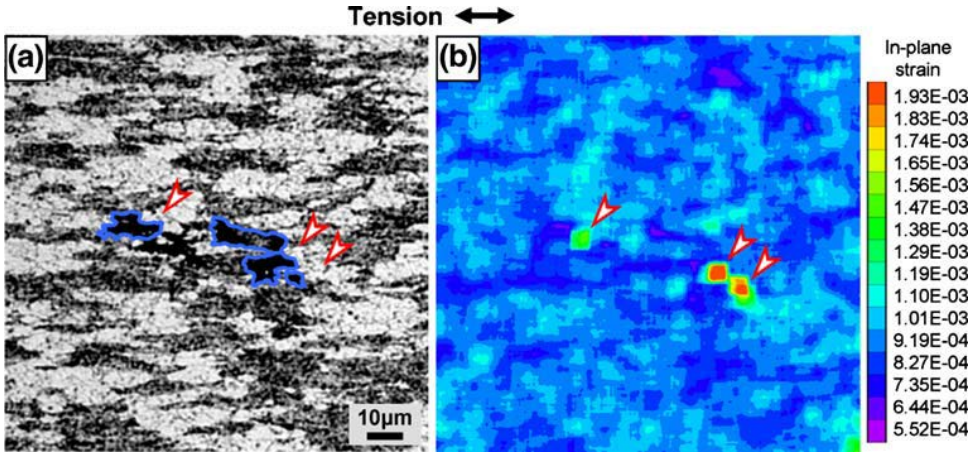

Figure 1.35: (a) Optical micrograph and (b) corresponding in-plane strain field obtained from DIC in UFG (cryomilled) Al 5083 alloy [82].

Kammers et al. [85] even used DIC during high temperature *in situ* tensile tests in a SEM for a local estimate of the SRS, close to LAGBs, HAGBs or inside grains, based on measurements of the local increment in plastic strain after a change in strain rate.

DIC will also be used in the present work to document plastic strain distribution, depending on the strain level, strain rate and temperature and to compare this distribution in CG and UFG materials. Furthermore, due to meso-scale microstructural heterogeneities in ECAPed materials, it is important not to focus only on a small area containing a few grains, but also to monitor strain fields over several hundreds of microns. That is why two-scale DIC will be used here.

1.4 Introduction to Al 5083 alloy and previous work on its UFG form

Al 5083 aluminium alloy contains 4-5% Magnesium and traces of other elements: Mn, Fe, Cr and Si. It is a non-heat treatable, but strain hardenable alloy, which derives its strength from solid solution strengthening by Mg addition. It is an important commercial Al-Mg alloy owing to its high strength to weight ratio, high corrosion resistance, especially in sea water. It is also amenable to superplastic forming above 500°C, for a mean grain size in the range of 2-10 μm and has been exploited commercially for long time by automobile, marine and defense industries. It has good low-temperature tensile and fatigue properties and thus is also widely used for cryogenic applications.

Since it contains more than 3% Mg, it is supersaturated at RT (Figure 1.36). Thus, some of the magnesium precipitates in the form of β-phase (Mg_2Al_3) particles, distributed along the grain boundaries [86]. Secondary Mn and Fe rich coarse intermetallic particles and Al-Mn-Fe-Cr–type rod shaped nano-dispersoids can also be found in this material.

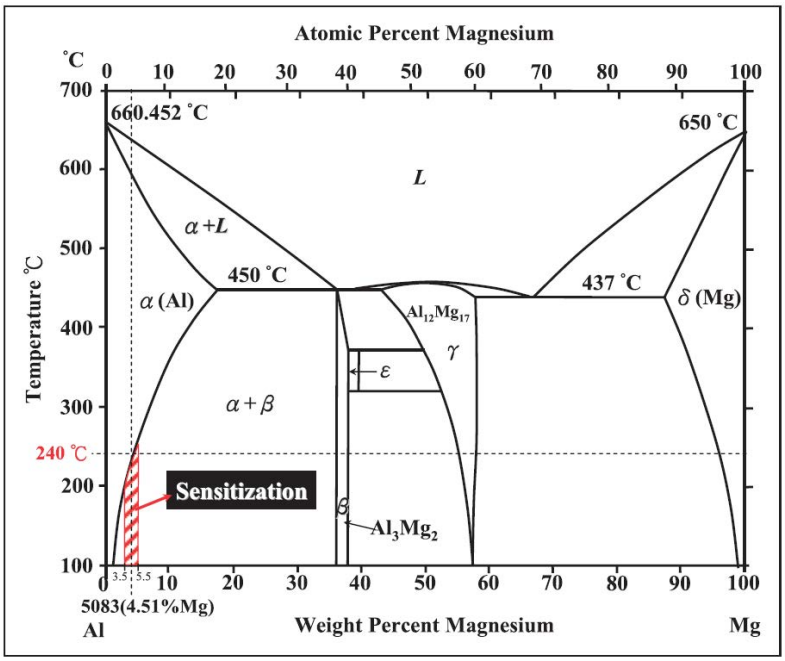

Figure 1.36: Phase diagram for Al-Mg binary system [86].

Figure 1.37, from Chen et al. shows that an annealing treatment of 30 min up to 200°C does not significantly alter the RT yield stress, UTS and ductility of the material, and neither does it change the precipitates size or distribution. This point is important for the present study in which tension or relaxation tests were run up to 200°C [86].

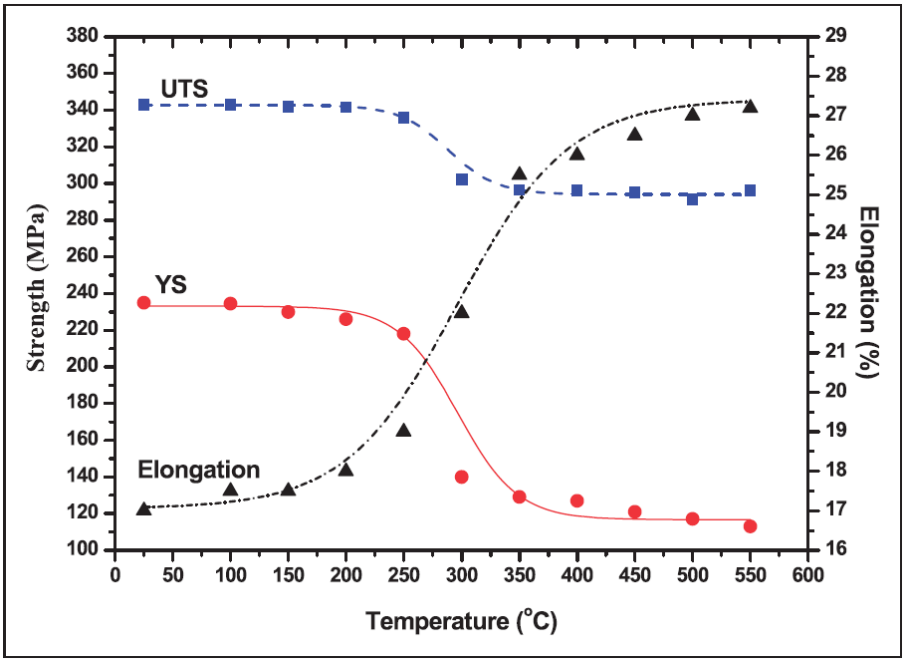

Figure 1.37: Tensile properties of Al 5083 alloy versus annealing temperatures [86].

1.4.1 UFG Al 5083 and its tensile properties at RT

Several studies on UFG Al 5083 can be found in the literature. Many of those deal with UFG or bimodal alloys obtained by cryomilling, powder compaction + extrusion or rolling[82], [84], while others concern UFG alloys obtained by ECAP, generally performed between 150 and 200°C [5], [17], [87].

Figure 1.38a, from Dupuy et al. [88] shows the evolution of the tensile stress-strain curve of Al 5083 at RT with the number of ECAP passes following route Bc, at 150°C, while figure 1.38b, compares the tensile curves after 8 passes of route A, Ba, Bc or C.

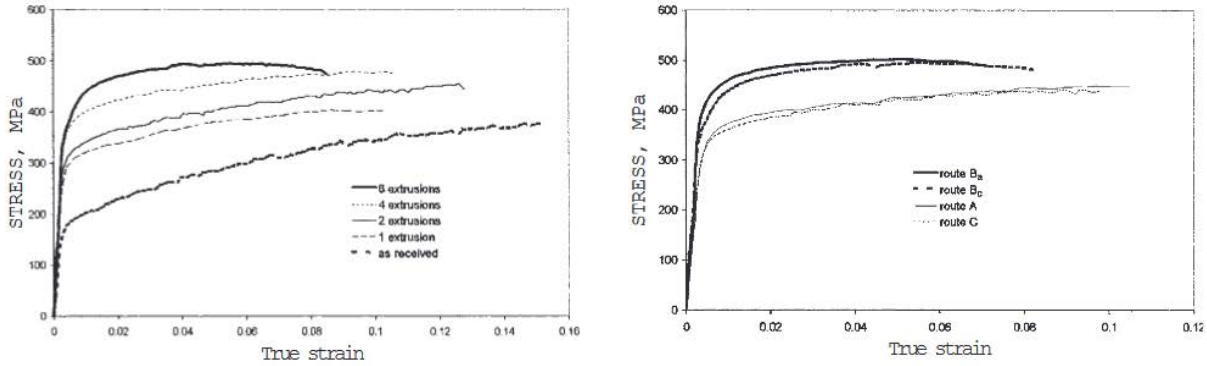

(a) (b)

Figure 1.38: RT evolution of tensile stress-strain curves with (a) number of ECAP passes for route Bc and (b) different routes after 8 ECAP passes for Al 5083 [88].

The increase in yield stress due to grain refinement is quite substantial in Al-Mg alloys, for which the Hall-Petch coefficient, k_y ($\sigma_y = \sigma_0 + k_y d^{-1/2}$) ranges from 0.12 to 0.28 MPa/m$^{1/2}$ as shown in table 1.1.

Alloy	k_y (MPa/m$^{1/2}$)	Reference
cryomilled Al5083	0.28	[89]
ECAPed Al-1%Mg	0.13	[90]
ECAPed Al-3%Mg	0.15	[90]
ECAPed Al 5083	0.10-0.16	[91]
CG Al-4%Mg	0.22	[92]
CG Al-5%Mg	0.12	[93]

Table 1.1: Values of Hall-Petch coefficients for Al-Mg alloys

Dupuy et al. have shown that although the coarse intermetallic particles, initially present in CG Al 5083, get fragmented and redistributed during ECAP, it does not prevent cavity nucleation from clusters of fragmented particles during tension (Figure 1.39b) [94]. The shape, size and spatial distribution of intermetallic particles can thus play an important role in determining the ductility of both CG and UFG Al alloys. However, many papers on UFG Al alloys thoroughly describe grain size, shape and texture, but do not even mention these particles, whose role is seldom discussed.

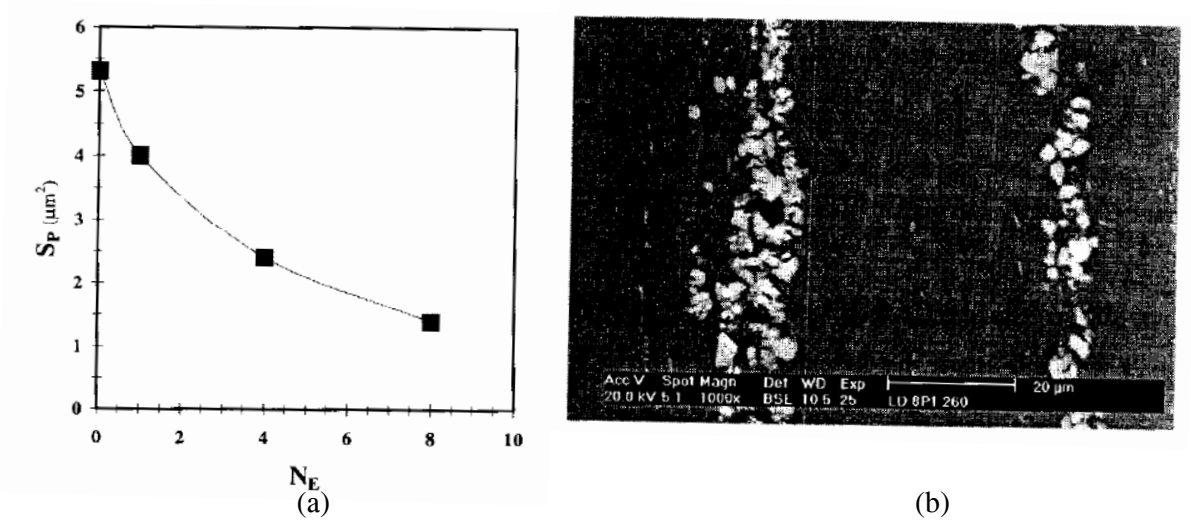

(a) (b)

Figure 1.39: (a) Effect of number of extrusions (N_E) on the mean surface of second phase particles, (b) SEM image of cavity nucleation at broken second phase particles [94].

1.4.2 Dynamic strain ageing

Like in all Al-Mg alloys, due to the dynamic interaction between solute Mg atoms and mobile dislocations, serrated flow is observed in Al 5083 alloy. This effect, also known as Portevin Le-Chatelier (PLC) effect is a manifestation of dynamic strain aging (DSA). Al-Mg alloys have often been chosen as model materials for the study of DSA, since the amplitude of the phenomenon can easily be changed by a change in Mg content, as illustrated by figure 1.40 [95].

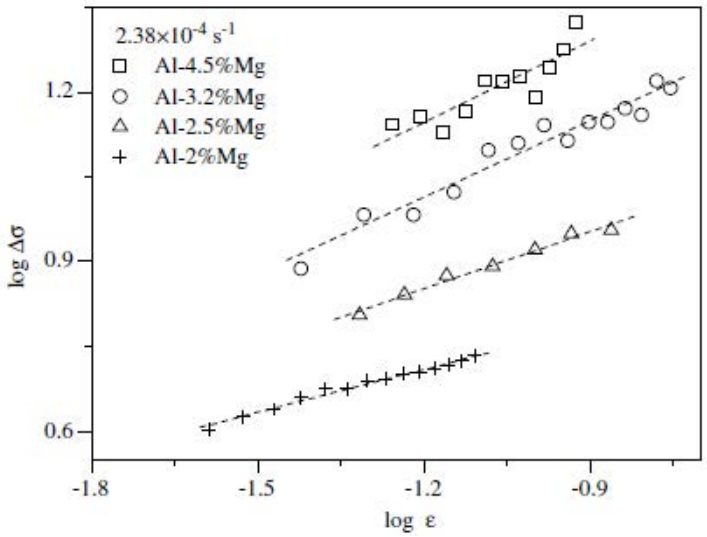

Figure 1.40: Effects of strain and Mg content on the magnitude of the stress drops at RT in Al-Mg alloys [95].

Tell-tale signs of PLC effects are shear-mode failure instead of necking, negative strain rate sensitivity and serrated flow. The stress serrations are a result of repeated

pinning-unpinning of mobile dislocations by Mg atoms if the temperature and strain rates allow the atoms to diffuse at a rate comparable to the dislocation glide velocity.

PLC bands are generally classified, based on their frequency and the shape of the serrations on the stress-strain curve, into 3 types, type A: avalanche-like shearing pattern, with continuously propagating bands, type B: discontinuous hopping like behaviour with hopping distance almost the same scale as the specimen thickness, and type C: strong and regular stress drops at relatively high frequency (Figure 1.41) [96], [97].

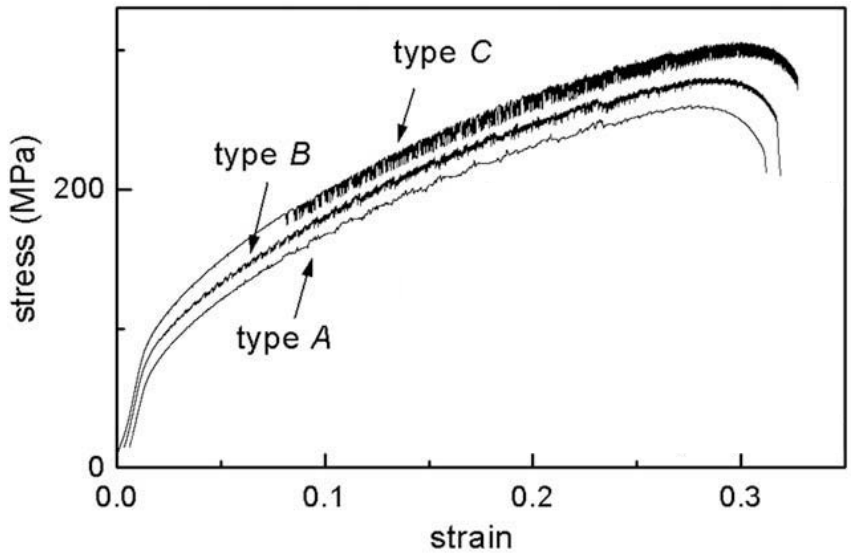

Figure 1.41: True stress-strain curves representing conventional PLC types [97].

PLC instabilities shift from one type to the other or disappear depending upon the applied strain rate and temperature (Figure 1.42). At low strain rate and high temperature, the PLC effect disappears because mobile dislocations keep dragging solute atoms. The high strain rate and low temperature domain, where PLC effect also disappears, corresponds to friction of unpinned dislocations on the crystal lattice. And in-between those two regimes, type A, B or C bands can be observed.

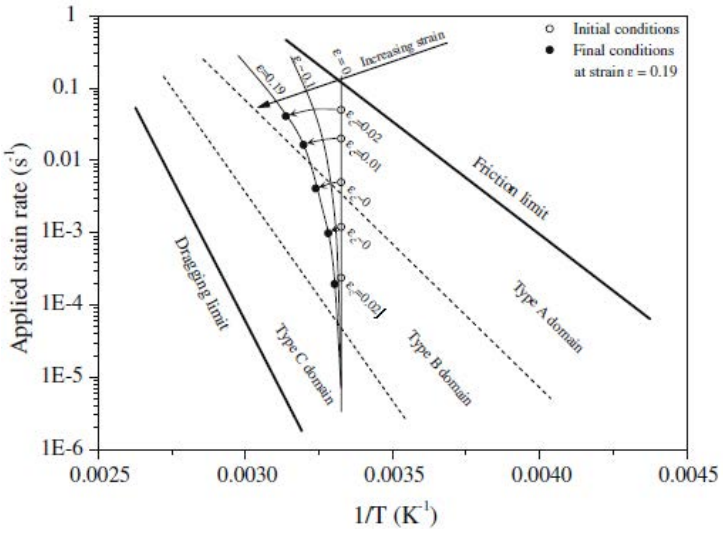

Figure 1.42: Temperature and strain rate regimes of PLC effect in Al-Mg alloys [98].

A few research was done to study the effect of grain refinement down to UFG regime on DSA in AL-MG alloys. There is no consensus on the effect of grain refinement on PLC effect, however, a trend seems to emerge. The amplitude of stress serrations was reduced in UFG Al-Mg alloys with less than 3% Mg [99]–[101], while for Al-Mg alloys with more than 3% Mg elevated stress serrations were reported after ECAP [102]–[104]. The trend seems logical since Mg is dissolved completely below 3%, and there might not be enough solute Mg atoms to pin the increased dislocation density after ECAP. Kaneko et al. [105] have shown that SPD processing can produce supersaturated Al-Mg solutions (up to 30% Mg without any precipitation). If ECAP fragments Mg-rich second phase particles and even dissolves some of it, the UFG alloy might be supersaturated in Mg, and contain enough solute atoms to interact with their high dislocation density, this leading to larger serrations than in their CG counterparts.

1.4.3 Superplasticity

CG Al 5083 alloy (with grain size$\sim$2-10 μm) exhibits superplasticity at low strain rate (<10^{-3} s^{-1}) and high temperature (>450°C) [106]–[108]. Elongations to failure as high as 450% were achieved at 550°C and $\sim 10^{-4}$ s^{-1}, as show in figure 1.43.

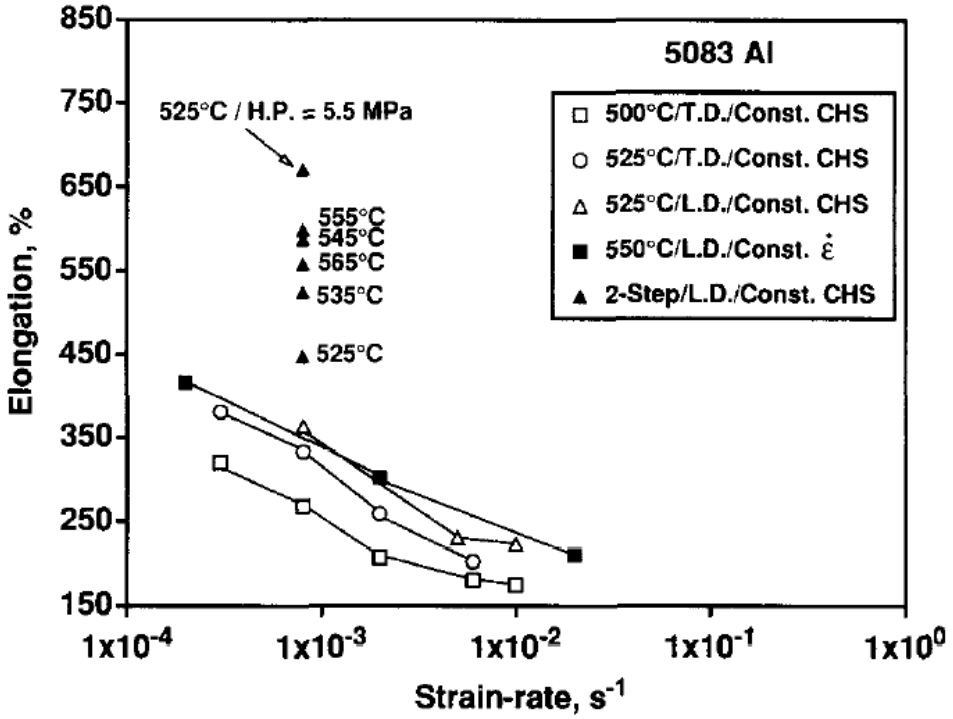

Figure 1.43: Maximum elongation to failure as a function of initial strain rate and temperature for CG (∼9 μm) Al 5083 alloy (T.D. and L.D. denotes specimens cut with tensile axis parallel to transverse and longitudinal directions, respectively and CHS stands for constant cross-head speed) [107].

According to Chauhan et al., superplasticity can be achieved at higher strain rates in UFG Al 5083. They obtained an elongation of about 350% at 0.1 s^{-1} and 523 K, as shown on figure 1.44 [109].

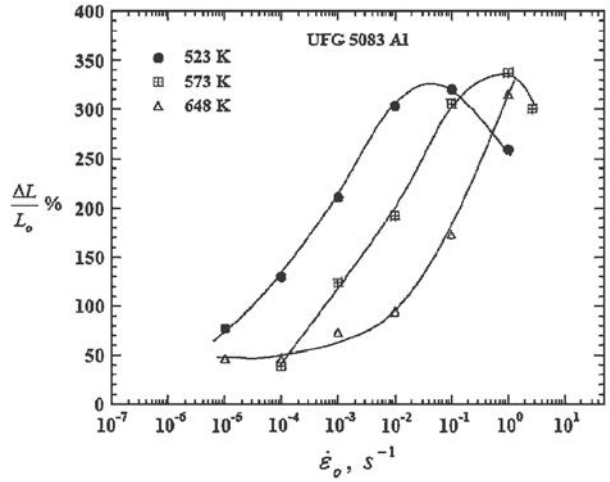

Figure 1.44: Maximum elongation to failure as a function of initial strain rate at temperatures 523-648 K [109].

Similar results were obtained by Chang et al. [17], Ko et al. [108], Park et al. [110]

for ECAPed Al5083 alloy. The tensile elongation to failure not only varied with average grain size but also with the percentage of HAGBs. Elongations of up to 300% were achieved at 548 K for UFG Al5083 (with 300 nm mean grain size), after 8 ECAP passes at 200°C (50% of HAGBs), while after 4 passes (similar grain size, but only 35% HAGBs) the maximum elongation was "only" 140%, as shown in figure 1.45.

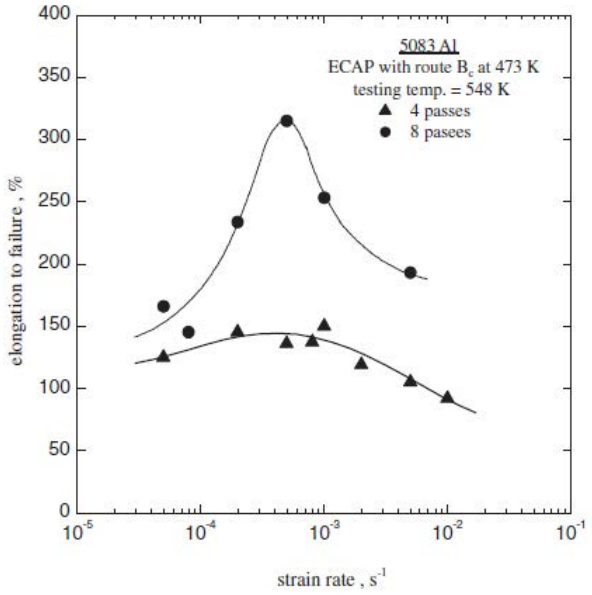

Figure 1.45: Variation of elongation to failure as a function of initial strain rate at 548 K [110].

Most studies on the high temperature properties of UFG Al 5083 aimed at allowing superplastic forming at lower temperature and higher strain rate than in CG material, and were thus performed above 530 K. The number of studies of the viscoplastic behaviour of this material at lower temperatures is actually limited. Such temperatures might however be encountered in service and it is important, for example, to document and analyse the transition from GB-induced strengthening to GB-induced softening in Al 5083, as it was done for other alloys.

1.4.4 Creep behaviour

Outside the superplastic regime, the creep behaviour of CG Al-Mg alloys shows a typical class I (Alloy type) solid solution behaviour with a stress exponent of 3, indicating solute-drag as a controlling mechanism, and a power-law breakdown at high stresses (Figure 1.46a) [111]. The activation energy of $\sim$142 kJ/mol which is generally observed corresponds both to the activation energy of solute Mg diffusion in Al and self diffusion of Al in Al matrix.

The creep behaviour of Al-Mg alloys becomes more complicated below 0.5Tm [111], a regime where very limited data is available. Figure 1.46b shows the low temperature creep behaviour of Al-3%Mg [111]. The stress exponent and the activation energy for creep approach infinity. It is well accepted that in this region creep is controlled by

the interaction of solute atmospheres with moving dislocations to such a level that an athermal type trend is achieved.

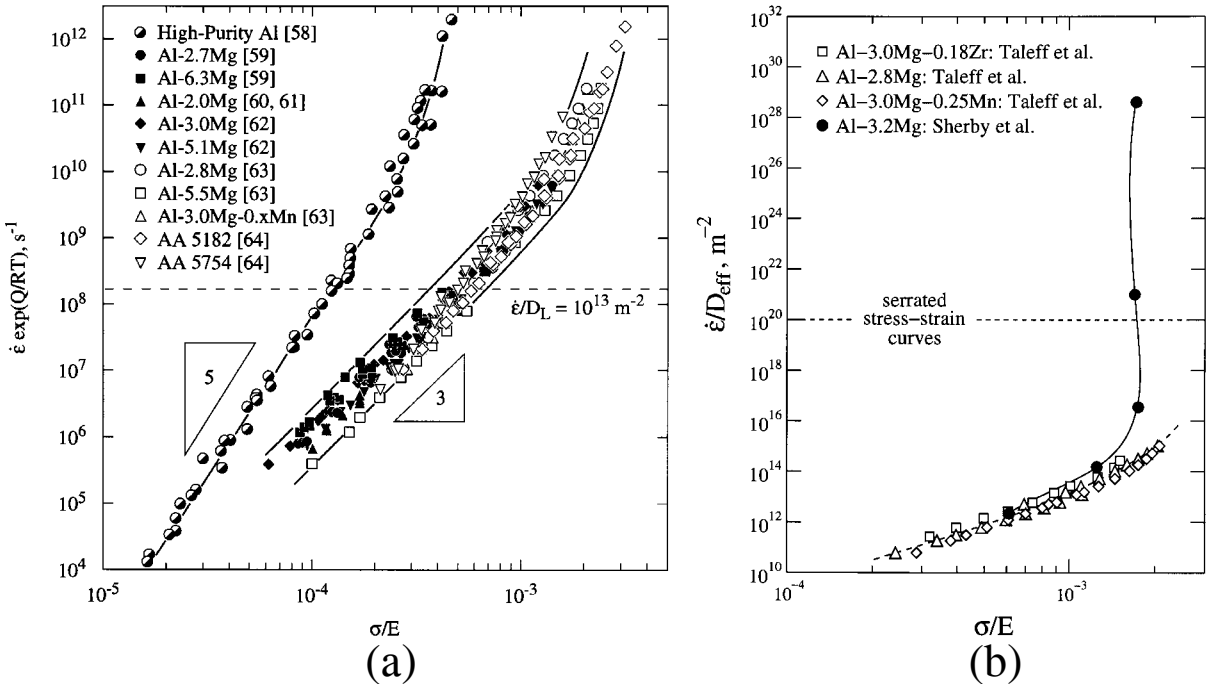

Figure 1.46: (a) Zener-Hollomon parameter as a function of modulus compensated stress for Al-Mg alloys. (b) Low temperature data of an Al-3%Mg alloy plotted with high temperature data from similar alloys [111].

The creep behaviour of UFG (ECAPed) Al 5083 alloy was analysed by Kim et al. in the temperature range of 498 to 548 K [112]. The value of stress exponent was observed to be 3.5 at low stresses and increased to 4.5 at high stress (Figure 1.47). Even though creep is controlled by solute-drag processes, the creep curve exhibited a class II (Metal type) creep behaviour. Activation energies of 72.6 and 96.1 kJ/mol were determined at low and high stresses, respectively. This indicates that at low stresses, creep deformation is controlled by dislocation glide while at high stresses, it is controlled by dislocation climb.

The existence of a thermally activated threshold stress was detected in various studies for both CG and UFG materials [109], [112]–[114]. However, it was only introduced as a fitting parameter to obtain a power-law relation for creep data. The physical basis of such a parameter is not clear. According to Chauhan et al. [109] and Kaibyshev et al. [113], the threshold stress originates from the interaction of dislocations with nano-dispersoids or other incoherent particles, while Kim et al. assume that the threshold stress is related to the initiation of glide at triple junctions, ledges, or particles at GBs. They use this reasoning to explain the lower threshold stresses in UFG materials which have more grain corners as well as particles per unit volume lying on GBs and thus more glide sources can be activated.

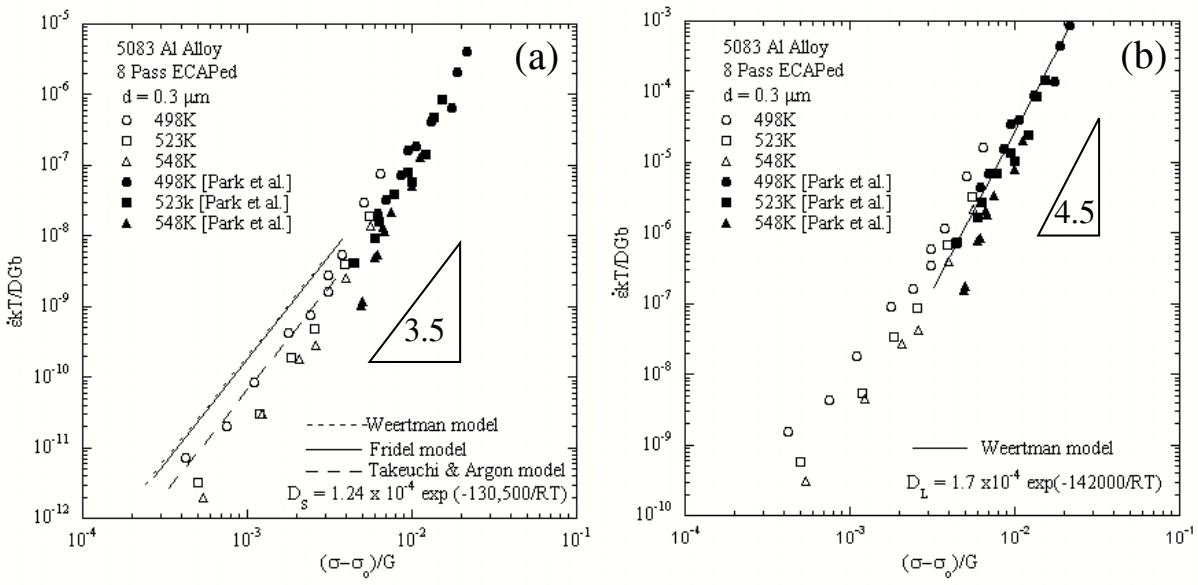

Figure 1.47: Normalised strain rate against normalised stress for UFG Al 5083 between 498 and 548K [112].

1.4.5 Fatigue behaviour

Conflicting results were reported concerning the resistance of UFG Al 5083 to low-cycle fatigue. Sedighi et al. reported lower fatigue lives as compared to CG material (Figure 1.48a), in total strain controlled, with an R ratio of 0.75 [115]. By contrast, Walley et al. did not find any difference in lives between CG and UFG Al 5083, for fully-reversed plastic strain-controlled tests (Figure 1.48b). However, they observed earlier crack initiation and more profuse damage in CG material, and slight grain growth plus a tendency to form sharp macroscopic slip bands in UFG material [116]. The reason why this did not lead to a reduced resistance to fatigue in UFG material thus remained unexplained.

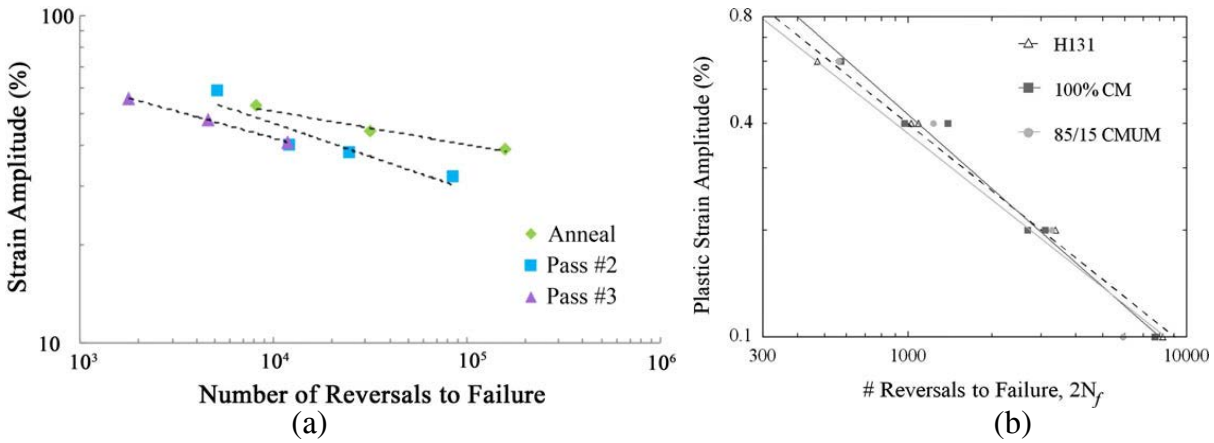

Figure 1.48: (a) LCF behaviour of CG (anneal) and UFG (ECA rolled for 2 or 3 passes) Al 5083 for an R ratio of 0.75 [115], (b) Coffin–Manson plot for CG (H131) and UFG (cryomilled-CM, 85% or 100%) Al 5083 [116].

The push-pull tests run by Walley et al. for CG and UFG (cryomilled) Al5083 alloy revealed a persistent tension-compression asymmetry, the minimum compressive stress remaining higher (by a few %) than the maximum tensile stress (Figure 1.49) [116]. Apart from a short initial softening, due to relaxation of residual stresses, cyclic hardening was observed in UFG material, while the CG material, which was in a strain-hardened condition, did not exhibit any hardening. But the nature of this cyclic hardening (isotropic or kinematic?) which might shed light on its mechanisms was not investigated. This is thus a point that deserves an investigation.

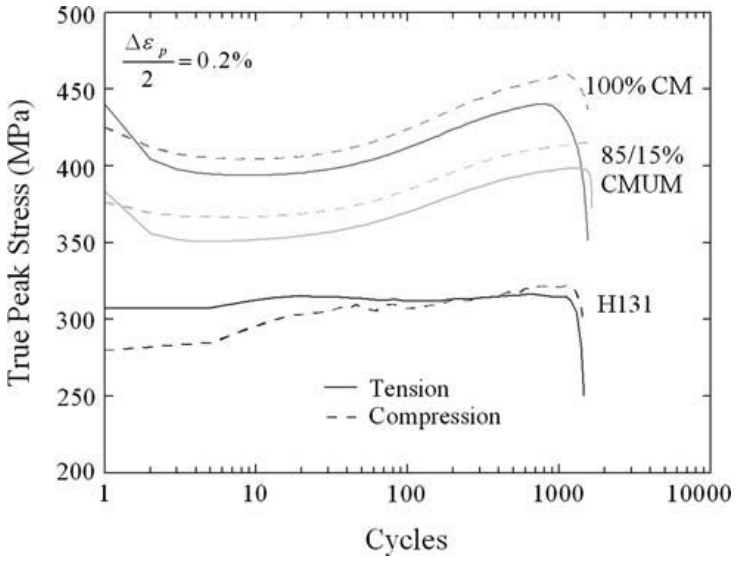

Figure 1.49: Evolutions of tensile and compressive peak stresses during plastic-strain controlled push-pull tests in CG (H131) and UFG (cryomilled-CM) Al 5083 alloys [116].

In HCF regime, Singh et al. found that the S-N curve of UFG Al 5083 stands well above that of its CG counterpart [117] and attributed it mainly to the fragmentation and redistribution of coarse intermetallic particles during the cold and warm rolling

processes used to produce UFG Al 5083 (Figure 1.50).

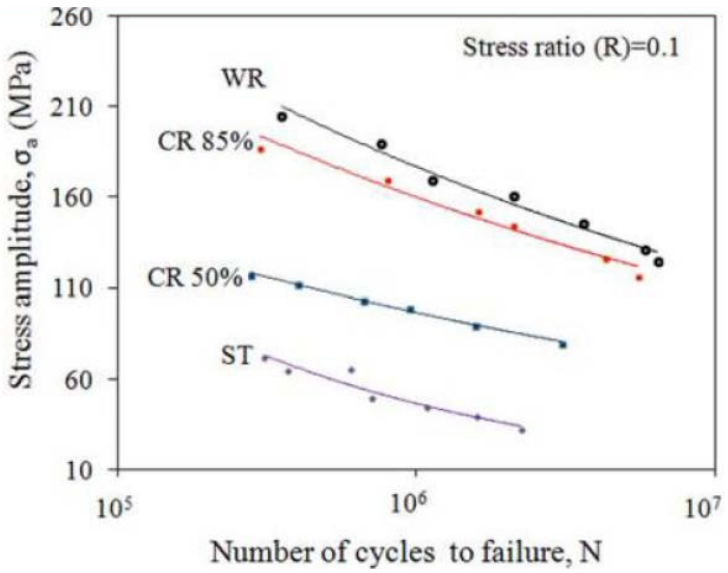

Figure 1.50: HCF behaviour of CG(solution treated, ST) and UFG (cryomilled and cold-rolled, CR) Al5083 alloy for R = 0.1 [117].

None of the above mentioned studies were run on ECAPed materials. Since the resistance to fatigue is quite sensitive to microstructural details, themselves very dependent on the manufacturing process, it is worth investigating the behaviour of ECAPed UFG Al 5083 in LCF and HCF regimes. In addition, no paper from the literature provides any quantitative element about fatigue damage of UFG and CG alloys (micro-cracks density, orientations and lengths) that would allow a more reliable comparison than qualitative elements about "diffuse" or "localized" damage. An effort to provide such quantitative elements was thus made in the present work.

1.5 Open questions

Keeping this background in mind, there are several open question that one can evoke:

- What is the importance of GBS in UFG materials at each stage of deformation ?
- What is the impact of GBS on the stress-strain curves ?
- Is there a threshold stress for GBS and how does it vary with the temperature ?
- What is the effect of GBS on the strain rate sensitivity ?
- What is the influence of microstructural refinement on cyclic plasticity and damage mechanisms ?
- Is the crack growth mechanism similar in CG and UFG materials? Does texture play any role for crack growth ?

- Under what conditions does a UFG material have a better fatigue life than its CG counterpart, and why ?

Such questions will be addressed in forthcoming chapters.

References

[1] V. M. Segal, “Materials processing by simple shear,” *Materials Science and Engineering: A*, vol. 197, pp. 157–164, 1995.

[2] R. Z. Valiev and T. G. Langdon, “Principles of equal-channel angular pressing as a processing tool for grain refinement,” *Progress in Materials Science*, vol. 51, pp. 881–981, 2006.

[3] Y. Iwahashi, J. Wang, Z. Horita, M. Nemoto, and T. G. Langdon, “Principle of equal-channel angular pressing for the processing of ultra-fine grained materials,” *Scripta Materialia*, vol. 35, pp. 143–146, 1996.

[4] A. R. Eivani and A. Karimi Taheri, “An upper bound solution of ECAE process with outer curved corner,” *Journal of Materials Processing Technology*, vol. 182, pp. 555–563, 2007.

[5] L. Dupuy, “Mechanical behavior of an aluminium alloy subjected to severe plastic deformation,” PhD thesis, 2000.

[6] J. R. Bowen, A. Gholinia, S. M. Roberts, and P. B. Prangnell, “Analysis of the billet deformation behaviour in equal channel angular extrusion,” *Materials Science and Engineering A*, vol. 287, pp. 87–99, 2000.

[7] A. Shan, I.-G. Moon, H.-S. Ko, and J.-W. Park, “Direct observation of shear deformation during equal channel angular pressing of pure aluminum,” *Scripta Materialia*, vol. 41, no. 4, pp. 353–357, 1999.

[8] F. Djavanroodi and M. Ebrahimi, “Effect of die channel angle, friction and back pressure in the equal channel angular pressing using 3D finite element simulation,” *Materials Science and Engineering A*, vol. 527, no. 4-5, pp. 1230–1235, 2010.

[9] Z. Horita, T. Fujinami, and T. G. Langdon, “The potential for scaling ECAP: Effect of sample size on grain refinement and mechanical properties,” *Materials Science and Engineering A*, vol. 318, no. 1-2, pp. 34–41, 2001.

[10] R. Lapovok, “Damage evolution under severe plastic deformation,” *International Journal of Fracture*, vol. 115, pp. 159–172, 2002.

[11] V. V. Stolyarov and R. Lapovok, “Effect of backpressure on structure and properties of AA5083 alloy processed by ECAP,” *Journal of Alloys and Compounds*, vol. 378, no. 1-2, pp. 233–236, 2004.

[12] F. Djavanroodi and M. Ebrahimi, “Investigation of Strain Behavior in the Modified Equal Channel Angular Pressing Die by 3D Finite Element Method,” *Journal of Applied Sciences*, vol. 10, no. 20, pp. 2411–2418, Dec. 2010.

[13] J. Papasidero, V. Doquet, and D. Mohr, "Ductile fracture of aluminum 2024-T351 under proportional and non-proportional multi-axial loading: Bao–Wierzbicki results revisited," *International Journal of Solids and Structures*, vol. 69-70, pp. 459–474, 2015.

[14] F. A. Mohamed, "A dislocation model for the minimum grain size obtainable by milling," *Acta Materialia*, vol. 51, pp. 4107–4119, 2003.

[15] T. Morishige, T. Hirata, T. Uesugi, Y. Takigawa, M. Tsujikawa, and K. Higashi, "Effect of Mg content on the minimum grain size of Al-Mg alloys obtained by friction stir processing," *Scripta Materialia*, vol. 64, pp. 355–358, 2011.

[16] K. Edalati, D. Akama, A. Nishio, S. Lee, Y. Yonenaga, and Z. Horita, "Influence of dislocation – solute atom interactions and stacking fault energy on grain size of single-phase alloys after severe plastic deformation using high-pressure torsion," *Acta Materialia*, vol. 69, pp. 68–77, 2014, ISSN: 1359-6454. DOI: 10.1016/j.actamat.2014.01.036. [Online]. Available: http://dx.doi.org/10.1016/j.actamat.2014.01.036.

[17] S. Y. Chang, L. Jung Guk, K. T. Park, S. Dong Hyuk, J. G. Lee, K. T. Park, and D. H. Shin, "Microstructures and mechanical properties of equal channel angular pressed 5083 Al alloy," *Materials Transactions*, vol. 42, pp. 1074–1080, 2001.

[18] S. G. Chowdhury, A. Mondal, J. Gubicza, G. Krállics, and Á. Fodor, "Evolution of microstructure and texture in an ultrafine-grained Al6082 alloy during severe plastic deformation," *Materials Science and Engineering A*, vol. 490, pp. 335–342, 2008.

[19] a. Goloborodko, O. Sitdikov, R. Kaibyshev, H. Miura, and T. Sakai, "Effect of pressing temperature on fine-grained structure formation in 7475 aluminum alloy during ECAP," *Materials Science and Engineering A*, vol. 381, pp. 121–128, 2004.

[20] K. V. Ivanov and E. V. Naidenkin, "Effect of the velocity of equal-channel angular pressing on the formation of the structure of pure aluminum," *Physics of Metals and Metallography*, vol. 106, no. 4, pp. 411–417, 2008.

[21] P. B. Berbon, M. Furukawa, Z. Horita, M. Nemoto, and T. G. Langdon, "Influence of pressing speed on microstructural development in equal-channel angular pressing," *Metallurgical and Materials Transactions A*, vol. 30A, pp. 1989–1997, 1999.

[22] P. N. Fagin, J. O. Brown, T. M. Brown, K. V. Jata, and S. L. Semiatin, "Failure modes during equal channel angular extrusion of aluminum alloy 2024," *Metallurgical and Materials Transactions A*, vol. 32A, pp. 1869–1871, 2001.

[23] J. M. García-Infanta, A. P. Zhilyaev, C. M. Cepeda-Jiménez, O. A. Ruano, and F. Carreño, "Effect of the deformation path on the ductility of a hypoeutectic Al-Si casting alloy subjected to equal-channel angular pressing by routes A, B_A, B_C and C," *Scripta Materialia*, vol. 58, no. 2, pp. 138–141, 2008.

[24] Y. Iwahashi, Z. Horita, M. Nemoto, and T. Langdon, "An investigation of microstructural evolution during equal-channel angular pressing," *Acta Materialia*, vol. 45, no. 11, pp. 4733–4741, 1997.

[25] Y. Iwahashi, Z. Horita, M. Nemoto, and T. G. Langdon, "The process of grain refinement in equal-channel angular pressing," *Acta Materialia*, vol. 46, no. 9, pp. 3317–3331, 1998.

[26] V. V. Stolyarov, Y. Zhu, I. V. Alexandrov, T. C. Lowe, and R. Z. Valiev, "Influence of ECAP routes on the microstructure and properties of pure Ti," *Materials Science and Engineering: A*, vol. 299, no. 1-2, pp. 59–67, 2001.

[27] T. G. Langdon, "The principles of grain refinement in equal-channel angular pressing," *Materials Science and Engineering: A*, vol. 462, no. 1-2, pp. 3–11, 2007.

[28] P. R. Cetlin, M. T. P. Aguilar, R. B. Figueiredo, and T. G. Langdon, "Avoiding cracks and inhomogeneities in billets processed by ECAP," *Journal of Materials Science*, vol. 45, no. 17, pp. 4561–4570, 2010.

[29] M. S. Soliman, E. A. El-Danaf, and A. A. Almajid, "Enhancement of static and fatigue strength of 1050 Al processed by equal-channel angular pressing using two routes," *Materials Science & Engineering A*, vol. 532, pp. 120–129, 2012.

[30] E. Prados, V. Sordi, and M. Ferrante, "Tensile behaviour of an Al–4wt% Cu alloy deformed by equal-channel angular pressing," vol. 503, pp. 68–70, 2009.

[31] W. Liang, L. Bian, G. Xie, W. Zhang, H. Wang, and S. Wang, "Transformation matrix analysis on the shear characteristics in multi-pass ECAP processing and predictive design of new ECAP routes," *Materials Science and Engineering A*, vol. 527, no. 21-22, pp. 5557–5564, 2010.

[32] Z. Horita, D. J. Smith, M. Furukawa, M. Nemoto, R. Z. Valiev, and T. G. Langdon, "An investigation of grain boundaries in submicrometer-grained Al-Mg solid solution alloys using high-resolution electron microscopy," *Journal of Materials Research*, vol. 11, no. 8, 1996.

[33] V. N. Danilenko, D. V. Bachurin, and R. R. Mulyukov, "In-situ measurements of grain rotation during annealing in ultrafine grained aluminum alloy," *Letters on materials*, vol. 4, no. 4, pp. 233–236, 2014.

[34] G. S. Dyakonov, C. F. Gu, L. S. Toth, R. Z. Valiev, and I. P. Semenova, "Microstructure and mechanical properties of continuous equal channel angular pressed Titanium," *IOP Conference Series: Materials Science and Engineering*, vol. 63, p. 012 067, 2014.

[35] X. Sauvage, N. Enikeev, R. Valiev, Y. Nasedkina, and M. Murashkin, "Atomic-scale analysis of the segregation and precipitation mechanisms in a severely deformed Al-Mg alloy," *Acta Materialia*, vol. 72, pp. 125–136, 2014.

[36] T. Fujita, Z. Horita, and T. G. Langdon, "Using grain boundary engineering to evaluate the diffusion characteristics in ultrafine-grained Al – Mg and Al – Zn alloys," *Materials Science & Engineering A*, vol. 371, pp. 241–250, 2004.

[37] I. Sabirov, Y. Estrin, M. R. Barnett, I. Timokhina, and P. D. Hodgson, "Enhanced tensile ductility of an ultra-fine-grained aluminum alloy," *Scripta Materialia*, vol. 58, pp. 163–166, 2008.

[38] I. Sabirov, M. R. Barnett, Y. Estrin, and P. D. Hodgson, "The effect of strain rate on the deformation mechanisms and the strain rate sensitivity of an ultra-fine-grained Al alloy," *Scripta Materialia*, vol. 61, no. 2, pp. 181–184, 2009.

[39] E. Hart, "Theory of the tensile test," *Acta metallurgica*, vol. 15, 1967.

[40] Y. J. Wei and L. Anand, "Grain-boundary sliding and separation in polycrystalline metals: Application to nanocrystalline fcc metals," *Journal of the Mechanics and Physics of Solids*, vol. 52, no. 11, pp. 2587–2616, 2004.

[41] S. Cheng, J. A. Spencer, and W. W. Milligan, "Strength and tension / compression asymmetry in nanostructured and ultrafine-grain metals," *Acta Materialia*, vol. 51, pp. 4505–4518, 2003.

[42] J. E. Carsley, W. W. Milligan, X. H. Zhu, and E. C. Aifantis, "On the failure of pressure sensitive plastic materials. Part II : Comparisns with experiments on ultra-fine grained Fe-10% Cu alloys," *Scripta Materialia*, vol. 36, no. 6, pp. 727–732, 1997.

[43] B. Q. Han, Z. Lee, S. R. Nutt, E. J. Lavernia, and F. A. Mohamed, "Mechanical Properties of An Ultrafine-Grained Al-7 . 5 Pct Mg Alloy," *Metallurgical and Materials Transactions A*, vol. 34A, no. March, 2003.

[44] C. Y. Yu, P. L. Sun, P. W. Kao, and C. P. Chang, "Mechanical properties of submicron-grained aluminum," *Scripta Materialia*, vol. 52, pp. 359–363, 2005.

[45] B. Q. Han, E. J. Lavernia, and F. A. Mohamed, "Mechanical Properties of Iron Processed by Severe Plastic Deformation," *Metallurgical and Materials Transactions A*, vol. 34A, no. 1, pp. 71–83, 2003.

[46] K. Zhou, B. Liu, S. Shao, and Y. Yao, "Molecular dynamics simulations of tension–compression asymmetry in nanocrystalline copper," *Physics Letters A*, vol. 381, no. 13, pp. 1163–1168, Apr. 2017.

[47] E. Gürses and T. El Sayed, "On tension–compression asymmetry in ultrafine-grained and nanocrystalline metals," *Computational Materials Science*, vol. 50, no. 2, pp. 639–644, Dec. 2010.

[48] T. Tsuru, "Origin of tension-compression asymmetry in ultrafine-grained fcc metals," *Phys. Rev. Materials*, vol. 1, p. 033 604, 3 Aug. 2017.

[49] M. Haouaoui, I. Karaman, and H. J. Maier, "Flow stress anisotropy and Bauschinger effect in ultrafine grained copper," *Acta Materialia*, vol. 54, pp. 5477–5488, 2006.

[50] C. Reyes-Ruiz, I. A. Figueroa, C. Braham, J. M. Cabrera, O. Zanellato, S. Baiz, and G. Gonzalez, "Residual stress distribution of a 6061-T6 aluminum alloy under shear deformation," *Materials Science & Engineering A*, vol. 670, pp. 227–232, 2016.

[51] H. H. Lee, K. D. Gangwar, K.-T. Park, W. Woo, and H. S. Kim, "Neutron diffraction and finite element analysis of the residual stress distribution of copper processed by equal-channel angular pressing," *Materials Science & Engineering A*, vol. 682, pp. 691–697, 2017.

[52] Y. Li, X. Zeng, and W. Blum, "Transition from strengthening to softening by grain boundaries in ultrafine-grained Cu," *Acta Materialia*, vol. 52, no. 17, pp. 5009–5018, Oct. 2004.

[53] R. Kapoor, J. B. Singh, and J. K. Chakravartty, "High strain rate behavior of ultrafine-grained Al-1.5 Mg," *Materials Science and Engineering A*, vol. 496, no. 1-2, pp. 308–315, 2008.

[54] Y. Furukawa, T. Fujii, S. Onaka, and M. Kato, "Cyclic Deformation Behavior of Ultra-Fine Grained Copper Produced by Equal Channel Angular Pressing," *Materials Transactions*, vol. 50, no. 1, pp. 70–75, 2009.

[55] H. Mughrabi and H. W. Höppel, "Cyclic deformation and fatigue properties of very fine-grained metals and alloys," *International Journal of Fatigue*, vol. 32, pp. 1413–1427, 2010.

[56] P. Cavaliere, "Fatigue properties and crack behavior of ultra-fine and nanocrystalline pure metals," *International Journal of Fatigue*, vol. 31, pp. 1476–1489, 2009.

[57] Y. Estrin and A. Vinogradov, "Fatigue behaviour of light alloys with ultrafine grain structure produced by severe plastic deformation : An overview," *International Journal of Fatigue*, vol. 32, pp. 898–907, 2010.

[58] T. Niendorf, F. Rubitschek, H. J. Maier, D. Canadinc, and I. Karaman, "On the fatigue crack growth-microstructure relationship in ultrafine-grained interstitial-free steel," *Journal of Materials Science*, vol. 45, no. 17, pp. 4813–4821, 2010.

[59] T. Zhai, X. P. Jiang, J. X. Li, M. D. Garratt, and G. H. Bray, "The grain boundary geometry for optimum resistance to growth of short fatigue cracks in high strength Al-alloys," *International Journal of Fatigue*, vol. 27, no. 10-12, pp. 1202–1209, 2005.

[60] G. Bertolino, V. Doquet, and M. Sauzay, "Modelling of the scatter in short fatigue cracks growth kinetics in relation with the polycrystalline microstructure," *International Journal of Fatigue*, vol. 27, pp. 471–480, 2005.

[61] F. Crossman and M. Ashby, "The non-uniform flow of polycrystals by grain-boundary sliding accommodated by power-law creep," *Acta Metallurgica*, vol. 23, pp. 425–440, 1975.

[62] M. F. Ashby and R. A. Verrall, "Diffusion-accommodated flow and superplasticity," *Acta Metallurgica*, vol. 21, 1973.

[63] R. Raj and M. F. Ashby, "On grain boundary sliding and diffusional creep," *Metallurgical Transactions*, vol. 2, no. 4, pp. 1113–1127, 1971.

[64] J. Koike, R. Ohyama, T. Kobayashi, M. Suzuki, and K. Maruyama, "Grain-Boundary Sliding in AZ31 Magnesium Alloys at Room Temperature to 523 K," *Materials Transactions*, vol. 44, no. 4, pp. 445–451, 2003.

[65] K. Yang, H.-J. Fecht, and Y. Ivanisenko, "First Direct In Situ Observation of Grain Boundary Sliding in Ultra fi ne Grained Noble Metal," *Advanced Engineering Materials*, vol. 16, no. 5, pp. 517–521, 2014.

[66] T. Matsunaga and E. Sato, "Estimation of grain boundary sliding during ambient-temperature creep in hexagonal close-packed metals using atomic force microscope," in *Scanning Probe Microscopy*, V. Nalladega, Ed., Rijeka: IntechOpen, 2012, ch. 9.

[67] A. Soula, Y. Renollet, D. Boivin, J. Pouchou, D. Locq, P. Caron, and Y. Bréchet, "Analysis of high-temperature creep deformation in a polycrystalline nickel-base superalloy," *Materials Science & Engineering A*, vol. 511, pp. 301–306, 2009.

[68] R. L. Bell and T. G. Langdon, "An investigation of grain boundary sliding during creep," *Journal of Materials Science*, vol. 2, 1967.

[69] R. C. Gifkins, A. Gittins, R. L. Bell, and T. G. Langdon, "The dependence of grain boundary sliding on shear stress," *Journal of Materials Science*, vol. 3, pp. 306–313, 1968.

[70] R. L. Bell, C. Graeme-Barber, and T. G. Langdon, "The contribution of grain boundary sliding to the overall strain of a polycrystal," *Transactions of the metallurgical society of aime*, vol. 239, 1967.

[71] L. Clarisse, A. Bataille, Y. Pennec, J. Crampon, and R. Duclos, "Investigation of grain boundary sliding during superplastic deformation of a fine-grained alumina by atomic force microscopy," *Ceramics International*, vol. 25, pp. 389–394, 1999.

[72] J. H. Han and F. A. Mohamed, "Quantitative Measurements of Grain Boundary Sliding in an Ultrafine-Grained Al Alloy by Atomic Force Microscopy," *Metallurgical and Materials Transactions A*, vol. 42A, pp. 3969–3978, 2011.

[73] K. V. Ivanov and E. V. Naydenkin, "Tensile behavior and deformation mechanisms of ultrafine-grained aluminum processed using equal-channel angular pressing," *Materials Science and Engineering A*, vol. 606, pp. 313–321, 2014.

[74] M. Chauhan, I. Roy, and F. A. Mohamed, "High-strain-rate superplasticity in bulk cryomilled ultra-fine-grained 5083 Al," *Metallurgical and Materials Transactions A*, vol. 37A, no. 9, pp. 2715–2725, 2006.

[75] S. V. Bobylev, A. K. Mukherjee, and I. A. Ovid'Ko, "Transition from plastic shear into rotation deformation mode in nanocrystalline metals and ceramics," *Reviews on Advanced Materials Science*, vol. 19, pp. 103–113, 2009.

[76] Y. Ivanisenko, E. D. Tabachnikova, I. A. Psaruk, S. N. Smirnov, and A. Kilmametov, "Variation of the deformation mechanisms in a nanocrystalline Pd – 10 at .% Au alloy at room and cryogenic temperatures," *International Journal of Plasticity*, vol. 60, pp. 40–57, 2014.

[77] E. Izadi, A. Darbal, R. Sarkar, and J. Rajagopalan, "Grain rotations in ultra fi ne-grained aluminum fi lms studied using in situ TEM straining with automated crystal orientation mapping," *Materials and design*, vol. 113, pp. 186–194, 2017.

[78] N. I. Noskova and E. G. Volkova, "In situ Investigations of deformation in nanocrystalline Fe73.5Cu1Nb3Si13.5B9 alloy," *The Physics of Metals and Metallography*, vol. 92, no. 10, pp. 421–425, 2001.

[79] W. Milligan, S. Hackney, M. Ke, and E. Aifantis, "In situ studies of deformation and fracture in nanophase materials," *Nanostructured Materials*, vol. 2, no. 3, pp. 267–276, May 1993.

[80] F. Mompiou and M. Legros, "Quantitative grain growth and rotation probed by in-situ TEM straining and orientation mapping in small grained Al thin films," *Scripta Materialia*, vol. 99, pp. 5–8, 2015.

[81] I. Sabirov, Y. Estrin, M. R. Barnett, I. Timokhina, and P. D. Hodgson, "Tensile deformation of an ultrafine-grained aluminium alloy : Micro shear banding and grain boundary sliding," *Acta Materialia*, vol. 56, pp. 2223–2230, 2008.

[82] B. Ahn and S. R. Nutt, "Strain Mapping of Al – Mg Alloy with Multi-scale Grain Structure using Digital Image Correlation Method," *Experimental Mechanics*, vol. 50, pp. 117–123, 2010.

[83] A. D. Kammers, J. Wongsa-Ngam, T. G. Langdon, and S. Daly, "The effect of microstructure heterogeneity on the microscale deformation of ultrafine-grained aluminum," *Journal of Materials Research*, vol. 29, 2014.

[84] Y. Zhang, T. D. Topping, E. J. Lavernia, and S. R. Nutt, "Dynamic Micro-strain Analysis of Ultrafine-grained Aluminum Magnesium alloy using Digital Image Correlation," *Metallurgical and Materials Transactions A*, vol. 44A, no. 6, pp. 1–23, 2013.

[85] A. D. Kammers, J. Wongsa-Ngam, T. G. Langdon, and S. Daly, "The microstructure length scale of strain rate sensitivity in ultrafine-grained aluminum," *Journal of Materials Research*, vol. 30, no. 7, pp. 981–992, 2015.

[86] R.-Y. Chen, H.-Y. Chu, C.-C. Lai, and C.-T. Wu, "Effects of annealing temperature on the mechanical properties and sensitization of 5083-H116 aluminum alloy," *Journal of Materials Design and Applications*, vol. 229, no. 4, pp. 339–346, 2015.

[87] N. Llorca-Isern, C. Luis Pérez, P. A. González, L. Laborde, and D. Pati, "Analysis of Structure and Mechanical Properties of Aa 5083 Aluminium Alloy Processed By Ecae," *Reviews on Advanced Materials Science*, vol. 10, pp. 473–478, 2005.

[88] L. Dupuy, J. J. Blandin, and E. F. Rauch, "Structural and mechanical properties in AA 5083 processed by ECAE," *Materials Science and Technology*, vol. 16, no. 11-12, pp. 1256–1258, 2000.

[89] D. B. Witkin and E. J. Lavernia, "Synthesis and mechanical behavior of nanostructured materials via cryomilling," *Progress in Materials Science*, vol. 51, no. 1, pp. 1–60, 2006.

[90] H. Hasegawa, S. Komura, A. Utsunomiya, Z. Horita, M. Furukawa, M. Nemoto, and T. G. Langdon, "Thermal stability of ultrafine-grained aluminum in the presence of Mg and Zr additions," *Materials Science & Engineering A*, vol. 265, pp. 188–196, 1999.

[91] Y. S. Sato, M. Urata, H. Kokawa, and K. Ikeda, "Hall-Petch relationship in friction stir welds of equal channel angular-pressed aluminium alloys," *Materials Science and Engineering A*, vol. 354, pp. 298–305, 2003.

[92] E. L. Huskins, B. Cao, and K. T. Ramesh, "Strengthening mechanisms in an Al-Mg alloy," *Materials Science and Engineering A*, vol. 527, no. 6, pp. 1292–1298, 2010.

[93] D. J. Lloyd and S. A. Court, "Influence of grain size on tensile properties of Al-Mg alloys," *Materials Science and Technology*, vol. 19, no. 10, pp. 1349–1354, 2003.

[94] L. Dupuy, J. J. Blandin, and E. F. Rauch, "Microstructure and high temperature deformation of an ECAE processed 5083 Al alloy," *Materials Science Forum*, vol. 357-359, pp. 437–442, 2001.

[95] H. Ait-Amokhtar, S. Boudrahem, and C. Fressengeas, "Spatiotemporal aspects of jerky flow in Al-Mg alloys, in relation with the Mg content," *Scripta Materialia*, vol. 54, no. 12, pp. 2113–2118, 2006.

[96] H. Jiang, Q. Zhang, X. Chen, Z. Chen, Z. Jiang, X. Wu, and J. Fan, "Three types of Portevin – Le Chatelier effects : Experiment and modelling," *Acta Materialia*, vol. 55, pp. 2219–2228, 2007.

[97] T. A. Lebedkina and M. A. Lebyodkin, "Effect of deformation geometry on the intermittent plastic flow associated with the Portevin – Le Chatelier effect," *Acta Materialia*, vol. 56, no. 19, pp. 5565–5572, 2008.

[98] H. Ait-Amokhtar and C. Fressengeas, "Crossover from continuous to discontinuous propagation in the Portevin-Le Chatelier effect," *Acta Materialia*, vol. 58, no. 4, pp. 1342–1349, 2010.

[99] O. Andreau, J. Gubicza, N. X. Zhang, Y. Huang, P. Jenei, and T. G. Langdon, "Effect of short-term annealing on the microstructures and fl ow properties of an Al – 1 % Mg alloy processed by high-pressure torsion," *Materials Science & Engineering A*, vol. 615, pp. 231–239, 2014.

[100] T. A. Lebedkina, M. A. Lebyodkin, T. T. Lamark, M. Janecek, and Y. Estrin, "Effect of equal channel angular pressing on the Portevin – Le Chatelier effect in an Al3Mg alloy," *Materials Science & Engineering A*, vol. 615, pp. 7–13, 2014.

[101] M. A. Muñoz-Morris, C. G. Oca, and D. G. Morris, "Mechanical behaviour of dilute Al – Mg alloy processed by equal channel angular pressing," *Scripta Materialia*, vol. 48, pp. 213–218, 2003.

[102] A. Mogucheva, D. Yuzbekova, R. Kaibyshev, T. Lebedkina, and M. Lebyodkin, "Effect of Grain Refinement on Jerky Flow in an Al-Mg-Sc Alloy," *Metallurgical and Materials Transactions A*, 2016.

[103] M. Komarasamy and R. S. Mishra, "Serration behavior and shear band characteristics during tensile deformation of an ultrafine-grained 5024 Al alloy Materials Science & Engineering A Serration behavior and shear band characteristics during tensile deformation of an ultra fi ne-grained 5024 Al alloy," *Materials Science & Engineering A*, vol. 616, no. October, pp. 189–195, 2014.

[104] S. P. Joshi, C. Eberl, B. Cao, and K. T. Ramesh, "On the Occurrence of Portevin – Le Châtelier Instabilities in Ultrafine-Grained 5083 Aluminum Alloys," pp. 207–218, 2009.

[105] K. Kaneko, T. Hata, T. Tokunaga, and Z. Horita, "Fabrication and Characterization of Supersaturated Al-Mg Alloys by Severe Plastic Deformation and Their Mechanical Properties," *Materials Transactions*, vol. 50, no. 1, pp. 76–81, 2009.

[106] W. A. Soer, A. R. Chezan, and J. T. M. De Hosson, "Deformation and reconstruction mechanisms in coarse-grained superplastic Al – Mg alloys," *Acta Materialia*, vol. 54, pp. 3827–3833, 2006.

[107] R. Verma, A. K. Ghosh, S. Kim, and C. Kim, "Grain refinement and superplasticity in 5083 Al," *Materials Science & Engineering A*, vol. 191, pp. 143–150, 1995.

[108] Y. G. Ko, D. H. Shin, K. T. Park, and C. S. Lee, "Superplastic deformation behavior of ultra-fine-grained 5083 Al alloy using load-relaxation tests," *Materials Science and Engineering A*, vol. 448-451, pp. 756–760, 2007.

[109] M. Chauhan, I. Roy, and F. A. Mohamed, "Creep behavior in near-nanostructured Al 5083 alloy," *Materials Science and Engineering A*, vol. 410-411, pp. 24–27, 2005.

[110] K. T. Park, H. J. Lee, C. S. Lee, B. D. Ahn, H. S. Cho, and D. H. Shin, "Effect of ECAP strain on deformation behavior at low temperature superplastic regime of ultrafine grained 5083 Al alloy fabricated by ECAP," *Materials Transactions*, vol. 45, no. 3, pp. 958–963, 2004.

[111] O. D. Sherby and E. M. Taleff, "Influence of grain size, solute atoms and second-phase particles on creep behavior of polycrystalline solids," *Materials Science and Engineering A*, vol. 322, no. 1-2, pp. 89–99, 2002.

[112] H.-K. Kim, "Low-temperature creep behavior of ultrafine-grained 5083 Al alloy processed by equal-channel angular pressing," *Journal of mechanical science and technology*, vol. 24, no. 10, pp. 2075–2081, 2010.

[113] R. Kaibyshev, F. Musin, E. Avtokratova, and Y. Motohashi, "Deformation behavior of a modified 5083 aluminum alloy," *Materials Science & Engineering A*, vol. 392, pp. 373–379, 2005.

[114] I. C. Hsiao and J. C. Huang, "Deformation mechanisms during low-and high-temperature superplasticity in 5083 Al-Mg alloy," *Metallurgical and Materials Transactions A*, vol. 33, no. 5, pp. 1373–1384, 2002.

[115] M. Sedighi, P. Monshi, and J. Joudaki, "Investigation of mechanical properties and fatigue life of ECARed AA5083 aluminium alloy," *Fatigue & Fracture of Engineering Materials & Structures*, vol. 40, pp. 412–422, 2017.

[116] J. L. Walley, E. J. Lavernia, and J. C. Gibeling, “Low-Cycle Fatigue of Ultra-Fine-Grained Cryomilled 5083 Aluminum Alloy,” *Metallurgical and Materials Transactions A*, vol. 40A, 2009.

[117] D. Singh, P. N. Rao, and J. Rengaswamy, “High cycle fatigue behaviour of Ultra-fine grained Al 5083 alloy,” *Materials Science and Technology*, vol. 000, 2014.

Chapter 2

Investigated Materials

Two different batches of Al5083 alloy were used. For the sake of simplicity, we will call them batch-A and B respectively. The measured composition of the materials is presented in table 2.1.

Composition	**Weight percent**	
	Batch-A	Batch-B
Magnesium	5.2	4.6
Iron	0.24	0.36
Copper	-	0.16
Manganese	0.45	0.46
Silicon	0.27	0.22
Chromium	0.09	0.15
Aluminium	Balance	Balance

Table 2.1: Composition of the two batches of Al5083 alloy measured with EDS

To analyse the microstructure of the observed materials, the sample surface is first mechanically polished using 800-4000 grit SiC papers and later electro-polished at 17 V for 35s using A2 electrolyte. The electrolyte was always kept in an ice bath to avoid heating during electro-polishing. Philips Quanta 600 ESEM, with a Field emission gun and a large chamber to accommodate small testing machines was used to capture images of the polished specimens. For EBSD and EDS, AZtec HKL software by Oxford Instruments was used. The grain detection angle was fixed at 10° for all the analysed materials. The dislocation density and the percentage of high angle grain boundaries (HAGB) i.e. with a misorientation >15° and low angle grain boundaries(LAGB) i.e. <15° were calculated using the ATOM software developed at LEM3, Metz

2.1 Coarse-grained (CG) materials

Batch A CG Al5083 was obtained in the form of an as-cast, milled and annealed plate of thickness 20 mm. Figure 2.1 shows the BSE high contrast image of the polished section normal to the plate thickness. This material contains large equiaxed grains with grain size ranging from 10 to 250 μm, with a mean value of 93 μm (Figure 2.2). It also contains a high amount of large (equivalent diameter $\sim 11.4 \pm 6$ μm), dendritic, intermetallic particles which are mostly present at grain boundaries. No preferential alignment was observed for these second phase particles.

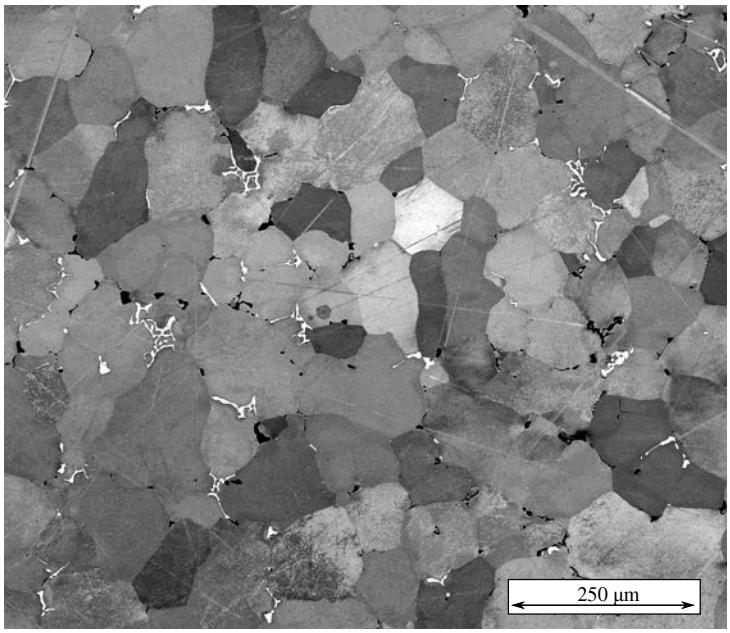

Figure 2.1: BSE image of section normal to the CG-A plate thickness

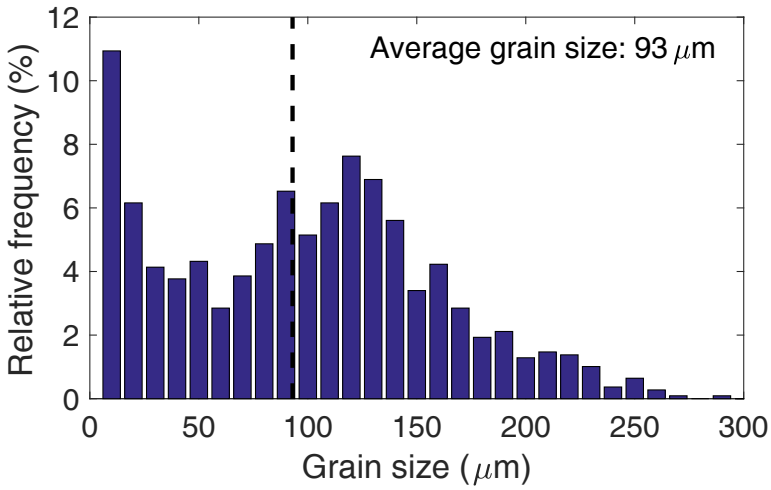

Figure 2.2: Grain-size distribution of CG-A specimen calculated from the elliptical fits using EBSD software (same for transverse and longitudinal section).

EDS reveals that the black coloured particles (see figure 2.3) are rich in Mg and Si while white coloured particles contains mostly Fe, Mn and Al (Figure 2.4).

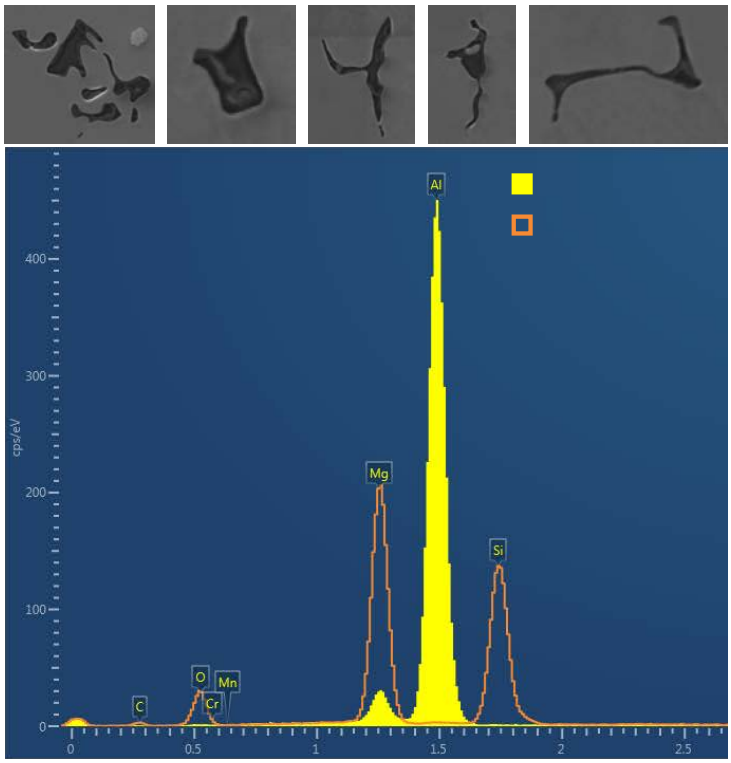

Figure 2.3: Spectrometry of black second phase particles

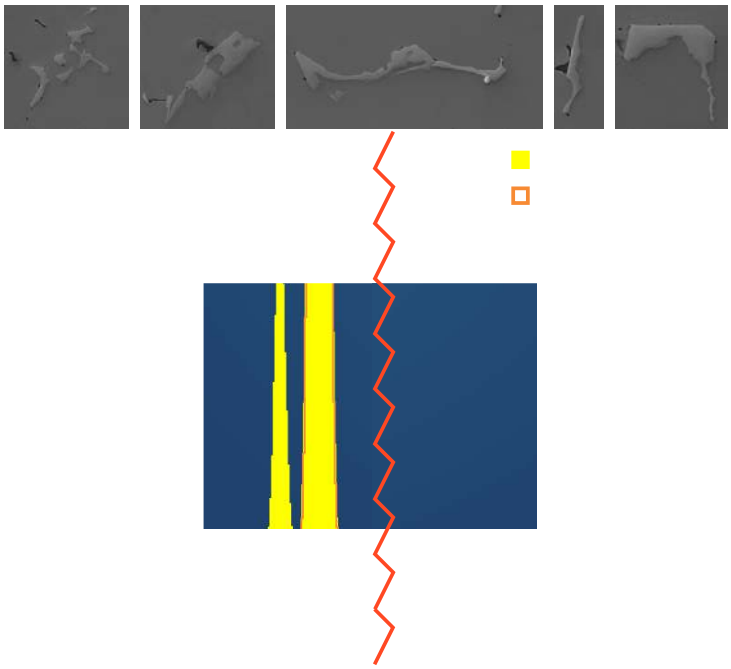

Figure 2.4: Spectrometry of white second phase particles

Figure 2.5 presents a magnified BSE image of the material. Rod-shaped dispersoids of length 144 ± 65 nm and width 71 ± 28 nm were observed. These dispersoids are not necessarily located at the grain boundaries, but are distributed uniformly in some areas (mean spacing $\sim$690 nm) while some regions are completely devoid of them. Various evidences of such nano dispersoids are found in literature [1]–[3], where their chemical composition is identified as Al_6(Fe, Mn) containing small amounts of Cr.

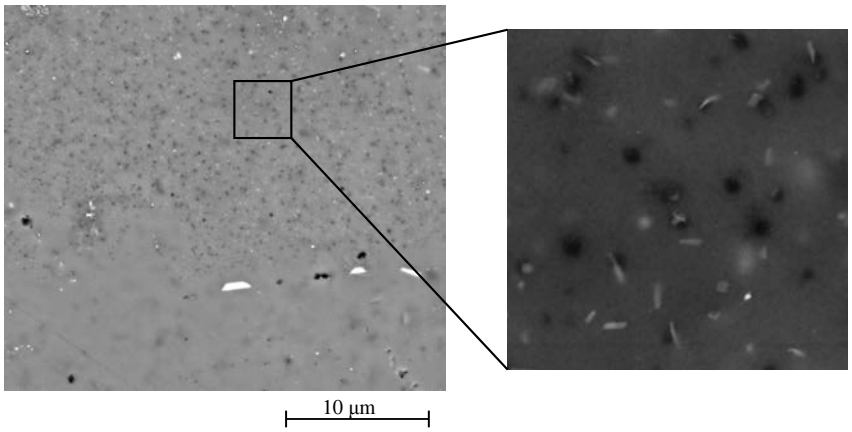

Figure 2.5: Nanoscale dispersoids in CG-A material

EBSD was done on a $\sim$10 mm^2 area (containing approx. 1000 grains) of the lateral and the normal section of the plate with a step size of 2 μm. The obtained "All-Euler" maps and corresponding pole figures are shown in figures 2.6, 2.7 and 2.8. The CG-A material is isotropic and texture-free.

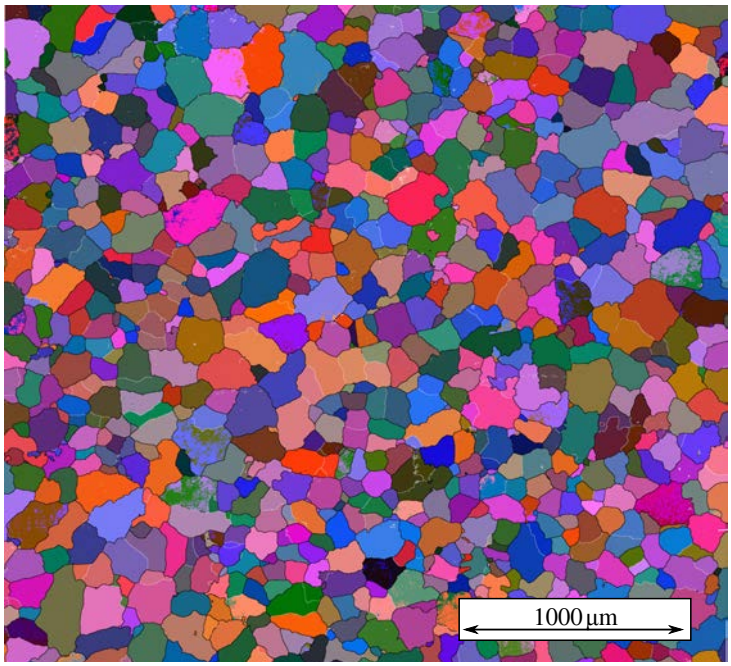

Figure 2.6: Microstructure of CG-A material perpendicular to the plate normal

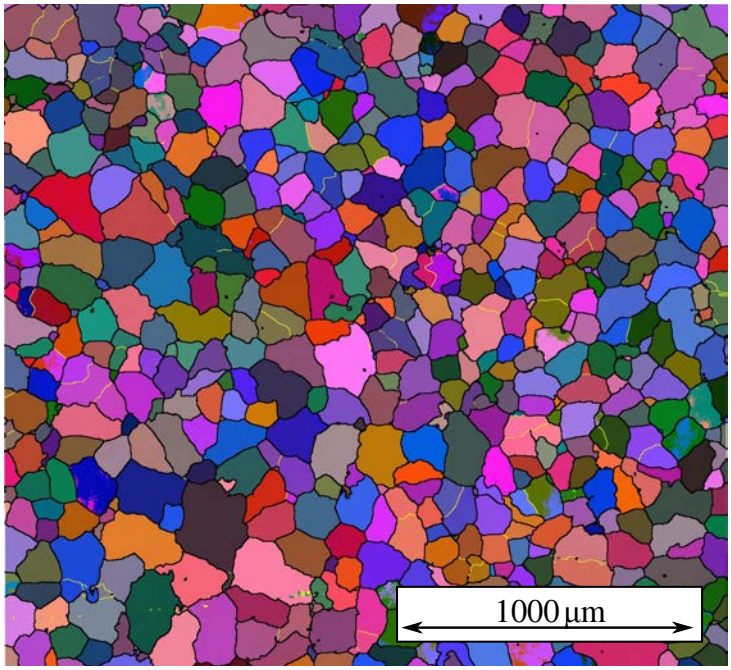

Figure 2.7: Microstructure of CG-A material on a longitudinal section of the plate

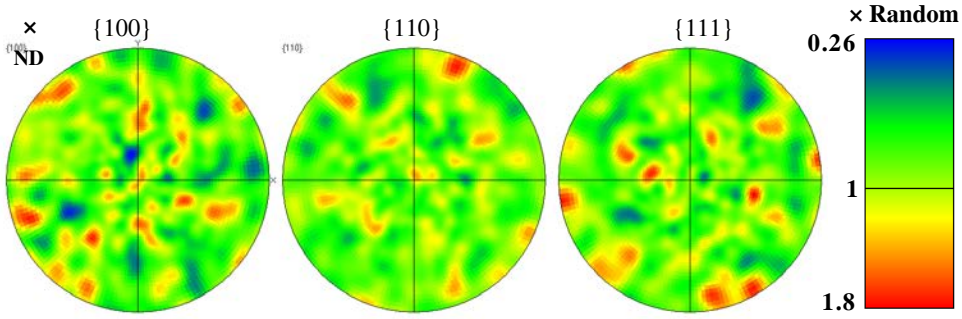

Figure 2.8: Pole figures of CG-A materials

Batch B CG Al5083 material was received in the form of a 20 mm diameter extruded bar in the H112 condition, that is: annealed and then slightly strain hardened. Figures 2.9a,b show the EBSD maps of $\sim$0.75 mm^2 area (containing nearly 2000 - 3000 grains each) of the planes perpendicular and parallel to the bar axis respectively. Step size for EBSD was 0.7 μm. Grains are almost equiaxed in the plane normal to the axis with non-equillibrium grain boundaries (wavy in shape). The grain size is quite heterogeneous (Figure 2.9c. It ranges from 4 to 90 μm, with a mean value of 17 μm in transverse section. The grains are elongated along the bar axis (with aspect ratio as high as 8 for some grains). The distribution of their intercepts along bar axis is presented in figure 2.9d. Grain length as long as 150 μm were observed with a mean value of 35 μm. The dislocation density was estimated to be 3.6×10^{13} m^{-2}.

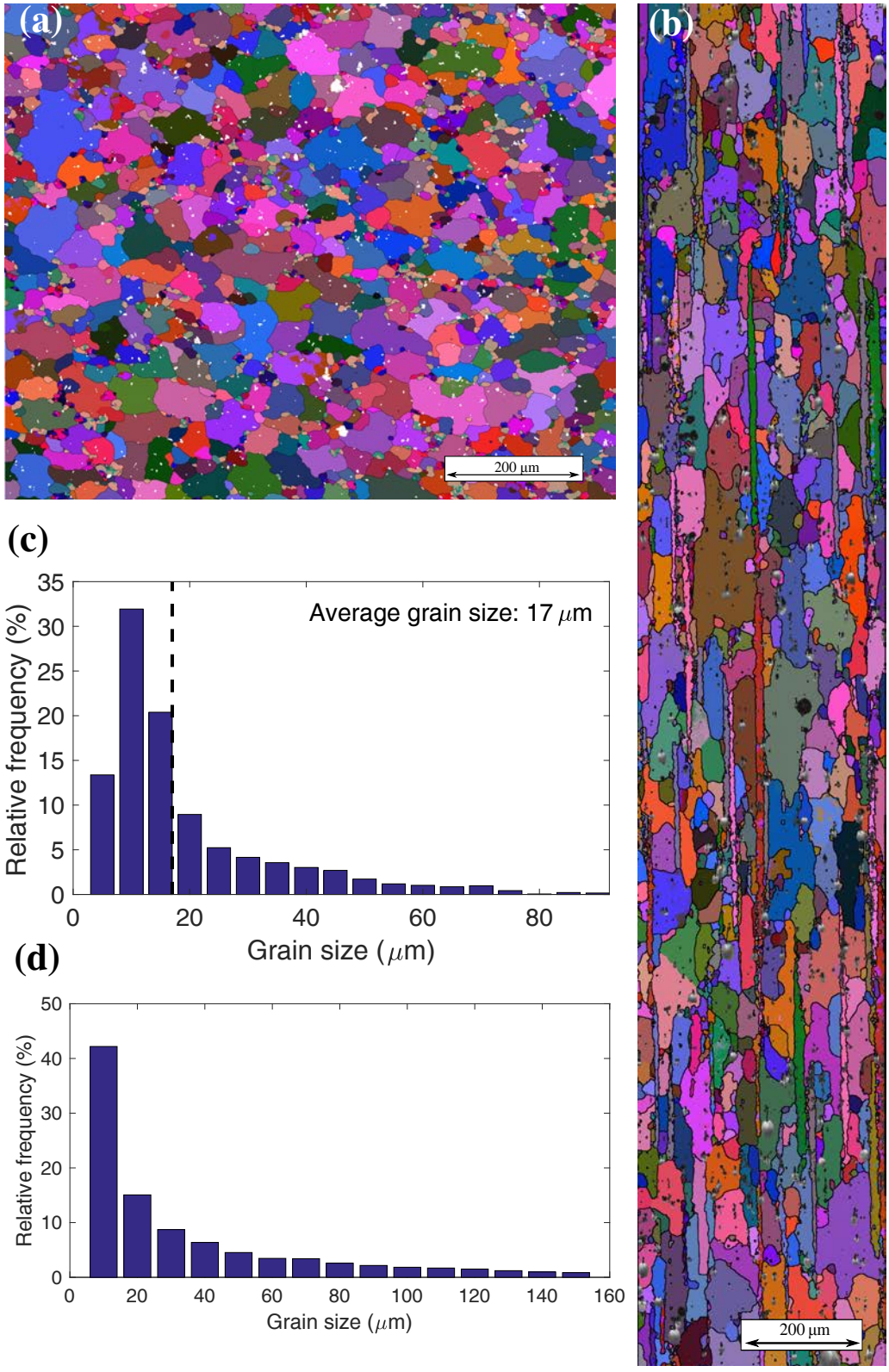

Figure 2.9: "All-Euler" maps of (a) transverse section and (b) longitudinal section of CG-B material, its grain-size distribution (c) on the transverse section and (d) distribution of grain intercepts along bar axis.

BSE contrast image is shown in figure 2.10. Rows of broken second phase particles with size ranging from 500 nm to 9 μm are observed along the bar axis. Manganese and chromium segregation bands parallel to bar axis seem to exist, in which region 1, covered with small white particles is enriched with those elements, compared to region 2, where these particles are less numerous as illustrated by figure 2.11. The second phase particles for this material have the same chemical composition as in batch A CG material. The presence of nanoscale (35 ± 1.3 nm) rod shaped dispersoids is observed in for this material as well (Figure 2.12).

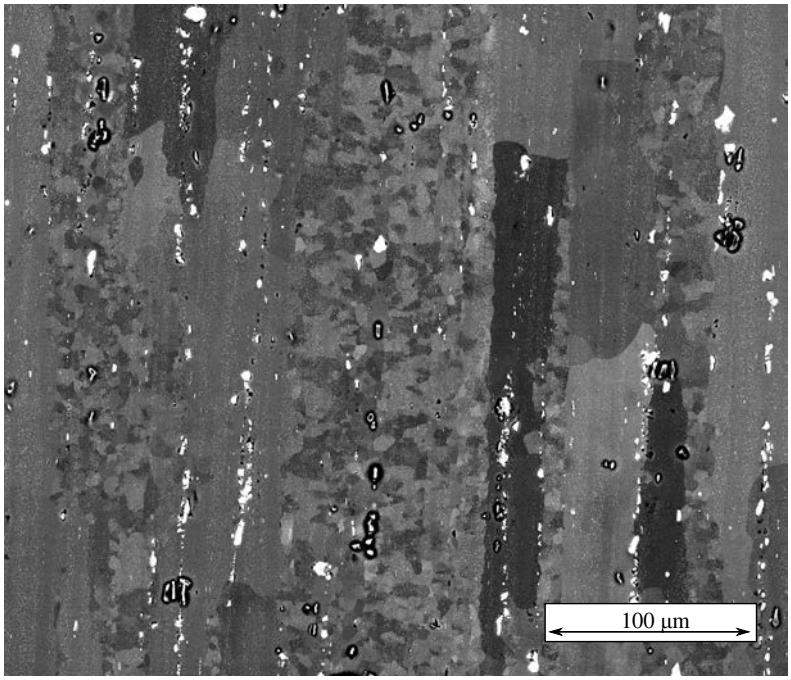

Figure 2.10: BSE-SEM image of CG-B material parallel to bar axis

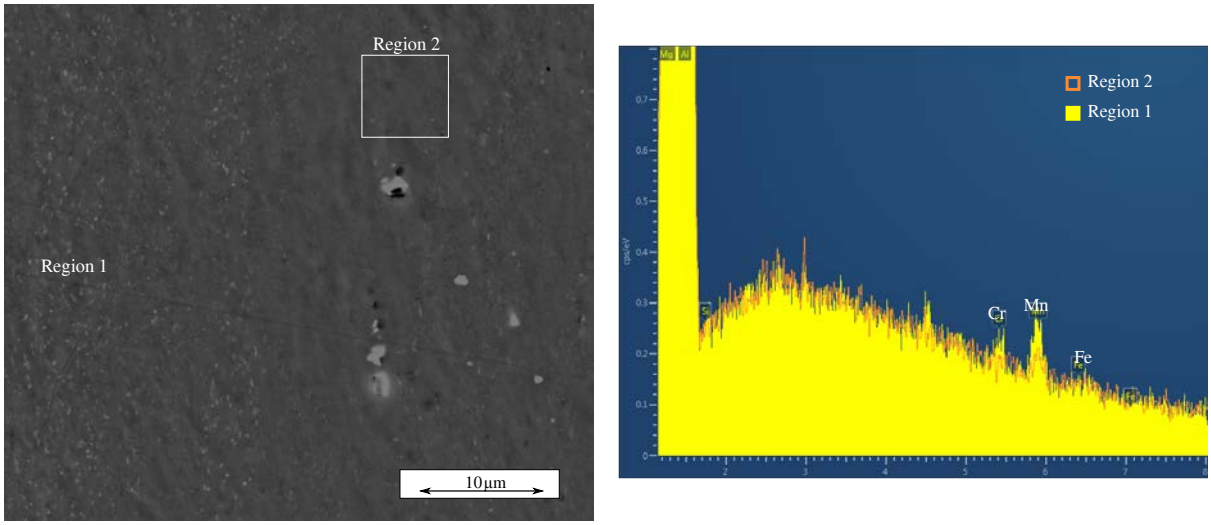

Figure 2.11: EDS analysis of different regions in CG-B material

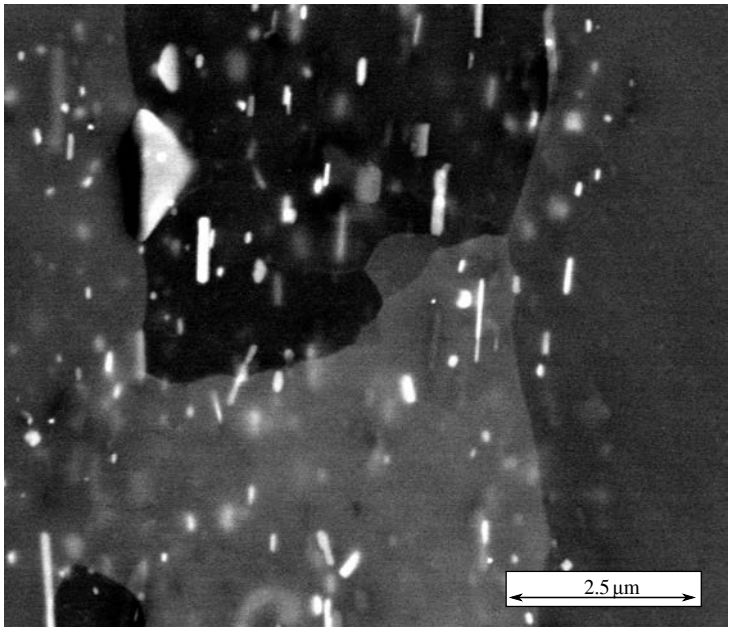

Figure 2.12: BSE-SEM image of CG-B material parallel to bar axis

Pole figures for the analysed microstructure are presented in figure 2.13. The texture is strong and fibres <111> and <100> can be identified in accordance with the literature ([4], [5]).

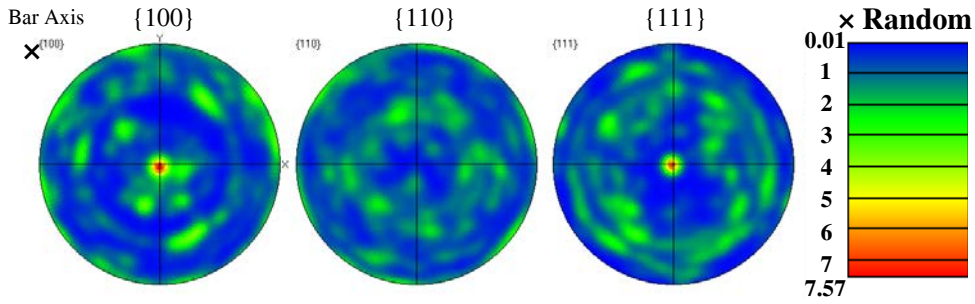

Figure 2.13: Pole figures of CG-B materials

2.2 Grain refinement by ECAP

At the beginning of this work, the ECAP facility at LMS was not yet operational. ECAP specimens (20×20×105 mm) from batch A CG material were produced with the assistance of Dr. Jean-Jacques Fundenberger using the ECAP facility at LEM3, Metz (Figure 2.14). ECAP was done following route C at room temperature with a pressing speed of ∼5 mm/s and a back pressure of ∼ 60 MPa, using a lubricant (MolyDuval Paste Z). Due to the lack of ductility of the material at RT, only 3 ECAP passes could be achieved without deep cracking (Figure 2.15).

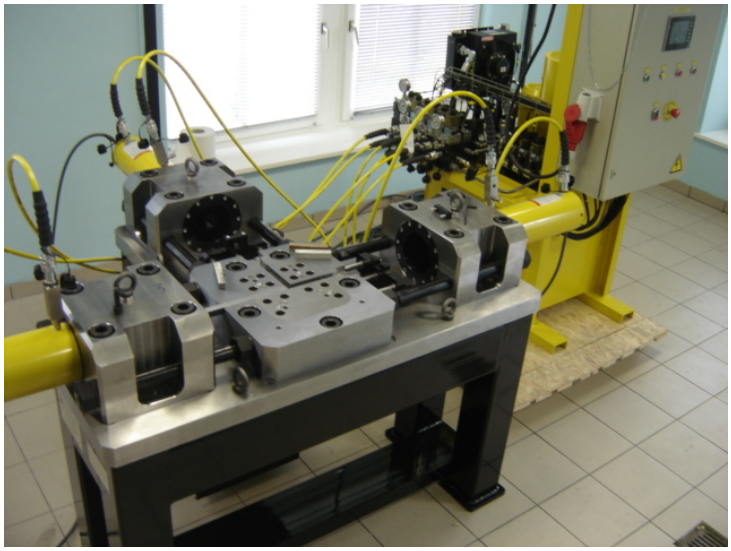

Figure 2.14: ECAP facility at LEM3, Metz

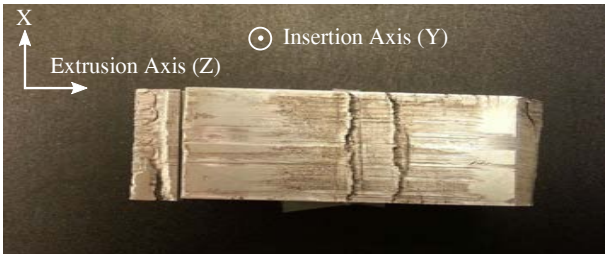

Figure 2.15: Specimen after 3 ECAP passes

Figure 2.16 presents the Vickers hardness of batch A UFG specimens with increasing number of passes. To measure the Vickers micro-hardness, 500 g was applied for 20 s and atleast 5 measurements were made to get an averaged value. The hardness was measured near the center of a transverse section of the ECAPed specimens.

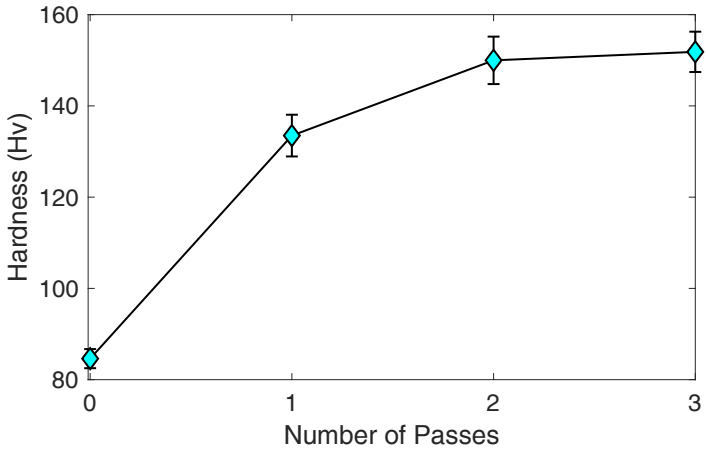

Figure 2.16: Hardness of batch-A material as a function of number of ECAP passes following route C, at room temperature

The hardness of the material nearly doubles after 2 passes but reaches a stable value after the 3rd pass. To analyse the thermal stability of UFG-A material after the 3rd ECAP pass, the material was annealed at different temperatures and its hardness was measured and plotted as a function of the annealing time (Figure 2.17). A sharp decrease in hardness after 3 hours of annealing at 300 and 400°C indicates grain growth. However after annealing at 200°C, the change in hardness is approximately 10%, and a stable value is obtained with further annealing, indicating a stable microstructure with limited grain growth (also observed from EBSD maps). In consequence, such an annealing treatment was always performed before microstructural and mechanical characterization of UFG-A material.

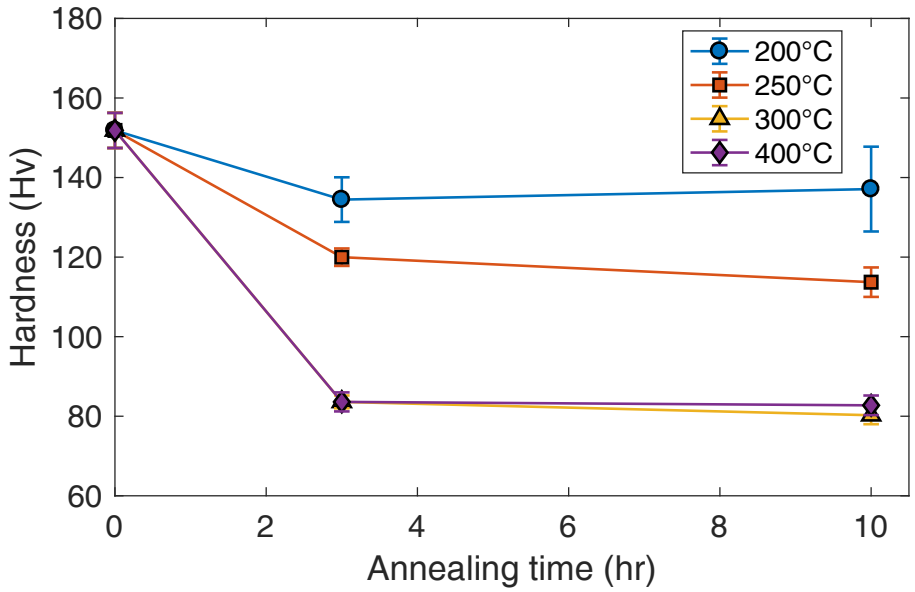

Figure 2.17: Hardness near the center of a transverse section as a function of annealing time at different temperatures for UFG-A after 3 ECAP passes

Batch B materials were processed using the ECAP die equipped with heating elements developed at LMS to process cylindrical specimens of diameter 20 mm (Figure 2.18). The samples were 100 mm long and lubricated with Omega 99 lubrificant. The exit channel diameter was reduced to 19.5 mm to apply some back pressure, at least during the first passes, for which the diameter of the samples is still higher than 19.5 mm. ECAP was done following route Bc at 150°C with a pressing speed of 0.1 mm/s until 6 passes (Figure 2.19). After that, severe cracking occured. An attempt to add two more passes at 200°C was made without damage, but the improvement in the homogeneity of the microstructure was found insufficient to justify the extra processing time.

(a)

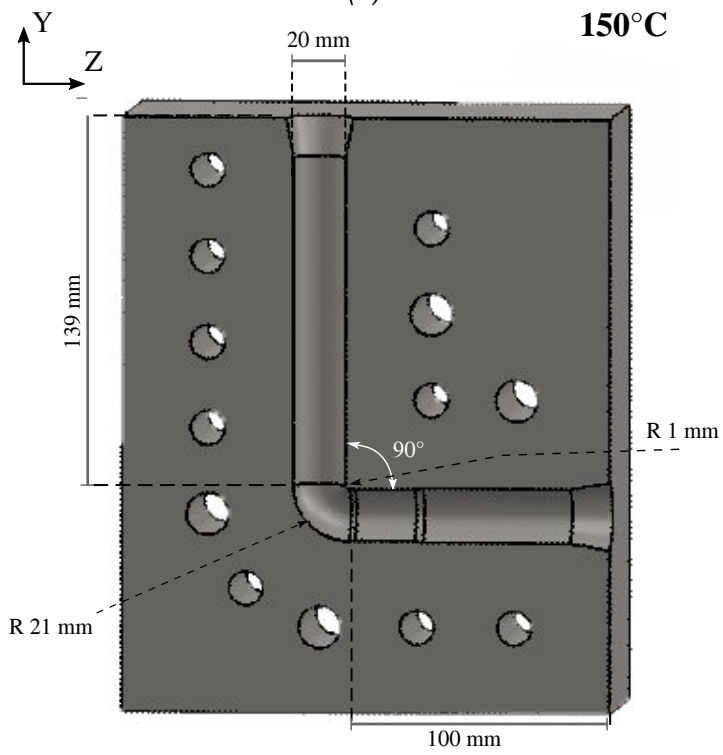

(b)

Figure 2.18: ECAP facility at LMS, made of quenched and tempered DH13 steel.

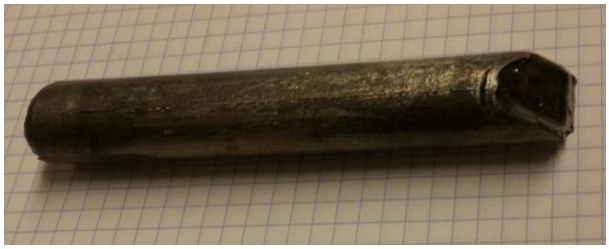

Figure 2.19: Batch B specimen after 6 ECAP passes following route Bc at 150° C.

After removing the two "dead zones" at both ends of ECAPed samples [6], flat dog-bone shaped or cylindrical specimens were machined parallel to the extrusion axis for tensile and fatigue tests as shown in figure 2.20.

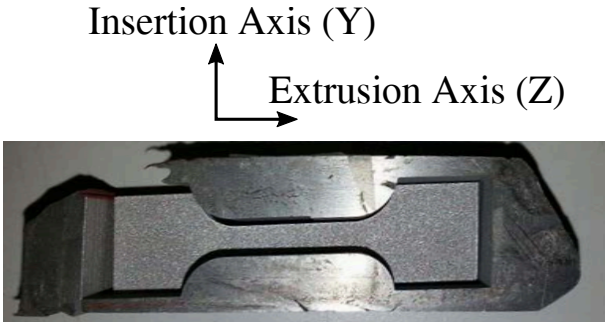

Figure 2.20: Schematics of the tensile specimens cut from UFG-A material.

In case of CG materials, the specimens were machined in such a way that the tensile axis was along the plate length for CG-A and along the bar axis for CG-B materials.

Cylindrical specimens of 8 mm height and 8 mm diameter were machined to perform relaxation tests in compression. Again, the compression axis was parallel to the bar axis, the plate length or the extrusion axis for CG-B, CG-A and UFG-A materials, respectively (Figure 2.21).

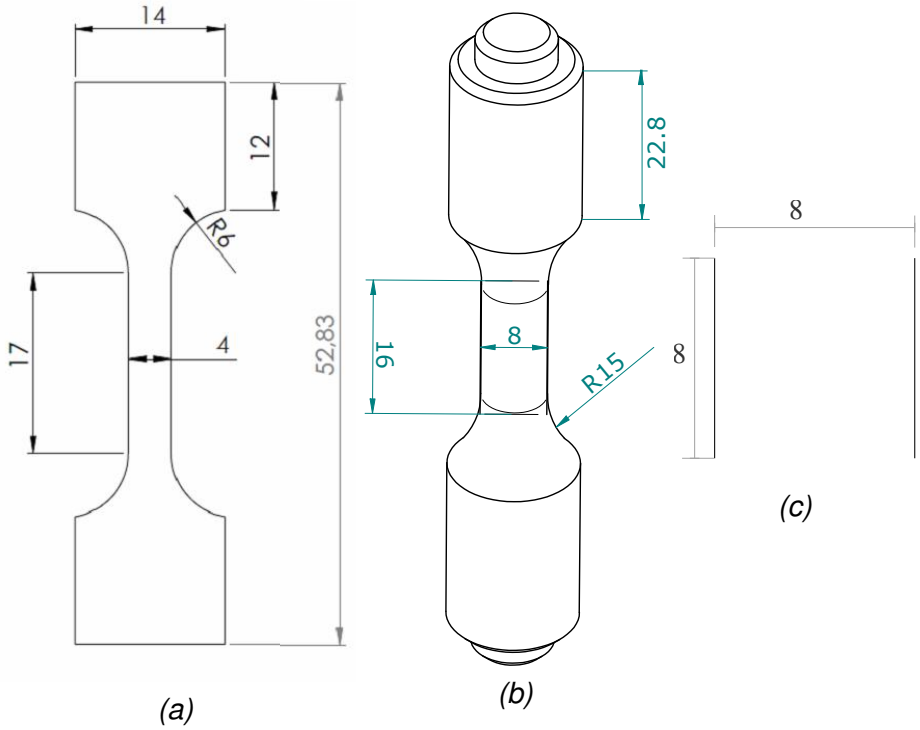

Figure 2.21: Specimen geometries for experimentation: (a) Flat dog-bone shaped specimen for tensile testing, (b) cylindrical specimens for fatigue and (c) cylindrical specimens for relaxation tests in compression (All the units are in mm).

2.3 Ultrafine-grained (UFG) materials

Figure 2.22 presents the SEM image of the plane parallel to the extrusion axis. Initially dendritic particles broke down into rows of small particles aligned at 30° from the extrusion axis. The average length of these arrays of 2^{nd} phase particles is approximately 50 μm, but it can extend up to 100 μm.

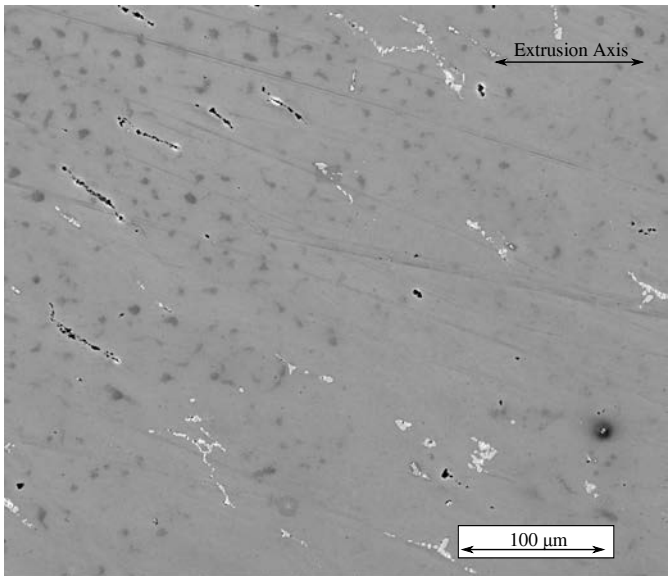

Figure 2.22: SEM image of UFG-A material

Dispersoids are still present after ECAP, as seen in figure 2.23 (Image was taken during SEM observation of a thin foil cut by FIB after a tensile test at room temperature as detailed in chapter 4). The length and width of rod shaped nano-dispersoids are 97 ± 47 and 58 ± 25 nm respectively which is somewhat smaller than in CG material where their length was 144 ± 65 nm and their width was 71 ± 28. However, the mean spacing between the particles, which is 600 nm after ECAP, is similar to that for CG materials (690 nm). It can also be noted that the dispersoids in this case are mostly located at the grain boundaries.

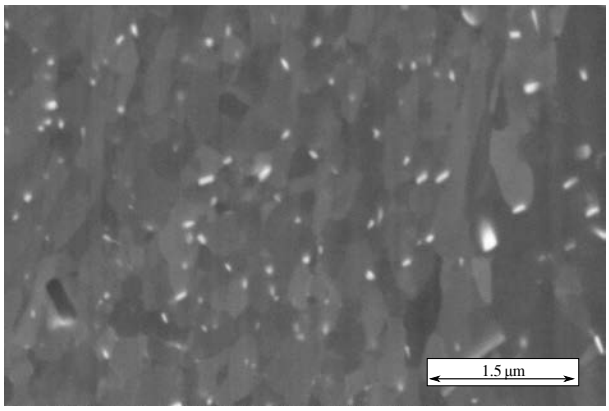

Figure 2.23: Presence of dispersoids after ECAP in the section normal to the extrusion axis for UFG-A material (SEM observation of a thin foil cut by FIB after a tensile test at RT).

Figure 2.24 presents the "All-Euler" EBSD maps of the transverse and the two longitudinal sections of a UFG-A specimen. Many difficulties were encountered while performing EBSD on UFG-A material, which were not met for UFG -B or any of the CG materials. During the 62 hours necessary to scan a representative area with a sufficiently small step (75 nm), a progressive deterioration of the indexation rate was observed, as well as a strong contamination of the scanned area. It may be due to the presence of a high dislocation density, in spite of the annealing treatment, which would make the metal highly chemically reactive. On several occasions, due to the small size of grains, 2 overlapping Kikuchi patterns were observed, hence confusing the software which also contributed to the poor indexation rate. The UFG-A material is bimodal in terms of grain size, as can also be seen from the histogram of grain-size in transverse plane (Figure 2.25). Although less than 1% of the grains are larger than 2 μm, their volume fraction is significant. Similar observation can be made for grain size distribution in longitudinal plane. However the bimodal character of grain size in not so evident in this plane (Figure 2.26). The average grain size of UFG-A material is 680 nm. Grains are slightly elongated with an average elongation angle of 25° with the extrusion axis in y-z plane and an average aspect ratio of 2.2.

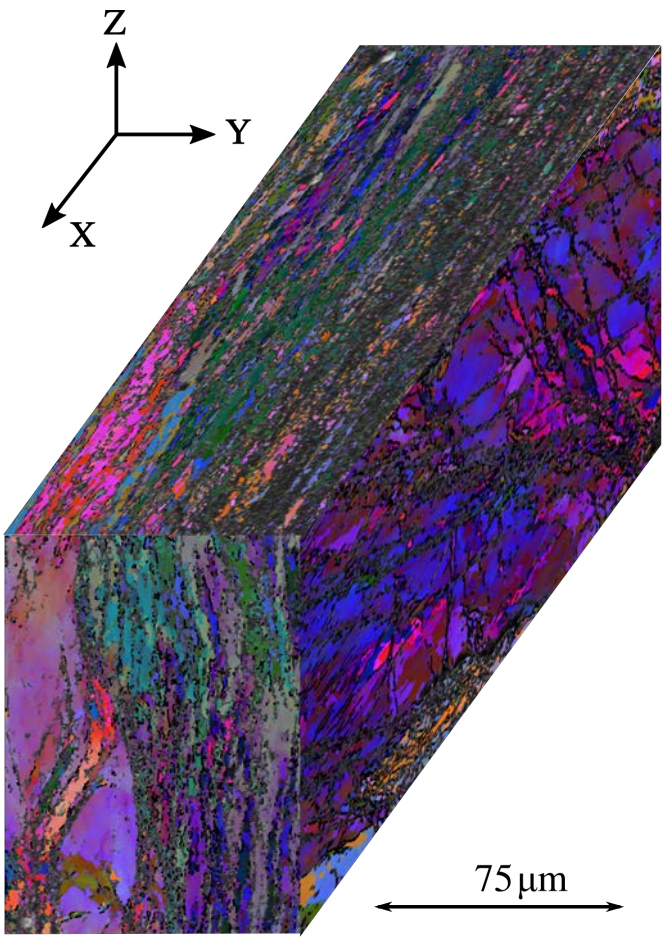

Figure 2.24: Pseudo 3D assembly of "All Euler" maps (Step size: 75 nm in xy and xz planes, 160 nm in yz plane) of UFG-A material.

The percentage of HAGBs was 77% in the X-Z longitudinal plane. Due to the presence of large grains in the transverse and Y-Z longitudinal plane, the percentage of HAGBs was reduced to 55%. The dislocation density estimated from EBSD maps was 9×10^{14} m^{-2}.

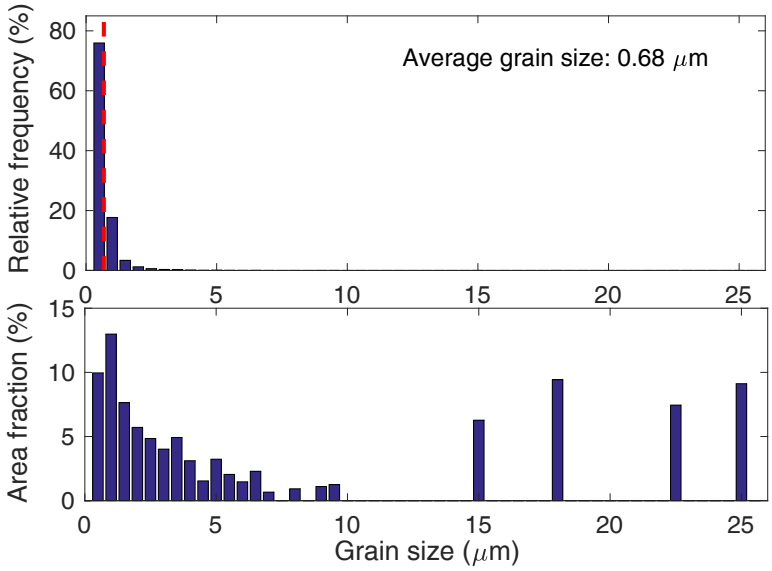

Figure 2.25: Grain size distribution of UFG-A specimen in transverse plane.

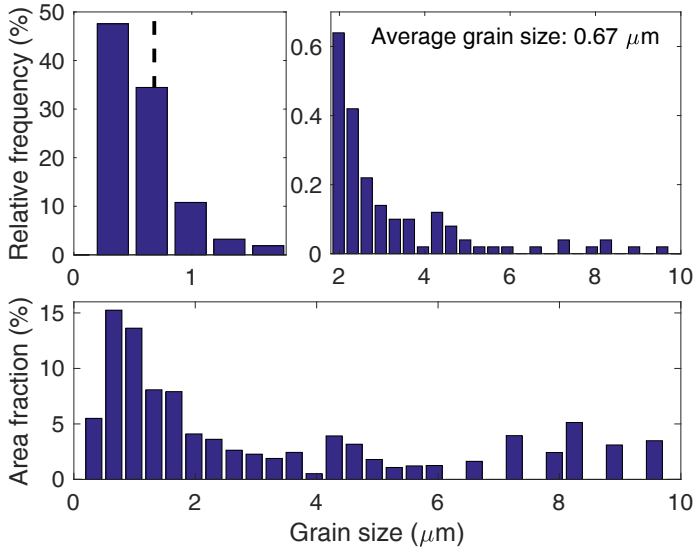

Figure 2.26: Grain size distribution of UFG-A specimen in X-Z longitudinal plane.

Figures 2.27 presents the pole figures of a UFG-A specimen. No doubt the material is highly textured, but no classical ECAP related texture was identified. However, when the pole figures were replotted considering only one point per grain (Figure 2.28) to remove the effect of grain size, the <110> fibre typical of an ECAP route C texture was identified [7].

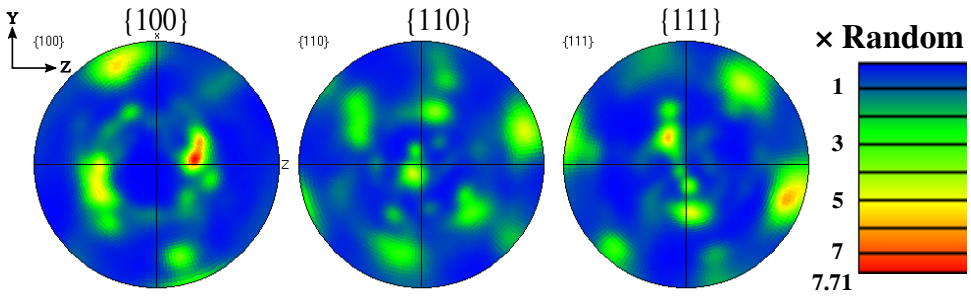

Figure 2.27: Pole figures of UFG-A material considerening all the pixels.

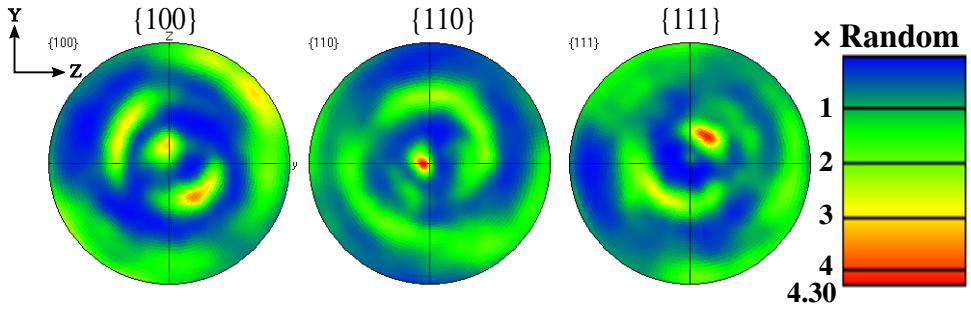

Figure 2.28: Pole figures of UFG-A material considering one point per grain.

Figure 2.29 shows the microstructure of the batch B UFG material in longitudinal plane. The intermetallic particles form rows of broken particles along the bar axis. Thanks to the ECAP route, the distribution of broken 2^{nd} phase particles is more homogeneous for UFG-B material than UFG-A. Segregation bands, with excess and deficit in Mn and Cr, similar to the ones present in CG-B material exist parallel to the extrusion axis. The rod-shaped dispersoids are still present after ECAP (Figure 2.30). Like for the UFG-A material, they are mostly located at the grain boundaries. The segregation of dispersoids is also seen for this material.

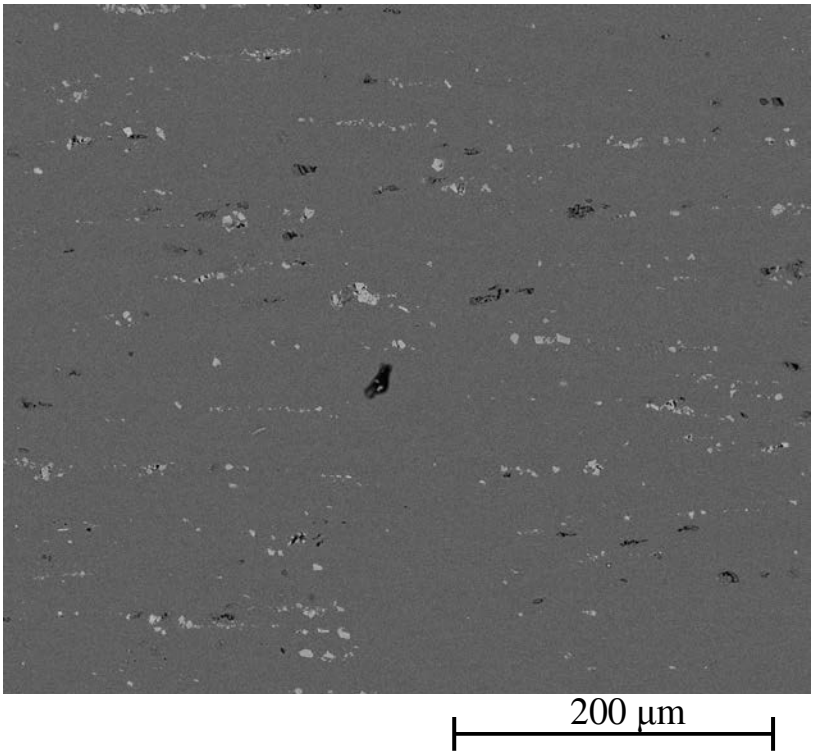

Figure 2.29: BSE image of the longitudinal section of UFG-B material with extrusion axis along the horizontal line.

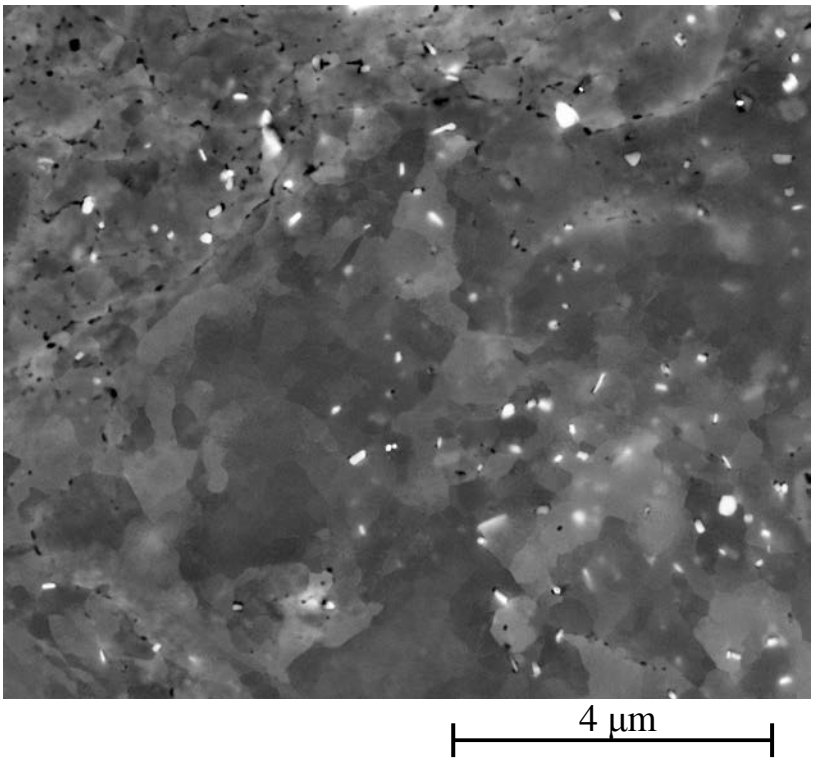

Figure 2.30: Presence of dispersoids after ECAP in the transverse section for UFG-B material.

Figure 2.31 and 2.32 presents the EBSD maps of the normal and the transverse section of a UFG-B specimen. The distribution of grain size is similar in both planes and is presented in figure 2.33. The grains are elongated at an angle of 33° with respect to extrusion axis with an average aspect ratio of 1.9 in transverse and 2.6 in longitudinal section. The distribution of grain size of UFG-B material is much more homogeneous than that of UFG-A, but with a comparable average value of 597 nm. The percentage of HAGBs is higher (> 80%) than in UFG-A material in both planes. This can be due to the higher number of ECAP passes for UFG B material. The dislocation density after ECAP increases to 9×10^{14} m^{-2}.

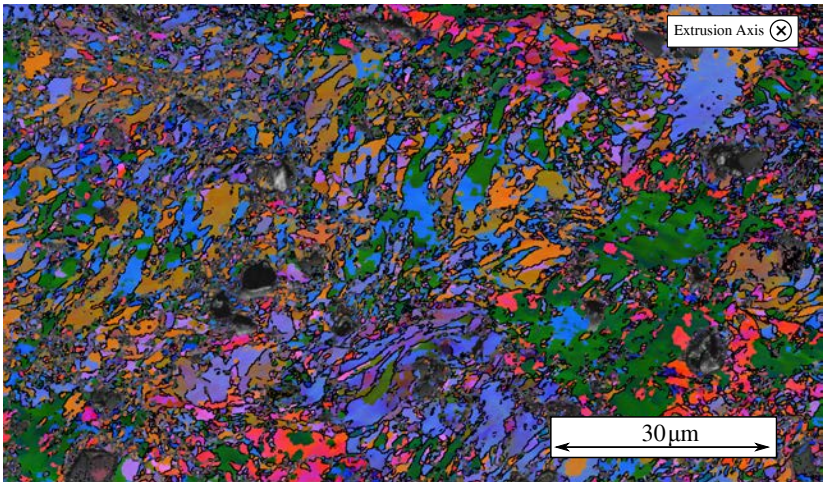

Figure 2.31: EBSD "All-Euler" map (Step size: 75 nm) of UFG-B material perpendicular to the extrusion axis.

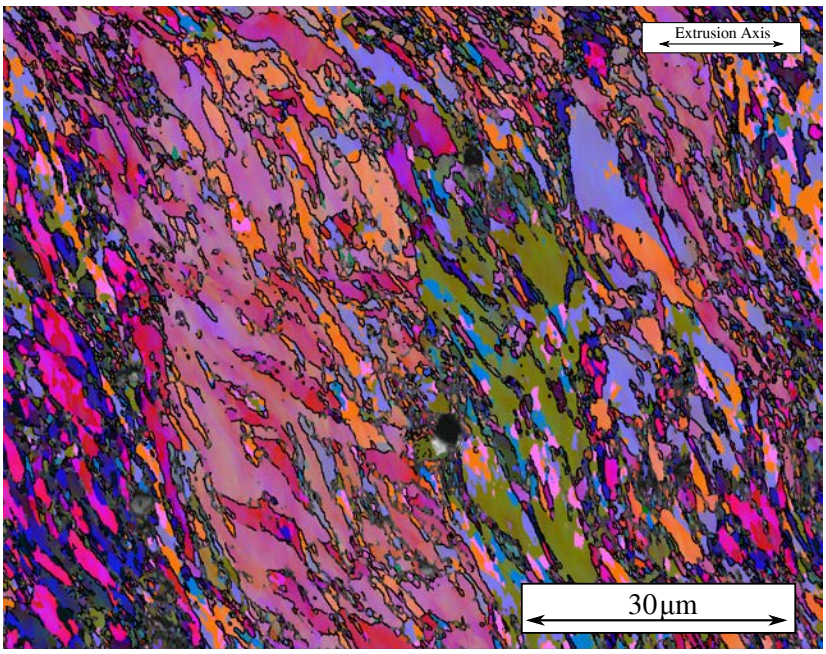

Figure 2.32: EBSD "All-Euler" map (Step size: 75 nm) of UFG-B material parallel to the extrusion axis.

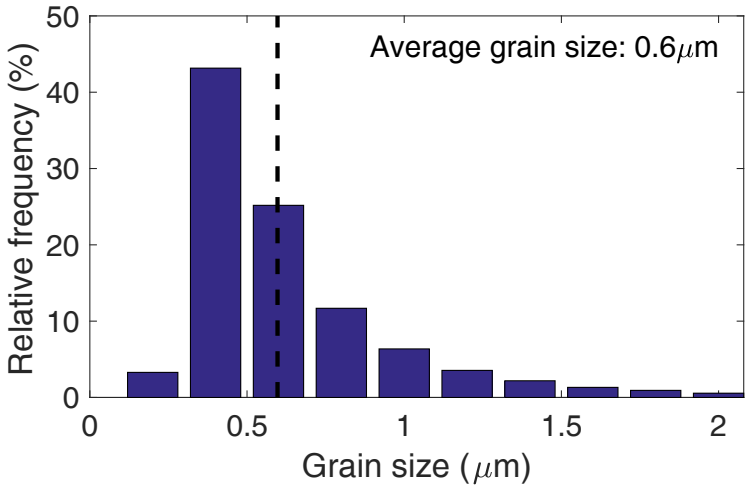

Figure 2.33: Grain-size distribution of UFG-B specimen calculated from the elliptical fits using EBSD software (Same for both transverse and longitudinal planes).

Figures 2.34 and 2.35 show the pole figures considering all the pixels or one point per grain, respectively. A strong <110> texture is observed in one of the radial directions with or without normalising the effect of grain size. This type of texture is typical for fcc materials processed by ECAP along route B_c [8].

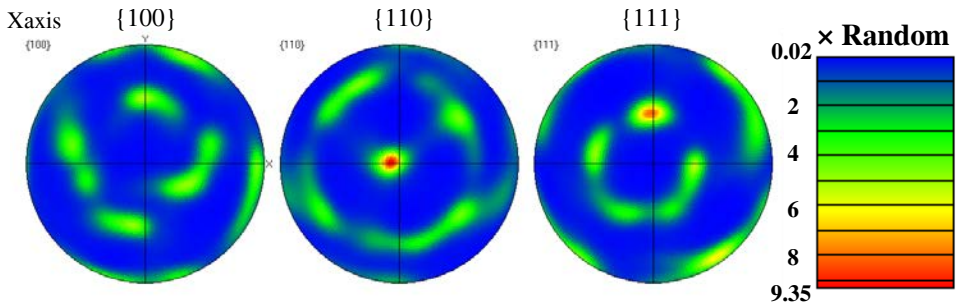

Figure 2.34: Pole figures of UFG-B material.

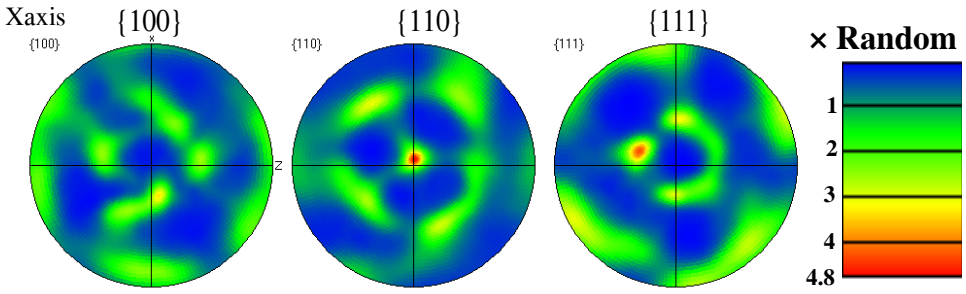

Figure 2.35: Pole figures of UFG-B material considering one point per grain.

References

[1] S.-L. Lee and S.-T. Wu, “Identification of Dispersoids in Al-Mg Alloys Containing Mn,” *Metallurgical Transactions A*, vol. 18, no. August, pp. 1353–1357, 1987.

[2] R. Goswami and R. L. Holtz, “Transmission electron microscopic investigations of grain boundary beta phase precipitation in Al 5083 aged at 373 K (100 C),” *Metallurgical and Materials Transactions A: Physical Metallurgy and Materials Science*, vol. 44, no. 3, pp. 1279–1289, 2013.

[3] T. Radetić, M. Popović, and E. Romhanji, “Microstructure evolution of a modified AA5083 aluminum alloy during a multistage homogenization treatment,” *Materials Characterization*, vol. 65, pp. 16–27, 2012.

[4] B. Chenal and J. Driver, *Écrouissage d’alliages d’aluminium*, 1999.

[5] D. N. Lee, Y. H. Cgung, and M. C. Shin, “Preferred orientation in extruded aluminum alloy rod,” *Scripta metallurgica*, vol. 17, pp. 339–342, 1983.

[6] L. Dupuy, “Mechanical behavior of an aluminium alloy subjected to severe plastic deformation,” PhD thesis, 2000.

[7] S. Li, I. J. Beyerlein, C. T. Necker, D. J. Alexander, and M. Bourke, “Heterogeneity of deformation texture in equal channel angular extrusion of copper,” *Acta Materialia*, vol. 52, no. 16, pp. 4859–4875, 2004.

[8] A. P. Zhilyaev, D. L. Swisher, K. Oh-ishi, T. G. Langdon, and T. R. McNelley, “Microtexture and microstructure evolution during processing of pure aluminum by repetitive ECAP,” *Materials Science and Engineering A*, vol. 429, pp. 137–148, 2006.

Chapter 3

Experimental investigation of the viscoplastic behaviour of CG and UFG Al5083 (Macroscopic aspect)

As explained in the previous chapter, ECAP not only results in grain size reduction but also changes the microstructural features such as texture, dislocation density, GB misorientations, distribution of second phase particles, etc. Such microstructural changes can highly influence the way dislocations interact inside the grains and at the GBs which can also change with temperature and strain-rate. To study the strain rate and temperature effects on the mechanical behaviour of CG and UFG materials, tension at various strain rates as well as relaxation tests were performed at various temperatures. The experimental procedure and the results of the tensile tests are presented in the first section of this chapter. The second section elaborates on the procedure and the results of the relaxation and strain-rate jump tests. In the last section, the results from the two previous sections are compiled, discussed and interpretations are proposed based on the macro-scale behaviour. The underlying deformation mechanisms will however be investigated at a finer scale in the next chapter, allowing a more complete discussion.

3.1 Tensile Tests

3.1.1 Procedure

For the tensile tests, flat dog-bone samples and cylindrical specimens (Figure 2.21 chapter 2) were used, as specified in table 3.1. Surface preparation of the specimens is described in the next chapter. The room temperature tensile tests were performed either on a 100 kN hydraulic press or a 4.4 kN electro-mechanical micromachine that can be fitted into a SEM (Figure 3.1).

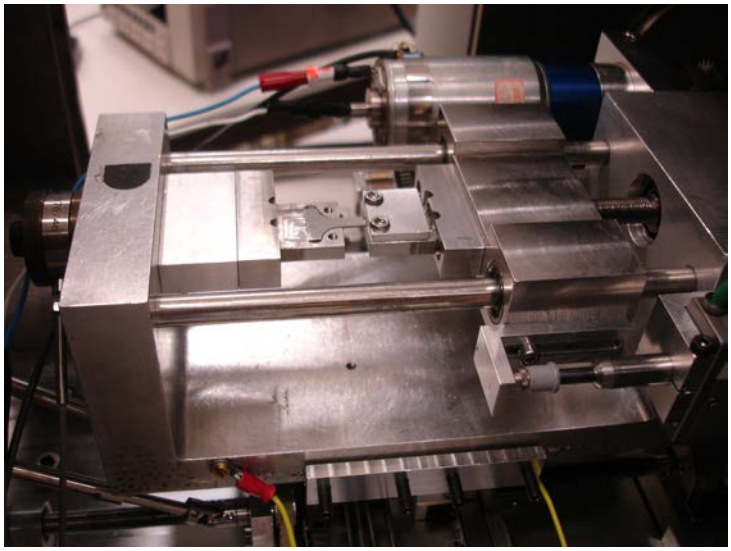

Figure 3.1: Micro-machine with a 4.4 kN load cell for tensile testing in the SEM

Strain measurement for the tests performed on the hydraulic press was done using an extensometer with a 10 mm gage length and a full range of 40% while 2 types of extensometry were used for tests performed on the micro-machine: 1. optical macro extensometry and 2. DIC (described in next chapter). Two dots approximately 1 mm in diameter are painted near the ends of the gauge length (previously covered with a layer of white paint, to avoid undesirable reflections) using a thermally resistant black paint (Figure 3.2). The digital image correlation (DIC) technique is used for real-time monitoring of the position of 2 dots, projected along a vertical line on the specimen, and to calculate the axial strain, based on their initial distance (= gage length).

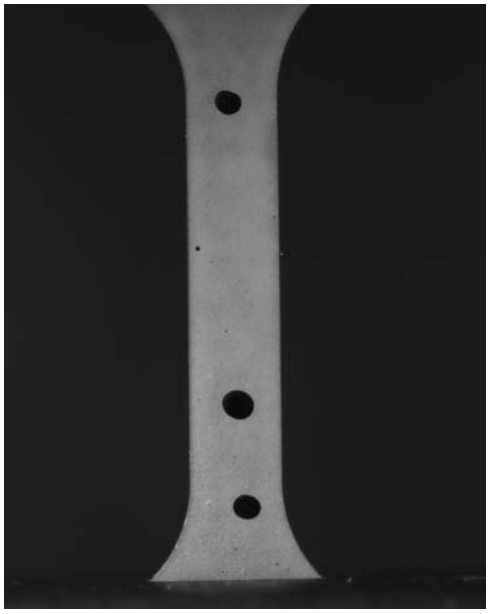

Figure 3.2: Macro-scale patterning for optical measurement of axial strain

High temperature tensile tests were performed using a 10 kN load cell on a 250 kN hydraulic press equipped with a thermal chamber including a resistive heating device, a closed-loop control of the temperature inside and a fan to homogenise it. The strain was measured by optical extensometry, thanks to the transparent window in the chamber. An additional thermocouple was attached inside the chamber, near the specimen. Special attention was given while heating: to avoid buckling, the specimens were held in force control mode with a small, positive force (approx. 50 N). Both the displacement of the crosshead and the strain of the sample were monitored during this heating time. The tensile test was run at least 1 hour after the required temperature was reached and only after both the displacement and strain reached a steady-state (representing the thermal equilibrium). All the tensile tests were displacement-controlled. The strain rates reported in table 3.1 and 3.4 are thus approximations based on the imposed displacement rate, and the sample gage length. All the experiments were run until fracture.

3.1.2 Results at room temperature (RT)

The engineering stress-strain curves and the corresponding hardening rates at RT measured on the batch A materials are presented in figure 3.3 and 3.4 respectively. The results of all the tests are summarised in table 3.1.

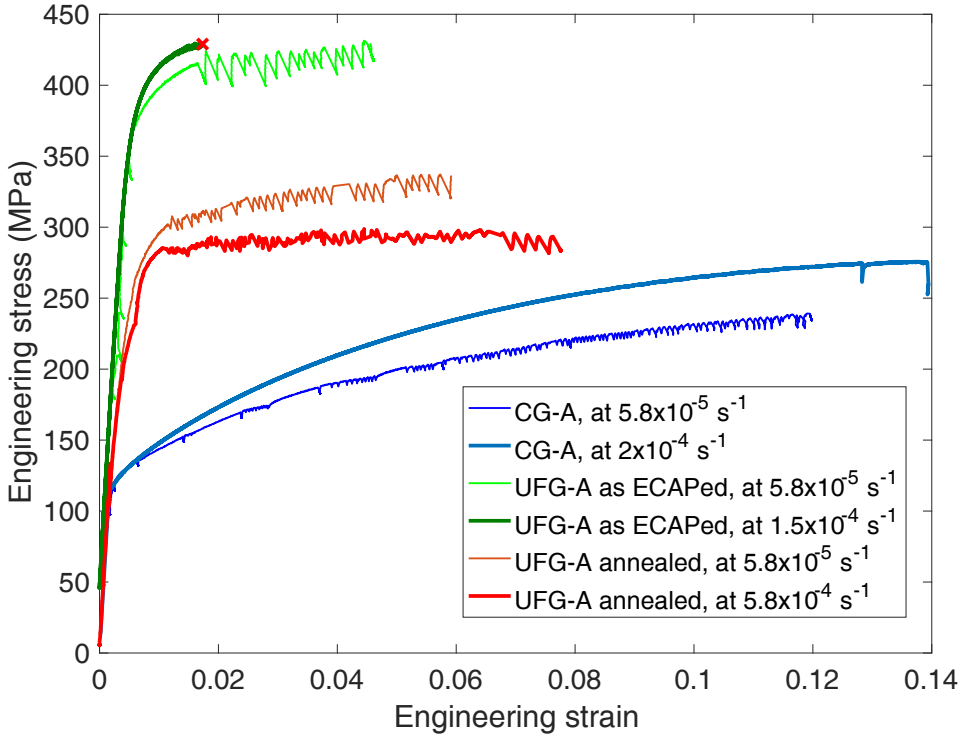

(a)

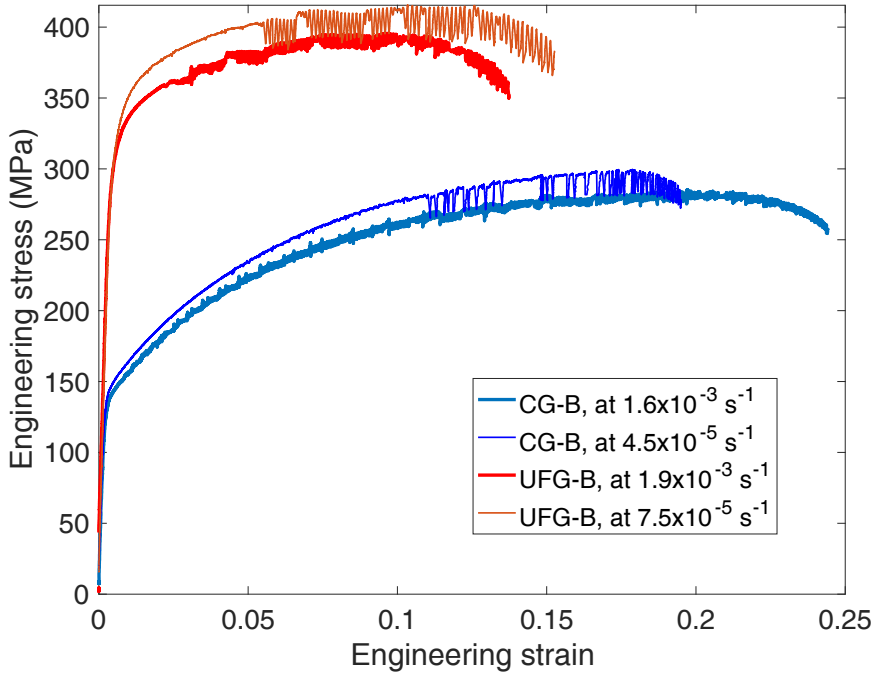

(b)

Figure 3.3: Engineering stress-strain curves for tensile tests on a) batch A and b) batch B materials at RT.

Material Al5083	CG-A		UFG-A				CG-B		UFG-B	
Heat treatment	na.		na.		6h at 200°C		na.		na.	
Testing machine	MTS	Micro	Micro	MTS	Micro	Micro	MTS	MTS	MTS	MTS
Specimen geometry	cylindrical	flat	flat	flat	flat	flat	flat	flat	flat	flat
Strain-rate (s^{-1})	2×10^{-4}	5.8×10^{-5}	5.8×10^{-5}	1.5×10^{-4}	5.8×10^{-5}	5.8×10^{-4}	1.6×10^{-3}	4.5×10^{-5}	1.9×10^{-3}	7.5×10^{-5}
Young's Modulus (GPa)	70.3	70.8	70.3	70.3	69.8	70.2	67.2	57.9	70.1	71.4
0.2% Yield stress (MPa)	127	128	382	391	265	225	139	145	313	323
UTS (MPa)	276	241	431	430*	337	299	285	299	396	415
Uniform Elongation (%)	13.8	12.2	4.5	1.7	5.7	6.5	19.7	17.6	10.2	10.9
Fracture strain (%)	14.0	12.6	4.6	1.7*	5.9	7.8	24.5	19.5	16.0	16.5

Table 3.1: Details of tensile tests at RT (premature failure from extensometer)*

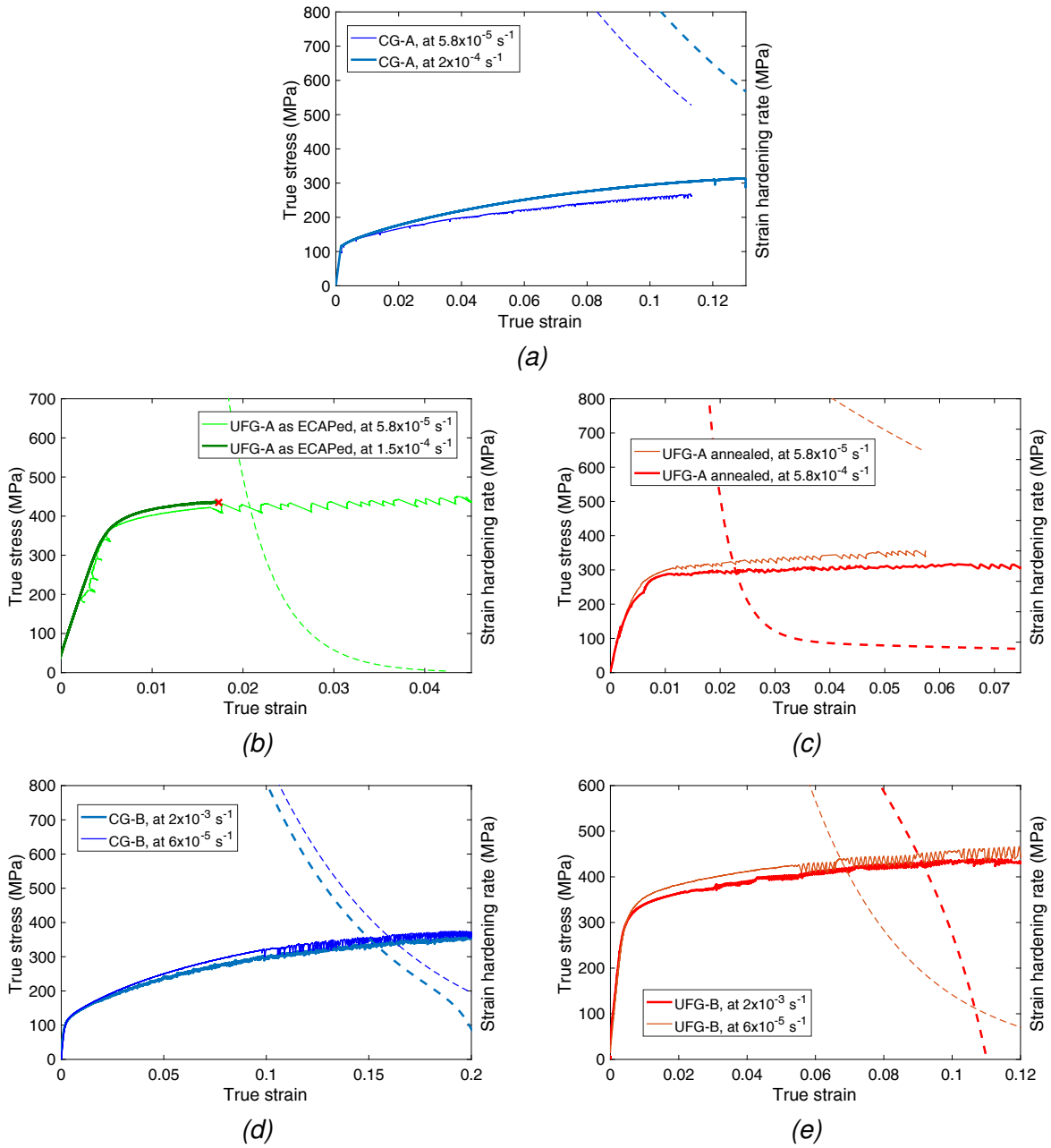

Figure 3.4: True stress-strain curves superimposed with the evolution of the strain hardening rate on (a) CG-A , (b) UFG-A (annealed), (c) UFG-A (as ECAPed), (d) CG-B and (e) UFG-B Al5083 materials at RT.

At this temperature, UFG materials have a higher yield stress than CG materials for all the investigated rates. Various factors are responsible for this increased yield stress: not only grain refinement (Hall-Petch strengthening), but also an increased dislocation density in as-ECAPed condition and a possible increase in solute Mg content due to fragmentation of second-phase particles. The strain hardening capacity of the materials, measured by the ratio $(UTS - 0.2\%YS)/0.2\%YS$, is approximately 5 times higher in CG than in UFG materials, as shown in figure 3.5. Dislocation density of the UFG material is $9 \times 10^{14} m^{-2}$ (refer to chapter 2 for more details on microstructure), which is

quite close to its saturation. This implies that after ECAP, a UFG material looses most of its dislocation storage capability. However annealing the ECAPed material, as in the case of UFG-A, decreased the yield strength, while increasing the strain hardening capacity and the fracture strain.

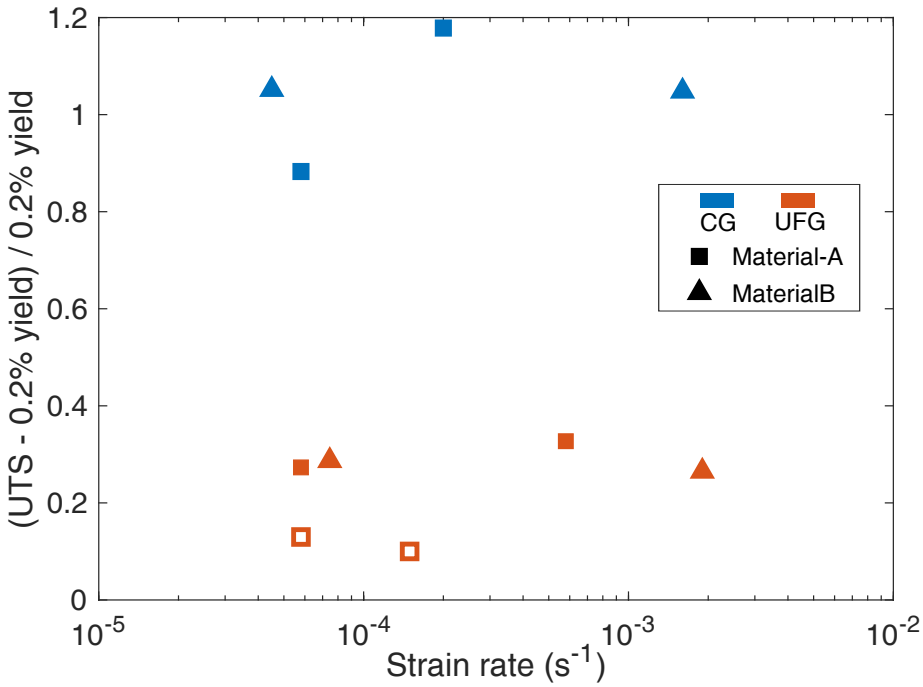

Figure 3.5: Relative hardening of the CG and UFG materials (open symbols square symbols for as ECAPed UFG-A and filled for annealed UFG-A material)

UFG materials are less ductile than their CG counterparts. Macroscale pictures of the broken samples are presented on figure 3.6 and 3.7 for batch A and B respectively (SEM fractographic observations will be shown and discussed in the next chapter).

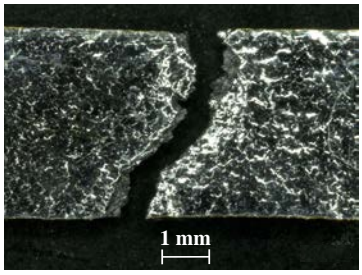

(a) CG-A, $5.8 \times 10^{-5} s^{-1}$

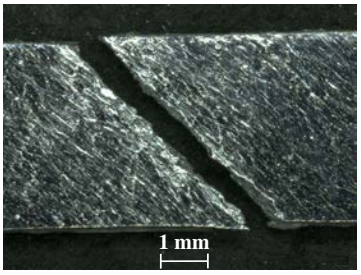

(b) UFG-A annealed, $5.8 \times 10^{-4} s^{-1}$

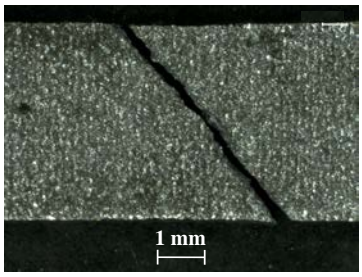

(c) UFG-A as ECAPed, $1.5 \times 10^{-4} s^{-1}$

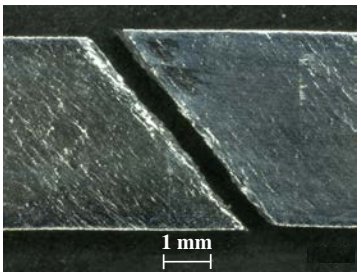

(d) UFG-A as ECAPed, $5.8 \times 10^{-5} s^{-1}$

Figure 3.6: Optical images of broken batch-A samples after the tensile tests (UFG-A(annealed) specimen tested at 5.8$\times 10^{-5} s^{-1}$ *fractured at the ends and is not presented here).*

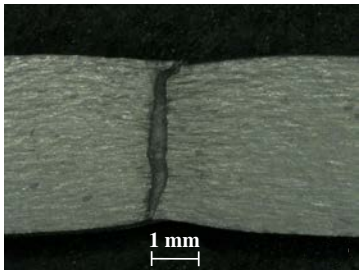

(a) CG-B, $1.6 \times 10^{-3} s^{-1}$

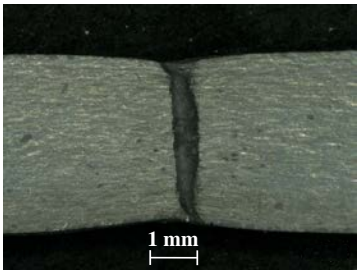

(b) CG-B, $4.2 \times 10^{-5} s^{-1}$

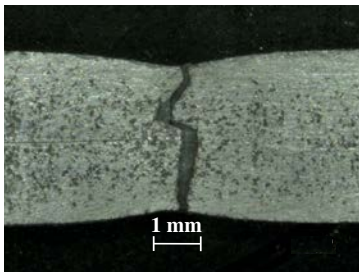

(c) UFG-B, $1.9 \times 10^{-3} s^{-1}$

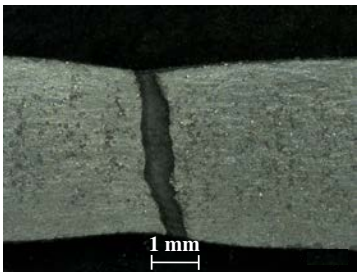

(d) UFG-B, $7.5 \times 10^{-5} s^{-1}$

Figure 3.7: Optical images of fracture batch-B samples after the tensile tests

While both CG and UFG batch B materials exhibit some necking associated with a drop in engineering stress before fracture, no such drop was observed for batch A materials, which do not exhibit necking (see figure 3.6) but rather shear dominated slanted fracture. Even though batch B materials exhibit ductile fracture and necking, the fracture surface is actually slanted as well, but into the depth as shown in the lat-

eral view of the fractured samples (Figure 3.8).

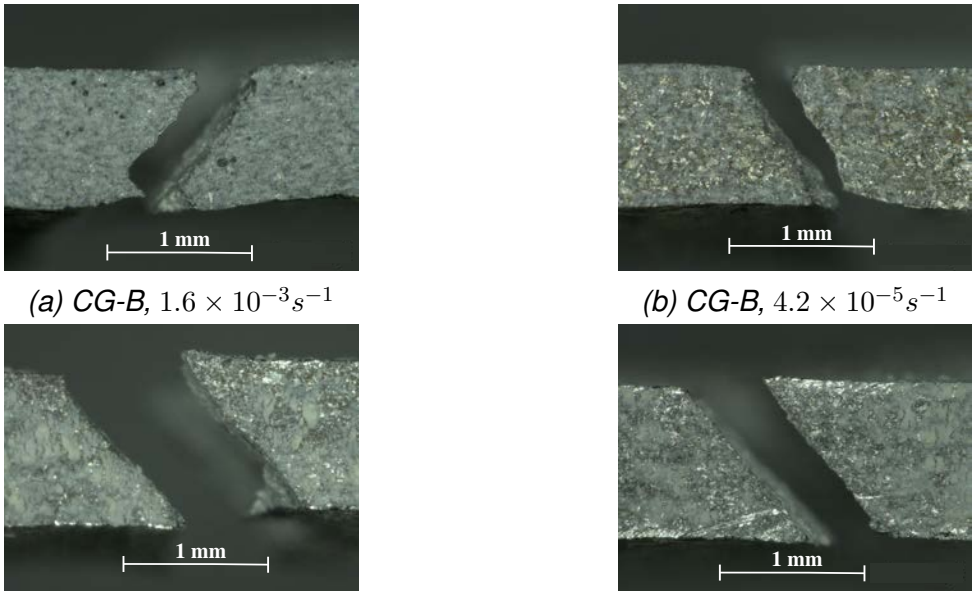

(a) CG-B, $1.6 \times 10^{-3} s^{-1}$ *(b) CG-B,* $4.2 \times 10^{-5} s^{-1}$

(c) UFG-B, $1.9 \times 10^{-3} s^{-1}$ *(d) UFG-B,* $7.5 \times 10^{-5} s^{-1}$

Figure 3.8: Optical images of the lateral side of fractured batch-B samples after the tensile tests at RT (have to retake the images to change the scale)

These slanted fractures, as explained in chapter 1, can explain why failure does not follow Considere's criterion (Equation 1.3), even in batch B materials as seen from figure 3.4.

Highly serrated flow, symptomatic of dynamic strain aging was observed during all the tests done on flat samples. Furthermore, the relative positions of the tensile curves obtained at different rates on UFG-A and B as well as on CG-B material, suggest a negative strain rate sensitivity (SRS) at RT and approximate values derived from the comparison of flow stresses at 5% strain are indicated in table 3.2. Such negative SRS is favourable to strain localisation. But the direction in which localisation occurs is controlled by the anisotropy of the microstructure. In case of UFG-A materials, a strong microstructural anisotropy (grain elongation, rows of broken particles and texture) was inherited from ECAP route C (refer to the figures in the previous chapter). It will be shown in the next chapter that intense plastic flow occurs along the direction of grains and particles elongation, and after strain localisation assisted by this negative SRS, this leads to slanted fracture that cannot be predicted by Considere's criterion.

Material	SRS
UFG-A	-0.062
CG-B	-0.017
UFG-B	-0.019

Table 3.2: Strain-rate sensitivity calculated from RT tensile curves

Based on their frequency and shape, the serrations are classified into 3 types, described in the literature review. Details about the character of these serrations and the strain at their onset are provided in table 3.3. At the highest strain rate, A type serrations were observed and with decreasing strain rate, the type of serrations gradually changed to B and to C at the lowest strain rate (Figure 3.9). Similar observation was made by Lebedkina and Lebyodkin [1].

Material	Strain rate (s^{-1})	Strain at onset of serrations	Type
CG-A	5.8×10^{-5}	2.45%	B+C
UFG-A	5.8×10^{-5}	1.15%	C
UFG-A	5.8×10^{-4}	1.06%	B+C
CG-B	1.6×10^{-3}	0.8%	A+B
CG-B	4.5×10^{-5}	11.0%	C
UFG-B	1.9×10^{-3}	2.2%	A+B
UFG-B	7.5×10^{-5}	5.4%	B+C

Table 3.3: Details of the serrated yielding during the RT tensile test

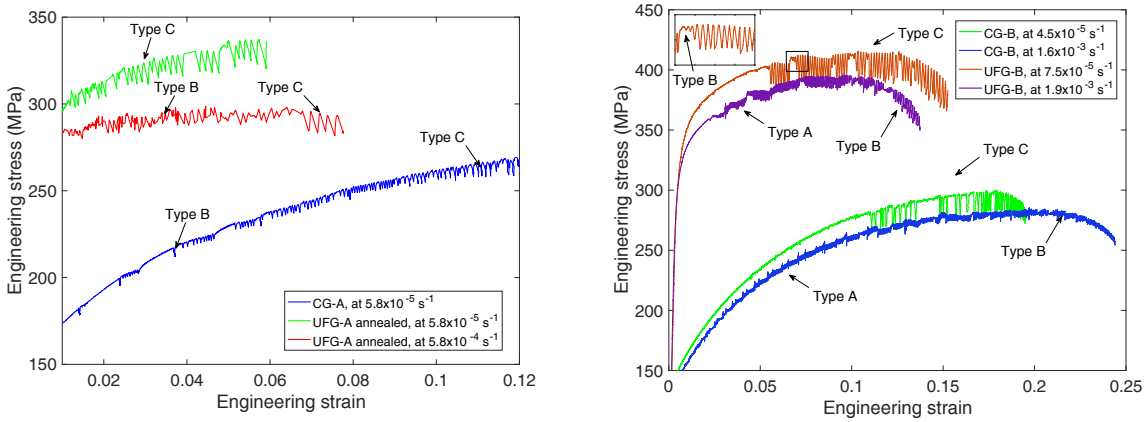

Figure 3.9: Nature of serrations for (a) batch-A and (b) batch-B Al5083 materials.

A statistical analysis of the amplitude of the serrations was done and figures 3.10 and 3.11 show their measured distributions. Stress serrations of less than 1 MPa corresponding to $\sim$5 N are not considered. It can be observed that the amplitude of the serrations is higher in each batch for UFG materials. There maybe several reasons for such behaviour: first, increased dislocation density and the amount of GBs leading to more arrest periods; second, Mg segregation at GBs or fragmentation of intermetallic particles during ECAP, both of which can alter the amount of obstacles available for mobile dislocations (X-ray diffraction measurement of lattice parameter along with atom probe tomography to measure spatial distribution could provide a better insights [2], [3]); third, the long range synchronisations which are possible in UFG materials due to its highly textured grains [4]. This observation is contrary to those made by Lebedkina and Lebyodkin [1] who reported that the amplitude of serrations for UFG material was 20 times smaller as compared to the CG counterpart. However their observations were made on Al-3%Mg which did not contain iron and silicon-rich intermetallic particles. The lower Mg content can also explain the lower amplitudes of serrations for their CG alloy as compared to the present one.

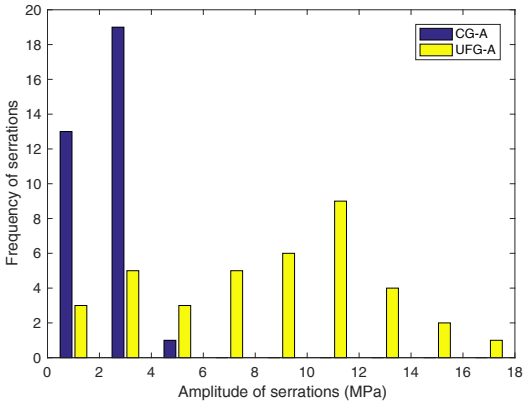

Figure 3.10: Histograms of the amplitude of stress serrations for batch A materials when tested at $\sim 6 \times 10^{-5} s^{-1}$

Contrary to Lebedkina et al. [5], and in accordance with the present observations, Perisse et al. [6] also reported a larger amplitude of serrations in UFG titanium. They proposed an explanation based on Orowan's equation, which predicts that for a given strain rate, the ratio of mean dislocation glide velocities in UFG and CG has to be the inverse of the ratio of mobile dislocation densities. Since the latter can be quite large (because of the larger density of dislocation sources at grain boundaries), the mean dislocation glide velocity would be much lower in UFG material, this allowing more interactions with solute atoms, and thus larger stress drops.

Histograms of the amplitude of serrations are plotted in figure 3.12 for the each material to analyse the effect of applied strain rate. The maximum amplitude of the serrations increases 2-fold with decreasing strain rate from $\sim 2 \times 10^{-3} s^{-1}$ to $\sim 6 \times 10^{-5} s^{-1}$ for batch B materials and from $5.8 \times 10^{-4} s^{-1}$ to $5.8 \times 10^{-5} s^{-1}$ for batch A materials. With decreasing strain rate, the waiting time of dislocations at obstacles increases, resulting

in an increase in aging time locally at the obstacles and hence the increase in stress drops. For a given strain rate, the strain at the onset of the serrations tends to be smaller in UFG than in CG material. This might be due to a faster diffusion in UFG material, and/or to a smaller mean free path for the dislocations.

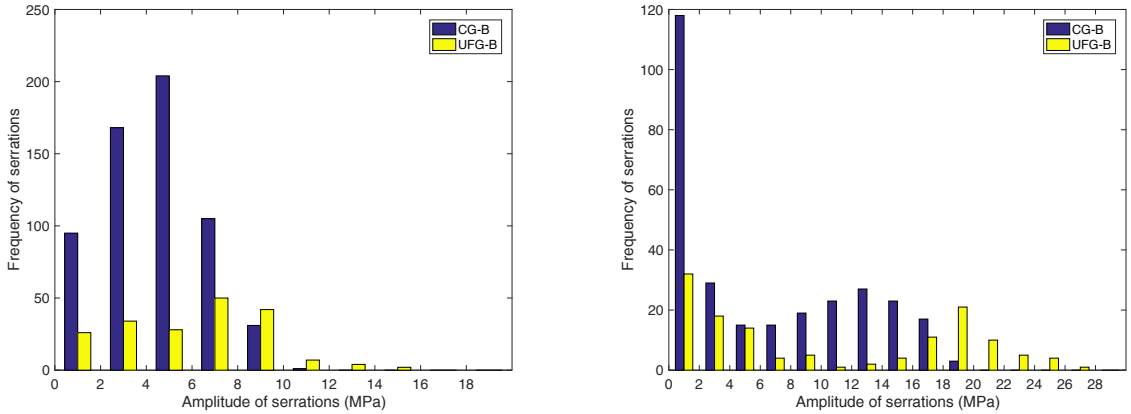

(a) Strain Rate: $\sim 2 \times 10^{-3} s^{-1}$ *(b) Strain Rate:* $\sim 6 \times 10^{-5} s^{-1}$

Figure 3.11: Histograms of the amplitude of stress serrations for batch B materials

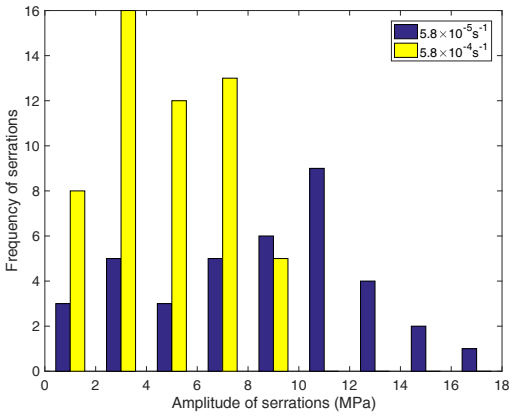

(a) UFG-A (annealed)

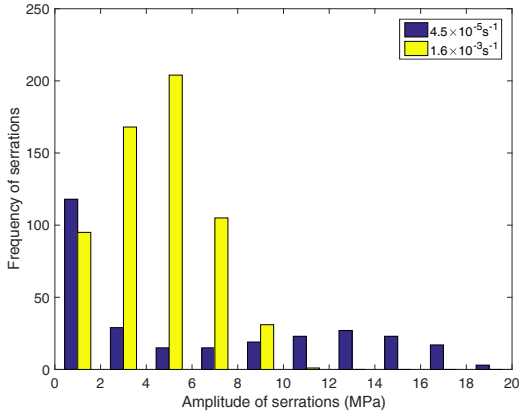

(b) CG-B

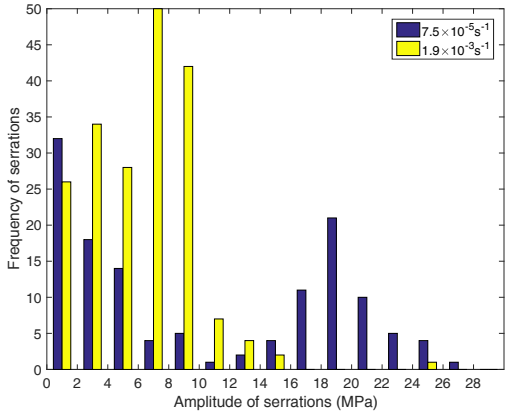

(c) UFG-B

Figure 3.12: Effect of applied strain rate on the amplitude of stress serrations

3.1.3 Results at high temperature (HT)

High temperature tensile tests were performed at 100, 150 and 200°C only on CG-A and UFG-A(annealed) specimens. The tests were not run at similar strain rates for CG and UFG, but inspired from the work of Kapoor and Chakravarty [7], the strain rates at each temperature were chosen so as to observe the transition in strength with the strain rate for CG and UFG materials with the limited number of available samples. Details of all the high temperature tensile tests are presented in the table 3.4. Some additional tensile tests were done on CG material at higher strain rates and are presented in the Appendix 3.B. They will later be used for the identification of material parameters in the constitutive model presented in chapter 5.

The engineering stress-strain curves at 100°C are presented in figure 3.13. At 100°C, the UFG material has a higher yield stress than CG for the two investigated rates. CG material shows higher hardening capacity and higher uniform strain than UFG material. The fracture strain of the former is also higher than that of UFG materials. The strain rate has a strong effect on the tensile behaviour of UFG material. As the strain

Material Al5083	**CG-A**						**UFG-A (annealed)**				
Temperature ($^{\circ}C$)	**100**		**150**	**200**			**100**		**150**	**200**	
Strain-rate (s^{-1})	3.8×10^{-6}	1.5×10^{-5}	1.5×10^{-5}	2.0×10^{-4}	1.8×10^{-3}	4.1×10^{-3}	3.0×10^{-6}	1.8×10^{-5}	1.6×10^{-5}	1.4×10^{-4}	4.5×10^{-3}
Young's Modulus (GPa)	50.0	56.4	55.2	55.8	55.8	58	45.5	64.1	50.7	24.2	39.5
0.2% Yield stress (MPa)	129	131	115	145**	102	114	146	279	84	48	138
UTS (MPa)	193	210	160	174**	166	174	241	323	150	105	203
Uniform Elongation (%)	15.5	14.8	9.9	4.8	10.2	8.8	7.4	3.5	11.2	13.9	5.0
Fracture strain (%)	28.9*	19.9*	27.7	42.2	20.9	12.1	22.7	12.9	27.5	49.8	33.9

*Table 3.4: Details of tensile tests at HT (*test stopped while specimen was not broken, **cylindrical specimen as opposed to flat specimens used for all other tests)*

rate decreases, the yield stress and UTS decrease (this suggesting a positive SRS), while the uniform elongation and fracture strain increase. Obviously, the rate dependence of the fracture strain cannot be captured by Considere's criterion, and the role of viscosity will be discussed later. In spite of the apparently positive SRS, small type B serrations for UFG material and large type C serrations for CG material were observed. The amplitude of these serrations for UFG material was however less than 3 MPa. However, the amplitude of serrations for CG material is higher at both strain rate. Maximum amplitude of stress drops reaches 6 MPa at $1.5 \times 10^{-5} s^{-1}$, while it reaches 38 MPa (approx. 6 times higher than at the fastest rate) at $3.8 \times 10^{-6} s^{-1}$ (Figure 3.15). Figure 3.14 shows the fractured specimens. Fracture surfaces are slanted for UFG materials, as previously observed at room temperature.

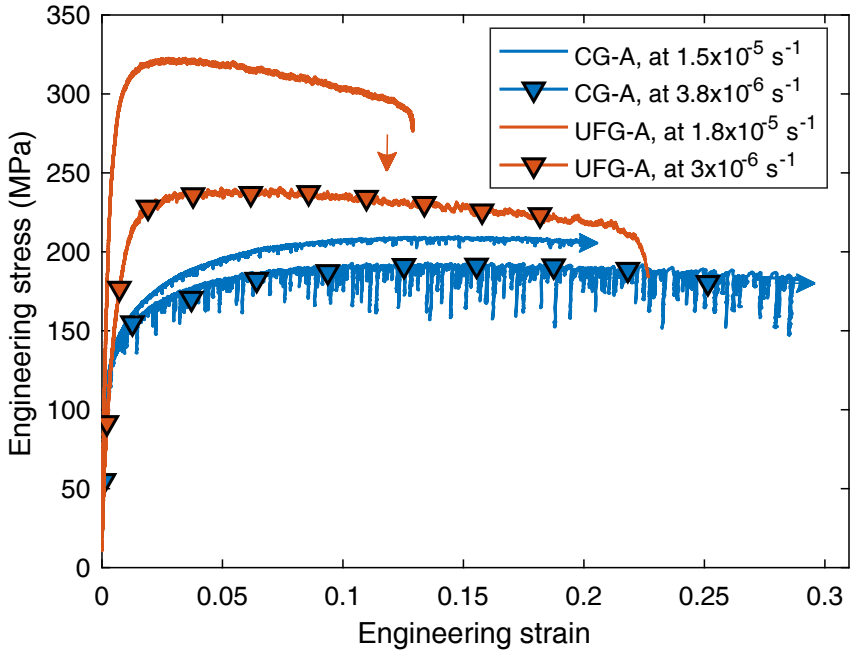

Figure 3.13: Engineering stress-strain curves for tensile tests at 100° C.

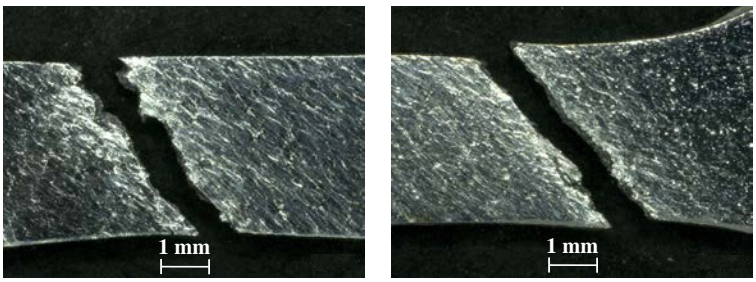

(a) UFG, $1.8 \times 10^{-5} s^{-1}$ *(b) UFG,* $3 \times 10^{-6} s^{-1}$

Figure 3.14: Optical images of the fractured samples at 100° C

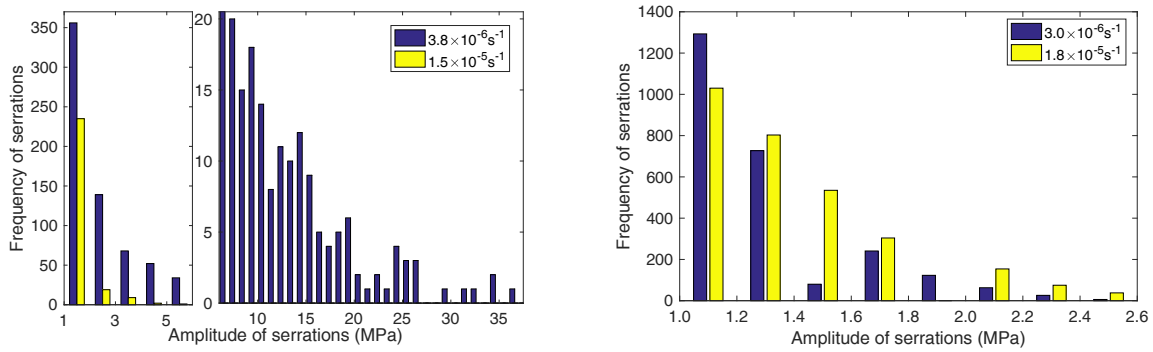

(a) CG-A *(b) UFG-A*

Figure 3.15: Histograms of serrations at 100° C

The engineering stress-strain curves obtained at 150°C are plotted on figure 3.16. At a nearly similar strain rate, the yield stress of UFG material is now lower than that of CG material. The uniform strain of UFG material is slightly higher than that of CG material while the fracture strain of both the materials is much larger than their uniform strain, and almost similar. A 400% increase in fracture strain is observed for CG material as compared to the test done at 100°C at a similar strain rate, but this is mostly due to a longer "post-peak" regime. Small serrations of less than 2 MPa are observed for UFG material while the curve for CG material is mostly smooth with sporadic serrations of less than 1 MPa. Figure 3.17 show the images of fractured samples at 150°C. No necking is observed for either of the materials, but the slanted fracture in UFG material is again clearly associated with localised plastic flow.

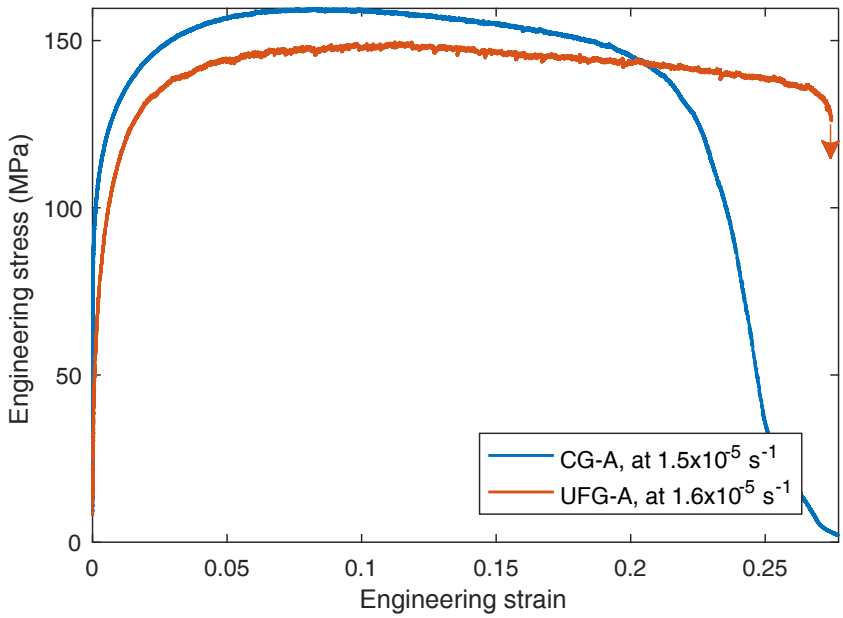

Figure 3.16: Engineering stress-strain curves for tensile tests at 150° C.

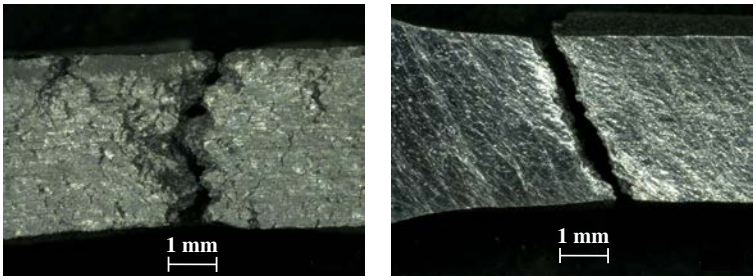

(a) CG, $1.5 \times 10^{-5}s^{-1}$ *(b) UFG,* $1.6 \times 10^{-5}s^{-1}$

Figure 3.17: Optical images of the fractured samples at 150° C

At 200°C (figure 3.18), the change in strength of UFG material with strain rate is even more pronounced indicating a high and positive SRS. At $\sim 4 \times 10^{-3}s^{-1}$ UFG is stronger than CG while at $\sim 2 \times 10^{-4}s^{-1}$ UFG is softer. The apparent Young's modulus of the UFG material (see table 3.4) is much lower than that of CG material and decreases by nearly a factor of two with decreasing strain rate (figure 3.19a). The word "apparent" is used here, because a non-linear pseudo-elastic regime (Figure 3.19b) makes it difficult to define the yield stress of UFG material at small strain rates. This effect, probably due to grain boundary sliding, will be discussed in chapter 5. The apparent yield stress of the UFG material also decreases by a factor of 3 when the strain rate decreases from $4.5 \times 10^{-3}s^{-1}$ to $1.4 \times 10^{-4}s^{-1}$. Similar trend is observed for the UTS. Meanwhile, the uniform strain and fracture strain increase with this decrease in strain rate. Small sporadic serrations of less than 2MPa can be observed at the slowest rate for UFG material. Serrations of amplitude less than 1MPa (observed in the case of the UFG material at $4.5 \times 10^{-3}s^{-1}$) are not considered.

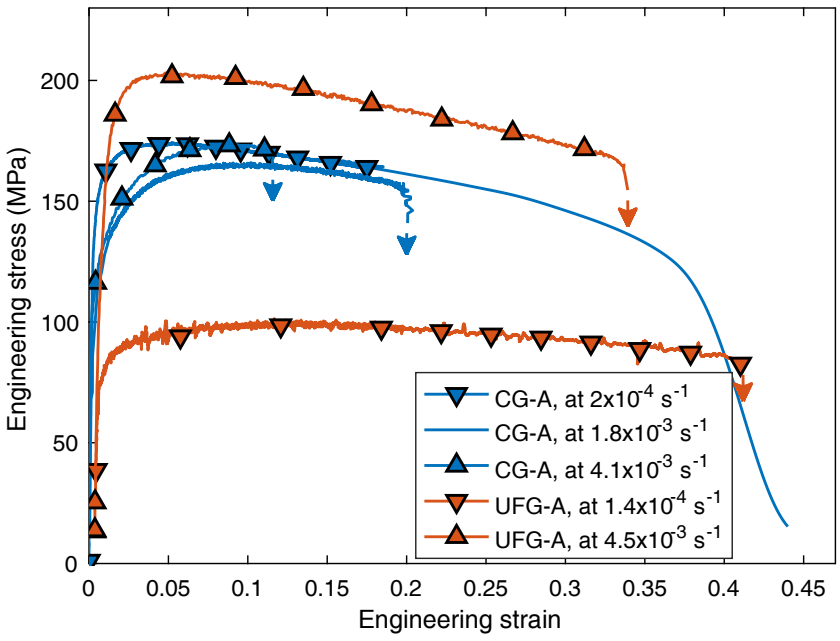

Figure 3.18: Engineering stress-strain curves for tensile test at 200° C.

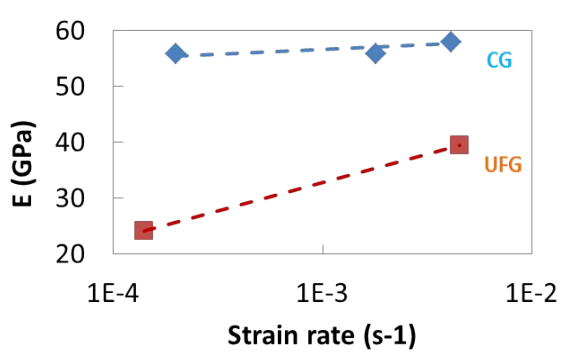

(a)

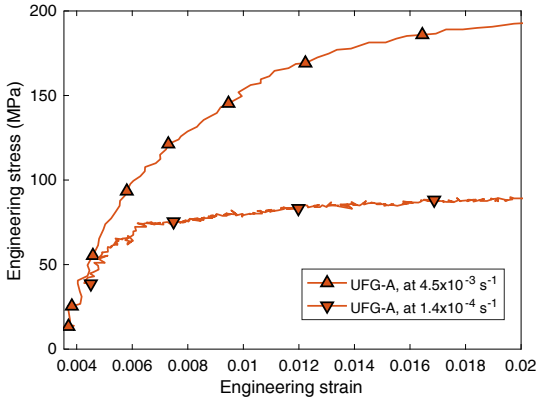

(b)

Figure 3.19: (a) Young's modulus as a function of strain rate at 200°C and (b) a zoom of engineering stress-strain plot at 200°C for UFG material.

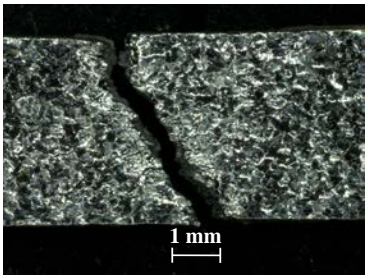

(a) CG, $1.8 \times 10^{-3} s^{-1}$

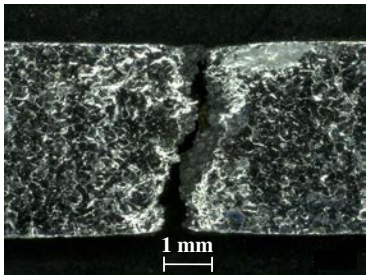

(b) CG, $4.1 \times 10^{-3} s^{-1}$

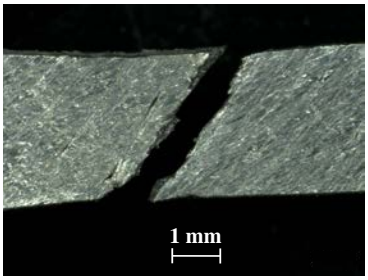

(c) UFG, $1.4 \times 10^{-4} s^{-1}$

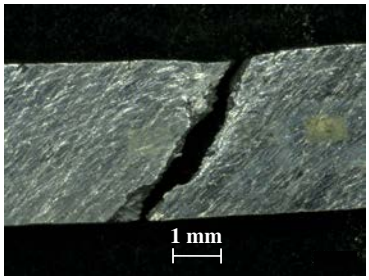

(d) UFG, $4.5 \times 10^{-3} s^{-1}$

Figure 3.20: Optical images of the fractured samples at 200°C

A comprehensive details of the activity of serrated flow for high temperature tensile tests is presented in table 3.5. Full (respectively, hollow) symbols have been plotted on figure 3.21, to indicate the temperature and strain rates for which serrations have (respectively, have not) been observed in CG and UFG materials. The solid lines correspond to the limits of the solute drag or friction regimes determined by Amokhtar and Fressengeas [8] for Al-Mg alloys. Serrations should normally be observed in-between the two lines. The PLC regime defined by those lines in each case is pushed towards higher temperatures and/or lower strain rates i.e. 100°C for CG materials and 200°C for UFG.

Material	Temperature (°C)	Strain rate (s^{-1})	Strain at onset of serrations	Type
CG-A	100	3.8×10^{-6}	0.37%	C
CG-A	100	1.5×10^{-5}	1.02%	C
CG-A	150	1.5×10^{-5}	11.68%	B+C
CG-A	200	1.8×10^{-3}	na.	
CG-A	200	4.1×10^{-3}	na.	
CG-A	200	2×10^{-4}	na.	
UFG-A	100	3.0×10^{-6}	1.56%	B
UFG-A	100	1.8×10^{-5}	1.58%	B
UFG-A	150	1.6×10^{-5}	3.39%	B+C
UFG-A	200	1.4×10^{-4}	3.24%	B
UFG-A	200	4.5×10^{-3}	na.	

Table 3.5: Details of the serrated yielding during the HT tensile tests

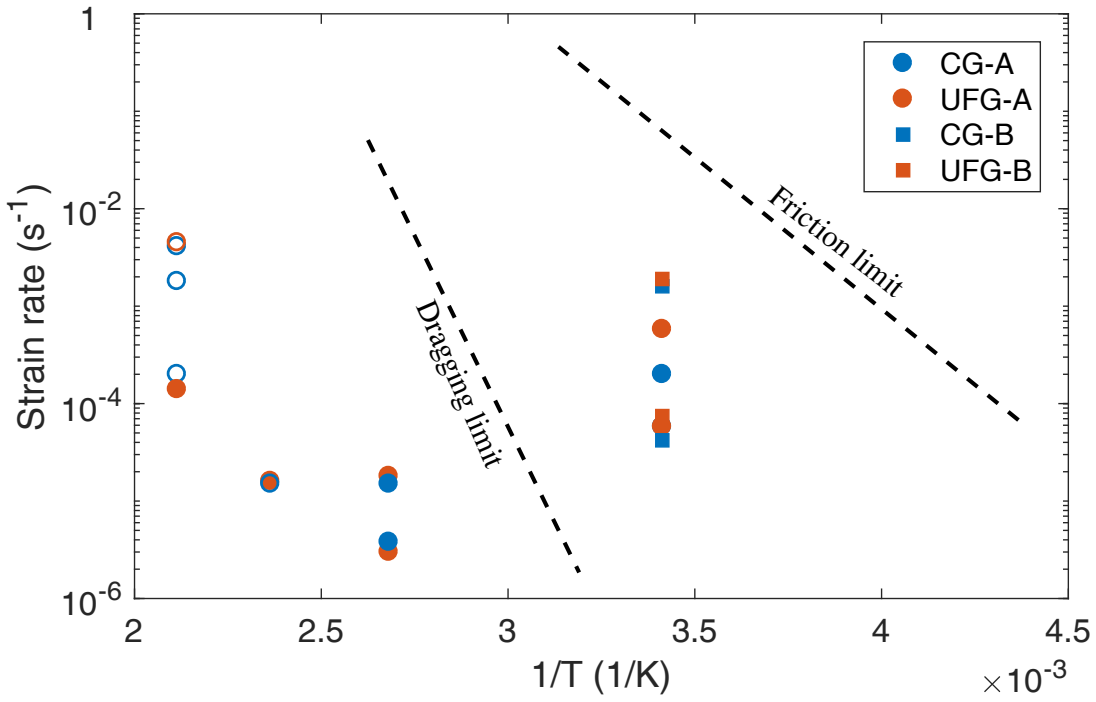

Figure 3.21: Schematic diagram of the temperature and strain rate regimes of PLC effect in Al-Mg alloys. Dragging and Friction limits are taken from [8] (Filled symbols represent serrated flow while open symbols represent smooth curves)

3.2 Relaxation tests and SRS measurements

3.2.1 Procedure

Cylindrical specimens as described in section 2.2 of chapter 2 were used to perform relaxation tests in compression. The specimens well-greased with a Teflon spray were mounted between the flat surfaced punch of a 250 kN hydraulic press equipped with the thermal chamber described in section 3.1.1. Special attention was given to the alignment of the compression axis with the cylinder axis. The optical procedure described above was used to measure the true strain. While heating, the specimens were held in compression at 200 N (4 MPa) until thermal equilibrium was achieved. All the compression tests were displacement-controlled.

To perform the relaxation tests, the specimens were initially deformed with a constant displacement rate of 1.6×10^{-2}mm/s (which approximately corresponds to a strain rate of $2 \times 10^{-3} s^{-1}$) until 3-5% compressive strain. Then the crosshead displacement was held constant for 2 hrs, while the stress and strain were recorded, each time the force changed by 50 N. Since the tests were displacement- controlled, the total strain was not perfectly constant, but the increase in strain during the relaxation period was not more than 2%, so that the evolution of the microstructure was probably limited. Figure 3.22 shows a typical true stress relaxation curve.

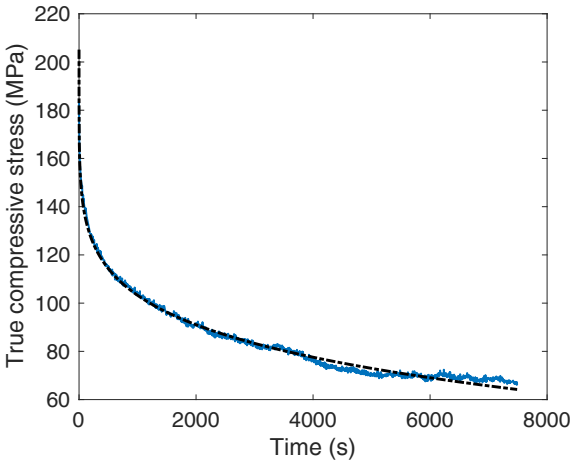

Figure 3.22: Stress evolution with time during a relaxation test (CG at 200° C) and power law fit

An exponential or power law fit was obtained for the stress relaxation data, and the stress rate ($\dot{\sigma}$) was calculated from these fitted laws.
To compare the relaxation tests done at various temperatures on CG and UFG microstructures, the relaxed fraction of the flow stress, RF was calculated as follows:

$$RF = \frac{\sigma_0 - \sigma}{\sigma_0} \tag{3.1}$$

Here, σ is the current true stress during the relaxation period and σ_0 is the true stress just before the start of relaxation period.

The plastic strain rate, $\dot{\epsilon_p}$ was calculated using 2 methods:
Method 1:
Plastic strain, ϵ_p is calculated by subtracting the elastic strain, ϵ_e from the total strain, ϵ obtained using the optical measurement.

$$\epsilon = \epsilon_e + \epsilon_p = \frac{\sigma}{E} + \epsilon_p \tag{3.2}$$

$$\dot{\epsilon_p} = \dot{\epsilon} - \frac{\dot{\sigma}}{E} \tag{3.3}$$

Here, E is the young's modulus of the specimen calculated from the ramp before each relaxation test.
Method 2:
This method was proposed by Lee and Hart [9] and used by Kapoor [7] to analyze displacement-controlled relaxation tests. During relaxation, the total displacement, d is constant and can be written as:

$$\begin{aligned} d &= d_{machine} + d_{elastic} + d_{plastic} \\ &= \frac{F}{K_m} + \frac{F \cdot h}{A \cdot E} + \epsilon_p \cdot h \end{aligned} \tag{3.4}$$

where F is the applied force, K_m is the stiffness of the machine and A and h are the cross-section and height of the specimen respectively. Displacement, d can also be written as:

$$d = \frac{F}{K} + \epsilon_p \cdot h = \frac{\sigma \cdot A}{K} + \epsilon_p \cdot h \tag{3.5}$$

where K is the combined stiffness, which includes the elastic stiffness of the specimen, $h/A \cdot E$ and the stiffness of the machine, K_m. It was obtained for each test within the elastic regime. Taking the derivative of the equation 3.5:

$$\frac{\dot{\sigma} \cdot A}{K} + \frac{\sigma \cdot \dot{A}}{K} + \dot{\epsilon_p} \cdot h = 0 \tag{3.6}$$

Assuming the specimen's volume, $V = A \cdot h$ to remain constant during the plastic flow:

$$\begin{aligned} \dot{A} \cdot h + A \cdot \dot{h} &= 0 \\ \dot{A} = -A \cdot \frac{\dot{h}}{h} = -A\dot{\epsilon} &\approx -A\dot{\epsilon_p} \end{aligned} \tag{3.7}$$

Neglecting second order term in strain in equation 3.6:

$$\epsilon_p \dot{h} = \dot{\epsilon_p} \cdot h\dot{\epsilon} \tag{3.8}$$

we have,

$$\frac{\dot{\sigma} \cdot A}{K} - \frac{\sigma \cdot A\dot{\epsilon_p}}{K} + \dot{\epsilon_p} \cdot h = 0 \tag{3.9}$$

and finally,

$$\dot{\epsilon_p} = \frac{-\dot{\sigma}}{\left[\frac{Kh}{A} - \sigma\right]} \tag{3.10}$$

The evolutions of the plastic strain rate with the true compressive stress obtained by both methods are compared in figure 3.23, for CG material at 200°C. The two curves nearly overlap. This holds true for tests done at high temperature, which gave rise to a substantial stress relaxation, but with decreasing temperature, the plastic strain rate obtained by method 1 is always smaller than that obtained using method 2. One of the reasons for this could be the error associated with the optical measurement of strain. With the decreasing stress, the change in strain decreases, which increases the sensitivity to the noise in the optical strain measurement. Furthermore, with decreasing strain rate and decreasing temperature there is a substantial increase in strain bursts. This is probably due to the PLC effect, which becomes active in low temperature and low strain rate regime and makes the fluctuating strain signal difficult to analyse. Hence for all the tests, the plastic strain rate was calculated using method 2.

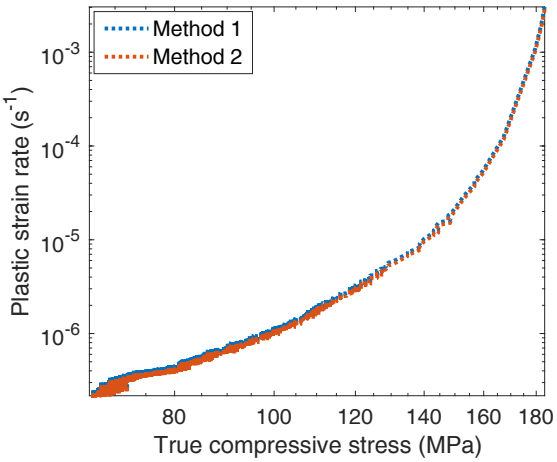

Figure 3.23: Plastic strain rate evolution with true stress (CG at 200° C)

SRS was calculated from the slope of plastic strain rate and true compressive stress in a log-log plot. Since the slope was not constant, piecewise linear regression was made around a particular strain value. To cover a wider range of strain rate, strain rate jump tests were also performed on the same specimen after the relaxation tests. Once again the strain rate jump tests were displacement-controlled and the displacement rate was changed after every 0.05 mm or 0.1 mm for ten times lower or higher rates. The data acquisition rate was 10 Hz for low displacement rates, and 100 Hz for high displacement rates (Figure 3.24).

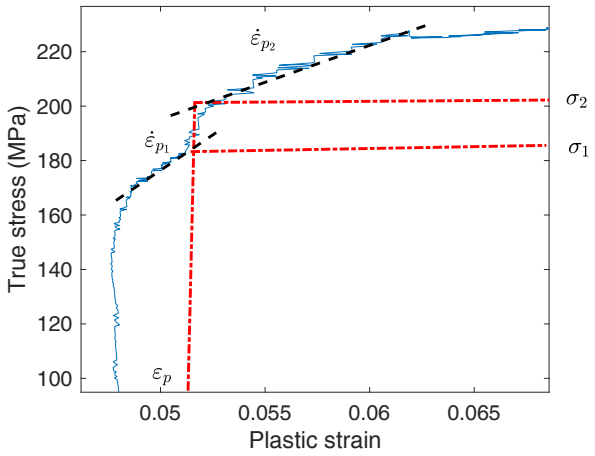

Figure 3.24: Principle of strain rate jump test analysis (CG at 200° C)

SRS from the strain rate jump tests was calculated as follows:

$$m = \left[\frac{\Delta ln\sigma}{\Delta ln\dot{\epsilon_p}}\right]_{T,\mu S} = \left[\frac{ln\sigma_1 - ln\sigma_2}{ln\dot{\epsilon_{p,1}} - ln\dot{\epsilon_{p,2}}}\right]_{T,\mu S} \tag{3.11}$$

3.2.2 Results

Influence of strain-level

The results of two consecutive relaxation tests done at different strain levels: 2.3% (corresponding an initial stress of 185 MPa) and 4.3% (corresponding to an initial stress of 190 MPa) on CG material at 200°C; and 1.7% (corresponding an initial stress of 426 MPa) and 5.1% (corresponding to an initial stress of 526 MPa) on UFG material at room temperature (RT) are plotted in figure 3.25 and 3.26 respectively.

In the first case, the strain levels have almost no influence on stress relaxation. In the second case, the initial strain level has a significant influence: nearly 8% of the flow stress is relaxed after 2 hours, for an initial strain of 5.1% (initial stress: 526 MPa), while the relaxed fraction is only 5.5% for an initial strain of 1.7% (initial stress: 426 MPa). This difference in stress relaxation can be attributed to the much larger difference in the initial stress levels than in the previous case.

Hence, to compare all the relaxation tests at different temperatures and different microstructures, only data corresponding to an initial strain in the range of 4-5% were thus used.

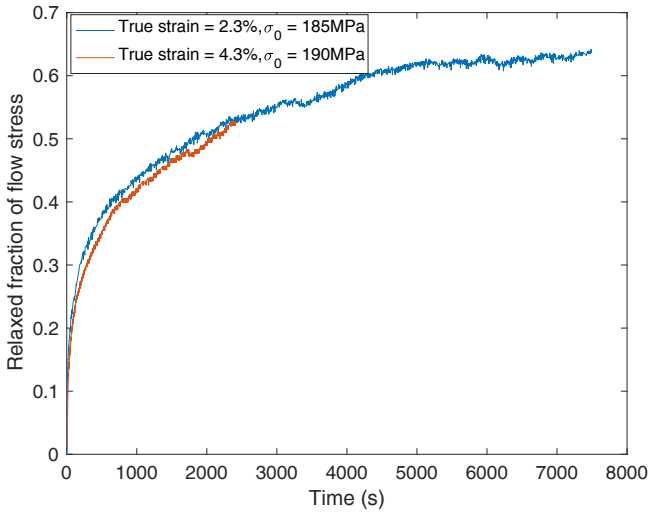

Figure 3.25: Comparison of the relaxation kinetics for two strain levels in CG material at 200° C)

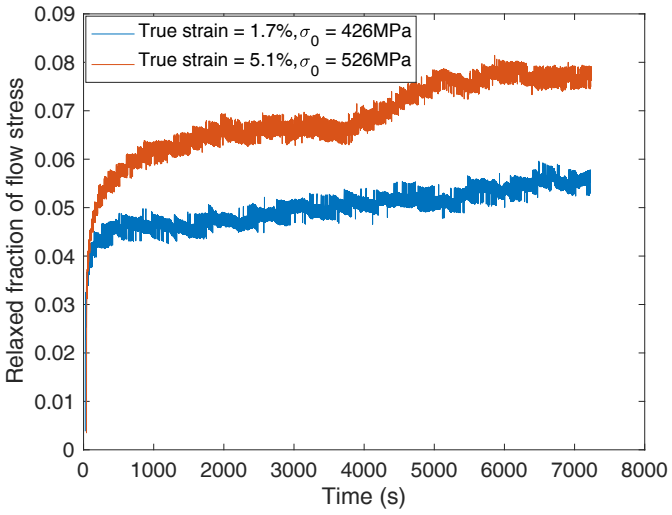

Figure 3.26: Comparison of the relaxation kinetics for two strain levels in UFG material at 20° C)

Influence of temperature

As evident from figures 3.27 and 3.30, the relaxed fraction (RF) of flow stress increases with the temperature for both CG and UFG materials. As compared to the tests done at RT, the final RF is 11 times more for tests done at 200°C for both CG and UFG materials. This increase in relaxed fraction of flow stress is not only due to an increase in stress drop, (which is not observed for the relaxation test at 200°C on UFG material (Table 3.6), but also to the decrease in strength of the material, i.e. a decrease in σ_0. At all temperatures, the plastic strain rate is quite high ($\approx 10^{-3}s^{-1}$) at the onset of relaxation, and progressively drops to ($\approx 10^{-7} - 10^{-8}s^{-1}$), as the stress relaxes. The strain-rate versus stress plots shown on Figures 3.28 and 3.31 do not have a constant

slope over the strain rate range covered in each test and they are not parallel at different temperatures, which suggest a temperature and strain-rate dependence of the SRS, as shown below.

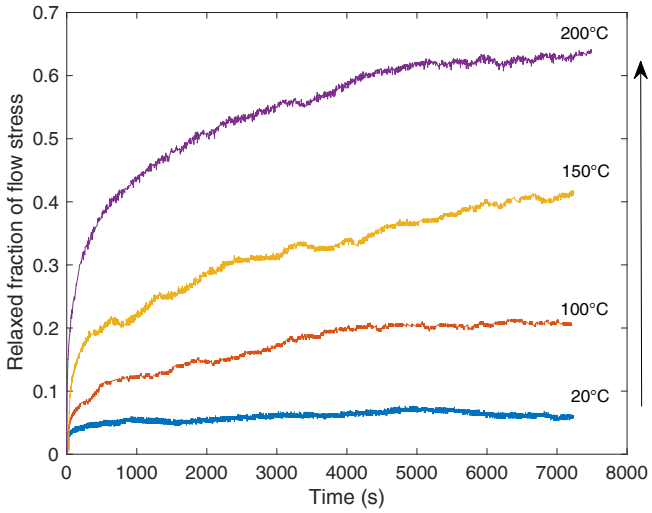

Figure 3.27: Influence of temperature on the relaxation kinetics in CG material

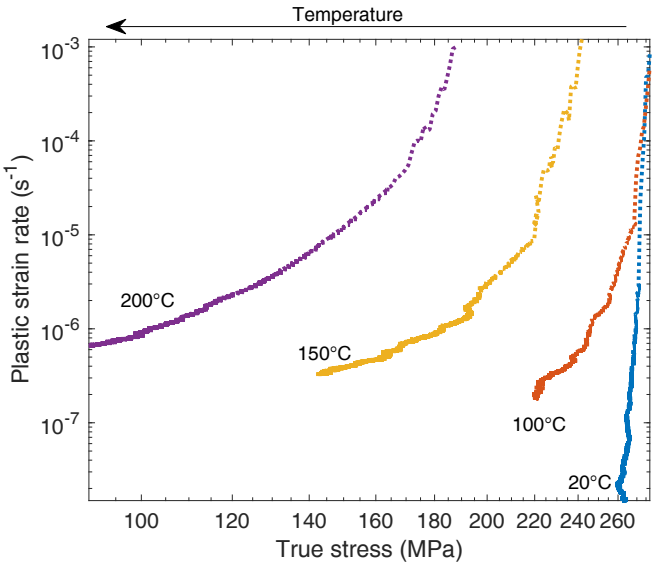

Figure 3.28: Plastic strain rate vs true stress during relaxation for CG Al5083

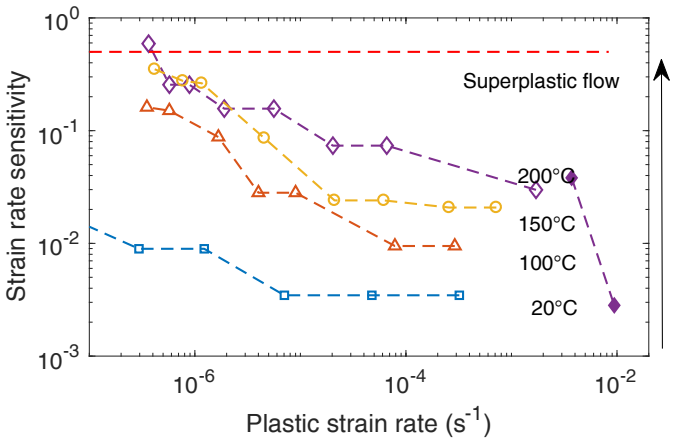

Figure 3.29: Influence of temperature on strain-rate sensitivity of CG Al5083, open symbols for relaxation tests and filled symbols for strain rate jump tests

Temperature (K)	**CG**			**UFG**		
	Initial true stress (MPa)	Stress drop after 2h (MPa)	RF (%)	Initial true stress (MPa)	Stress drop after 2h (MPa)	RF (%)
293	280	16	6	525	40	8
373	278	58	21	451	174	39
423	243	101	42	373	283	76
473	184	118	64	225	201	90

Table 3.6: True stress values during relaxation tests

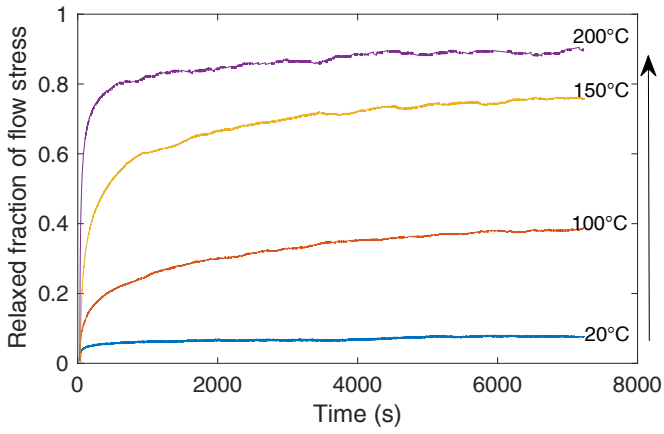

Figure 3.30: Influence of temperature on the relaxation kinetics in UFG material

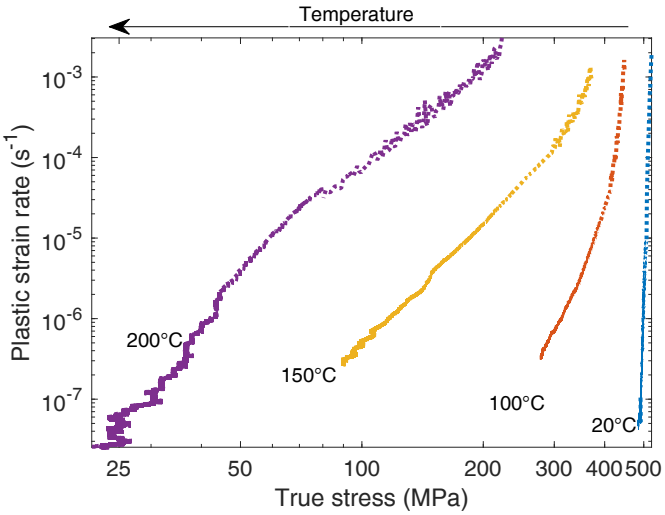

Figure 3.31: Plastic strain rate vs true stress during relaxation for UFG Al5083

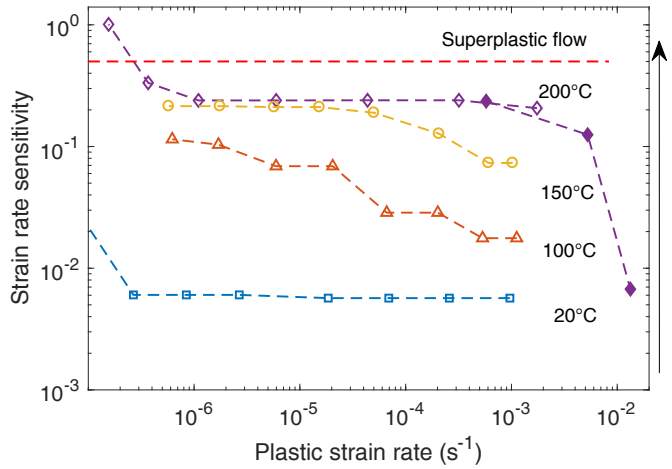

Figure 3.32: Influence of temperature on strain-rate sensitivity of UFG Al5083, open symbols for relaxation tests and filled symbols for strain rate jump tests

Influence of microstructure

To analyse the influence of microstructure, RF evolution curves are plotted at same temperature for both the materials (Figure 3.33). Relaxation is faster and more pronounced in UFG material, where the final RF is sometimes even more than twice higher. Mohebbi et al. [10] performed stress relaxation tests in plane strain compression at room temperature on UFG Al obtained by various numbers of ARB passes. They found that the relaxed fraction of stress increases with the number of ARB passes, which is consistent with the present observations made on CG and UFG Al5083. Based on TEM observations showing a decrease in dislocation density and dislocations rearrangement into sharper sub-boundaries after relaxation, they attributed the enhancement of relaxation by grain refinement to easier dislocation annihilation and a contribution of grain boundary sliding.

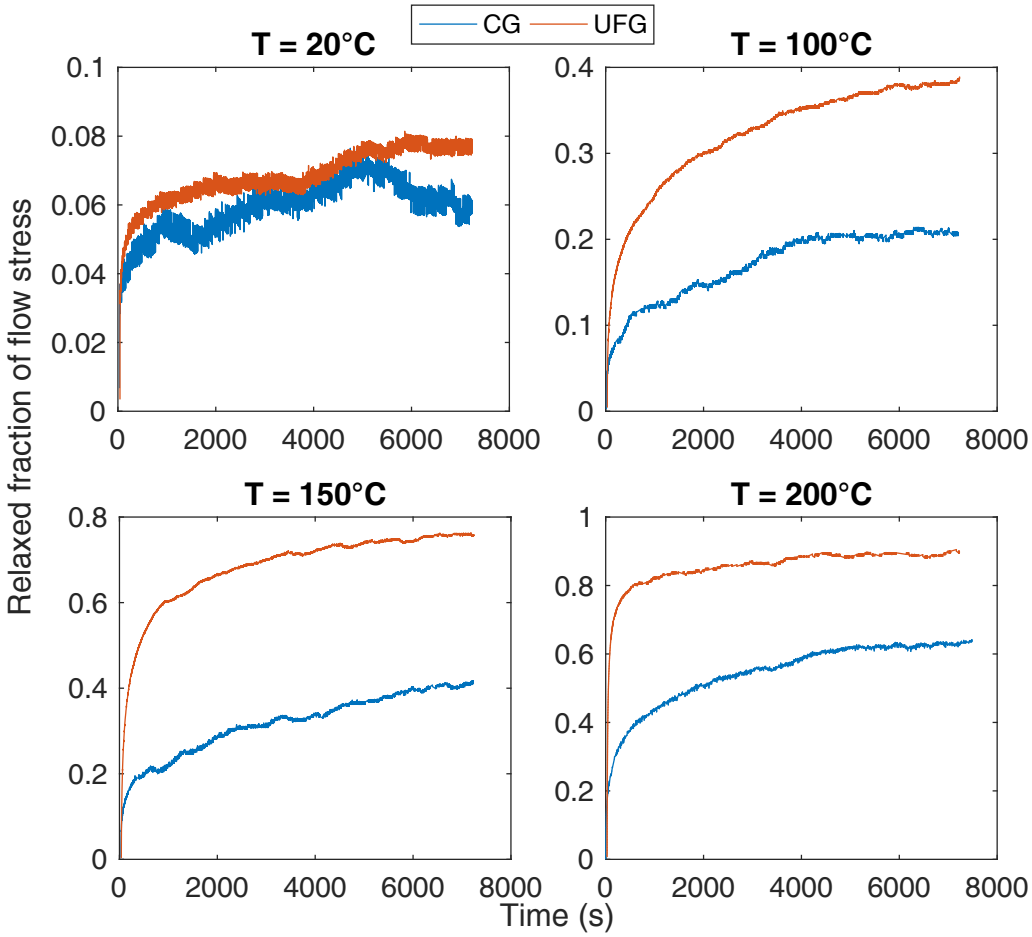

Figure 3.33: Influence of microstructure of relaxation kinetics at different temperatures.

The plastic strain rate vs. true stress curves for both microstructures are compared in figure 3.34. For a given temperature, they are not parallel, which clearly shows that microstructure refinement modifies the SRS. Their relative positions along the stress axis is also observed to change with temperature: while a higher stress is always required to produce a given strain rate in UFG material than in CG at 20 and 100°C, this is no more the case above 150°C.

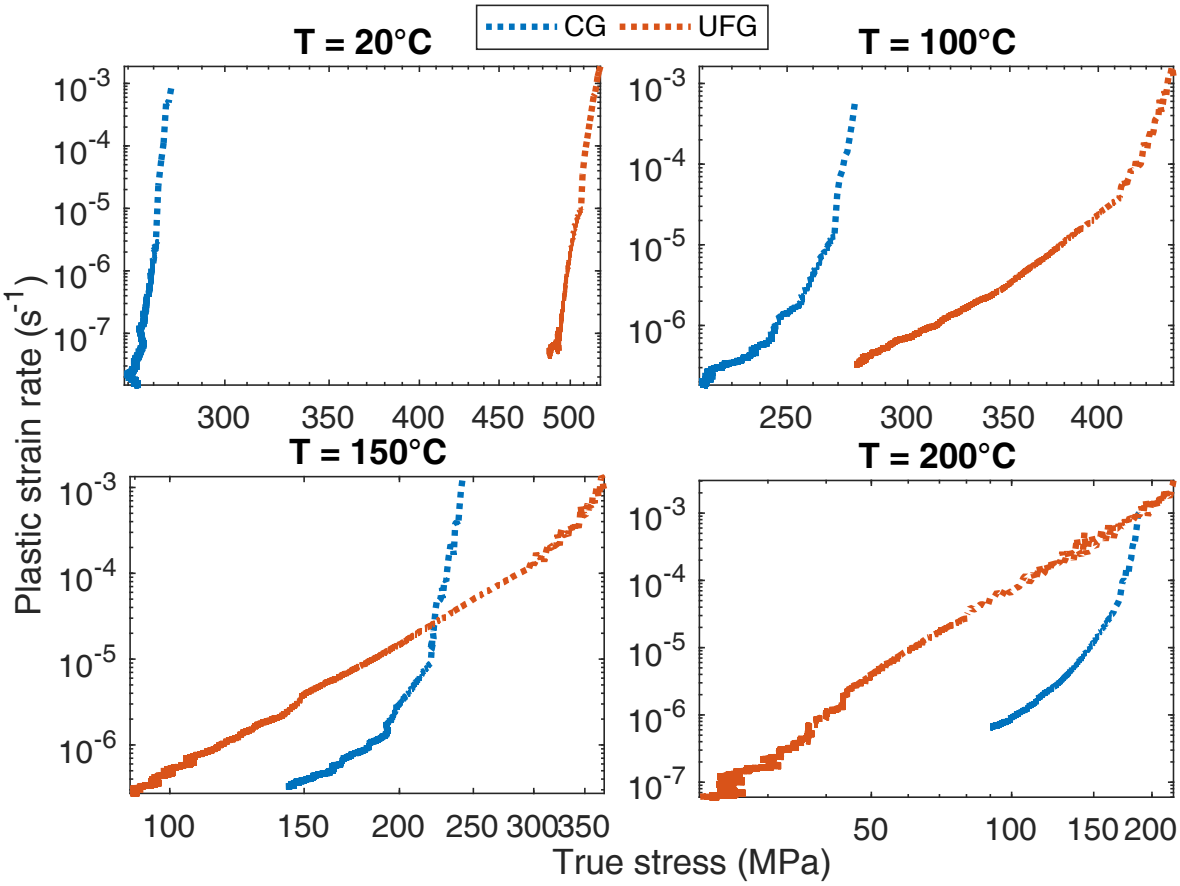

Figure 3.34: Plastic strain rate vs true stress for CG and UFG materials at different temperatures.

SRS is plotted for each material at different temperatures (Figure 3.35). There is a decrease in SRS with the increasing plastic strain rate at all temperatures and for both the materials. SRS also increases with increasing temperature. Several phenomena can explain such changes: onset of dislocation climb, transition from solute drag to dislocation escape regime, activation of non-octahedral slip systems, as well as grain boundary sliding. This will be discussed in the following chapter after further analysis of the deformation mechanism.

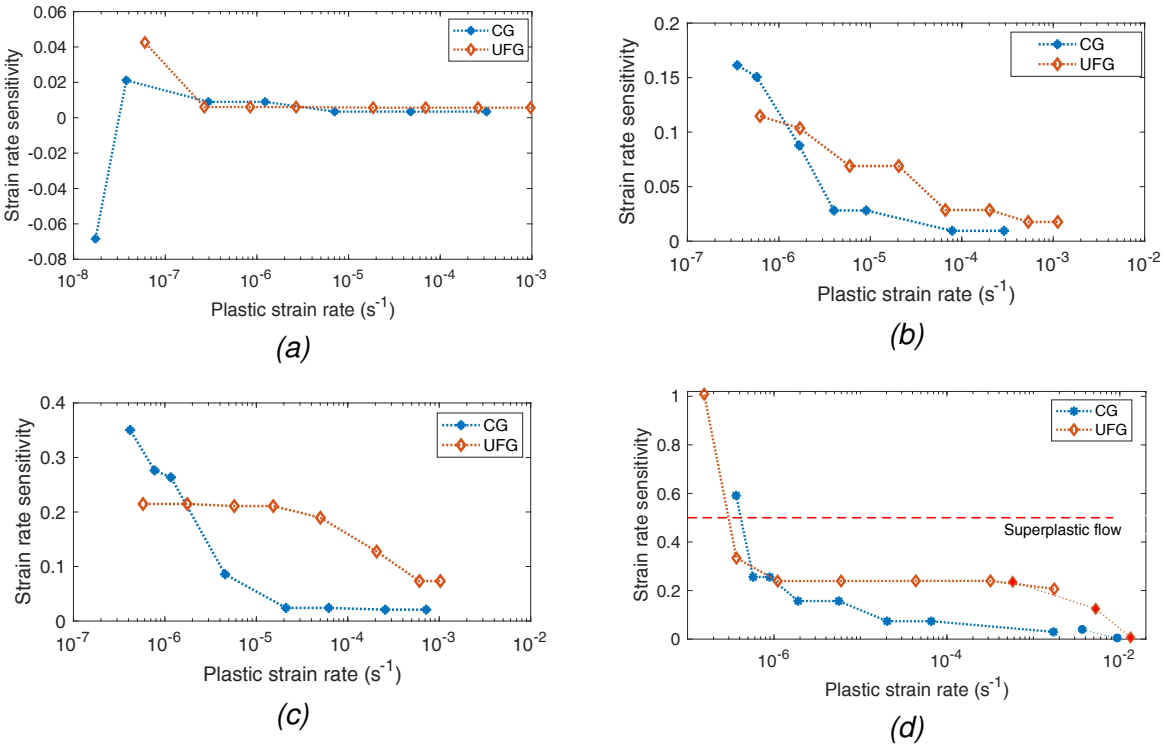

Figure 3.35: Influence of microstructure on SRS at (a) 20°C, (b) 100°C, (c) 150°C and (d) 200°C, open symbols for relaxation tests and filled symbols for strain rate jump tests

SRS is plotted for each material versus true stress in figure 3.36. For UFG material, irrespective of the temperature and the strain rate, the data points fall on a single curve, which suggests that the transitions in mechanisms with temperature or strain rate are stress-controlled. This is consistent with the model of Duhamel et al. [11]. Such a "master curve" is however not obtained in CG material.

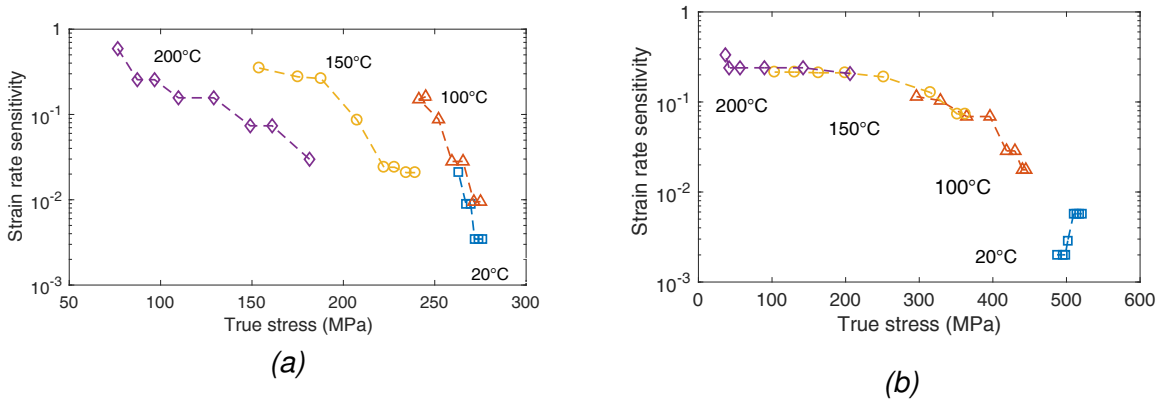

Figure 3.36: Strain-rate sensitivity as a function of true stress at all temperatures for (a) CG and (b) UFG materials.

Plastic strain rate vs. true stress curves are compared with those obtained by Kapoor

et al. [7] (see figure 3.37). Even though the shape of the curves is almost similar, their curves lie above the curves for the current material i.e. for the same stress level they obtain a higher strain rate. This can be explained by the lower Mg content (1.5%) in their material which can lower the threshold stress for relaxation.

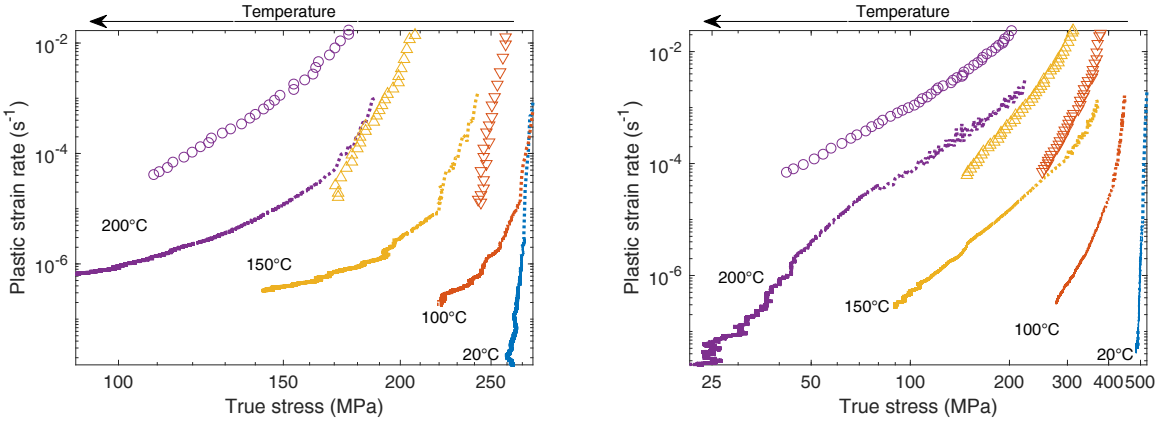

Figure 3.37: Plastic strain rate as a function of stress for (a) CG and (b) UFG materials in comparison with the data from Kapoor et al. [7] on Al-1.5%Mg

The activation volume of the Al5083 CG and UFG materials is calculated as:

$$V_a = MkT\frac{\partial ln\dot{\epsilon}}{\partial \sigma} = \frac{MkT}{\sigma}\frac{\partial ln\dot{\epsilon}}{\partial ln\sigma} = \frac{MkT}{\sigma \cdot m} \tag{3.12}$$

Here, M = 3.06 is the Taylor factor for isotropic fcc materials and k = $1.38 \times 10^{-23} J/K$ is the Boltzmann constant. Note that the value of M is controversial for UFG materials, whose deformation is not purely controlled by dislocation glide. A value of square root of 3 is often used instead [11]. The M factor should also depend on texture, which is quite pronounced in UFG-batch A material. The activation volume normalised with Burger's vector, b = $2.86 \times 10^{-10} m$ is plotted versus the flow stress (normalised with the shear modulus, G = $3.82 \times 10^4 - 39T$ MPa) for both CG and UFG materials in figure 3.38, in which the black dotted line represents the case where V_a would vary as

$$\frac{V_a}{b^3} = \frac{2}{3}\frac{\mu}{\sigma} \tag{3.13}$$

Equation 3.13 (Cottrel-Stokes law) represents the case of pure metals where dislocation-dislocation interaction controls deformation [7]. Due to the uncertainties on the correct value of M, this plot is qualitative and rather reflects trends than absolute values.

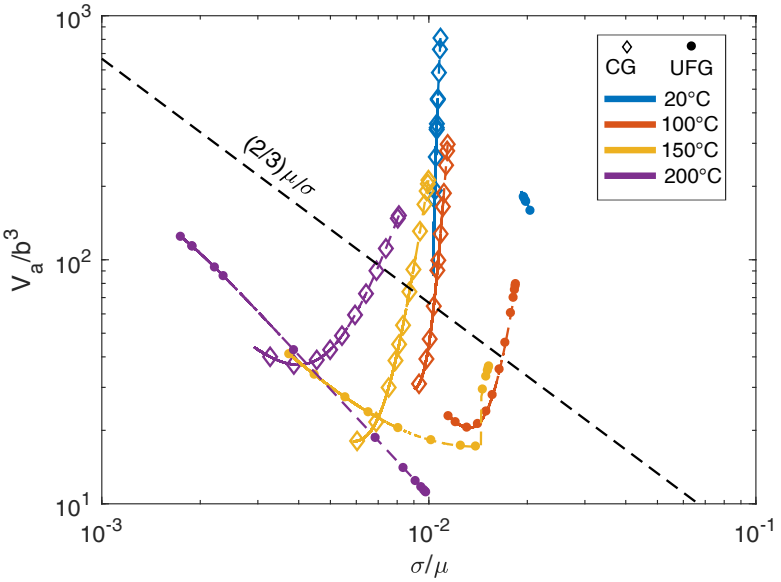

Figure 3.38: Normalised activation volume vs. normalised flow stress for CG and UFG batch A materials

The activation volume of UFG material is lower than that of CG material at all the temperatures indicating a reduction in the spacing between obstacles for UFG materials. The use of M = $\sqrt{3}$ would shift the activation volume for the UFG material to even smaller values.

For the UFG material, all data-points more or less fall on a unique parabolic curve which, again, suggests that in this material, the transition in deformation mechanisms is merely stress-controlled. At high stress (low temperature), the activation volume increases with the stress (Inverse Cottrel-Stokes behaviour). At moderate stress, it is nearly constant, while at low stress, it increases with the decrease in stress ("normal" or Cottrel-Stokes behaviour). For CG material, the activation volume is either nearly constant or rises with the stress and the data-points obtained at different temperatures do not fall on a single curve. According to Kapoor et al. [7] who observed similar evolutions in Al-1.5%Mg, the direct proportionality regime is dominated by dislocation break-away, while the inverse proportionality regime indicates viscous drag. Note that Duhamel's model [11] for pure ultrafine grained metals is able to predict the 3 regimes observed here (Figure 3.39). However, the fact that CG Al 5083 also exhibits an inverse Cottrel-Stokes behaviour suggests that the interpretation of Kapoor et al. based on a change in dislocations-solutes interaction is more relevant here. Nonetheless, both consider that in the intermediate stress range where the activation volume remains nearly constant, grain boundary mediated plasticity is predominant.

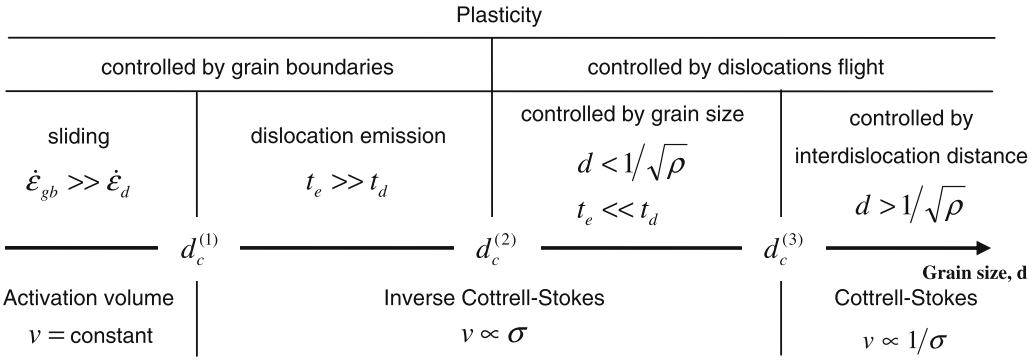

$\dot{\varepsilon}_{gb}$: strain rate at the grain boundaries, $\dot{\varepsilon}_d$: strain rate inside grain by dislocation motion, t_e : dislocation emission time by grain boundary, t_d : dislocation emission time by regular intragranular sources, d : grain size, ρ : dislocations density, v : activation volume, σ : applied stress.

Figure 3.39: Controlling events and resulting laws, with change in grain size, involving dislocations and grain boundaries in plasticity of pure fcc metals, according to Duhamel et al. [11].

3.3 Discussion

3.3.1 GB-hardening and softening

Using the experimental data from tensile and relaxation tests, temperature and strain rate domains for which the microstructural refinement leads to hardening or to softening are identified and plotted in figure 3.40, where data obtained by Ko et al. [12] and Kapoor et al. [7] on Al-1.5Mg are also plotted. The data points represent the conditions for which the flow stress of CG and UFG materials was similar. At low temperature and high strain rate, GBs act as effective barriers for lattice dislocations. A regime of strengthening of UFG materials as compared to CG Al5083 is thus observed. With an increase in temperature and decrease in strain rate, however, GBs act as sinks for mobile dislocations which leads to dynamic recovery, and also accommodate part of the plastic strain (as will be shown in the 5^{th} chapter), which leads to the softening as compared to the CG material.

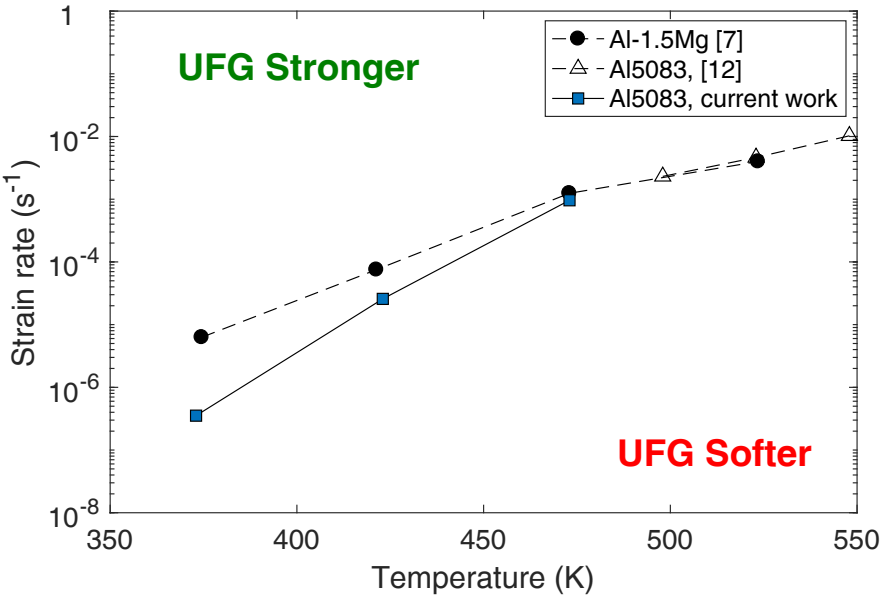

Figure 3.40: Domains of grain boundary-induced hardening or softening for batch-A materials

3.3.2 Influence of viscosity on ductility

The fracture strain obtained after the tensile tests on batch-A materials is plotted as a function of strain rate in figure 3.41, where the measured values of the SRS are indicated, for each testing condition. At RT, UFG is less ductile than CG and the influence of the strain rate is limited, even though the fracture strain slightly decreases with the decrease in strain rate, which can be attributed to rising DSA. By contrast, at 100 and 200°C, UFG is more ductile than CG and the fracture strains of both the materials rise with the decrease in strain rate, and thus an increase in SRS, as also reported by Sabirov et al. [13].

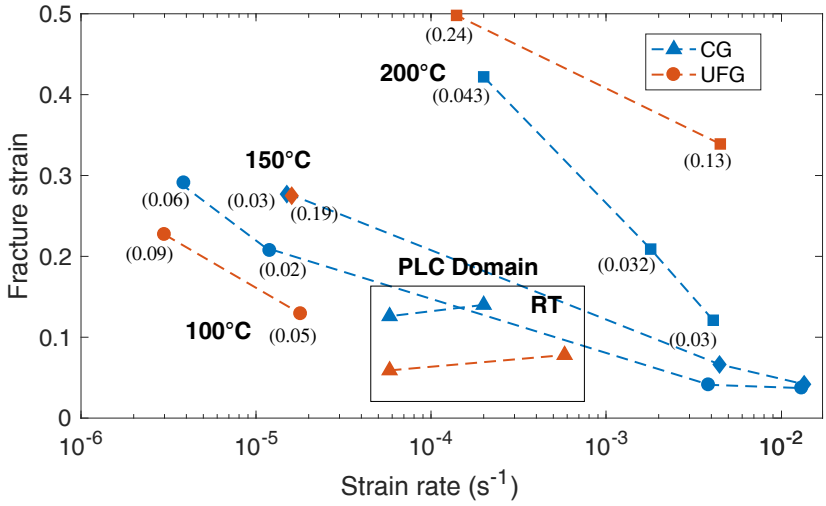

Figure 3.41: Influence of the strain rate on fracture strain for batch-A materials (Corresponding SRS values are mentioned in parenthesis).

Fracture strain is also plotted as a function of SRS in figure 3.42. It is observed that irrespective of strain rate or temperature, a linear correlation is obtained, although the slope is different for CG and UFG materials. This indicates that SRS is one of the controlling factors for fracture. Fracture strain increases with the increase in SRS, because the localisation of plastic deformation leads to a local increase in strain rate. The higher the subsequent increase in flow stress, the more difficult is further localization.

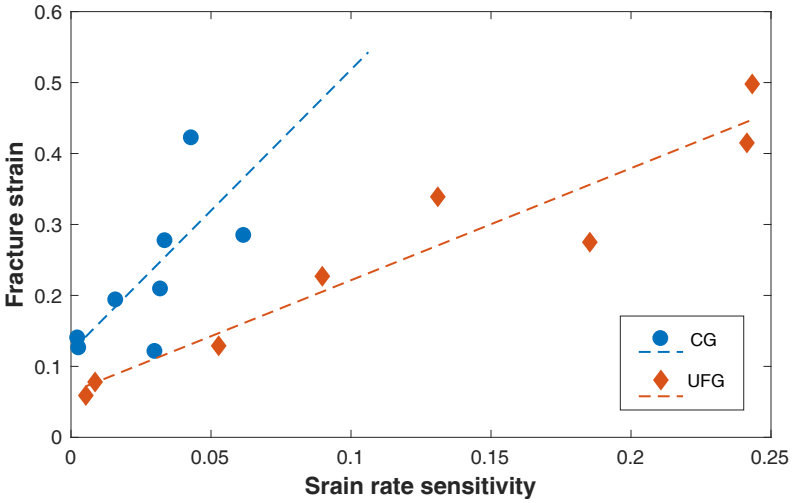

Figure 3.42: Fracture strain as a function of SRS for batch-A materials

The plastic instability criteria (Considere's and Hart's described in chapter 1, while Hahner described below) are used to analyse the tensile tests done at 200°C on batch A materials.

Haehner plastic instability criterion [14] extends to the superplastic regime and thus takes into account grain boundary sliding:

$$\frac{\theta(\varepsilon)}{\sigma(\varepsilon)} < 1 - \left(1 + \frac{\eta}{\varepsilon_0}\right) m(\varepsilon) \tag{3.14}$$

Here, η is the fraction of strain accommodated by grain boundary sliding and $\epsilon_0 \approx 0.5$ is the elementary deformation step assumed to occur during superplastic flow according to Ashby and Verral [15]. If all the deformation is accommodated by GBS, Haehner's criterion reads:

$$\frac{\theta(\epsilon)}{\sigma(\epsilon)} < 1 - 3m(\epsilon) \tag{3.15}$$

For this analysis, the values of SRS are taken as constant (although it might slightly change with strain) so that the second members of equations 1.3, 1.4 and 3.15 are represented by 3 horizontal lines on figure 3.43 where θ/σ is plotted versus ϵ. The fracture strains predicted by each criterion are compared to the measured ones in table 3.7.

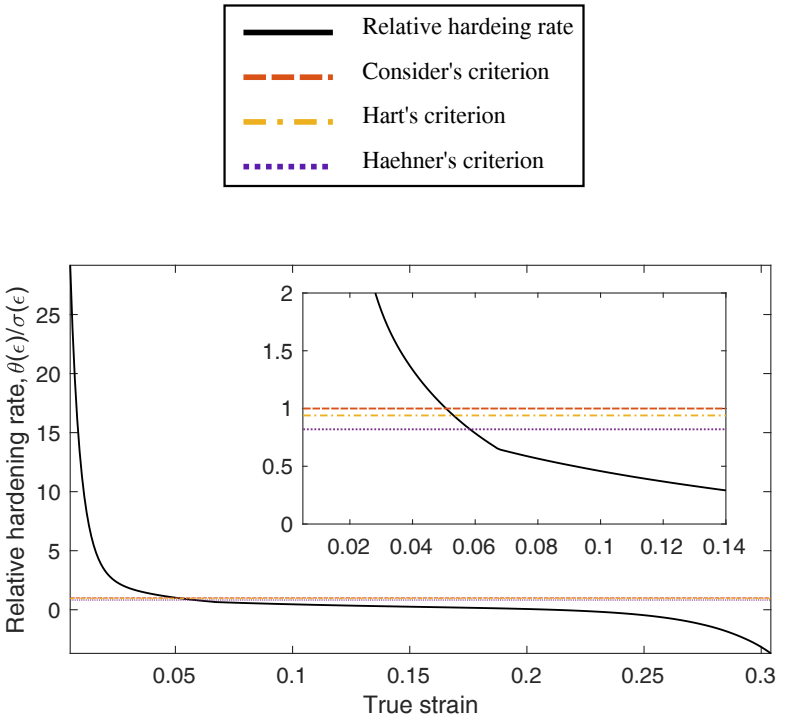

(a) CG-A, $2 \times 10^{-4} s^{-1}$

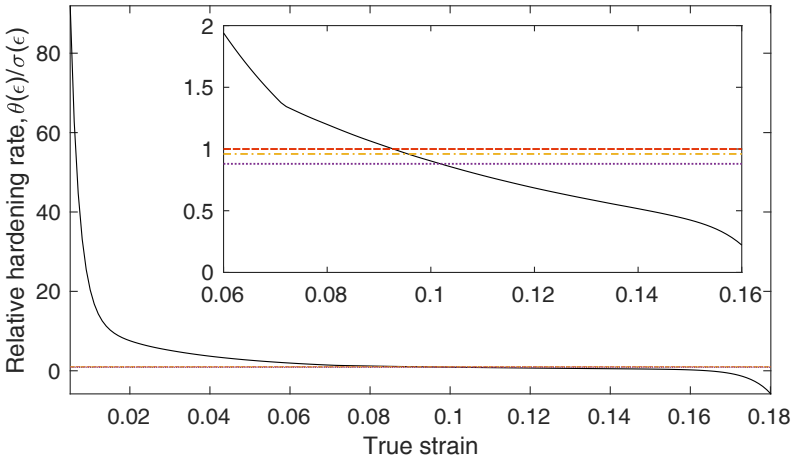

(b) CG-A, $1.8 \times 10^{-3} s^{-1}$

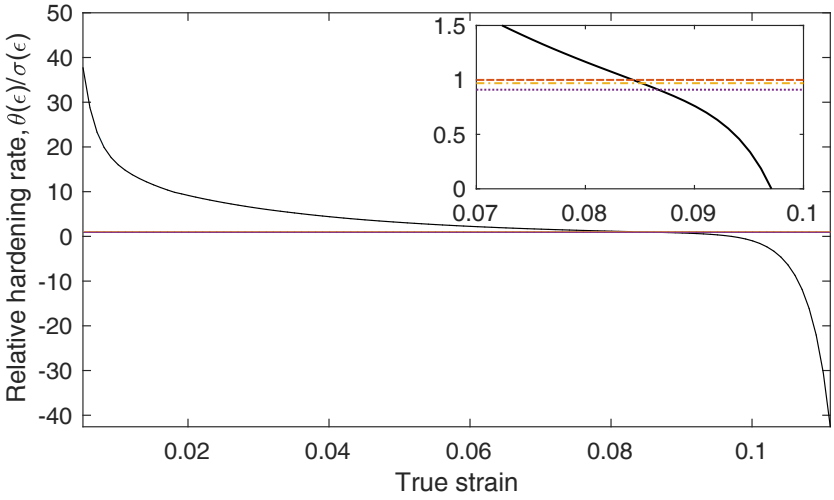

(c) CG-A, $4.1 \times 10^{-3} s^{-1}$

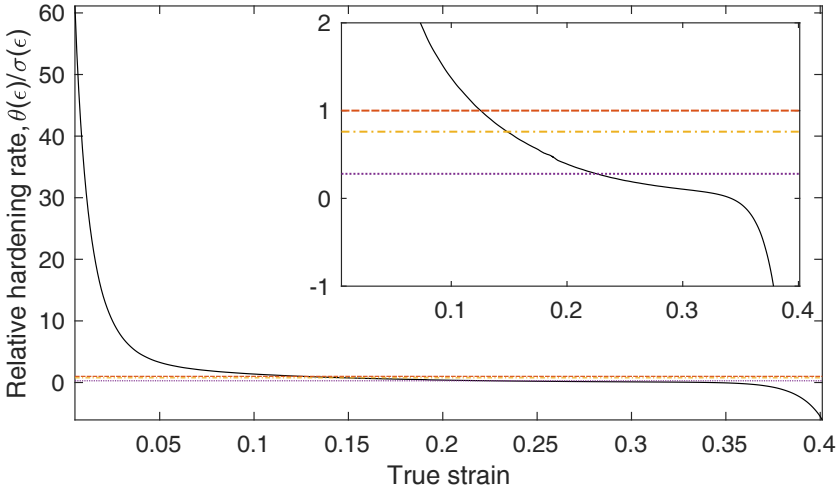

(d) UFG-A, $1.4 \times 10^{-4} s^{-1}$

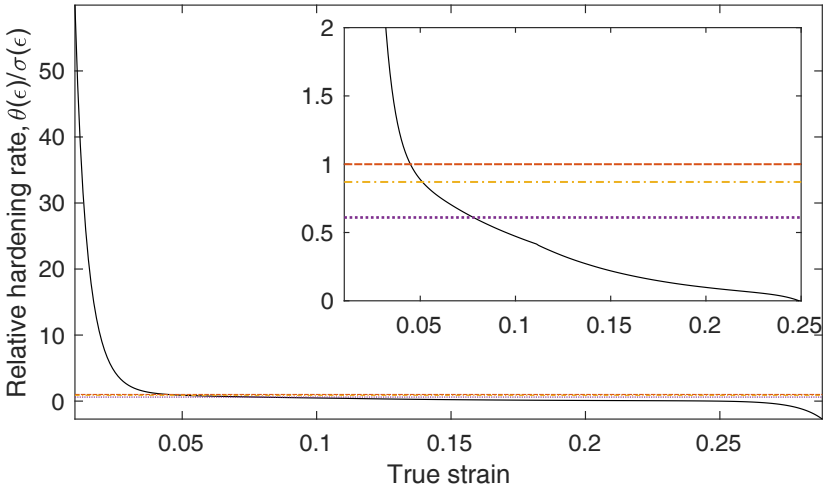

(e) UFG-A, $4.5 \times 10^{-3} s^{-1}$

Figure 3.43: Evaluation of plastic stability during tensile tests at 200° C

Indeed the Considere's criterion underestimates the stability limit of plastic deformation. But even though, Hart's and Haehner's criteria are somewhat closer to the measured fracture strains, their predictions are still not correct. For Haehners'criterion, this might be partly because it has been formulated for the superplastic regime, which was not reached here at 200°C, so that the assumption that GB sliding accommodates all the plastic strain, and the unit strain of 0.5 are probably not suitable.

Material	**Strain rate (s^{-1})**	**SRS**	**Fracture strain**	**Predicted strain at instability**		
				Considere	Hart	Haehner
CG-A	2.0×10^{-4}	0.043	0.422	0.057	0.060	0.067
CG-A	1.8×10^{-3}	0.032	0.209	0.093	0.096	0.102
CG-A	4.1×10^{-3}	0.030	0.121	0.084	0.085	0.087
UFG-A	1.4×10^{-4}	0.24	0.498	0.125	0.147	0.225
UFG-A	4.5×10^{-3}	0.13	0.339	0.045	0.051	0.078

Table 3.7: Predicted strain after which plastic flow is unstable (assuming constant SRS) at 200°C

3.4 Summary

In the present chapter, a macro-scale experimental analysis of the viscoplastic behaviour of CG and UFG materials was presented. It was based on relaxation and tensile tests carried out over a wide range of temperatures (20 to 200°C , that is 0.33 to 0.53 T_m) and strain rates (1×10^{-8} to 1×10^{-3} s^{-1}.

- The mechanical behaviour (yield stress , hardening, ductility) are highly temperature and strain rate dependent.
- With increasing temperature and decreasing strain rate, a transition from stronger to softer UFG material as compared to its CG counterpart was observed. The observed temperature and rate domains where UFG Al5083 is stronger/softer than CG material agree with existing literature on Al-Mg alloys.
- The ductility of both materials raised as the strain rate decreased. While UFG material was less ductile than CG at room temperature, its fracture strain was similar to that of CG at 150°C and finally it became more ductile above 200°C, whatever the strain rate, but mainly due to an increase in post-peak elongation.
- The Young's modulus of the UFG material was observed to be strain-dependant: it decreased with the decrease in strain rate at high temperatures which has not been reported so far, might be due to GB sliding, as discussed in chapter 5.
- The strain-rate sensitivity of UFG material, which was higher than that of CG material was observed to rise with the temperature and with the decrease in strain rate, at fixed T.
- PLC effect, a manifestation of DSA due to the solute Mg atoms was observed for all the materials at 20 and 100°C, and persisted, although with a much lower amplitude, up to 200°C for UFG materials. The three types of bands A, B and C, were observed, depending on the strain rate. At room temperature, the amplitude of the serrations was higher in UFG than in CG materials, while at 100°C, the opposite trend was noticed.
- A systematic slanted fracture was observed for UFG material at all temperatures, while CG material only exhibited slanted fracture within PLC regime.
- Direct linear correlations were obtained between SRS and ductility for both CG and UFG, although with different slopes. However, neither Hart's nor Hähner's plastic flow stability criteria, that take into account the moderating effect of a high SRS on strain localization could rationalize the measured fracture strains.
- The activation volume is smaller in UFG material, because of a decrease in the distance between obstacles. As the stress rises, it first decreases, then remains nearly constant, and finally rises. This change in trend is attributed to a transition from breakaway to viscous drag regimes, which seems to occur at higher temperatures for UFG materials.

- A unique correlation was obtained between SRS or activation volume and true stress for UFG material, indicating that the transition between different mechanisms is stress controlled.

  Further analysis of the mechanisms active during plastic deformation is presented in chapter 4.

Appendix

3.A Creep tests on CG Al5083

Since the creep tests run on batch A CG 5083 had no counterpart in UFG material, these tests are presented in appendix. Some results of these tests will be used in the simulations presented in the next chapter.

3.A.1 Procedure

For the creep tests, cylindrical specimens and flat dog-bone samples (Figure 2.21 chapter 2) were used. Surface preparation of the flat sample is same as for the high temperature tensile tests. Tests were performed using a 10 kN load cell on a 250 kN hydraulic press equipped with a thermal chamber including a resistive heating device, a closed-loop control of the temperature inside and a fan to homogenise it. In the literature, double shear specimens are usually used to keep the true stress constant during creep tests on ductile materials [16]. Here, the creep tests are run in tension, but an additional control loop that recomputes the necessary load based on the optically-measured strain was implemented. However this correction is valid only until necking. Creep tests are either performed until fracture or in a step-wise increment of stress for a given temperature.

3.A.2 Results

Creep tests run until failure

Two of the creep tests at 200°C were run until fracture. Figures 3.A.1, 3.A.2 and 3.A.3 present the creep strain as a function of time and creep rate as a function of time and creep strain respectively. For a stress of 130 MPa, a primary creep is observed where the creep rate decreases, followed by a steady-state where the creep rate reaches a minimun and remains almost constant and finally a tertiary stage where the creep rate increases continuously. For the stress of 100 MPa, no primary stage is observed. The minimum creep rate observed during this steady-state regime is chosen for the post-treatment of creep characteristics.

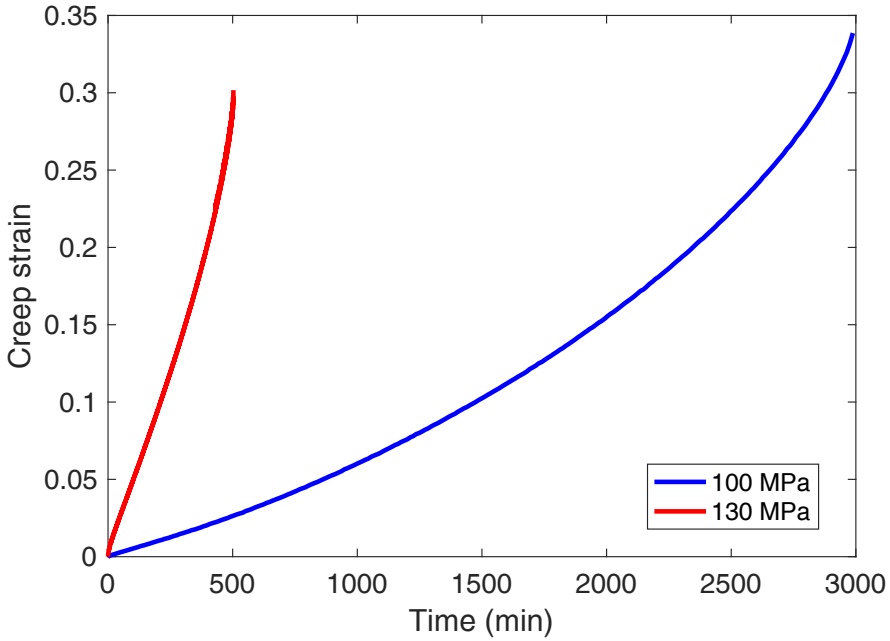

Figure 3.A.1: Evolution of creep strain with time at 200° C

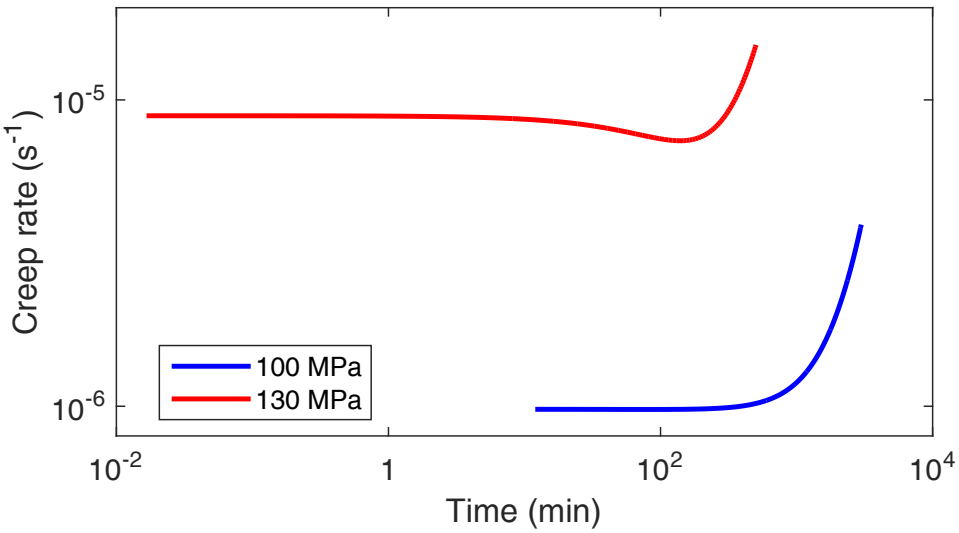

Figure 3.A.2: Evolution of creep rate with time at 200° C

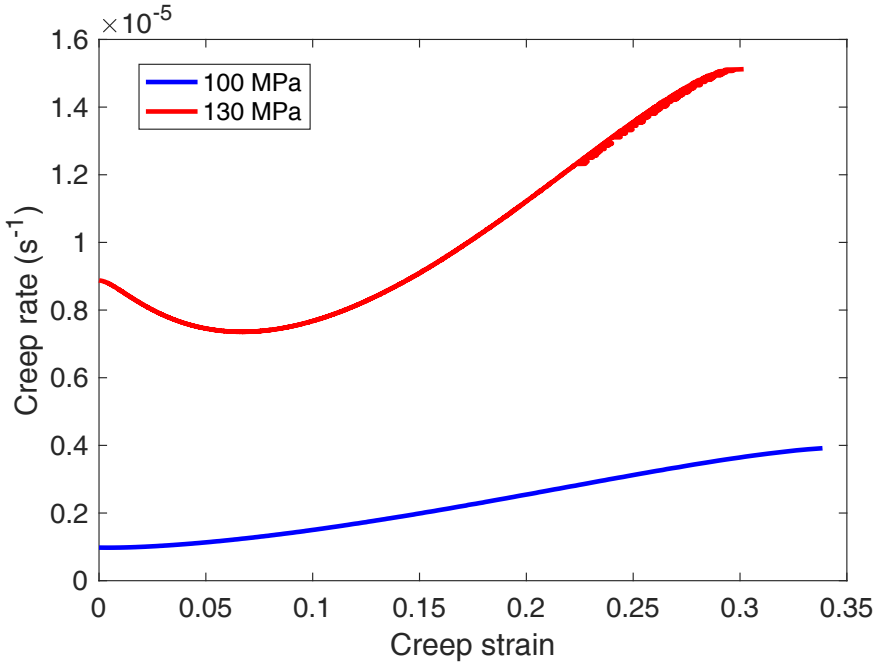

Figure 3.A.3: Evolution of creep rate with strain at 200° C

Step-wise incremental creep tests

All other creep tests were done on one specimen per temperature by stepwise incrementing the true stress from 75 to 150 MPa after an increase in the displacement of 0.1 mm at each stress level. The observed evolution of creep strain at different temperatures is presented in figure 3.A.4. At each stress level, a steady state regime is immediately reached. The creep strain increases linearly with time and hence the creep rate is calculated from the slope of creep strain vs. time curves.

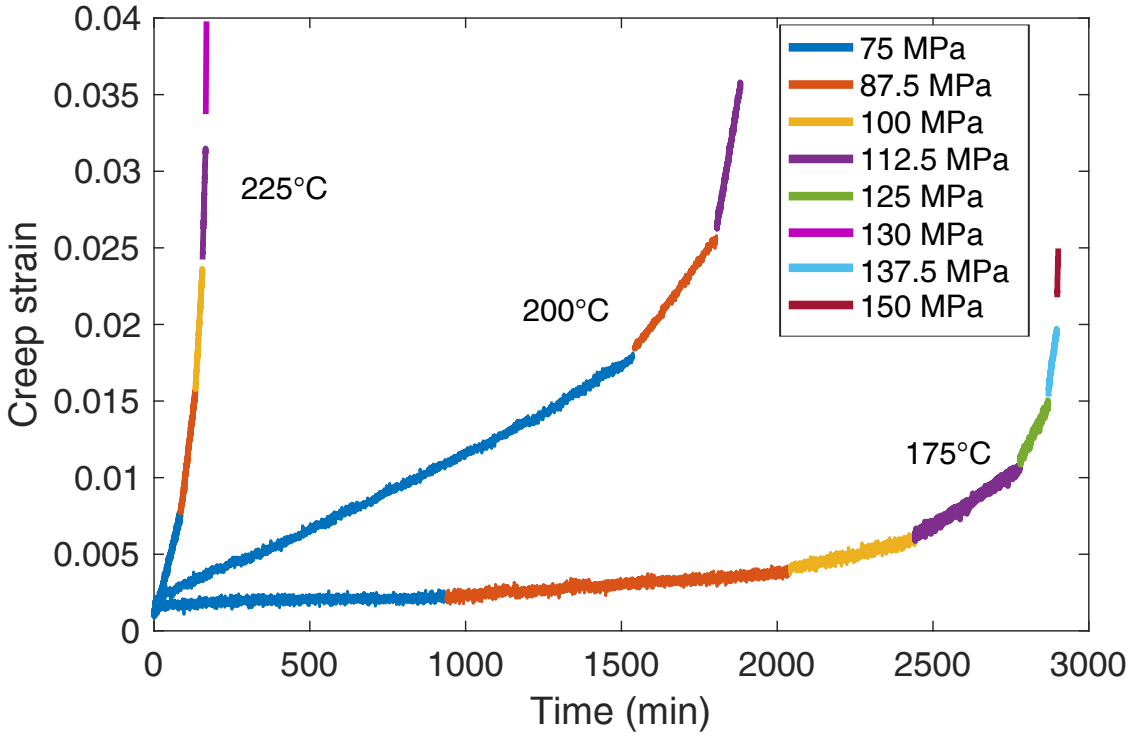

Figure 3.A.4: Evolution of creep strain with time for stepwise-incremental creep tests

Creep behaviour is generally represented as an Arhenius type function:

$$\dot{\epsilon} = A\left(\frac{\sigma}{G}\right)^{n} exp\left(-\frac{Q}{RT}\right) \tag{3.16}$$

Here, $\dot{\epsilon}$ is the steady state creep rate, σ is the true stress, G is the shear modulus of the material, Q is the activation energy for the active deformation mechanism, R is the universal gas constant and A is the proportionality constant. Figure 3.A.5 presents the steady state creep rates, $\dot{\epsilon}$ as a function of true stress, at each temperature on a log-log scale.

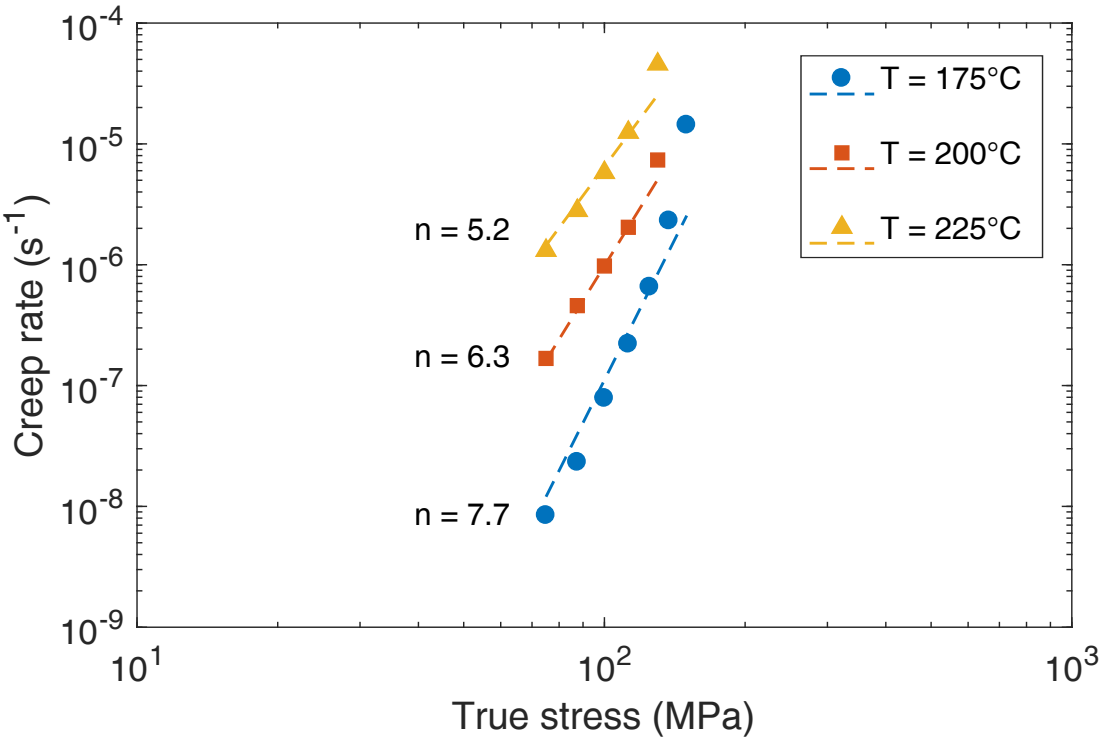

Figure 3.A.5: Creep behaviour of CG Al5083

The stress exponent, n ($= \partial\dot{\epsilon}/\partial\sigma$) calculated from the slope of the logarithmic curves is very high and not constant with temperature. This indicates the need of a temperature-dependent threshold stress, σ_0 to obtain a constant stress exponent. Equation 3.16 is hence modified as follows:

$$\dot{\epsilon} = A\left(\frac{\sigma - \sigma_0}{G}\right)^n exp\left(-\frac{Q}{RT}\right), \tag{3.17}$$

$$\frac{\sigma_0}{G} = Bexp\left(\frac{Q_{thresh}}{RT}\right) \tag{3.18}$$

Here, Q_{thresh} is the activation energy for threshold and B is the proportionality constant. To estimate the values of threshold stress, $\dot{\epsilon}^{1/n}$ is plotted against true stress for different integer values of n ranging from 2 to 6. The plot with n = 3 gives the best affine fit and is presented in figure 3.A.6. The threshold stresses correspond to the intercept of these curves with the x axis.

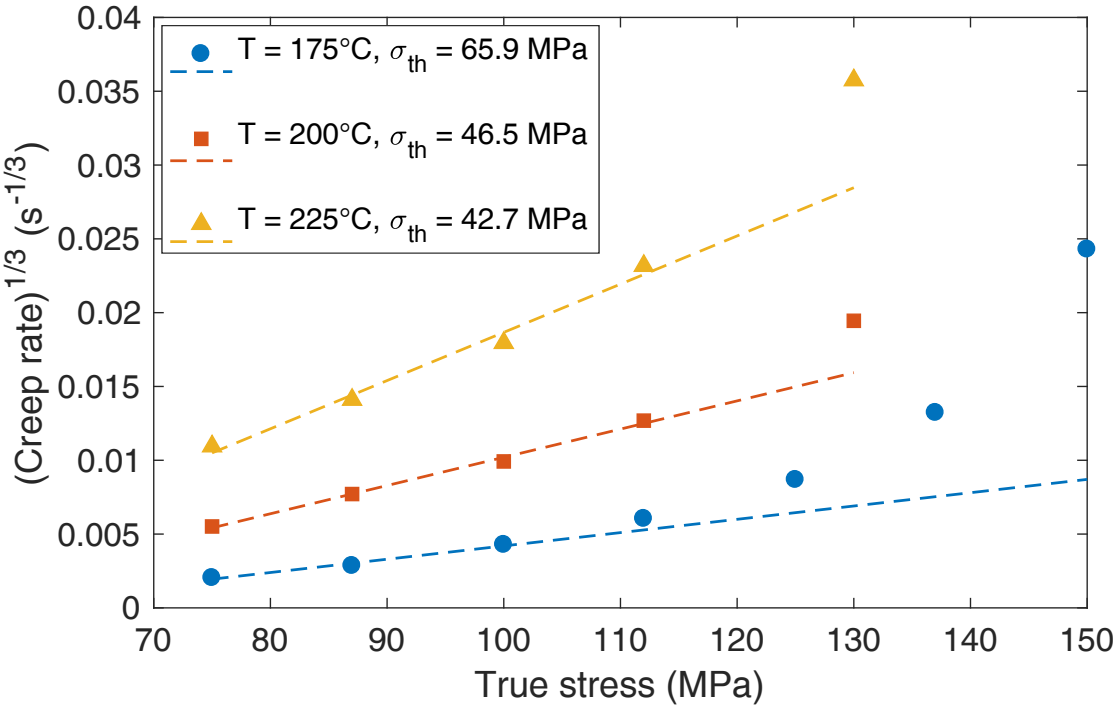

Figure 3.A.6: Plot of $\dot{\epsilon}^{1/n}$ vs. σ to calculated threshold stress at n = 3.

The estimated values of threshold stress are plotted on a log-log scale to obtain the activation energy for threshold, Q_{thresh} (Figure 3.A.7). The obtained values match very well with the ones reported in literature [17], [18].

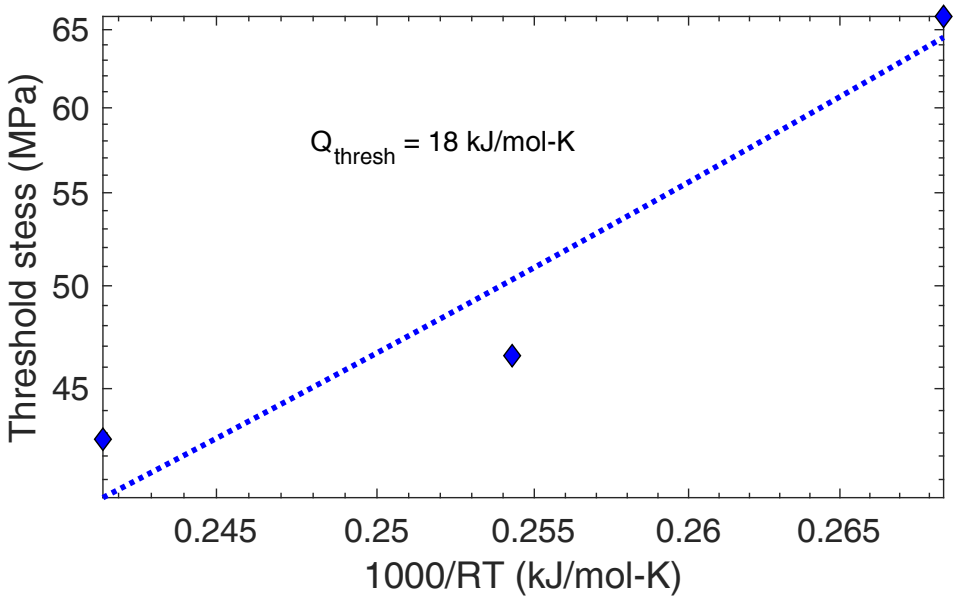

Figure 3.A.7: Plot of threshold stress as a function of 1000/RT to determine the activation energy for the threshold stress

The creep rate is plotted against the effective stress, $(\sigma - \sigma_0)$, on a log-log scale in figure 3.A.8. The stress exponent, n in this case is equal to 2.8 which is close to the stress exponent for viscous glide of dislocations dragging solute atoms (n = 3).

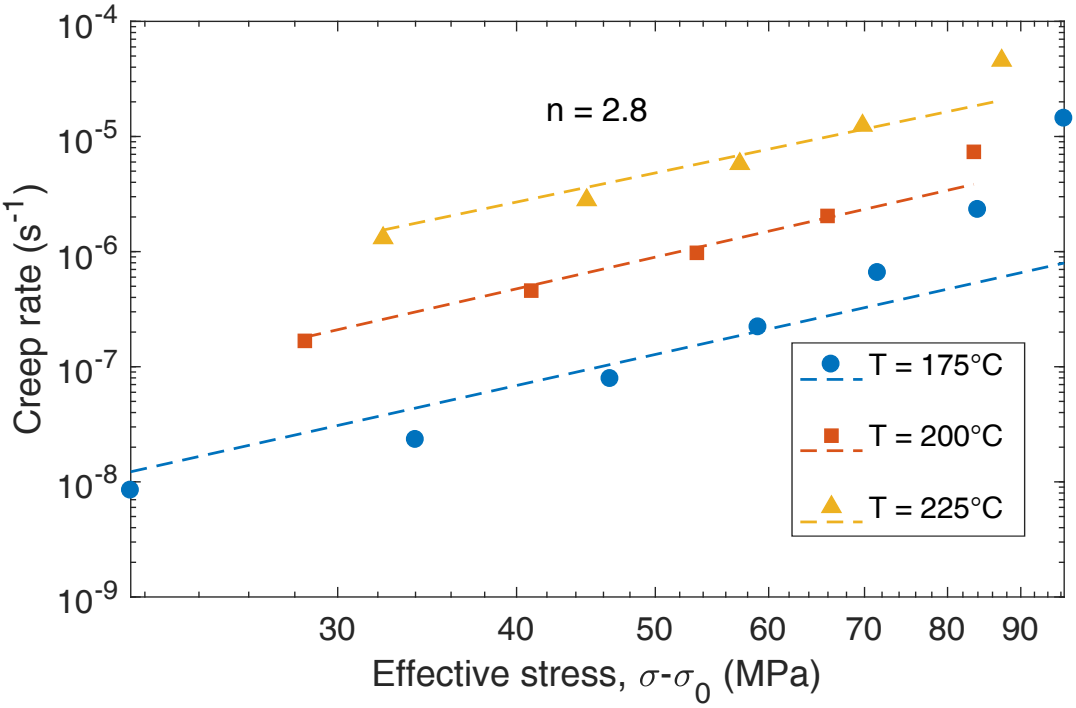

Figure 3.A.8: Modified creep behaviour after considering threshold stresses for creep

To determine the activation energy, the creep rate is plotted as a function of 1000/RT at a constant effective stress on a logarithmic scale in figure 3.A.9. The activation energy is calculated from the exponent of the exponential fit and is equal to 124kJ/mol. This value is quite close to the activation energy for the diffusion of Mg in Al ($\sim 130.5kJ/mol$) and is further from the activation energy of lattice self diffusion for Al ($\sim 142kJ/mol$). This suggests that indeed the rate controlling step is the viscous glide of dislocations in the atmosphere of solute magnesium atoms.

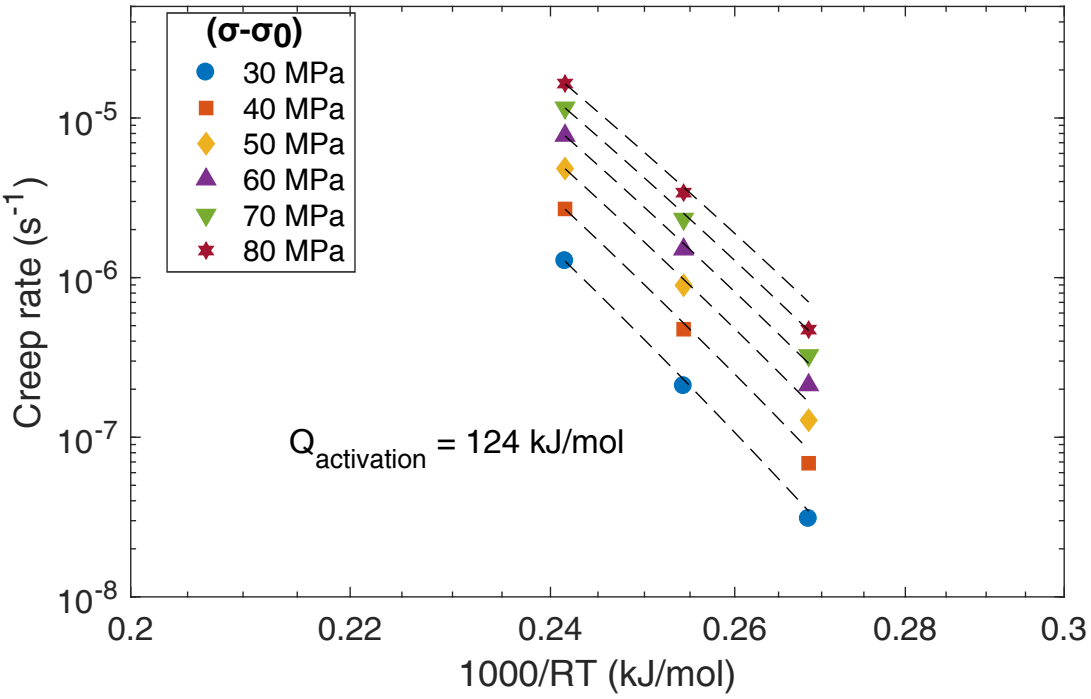

Figure 3.A.9: Plot of creep rate as a function of 1000/RT to determine activation energy

3.B Tensile tests for CG material

Additional tensile tests, as shown in figurs 3.B.1 and 3.B.2, were done on CG material at very high strain rates to have minimum contribution of viscous strain during the high temperature deformation of CG material. Table 3.B.1 presents the detailed information regarding these tests. Information from these tests was later used to identify the isotropic hardening parameters for the constitutive model proposed in chapter 5.

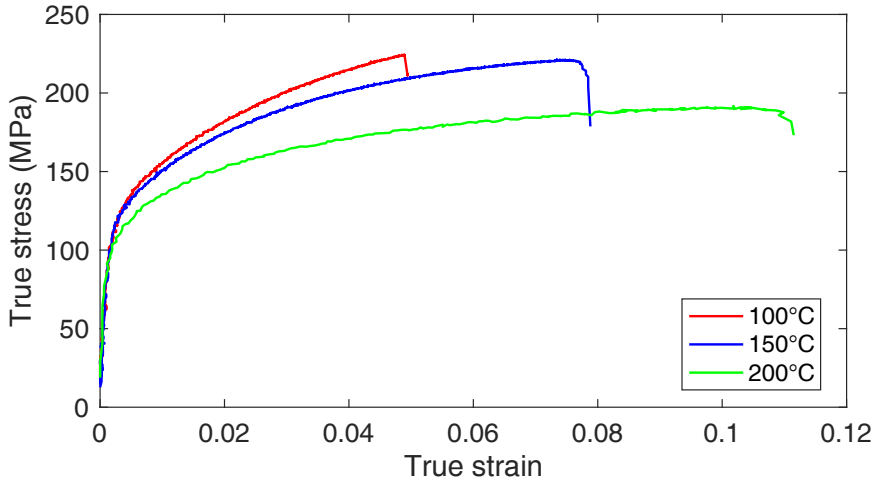

Figure 3.B.1: True stress-strain curves for CG material strained at $5\times10^{-3}\ s^{-1}$

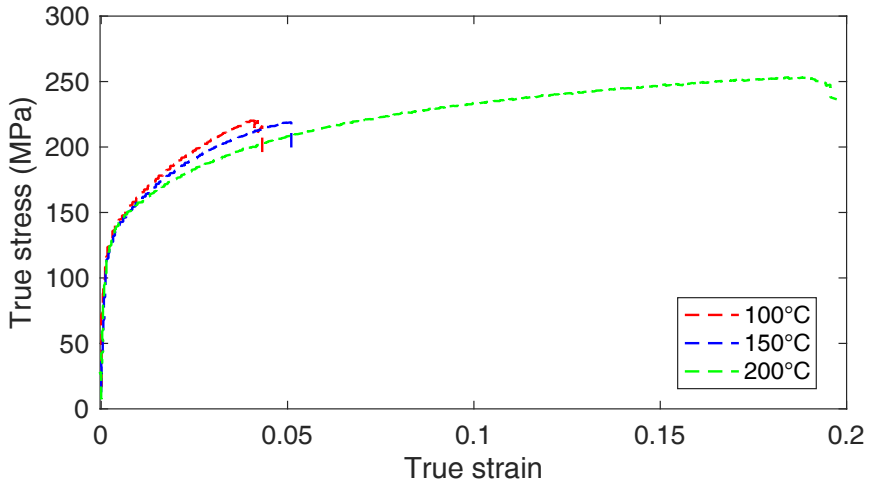

Figure 3.B.2: True stress-strain curves for CG material strained at $2\times10^{-2}\ s^{-1}$

Temperature ($^{\circ}C$)	**100**		**150**		**200**	
Strain-rate (s^{-1})	5×10^{-3}	2×10^{-2}	5×10^{-3}	2×10^{-2}	5×10^{-3}	2×10^{-2}
Young's Modulus (GPa)	51.4	-	55.2	56.9	58.0	68.4
0.2% Yield stress (MPa)	130	-	126	135	114	136
UTS (MPa)	213	211	205	208	174	213
Fracture strain (%)	5.2	4.7	8.4	5.3	12.1	18.8

Table 3.B.1: Details of additional tensile tests done on CG-A material

References

[1] T. A. Lebedkina and M. A. Lebyodkin, “Effect of deformation geometry on the intermittent plastic flow associated with the Portevin – Le Chatelier effect,” *Acta Materialia*, vol. 56, no. 19, pp. 5565–5572, 2008.

[2] X. Sauvage, N. Enikeev, R. Valiev, Y. Nasedkina, and M. Murashkin, “Atomic-scale analysis of the segregation and precipitation mechanisms in a severely deformed Al-Mg alloy,” *Acta Materialia*, vol. 72, pp. 125–136, 2014.

[3] R. Z. Valiev and T. Langdon, “Developement in the use of ECAP processing for grain refinement,” *Reviews on Advanced Materials Science*, vol. 13, pp. 15–26, 2006.

[4] D. Zhemchuzhnikova, “Influence of the extreme grain size reduction on plastic deformation instability in an AlMg and AlMgScZr alloys,” PhD thesis, University of Lorraine, 11th December, 2018.

[5] T. A. Lebedkina, M. A. Lebyodkin, T. T. Lamark, M. Janecek, and Y. Estrin, “Effect of equal channel angular pressing on the Portevin – Le Chatelier effect in an Al3Mg alloy,” *Materials Science & Engineering A*, vol. 615, pp. 7–13, 2014.

[6] F. P. D. Lopes, C. H. Lu, S. Zhao, S. N. Monteiro, and M. A. Meyers, “Room Temperature Dynamic Strain Aging in Ultrafine-Grained Titanium,” *Metallurgical and Materials Transactions A*, vol. 46, no. 10, pp. 4468–4477, 2015.

[7] R. Kapoor and J. K. Chakravartty, “Deformation behavior of an ultrafine-grained Al-Mg alloy produced by equal-channel angular pressing,” *Acta Materialia*, vol. 55, no. 16, pp. 5408–5418, 2007.

[8] H. Ait-Amokhtar and C. Fressengeas, “Crossover from continuous to discontinuous propagation in the Portevin-Le Chatelier effect,” *Acta Materialia*, vol. 58, no. 4, pp. 1342–1349, 2010.

[9] D. Lee and E. W. Hart, “Stress Relaxation and Mechanical Behavior of Metals,” *Metallurgical Transactions*, vol. 2, pp. 1245–1248, 1971.

[10] M. S. Mohebbi and A. Akbarzadeh, “Development of equations for strain rate sensitivity of UFG aluminum as a function of strain rate,” *International Journal of Plasticity*, vol. 90, pp. 167–176, 2017.

[11] C. Duhamel, Y. Brechet, and Y. Champion, “Activation volume and deviation from Cottrell-Stokes law at small grain size,” *International Journal of Plasticity*, vol. 26, no. 5, pp. 747–757, 2010.

[12] Y. G. Ko, D. H. Shin, K. T. Park, and C. S. Lee, “Superplastic deformation behavior of ultra-fine-grained 5083 Al alloy using load-relaxation tests,” *Materials Science and Engineering A*, vol. 448-451, pp. 756–760, 2007.

[13] I. Sabirov, M. R. Barnett, Y. Estrin, and P. D. Hodgson, “The effect of strain rate on the deformation mechanisms and the strain rate sensitivity of an ultra-fine-grained Al alloy,” *Scripta Materialia*, vol. 61, no. 2, pp. 181–184, 2009.

[14] P. Hahner, “A generalised criterion of plastic instabilities and its application to creep damage and superplastic flow,” *Acta Metallurgica*, vol. 43, no. 11, pp. 4093–4100, 1995.

[15] M. F. Ashby and R. A. Verrall, “Diffusion-accommodated flow and superplasticity,” *Acta Metallurgica*, vol. 21, 1973.

[16] M. T. Abdu, S. S. Dheda, E. J. Lavernia, T. D. Topping, and F. A. Mohamed, “Creep and microstructure in ultrafine-grained 5083 Al,” *Journal of Materials Science*, vol. 48, pp. 3294–3303, 2013.

[17] R. Kaibyshev, F. Musin, E. Avtokratova, and Y. Motohashi, “Deformation behavior of a modified 5083 aluminum alloy,” *Materials Science & Engineering A*, vol. 392, pp. 373–379, 2005.

[18] K.-T. Park, E. J. Lavernia, and F. A. Mohamed, “High-temperature deformation of 6061 Al,” *Acta Metallurgica*, vol. 42, no. 3, 1994.

Chapter 4

Deformation, damage and fracture mechanisms

This chapter details the deformation and damage mechanisms active during the plastic deformation of CG and UFG batch A materials investigated at room or high temperature, through *in situ* tensile tests in a SEM, or *ex situ* tests, with SEM observations and fine-scale measurements of the strain field by correlation of SEM digital images (DIC) captured after straining. The first section presents the experimental procedures, especially the 2-scale patterning method developed for meso- and nano-scale digital image correlation. The second section presents the observations and analyses of the strain fields and fracture surfaces at 20, 100, 150 and 200°C. Lastly, the chapter concludes with a discussion and synthesis of the observed mechanisms in relation with the macroscopic behaviour reported in the previous chapter.

4.1 Experimental procedures

For observations of the deformation mechanisms, the surface preparation is a crucial step. The surface of flat dog-bone specimens was initially mechanically polished with 800 - 4000 grit SiC paper. It was then electro-polished at 17 V for 35 seconds using Struers A2 electrolyte kept in an ice bucket.

4.1.1 Surface patterning for DIC

To allow DIC using SEM images, a small-scale pattern, made of a ductile material, with a good adhesion to the surface of the object under deformation, and providing a good contrast for SE or BSE images has to be introduced. The spatial resolution of the strain measurement depends highly on the size and density of the features inside the domains of correlation.

To measure the micro and meso-scale strain fields for both CG and UFG materials, a meso-scale pattern was developed using electron-beam lithography denoted by EBL (Figure 4.1 illustrates the steps realised to obtain the desired pattern). 600$\times$600 μm patches of gold grids with 5 microns pitch were printed on the polished specimen surface as shown in figure 4.2. In case of CG material, 4 patches of grids were printed side to side in a square to give a larger observation window of 1200$\times$1200 μm. For UFG

materials, due to the heterogeneity in microstructure, several 600×600 μm patches of grids were printed along the gauge length (Figure 4.3).

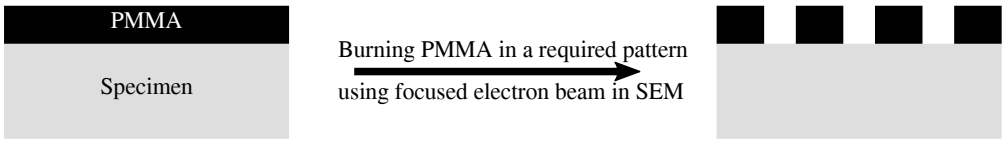

Step 1: A thin layer of liquid PMMA polymer (5g for 100cc) is spread on a polished surface using a spin coater at 3000 rpm for 90 secs.

Step 2: It is baked at 140°C for 30 mins for polymerisation.

Step 3: It is scanned by a focused electron beam in the SEM to draw the required pattern by burning the electron-sensitive polymer.

Step 4: It is then immersed in a Propanol+ Methyl ethylacetone solvent to disolve the exposed area.

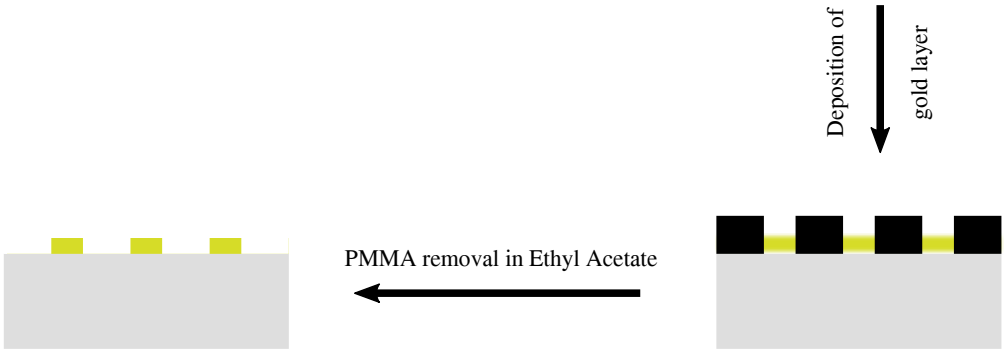

Step 5: The remaining PMMA is removed using Ethyl Acetate in an Ultrasonic bath

Step 5: The unmasked area of the specimen is covered with gold. First, a 3 nm thick gold layer is sputtered in argon plasma to ensure a good adhesion. Then, an additional 11 nm thick gold layer is deposited using vapor deposition technique in vacuum.

Figure 4.1: Procedure for patterning by electron beam lithography.

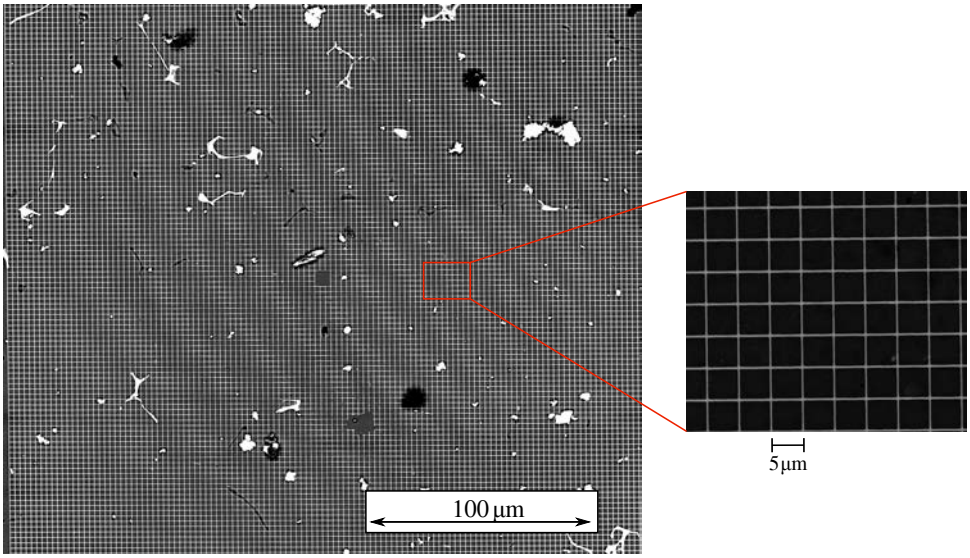

Figure 4.2: BSE image of the gold grids obtained from e-beam lithography.

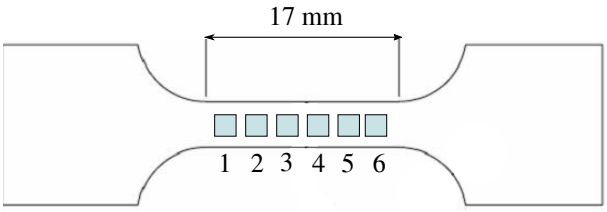

Figure 4.3: Schematic of the 600×600 μm^2 patches of gold grids along the gauge length for UFG specimens.

For UFG material, even though microgrids patches were useful to monitor "large scale" localization phenomena, a spatial resolution of a few tens of nanometers was however needed for grain-scale high resolution or HR-DIC monitoring of plastic deformation. A nano-scale surface patterning method had thus to be developed.

Several teams have succeeded in obtaining micro-scale speckle patterns for DIC, but research on the creation of nano-scale patterns which is not only reproducible, reliable but also cost and time efficient is still going on. Wang et al. [1] spread a thin film of liquid epoxy resin containing graphite powder particles of 3 μm size on a sample surface, using a spin coater, and then polymerized the resin, to create the micro-scale speckle pattern. Problems of agglomeration of the particles decreased the resolution of the DIC. Collette et al. [2] used porous alumina membranes with 200 nm pores, entrapping gold particles to pattern the surface by stamping. The pattern exhibited a good contrast in ESEM, an excellent adherence and ductility, with a small thickness (< 0.1 μm). But the minimum size of the patterns obtained was 200 nm. Tanaka et al. [3] used the AFM nanolithography technique to create grids with 500 nm spacing, by scratching with the AFM tip a 30 nm thick gold layer deposited on the specimen surface, along two orthogonal directions. In all the above-mentioned cases, the size of the patterns were too large to allow detection of any grain boundary plastic activity in

the UFG materials.

A more suitable method to obtain a high density nano-scale pattern is electron beam lithography. Zhang et al. [4] obtained a 45 nm gold dots pattern on a 20 μm by 20 μm area on Al5083 alloy, using the smallest SEM diaphragm aperture (7.5 μm), a low acceleration voltage (10 kV) and a dose factor of 5 for a base dose level of 800pAs/cm^2.

This technique was thus attempted in the present study. To obtain the fine scale EBL pattern, a spot size of 2.5 was chosen with the smallest aperture (30 μm) and an acceleration voltage of 28 kV. After performing the dose test between 0.00194 and 0.1747 pC, an irradiation dose value 0.0194 pC was found most suitable. Two kinds of patterns were tested: one with a grid of evenly-spaced dots, and another one with a speckle pattern. The average size of the gold particles obtained was around 140 nm with a mean spacing of 370 nm for evenly spaced pattern (Figure 4.4a), while it was around 300 nm with an aspect ratio of 1.5 and mean spacing of 750 nm for the speckle pattern (Figure 4.4b). In both cases, this is still too large for HR-DIC on UFG materials. The accuracy and the size of the pattern obtained using EBL was actually controlled by the proximity effect i.e. spill over of the electrons into a nearby region, leading to over-exposure. Thus, depending upon the gap between 2 particles, they might merge to form a bigger particle, or might not even print at all. Additionally, this was not a very time efficient and cost friendly process.

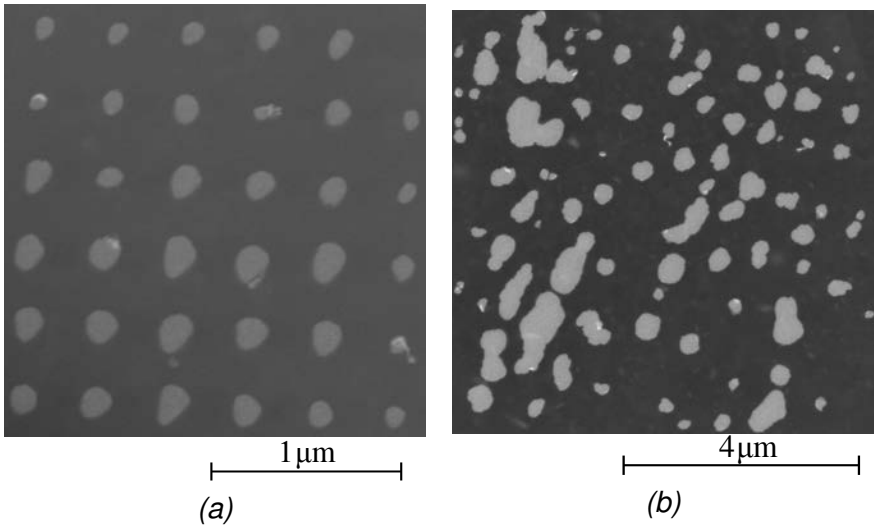

Figure 4.4: Nano-scale pattern using electron-beam lithography, (a) a regular dotted nano-pattern and (b) random speckle nano-pattern.

Another promising patterning method is vapour/gas-assisted remodelling of thin metal layers which was first described by Luo et al. [5] on glass slides, using water vapour or iodobenzene carried by N_2 to remodel 5-30 nm thick gold films. This technique was further elaborated by Scrivens et al. [6] to remodel not only Au but also Ag and Cr films. Later it was successfully used by Gioacchino and Fonseca [7], on stainless steel, and by Kammers and Daly [8] on Al2024. Bourcier et al. [9] also used the remodelling technique to pattern halite with gold dots of diameter approx. 1 μm. This technique

was thus also attempted.

Various thickness of gold films (3-50 nm) were vaporised on the polished surface. The specimen was kept on a heating plate at 200°C and exposed to water vapour for 3 hrs using the set-up proposed by Gioacchino and Fonseca [7] described in figure 4.5. This temperature was low enough to avoid grain growth in the UFG material.

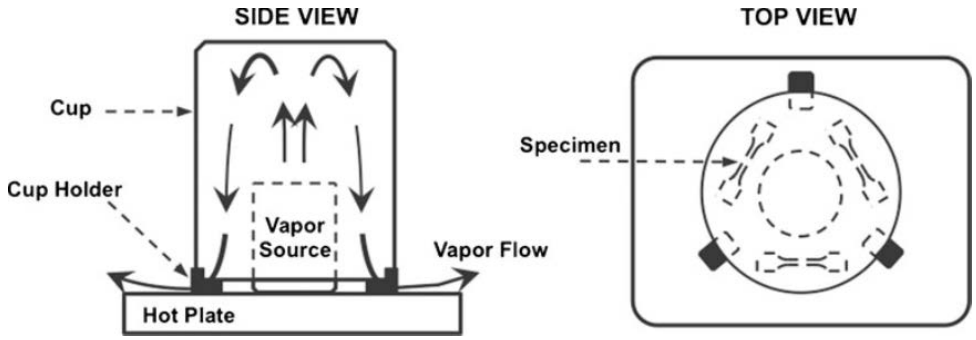

(a) Schematics proposed by Gioacchino and Fonseca [7]

(b) Experimental set-up used for remodelling

Figure 4.5: Apparatus for vapour-assisted gold remodelling

Due to minimisation of surface energy [10], the gold layer evolves into a speckle pattern. Beyond 8 nm thickness , the gold layers did not remodel into small individual particles, but into more or less connected "islands" (Figure 4.6 c-f). But for 3 and 5 nm, a uniform and dense ($\sim$ 3500 particle/sq. μm) pattern of 20 nm gold particles with a mean spacing of 17 nm was successfully obtained (Figure 4.6 a,b). The aspect ratio of the gold particles was closer to 1 for 5 nm gold layer than for the 3 nm gold layer. The spatial distribution of the resulting pattern was quite random and isotropic, with high density of gray-level contrast, favourable to DIC. Other than being cost effective, this technique was quite simple, easily repeatable and less time consuming than E-beam lithography. One additional benefit was the elimination of the additional annealing time necessary to get a stable, recovered UFG microstructure and obtain acceptable EBSD

mappings.

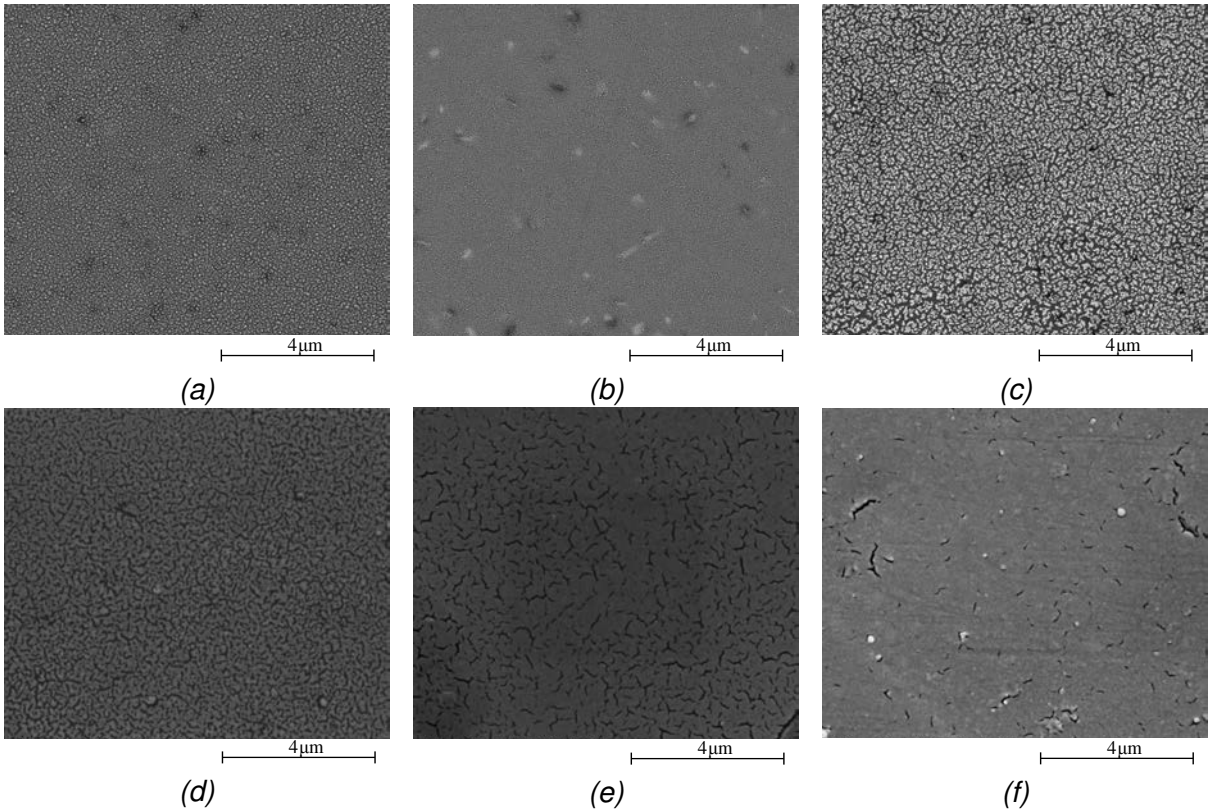

Figure 4.6: Vapour-assisted remodelling for (a) 3 nm, (b) 5 nm, (c) 8 nm, (d) 10 nm, (e) 30 nm and (f) 50 nm vaporised gold layers.

To determine the strain fields at macro and mesoscopic scales, as well as sub-grain scale in UFG material, a two-scale surface pattern was created. First, multiple 600×600 μm^2 gold grids were printed along the gauge length by EBL. Then, a nano-scale pattern was obtained over a 10×10 μm^2 area in the center of each grid using vapour-assisted remodelling, with a 5 nm thick gold layer (Figure 4.7).

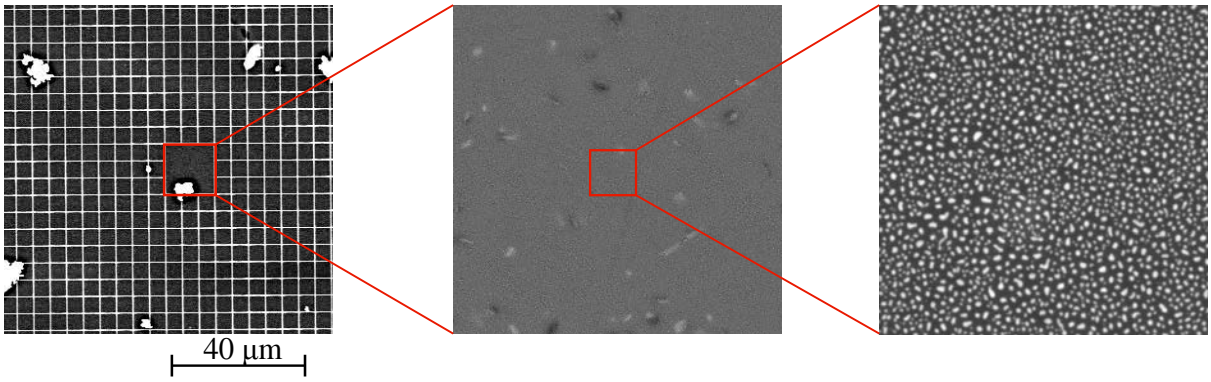

Figure 4.7: Meso and nano-scale patterning for DIC of UFG material.

4.1.2 Incremental tensile testing and image capture

All the *in situ* tensile tests done at RT on the miniature tensile machine shown on figure 3.1 were displacement controlled with a displacement rate of 1 μm/s or 10 μm/s (approximately 5.8×10^{-5} or 5.8×10^{-4} s^{-1} as described in the previous chapter). The data acquisition rate was 1 Hz for the slowest rate and 0.1 Hz for the fastest.

A single *in situ* tensile test was run at 5.8×10^{-5} s^{-1} on CG material. It was stopped at a regular stress interval of 17.5 MPa to capture 4096 $\times$3775 pixels images of a 1200$\times$1100 μm^2 area (which corresponds approximately to 293 nm/pixel) for DIC. The image was captured in the loaded configuration so that **total** strain fields were obtained by correlation with the reference image captured in the undeformed state. But, as discussed in the next section, pseudo strains were induced by the openings of cracks inside broken second phase particles. Thus, to minimise this effect during subsequent tests on UFG material, the specimen was unloaded after each strain increment (approximately 1%) before capturing 4096$\times$3775 pixels images of 600$\times$552 μm^2 areas equipped with grids (this corresponding to 146 nm/pixel) and 4096$\times$3775 pixels images of 20$\times$18 μm^2 remodelled areas which corresponds to 5 nm/pixel (This size is larger than 10$\times$10 μm^2 correlated area to compensate for the local deformation and the 4:3 image ratio)(Figure 4.8). **Plastic** strain fields were thus obtained by correlation with the reference image.

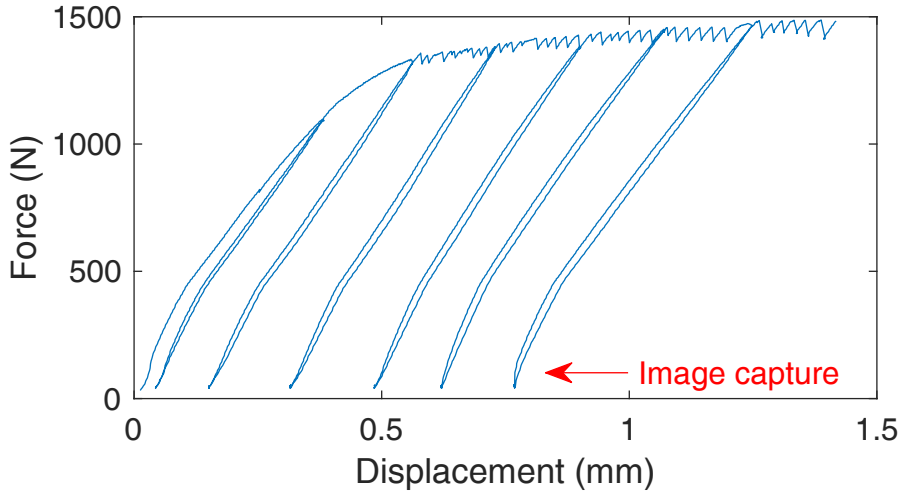

Figure 4.8: Typical force-displacement curve during in-situ test with unloading after each step for image capture.

The contrast in a BSE image is based on the chemical composition, which remains constant during the tensile test, as opposed to the contrast of the SE image, which is based on the topography, and changes with deformation. Since for a successful DIC the image contrast needs to be constant between consecutive steps, BSE images with optimal contrast settings were used for DIC.

4.1.3 DIC computation

The captured images were correlated using the in-house DIC software, CorrelManuv developed by M. Bornert [11]. A homologous position of a set of points (called correlation domain) in the reference and the deformed images is found through the minimisation of the correlation coefficient (which measures the level of resemblance between the spatial distribution of grey levels between identified and reference domains and is minimum for maximum correlation). For meso-scale DIC, the centres of the 4.4×4.4 μm^2 correlation domains were placed on the intersection points of the grids with a pitch such that adjacent correlation domains did not overlap. For high-resolution DIC based on nano-scale speckle pattern, the choice of correlation domain was crucial for the spatial resolution and error minimisation. Figure 4.9 compares axial strain maps obtained with different correlation domains. Even though the spatial resolution increases with decrease in the size of correlation domains, the error in strain calculation increases as explained below. Finally, correlation domains of 97×97 nm^2 were chosen and were placed line-by-line such that every correlation domain contained sufficient contrast for correlation. This DIC software also allowed sub-pixel optimisation based on linear or quadratic interpolation. A quadratic interpolation was used.

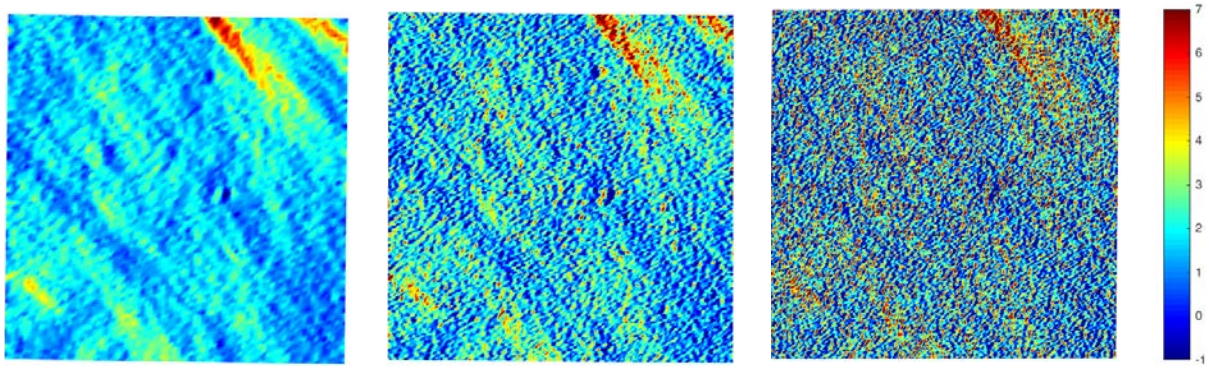

Correlation domain: 97 nm
Gauge length: 225 nm
Error in E11 = 0.31%

Correlation domain: 49 nm
Gauge length: 127 nm
Error in E11 = 0.95%

Correlation domain: 34 nm
Gauge length: 88 nm
Error in E11 = 2.00%

Figure 4.9: Effect of correlation domain size on the computed axial plastic strain field in a 10×10 μm^2 area.

In CorrelManuv software, the local in-plane Green-Lagrange strain components, as well as rigid boby rotations are computed using an integration domain where an average value of the displacement gradient is calculated from the positions of the center points of neighbouring correlation domains (assuming that the deformation varies linearly in between) [11]. Depending on the choice of correlation and integration domains sizes (Figure 4.10), it was possible to obtain very local but inaccurate and noisy strain values (smallest integration domain), or more accurate average value over a larger domain. Scheme 1 was chosen as it was the smallest but symmetric scheme of integration to calculate the deformation locally. Thus, the corresponding physical "gage length" for strain calculation was twice the spacing between the centres of neighbouring correlation domains, that is 10 and 0.23 μm for grids with 5 μm pitch and speckle pattern respectively.

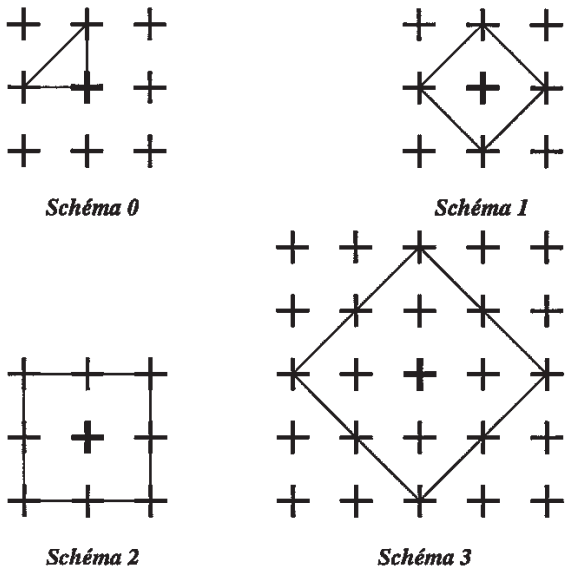

Figure 4.10: Available integration scheme in CorrelManuv software.

The error and the uncertainties related to local deformation depend on many factors, such as detector mode (SE/BSE), intensity of electron beam, speed of image acquisition, brightness and contrast and working distance. According to Doumalin [12], inherent noise related to the imaging technique inside the SEM can be reduced by decreasing the speed of acquisition and image averaging techniques. Dwell time of 10 μs per pixel was used in all cases as a compromise between image noise and time of acquisition. To estimate the error on the local deformation, two high resolution images, 4096$\times$3775 pixels with a difference in magnification of 0.15% ($\sim$ 6 pixels) were captured and correlated using the DIC software. The maximum error in axial strain was 0.31% for 10$\times$10 μm area and 0.07% for 600$\times$600 μm area.

4.2 Observations and Analysis

4.2.1 At room temperature

CG-A material at $5.8 \times 10^{-5}\ s^{-1}$

A tensile test on CG material at $5.8 \times 10^{-5}\ s^{-1}$ was realised in 9 steps at equal stress intervals of 17.5 MPa, as shown by blue dots in figure 4.11. Figure 4.12 shows the BSE images of the 1.2$\times$1.1 mm^2 monitored area at step 1 and 9, with a few zoomed details illustrating second phase particle cracking and the aspect of the slip lines. Particle cracking (which was not observed initially, and thus not due to polishing) started early, within the macro-scale elastic regime.

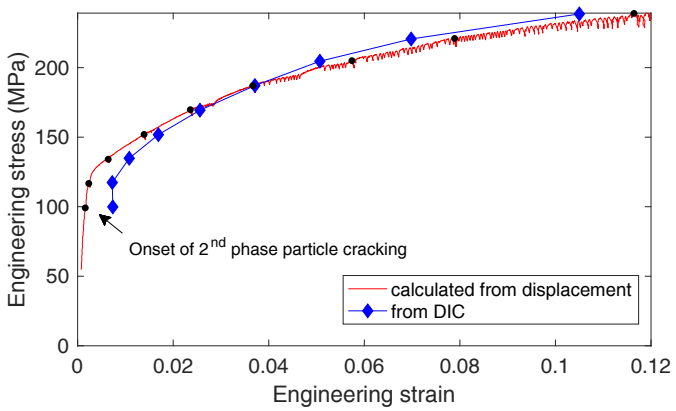

Figure 4.11: The stress-strain curve for an in-situ test on CG material at RT(Black circles represent the point of image capture at each step).

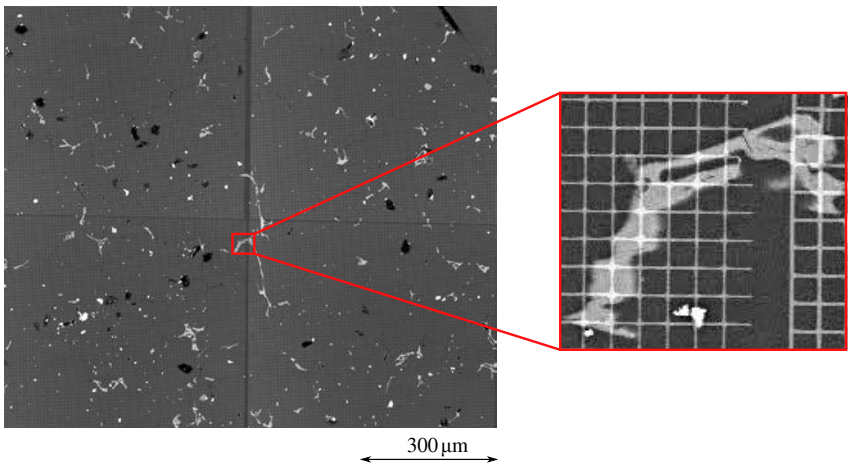

(a) Step 1: 100 MPa, E_{11}=0.7%

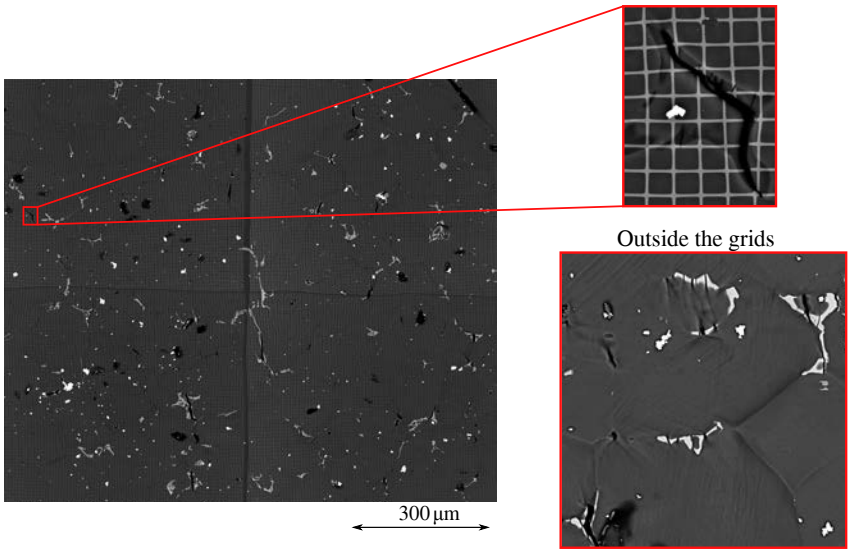

(b) Step 9: 240 MPa, E_{11}=10.5%

Figure 4.12: BSE image of the monitored area at steps 1 and 9 + zoomed details in CG-A material strained at $5.8 \times 10^{-5}\ s^{-1}$ at RT. Tensile axis is horizontal.

Big particles especially the ones with high number of dendrites or high aspect ratio, were observed to break first, more or less normal to the tensile axis, as expected for a brittle phase, while the small and circular particles broke later. Figure 4.13 presents the fraction of broken particles as a function of stress. It increases slowly until 140 MPa, after which it increases faster and tends to saturate around 240 MPa. The slip lines were generally straight, in accordance with the relatively low stacking fault energy of this alloy. Slip was observed to intensify near the broken particles (Figure 4.14). The optical image taken after the test shows that even after 12% strain, some grains hardly exhibit any slip trace, while others exhibit two or even three sets of slip traces. This suggests that plastic strain is quite heterogeneous.

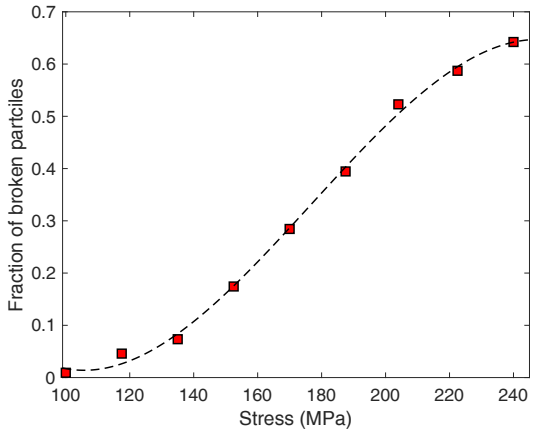

Figure 4.13: Fraction of broken particles as a function of applied stress in CG-A material strained at $5.8 \times 10^{-5}\ s^{-1}$ *at RT.*

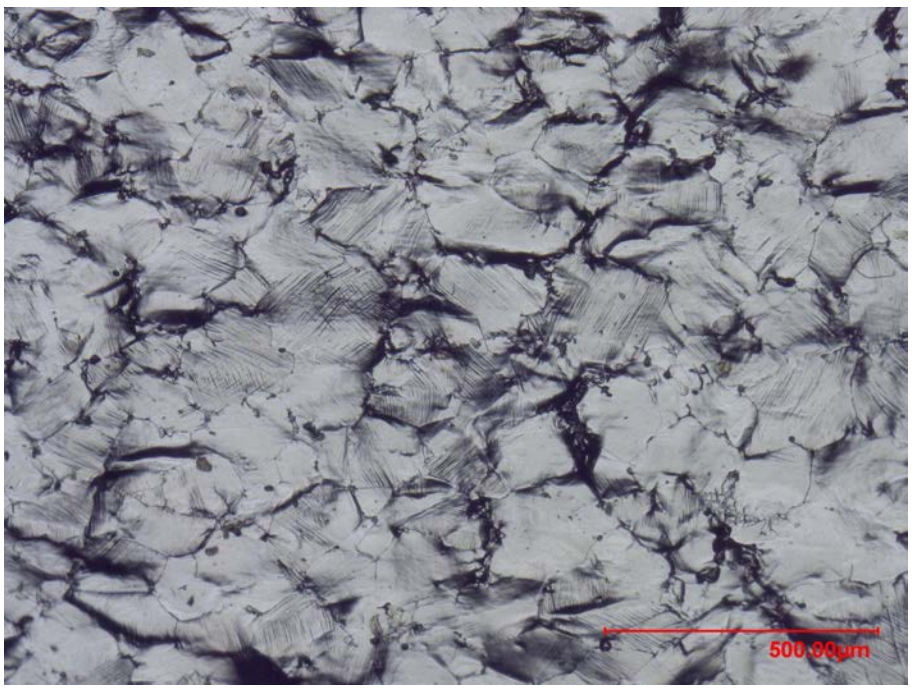

Figure 4.14: Post fracture optical image of the CG-A material strained at $5.8 \times 10^{-5}\ s^{-1}$ *at RT.*

Figure 4.15 shows a selection of longitudinal strain maps obtained from DIC using either the same color scale for all the steps, to emphasise the evolutions, or individual scales for each step, to emphasize the local gradients. The tensile axis is horizontal. The stress concentration near the broken particles triggers the formation of bands of strain localisation joining these broken particles. There is no preferential direction for the localised bands.

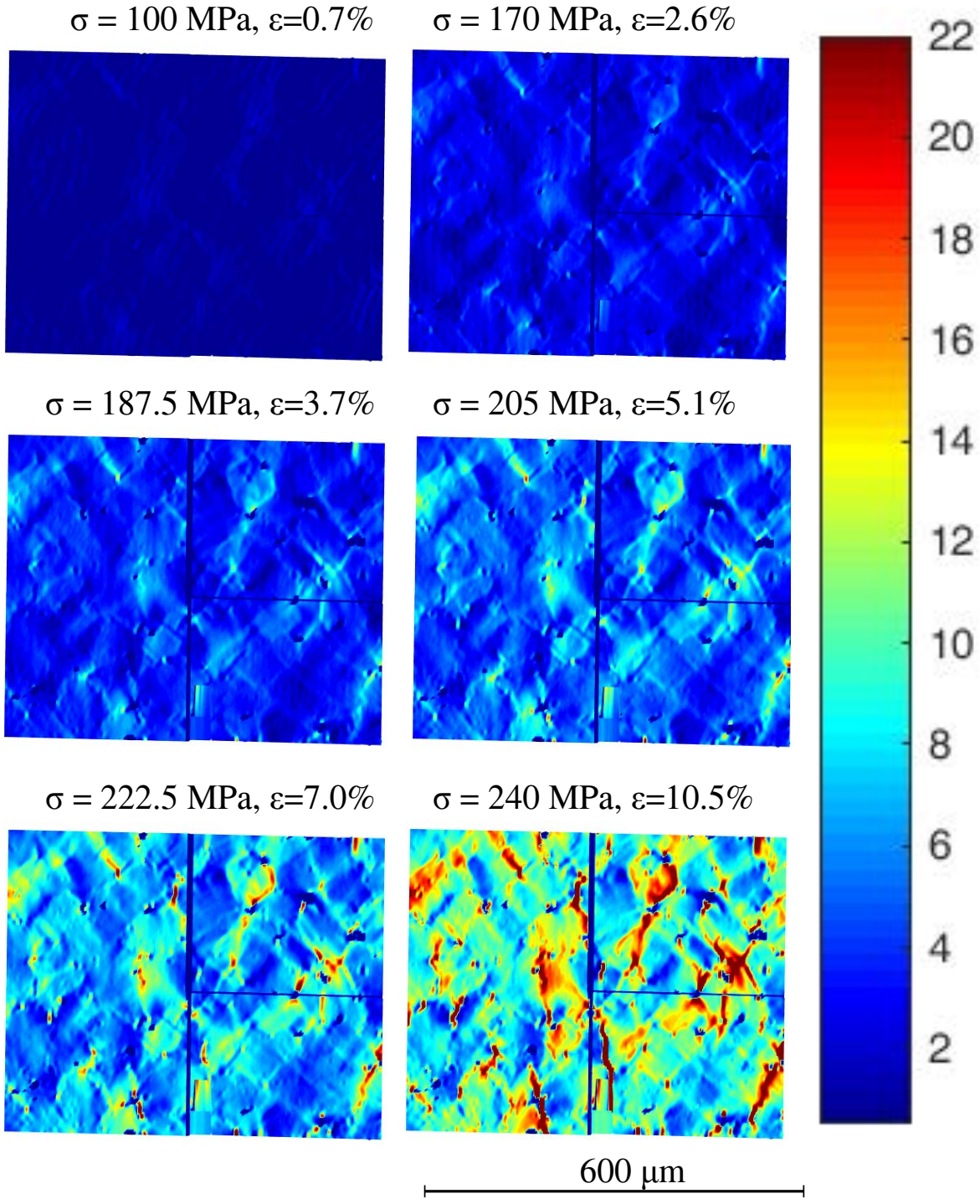

(a) Same-scale for all the maps

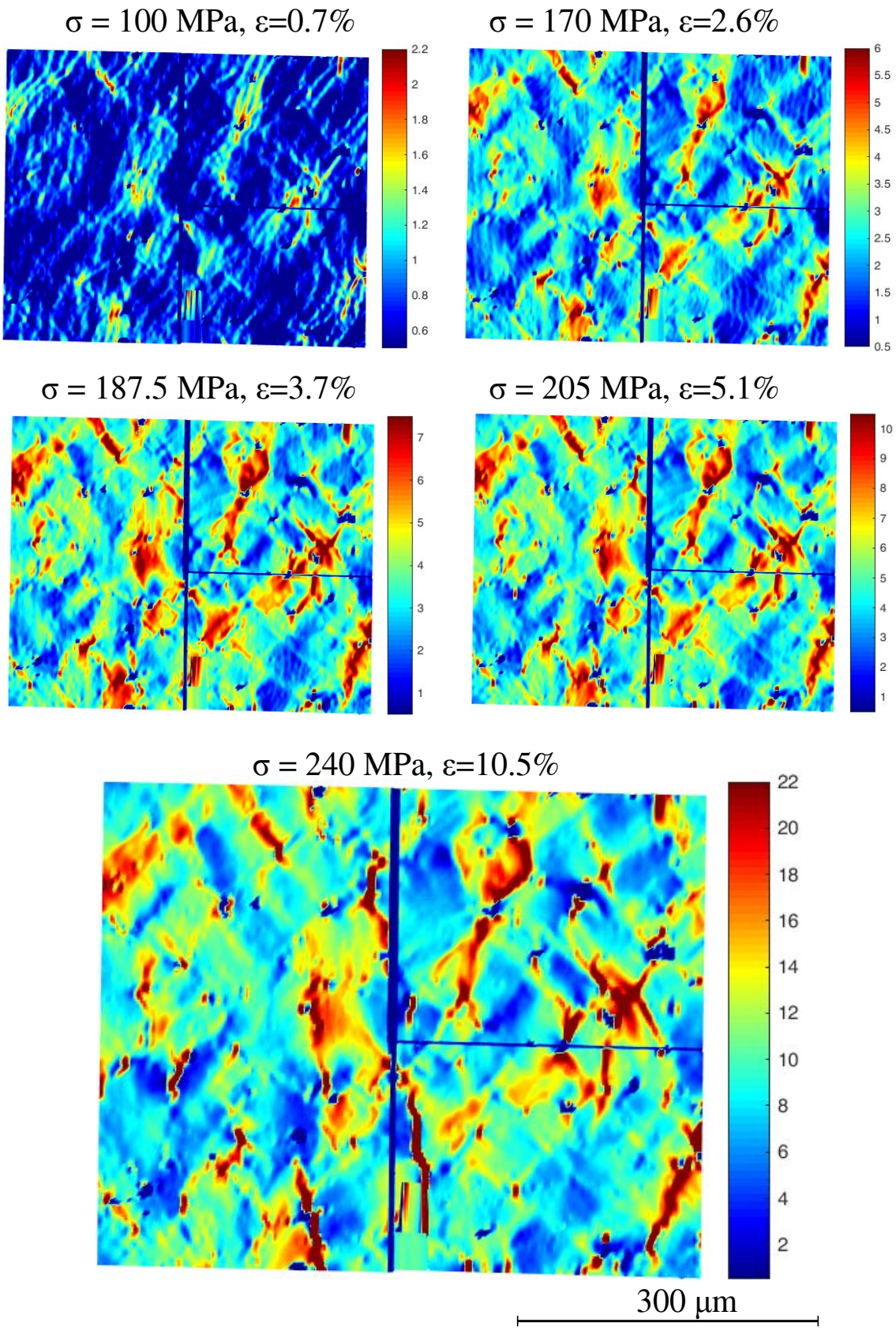

(b) Scale depending on local strain field

Figure 4.15: Total longitudinal strain fields for CG material at $5.8 \times 10^{-5}\ s^{-1}$*, RT*

Histograms of the normalised strain distribution (that is: the local strain divided by the mean strain) and their standard deviation at different steps are plotted in figures 4.16 and 4.17. The normalised histograms at different steps look more or less similar. As suggested by the optical image, some areas hardly deform, while some others deform up to 2.5 times more than average. In the latter case, this is partly due to pseudo strains that actually correspond to crack opening in the particles, but not in all cases, since intense slip bands do develop from these cracks. The standard deviation of the strain field slightly decreases, probably due to a progressive plastification of a growing fraction of the grains until approximately 5% strain. Beyond this point, it starts to rise sharply until fracture, indicating increased localisation.

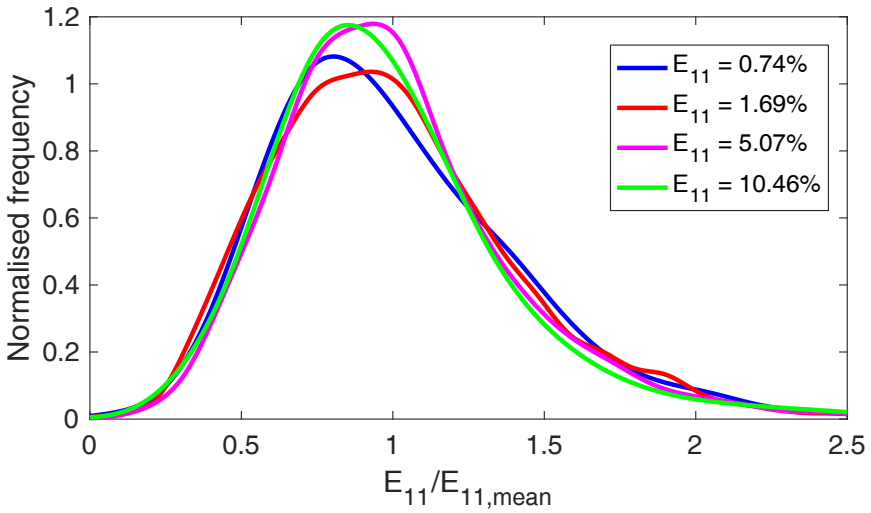

Figure 4.16: Histograms of normalised axial strain at different steps in CG material strained at $5.8 \times 10^{-5}\ s^{-1}$ *at RT*

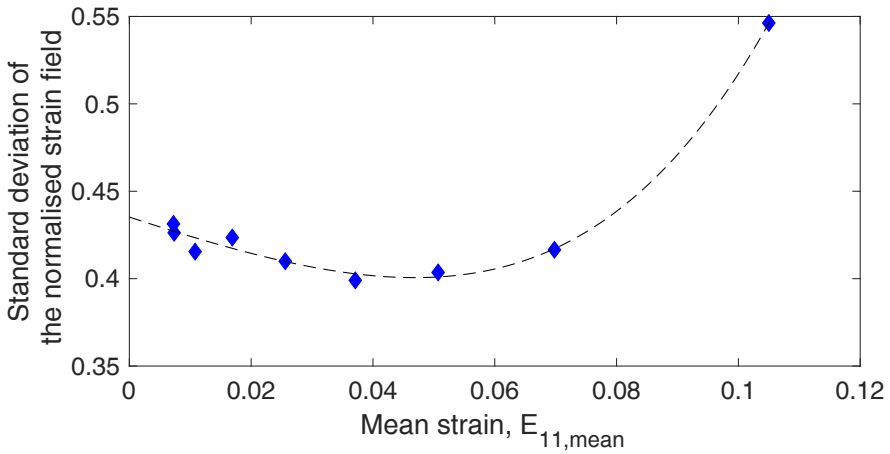

Figure 4.17: Standard deviation of the normalised strain field as a function of mean axial strain for CG material strained at $5.8 \times 10^{-5}\ s^{-1}$ *at RT*

SE and BSE SEM images of the fracture surfaces are shown in figure 4.18. Relatively smooth intergranular "facets" covered with debonded/fractured big intermetallic particles can be seen all over the fracture surface with transgranular ligaments, corresponding to the localised slip bands joining them, and containing smaller dimples.

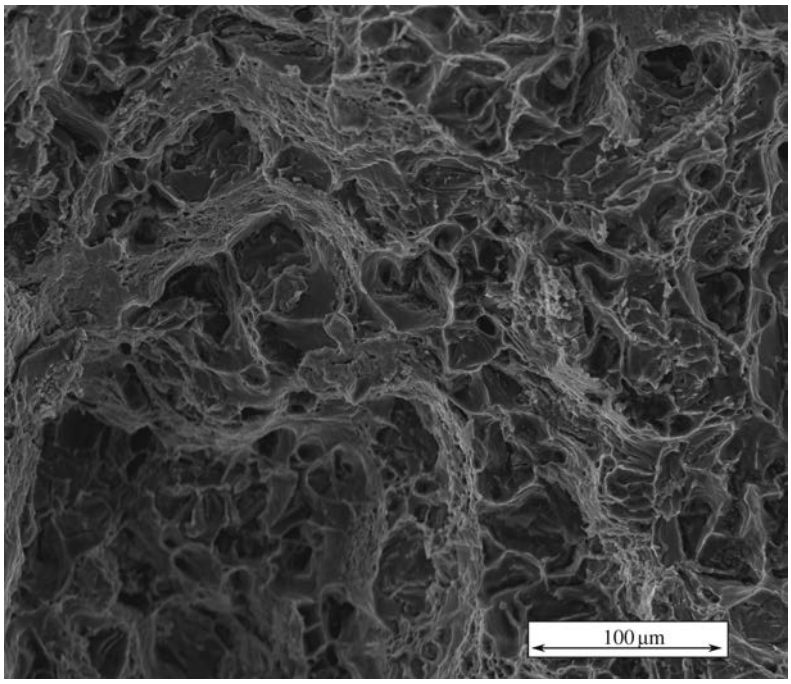

(a) SE image of the fracture surface

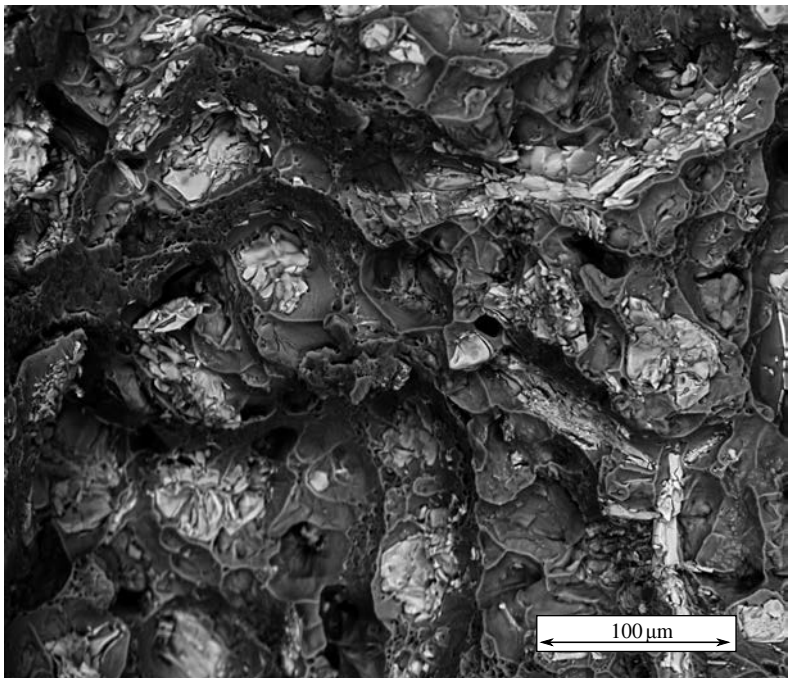

(b) BSE image of the fracture surface

Figure 4.18: Fracture surface of the CG material strained until 12% at $5.8 \times 10^{-5}\ s^{-1}$*, RT*

UFG-A material at $5.8 \times 10^{-5}\ s^{-1}$

Similar test was performed for UFG material except that after every step the specimen was unloaded for image capture. The plastic strain calculated from DIC is plotted against true stress in figure 4.19. Since six patches of grids are printed along the gauge length, 4 600×600 and 4 10×10 μm^2 areas were analysed at each step (The pitch of the grids for ZOI 3 and 4 was 10 μm instead of 5 μm and hence their strain maps are not presented here).

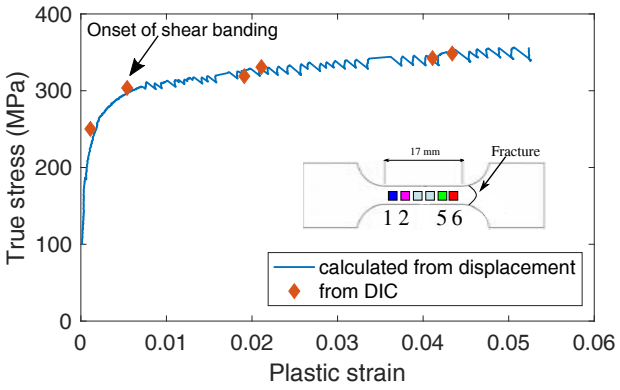

Figure 4.19: True stress vs plastic strain curve of UFG-A material at $5.8 \times 10^{-5}\ s^{-1}$, RT

Shear bands 10 to 100 times longer than the mean grain size were observed on the deformed surface (Figure 4.20). In some cases, these bands were generated due to the stress concentration induced by particle breaking (Figure 4.21b). The shear band angles were measured between 52° and 54° relative to the applied stress direction without any symmetry in the sign of these angles. These angles do not correspond with the planes of maximum shear, but the bands rather seem to follow the elongated grain structure.

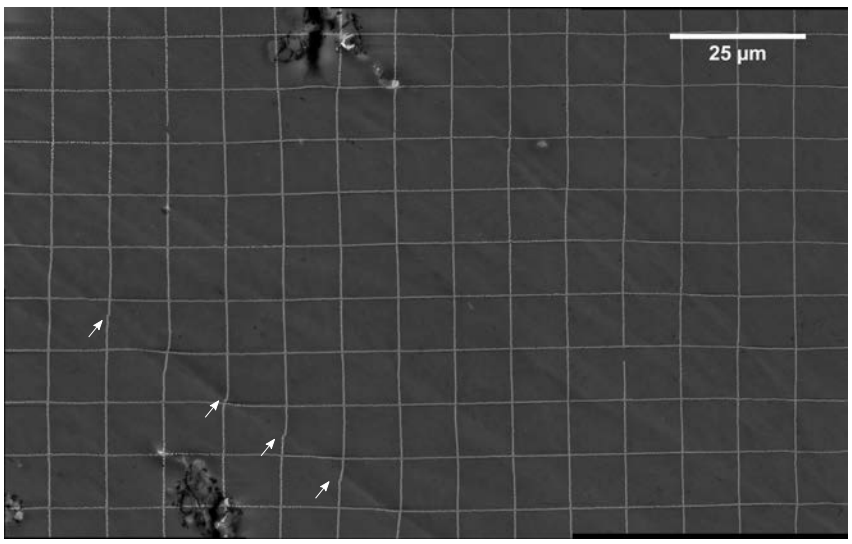

Figure 4.20: Shear band observed after 5.9% tensile strain on UFG-A material tested at $5.8 \times 10^{-5}\ s^{-1}$, RT. The white arrows point towards discontinuities of the grids.

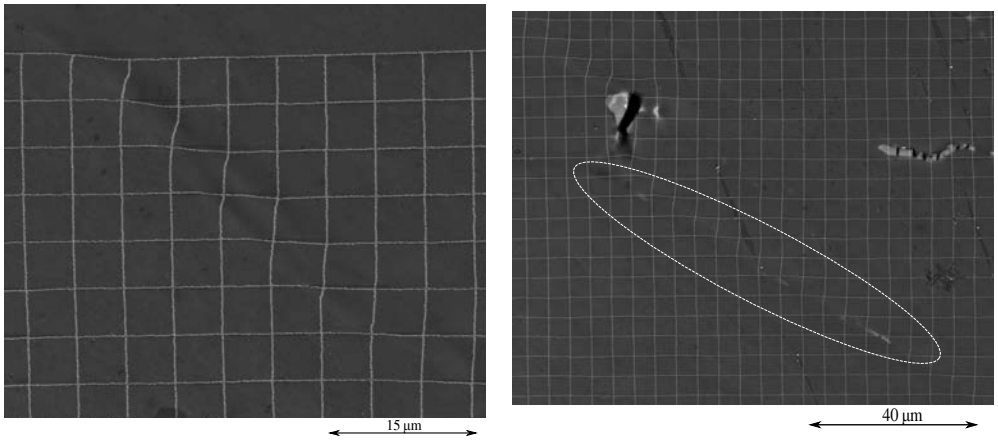

(a) *(b)*

Figure 4.21: BSE images of shear bands in UFG-A material strained at $5.8 \times 10^{-5}\ s^{-1}$, RT (a) due to grain structure and (b) triggered by particle breaking

Along some of these shear bands, the discontinuity in the grids, marked by white arrows in figure 4.20 suggest grain boundary sliding. Several evidences were found that GBS was triggered by stress concentration due to particle breaking (Figure 4.22). The length of grid discontinuities in figure 4.22b extends up to 20 μm which is 30 times the average grain size. Since GBS was observed over distances that are 10-100 times the mean grain size it suggests cooperative sliding along several grain boundaries.

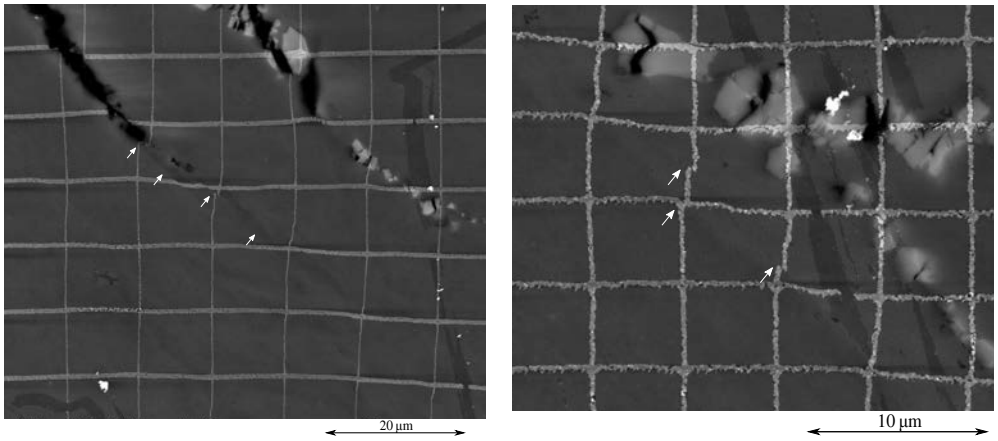

(a) *(b)*

Figure 4.22: GBS triggered near the broken 2nd phase particles in UFG material strained until 5.9% at $5.8 \times 10^{-5}\ s^{-1}$, RT. The white arrows point towards discontinuities of the grids.

Meso-scale plastic longitudinal strain fields at selected steps for two of the observed zones of interest (ZOI) are presented in figures 4.23 and 4.24 with a common or individual strain scale, respectively. Contrary to the CG material in which the particles were initially intact, many transverse microcracks are initially present in these particles. They open and then propagate along the interface with the matrix, giving rise to meso-cracks aligned with the particle row, which are loaded in mixed-mode. Meso-scale bands initiate from rows of broken particles. The orientation of the major bands

ranges from 40 to 55°, even though faint and weak bands in the orthogonal directions seem to appear. No symmetry was observed in the angles of the localisation bands and cracks. They seem to be fully determined by the particles and grains elongation direction, and not by the mixed-mode stress field ahead of the crack tip that would promote bifurcation in an isotropic material. This preferential orientation is due to the anisotropic polycrystalline microstructure of the UFG material.

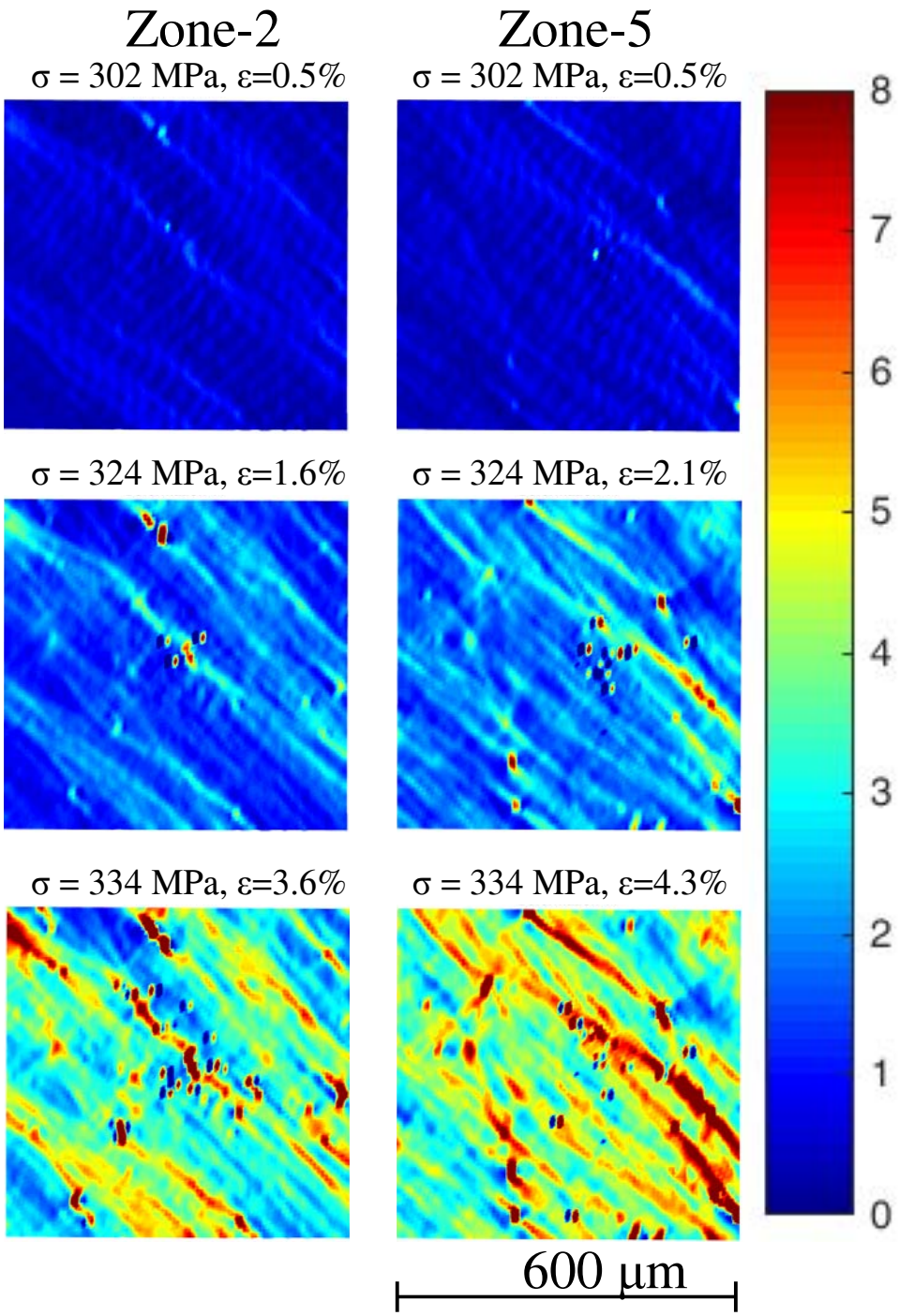

Figure 4.23: Meso-scale plastic longitudinal strain fields for UFG material at $5.8 \times 10^{-5}\ s^{-1}$*, RT*

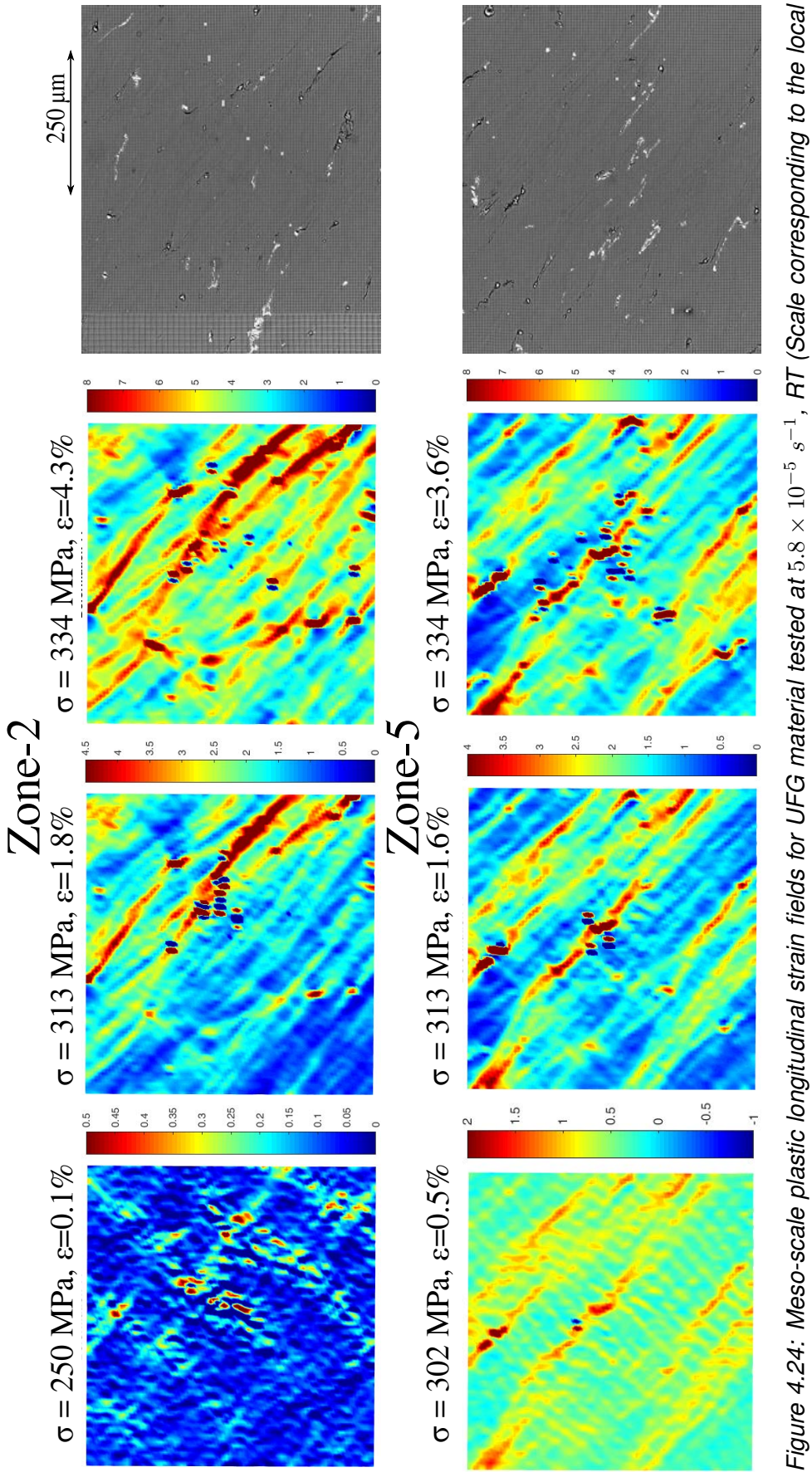

Figure 4.24: Meso-scale plastic longitudinal strain fields for UFG material tested at $5.8 \times 10^{-5}\ s^{-1}$*, RT (Scale corresponding to the local strain field)*

In figure 4.24, it can be seen that strain localisation in the form of shear bands sets in early. The local strain along the horizontal centerline is averaged along the vertical axis over ± 40 μm and is plotted in figure 4.25. Each peak in the local strain represents a shear band. The width/thickness of the shear bands remains almost constant. This suggests that it corresponds to the width of underlying "soft" grains (that is: larger than average, or more suitably oriented) surrounded by "harder" grains, or to the width of one layer of grains on each side of sliding grain boundaries.

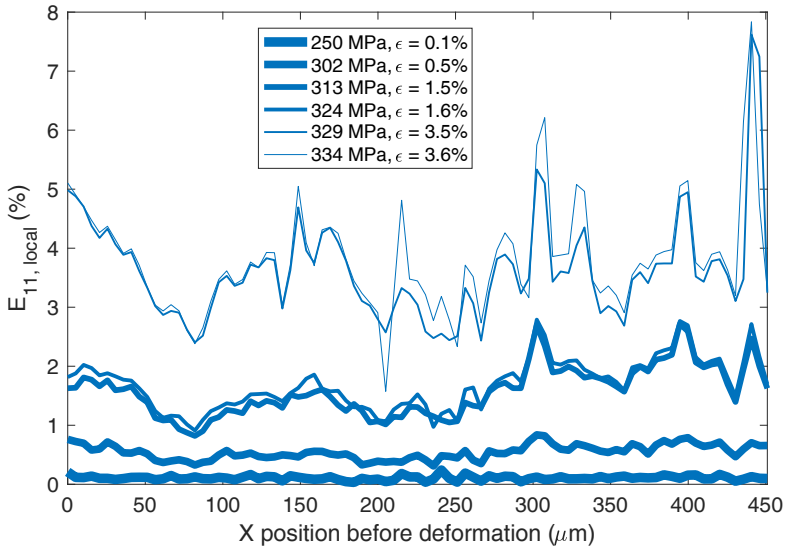

(a) ZOI-2

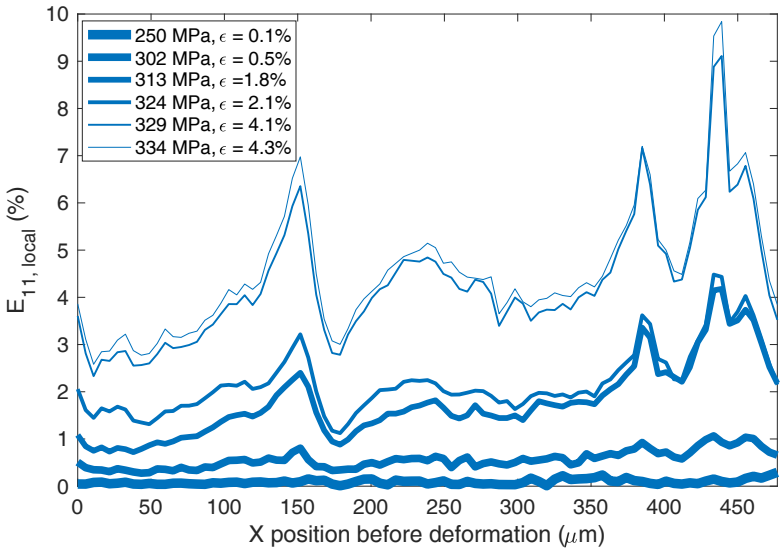

(b) ZOI-5

Figure 4.25: Local strain variation along the horizontal centreline in the strain fields and averaged in vertical direction for ± 40 μm from the centreline in UFG-A material deformed at 5.8×10^{-5} s^{-1} at RT

Histograms of the normalised plastic strain and their standard deviation at different steps are plotted in figures 4.26 and 4.27. The histograms become narrower indicating a decrease in heterogeneity of the strain field with increasing plastic strain, which can also be seen from the plot of standard deviation which decreases initially and then becomes almost constant for both the regions.

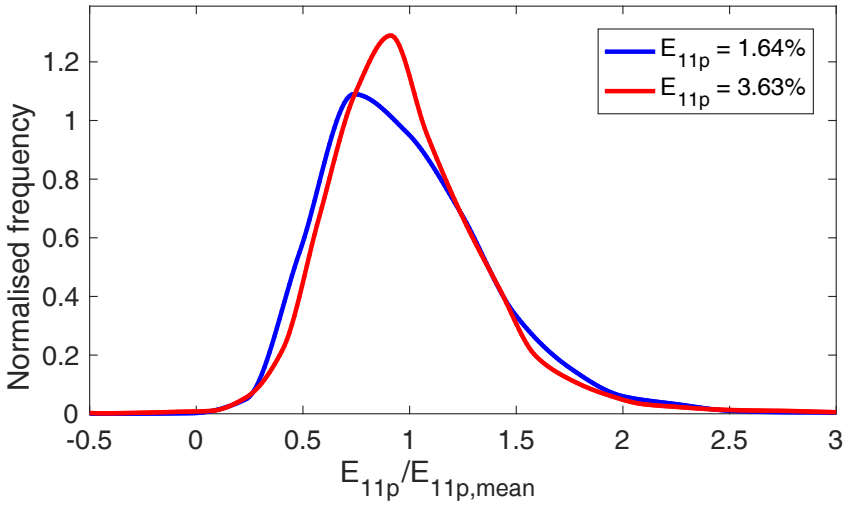

(a) ZOI-2

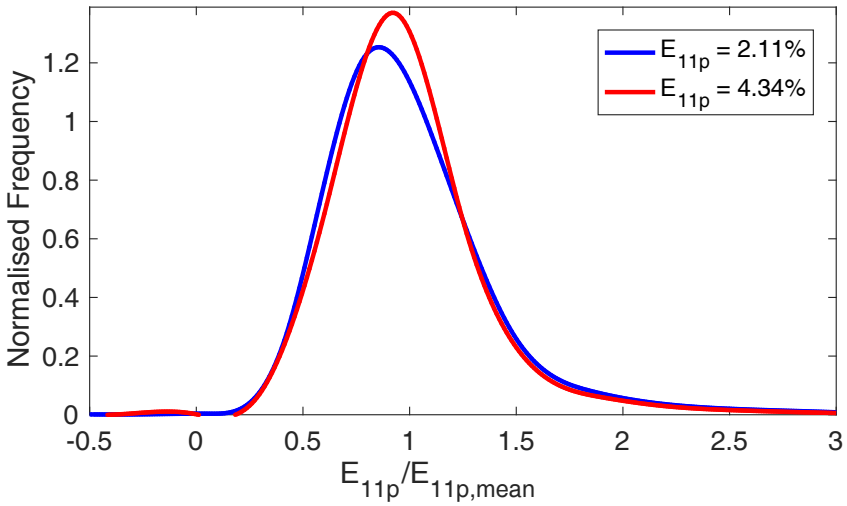

(b) ZOI-5

Figure 4.26: Histograms of normalised plastic strain at different steps in UFG material loaded at $5.8 \times 10^{-5}\ s^{-1}$ *at RT*

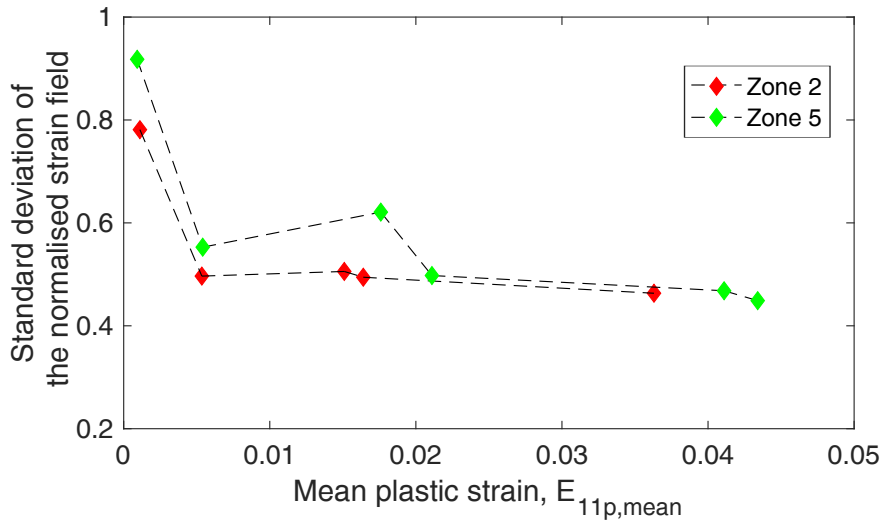

Figure 4.27: Evolution of the standard deviation of the normalised plastic strain fields for UFG material loaded at $5.8 \times 10^{-5}\ s^{-1}$ *at RT*

The standard deviation of the normalised plastic strain fields of both CG and UFG materials is plotted against the mean axial plastic strain in figure 4.28. The standard deviation is initially very high in UFG material and then decreases rapidly to a constant value which is higher than that for CG material. The existence of a few relatively "large" grains, prone to earlier and easier plastic flow in the ECAPed material, with a majority of "harder" refined grains might be responsible for the higher initial heterogeneity of plastic flow, compared to CG material.

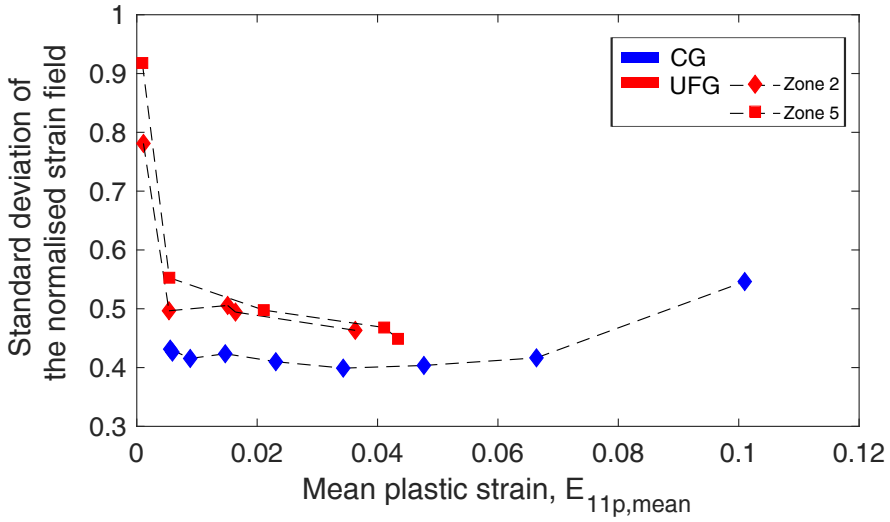

Figure 4.28: A comparison of the standard deviation of the of the normalised strain fields between CG and UFG materials at RT

Micro-scale plastic strain field were also observed in multiple 10×10 sq. μm areas. EBSD was done for these 10×10 sq. μm areas before the test, to be able to correlate

the strain distribution with the underlying microstructure. However, due to low indexation rate during EBSD, the orientation mapping was not completely successful. Since transmission Kikuchi diffraction (TKD) has a better resolution and allows sub-surface observations, FIB sectioning was performed at Equipex Matmeca normal to the bands. Figure 4.29 shows images of the steps followed to obtain the thin foil for TKD. As can be seen from the STEM-HAADF image of the thin foil, the distribution of dispersoids is heterogeneous. In addition, there are no visible signs of grain growth. The obtained TKD image correlates very well with the surface EBSD IPF map (Figure 4.30).

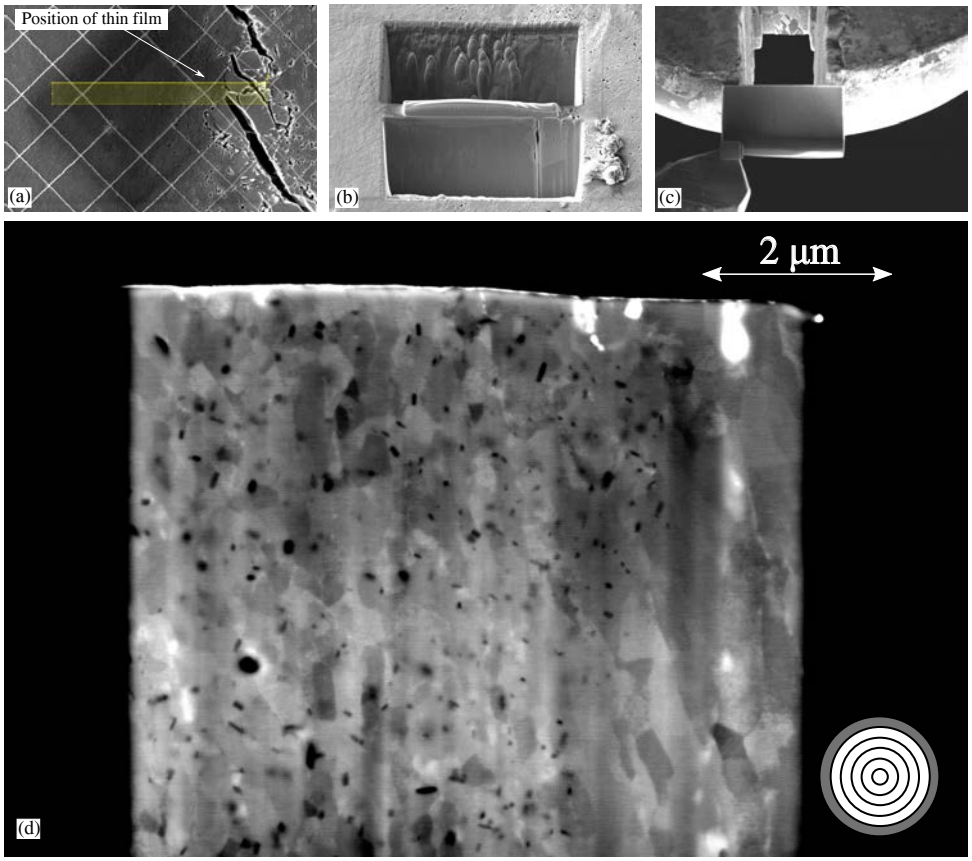

Figure 4.29: Steps for FIB sectioning: (a) Selection of the area of interest to be protected by Pt deposition, (b) Excavation on each side of the foil, (c) Placement of the foil in a support for observations and (d) observation through the foil thinned down to 200-300 nm (STEM-HAADF image).

The observed strain fields at each step was compared with the observed microstructure and are presented in figure 4.30. After 0.4% macro strain, shear bands become visible. With the increase in strain, an increase in the intensity of the strain in the bands and in their apparent widths can be observed. However, these shear bands occur mostly at the long, straight, high angle GBs with a high shear stress and at the interface between large and small grains, indicating a possibility of grain boundary sliding.

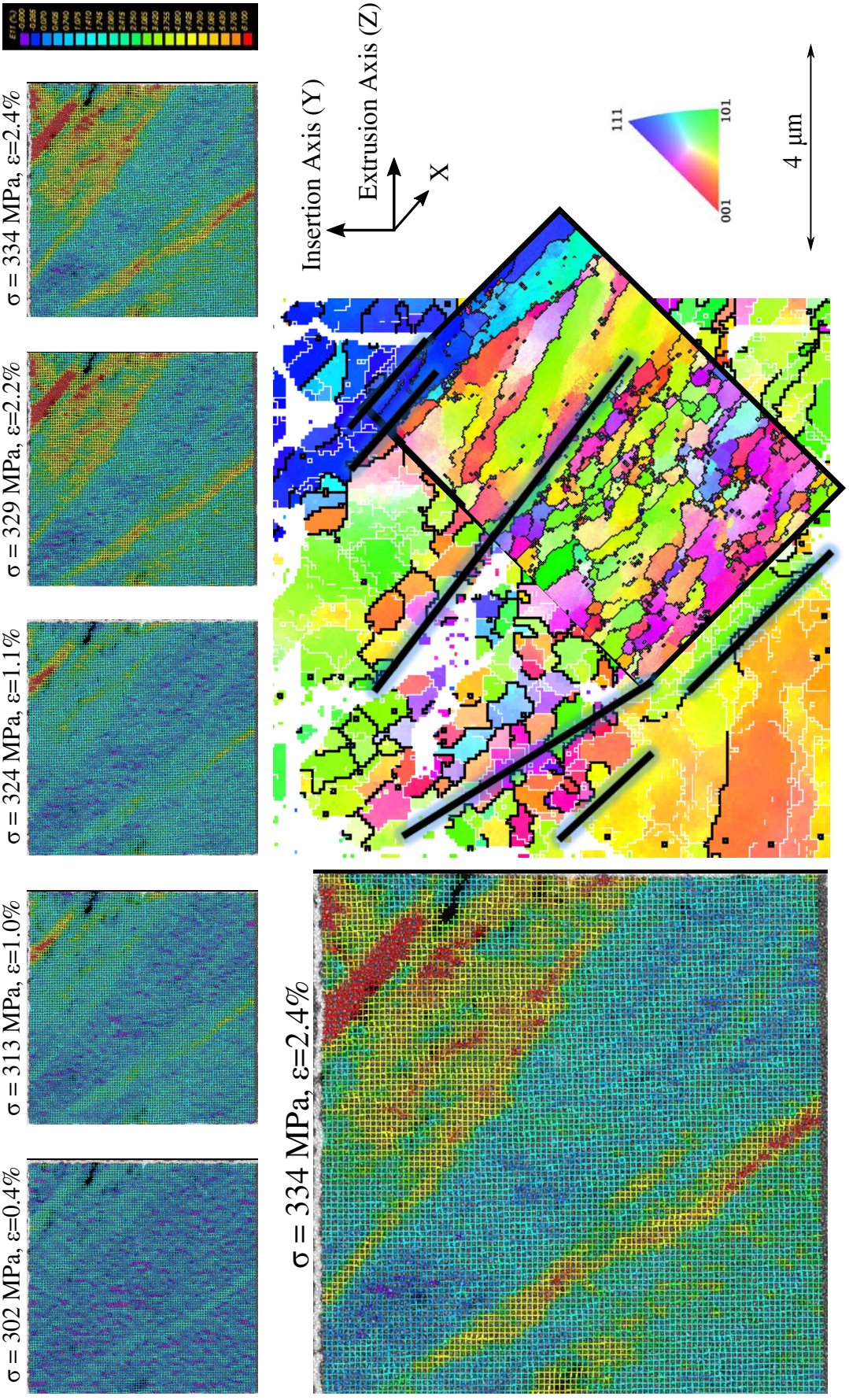

Figure 4.30: Micro-scale plastic longitudinal strain fields of 10× 10 μm area for UFG material tested at $5.8 \times 10^{-5}\ s^{-1}$, RT (Black lines on "IPF-X" maps represent the strain localisation bands)

A map of rigid body rotation at 334 MPa, 2.4% strain is shown in figure 4.31. The direction of rotation inside the bands is opposite to the rotation of the matrix. The evolutions of the local rotation inside and outside a band with the macro strain are compared in Figure 4.32. The rotation remains limited in the vicinity of the band while the progressively more negative rotation inside the band provides an evidence of grain rotation. According to Joshi and Ramesh [13], there is a difference in microstructure between inside and outside such bands in nanocrystalline or UFG materials. The grain structure of nano-structured Fe was equiaxed and random outside the bands but highly oriented within the bands. They further explained that within these bands, grains rotate and align during deformation to a preferable orientation which allows easy slip inducing a local geometric softening. Further analysis of grain rotation was difficult here. Even if the orientation of the grains in which rotation is observed was known, it would be difficult to determine if rotation is the natural result of dislocation glide, or non-crystallographic, because the number of active slip systems and the complete strain tensor of the grains are not known.

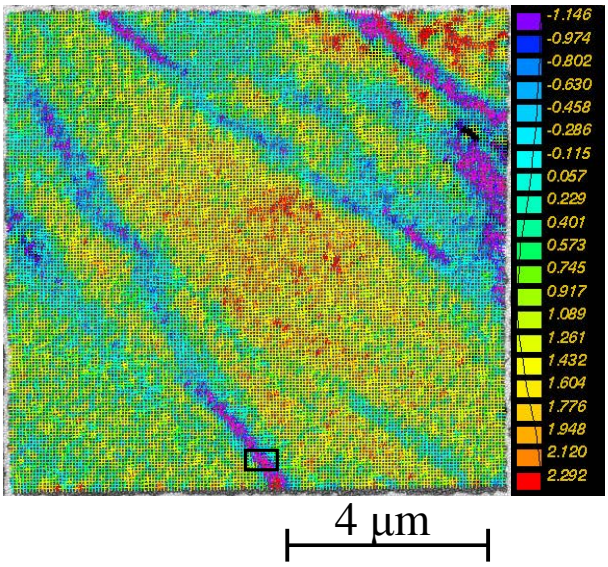

Figure 4.31: Rigid body rotation map (in degrees) at σ = 334 MPa, ϵ = 2.4% in UFG-A material tested at $5.8 \times 10^{-5}\ s^{-1}$ at RT

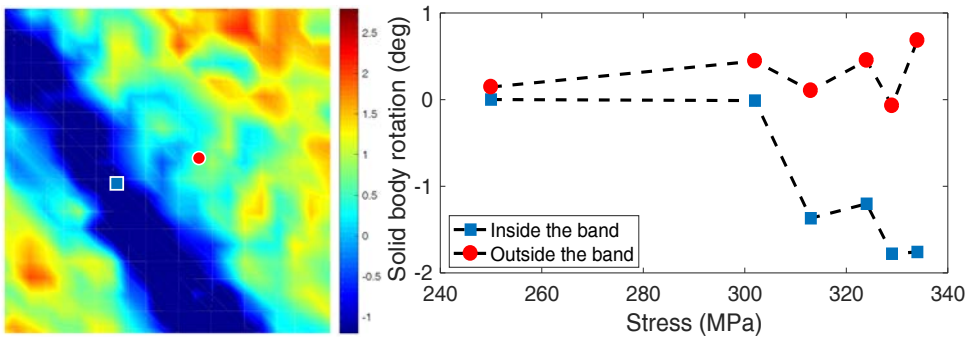

Figure 4.32: Compared evolutions of rigid body rotations inside and outside the band in the zone marked by a square in figure 4.31.

Figure 4.33 presents the series of strain maps in another 5×4.5 μm area together with an EBSD map of this area (not quite perfect, unfortunately, but sufficient to draw some conclusions). An intense shear band first appears along a long and straight high angle grain boundary suitably oriented to undergo a high shear stress. Upon further straining, the band extends along this grain boundary and later on, triggers sliding along 3 neighbouring grain boundaries whose trace is nearly normal to the tensile axis. This is an indication of the cooperative nature of grain boundary sliding.

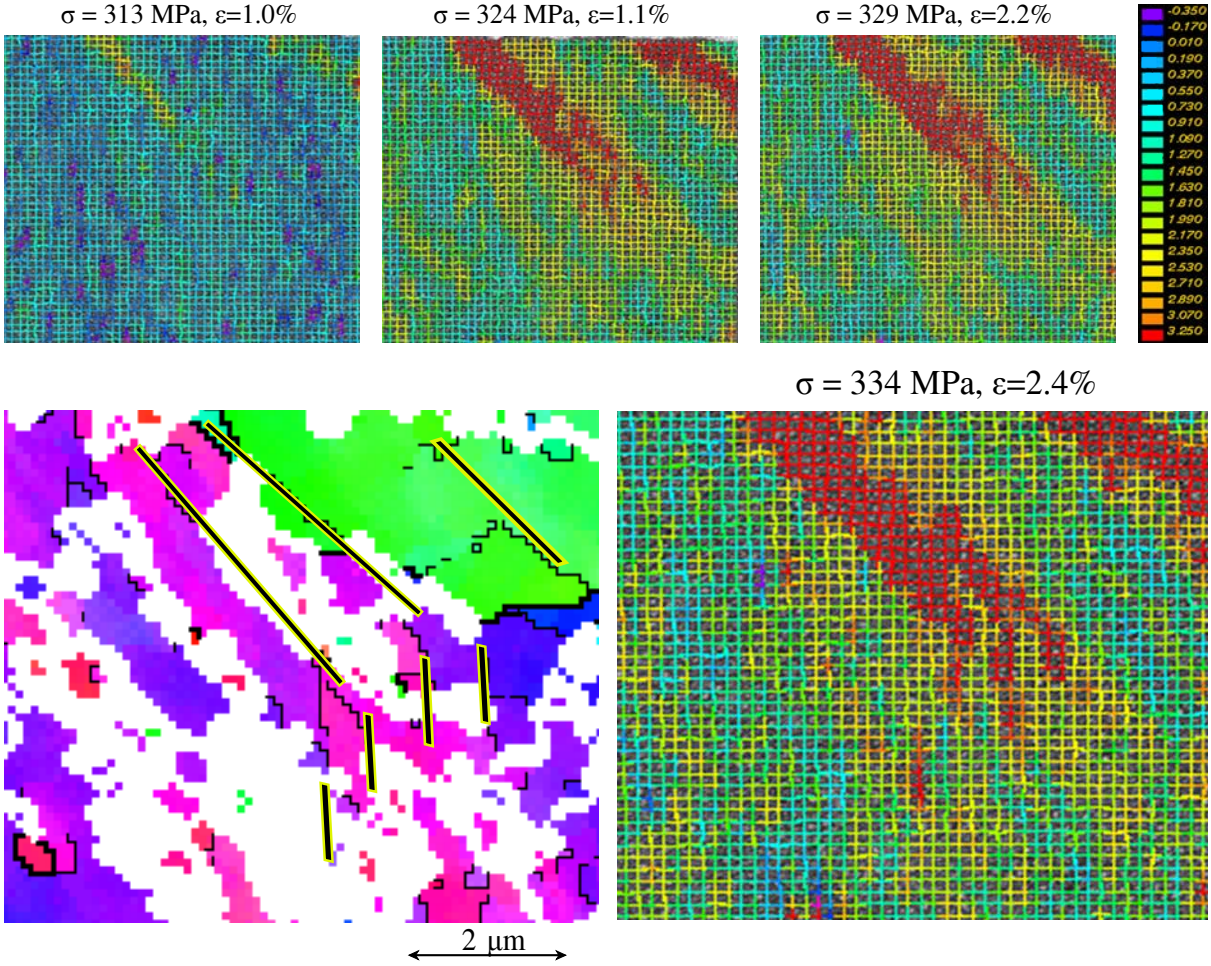

Figure 4.33: Micro-scale strain fields of 5×4.5 μm area for UFG material at 5.8×10^{-5} s^{-1}, RT

Figure 4.34 presents the micro-scale strain maps and the EBSD of a 10×10 μm area in ZOI-5. Black strain lines highlight the strain localisation bands on the EBSD map. Contrary to the expectations, the largest grains are not the most highly deformed areas, but the strain is more intense along the HAGBs.

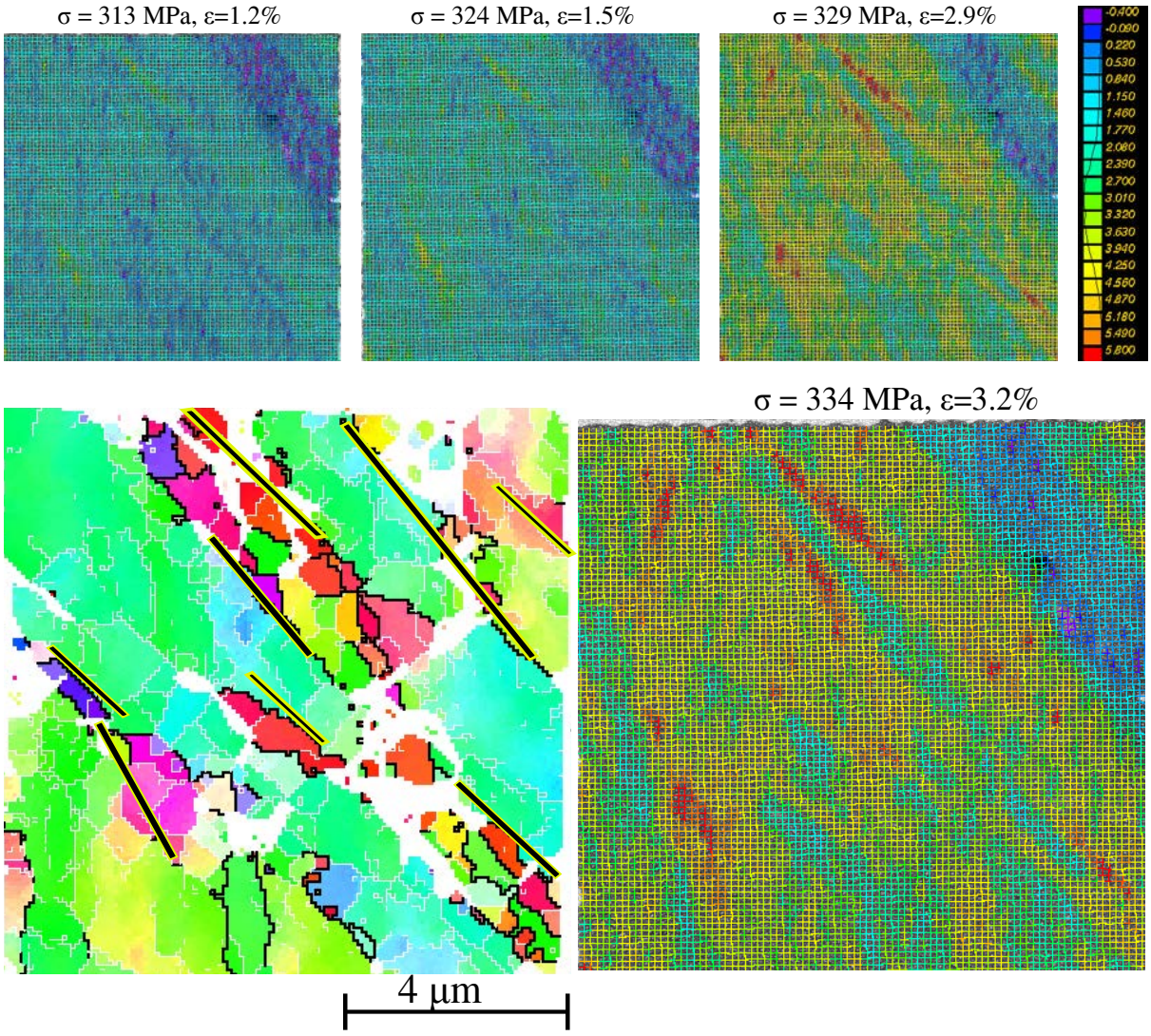

Figure 4.34: Micro-scale strain fields of 10×10 μm area for UFG material tested at 5.8×10^{-5} s^{-1} *at RT*

The evolution of the mean axial plastic strain in each of the four 600×600 μm^2 areas covered with microgrids along the sample axis and in the 10×10 μm^2 areas located in their centres is plotted as a function of the macroscopic stress in figure 4.35. First, significant differences in meso-scale deformation appear from one place to the other. Second, a step-wise evolution is observed both at meso- and micro-scale. Strain jumps in ZOI-1 alternate with the other ZOIs in accordance with the serrated flow.

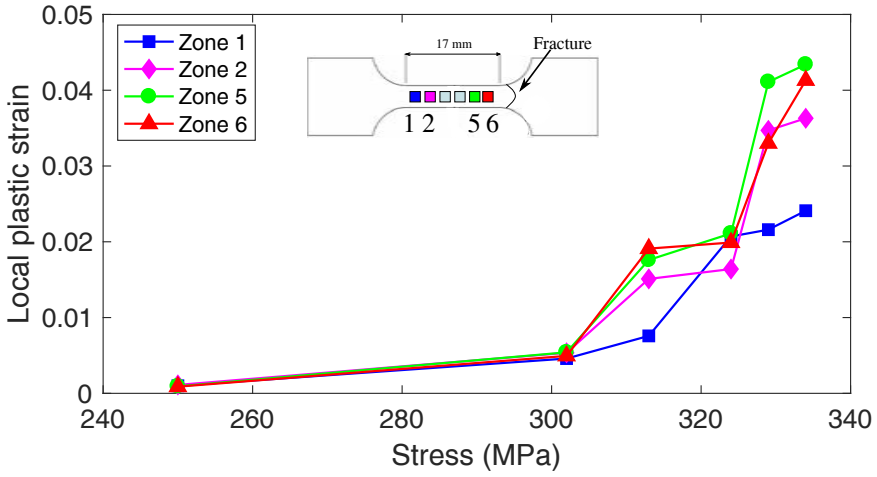

(a) 600×600 μm^2 area

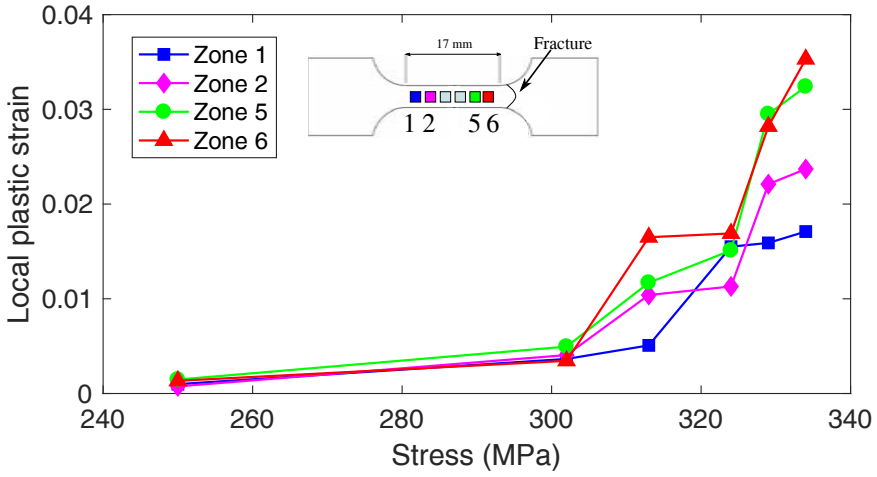

(b) 10×10 μm^2 area

Figure 4.35: Step-wise increment in mean axial strain in UFG-A material tested at 5.8×10^{-5} s^{-1} at RT

As expected from the strain gradient shown by figure 4.35, fracture finally took place in the curved area near ZOI-6. SE and BSE images of the fracture surface are shown in figure 4.36. In addition to the broken particles, the fracture surface is covered with ligaments containing small dimples (although these dimples are often larger than the mean grain size) corresponding to transgranular ductile fracture. Enlarged images of the dimples, inside which small particles can sometimes be found are presented in figure 4.37.

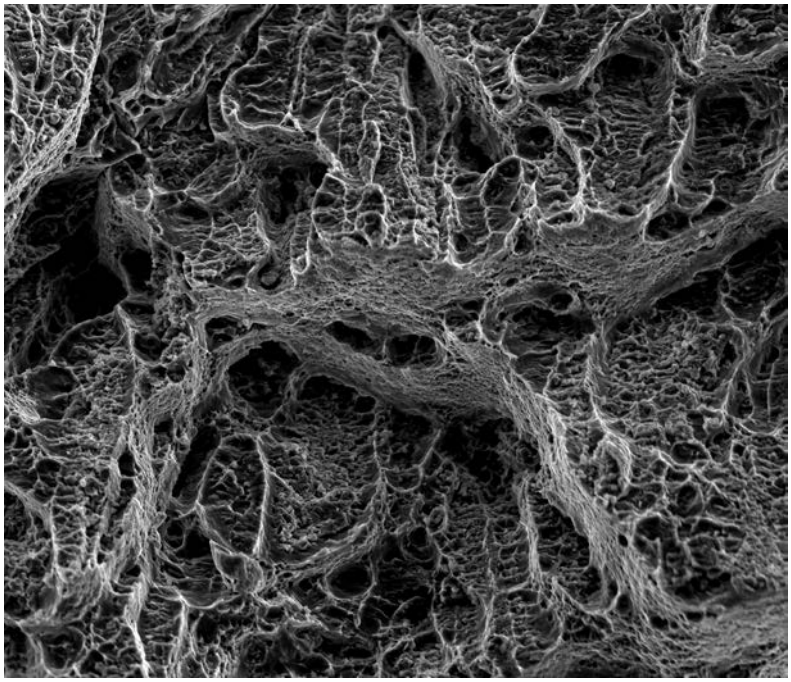

(a) SE image of the fracture surface

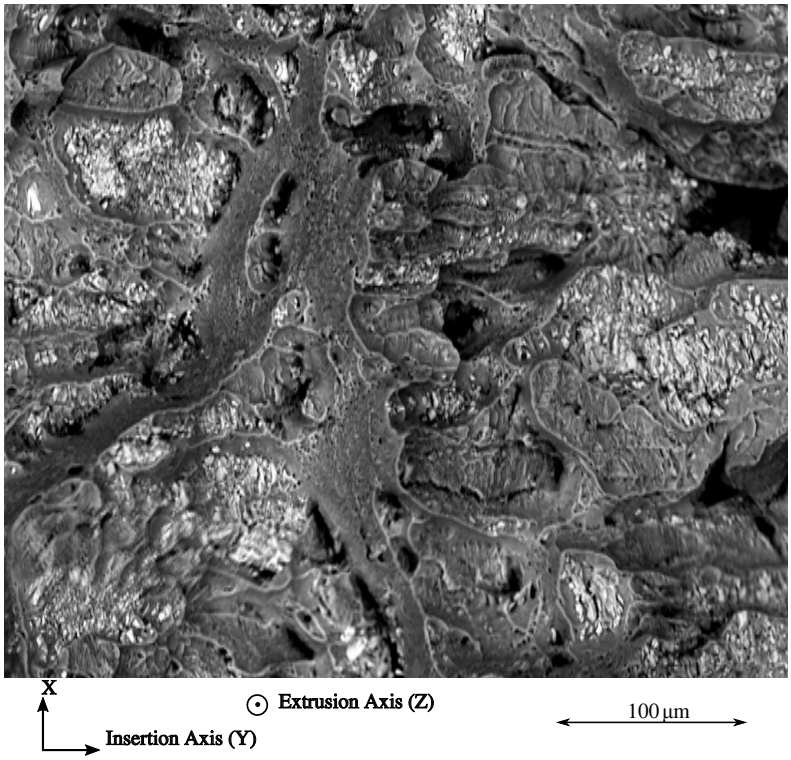

(b) BSE image of the fracture surface

Figure 4.36: Fracture surface of the UFG material tested at RT at $5.8 \times 10^{-5}\ s^{-1}$ *and broken at 5.9% strain*

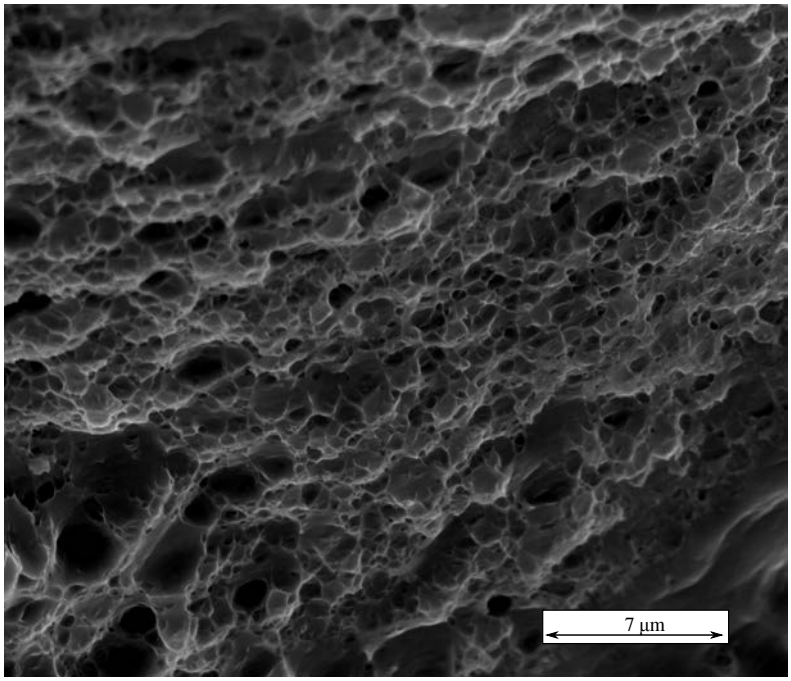

(a) SE image of the fracture surface

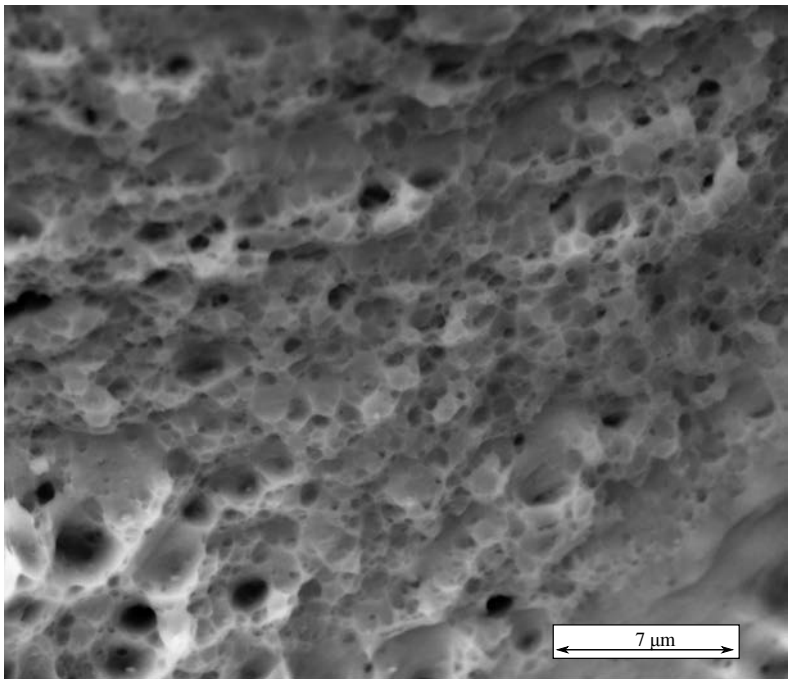

(b) BSE image of the fracture surface

Figure 4.37: Zoom of the fracture surface of the UFG material tested at RT at $5.8 \times 10^{-5}\ s^{-1}$

UFG-A material at $5.8 \times 10^{-4}\ s^{-1}$

Another test with 10-times faster displacement rate was performed on UFG material (Figure 4.38). This test was performed *ex-situ* to facilitate the measurement of the macro-scale strain, using two-marker points and an optical set-up. Again, 4 600×600 and 4 20×20 sq. μm area images were captured and analysed at each step. Plastic strain measured from DIC agrees very well with that measured from the optical extensometry, establishing the representatively of the analysed area (Figure 4.39). Similar to the UFG specimen tested at $5.8 \times 10^{-5}\ s^{-1}$, this specimen also gets covered with shear bands during deformation (Figure 4.40).

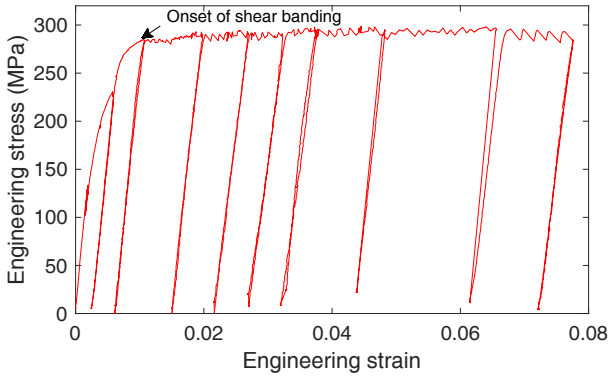

Figure 4.38: Engineering stress-strain curve for ex-situ tensile test on UFG material at $5.8 \times 10^{-4}\ s^{-1}$ *at RT (Strain is calculated from optical extensometry)*

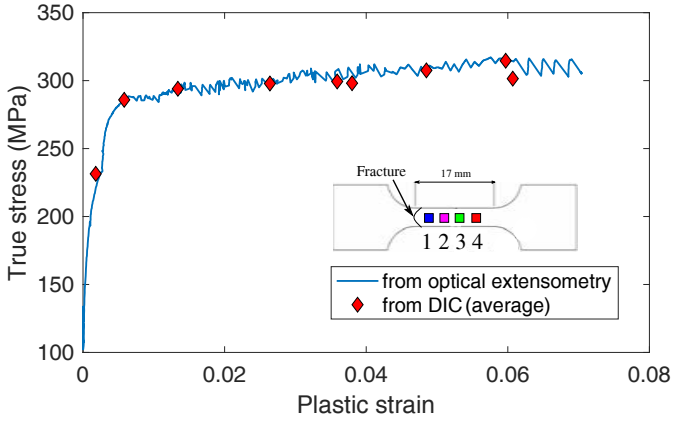

Figure 4.39: True stress vs plastic strain curve for ex-situ tensile test on UFG material at $5.8 \times 10^{-4}\ s^{-1}$ *at RT*

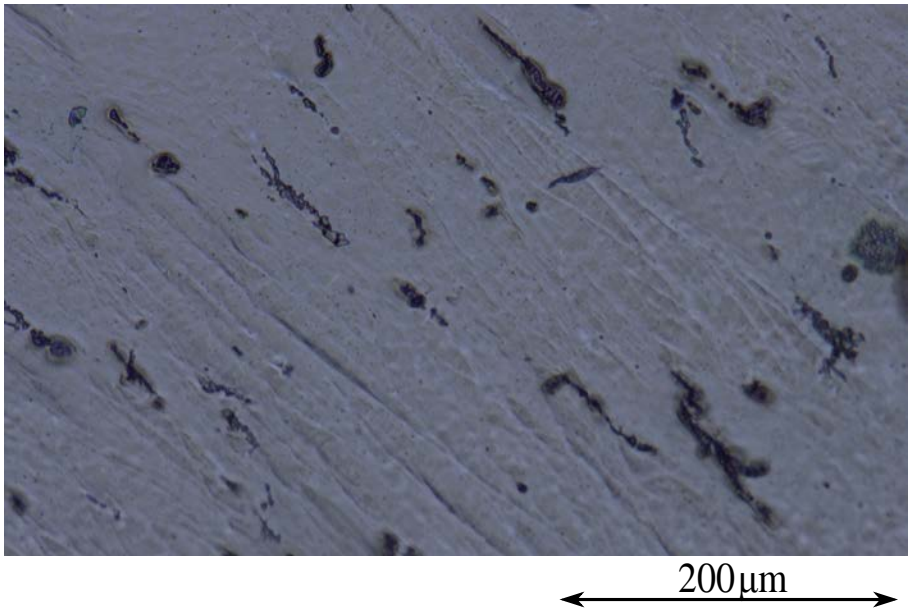

Figure 4.40: Optical image of a UFG specimen surface covered with shear bands after 3.3% strain at $5.8 \times 10^{-4}\ s^{-1}$ *at RT.*

Figure 4.41 shows selected meso-scale strain maps for ZOI 4. All meso-scale bands initiate from broken particles (especially the elongated rows of particles) beyond step 2, i.e. 285 MPa and 1.14% total strain. Their orientation ranges from 30 to 52° (no symmetry in the angles), and they seem to be fully determined by the particles and the grains elongation direction. Their length ranges from 50 to 360 μm with an average value of 107 μm, which is much higher than the mean grain size. The tensile strain inside the bands rises up to 11-12% (about twice the average strain). The local strain along the center line is averaged along the vertical axis in the shaded area (Figure 4.42a) and is plotted in figure 4.42b. The obtained results are similar to the ones obtained at $5.8 \times 10^{-5}\ s^{-1}$. The width of the shear bands is in the range of 20 to 200 μm and does not increase with increasing strain confirming that the principle cause of strain heterogeneity is the underlying heterogeneous microstructure, i.e. coexistence of small and large grains and HAGBs or LAGBs.

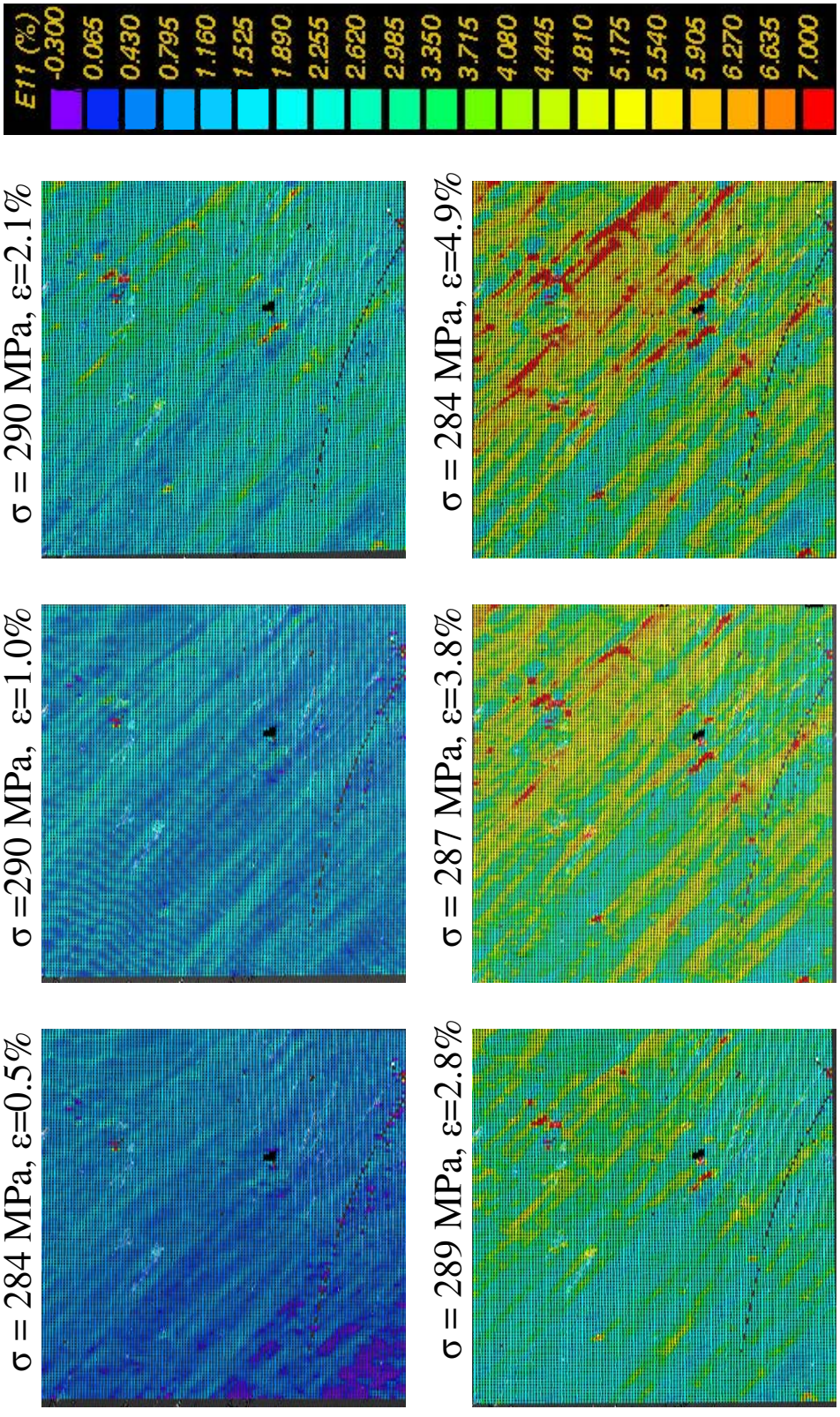

Figure 4.41: Meso-scale plastic longitudinal strain fields for UFG material tested at $5.8 \times 10^{-4}\ s^{-1}$ *at RT*

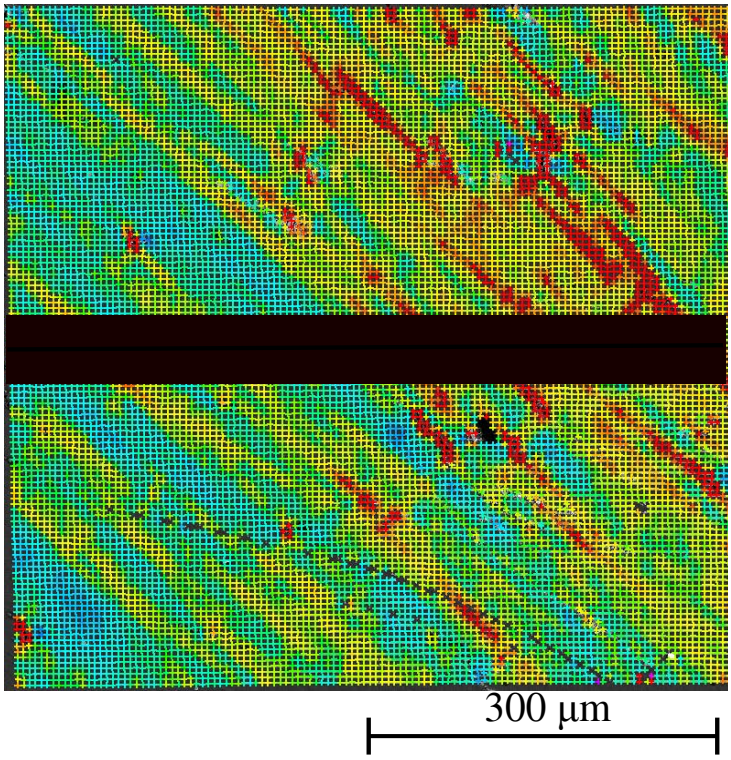

(a)

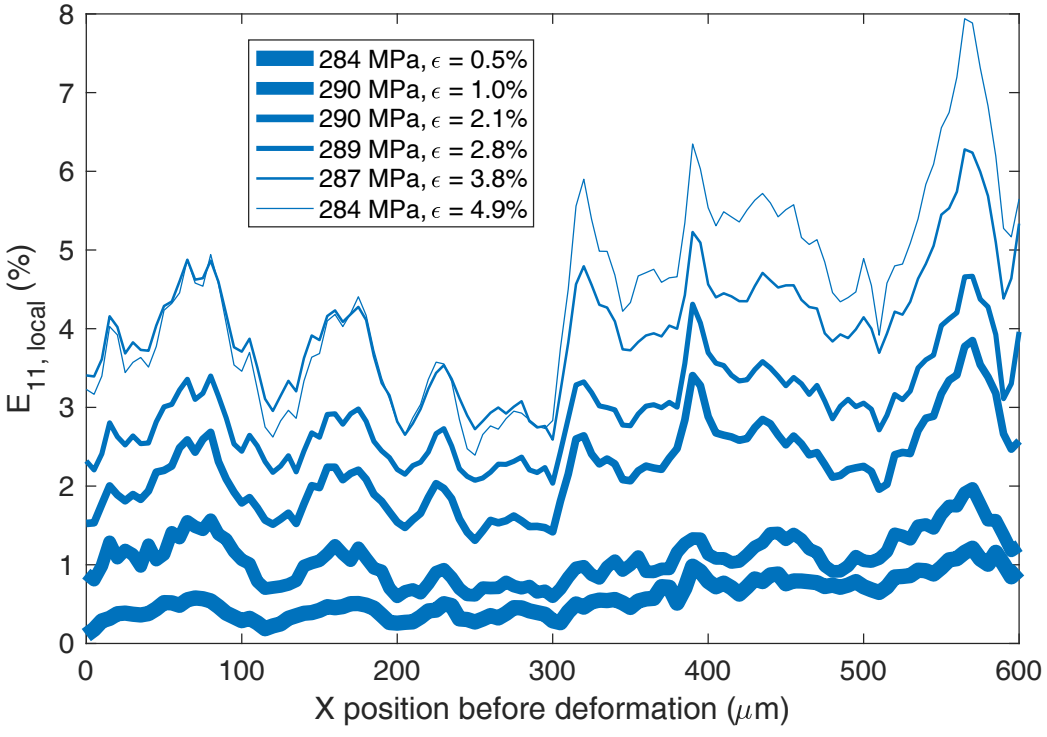

(b)

Figure 4.42: Local strain variation along the centerline (marked in black) averaged in vertical direction in the shaded area in (a) in UFG material loaded at $5.8 \times 10^{-4}\ s^{-1}$ *at RT.*

Figure 4.43 and 4.44 present the histograms of the normalised axial plastic strain for ZOI-4 and the evolutions of the strain fields standard deviations for all the analysed ZOIs. The histograms are wider at the start and the end of the deformation process. The standard deviation decreases sharply at first and then becomes almost constant with increase in plastic strain confirming that though shear banding sets in early, it remains restricted to a limited area/ number of grains. The standard deviation at this rate is similar to that at $5.8 \times 10^{-5}\ s^{-1}$.

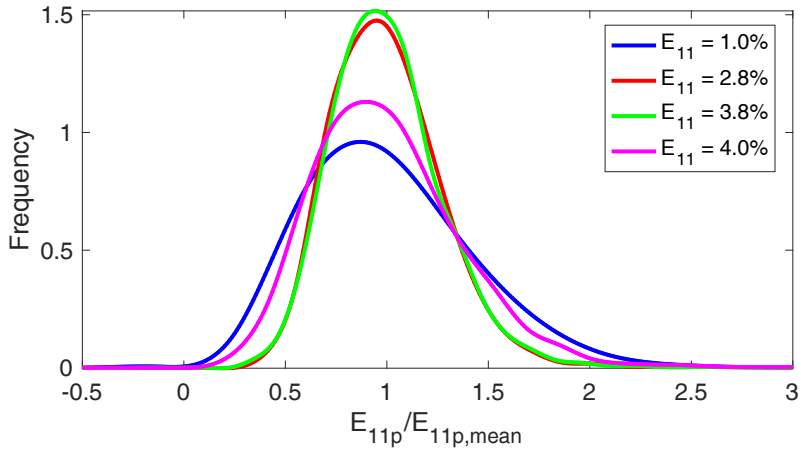

Figure 4.43: Histograms of normalised plastic strain at different steps for 600×600 μm^2 area of ZOI-4, UFG material tested at $5.8 \times 10^{-4}\ s^{-1}$ at RT

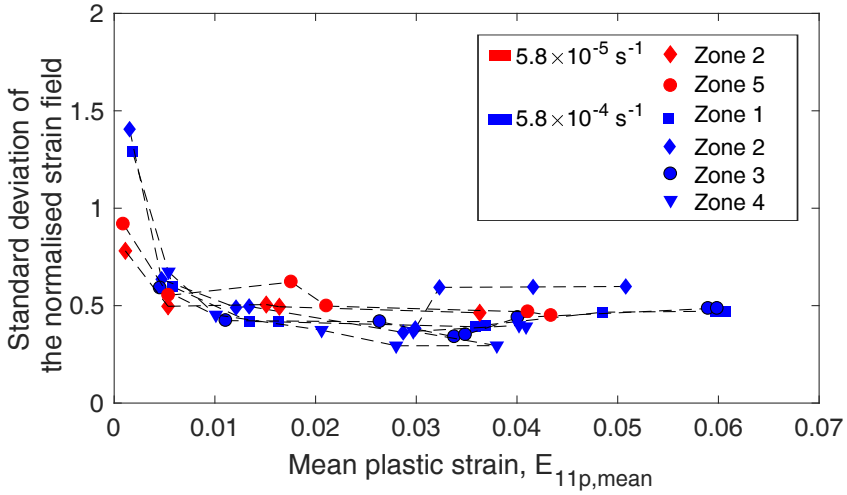

Figure 4.44: A comparison of the standard deviation of the normalised strain fields between the 2 tests run on UFG material at RT

Figure 4.45 presents the SE and BSE images of the fracture surface of the UFG specimen tested at $5.8 \times 10^{-4}\ s^{-1}$ which fractured after 7.8% strain. The fracture surface is again full of broken particles like at $5.8 \times 10^{-5}\ s^{-1}$. But the amount of the transgranular ligaments containing small dimples was decreased. Figure 4.46 shows BSE image of

one such rare sightings of the small ductile dimples sometimes with a tiny inclusion at their center.

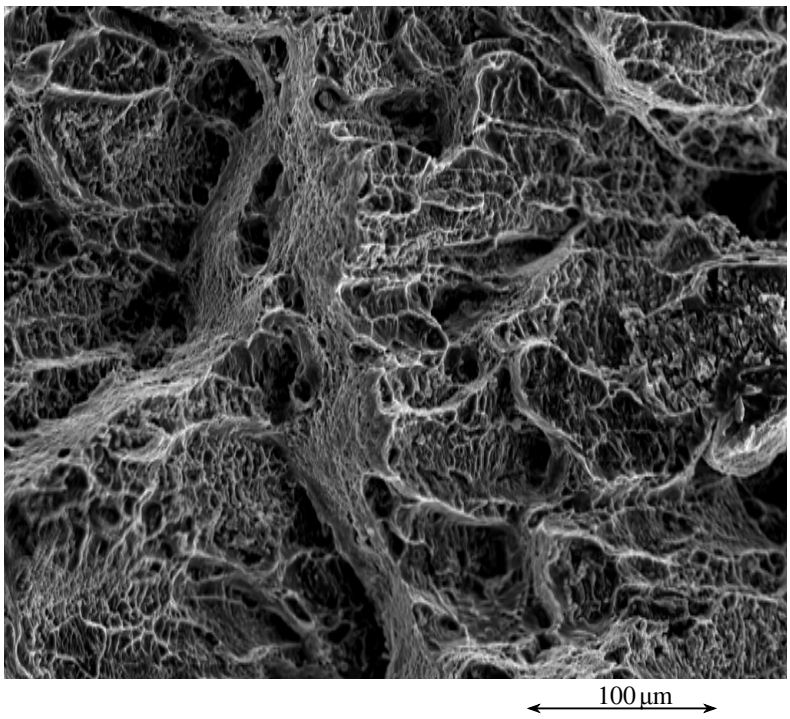

(a) SE image of the fracture surface

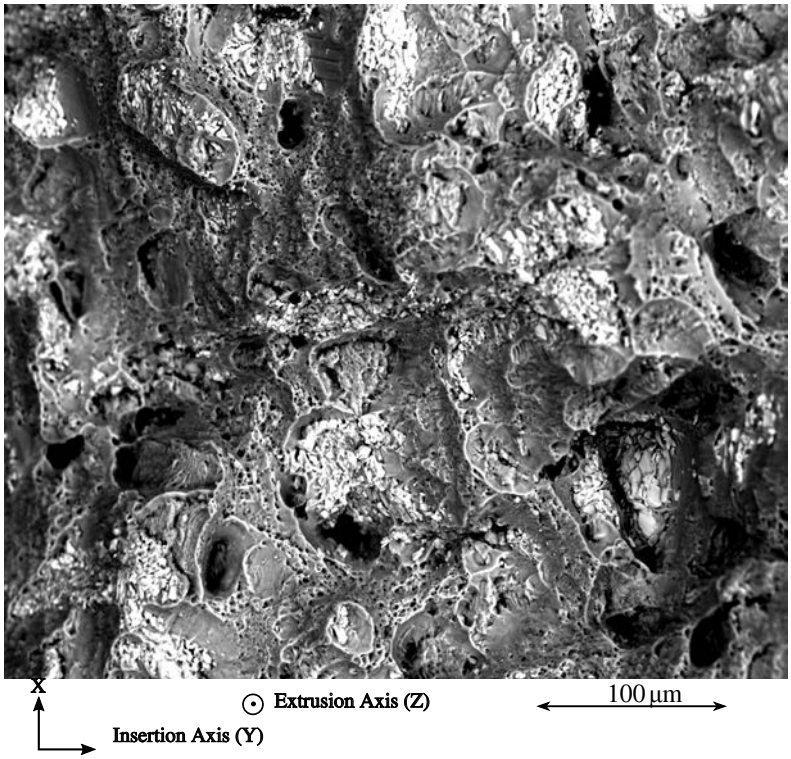

(b) BSE image of the fracture surface

Figure 4.45: Fracture surface of the UFG material tested at RT at $5.8 \times 10^{-4}\ s^{-1}$ *and broken at 7.8% strain*

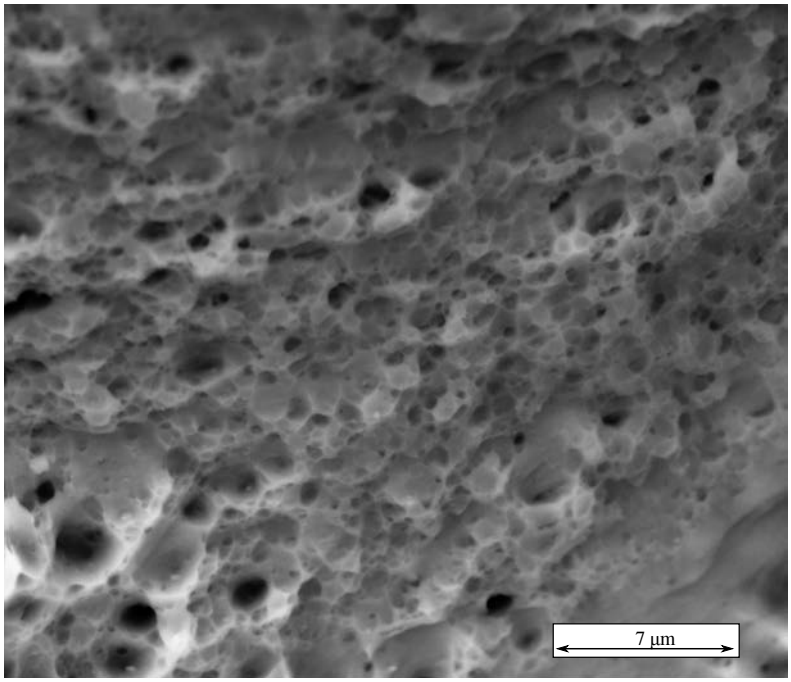

Figure 4.46: BSE image of the dimples on the fracture surface of the UFG material tested at RT at $5.8 \times 10^{-5}\ s^{-1}$

As-ECAPed UFG-A material at $5.8 \times 10^{-5}\ s^{-1}$

AFM observations are available for a similar tensile test done on the as-ECAPed UFG material at $5.8 \times 10^{-4}\ s^{-1}$, RT as shown in figure 3.3a of the previous chapter. Figure 4.47 shows the AFM images (both in deflection error contrast and topographic contrast) of the as-ECAPed UFG specimen after 4.6% strain scanned in contact-mode using a tip with a radius of 20 nm and a Dimension Icon AFM from Bruker. Image resolution is 44 nm/pixel. Several images were stitched to cover a wider area. In addition to the main shear bands observed along the grains and particles elongation direction, faint short bands normal to these shear bands were observed. To get a better resolution, the deformed surface was re-scanned in "peak-force tapping" mode with a sharper tip of radius 2 nm (Figure 4.48, with both peak force error and topographic contrasts). The image resolution was improved to 24 nm/pixel. The surface is highly deformed with significant roughness inside the shear bands. Figure 4.49 presents a magnified AFM image of one of the bands with a resolution of 2 nm/pixel. The scanned surface is full of nano-sized grains, each with a different out of plane height, while the polished surface before the test did not exhibit such "nano-hills". Like in the work of Han et al. [14], it suggests that grain boundary sliding induces out-of plane grain emergence.

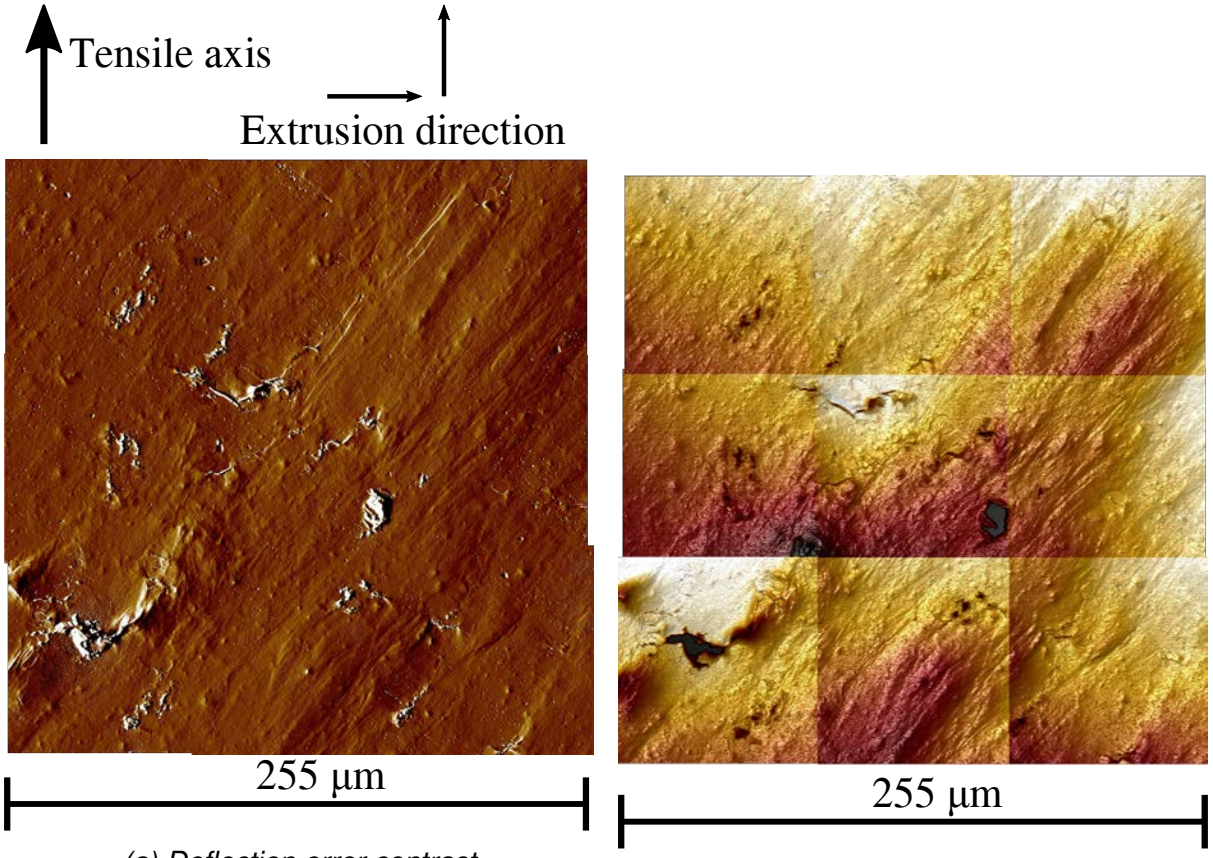

(a) Deflection error contrast

(b) Topography

Figure 4.47: AFM imaging in contact mode of as-ECAP UFG specimen deformed by 4.6% at $5.8 \times 10^{-5}\ s^{-1}$ *at RT*

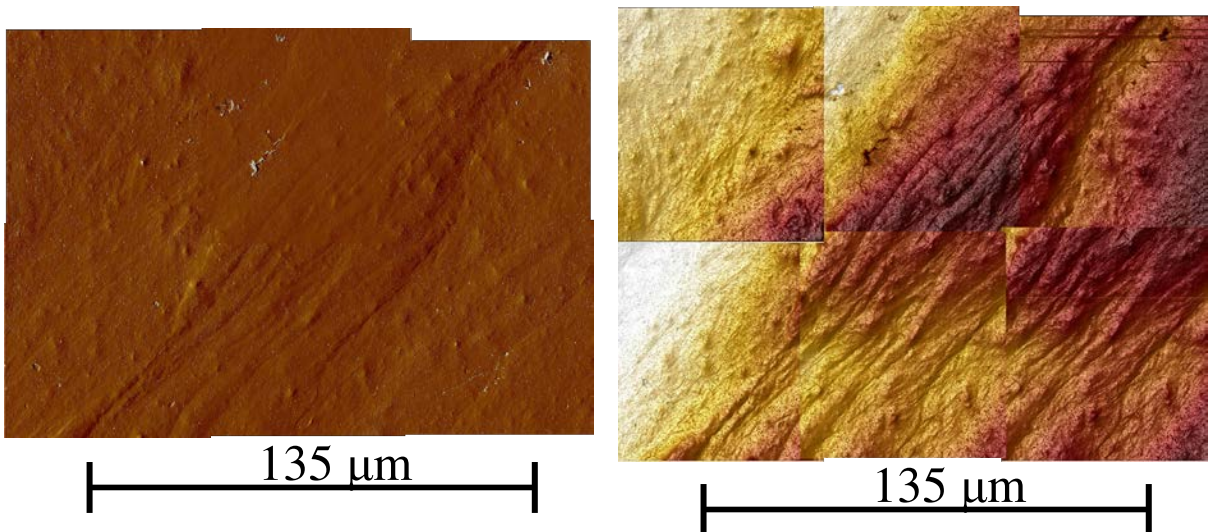

(a) Peak-force error contrast

(b) Topography

Figure 4.48: AFM imaging in "peak force tapping" mode of as-ECAP UFG specimen deformed by 4.6% at $5.8 \times 10^{-5}\ s^{-1}$ *at RT*

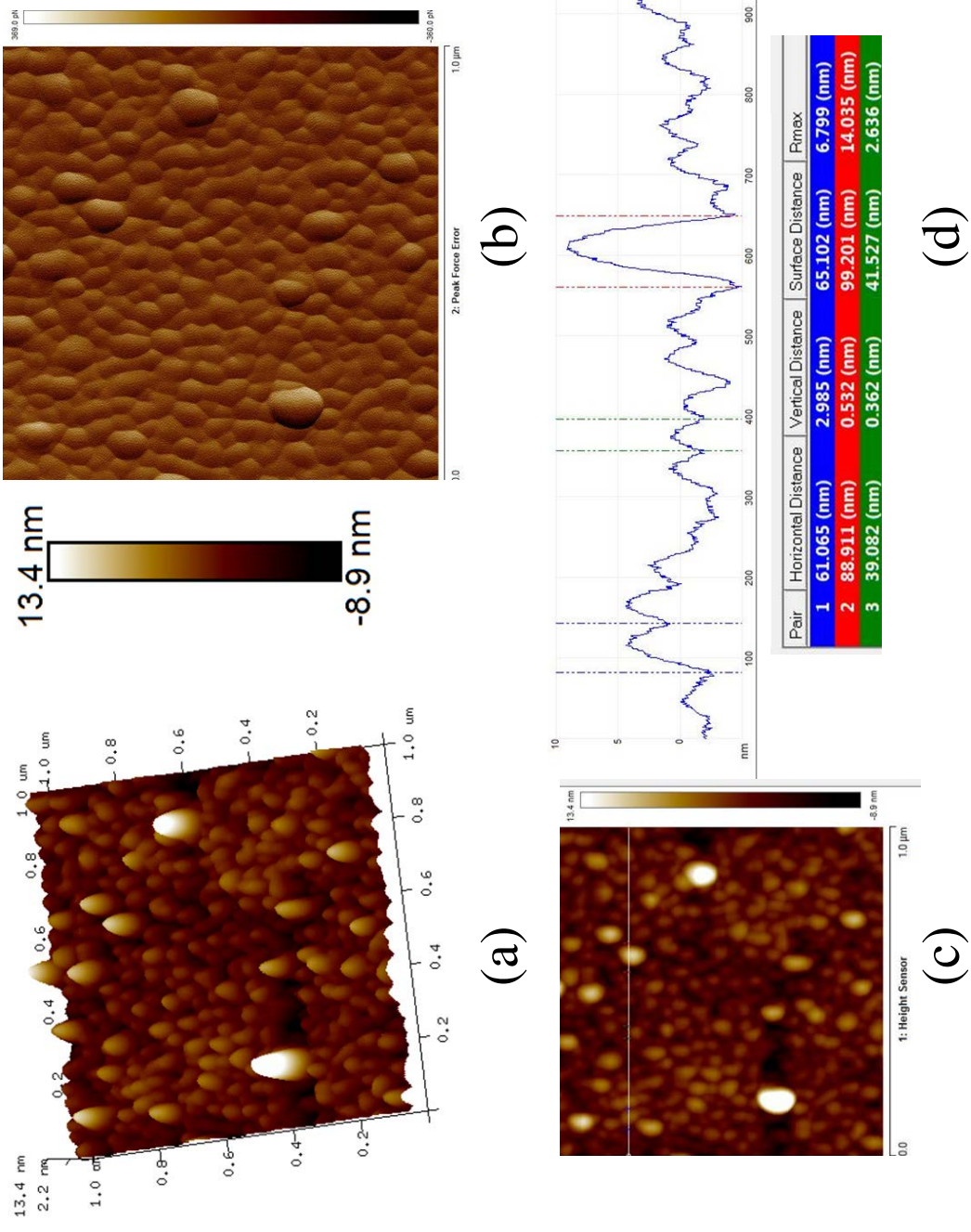

Figure 4.49: "Peak force tapping" mode AFM scan of a shear band in as-ECAP UFG specimen deformed by 4.6% at $5.8 \times 10^{-5}\ s^{-1}$ at RT: (a) High resolution 3D image, (b) Peak-force error contrast, (c) topographical profile and (d) hight variations along the horizontal line in (c).

4.2.2 At high temperature

Tensile tests were done using MTS hydraulic press at 100, 150 and 200°C on batch A CG and UFG materials using the optical extensometry described in previous chapter. The samples were however covered with microgrids, this allowing the measurement of the final plastic strain field by correlation of SEM images captured before and after the tests.

CG-A material at 100°C

Figure 4.50 presents the BSE image of the CG material strained by 6.5% at 1.5×10^{-5} s^{-1}, 100°C. Only 46% of the second phase particles were broken after 6.5% strain as compared to 60% at the similar strain level at RT. This may be due to a more ductile behaviour of the intermetallic particles and/or to the lower stress level. Signs of intragranular slip were also observed. Out of 50 grains, only 11 showed any observable slip lines.

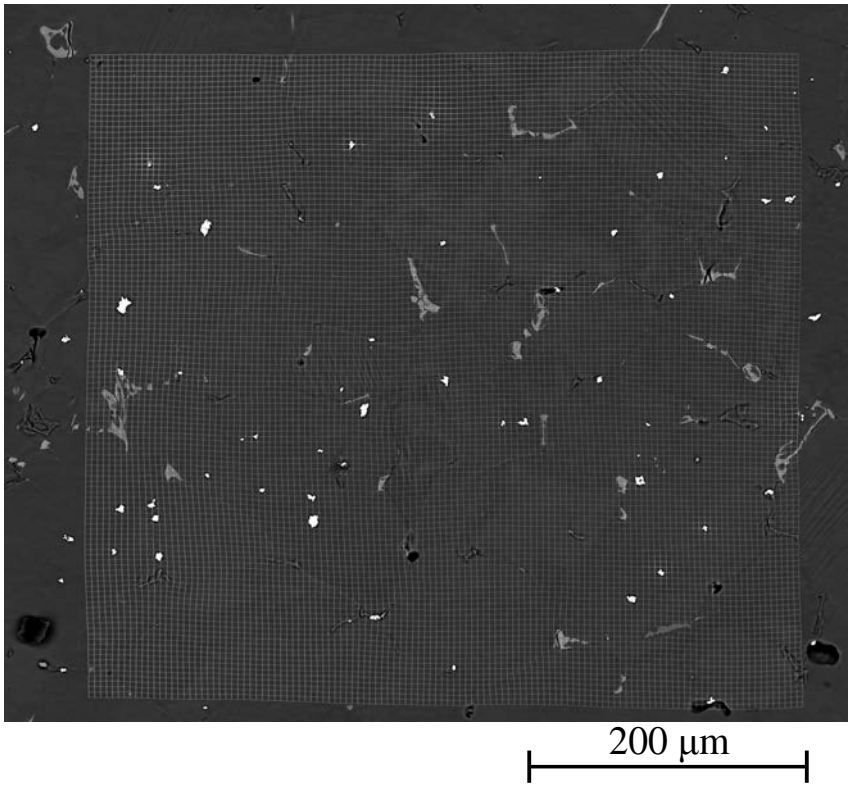

Figure 4.50: BSE image of the CG material strained at 6.5% at 1.5×10^{-5} s^{-1}*, 100°C*

Most of the slip lines were sharp and straight (Figure 4.51). In some cases, intragranular slip was accompanied by GBS (Figure 4.52). Several independent evidences of GB sliding were also observed (Figure 4.53), however they were limited in frequency and moderate in intensity making it difficult to measure the discontinuity in grids induced by GBS. The maximum value of the observed GBS-induced grid shift was 0.5 μm.

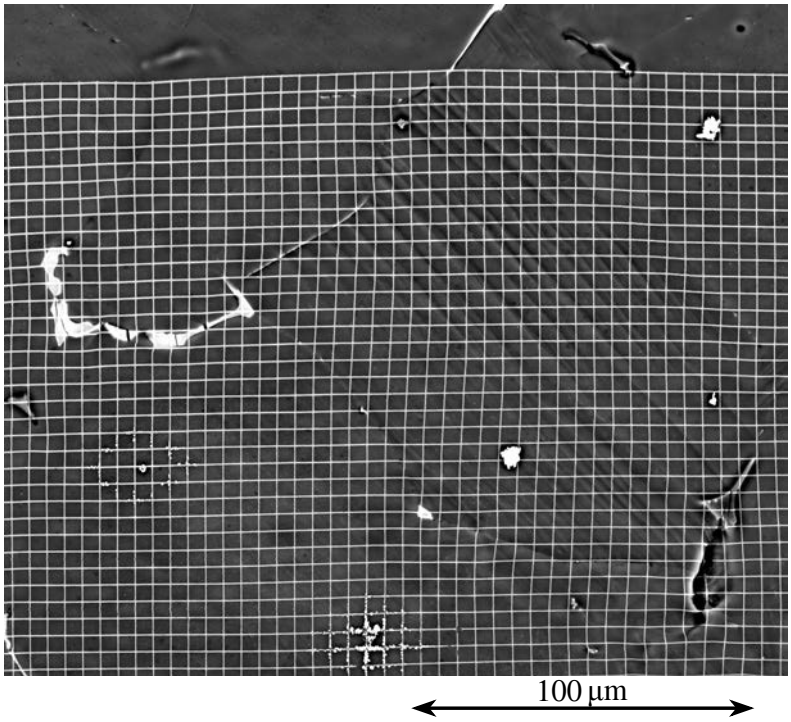

Figure 4.51: BSE image of the slip lines in CG material strained at 6.5% at $1.5 \times 10^{-5}\ s^{-1}$*, 100° C*

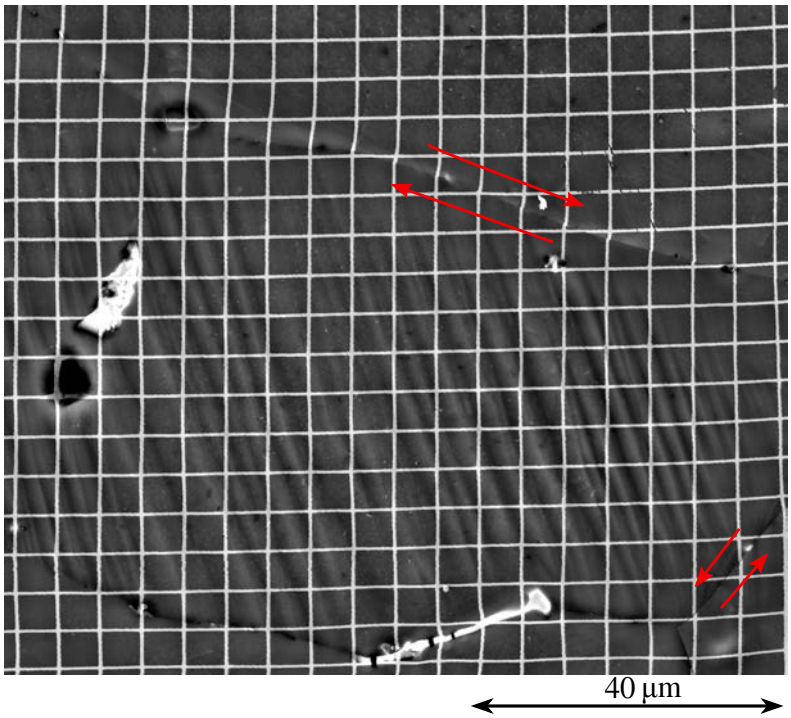

Figure 4.52: Slip lines accompanied by GBS in CG material after 6.5% strain at $1.5 \times 10^{-5}\ s^{-1}$*, 100° C*

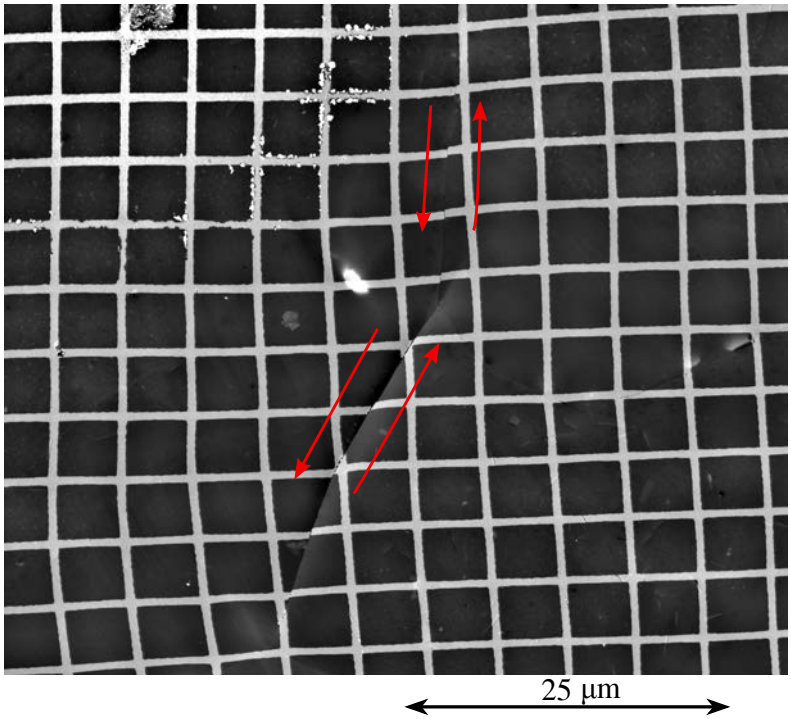

Figure 4.53: Grain boundary sliding in CG material strained at 6.5% at $1.5 \times 10^{-5}\ s^{-1}$*, 100°C*

An intercept method was used to obtain the fraction of sliding GBs (Figure 4.54). It was calculated by dividing the number of sliding GBs intercepted by the grid lines by the total number of intercepted GBs. The fraction of sliding GBs observed after 6.4% strain at $1.5 \times 10^{-5}\ s^{-1}$ was 9.5%.

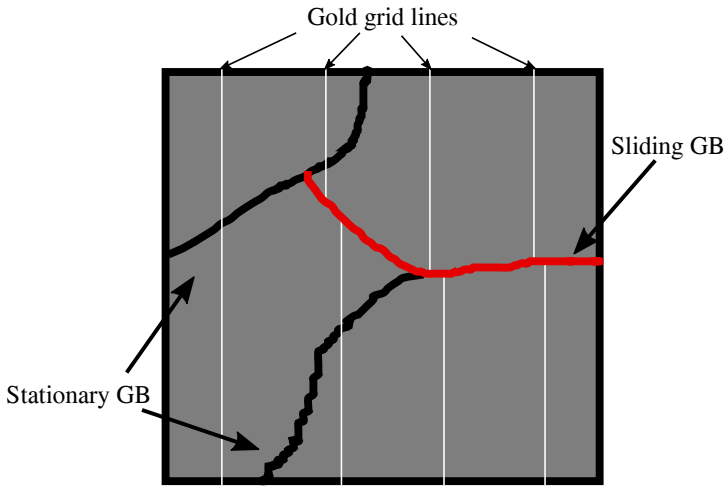

Figure 4.54: Schematic illustrating the intercept method used to calculate the fraction of sliding GBs

Figure 4.55 presents the post-fracture meso-scale axial strain field for CG material tested at $1.5 \times 10^{-5}\ s^{-1}$ superimposed with the contours of the grains, obtained by EBSD. The mean local plastic strain was approximately 6.5% with 70-180 μm long

localization bands, often along grain boundaries near which lattice rotation is visible, or which exhibit sliding.

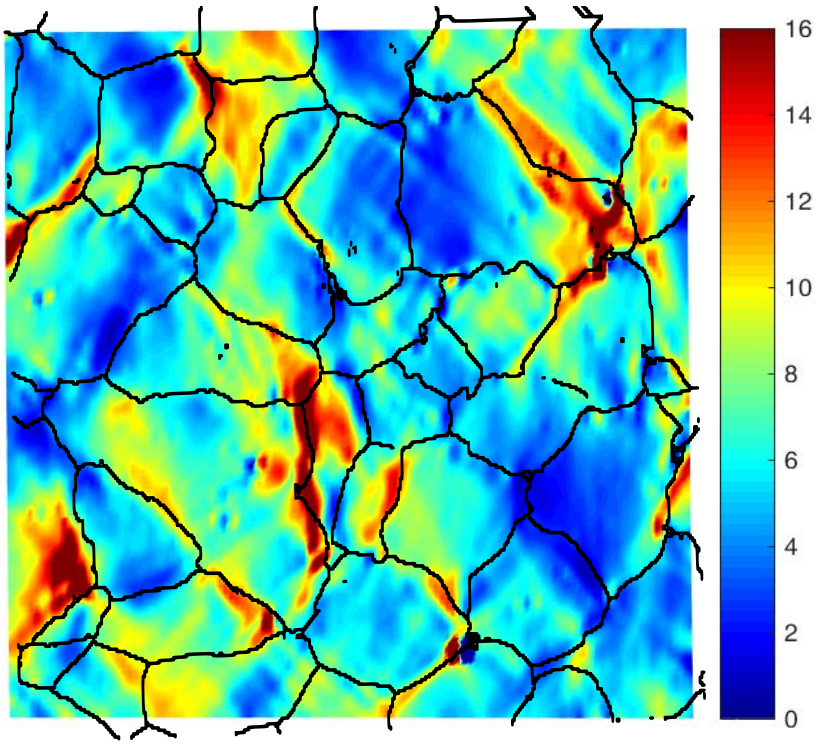

Figure 4.55: Meso-scale strain fields for CG material deformed by 6.5% at $1.5 \times 10^{-5}\ s^{-1}$*, 100°C*

The histogram of the normalised plastic strain field is compared with that of the total strain field obtained at ∼7% strain at RT in figure 4.56. The histogram is wider at 100°C with a standard deviation of 0.49 is higher as compared to 0.43 at RT. In spite of higher SRS, the strain field is less homogeneous than at RT. This might be due to a lower hardening rate.

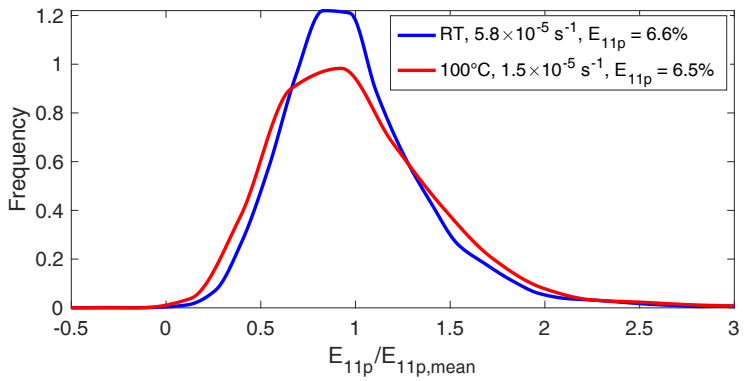

Figure 4.56: Histogram of normalised strain fields for CG material at RT and 100°C

SE and BSE SEM images of the fracture surface are presented in figure 4.57. The

fracture is mostly intergranular with broken particles however their density is less than that at RT, partly because of lower fracture strain. Some smooth and slanted surfaces are also observed suggesting grain boundary sliding.

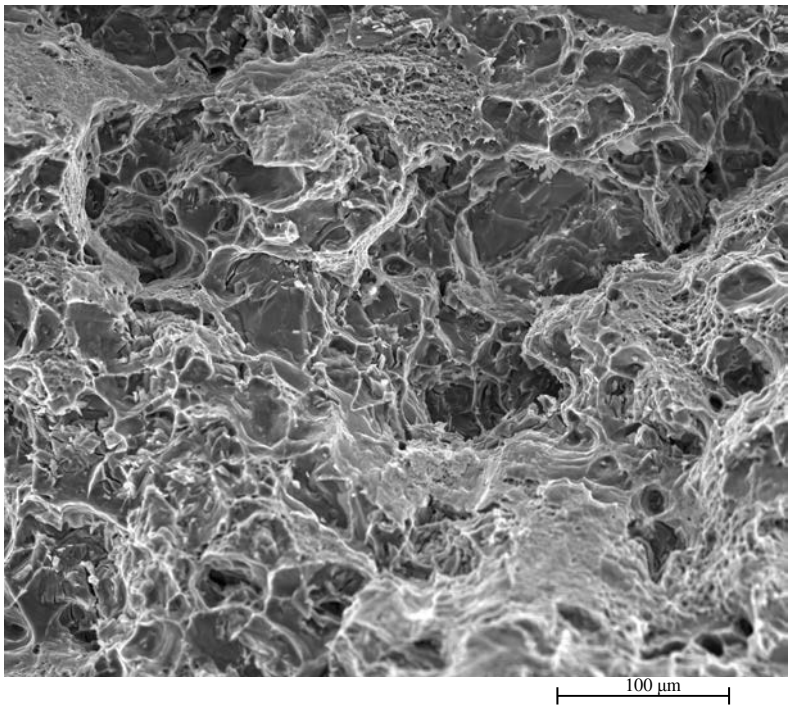

(a) SE image of the fracture surface

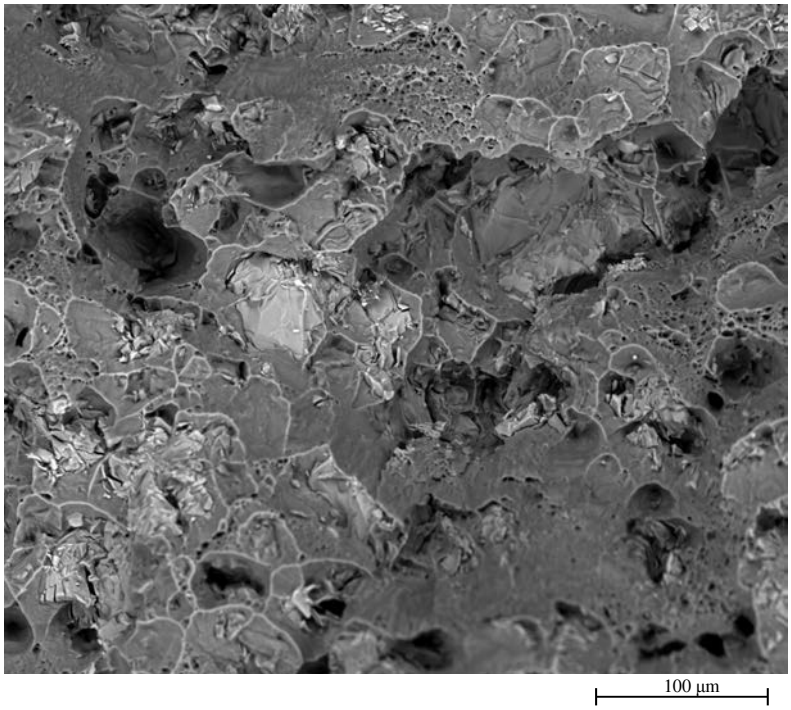

(b) BSE image of the fracture surface

Figure 4.57: Fracture surface of the CG material tested at 100° C at $1.5 \times 10^{-5}\ s^{-1}$ *and broken at 6.4% strain.*

UFG-A material at 100°C

Tensile tests for UFG material were performed at 2 strain rates: $1.8 \times 10^{-5}\ s^{-1}$ and $3.0 \times 10^{-6}\ s^{-1}$. Figure 4.58 presents the BSE images of the deformed grids after fracture at 12.9 and 22.7% strain, respectively. Both the surfaces are covered with shear bands up to 500 μm long. The shear bands were triggered by stress localisation due to particle cracking (Figure 4.59) and were more intense and longer at $3.0 \times 10^{-6}\ s^{-1}$. Such a mixed mode crack would induce non-coplaner shear bands in an isotropic material. In UFG material, it is however aligned with the crack and the shearing direction of ECAP. Figure 4.60 shows one of the thick shear bands observed at $3.0 \times 10^{-6}\ s^{-1}$. Its average thickness is approximately 13 μm which is 20 times the mean grain diameter. Although not in all cases, shear banding was accompanied by grain boundary sliding extending over 200 μm which can be detected by hatched grids, as shown in figure 4.61. This indicates towards cooperative nature of grain boundary sliding of preferentially aligned grains. Grain boundary sliding was easily detectable owing to its increased intensity (up to 0.4 μm shift in the grids) and frequency at $3.0 \times 10^{-6}\ s^{-1}$ than at the higher strain rate.

An estimate of the contribution of GBS to the global or local strain was obtained using equation 1.10 provided in the literature survey. Several transverse lines were chosen randomly from the deformed grids and all their horizontal offsets were measured, assuming that all discontinuities correspond to a sliding grain boundary. Since the orientation of each sliding GB is unknown, a common angle of 55°, representative of the orientation of the grain boundaries in the undeformed material is taken for the calculation. The measurement of the horizontal offsets is limited by the size of 1 pixel which is approximately 183 nm for a field of 600×600 μm^2 and goes down to approximately 5 nm for zoomed images. From figure 4.58a and b, the percentage contribution of GBS to their respective local plastic strain hence calculated was 9% for $1.8 \times 10^{-5}\ s^{-1}$ and 13% for $3.0 \times 10^{-6}\ s^{-1}$. Similar calculation was done on the regions highlighted by a red square on figure 4.59 and the local contribution of GBS reached 74% at $1.8 \times 10^{-5}\ s^{-1}$ and 81% at $3.0 \times 10^{-6}\ s^{-1}$.

Two types of microcracks can be observed: short ones, more or less normal to the tensile axis, in isolated bulky second phase particles, and longer ones along the elongated rows of particles that follow their interface with the matrix and are parallel to the shear bands.

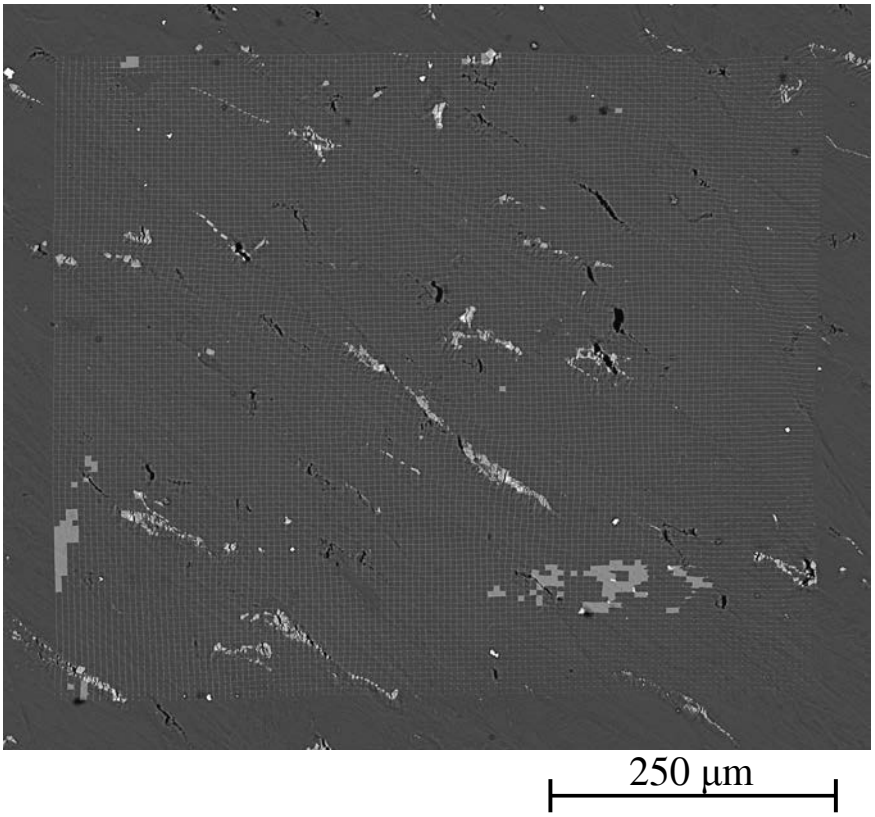

(a) Strain rate: $1.8 \times 10^{-5}\ s^{-1}$*, fracture strain: 12.9%*

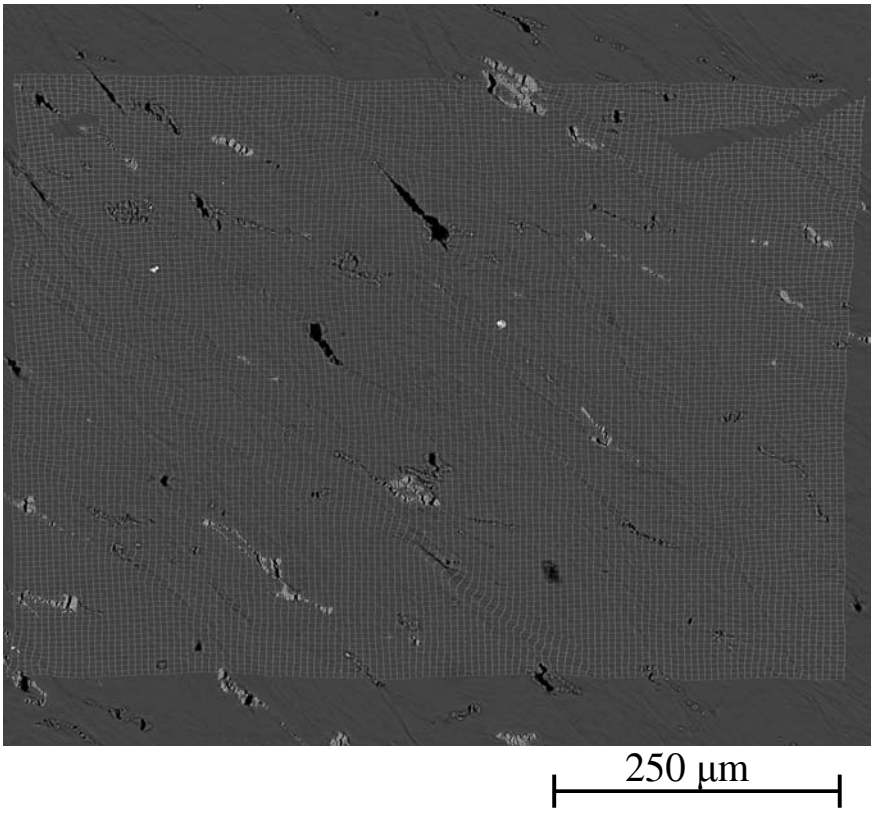

(b) Strain rate: $3.0 \times 10^{-6}\ s^{-1}$*, fracture strain: 22.7%*

Figure 4.58: Post-fracture BSE images of the deformed grids in UFG samples deformed at 100° C

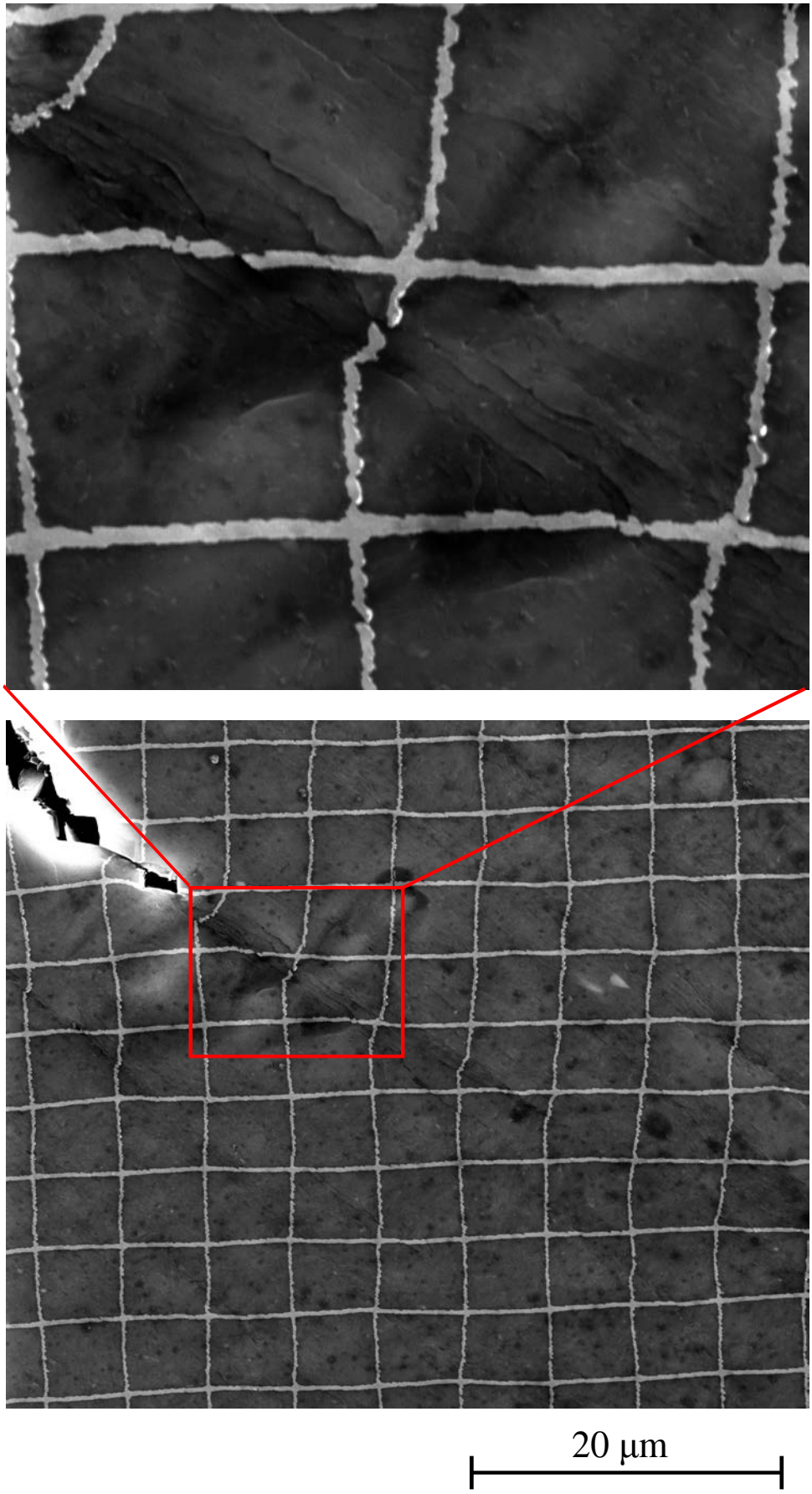

(a) Strain rate: $1.8 \times 10^{-5}\ s^{-1}$*, fracture strain: 12.9%*

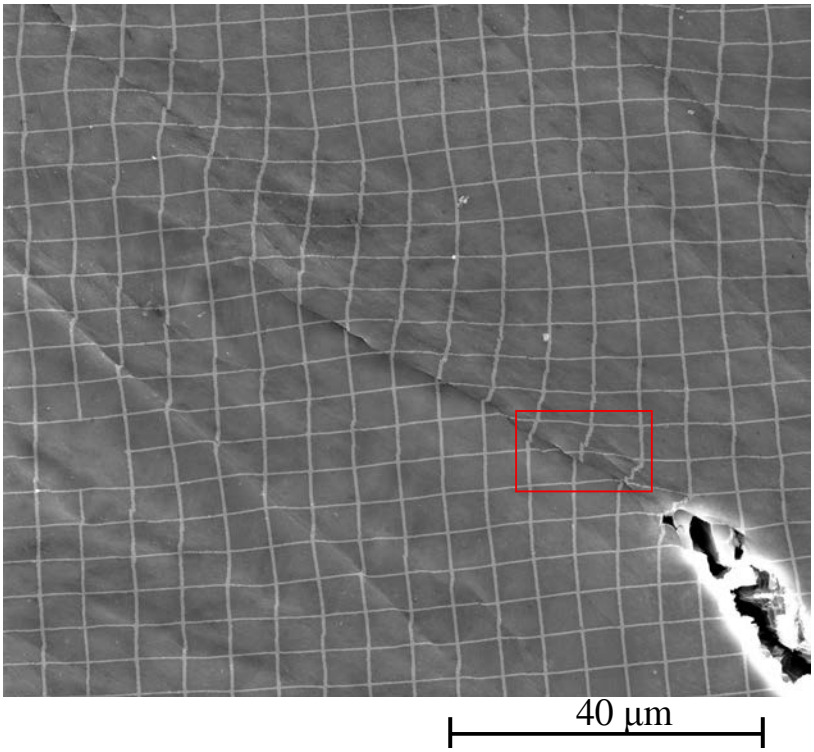

(b) Strain rate: $3.0 \times 10^{-6}\ s^{-1}$*, fracture strain: 22.7%*

Figure 4.59: Meso-scale shear bands triggered by particle cracking in UFG material at 100° C

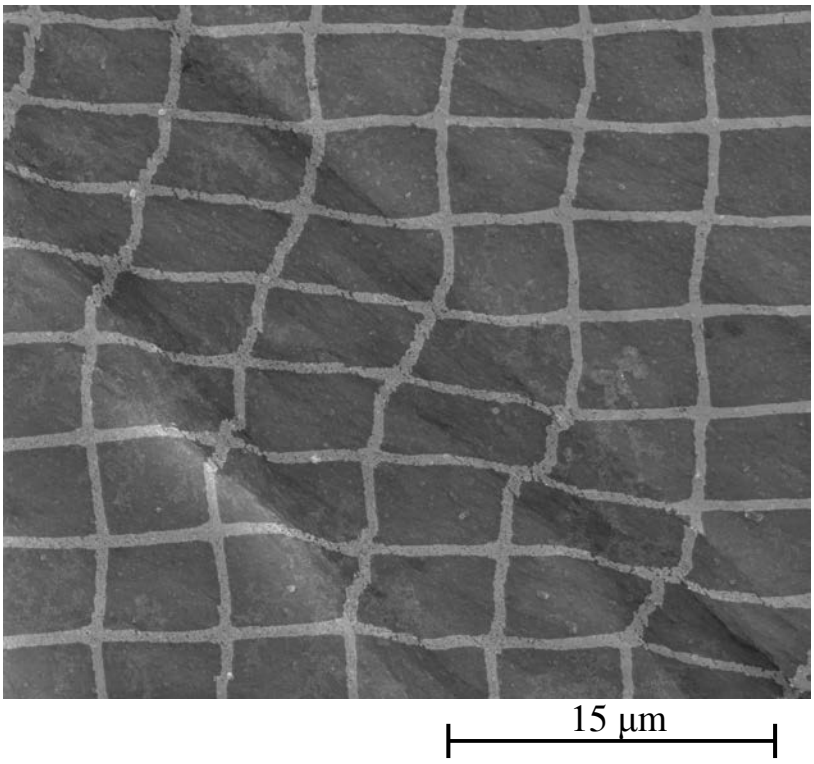

Figure 4.60: Thick meso-scale shear band at $3 \times 10^{-6}\ s^{-1}$ *in UFG material deformed by 22.7% at 100° C*

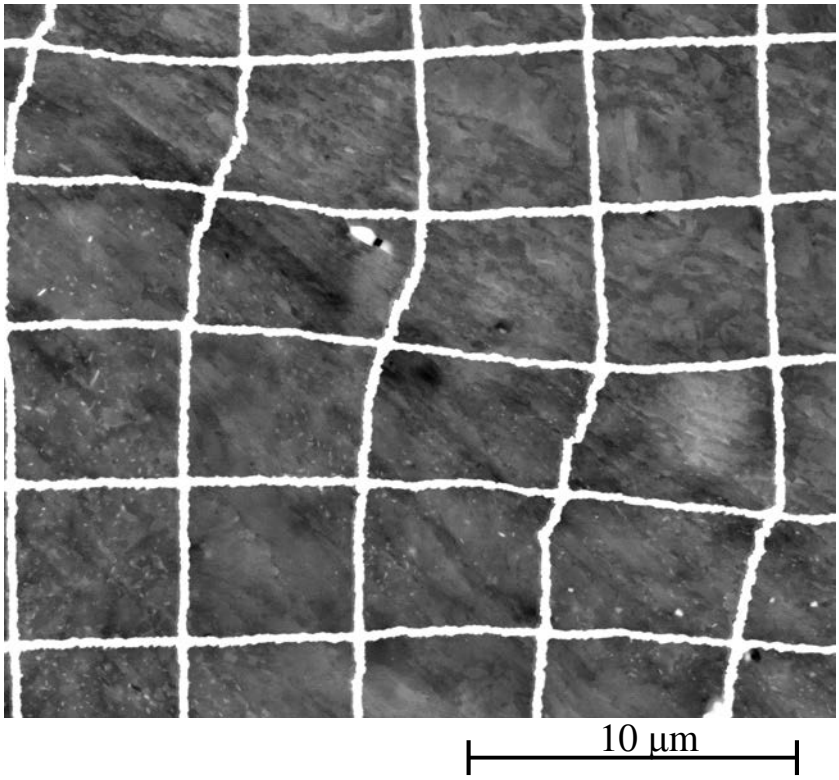

(a) Strain rate: $1.8 \times 10^{-5}\ s^{-1}$*, fracture strain: 12.9%*

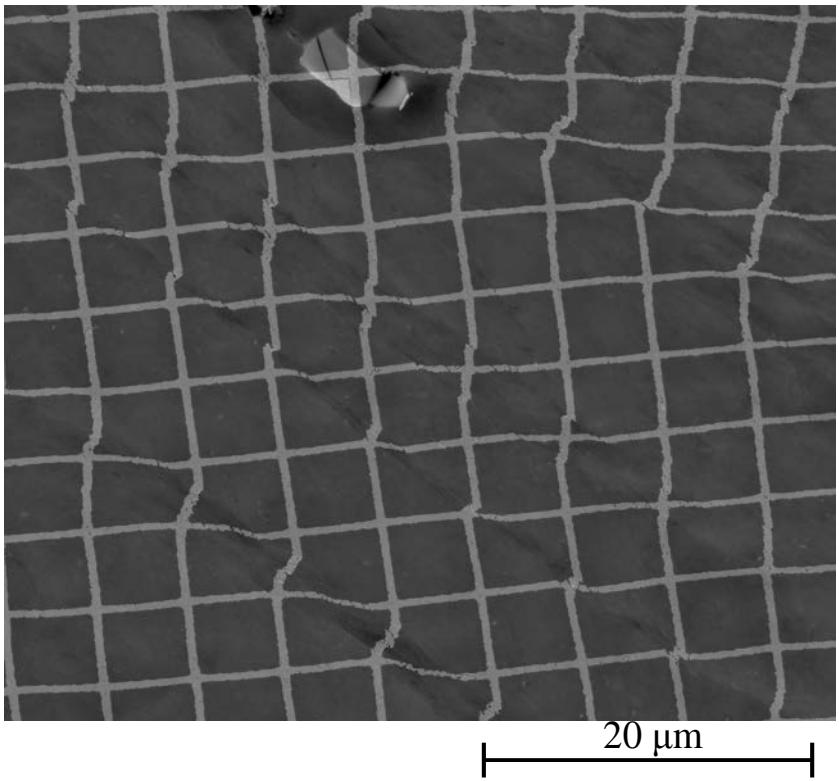

(b) Strain rate: $3.0 \times 10^{-6}\ s^{-1}$*, fracture strain: 22.7%*

Figure 4.61: Hatched grids indicating GBS in UFG material at 100° C

Figures 4.62 and 4.63 present the axial strain maps for UFG material tested at 100°C. Strain fields are heterogeneous.

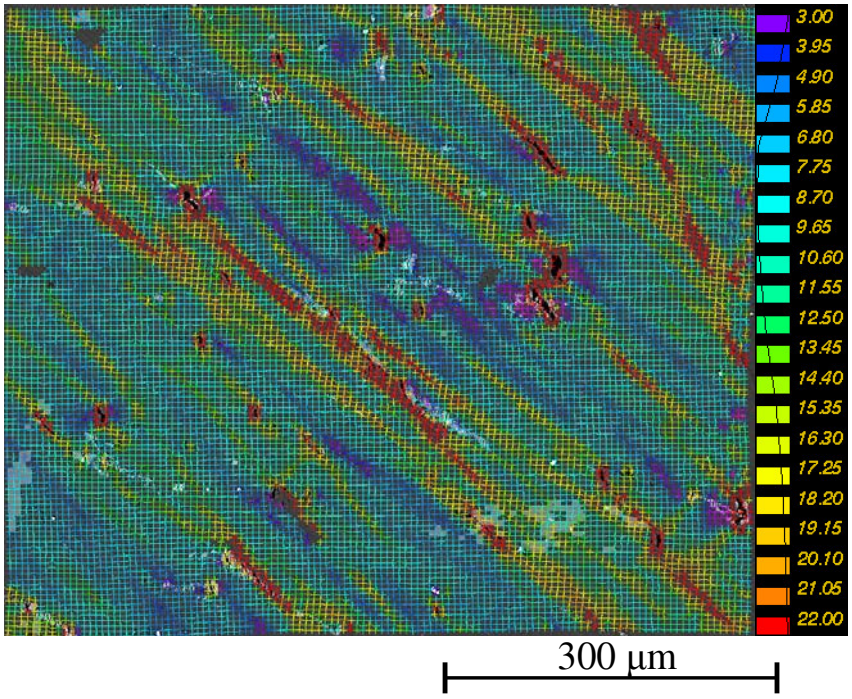

Figure 4.62: Axial plastic strain map of UFG material after 12.9% strain at $1.8 \times 10^{-5}\ s^{-1}$*, 100°C*

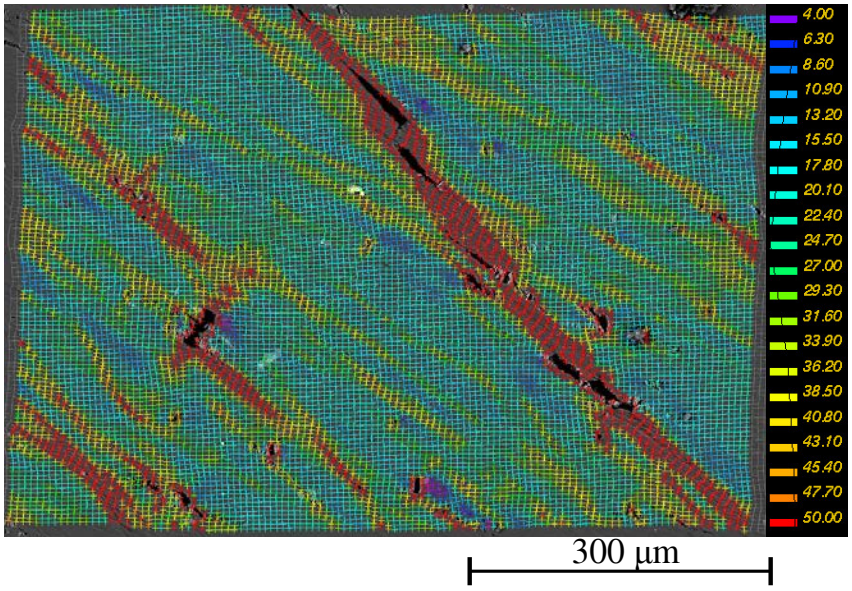

Figure 4.63: Axial plastic strain map of the UFG material after 22.7% strain at $3 \times 10^{-6}\ s^{-1}$*, 100°C*

At $3.0 \times 10^{-6}\ s^{-1}$, shear bands can be classified in two categories, high and low strain bands, depending upon their orientations and the accommodated strain. The high

strain bands, with orientations in the range of 34-54°, accommodated >70% strain and followed the elongation axis of the grains and broken particles. The low strain bands, with orientations in the range of 27-35°, accommodated up to 40% strain and no visible presence of particles was detected near these bands. These low angle bands are more frequent with increase in temperature and decrease in strain rate. Their length is 8 times larger than that at RT for a comparable strain rate. The axial strain inside the shear bands reaches 50% (with damage above 30%).

A sharp increase in these values is observed with an increase in fracture strain from 12.9 to 22.7% with a decrease in strain rate from $1.8 \times 10^{-5}\ s^{-1}$ to $3.0 \times 10^{-6}\ s^{-1}$. The axial strain accommodated inside the bands reaches 400 % (with damage above 100 % strain).

The histograms of the normalised strain fields are plotted in figure 4.64. At $3 \times 10^{-6}\ s^{-1}$, in spite of higher SRS, the standard deviation of the plastic strain distribution for a fracture strain of 22.7% was 1.07, which is twice that at 12.9% strain at $1.8 \times 10^{-5}\ s^{-1}$. This unexpected result might be due to the much higher strain level and to the presence of some damage, which induces "pseudo-deformation" in some bands. Because DIC was performed after fracture, a comparison at the same strain level was not possible.

The standard deviation for UFG material at 100°C is higher than that of CG material at the same temperature at similar strain rate, $1.5 \times 10^{-5}\ s^{-1}$ (= 0.49). It is also higher than UFG material at RT (= 0.45 after 5.9% strain at 5.8×10^{-5} and 0.39 after 7.8% strain at $5.8 \times 10^{-4}\ s^{-1}$). Again, this is contrary to what would be expected based only on the SRS (which rises with temperature), but it might be due to a lower strain hardening rate and a substantially larger strain level and maybe also due to "pseudo strains" induced by GBS.

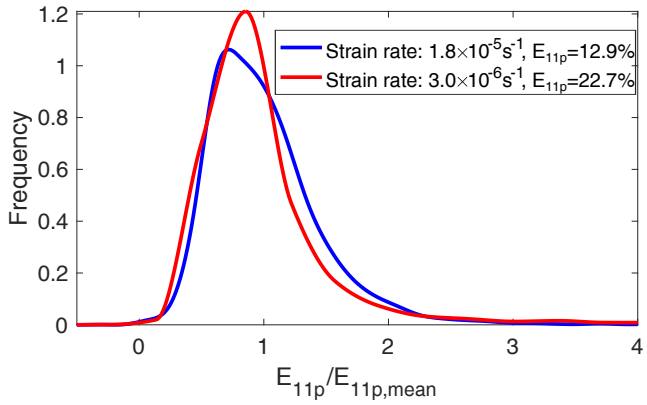

Figure 4.64: Histogram of the normalised plastic strain fields for UFG material at 100° C

Figures 4.65 and 4.66 present the SE and BSE images of the fracture surfaces of the UFG samples broken at 1.8×10^{-5} and $3.0 \times 10^{-6}\ s^{-1}$ respectively. At both rates, the fracture surface is full of broken particles. Some transgranular ligaments containing

ductile dimples can be observed at $1.8 \times 10^{-5}\ s^{-1}$. However, their presence is considerably reduced as compared to RT. Such ligaments are less visible at $3.0 \times 10^{-6}\ s^{-1}$, instead some incidences of tube-like smooth features indicative of GBS were observed.

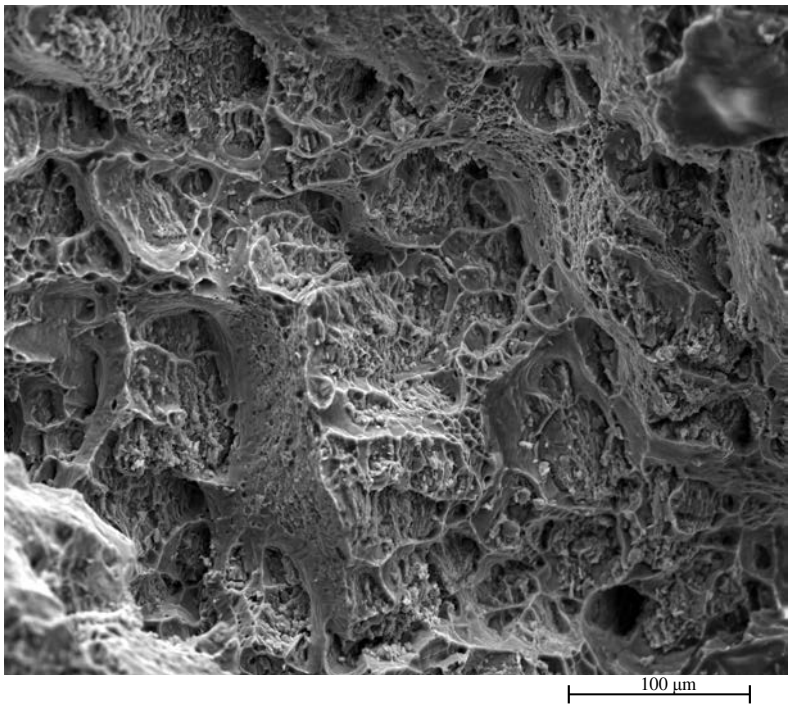

(a) SE image of the fracture surface

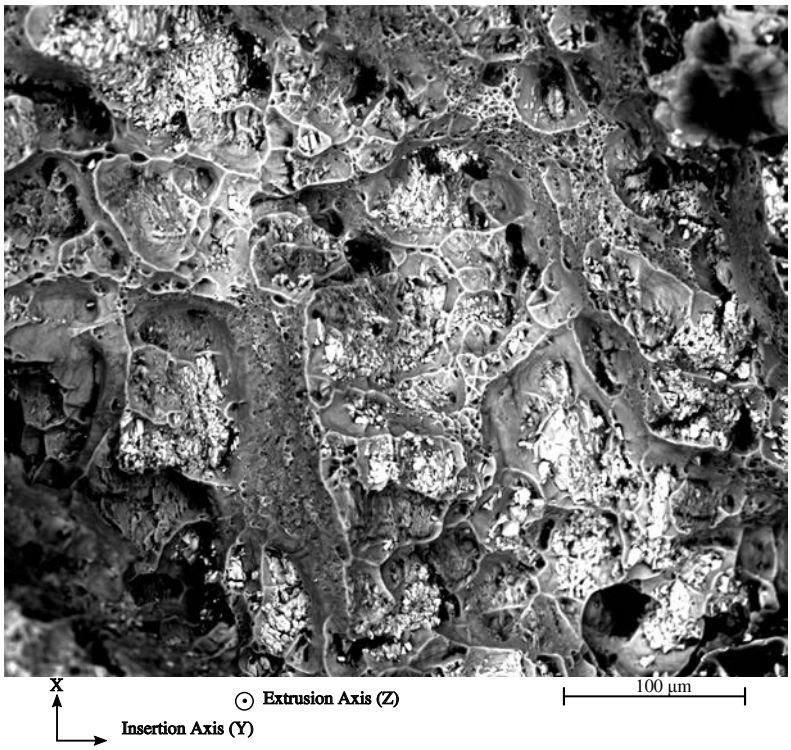

(b) BSE image of the fracture surface

Figure 4.65: Fracture surface of the UFG material after 12.9% strain at $1.8 \times 10^{-5}\ s^{-1}$, 100°C.

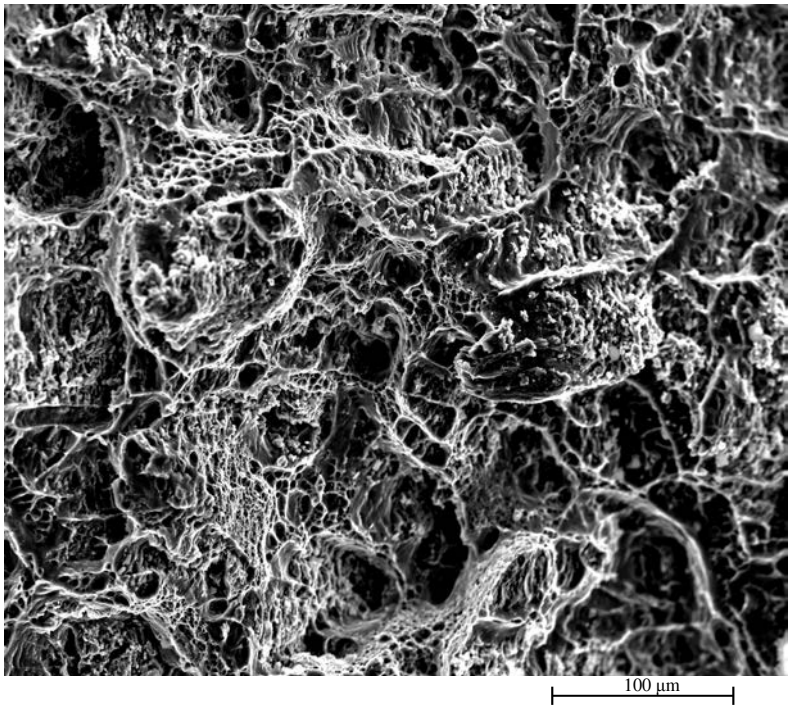

(a) SE image of the fracture surface

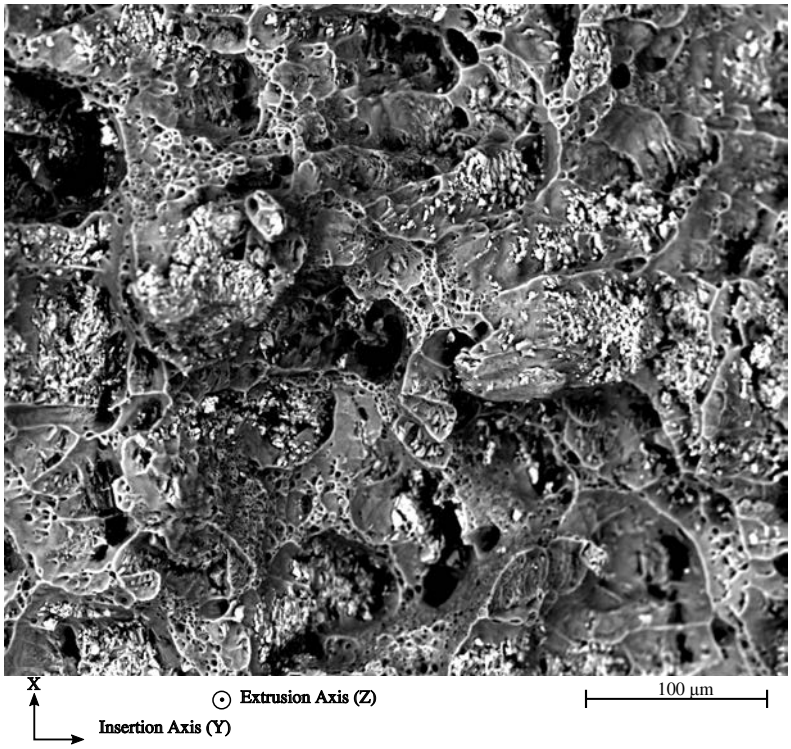

(b) BSE image of the fracture surface

Figure 4.66: Fracture surface of the UFG material tested at $3 \times 10^{-6}\ s^{-1}$, 100° C and broken at 22.7% strain.

UFG-A material at 150°C

No observations are available for CG material but only for UFG material at 150°C. Figure 4.67 shows the BSE image of the UFG material deformed by 27.5% at 1.6×10^{-5} s^{-1}. Meso-scale bands were observed all over the deformed surface with band angles in the range of 30-50° and an average length of 150 μm which is equivalent to 176 times the mean grain diameter. Some very sharp and wide shear bands were observed at this temperature. These shear bands are mostly accompanied by grain boundary sliding. The average width of the sharp shear band of 9.4 μm length shown in figure 4.68 is 1200 nm ($\sim$2 times the mean grain diameter) and indicates cooperative grain boundary sliding in approximately 14 grains along the band. Discontinuities in the grids are more evident as compared to the UFG specimen tested the same rate at 100°C. The grid discontinuities in figure 4.69 are marked with white dotted lines. Such discontinuities are visible along the bands over 26 and 46 μm corresponding to GBS in approximately 40 and 71 grains, respectively. As seen from the zoom on a sharp shear band in figure 4.69, grains were observed to slide in a step-like manner.

The percentage contribution of GBS to local plastic strain was calculated on the deformed grids of 600*600 μm^2 area (image not shown here) and also on a zoomed image to measure the local contribution. The contribution of GBS increased to 22% as compared to 13% at 100°C for a similar strain rate. The local contribution of GBS measured on figure 4.68 reached 58%.

Several micro-cracks were observed on the deformed surface. Most of them were due to strain localisation near cracked particles. Figure 4.70 shows the BSE image of a large crack formed due coalescence of multiple micro-scale cracks at the particles.

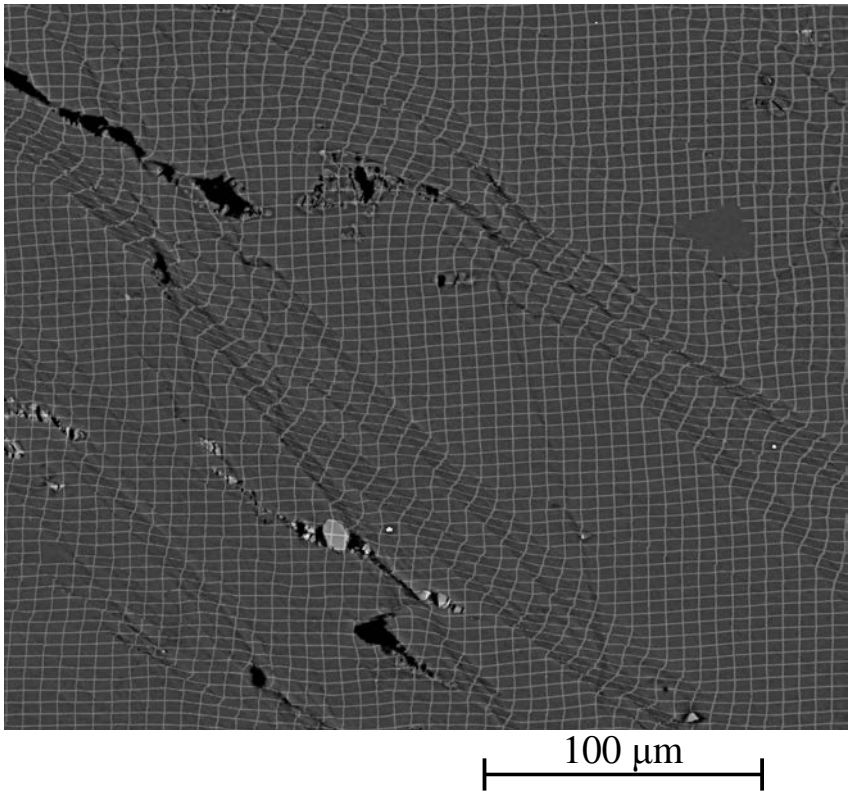

Figure 4.67: BSE image of the shear bands for UFG material strained by 27.5% at 1.6×10^{-5} s^{-1}*, 150° C*

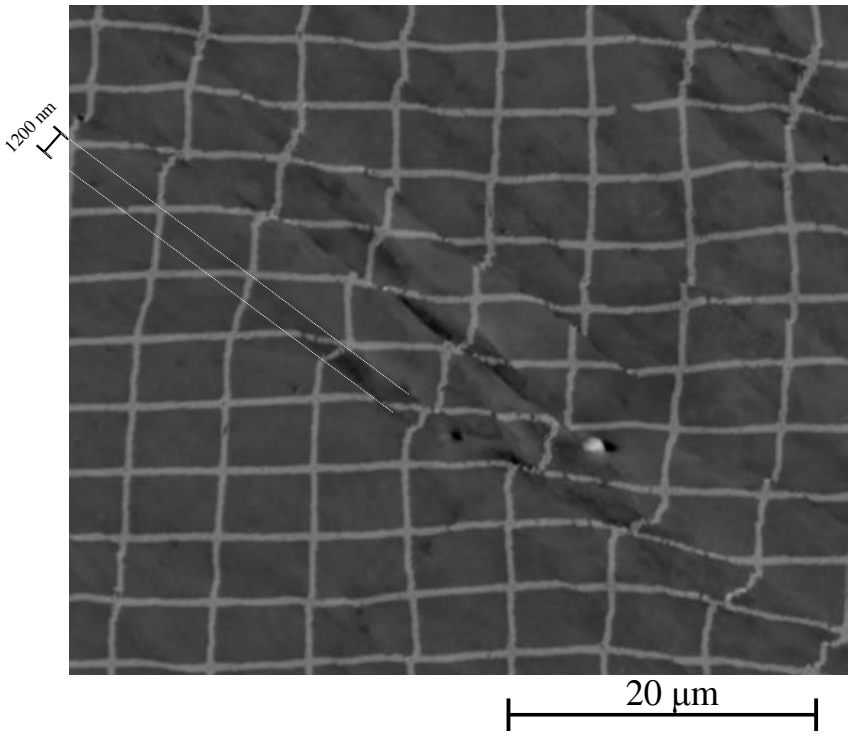

Figure 4.68: BSE image of the shear bands for UFG material strained by 27.5% at 1.6×10^{-5} s^{-1}*, 150° C*

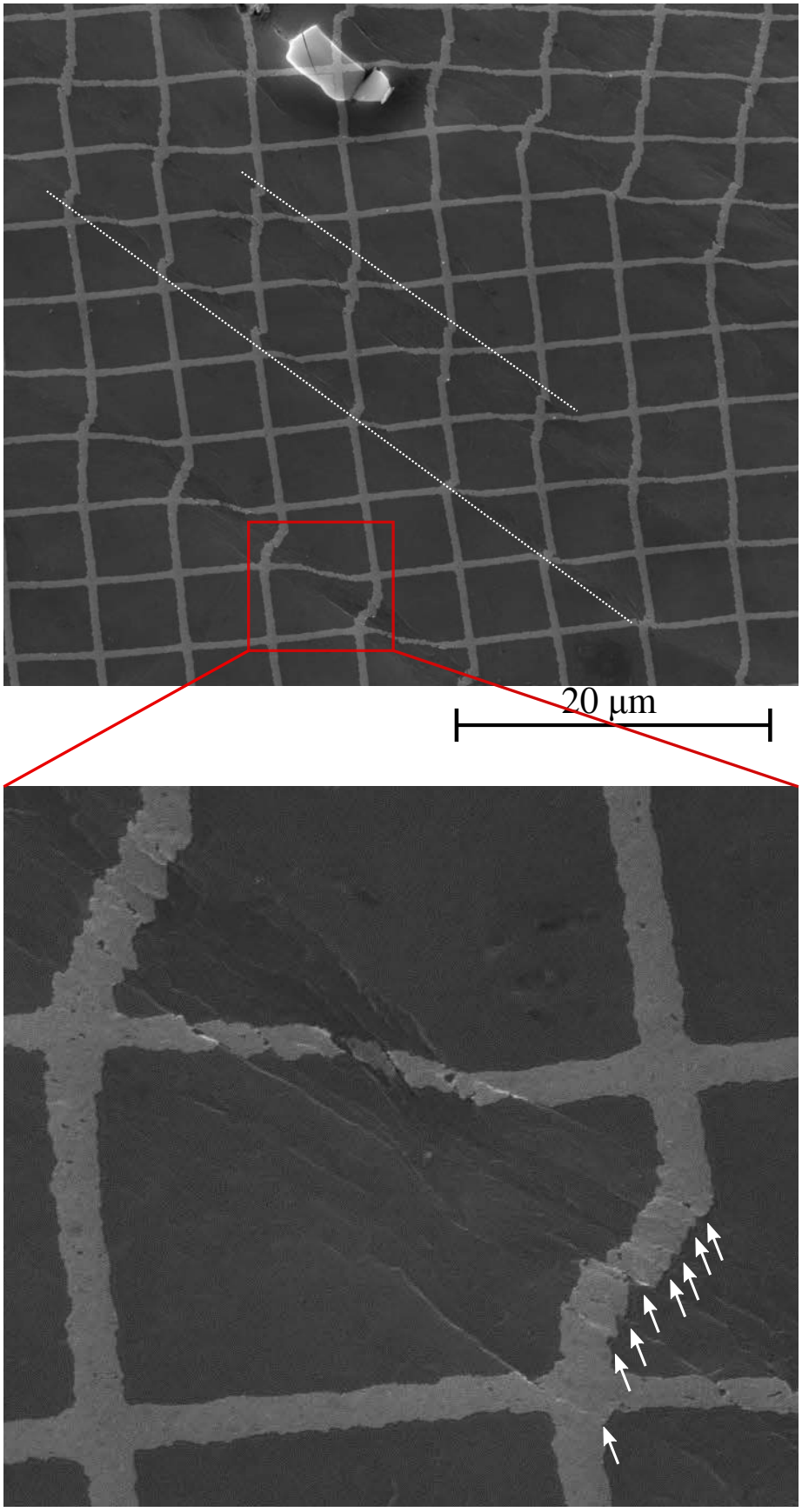

Figure 4.69: BSE image of the hatched grids due to GBS for UFG material strained by 27.5% at $1.6 \times 10^{-5}\ s^{-1}$*, 150°C*

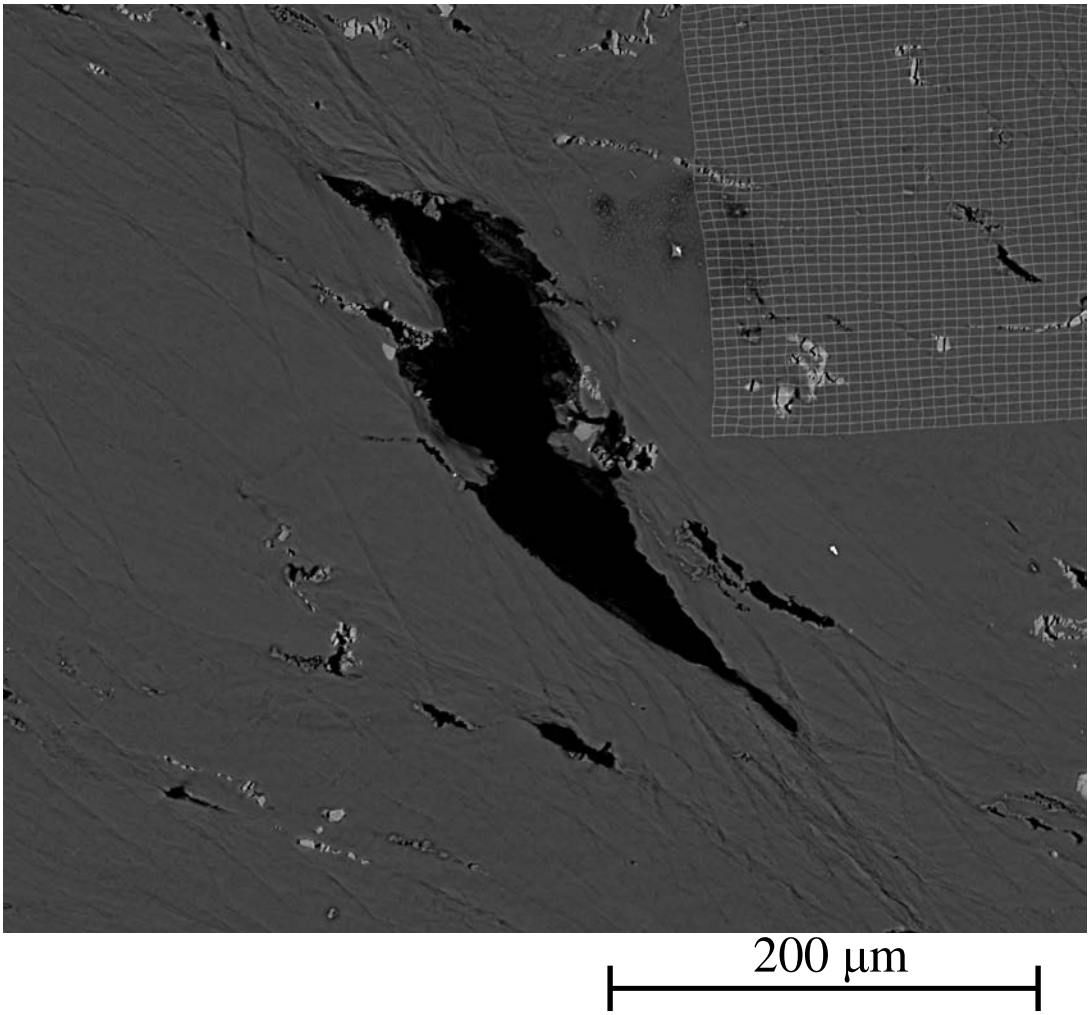

Figure 4.70: BSE image of a microcrack in UFG material strained by 27.5% at $1.6 \times 10^{-5}\ s^{-1}$*, 150°C*

CG-A material (tension and creep) at 200°C

At 200°C, tensile tests were done on flat samples of CG material at two different rates, $1.8 \times 10^{-3}\ s^{-1}$ and $4.1 \times 10^{-3}\ s^{-1}$ which led to fracture after 20.9 and 12.1% strain, respectively (see figure 3.18 in the previous chapter). Figure 4.71 presents the BSE images of the deformed specimens. The most common feature is the increased slip activity in the vicinity of grain boundaries accompanied by grain boundary sliding. The slip lines are more visible and intense than at RT and 100°C. Out of approximately 40 grains analysed for each sample, 80 and 72% of the grains showed observable slip lines at 1.8×10^{-3} and $4.1 \times 10^{-3}\ s^{-1}$, respectively. The fraction of broken second phase particle is decreased to approximately 50% out of which many particles do not fracture normal to the tensile axis, but parallel to a sliding GB.

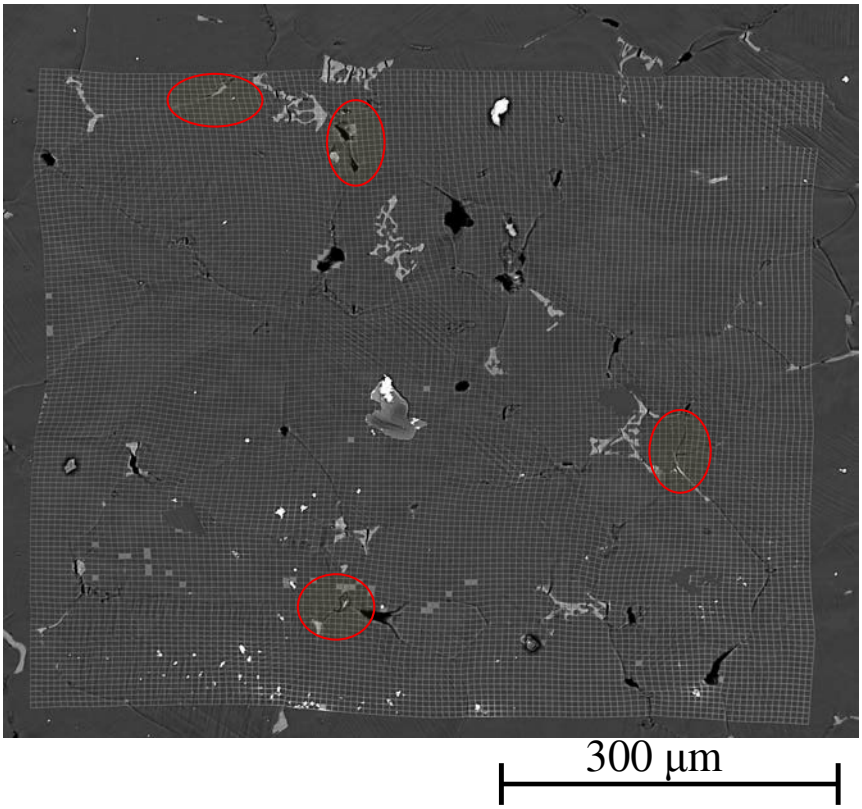

(a) Strain rate: $1.8 \times 10^{-3}\ s^{-1}$*, strain level: 20.9%*

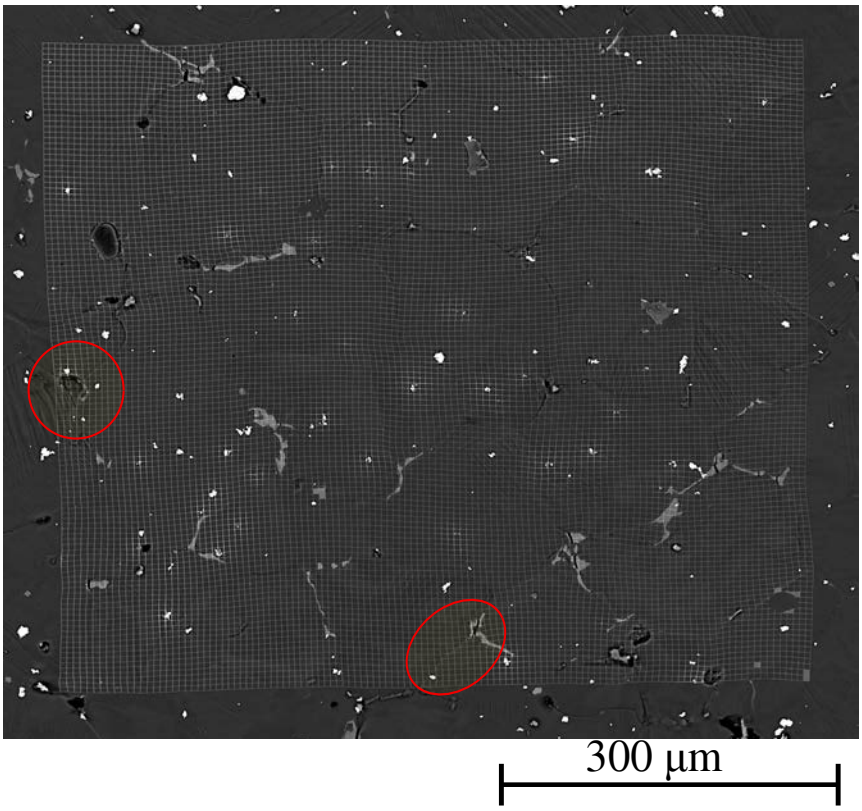

(b) Strain rate: $4.1 \times 10^{-3}\ s^{-1}$*, strain level: 12.1%*

Figure 4.71: BSE image of the CG material deformed at 200° C. Particles broken parallel to a sliding GB are circled in red.

In most cases, slip lines were straight and sharp, with some evidences of cross-slip. Active slip systems were identified for some grains for the test run at $1.8 \times 10^{-3}\ s^{-1}$ using the measured slip trace angles and the euler angles, characteristics of the grain orientation issued from EBSD. In addition to the common {111}<$\bar{1}$10> slip system, the presence of non-octahedral slip lines was detected. Out of 30 grains that showed any kind of slip lines, 17 showed slip activity in {111} plane, 3 in {110} plane, 3 in both {111} and {110} planes, and for the rest, no unambiguous identification was obtained. These non-octahedral slip lines look wavier and thicker than the slip lines along {111} planes (Figures 4.72 and 4.73).

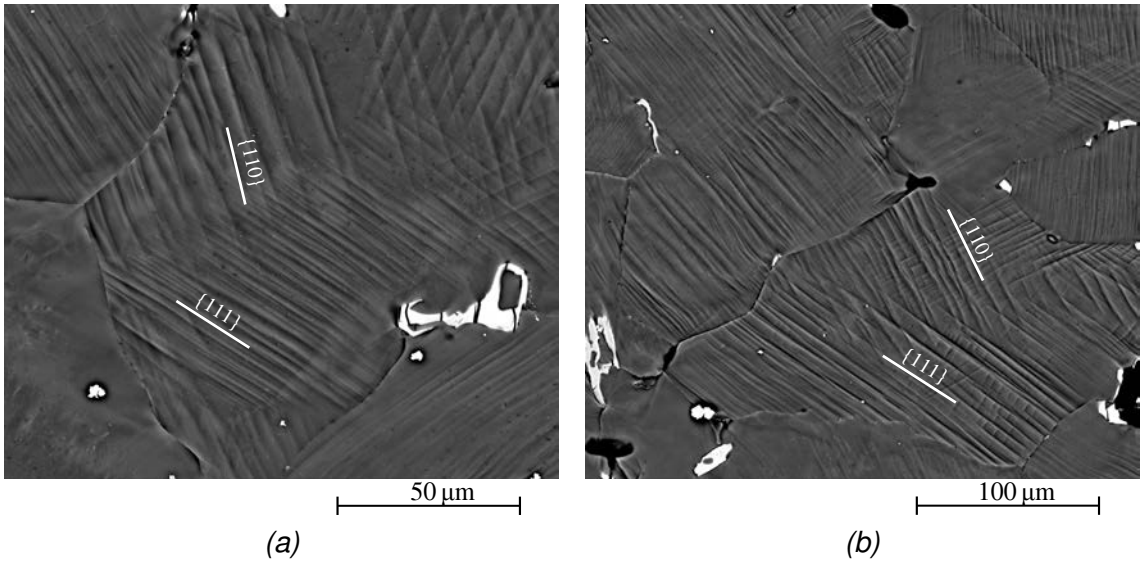

(a) (b)

Figure 4.72: BSE images of the grains showing slip in both {111} and {110} planes simultaneously for CG material strained at $1.8 \times 10^{-3}\ s^{-1}$ *at 200° C*

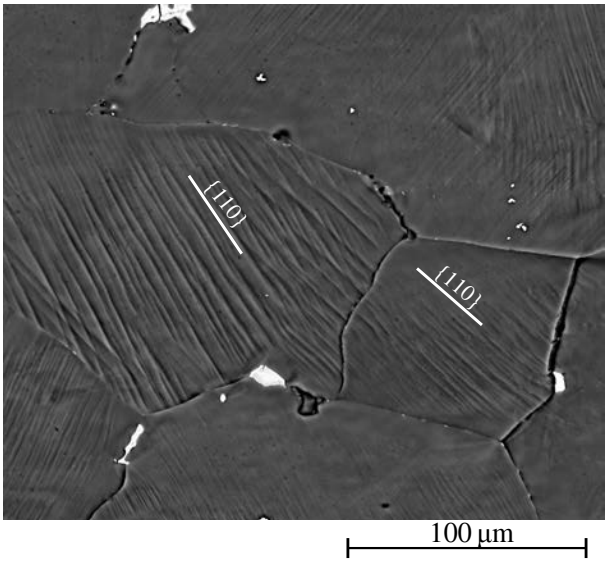

Figure 4.73: BSE image of a two grains showing slip only in {110} plane for CG material strained at $1.8 \times 10^{-3}\ s^{-1}$ *at 200° C*

The evidences of grain boundary sliding, as shown in figure 4.74 by discontinuities in the grids, are more frequent at this temperature than at 100°C and increase with a decrease in strain rate. In plane GBS was also accompanied by some out of plane GBS, as shown in figure 4.75. After 11.6% strain at $4.1 \times 10^{-3}\ s^{-1}$, 44% of the GBs sled and it increased to 68% at 14.0% strain at a lower rate of $1.8 \times 10^{-3}\ s^{-1}$.

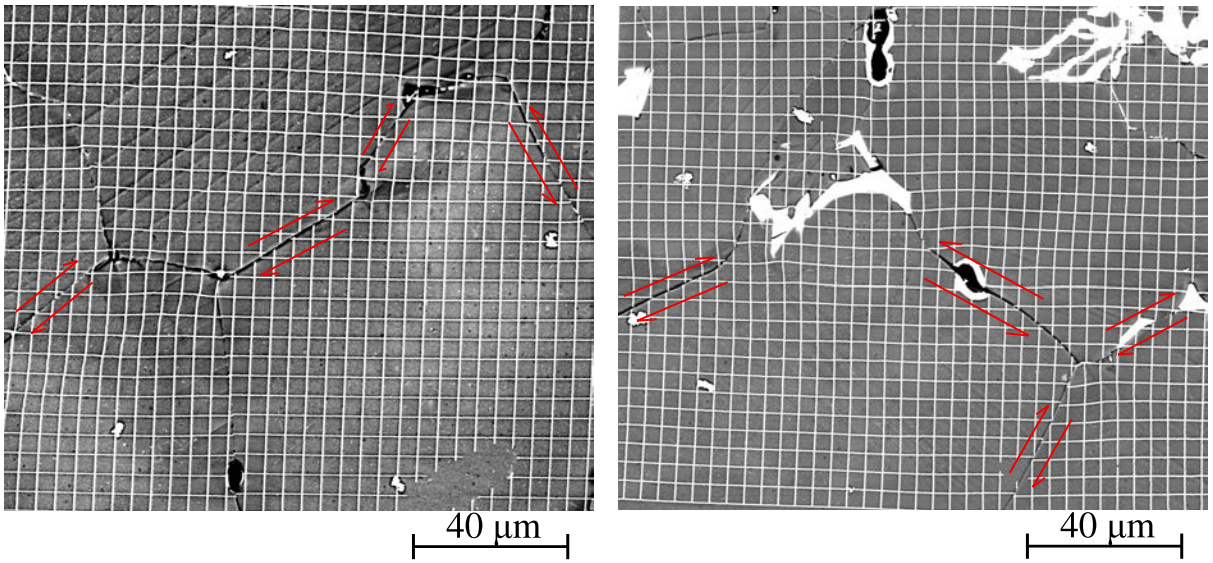

Figure 4.74: Examples of grain boundary sliding after 4.7% creep strain at $7.0 \times 10^{-6}\ s^{-1}$ in CG material at 200° C. The tensile axis is horizontal.

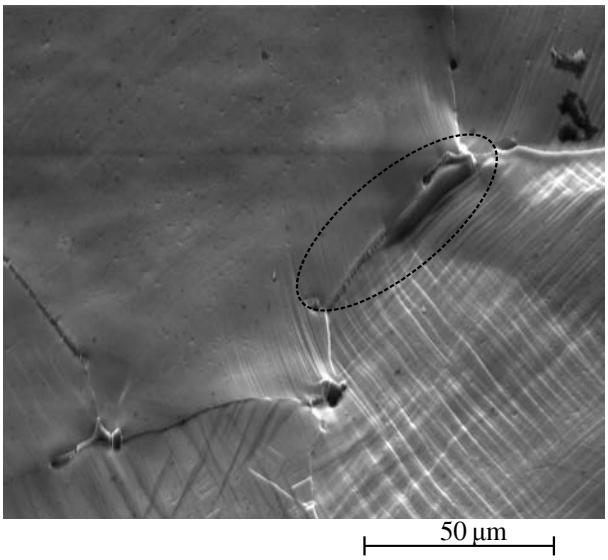

Figure 4.75: BSE image of out-of-plane GBS for CG material strained at $1.8 \times 10^{-3}\ s^{-1}$, 200° C

A creep test at 130 MPa on CG material at 200°C, which gave rise to a creep rate of $7.0 \times 10^{-6}\ s^{-1}$ was interrupted after 5% strain. After only 4.7% plastic strain at such low rate, 55% of the GBs had already sled.

The contribution of GB sliding to the global plastic strain, calculated from the intercept method similar to the one used for UFG material, is 4%. But, an alternative method based on DIC was also used. Figure 4.76 shows the plastic strain map after 4.7% creep strain superimposed with the GB contours. Each grain is identified as an individual phase and the contribution of GBS is calculated by subtracting the weighted sum (in terms of surface fraction) of the plastic strain from all the grains from the global plastic deformation of the correlation area, as shown in equation 4.1.

$$\varepsilon_{GBS} = \varepsilon_p - \sum_{grains} \frac{S_{grain}}{S_{total}} \cdot \varepsilon_p^{grain} \tag{4.1}$$

The contribution of GBS to the total plastic strain was calculated to be 10.3% (2.7 times higher than that calculated from the intercept method), which is quite limited considering the high fraction of sliding GBs.

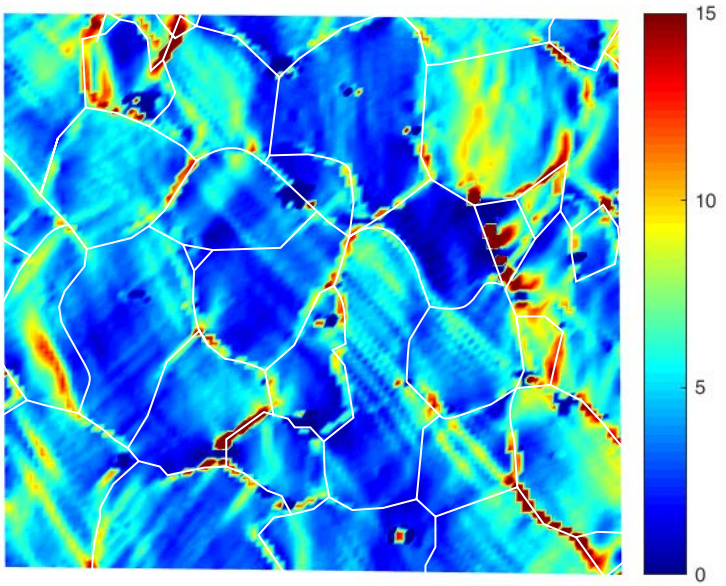

Figure 4.76: Axial plastic strain map after 4.7% creep strain for CG material at 200°C, superimposed with GB contours in white lines.

Figure 4.77 shows the axial strain maps of CG material strained by 14% and 11.6% at $1.8 \times 10^{-3}\ s^{-1}$ and $4.1 \times 10^{-3}\ s^{-1}$, respectively. Very few particles were broken during the test and thus it is not the main source of localisation. Strain tends to localize more along the sliding GBs. Strain localisation bands formed by GBS are more easily visible on the shear strain field map shown in figure 4.78 where bright red and violet regions represent GBS. The plastic strain in the bands induced by particle cracking reaches 150% at $1.8 \times 10^{-3}\ s^{-1}$ as opposed to 60% at $4.1 \times 10^{-3}\ s^{-1}$, while, a maximum of 40% strain was measured along sliding grain boundaries (visible from grid discontinuities at GB) for $1.8 \times 10^{-3}\ s^{-1}$ and 27% for $4.1 \times 10^{-3}\ s^{-1}$.

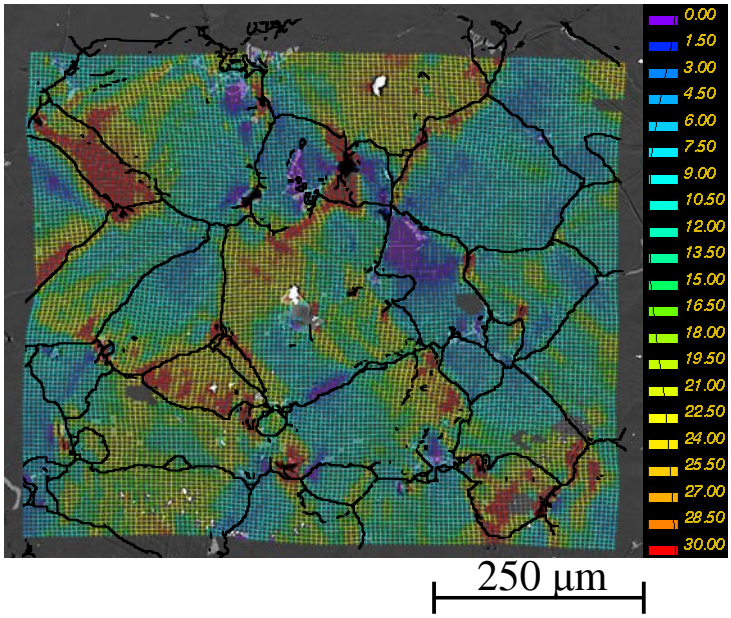

(a) Strain rate: $1.8 \times 10^{-3}\ s^{-1}$*, strain level: 14.0%*

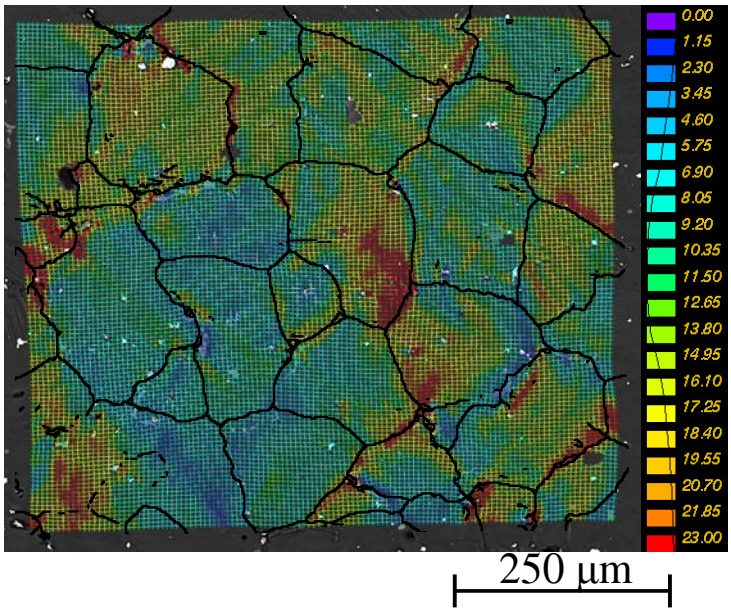

(b) Strain rate: $4.1 \times 10^{-3}\ s^{-1}$*, strain level: 11.6%*

Figure 4.77: Axial plastic strain fields in CG material at 200° C

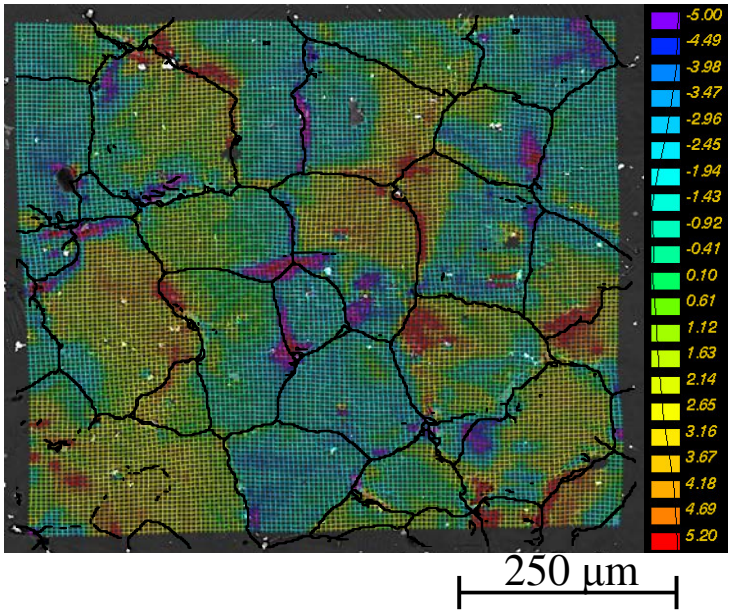

Figure 4.78: Plastic shear strain fields in CG material strained up to 11.6% at $4.1 \times 10^{-3}\ s^{-1}$*, 200°C*

Figure 4.79 compares the histograms of the normalised axial plastic strain fields for CG material for nearly the same strain level of 12% at 200°C and RT. In spite of rising SRS, strain fields are more and more heterogeneous with increasing temperature and decreasing strain rate. Their standard deviation is highest (= 0.65) for $1.8 \times 10^{-3}\ s^{-1}$ at 200°C and decreases to 0.45 for $4.1 \times 10^{-3}\ s^{-1}$ at 200°C which is almost same as that at RT at $5.8 \times 10^{-5}\ s^{-1}$ (= 0.43). This unexpected tendency might partly be due to a decreasing hardening rate with rising temperature (which favours strain localization), but more probably to the fact that GB sliding induces pseudo strains that artificially increase the standard deviation.

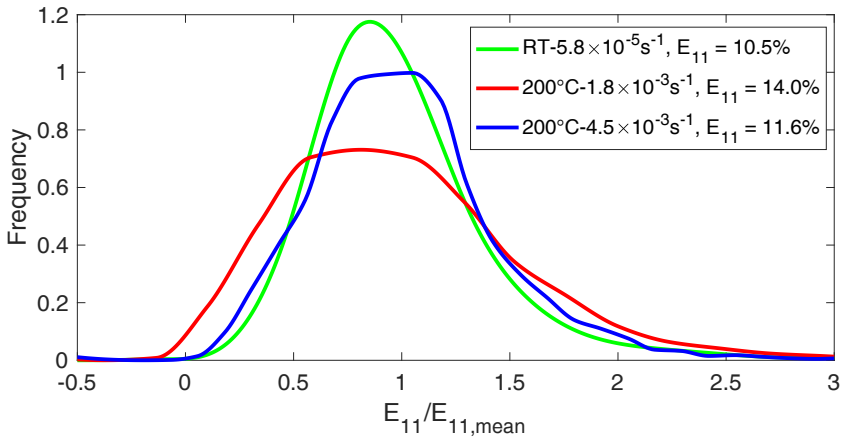

Figure 4.79: Histograms of normalised axial strain for CG material

Figures 4.80 and 4.81 present the fracture surfaces of CG material at 1.8×10^{-3} and $4.1 \times 10^{-3}\ s^{-1}$ respectively. The dimples observed at the lower strain rate are larger, in

accordance with the larger fracture strain (20.9% instead of 12.1%).

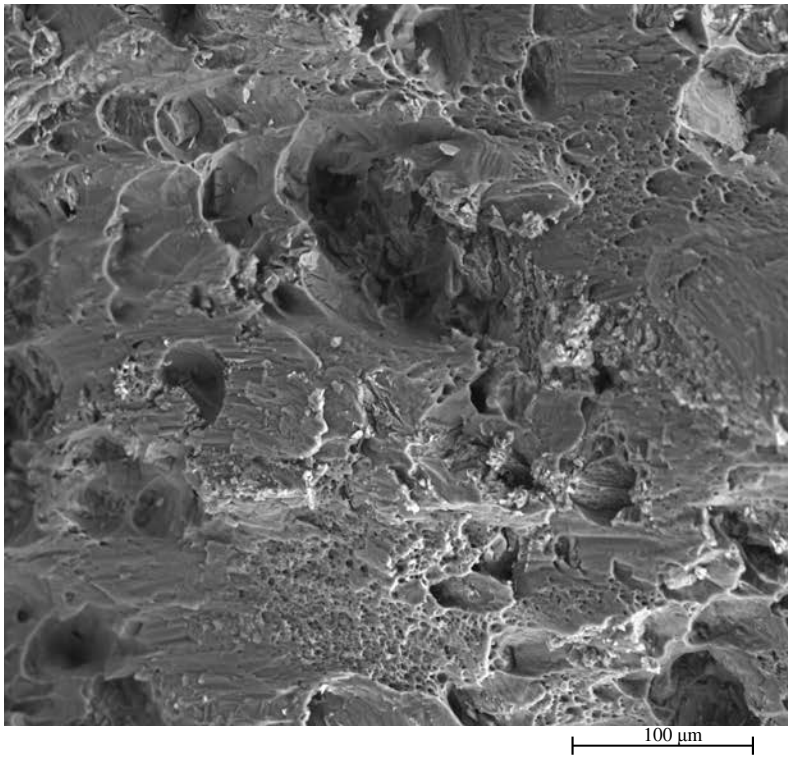

(a) SE image of the fracture surface

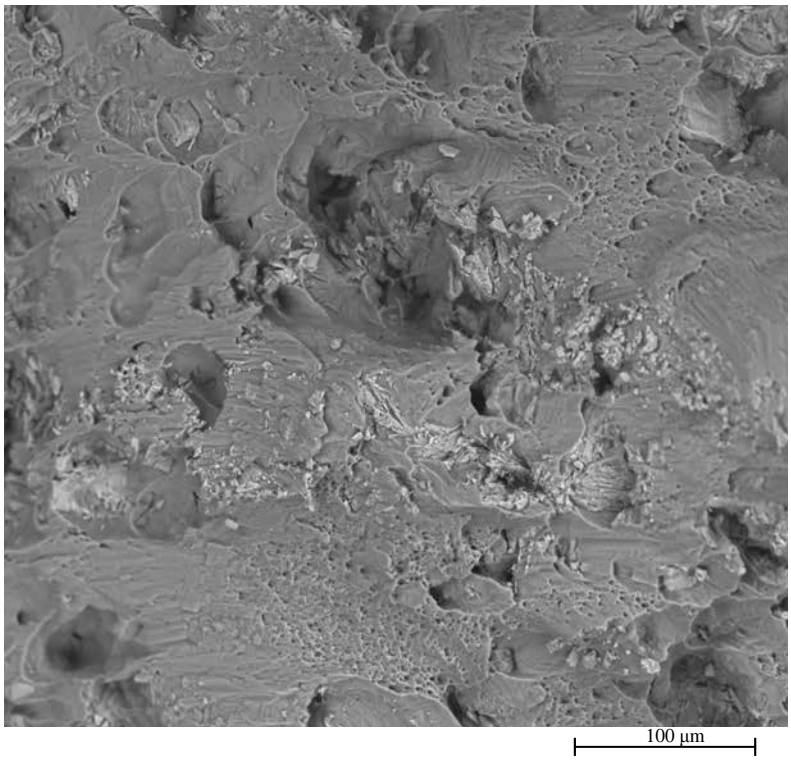

(b) BSE image of the fracture surface

Figure 4.80: Fracture surface of the CG material strained by 20.9% at 200° C at $1.8 \times 10^{-3}\ s^{-1}$

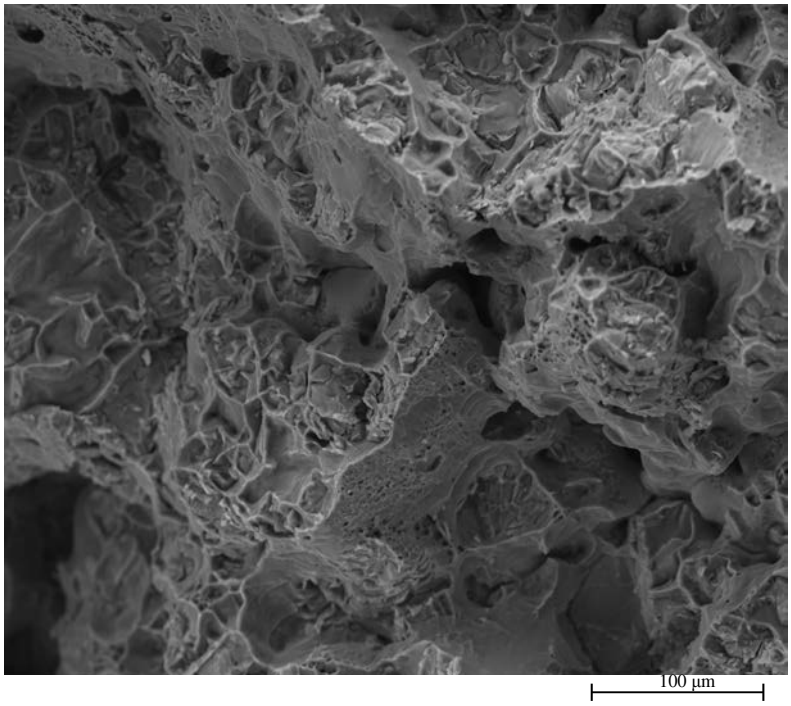

(a) SE image of the fracture surface

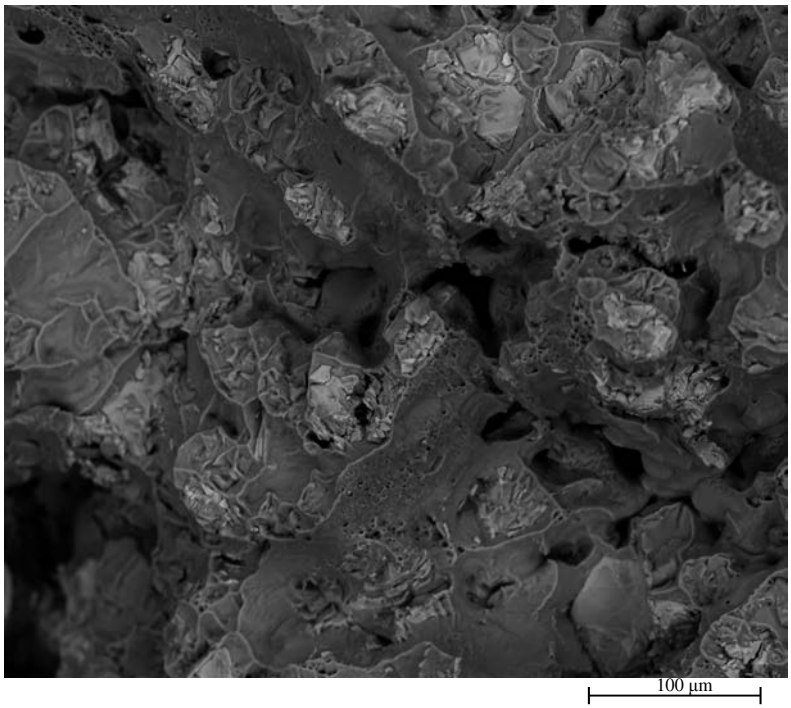

(b) BSE image of the fracture surface

Figure 4.81: Fracture surface of the CG material strained by 12.1% at 200° C at $4.1 \times 10^{-3}\ s^{-1}$

Figure 4.82 shows a zoom on the fracture surface of a CG sample crept under 130MPa at 200°C, with a secondary creep rate $\sim 7 \times 10^{-6}\ s^{-1}$ (fracture, which occurred around 30% strain). Polygonal shapes, and smooth facets, indicative of fracture along grain boundaries can be observed.

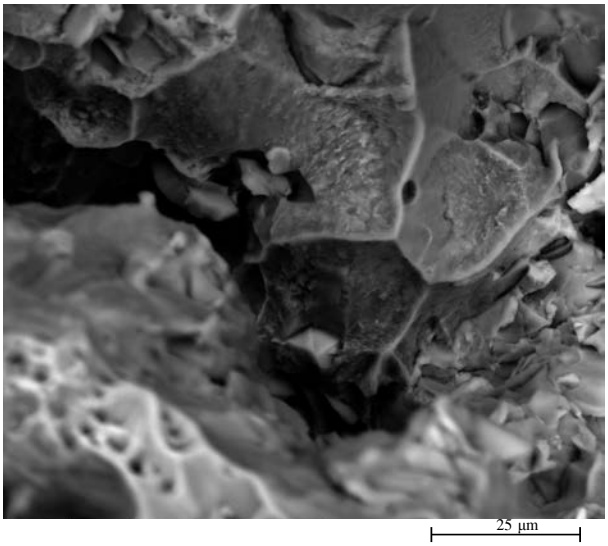

Figure 4.82: BSE image of the fracture surface of CG material crept upto 30% strain under 130 MPa at 200° C

The optical image of a longitudinal section shown on figure 4.83 reveals triangular-shaped cavities at triple points induced by GBS.

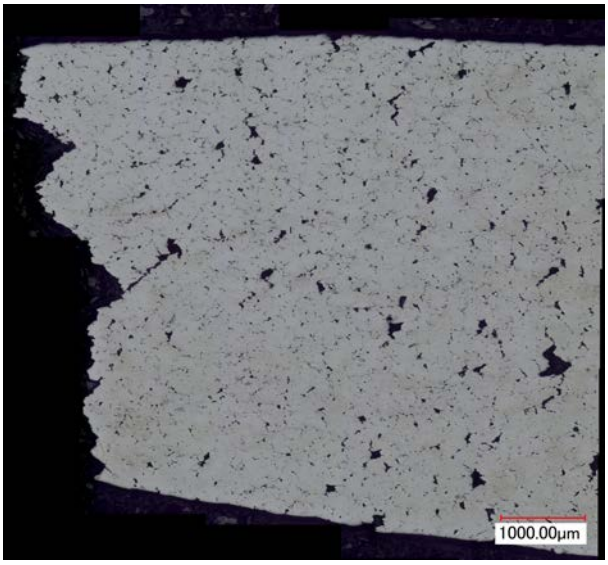

Figure 4.83: Optical image of the longitudinal section of CG sample crept under 130 MPa at 200° C

UFG-A material at 200°C

Similar to the tests done on CG material at 200°C, tensile tests on UFG material was done at two different rates, $1.4 \times 10^{-4}\ s^{-1}$ and $4.5 \times 10^{-3}\ s^{-1}$. Figure 4.84 shows the images of the deformed 600×600 μm^2 grids at the two rate. The grids are heavily deformed and more so at $1.4 \times 10^{-4}\ s^{-1}$, making it impossible to identify the intersection of the grid lies in some cases.

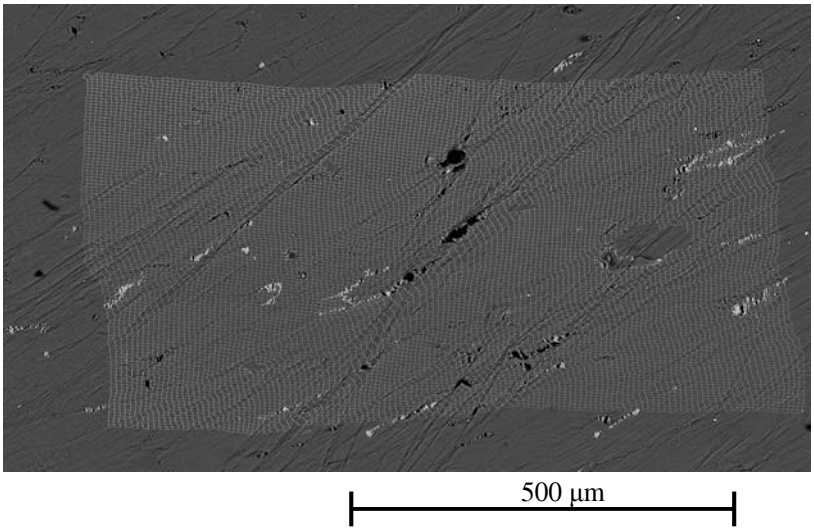

(a) Strain rate: 1.4$\times 10^{-4}$ s^{-1}, strain level:49.8%

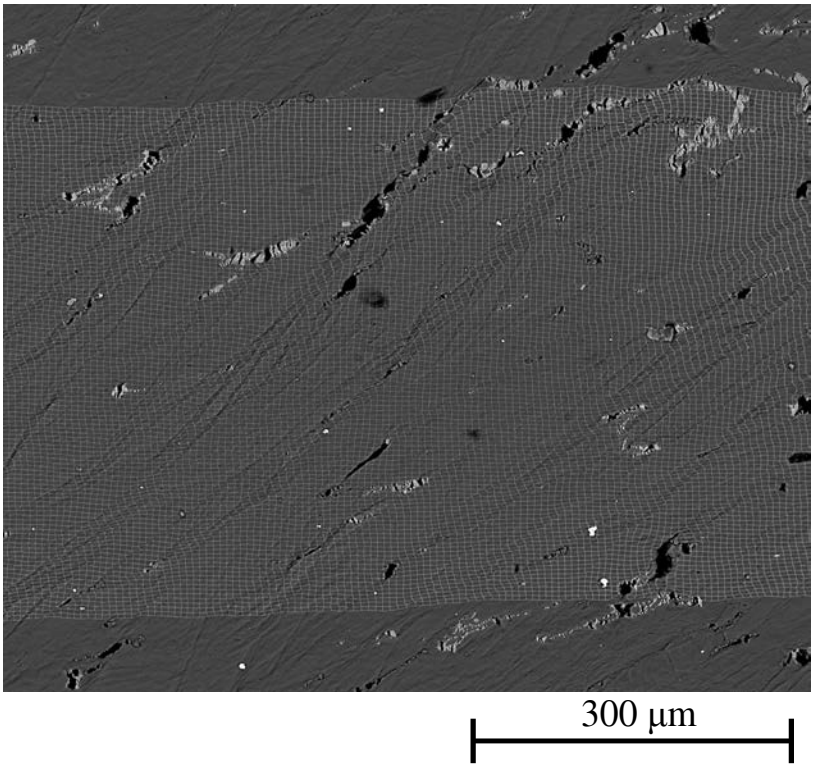

(b) Strain rate: 4.5$\times 10^{-3}$ s^{-1}, strain level: 33.9%

Figure 4.84: BSE images of the deformed grids for UFG material at 200° C

The specimen surface is covered with long shear bands which sometimes even cross the whole gauge width inducing steps on side surfaces. Some of these bands were more diffused and full of grid discontinuities (Figure 4.85, 4.87, 4.88). It resembled a collective motion of a packet of grains, while in some cases, very sharp, long and deep bands, with step like grid discontinuities were observed (Figure 4.86). Here, the width of the sharp band is 2.5 μm which is equivalent to 4 times the mean grain diameter indicating GBS in a steplike manner for 4 grains. These sharp bands were more visi-

ble at 4.5$\times 10^{-3}$ s^{-1} than at 1.4$\times 10^{-4}$ s^{-1} while for latter, the bands were more diffused.

The percentage contribution of GBS to the local plastic strain for the deformed grids in figure 4.84 was calculated to be 18 % at 4.5$\times 10^{-3}$ s^{-1} and 29% at 1.4$\times 10^{-4}$ s^{-1}. However, locally for the zoomed images, the percentage contribution of GBS is as high as 80% (Figure 4.87 left) at 1.4$\times 10^{-4}$ s^{-1} and 54% (Figure 4.88 left) at 4.5$\times 10^{-3}$ s^{-1}.

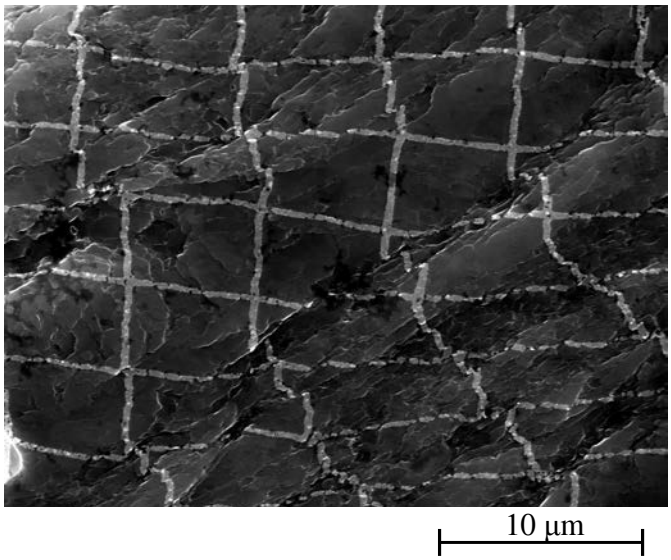

Figure 4.85: Diffused bands accompanied by hatched grids for UFG material strained until 49.8% at 1.4$\times 10^{-4}$ s^{-1} at 200° C

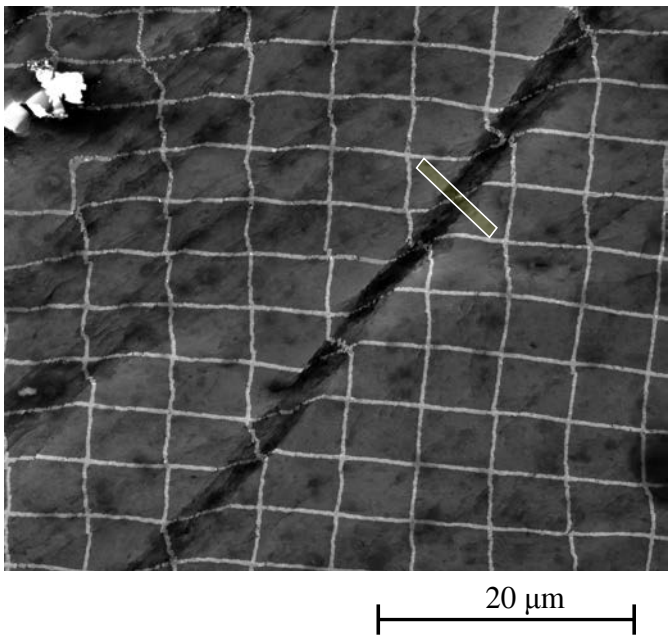

Figure 4.86: Sharp band accompanied by hatched grids for UFG material strained until 33.9% at 4.5$\times 10^{-3}$ s^{-1} at 200° C (highlighted square represents the zone for extraction of thin foil using FIB sectioning)

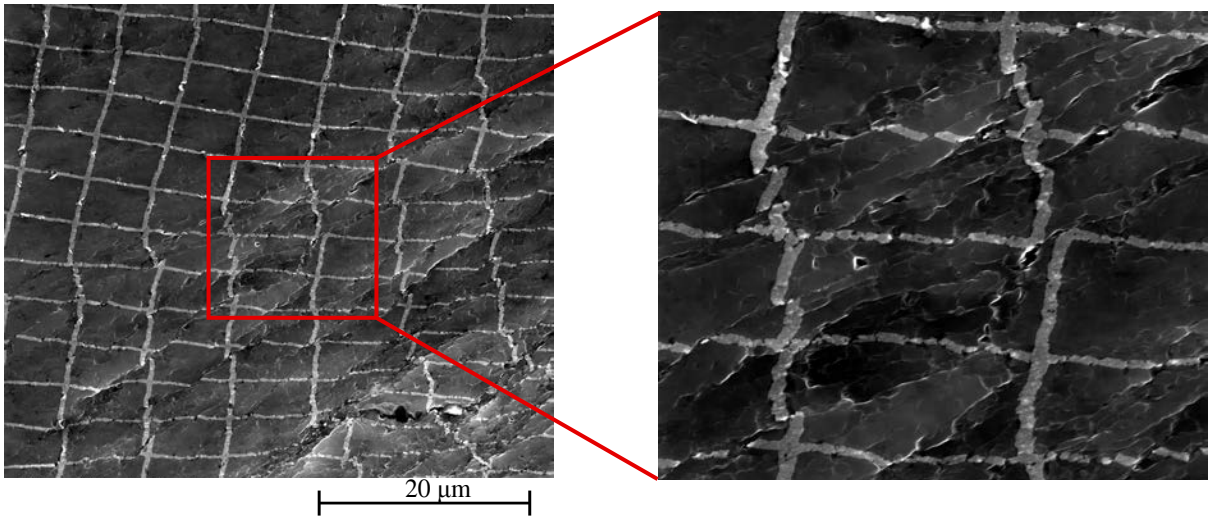

Figure 4.87: Diffused bands accompanied by hatched grids for UFG material strained until 49.8% at 1.4$\times 10^{-4}$ s^{-1} at 200° C

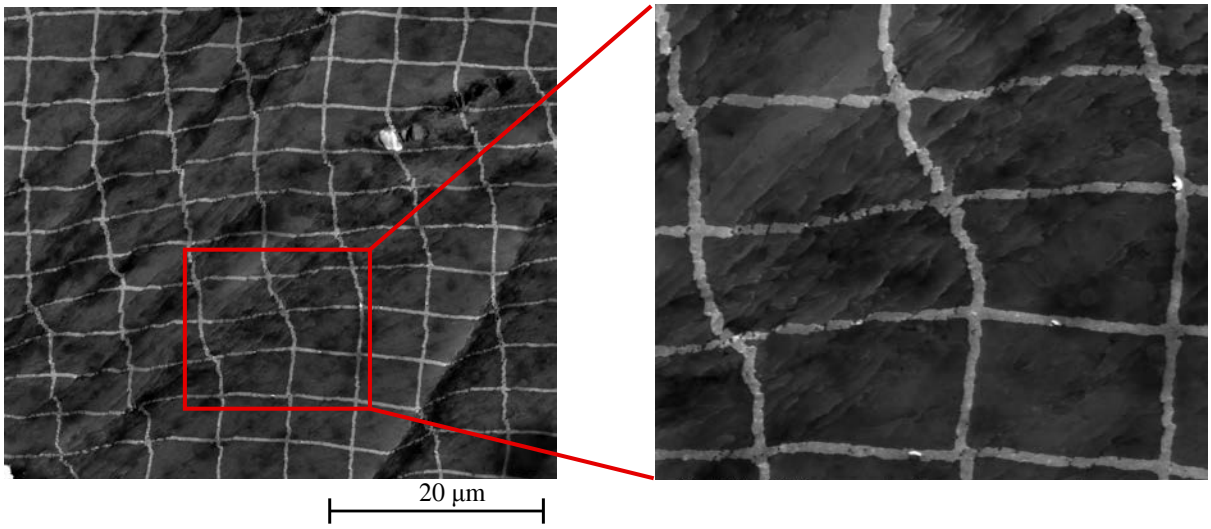

Figure 4.88: Diffused bands accompanied by hatched grids for UFG material strained until 33.9% at 4.5$\times 10^{-3}$ s^{-1} at 200° C

EBSD maps were collected after the test, in areas containing shear bands. Such maps, that do not reflect the initial microstructure, likely to evolve through grain rotations, dynamic recrystallization and grain growth must be interpreted with care. However, when GBS accommodates most of the plastic strain, texture evolutions are much less pronounced than when dislocation glide is the main deformation mechanism [15]. In the present case, if these evolutions were assumed to be moderate, the EBSD maps would suggest that deep and intense shear bands occurred mostly at the interface between coarse and ultrafine grains and were accompanied by GBS of the neighbouring ultrafine grains along their common long, straight GB. (Figure 4.89 and 4.90). GBS seems also exaggerated at HAGBs between small grains. Multiple grains were observed to slide together in a collaborative fashion.

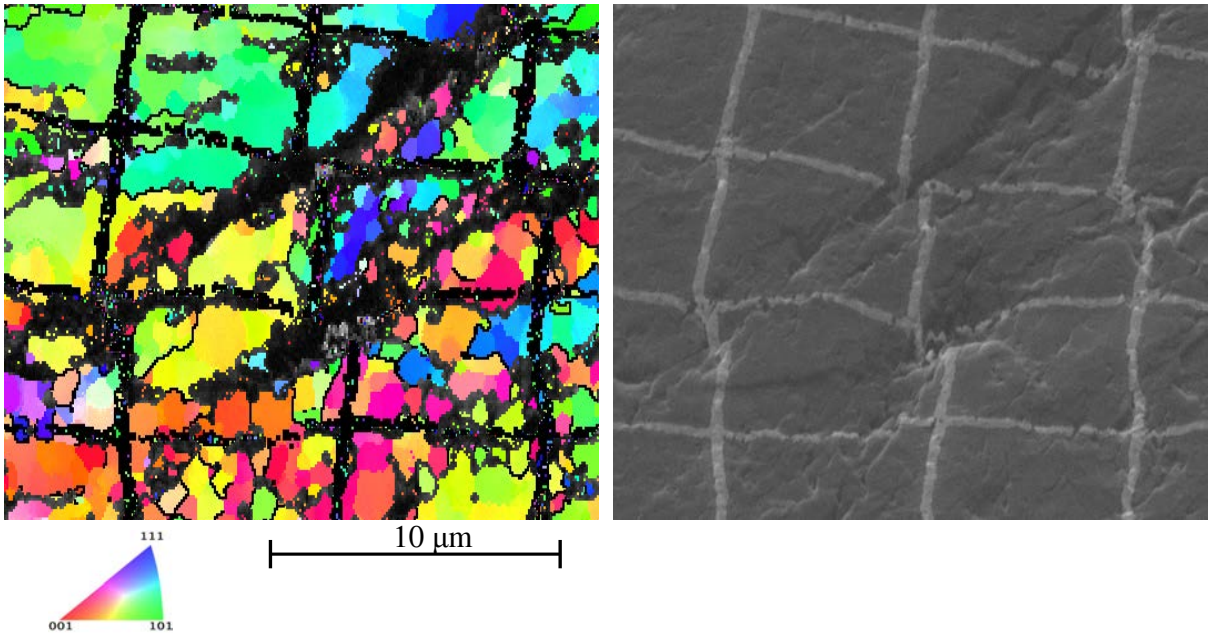

Figure 4.89: Post fracture IPF-Y map of the UFG material strained until 49.8% at 1.4$\times 10^{-4}$ s^{-1} at 200° C

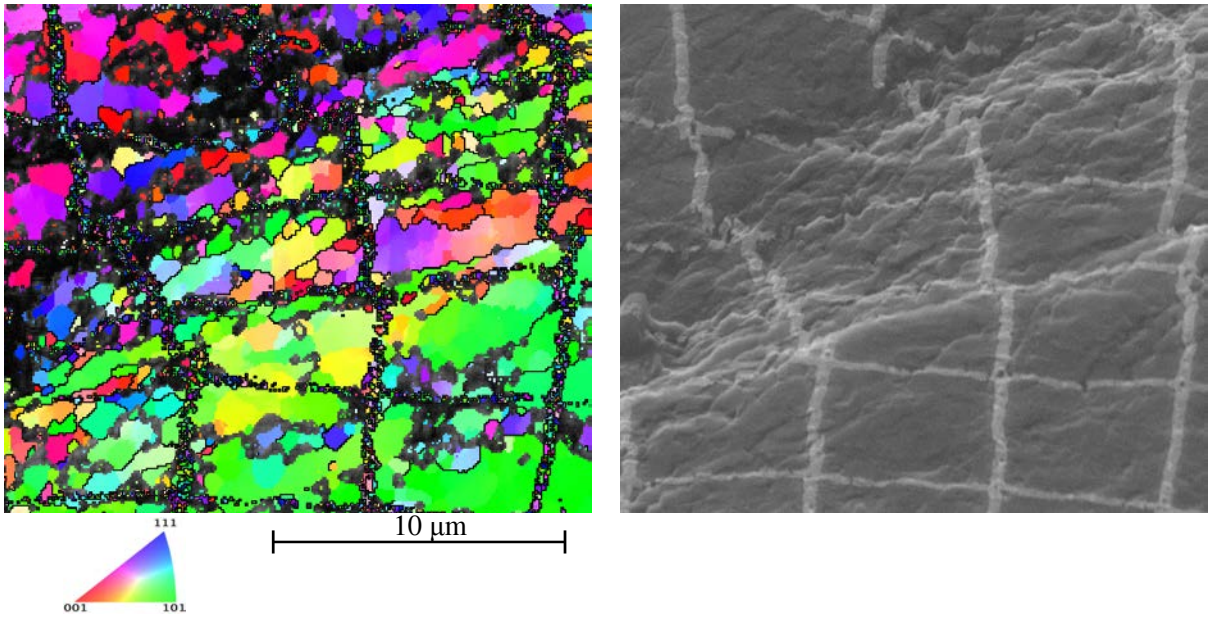

Figure 4.90: Post fracture IPF-Y map of the UFG material strained until 49.8% at 1.4$\times 10^{-4}$ s^{-1} at 200° C

To have more information about the final microstructure inside such bands, FIB sectioning (as described before) was done perpendicular to the sharp band shown in figure 4.86. Figure 4.91 shows the bright field and HAADF STEM images of the foil. Dislocation structures are visible inside some grains within the band, this suggesting that these grains were not recrystallised. Out of plane grain boundary sliding, marked by the step-wise movement of grains, was also observed in the "valley" created by the

sharp band where it emerges at the free surface. Such steps exposed by FIB sectioning were used by Ivanov & Naydenkin. [16] for a quantitative assessment of the contribution of GBS in UFG material, using Langdon's method. However, considering the limited size of FIB sections, the question of the statistical representativity of such an estimate can be raised.

White lines were also observed at the surface of the valley and at the grain boundaries. And since HAADF gives a diffraction contrast, bright colour should represent particles with high atomic number. This indicates a possibility of Mn diffusion along GBs towards the surface.

No clear evidence of local grain growth inside the band is obtained, however, dark coloured grains are observed in figure 4.91b in vertical direction indicating grains with similar orientation. This can also be seen from the IPF-X map of the foil obtained from TKD in figure 4.92. Two possible scenarios can be envisaged: first, some relatively large and thus "soft" grains like the big red grain shown in figure 4.92 ('supergrains' as defined by Kammers et al. [17]) deformed homogeneously to accommodate the localised strain, or second, small (or "hard") grains have rotated and aligned along the two sides of these "supergrains" to produce a homogeneous texture along the band, this forming a preferential path for GBS.

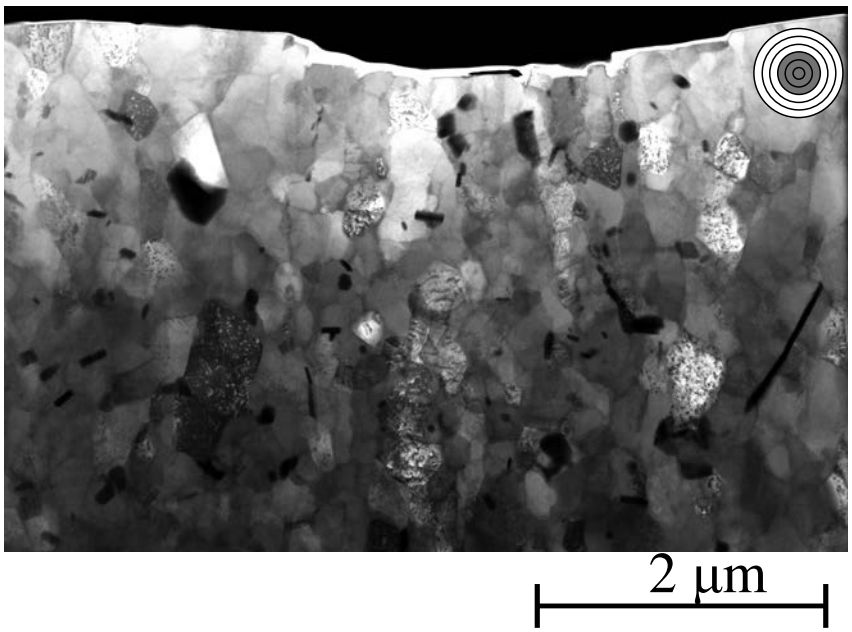

(a)

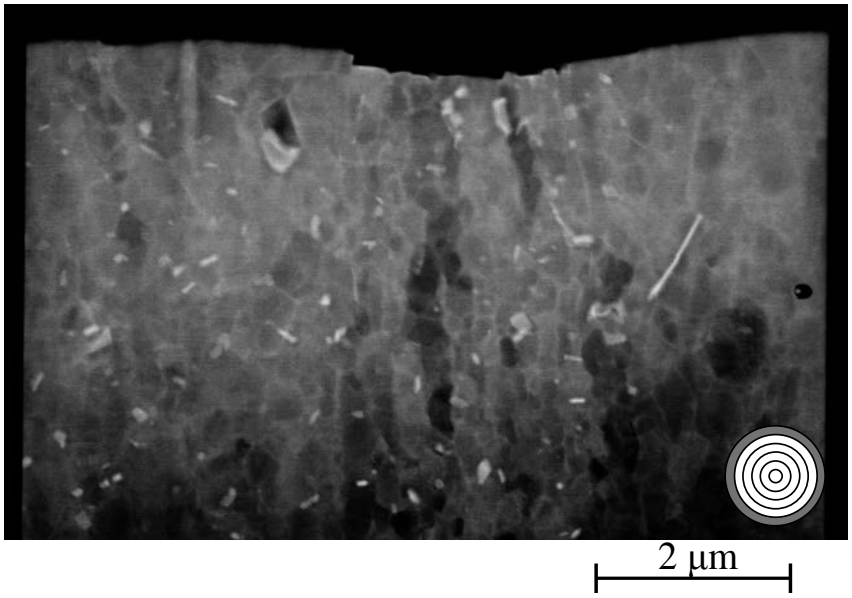

(b)

Figure 4.91: STEM images of the thin foil perpendicular to the band in figure 4.86 (Grey coloured circle represents (a) BF, DF1 and DF2 detectors and (b) HAADF detector used for respective STEM imaging)

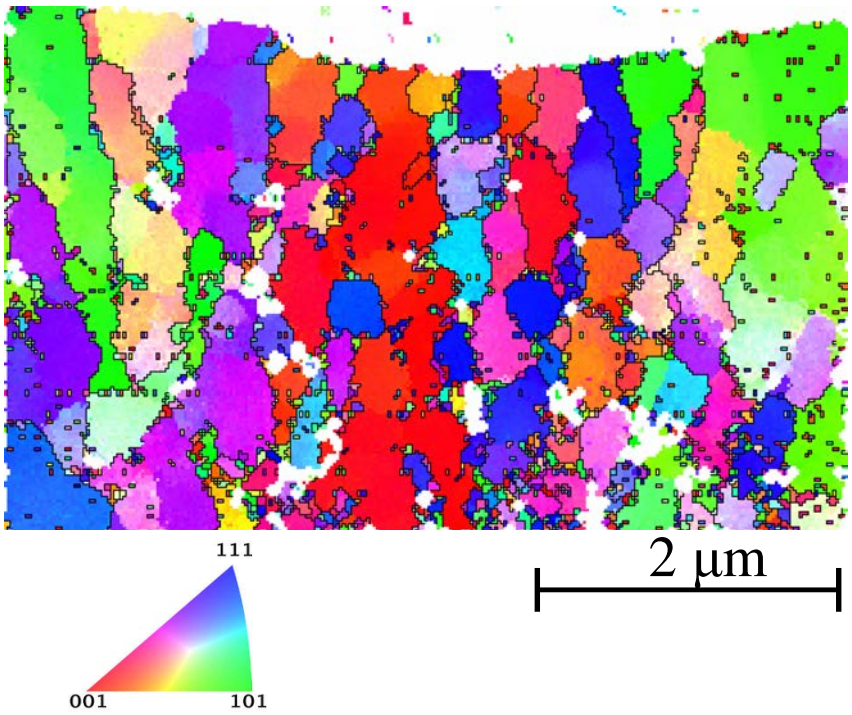

Figure 4.92: IPF-X map obtained from TKD on the thin foil cut by FIB perpendicular to the band in figure 4.86

In addition to the major, long shear bands along the elongated grains and broken particles, several 2 to 26 μm long minor lines perpendicular to these bands were observed

(Figure 4.93). They gave a slight curvature to the otherwise straight major lines. They were more numerous at 1.4$\times 10^{-4}$ s^{-1} than at 4.5$\times 10^{-3}$ s^{-1}. The change in local texture and maybe, dynamic recrystallization, might partially erase the preferred shearing direction inherited from ECAP, allowing shearing (either by dislocation glide or by GBS) in a secondary direction.

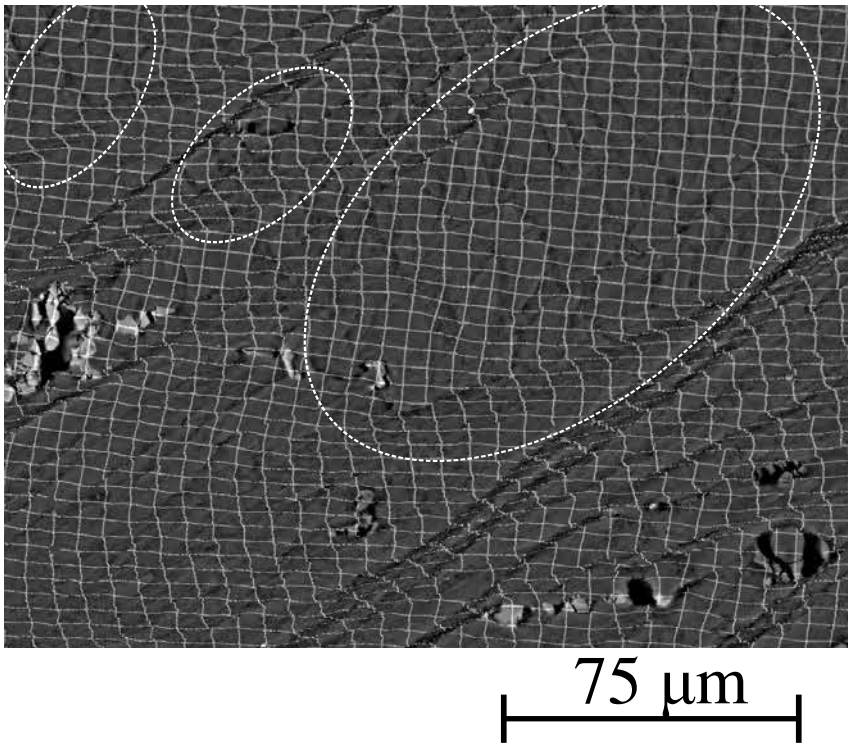

Figure 4.93: Lines perpendicular to the major shear bands at 1.4$\times 10^{-4}$ s^{-1} in UFG-A material stretched by 49.8% at 200° C

Figure 4.94 presents the maps of axial plastic strain fields at the two rates. The heavily deformed micro-grids for the UFG material tested at 1.4$\times 10^{-4}$ s^{-1} made it difficult to identify analogous patterns during DIC and thus the correlation was left unfinished. The specimen surface, in both cases, is covered with intense shear bands. Similar to the UFG material tested at 3.0$\times 10^{-6}$ s^{-1}, 100°C, these bands can be differentiated in two categories, high and low strain bands. "High strain" bands, with orientations in range of 33-55°, seem to originate from broken particles and follow their elongation axis. Although, the strain intensity inside these bands seems to be very high, this may be due to fake strains induced by particles cracking. The "low strain" bands, with orientations in the range of 22-31°, are damage-free and more dispersed (i.e. increased frequency but low in intensity). They appear independent from the particles, at least on the surface, and are probably related to the polycrystalline microstructure. Such bands were more frequent with a decrease in strain rate. In general, the strain intensity inside the bands was higher than at RT and 100°C. Up to 150% strain was accommodated in shear bands without damage at 4.5$\times 10^{-3}$ s^{-1}. This value increased to 300% at 1.4$\times 10^{-4}$ s^{-1}.

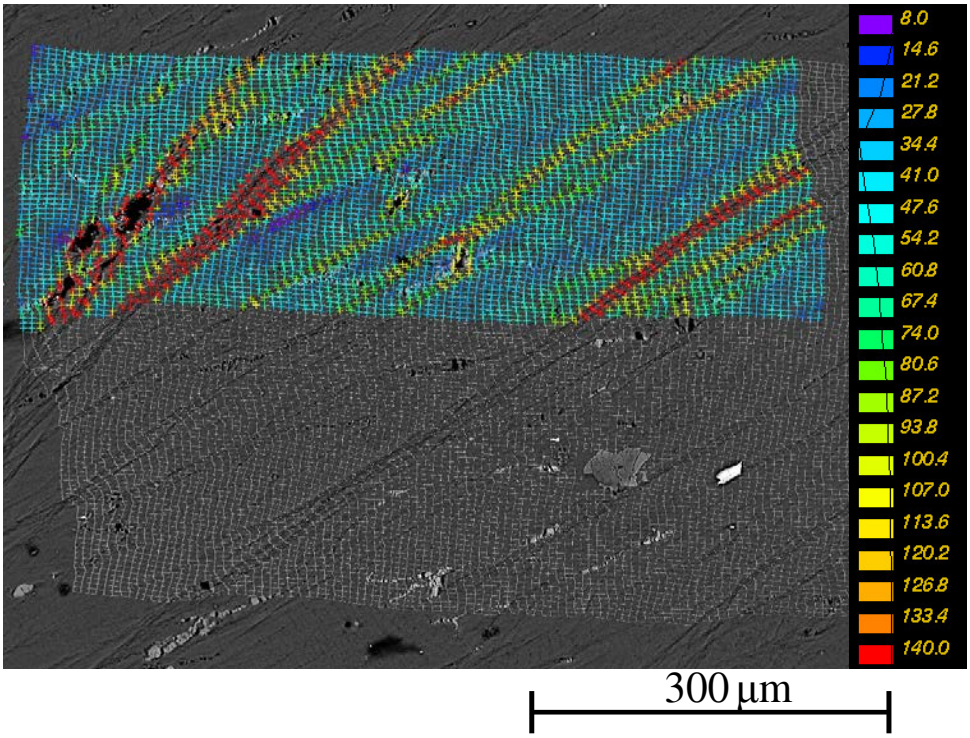

(a) Strain rate: 1.4$\times 10^{-4}$ s^{-1}, $E_{11,mean}$: 59.2%, $E_{fracture}$: 49.8%

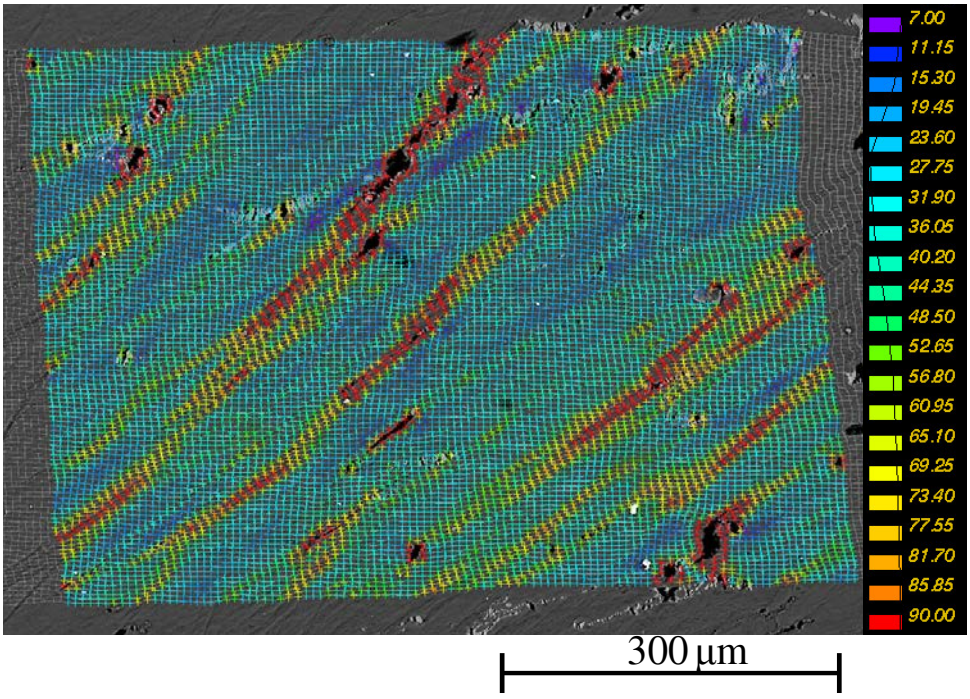

(b) Strain rate: 4.5$\times 10^{-3}$ s^{-1}, $E_{11,mean}$: 40.2%, $E_{fracture}$: 33.9%

Figure 4.94: Axial plastic strain maps of UFG material at 200° C

Figure 4.95 compares the histograms of the normalised strain fields for UFG material at 200°C. Similar to the trends observed in CG material, the standard deviation is higher for UFG material strained until 49.8% at 1.4$\times 10^{-4}$ s^{-1} than for that strained until

33.9% at 4.5$\times 10^{-3}$ s^{-1}. Note that the comparison is somewhat biased by the different size of correlated areas.

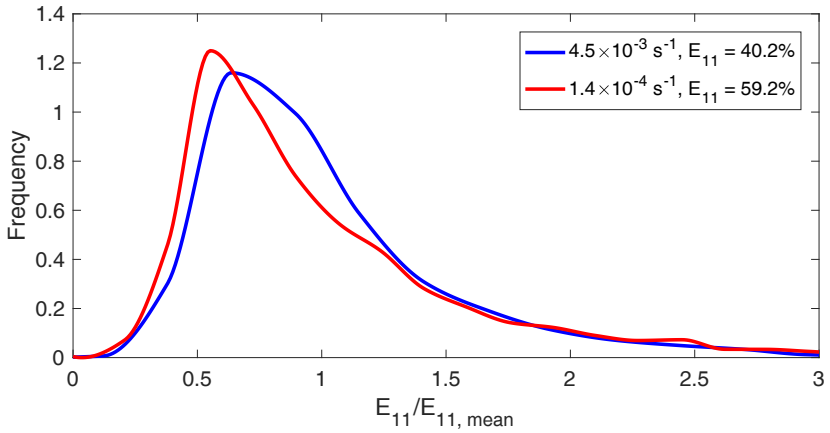

Figure 4.95: Histograms of normalised axial strain for UFG material at 200° C

SEM images of the fracture surfaces of UFG samples strained at 1.4$\times 10^{-4}$ s^{-1} and 4.5$\times 10^{-3}$ s^{-1} respectively are shown in figures 4.96 and 4.97. The fracture surfaces are covered with small tube-like features evoking groups of sliding grains. The width of these tubes was in the range of 2 to 28 μm. The small ductile dimples are still present at both the strain rates.

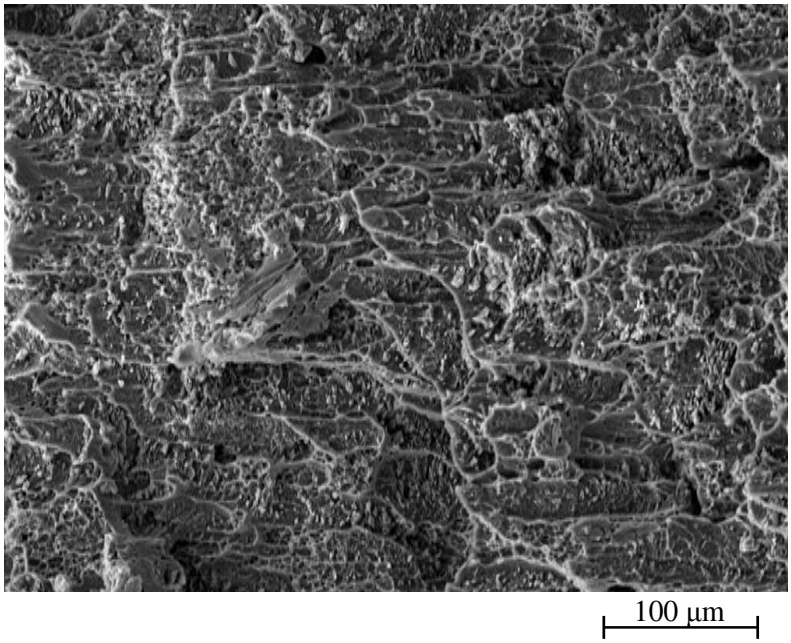

(a) SE image of the fracture surface

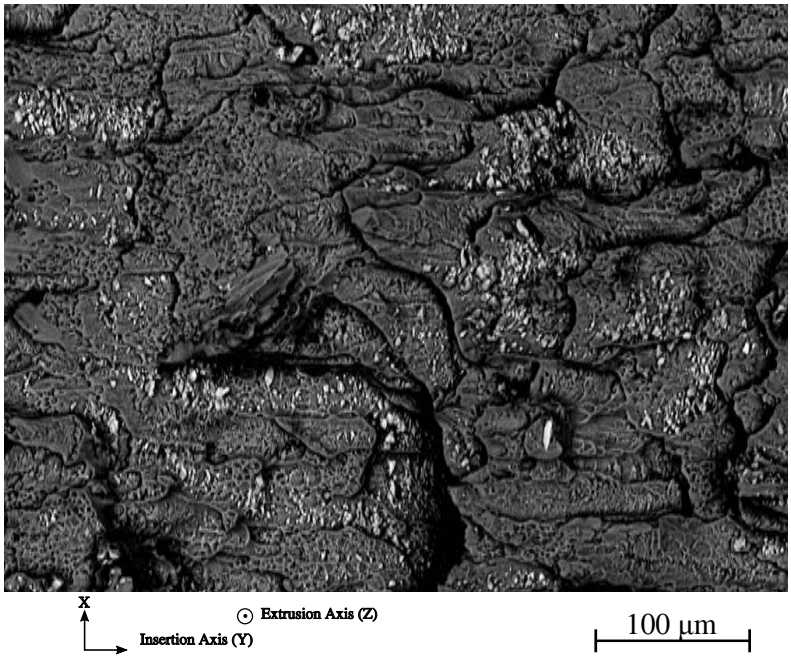

(b) BSE image of the fracture surface

Figure 4.96: Fracture surface of the UFG material strained up to 49.8% at 1.4$\times 10^{-4}$ s^{-1}, 200° C

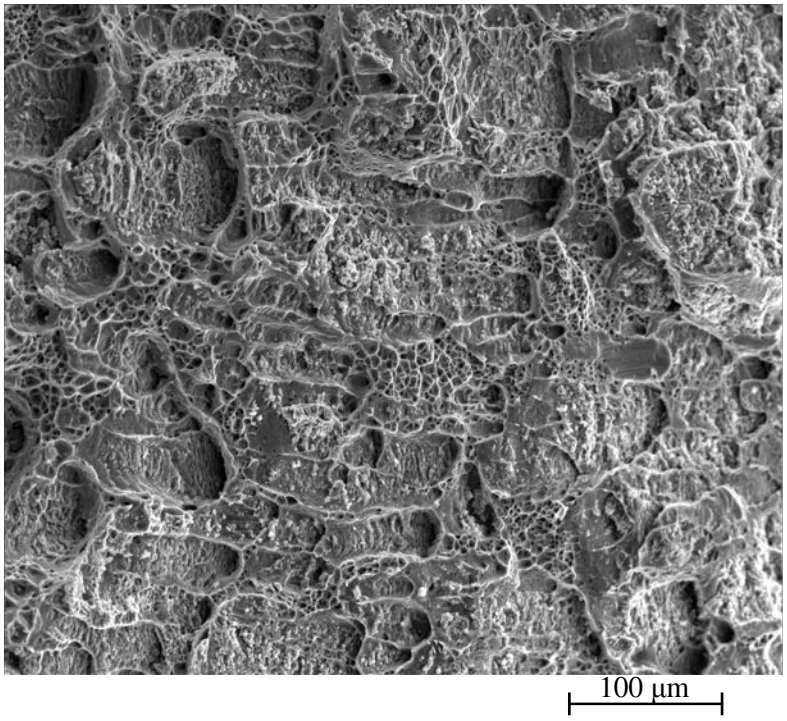

(a) SE image of the fracture surface

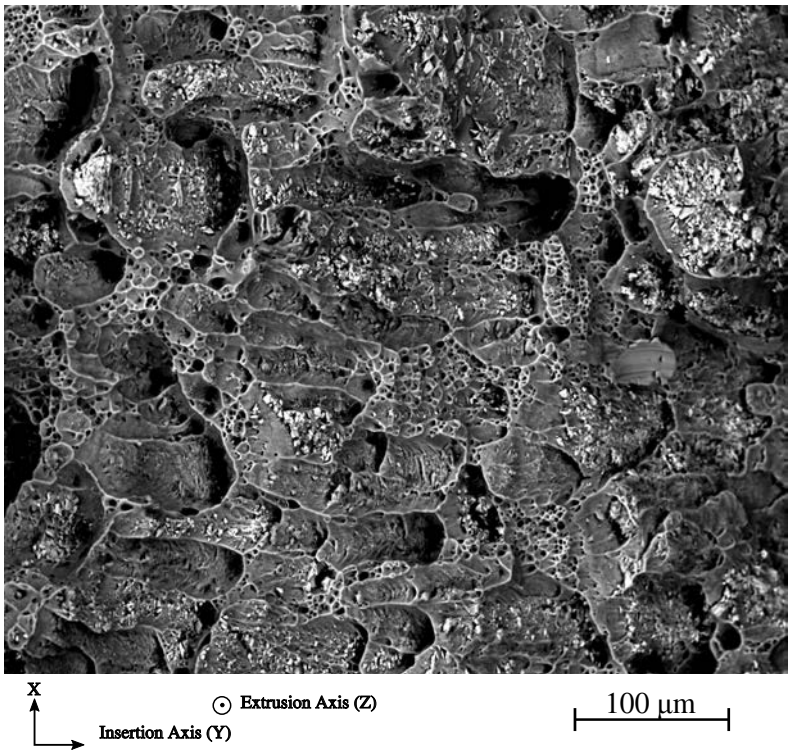

(b) BSE image of the fracture surface

Figure 4.97: Fracture surface of the UFG material strained up to 33.9% at 4.5$\times 10^{-3}$ s^{-1}, 200° C

4.3 Discussion

4.3.1 Strain heterogeneities in relation with mechanical and microstructural parameters

Irrespective of the testing temperature and strain rate, fracture was always slanted in UFG material, even outside the temperature and strain rate range for DSA. It is controlled by shear localization, which is not necessarily due to DSA, but comes from the microstructure i.e. the elongation of grains and the alignment of broken second phase particles in a slanted plane relative to the tensile axis. It is reminiscent of Arzaghi et al.'s [18] observations on UFG copper or by Niendorf et al. [19] on UFG steel, both with elongated grains formed by ECAP route C : mode I fatigue crack could not be grown in CT specimens that always fractured in a slanted plane, corresponding to the shearing direction during ECAP.

Higher and higher amounts of strain was accommodated in shear bands in UFG material, as the temperature rose and as strain rate decreased, which, at first, seems contradictory with the associated increase in SRS reported in the previous chapter. However, the SRS is not the only parameter that controls strain localization. Upon incipient strain localization, local strain hardening increases the flow stress in the incipient band, opposing further increase in strain, and the strain rate increases locally, leading on the one hand, -if the SRS is not too small- to an increase in viscous stress which tends to slow down further localization, but, on the other hand, -because the SRS is rate dependent- to a decrease in SRS, which on the contrary favours further localisation in the already deformed region. The evolution of shear bands is thus the result of a complex interplay between strain hardening and rate-dependent viscosity.

Figure 4.98 compares the normalised axial strain profiles measured at various temperatures and rates. Strain localization is more pronounced at 100 and 200°C than at RT, but this plot fails to reveal a clear influence of the strain rate on the degree of localization.

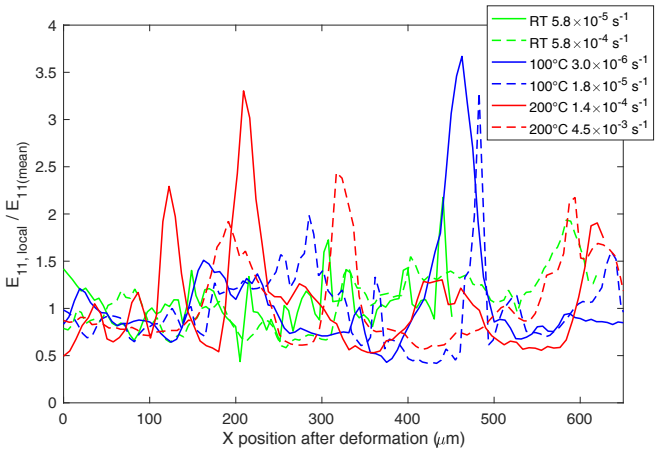

Figure 4.98: Normalized strain profiles at different temperatures

To analyse the parameters that control strain localization, the measured standard deviation of the normalized strain field (denoted below by SD) and the corresponding strain, strain rate, stress exponent and SRS have been reported in Table 4.1. Various attempts to correlate the data are also presented on figure 4.99.

As expected, although with a poor correlation, the SD decreases as the hardening exponent rises (Figure 4.99a), it also tends to rise with the strain level (Figure 4.99b) and, surprisingly, tends to rise with the SRS as well (Figure 4.99c). The latter result seems difficult to reconcile with the linear rise in ductility with increasing SRS reported in the previous chapter (Figure 3.42). This might be due the pseudo strains induced by damage and GBS, especially when the SRS and the fracture strain are high, that artificially increase the SD of the strain field.

Material	**T (°C)**	**Strain rate (s^{-1})**	**$E_{11,local}$**	**Hardening exponent, n**	**SD**	**SRS**
CG	RT	5.8×10^{-5}	10.5%	0.18	0.43	0.003
UFG	RT	5.8×10^{-5}	4.5%	0.09	0.50	0.009
UFG	RT	5.8×10^{-4}	6.2%	0.10	0.50	0.005
CG	100	1.5×10^{-5}	6.5%	0.25	0.49	0.02
UFG	100	1.8×10^{-5}	11.1%	0.05	0.53	0.05
UFG	100	3.0×10^{-6}	28.8%	0.06	1.07	0.09
CG	200	1.8×10^{-3}	14.0%	0.11	0.65	0.03
CG	200	4.1×10^{-3}	11.6%	0.13	0.45	0.03
UFG	200	1.4×10^{-4}	59.2%	0.10	0.88	0.24
UFG	200	4.5×10^{-3}	40.2%	0.05	0.77	0.13

Table 4.1: Hardening exponent, SRS, and standard deviation of the measured strain fields

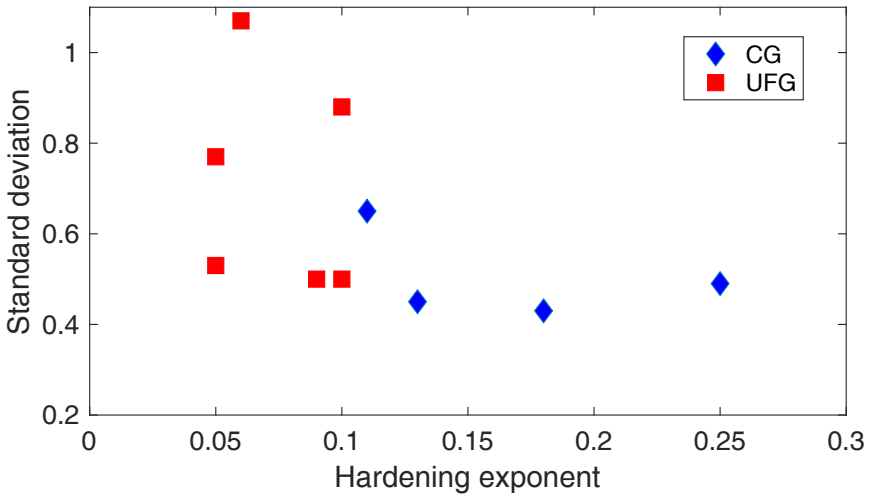

(a)

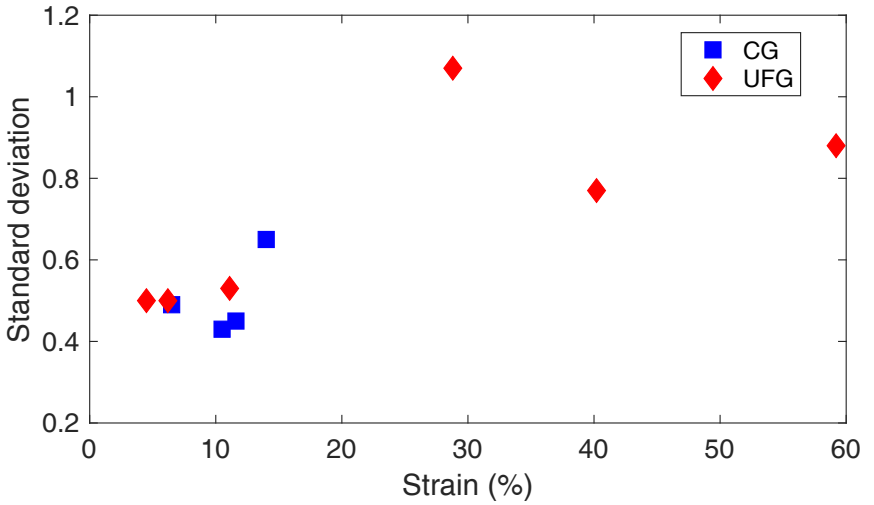

(b)

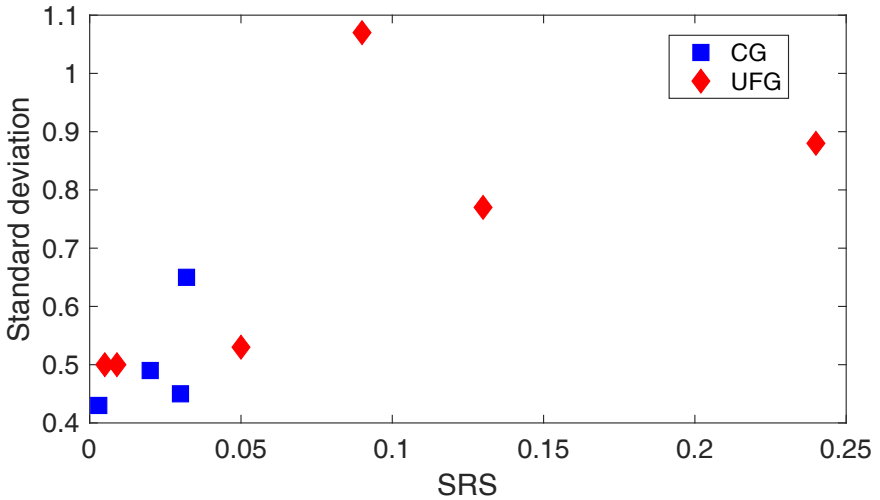

(c)

Figure 4.99: Standard deviation of the strain field as a function of (a) hardening exponent, (b) local strain level and (c) SRS.

4.3.2 Grain boundary sliding (GBS)

GB sliding was observed in both CG and UFG materials, especially at high temperature. For CG material, the fraction of sliding GBs and the contribution of GBS to the global inelastic strain could be measured and are reported in the table below.

T (°C)	Strain rate (s^{-1})	$E_{11,local}$	% Sliding GBs	contrib. GBS	SRS
100	$1.5\times10^{-5}\ s^{-1}$	6%	9%	0.6%	0.02
200	$4.1\times10^{-3}\ s^{-1}$	12%	44%	0.8%	0.03
200	$1.8\times10^{-3}\ s^{-1}$	23%	68%	1.8%	0.03
200	$7.0\times10^{-6}\ s^{-1}$	5%	55%	3.8%	0.14

Table 4.2: Quantification of GBS in CG-A material

The thermally-activated character of GBS clearly appears from the dramatic increase in its frequency at 200°C, as compared to 100°C. Figure 4.100a and b show the measured SRS versus percentage of sliding GBs and percentage contribution of GBS to local plastic strain. No correlation appears for fraction of sliding GBs with SRS, while a weak correlation can be observed between SRS and percentage contribution of GBS, which suggests that in CG material the rise in SRS at low strain rate and high temperature is not necessarily due to GBS.

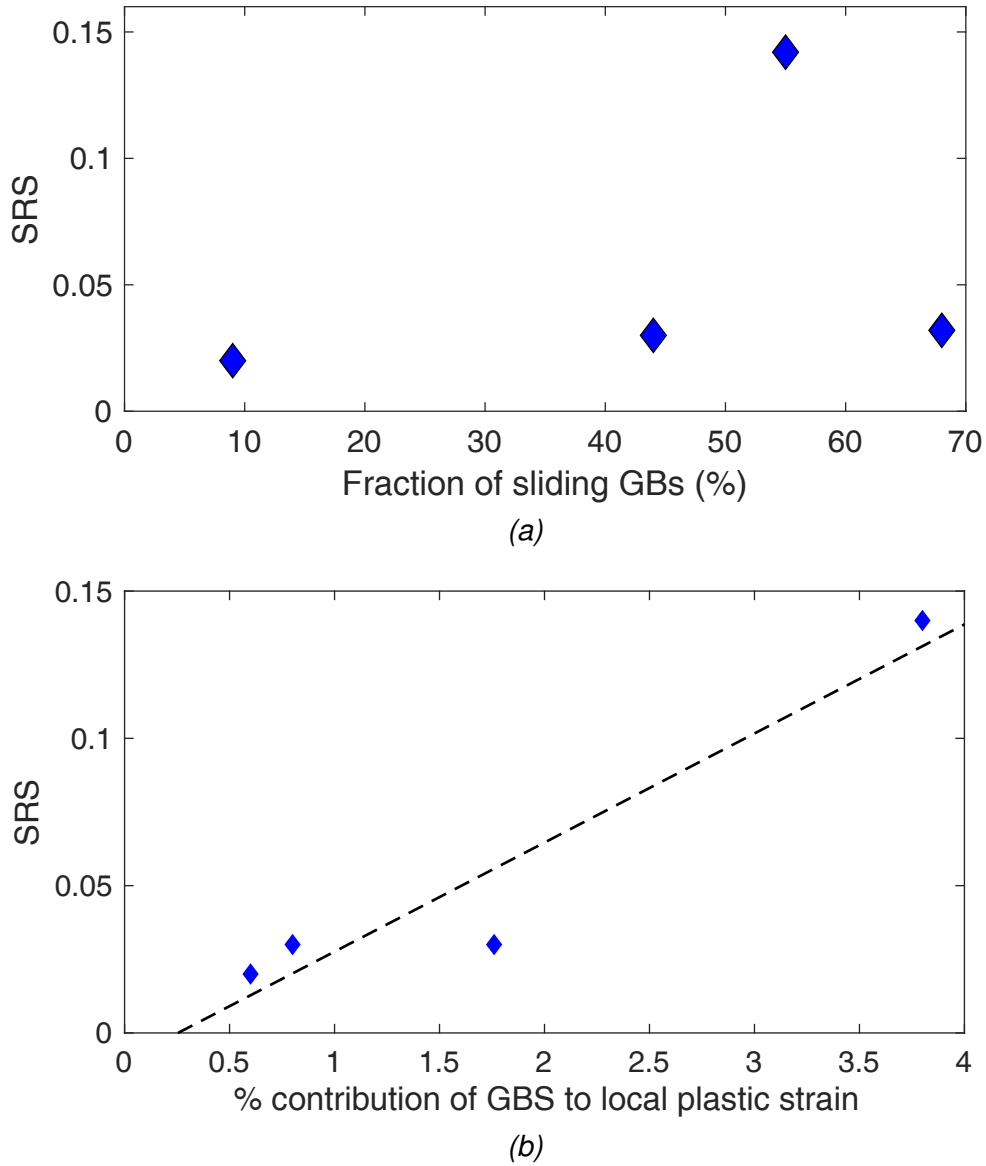

Figure 4.100: SRS versus (a) percentage of sliding GBs and (b) percentage contribution of GBS to global plastic strain for CG material

The rise in frequency of GBS in CG material as the strain rate decreases, which has negligible consequences on the stress-strain curve, might however influence significantly damage and fracture, promoting second phase particles debonding and creating cavities at triple points (see figure 4.71), but also accommodating grain-to-grain compatibility stresses. The second aspect seems to prevail, otherwise the ductility would drop with decreasing strain rate.

In the UFG material, GBS was mostly cooperative in nature i.e. a collection of grains slid in a collective manner leading to higher grids shifting as compared to CG. This can explain its higher ductility at 200°C as compared to CG material. The percentage contribution of GBS to local plastic strain was calculated using the intercept method

over 600×600 μm^2 areas, which rises as the temperature increases, and as the strain rate decreases is reported in table 4.3. Although the estimated values are approximate, a linear correlation is obtained with the SRS, as shown in figure 4.101 indicating a definitive role of GBS on the SRS and hence on the fracture strain.

T (°C)	Strain rate (s^{-1})	$E_{11,local}$	contrib. GBS	SRS
100	1.8×10^{-5} s^{-1}	11.1%	9%	0.05
100	3.0×10^{-6} s^{-1}	28.8%	13%	0.09
150	1.6×10^{-5} s^{-1}	46.8%	22%	0.19
200	4.5×10^{-3} s^{-1}	40.2%	18%	0.13
200	1.4×10^{-4} s^{-1}	59.2%	29%	0.24

Table 4.3: Contribution of GBS to local plastic strain for UFG-A material

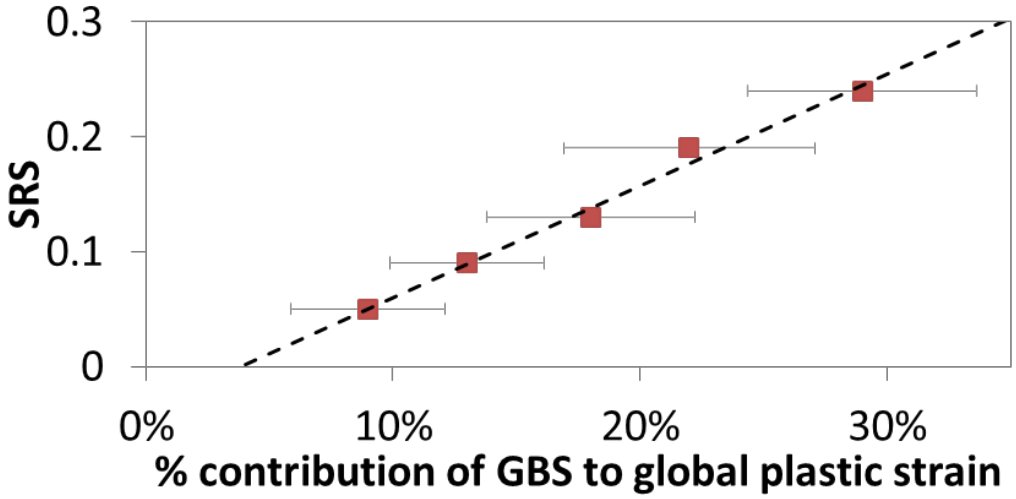

Figure 4.101: SRS versus percentage contribution of GBS to global plastic strain in UFG material

4.3.3 Role of second phase particles fracture on the strain rate dependence of ductility

The ductility of the CG material is actually more sensitive than that of the UFG material to the strain rate at 200°C (see figure 3.41 in the previous chapter) and to the SRS in general (see figure 3.42 in the same chapter). The purpose of this paragraph is to discuss this result in connection with second phase particle cracking which was shown to trigger strain localization in CG material. Figure 4.102 presents the fraction of broken particles as a function of ultimate stress (UTS) and fracture strain for CG material at all temperatures. Table 4.4 reports all the data used in the figures below.

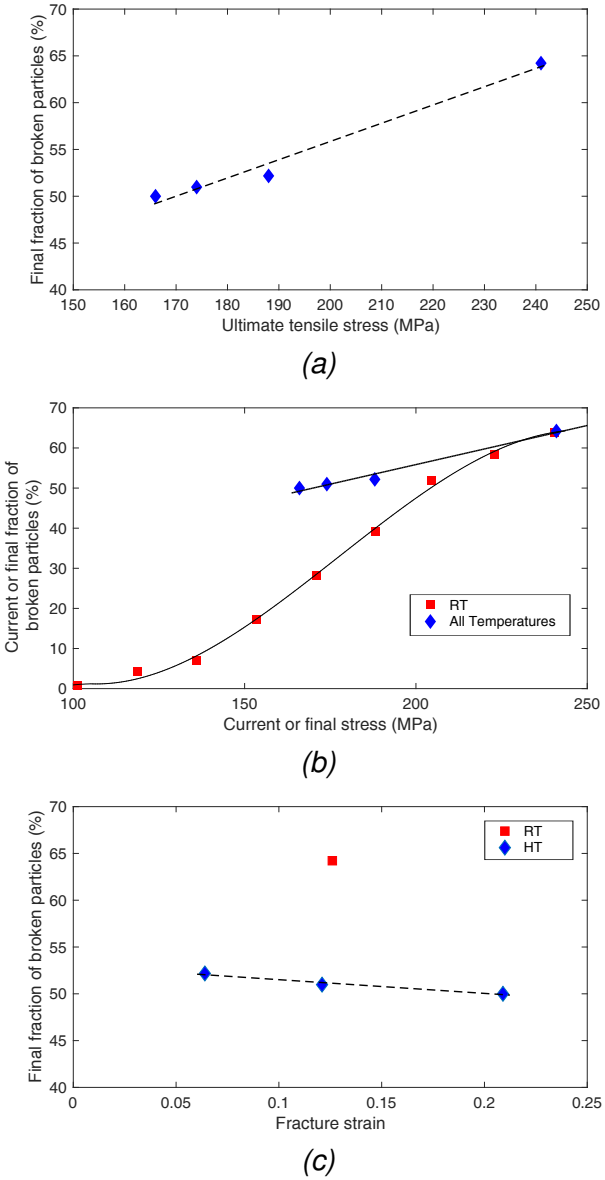

Figure 4.102: Fraction of broken particles in CG-A material (a) final fraction versus ultimate tensile stress, (b) current (RT) or final (HT) fraction versus current stress (RT) or UTS (HT) and (c) final fraction versus fracture strain.

T (°C)	Strain rate (s^{-1})	Fraction of broken particles (%)	UTS (MPa)	Fracture strain (%)
25	5.8×10^{-5}	64	241	12.6
100	1.5×10^{-5}	52	188	6.4
200	1.8×10^{-3}	50	166	20.9
200	4.1×10^{-3}	51	174	12.1

Table 4.4: Final fraction of broken particles for CG material

It appears that particles fracture is controlled by the stress rather than by the strain (a quasi inverse correlation with the strain appears at high temperature).

However, no unique correlation appears as a function of stress: at the same stress level, the percentage of broken particles at 100 and 200°C is higher than at RT. This might be due to a new fracture mode, in addition to brittle fracture normal to the tensile axis: GBS-induced fracture or debonding (parallel to the GBs). The decrease in flow stress when the strain rate decreases, and as a consequence, the reduction in the fraction of broken particles, might contribute to the increase in ductility. However, the large difference in ductility observed for the two rates at 200°C, for a limited difference in the fraction of broken particles suggests that this effect is not predominant.

4.3.4 Activation of non-octahedral slip

At 200°C, non-octahedral slip along {110} planes was activated in CG material. Similar evidences of non-octahedral slip along {110} plane in <110> direction were found in compression, at material-dependent temperatures, by Le Hazif et al. [20] in single crystal of various FCC metals (Al, Ag, Cu, Ni and Au, suitably oriented to get a higher Schmid factor on these systems than on octahedral ones, figure 4.103).

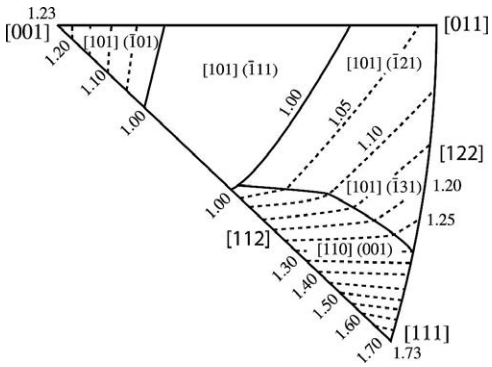

Figure 4.103: Ratio of Schmid factors between non-octaedral and octaedral slip systems [21].

They identified the temperature range for which each kind of slip activity was observed and plotted it as a function of $\mu b/\gamma$ (μ is the shear modulus, b is the Burgers vector and γ is the stacking fault energy in {111} plane) as shown in figure 4.104 (from Caillard and Martin [21] who replotted it from Le Hazif et al. [20]). They found a linear dependence between $\mu b/\gamma$ and the transition temperatures. Smaller the dislocation dissociation width, lower is the transition temperature for slip in {110} plane. The value of $\mu b/\gamma$ could be approximated for Al5083 alloy using the stacking fault energy of 33.1 mJ/m^2 provided by Morishige et al. [22]. The temperatures below which only {111}<$\bar{1}$10> slip system is expected and above which only non-octahedral slip should occur were found to be 174 and 400°C respectively for Al5083 alloy. These values are consistent with the observed evidences of a mixture of octahedral and non-octahedral slip lines in CG material at 200°C.

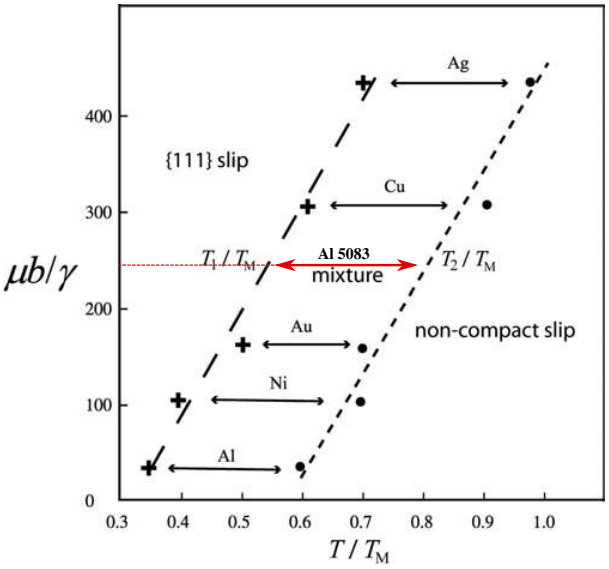

Figure 4.104: Domains of activation of non-octahedral {110} slip, as a function of reduced temperature and dislocations dissociation width $\mu b/\gamma$ (from Caillard and Martin [21] who replotted it from Le Hazif et al. [20])

Figure 4.105 [21] shows the variation of CRSS for glide in different non-octahedral slip planes in commercially pure aluminium. The CRSS decreases with increase in temperature and decrease in strain rate in the thermally-activated regime, which extends up to more than 300°C for {110} slip, and reaches a minimum steady-state value in the athermal regime. Unfortunately, no similar data was found for the octahedral slip systems and for Al 5083 alloy.

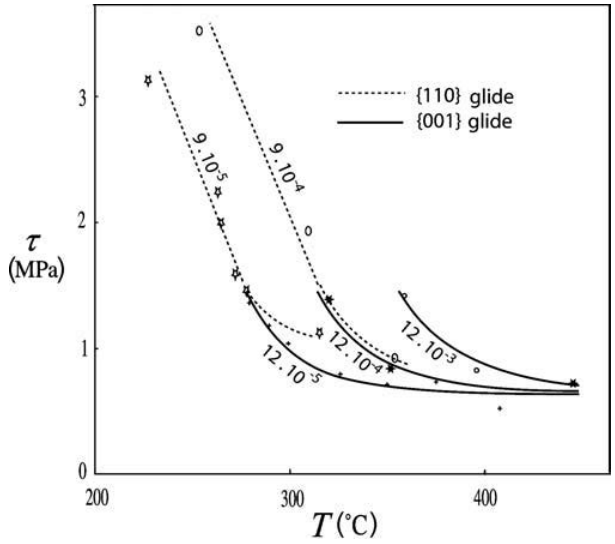

Figure 4.105: CRSS for the activation of non-octahedral slip in {110} and {100} planes in Al [21].

Note that the stress exponent for (110) glide in Al was found to be 4.2 [21], which corresponds to a SRS of 0.238 quite close to that measured here in both materials at 200°C and low strain rates. So, in principal, the activation of {110} glide might partly explain the observed rise in SRS. However, to have a substantial effect at the macro-scale, non-octahedral glide has to occur in a significant volume fraction of the materials.

To estimate this volume fraction, maps of maximum schmid factors (SF) for {110}<1$\bar{1}$0> and {111}<1$\bar{1}$0> slip systems were obtained over 3$\times$3 mm^2 and 100$\times$85 μm^2 areas in CG and UFG materials, respectively and are presented in figure 4.106. The surface fraction of grains where the SF for {110}<1$\bar{1}$0> slip systems was higher than for {111}<1$\bar{1}$0> slip systems was found to be 7.6% and 20.5% in CG and UFG materials, respectively. The difference is due to the change in texture induced by ECAP.

In CG material, this relatively low volume fraction added to the fact that at 200°C, octahedral slip coexists with {110} slip suggests that the activation of such slip systems is not responsible for the observed rise in SRS. By providing an additional accommodation mechanism, it might however improve the ductility.

For UFG material, the volume fraction of grains where {110} glide is potentially predominant is more substantial, but GBS also contributes more to the global strain, as will be shown in the next chapter. In that case, both effects might thus contribute to the rise in SRS at high temperature and low strain rate.

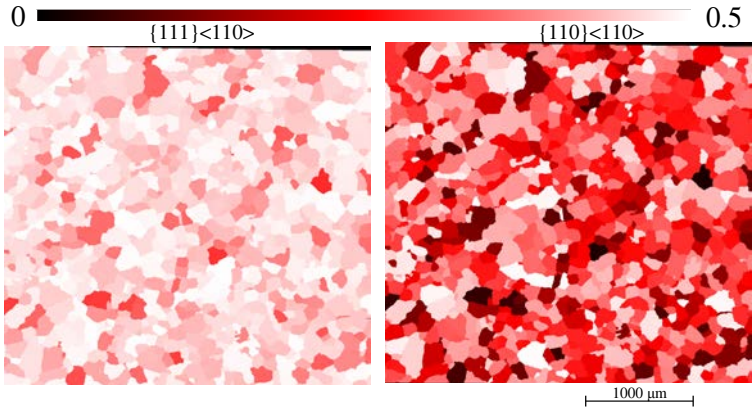

(a) CG material

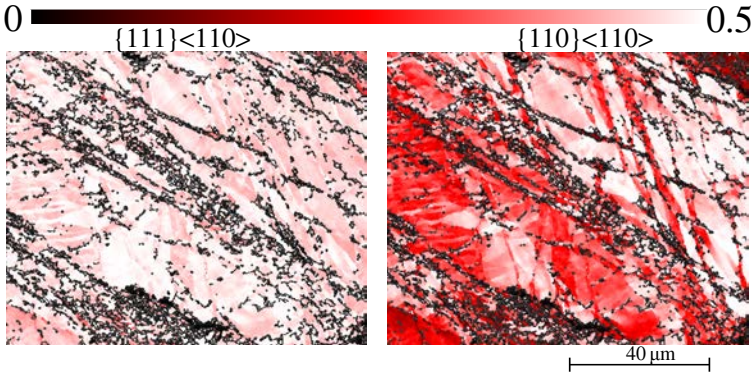

(b) UFG material

Figure 4.106: Schmid factor (SF) maps for slip activity in {110} and {111} planes.

4.4 Summary

In the present chapter, an analysis of the deformation and damage mechanisms was presented. A two-scale surface patterning method was successfully developed and exploited for meso- and sub-micron-scale measurement of strain fields for CG and UFG materials.

- Strain fields became heterogeneous very early for both CG and UFG materials. In CG material, it was due to the fracture of large second phase particles and to GBS at high temperature. However, for UFG material, the heterogeneity was due to its inhomogeneous grain refinement and occurred mostly at the interfaces between coarse and fine grains and, to a lesser extent, along rows of broken second phase particles.

- Grain boundary sliding was observed in both CG and UFG materials. As expected for a thermally-activated, viscous phenomenon, it was enhanced by a decrease in strain rate and increase in temperature.

- In CG material, GB sliding was mostly uncorrelated and accounted for at most 10% of the global strain. It was probably not responsible for the rise in SRS at high temperature/low strain rate. For UFG material, GB sliding was cooperative in nature accommodating locally up to 300% strain without apparent damage at 200°C. It is why the UFG material becomes more ductile than CG material at low strain rate/high temperature. The rise in SRS appears to be directly correlated with the increasing contribution of GBS to the plastic strain.

- Evidences of non-octahedral slip on {110}<1$\bar{1}$0> slip systems were observed for CG material at 200°C but over a volume fraction which is probably too low to induce a significant rise in SRS. In UFG material, due to a different texture, the volume fraction of grains in which such slip can occur is larger and this might partly explain the rise in SRS at high temperature/low strain rate. In both materials, this additional deformation mechanism certainly contributes to the rise in ductility observed with rising temperature.

References

[1] H. Wang, H. Xie, Y. Li, and J. Zhu, "Fabrication of micro-scale speckle pattern and its applications for deformation measurement," *Measurement Science and Technology*, vol. 23, 2012.

[2] S. A. Collette, M. A. Sutton, P. Miney, A. P. Reynolds, X. Li, P. E. Colavita, W. A. Scrivens, Y. Luo, T. Sudarshan, P. Muzykov, and M. L. Myrick, "Development of patterns for nanoscale strain measurements : I. Fabrication of imprinted Au webs for polymeric," *Nanotechnology*, vol. 15, 2004.

[3] Y. Tanaka, K. Naito, S. Kishimoto, and Y. Kagawa, "Development of a pattern to measure multiscale deformation and strain distribution via in situ FE-SEM," *Nanotechnology*, vol. 22, 2011.

[4] Y. Zhang, T. D. Topping, E. J. Lavernia, and S. R. Nutt, "Dynamic Micro-strain Analysis of Ultrafine-grained Aluminum Magnesium alloy using Digital Image Correlation," *Metallurgical and Materials Transactions A*, vol. 44A, no. 6, pp. 1–23, 2013.

[5] Y. Luo, J. Ruff, R. Ray, Y. Gu, H. J. Ploehn, and W. A. Scrivens, "Vapor-Assisted Remodeling of Thin Gold Films," *Chemistry of Materials*, vol. 17, no. 20, pp. 5014–5023, 2005.

[6] W. A. Scrivens, Y. Luo, M. A. Sutton, S. A. Collette, M. L. Myrick, P. Miney, P. E. Colavita, A. P. Reynolds, and X. Li, "Development of Patterns for Digital Image Correlation Measurements at Reduced Length Scales," *Experimental Mechanics*, vol. 47, pp. 63–77, 2007.

[7] F. D. Gioacchino and J. Q. Fonseca, "Plastic Strain Mapping with Sub-micron Resolution Using Digital Image Correlation," *Experimental Mechanics*, vol. 53, pp. 743–754, 2013.

[8] A. D. Kammers and S. Daly, "Small-scale patterning methods for digital image correlation under scanning electron microscopy," *Measurement Science and Technology*, vol. 22, 2011.

[9] M. Bourcier, M. Bornert, A. Dimanov, E. Héripré, and J. L. Raphanel, "Multi-scale experimental investigation of crystal plasticity and grain boundary sliding in synthetic halite using digital image correlation," *Journal of Geophysical Research: Solid Earth*, vol. 118, no. 2, pp. 511–526, 2013.

[10] C. V. Thompson, "Solid-State Dewetting of Thin Films," *Annual Review of Materials Research*, vol. 42, 2012.

[11] M. Bornert, F. Brémand, P. Doumalin, J. C. Dupré, M. Fazzini, M. Grédiac, F. Hild, S. Mistou, J. Molimard, J. J. Orteu, L. Robert, Y. Surrel, P. Vacher, and B. Wattrisse, "Assessment of digital image correlation measurement errors: Methodology and results," *Experimental Mechanics*, vol. 49, no. 3, pp. 353–370, 2009.

[12] P. Doumalin, "Microextensométrie locale par corrélation d ' images numériques. Application aux études micromécaniques par microscopie électronique à balayage.," PhD thesis, Ecole Polytechnique, 2000.

[13] S. P. Joshi and K. T. Ramesh, "Rotational diffusion and grain size dependent shear instability in nanostructured materials," *Acta Materialia*, vol. 56, pp. 282–291, 2008.

[14] J. H. Han and F. A. Mohamed, "Quantitative Measurements of Grain Boundary Sliding in an Ultrafine-Grained Al Alloy by Atomic Force Microscopy," *Metallurgical and Materials Transactions A*, vol. 42A, pp. 3969–3978, 2011.

[15] S. Agarwal, C. L. Briant, P. E. Krajewski, A. F. Bower, and E. M. Taleff, "Experimental validation of two-dimensional finite element method for simulating constitutive response of polycrystals during high temperature plastic deformation," *Journal of Materials Engineering and Performance*, vol. 16, pp. 170–178, 2007.

[16] K. V. Ivanov and E. V. Naydenkin, "Tensile behavior and deformation mechanisms of ultrafine-grained aluminum processed using equal-channel angular pressing," *Materials Science and Engineering A*, vol. 606, pp. 313–321, 2014.

[17] A. D. Kammers, J. Wongsa-Ngam, T. G. Langdon, and S. Daly, "The microstructure length scale of strain rate sensitivity in ultrafine-grained aluminum," *Journal of Materials Research*, vol. 30, no. 7, pp. 981–992, 2015.

[18] M. Arzaghi, C. Sarrazin-Baudoux, and J. Petit, "Fatigue Crack Growth in Ultrafine-Grained Copper Obtained by ECAP," *Advanced Materials Research*, vol. 891-892, pp. 1099–1104, 2014.

[19] T. Niendorf, F. Rubitschek, H. J. Maier, D. Canadinc, and I. Karaman, "On the fatigue crack growth-microstructure relationship in ultrafine-grained interstitial-free steel," *Journal of Materials Science*, vol. 45, no. 17, pp. 4813–4821, 2010.

[20] R. Le Hazif, P. Et-Dorizzi, and J.-P. Poirer, "Glissement {110}<110> dans les metaux de structure cubique a faces centrees," *Acta Metallurgica*, vol. 21, 1973.

[21] D. Caillard and J. L. Martin, "Glide of dislocations in non-octahedral planes of fcc metals: A review," *International Journal of Materials Research*, vol. 100, pp. 1403–1410, 2009.

[22] T. Morishige, T. Hirata, T. Uesugi, Y. Takigawa, M. Tsujikawa, and K. Higashi, "Effect of Mg content on the minimum grain size of Al-Mg alloys obtained by friction stir processing," *Scripta Materialia*, vol. 64, pp. 355–358, 2011.

Chapter 5

Modeling and simulation of the viscoplastic behaviour of CG and UFG Al 5083

5.1 Literature Review

Various models have been proposed to capture GB related mechanisms (GB sliding, GB migration, dislocation-GB interaction, grain rotation, etc). In the early 70s, the focus was mostly on creep and superplasticity, which is useful for quick plastic forming. Raj and Ashby [1] proposed an analytical model of grain boundary sliding accommodated either elastically (inducing internal back stresses that finally stop it), or by diffusion. They studied the effects of GB roughness and of the presence of particles along the GBs on their sliding "viscosity" and hence their effect on the creep rate of a polycrystal constituted of a regular array of hexagonal grains. They considered 2 types of sliding paths, saw toothed and jagged (Fig. 5.1).

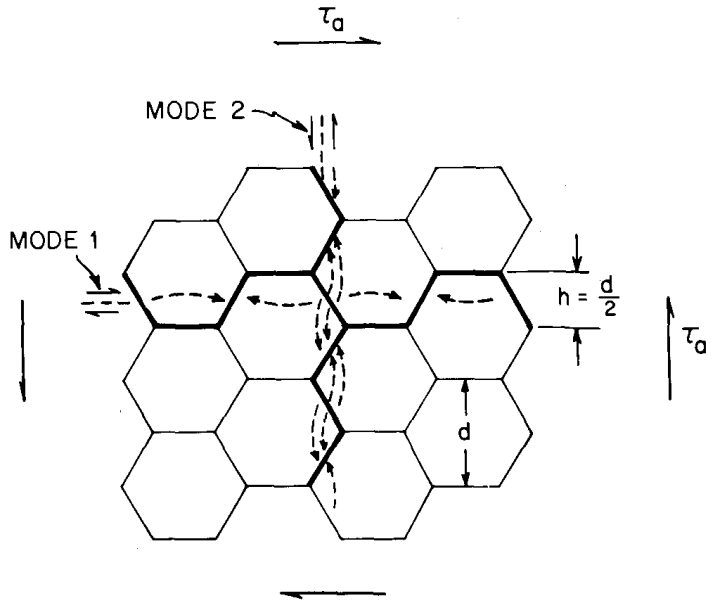

Figure 5.1: A polycrystal, idealised as an array of hexagons can deform by sliding in two orthogonal modes. Broken lines show the vacancy flux. [1]

They formulated a linear threshold-free relation between the GB sliding rate, $\dot{\gamma}$ and the applied shear stress, τ_a using a "*Newtonian viscosity*", η:

$$\dot{\gamma} = \frac{\tau_a}{\eta} \tag{5.1}$$

Their expressions for GB viscosity predicted an increase with GB roughness and the presence of particles, and was very similar to the expressions for Nabarro-Herring and Coble diffusional creep. Later, Ashby and Verral [2] focussed on the high strain regime encountered in superplasticity and introduced a GB sliding induced neighbour switching mechanism for grains, without any elongation or change in orientation (Fig. 5.2).

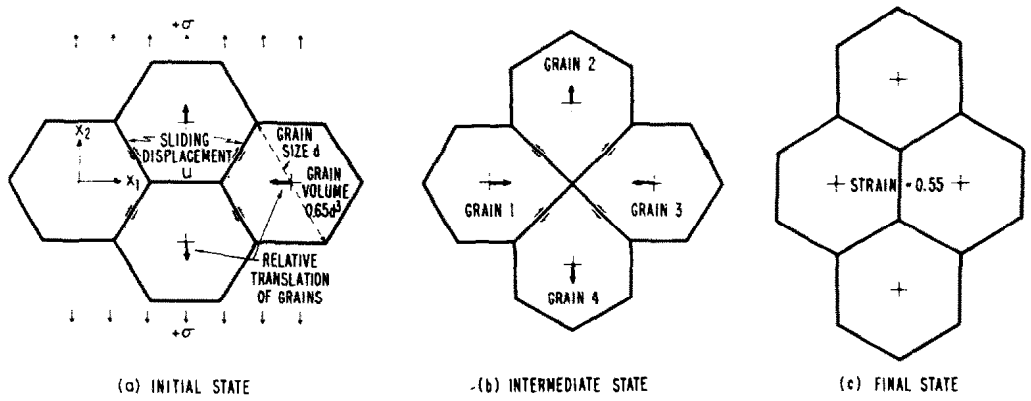

Figure 5.2: Neighbour switching mechanism as illustrated in [2]. The initial and final states of the polycrystal are thermodynamically identical, although it has suffered a true strain ϵ_0 = 0.65

They predicted a grain size-dependent evolution of the strain rate sensitivity associated with the transition from this deformation mechanism to dislocation-controlled creep as the strain rate changes (Fig. 5.3). A 2D, plane strain finite element analysis of creep with free grain boundary sliding accommodated by elastic and diffusion processes was later done by Crossman and Ashby [3]. They considered a regular array of hexagonal grains (with power law creep inside) and used the geometrical symmetries to reduce their F.E. model (Fig. 5.4). They investigated the influence of the viscous stress exponent, n inside the grains and of the strain rate on the contribution of GB sliding to the overall deformation (Fig. 5.5). For temperatures above $0.3T_M$, they predicted faster creep rates at large strains as compared to Nabarro-Herring or Coble creep which has a better agreement with the experimental data. They obtained a modified power law equation for steady state creep rate in the case of the freely sliding GBs (equation 5.2) that predicts an acceleration by a factor f, but no modification of the creep exponent, as illustrated by fig. 5.6.

$$\dot{\gamma}_A = A\left(f\frac{\tau}{\mu}\right)^n \begin{cases} f = 1 & \text{for no sliding} \\ f > 1 & \text{for freely sliding GBs} \end{cases} \tag{5.2}$$

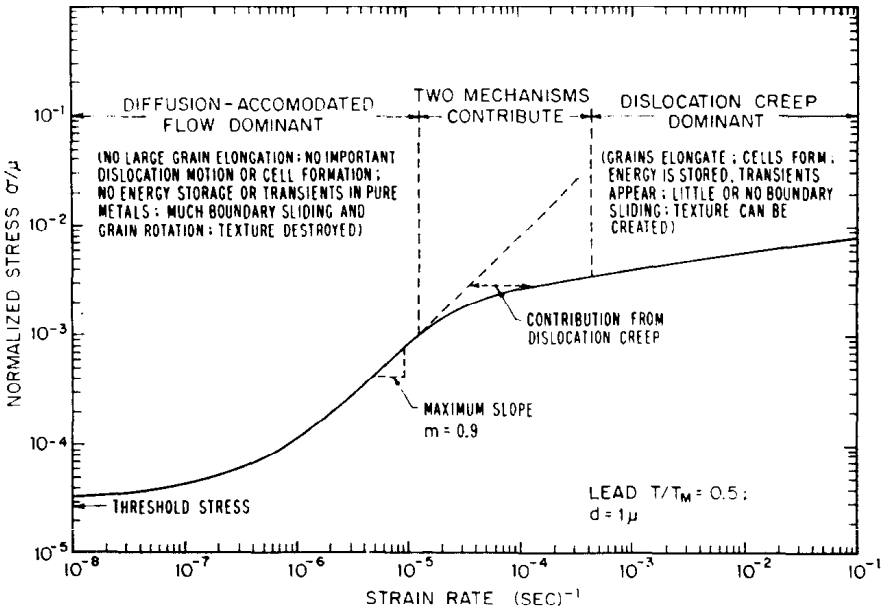

Figure 5.3: Evolution of the flow stress of a polycrystal with strain rate predicted by Ashby and Verral's model [2].

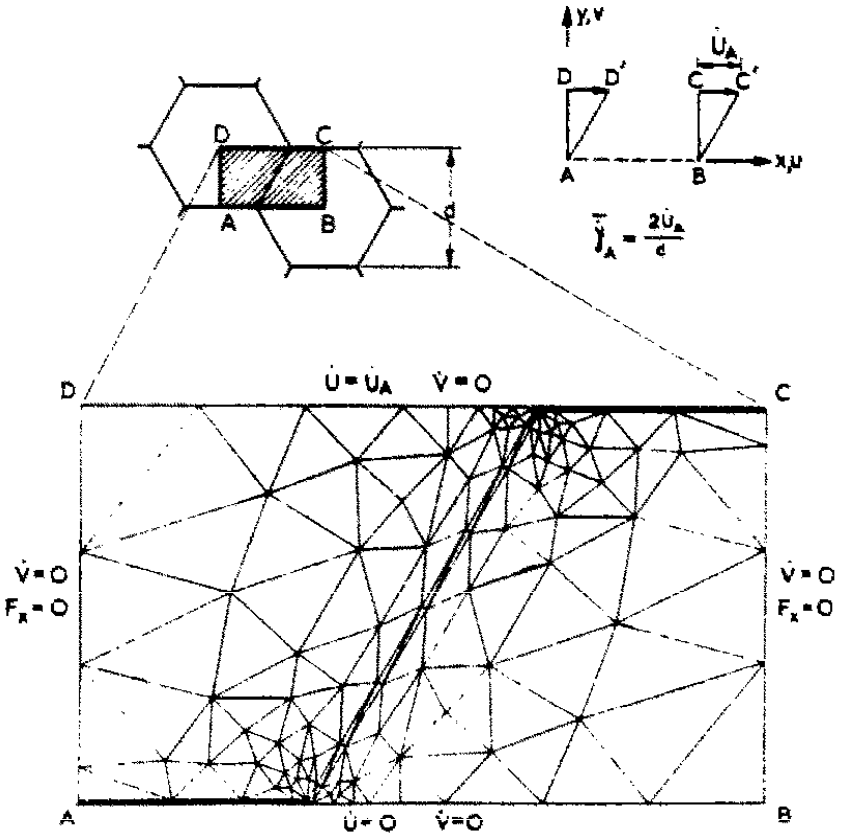

Figure 5.4: The FE model for the polycrystal used by Crossman & Ashby [3].

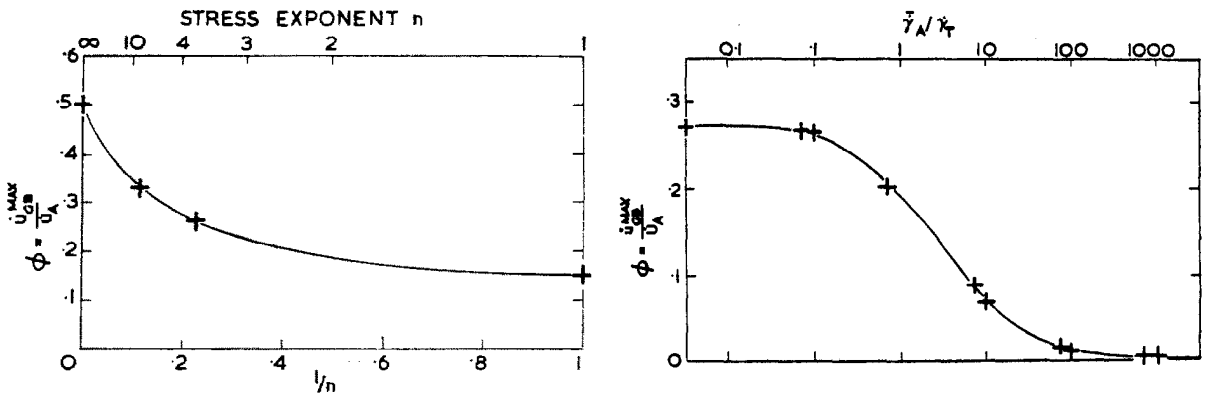

Figure 5.5: A plot of maximum contribution of GBS vs. reciprocal of stress exponent (left) and dimensionless strain-rate (right) from Crossman & Ashby [3].

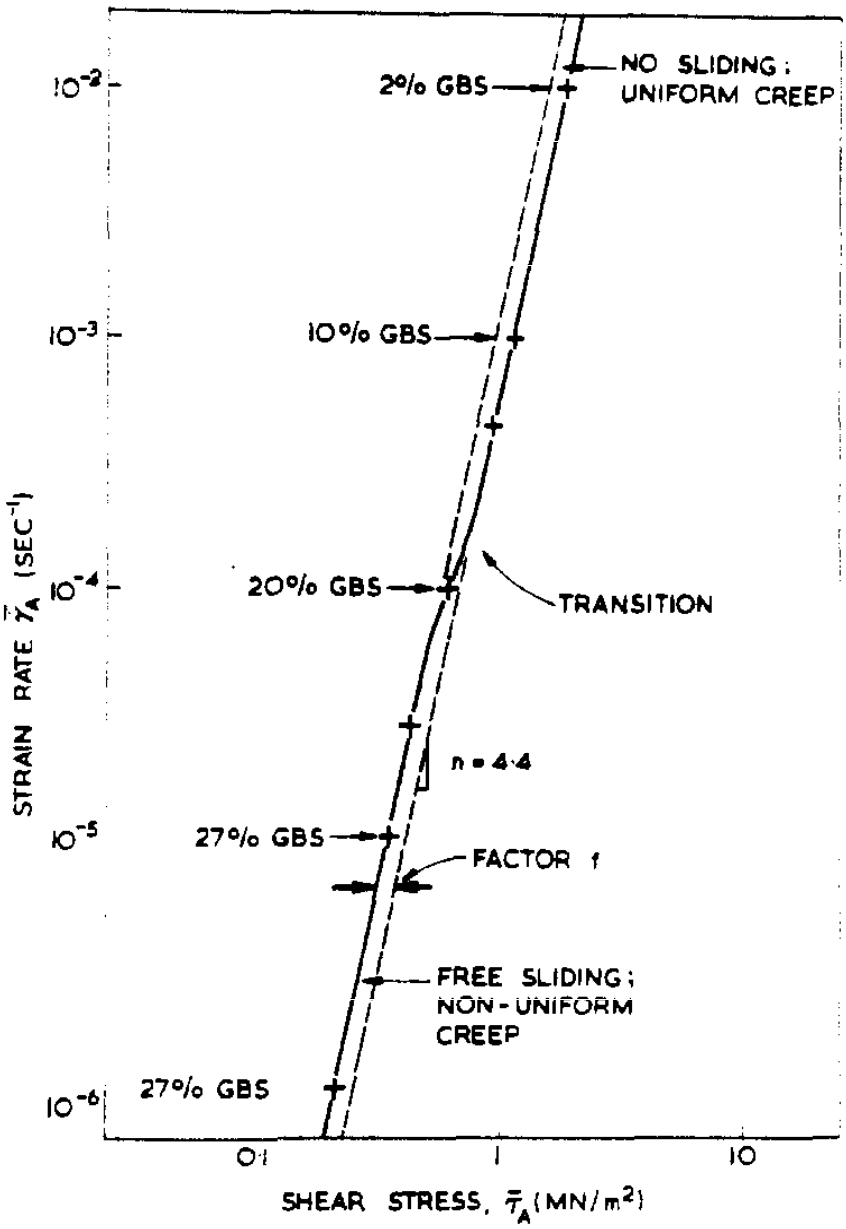

Figure 5.6: Creep rate evolution with applied stress predicted by Crossman & Ashby [3].

The 2D computational approach of Tvergaard [4], [5] in the eighties was close to that of Crossman and Ashby, but laid emphasis on the consequences of GB sliding in terms of cavities nucleation and growth along the grain boundaries normal to the tensile axis, while Hsia et al. [6] directly introduced a density, ρ of microcracks along such GBs and investigated the effect of GB sliding on the growth rate of such cracks (Fig. 5.7).

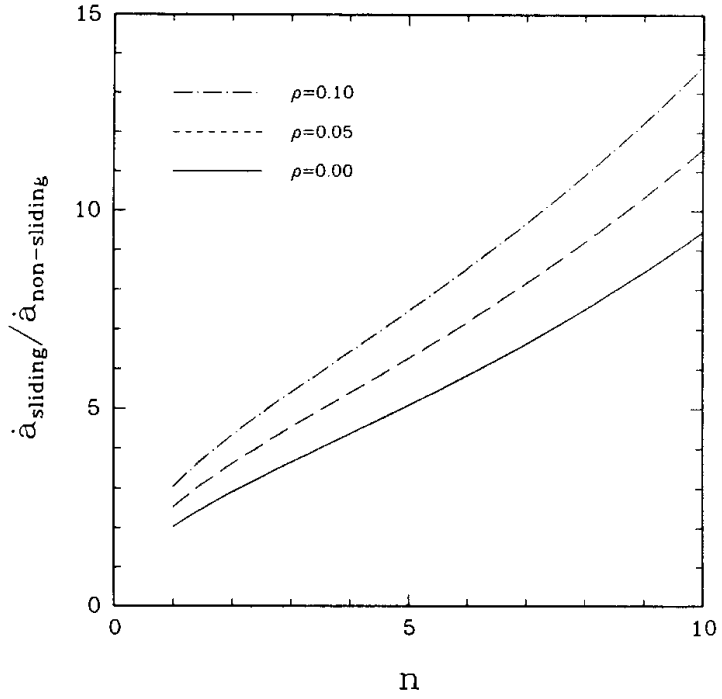

Figure 5.7: Effect of GB sliding on intergranular crack growth rate, as a function of creep exponent, n and their facet crack densities, ρ predicted by Hsia et al. [6].

All the above mentioned research was done on regular and periodic arrays of hexagonal grains. In 1996, Onck and Van Der Giessen [7] investigated the effect of (limited) microstructural variations on the creep rate of a polycrystalline aggregate with freely sliding boundaries, by slightly perturbating an initially regular array of hexagons generated by Voronoi tessellation (Fig. 5.8a) keeping the grains hexagonal. They also investigated the convergence of simulated behaviour as a function of mesh refinement (Fig. 5.8b). It was shown that the creep-rate was enhanced by up to 60% by the introduction of some microstructural irregularity due to increased GB sliding, also responsible for an increase in normal stresses on the GBs normal to the tensile axis, which is important for creep fracture.

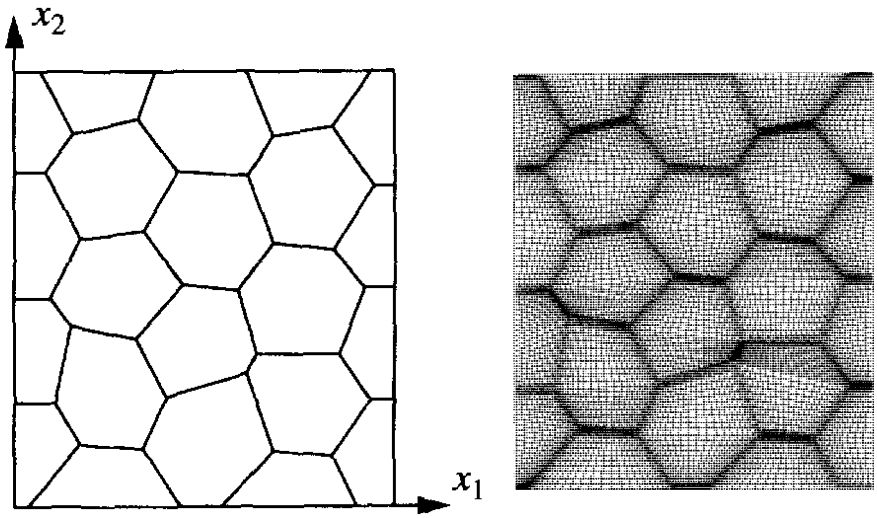

Figure 5.8: Perturbated hexagonal microstructure and the mesh used by Onck et al. [7]

Bower and Wininger [8] proposed a sophisticated 2D crystal visco-plasticity approach where, in addition to a GB sliding model quite similar to that proposed by Raj and Ashby [1], GB migration assisted by diffusion perpendicular to GB was modelled. They used a front tracking scheme and adaptive mesh generation techniques to follow the changes in grain structure. The model was applied by Agarwal et al. [9] to predict the creep behaviour and changing strain rate sensitivity of fine-grained (7-10 μm) Al5083 alloy above 450°C with a limited agreement (Fig. 5.9a), later improved by Du et al. [10] who introduced a threshold shear stress for GB sliding (Fig. 5.9b). Both studies used the same 2D C.P.F.E. model with only 18 grains (Fig. 5.10), and did not show or vary the FE mesh, nor specify how the grains orientations were assigned or varied. The lack of consideration to the representativity of the model decreases the credibility of their results. More recently, Taleff, Bower et al. [11] investigated gas pressure superplastic forming of Al5083 plates, and simulated it with a phenomenological constitutive model taking GB sliding into account. Their experiments revealed a higher creep rate under biaxial tension, which they attributed to an enhancement of of GB sliding by a positive hydrostatic pressure.

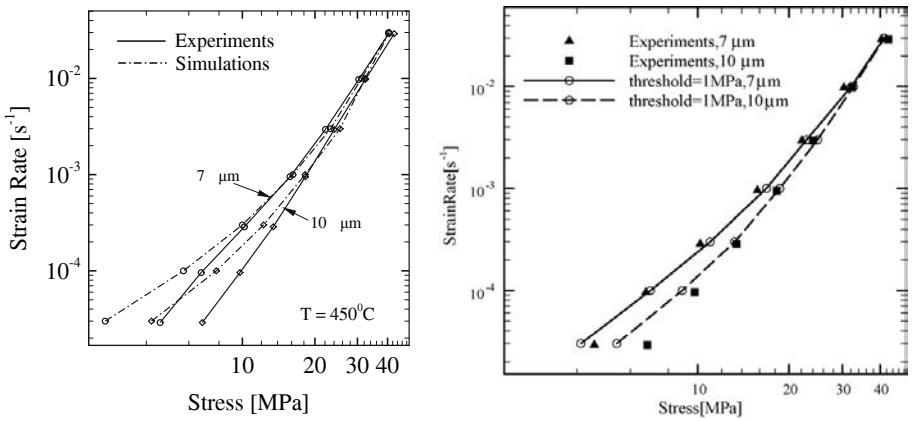

Figure 5.9: Simulated creep behaviour (a) without threshold [9] and (b) with threshold [10].

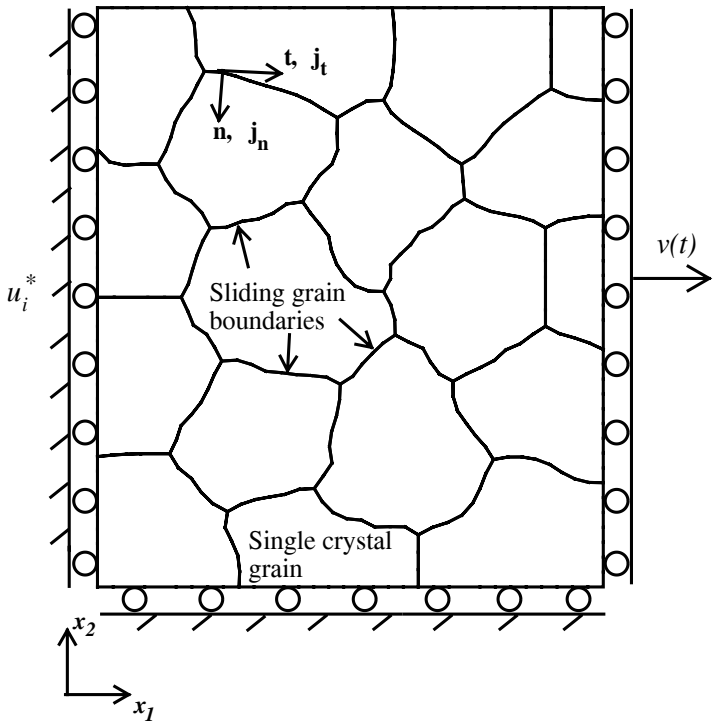

Figure 5.10: 2D C.P.F.E. model used by [9], [10]

In early 21st century, the focus of these studies shifted towards the study of grain boundary sliding in nanocrystalline (NC) or UFG materials [12]–[17].

Duhamel et al. [12] presented an analytical model based on a modified Orowan's equation to integrate grain boundary sliding, dislocation emission from the GBs and the dynamics of their "flight" accross the grains. It worked well to predict the trends in activation volume with varying temperatures (RT-120°C for pure Cu (grain size $\sim$ 100nm).

Many authors used molecular dynamics (MD) simulations to investigate GB mobility. Cheng et al. [15] modelled stress-induced GB migration for different GB structures and found that sliding and migration are coupled. Another interesting results was obtained on aluminium at 750K by Qi and Krajewski [18] who classified sliding behaviour in 3 categories depending on the applied stress: (i) at low applied stress, no sliding was observed indicating towards the existence of threshold; (ii) at intermediate stress, the amount of sliding increased linearly with time confirming the linear viscous nature of sliding GBs as described by Raj and Ashby; and (iii) at high stress, the amount of sliding increased parabolically with time (Fig: 5.11). According to the MD simulations done by Du et al. [19], the segregation of solute atoms (Mg and Si in Al5083 alloy) at GBs affects the threshold stress for GB sliding. These atomic simulations, provide interesting results regarding the qualitative behaviour of these GB deformation mechanisms and their variations from one type of GB to another. But it is nearly impossible to get any quantitative data since the simulations are run at nano-scales and pico-seconds time scales. Moreover, such analysis can only be done for a limited number of GB configurations and generally includes only two neighbouring grains, without any triple point, as in a polycrystal. A nice solution for scale transition might be that adopted by Warner et al. [20] to perform "atomistics-informed" crystal plasticity simulations, with GB constitutive equations derived from prior MD simulations.

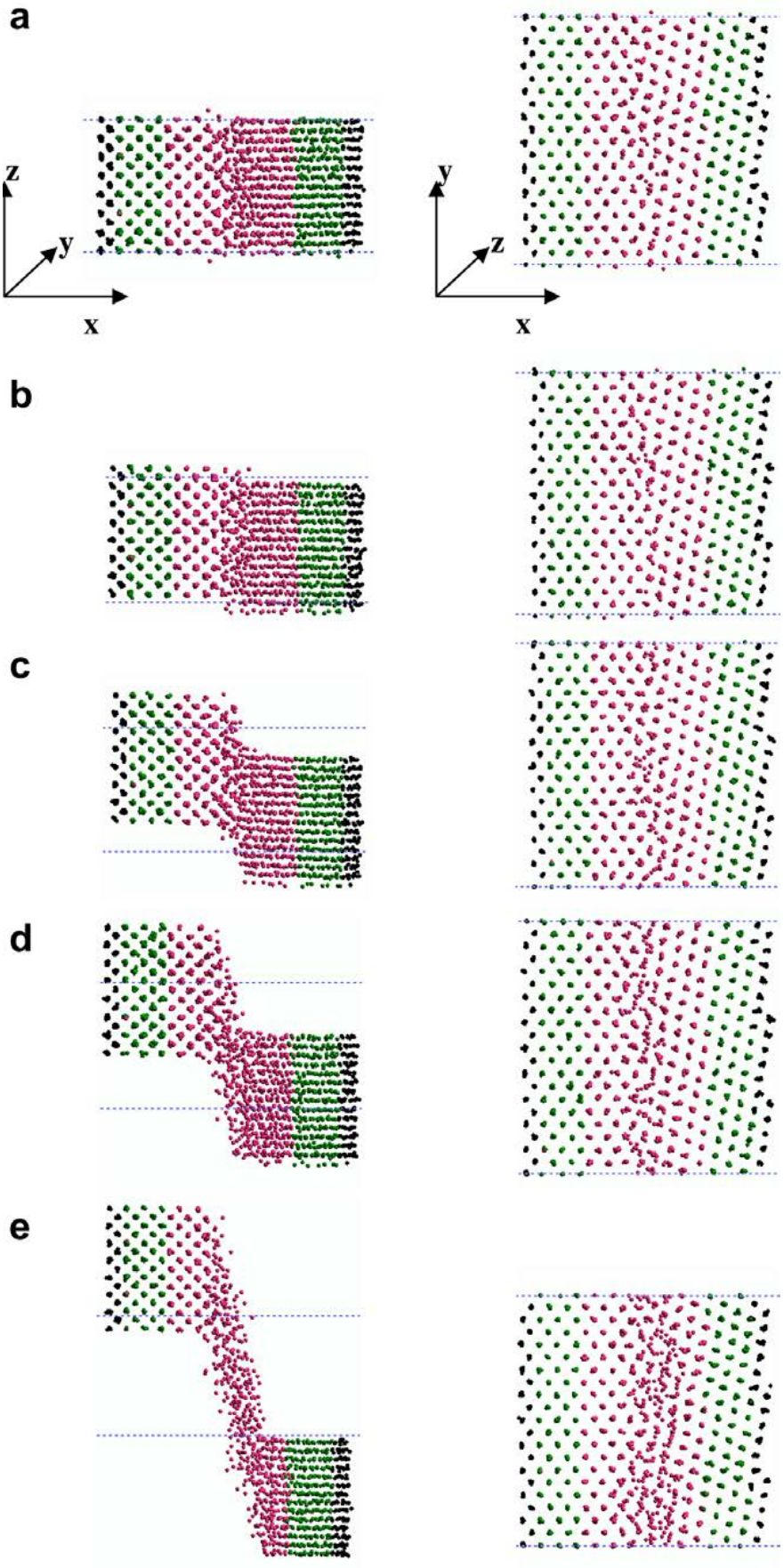

Figure 5.11: Atomistic simulations of GB sliding by Qi & Krajewski [18]

In a very ambitious study, Ahmed et al. [14] coupled 2D discrete dislocation dynamics and diffusion kinetics to model dislocation-induced GB sliding in UFG copper. The modelling cell was constituted of 4 hexagonal grains (with periodic boundary conditions) (Fig. 5.12) and 2 types of GBs were considered- one that acts as impenetrable barrier and the second that adsorbs dislocations.

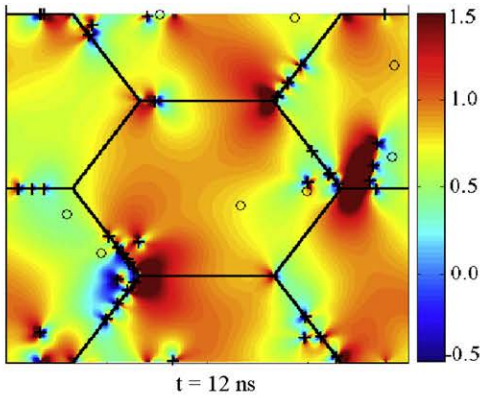

Figure 5.12: 2D model constituting 4 hexagonal grains used by Ahmed et al. [14] and superimposed tensile stress in the loading direction induced by discrete dislocations.

In the second case, they split the lattice dislocation into two components, one with the Burgers vector parallel (dislocation glide along GB, thus inducing GB sliding) and one with the Burgers vector orthogonal to the GB (dislocation climb). They obtained grain size and temperature-dependent predictions of the contribution of GBS (Fig. 5.13) and of the SRS (Fig. 5.14). They finally concluded that the dynamic recovery processes at GBs and GB diffusion are the rate-limiting processes during plastic deformation of UFG metals. A somewhat similar approach regarding decomposition of lattice dislocations at GBs was used by Shi and Zikry [17] but they rather used a dislocation density-GB interaction scheme (Fig. 5.15) instead of discrete dislocation dynamics and they made this interaction dependent on neighbouring grain misorientations. Their model considered regular arrays of hexagonal grains. Let us note that, as for the work of Bower et al. [8]–[11] or Ahmed et al. [14], the enrichment of the model with physical mechanisms comes at the expense of the description of the polycrystalline microstructure and its variability.

Another strategy is to use self-consistent models as described by Jiang & Weng [21], Benkassem, Capolungo et al. [22], [23] or Ramtani et al. [24] where the polycrystalline material is modelled as a three phase material: 1. inclusion phase representing grain cores with a crystal plasticity behaviour or a continuum law based on dislocation densities, 2. an amorphous and very thin coating phase representing GBs and 3. a homogeneous equivalent medium around the coated inclusion (Fig. 5.16). The proportions of these phases determines the mean grain size. Even though the micromechanical models proposed by Jiang and Weng [21] and used by Ramtani et al. [24] or Benkassem [22] conside perfect interfaces and thus do not explicitly include GB sliding but only "GB mediated plasticity", they are quite efficient in capturing the effect of grain size on the yield stress predicted to follow the Hall-Petch law down to a critical

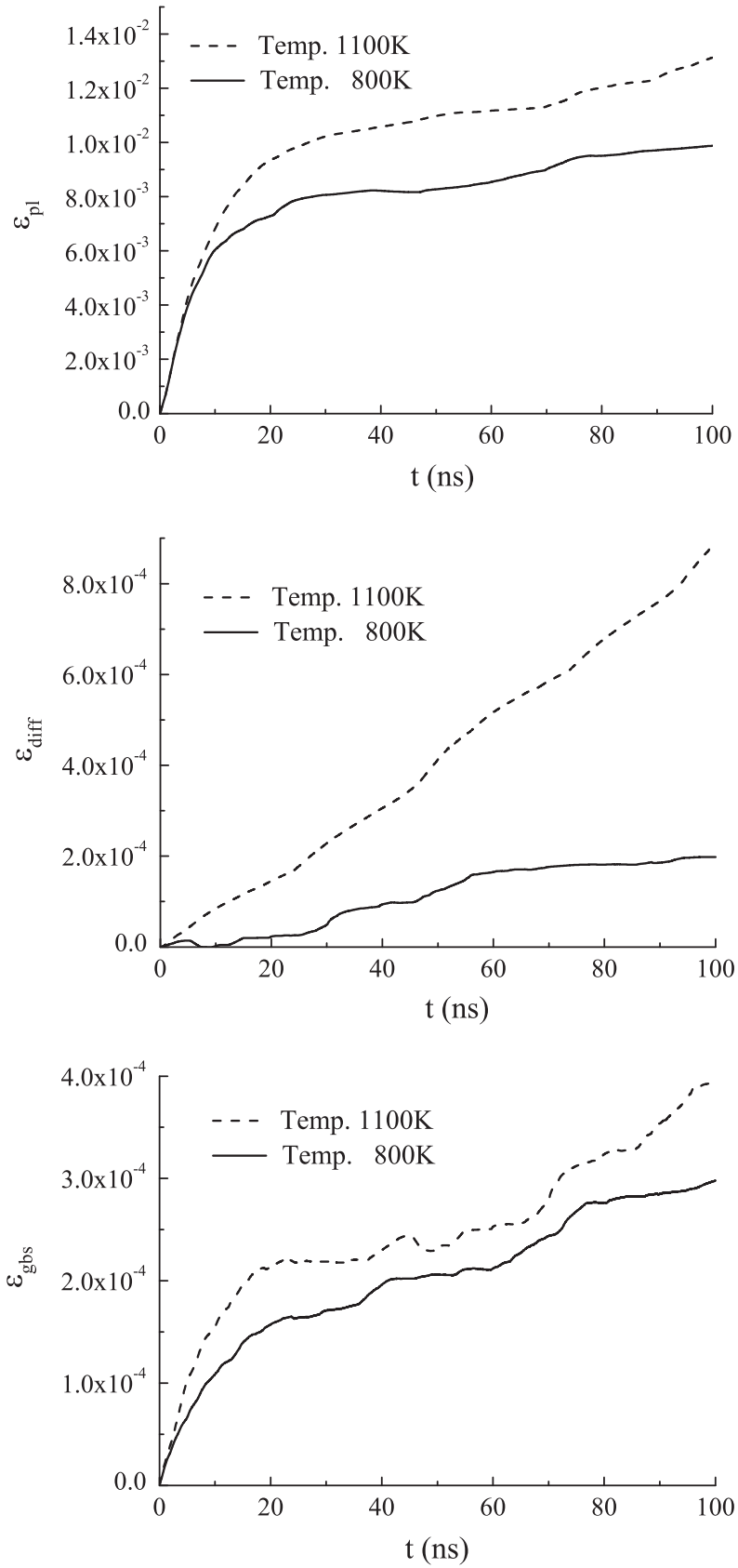

Figure 5.13: Time evolution of total plastic strain (top), strain caused by diffusion (middle) and strain produced by GBS (bottom) in 300nm grain-sized material [14].

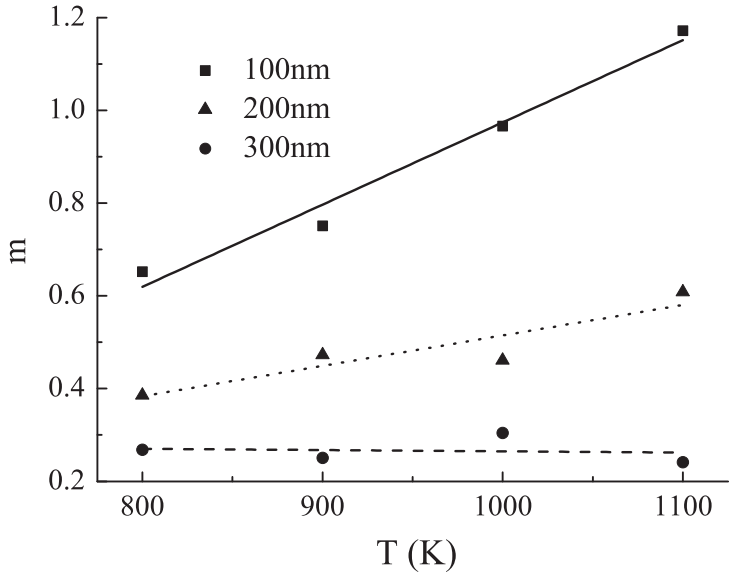

Figure 5.14: Temperature dependence of strain-rate sensitivity m for different grain sizes [14].

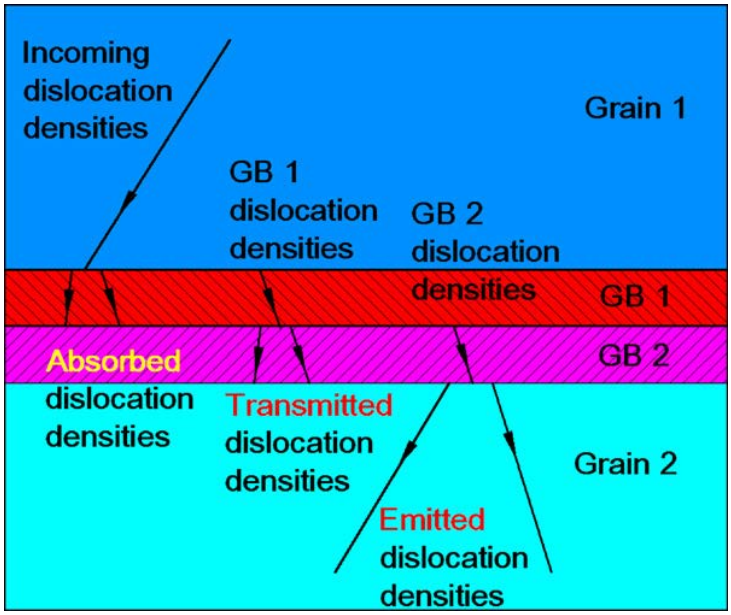

Figure 5.15: The dislocation–density grain boundary interaction (DDGBI) scheme [17].

grain size, followed by a breakdown of this law. Capolingo et al. [23] proposed a more advanced modelling technique with imperfect interfaces to explicitly model GB sliding, using the stick-slip mechanism predicted by MD simulations and mentioned by Warner et al. [20]. A limitation is that these models require 10 times more computation time that phenomenological models.

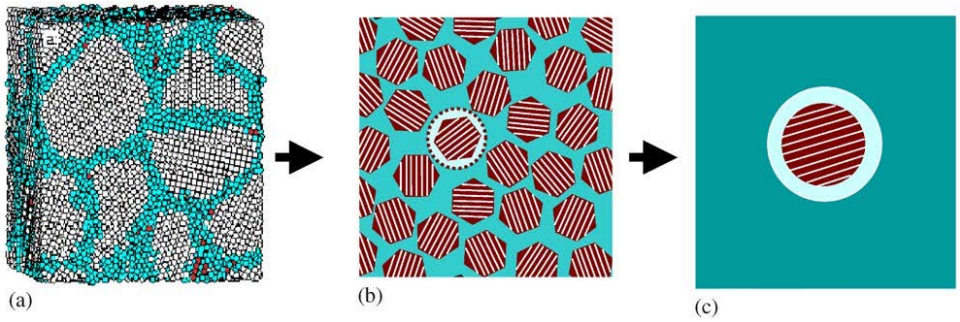

Figure 5.16: A rationale for the generalised self-consistent polycrystal model.

All previous models were two-dimensional, but 3D models have also been proposed, mostly to investigate intergranular damage and fracture after some opening or sliding displacement, using either a layer of elements with a viscous-damageable behaviour, like Musienko and Cailletaud [25] or cohesive elements like [26]–[28]. Cohesive models use traction-separation and shearing-sliding responses (Fig. 5.17). The use of cohesive elements permits a progressive softening of GB prior to decohesion or free sliding. Benedetti et al. [29] proposed a 3D crystal plasticity model with a cohesive frictional GB formulation for small strains. However it requires powerful computational resources especially considering the number of grains required to model a representative volume, with a representative texture. In addition, El Shawish et al. [30] questioned the accuracy of cohesive elements at GBs, specially in plastic regime. The accuracy of cohesive elements was found specially low close to triple lines and did not improve with mesh refinement. Since the analysis was done on microstructures generated using Voronoi tessellation (=straight boundaries and thus sharp edges) and on real microstructures obtained using 3D-EBSD (=rough boundaries), the authors partially attribute the scatter on computed macroscopic stress to GB roughness.

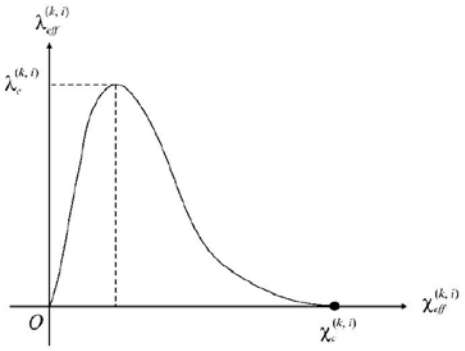

Figure 5.17: Cohesive zone model: a typical effective traction–displacement relation [27].

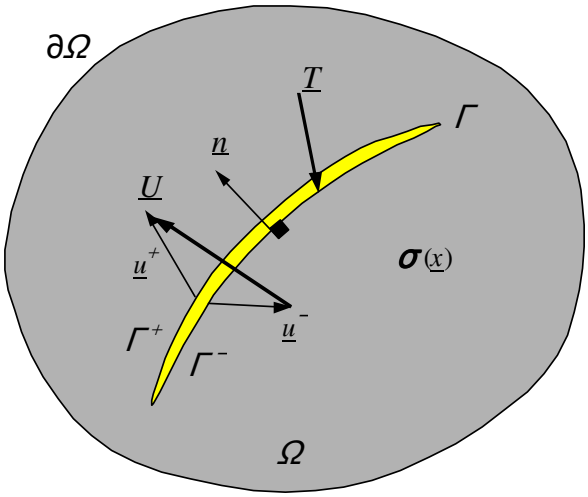

Figure 5.18: Displacement discontinuity at the grain boundary [31].

5.2 Aim and principle of the present model

As shown in previous chapters, at high temperatures, grain boundary sliding is an important mechanism contributing to the deformation of both CG and UFG Al5083. This calls for a model significantly different from conventional continuum plastic flow or crystal plasticity. The aim of these simulations is to capture the mechanical behaviour of both CG and UFG materials within the same framework (allowing some parameters to differ). The tensile and relaxation tests presented in chapter 2 are simulated for both the materials to capture the macroscopic response specially regarding the observed transition from harder to softer UFG material as a function of temperature and strainrate. The same model will later be used for a qualitative investigation of local phenomena described in chapter 3 like cooperative GBS, grain rotation, or grain shape/GB orientation effects.

To model the GBS effect on viscoplastic behaviour of CG and UFG alloy, a 2D finite element model with viscoplastic behavior for the matrix and elastic-viscous sliding interfaces is adopted. The DISROC FE code used for this simulation (thanks to Amade Pouya from Laboratoire Navier, IFSTAR, Ecole des Ponts) was initially developed to deal with multiple fractures in rock masses which in our belief bears some similarities with the deformation of a polycrystalline material with sliding grain boundaries. In both cases, the macroscopic strain sees the contributions from the matrix and from the displacement jump across the grain boundary (Fig.5.18) and can be described as follows [31]:

$$\mathbf{E} = \frac{1}{V}\left[\int_{\Omega} \epsilon \, dv + \sum_{k} \int_{\Gamma_k} \frac{1}{2} \left(\underline{U} \otimes \underline{n} + \underline{n} \otimes \underline{U}\right) \, ds\right] \tag{5.3}$$

A 2D model where the solid is idealised as a collection of polygonal blocks ("grains") with continuum viscoplastic behaviour, and straight-lines as grain boundaries is chosen, not only for its simplicity, or to reduce the computational cost, but for several

additional reasons listed below. First, since a 2D approach is used, only "degenerate" crystal plasticity (with slip directions all lying in the same plane, and particular misorientations at the grain boundaries) and thus a non representative texture would have to be used. Second, to avoid drawing non general conclusions from simulations run on specific, arbitrary-selected grain orientation sets, it would be necessary to repeat the simulations with various orientations. Third, at high temperature, cross-slip and dislocation climb become increasingly frequent, which is difficult to account for in a crystal plasticity model, not to mention the chance of non-octahedral slip. Finally, the investigated material has a weak elastic and plastic anisotropy, and thus limited grain-to-grain compatibility stresses that do not play a dominant role in GB sliding. Considering all these arguments, crystal plasticity is not "the perfect" solution for the present study. The "grains" are thus considered homogeneous with an isotropic viscoplastic behaviour. The pronounced texture of the ECAPed material and its mechanical anisotropy are not modelled, but the main aim of these simulations is to capture the unidirectional response only. To further simplify the model, the presence of the large second phase particles, and the dispersoids is ignored.

5.3 Detailed description of the model

5.3.1 Constitutive model for the grain interior

Based on the assumption of additive strain rates, the total strain rate inside a grain, $\dot{\epsilon}_g$, is defined as:

$$\dot{\epsilon}_g = \dot{\epsilon}_{el,g} + \dot{\epsilon}_{p,g} + \dot{\epsilon}_{v,g} \tag{5.4}$$

where $\dot{\epsilon}_{el,g}$, $\dot{\epsilon}_{p,g}$ and $\dot{\epsilon}_{v,g}$ respectively are the elastic, plastic and viscous strain rates of that grain.
As shown in the previous chapter, the Young's modulus of this material is highly temperature dependent and will be denoted by $E(T)$. Poisson's ratio, ν will be assumed to remain constant.
An isotropic strain hardening model is chosen. In spite of its strong contribution to the flow stress, kinematic hardening is deliberately ignored, for the simplicity of the model. This simplification has no or very little impact, because no stress reversal is simulated and since the stress drop during relaxation is not sufficient to trigger reverse plastic flow. Voce type hardening function is adopted for the isotropic stress variable R_i (equation 5.5).

$$R_i = R_0 + Q\left(1 - e^{-b\epsilon_{p,g}}\right) \tag{5.5}$$

where R_0, Q and b are material constants. In addition, even though our UFG material is highly anisotropic, Von-Mises yield criterion is chosen because the focus of the current simulations is on unidirectional tests only. The yield function is described in equation 5.6.

$$F(\sigma, R_i) = \sqrt{3J_2(\sigma)} - R_i = 0 \tag{5.6}$$

The viscous strain inside the grains is calculated using a standard Arrhenius-type equation with power law in effective stress as follows:

$$\dot{\epsilon}_{v,g} = a\left(\sigma - \sigma_0\right)^n, \qquad a = A\frac{1}{E(T)^n} exp\left[\frac{-Q}{RT}\right] \tag{5.7}$$

$$\sigma_0 = B \cdot exp\left[\frac{Q_{thresh}}{RT}\right] \tag{5.8}$$

where σ_0 is the threshold stress, Q and Q_{thresh} are the activation energies for creep and threshold stress respectively, n is the stress exponent, A and B are material constants and R is the universal gas constant.

5.3.2 Constitutive model for the grain boundaries

The ECAPed material has plenty of LAGBs that are less likely to slide than HAGBs. This is also the case for GBs with or without particles. Ideally, a stochastic model should be used, but at that stage, the grain boundaries are all treated the same.

The displacement rate at the grain boundaries, $\underline{\dot{U}}$ has 2 components, elastic, $\underline{\dot{U}}^e$ and viscous, $\underline{\dot{U}}^v$ and the stress is related to the elastic stiffness, K defined as follows

$$\underline{\dot{U}} = \underline{\dot{U}}^e + \underline{\dot{U}}^v \tag{5.9}$$

$$\underline{\sigma} = \mathbf{K}(\underline{U} - \underline{U}^v), \qquad \begin{pmatrix}\tau\\ \sigma\end{pmatrix} = \begin{bmatrix}K_t & K_{tn}\\ K_{nt} & K_n\end{bmatrix}\begin{pmatrix}U_t - U_t^v\\ U_n - U_n^v\end{pmatrix} \tag{5.10}$$

Here, t and n respectively represent tangential and normal directions to the GB. For the current simulations, we did not introduce any coupling and hence $K_{nt} = K_{tn} = 0$. To limit the inter-penetration of the two grains in case of normal compression, a hyperbolic expression (equation 5.11) is adopted for the normal stiffness, K_n.

$$K_n = \frac{k_0}{1 + U_n/e} \tag{5.11}$$

The closure displacement in this case is limited by the initial(purely computational) "thickness", e of the interface. It is taken to be 1% of the simulation box size. The normal stiffness, K_n will approach infinity when the closure displacement, U_n tends to $-e$ (Fig. 5.19). The normal stress, σ_n will be proportional to the normal displacement for small openings (with a proportionality constant k_0) and will saturate at $k_0 e$ for positive great openings (never reached in our simulations). In order not to modify the global elastic behaviour due to the presence of elastic GBS, the GB elastic stiffness parameters, k_0 and K_t are not independent parameters but are related to Young's modulus, $E(T)/e$ and to the shear modulus, $\mu(T)/e$ respectively.
For the viscous part, normal creep is suppressed and only sliding is considered to avoid decohesion. Various authors propose different constitutive relationship for the

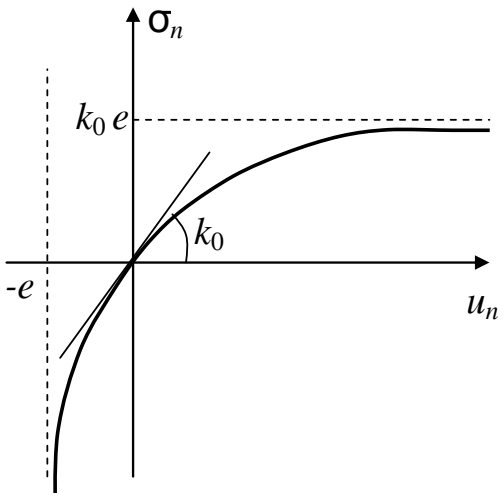

Figure 5.19: Hyperbolic normal elasticity.

GB sliding rate. As discussed above, MD simulations by Qi and Krajewski [18] confirm the linear relationship with the shear stress provided by Raj and Ashby (Equation 5.1), while Gouissem et al. [32] propose a hyperbolic sine function, which for low stresses can be approximated by a linear function. As predicted by the MD simulations [18], [19] and from TEM observations [33], a temperature dependent threshold (the same for all GBs, at that stage) is introduced, i.e. the sliding rate is supposed to be zero if the shear stress does not reach the temperature dependent threshold, τ_c and is proportional to the net shear stress otherwise.

$$U_n^v(t) = 0 \tag{5.12}$$

$$U_t^v(t) = b_t \langle |\tau| - \tau_c \rangle t \tag{5.13}$$

To take into account the thermally activated nature of GB sliding, an Arrhenius type expression inspired from Raj and Ashby [1] and Agarwal et al. [9], is assumed for the proportionality constant, b_t (equation 5.14).

$$b_t = \frac{\Omega \eta_0 exp(-Q_{GBs}/kT)}{kT} \tag{5.14}$$

Here, Ω, η_0, Q_{GBs} and k are the activation volume, characteristic sliding velocity, activation energy for GBS and Boltzmann constant, respectively.

5.3.3 Mesh generation and boundary conditions

Different microstructures are randomly generated using 2D Voronoi tessellation. In this technique, a given number of points (called seeds) are randomly generated in a given domain. Each seed is later bounded with lines such that every point within that region is closest to that seed than to any other. The mean grain size, d_{grain} (or equivalently the line density of grain boundaries) is controlled by the model size (or Area of the box,

A_{box}) and the number of grains, N (equation 5.15) and is taken from experiments to be 77 μm and 300 nm for CG and UFG materials, respectively.

$$d_{grain} = \sqrt{A_{box}/N} \tag{5.15}$$

Fig.5.20 represents the applied boundary conditions and loadings for the model. The bottom left corner node is pinned and the vertical displacement of the bottom line is zero. A constant vertical displacement rate, $\dot{u}_y$, corresponding to a constant global strain rate, $\dot{u}_y/L$ is imposed at the top line, to simulate tensile tests, while a constant vertical displacement, corresponding to a fixed strain, is applied on the top surface, to simulate stress relaxation. Due to the unavailability of periodic boundary conditions in the Disroc FE code, the left and right borders are just kept as free surfaces.

One of the short comings of this model is that the motions of GBs cutting a side surface are unconstrained and thus are more pronounced than for GBs ending inside the model. When the number of grains is small, these GB displacements are not negligible and have a significant effect on the displacement field, but it will be shown below that this artefact gets smaller and smaller as the number of grains increases.

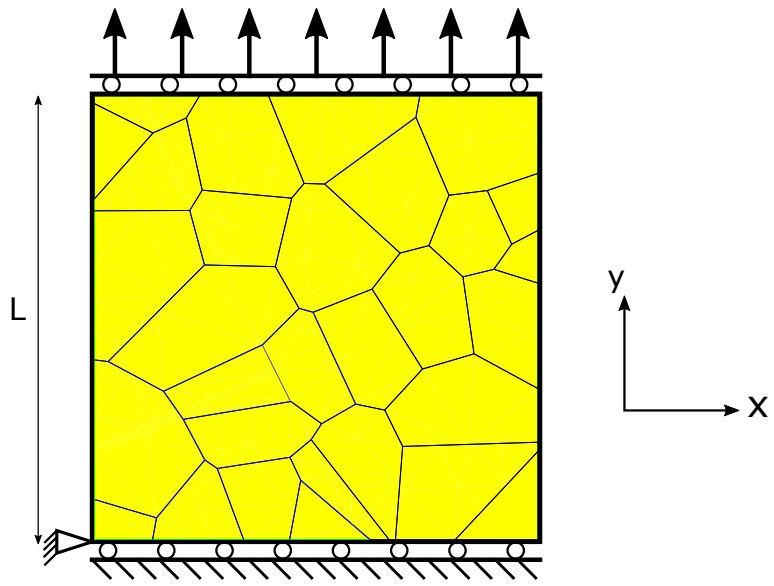

Figure 5.20: A schematic of the 2D model used for the simulations.

A 2D mesh with linear triangular elements (T3) for the grains and linear quadilateral elements(Q4) for the grain boundaries is chosen. Different mesh refinement ratios are examined for a microstructure with 15 grains in a $1 \times 1 \mu m^2$ simulation box until a convergence of the simulated stress-strain curves during a tensile test run at $5 \times 10^{-3} s^{-1}$ until 15% strain is achieved. Table 5.1 presents the details of the examined meshes shown in Fig. 5.21.

It was observed that the mesh refinement at the grain boundaries plays an important role, while mesh refinement inside the grains did not change the macroscopic

response. Furthermore, using an approximately 1.5 times coarser mesh for the grains core reduced the computation time by a factor of 2.4 (Fig. 5.22a, 5.22b). At the microscale, as shown on (Fig. 5.22c), refining the mesh at GBs leads to an increase in the contribution of GBS to the total strain which reaches a stable value, instead of decreasing with further strain as with coarser meshes.

Finally, a uniform mesh (mesh-1 with 0.03μm sized elements for GBs and 0.03μm sized elements for grain core in the present case, or 3% of the simulation box edge size, in general) is chosen for the identification purposes while post-identification analyses is done on mesh-4 with 0.01μm sized elements (1% of the box edge) for GBs and 0.05μm sized elements (5% of the box edge) for grain core.

	Mesh 1	**Mesh 2**	**Mesh 3**	**Mesh 4**	**Mesh 5**
Mesh type	uniform	non-uniform	non-uniform	non-uniform	non-uniform
Element size*					
GBs:	0.03	0.01	0.005	0.01	0.003
Grain core:	0.03	0.03	0.03	0.05	0.06
Mean no. of elements per GB	9	28	56	28	93
Calculation time	2.8 hrs	13.2 hrs	35.6 hrs	5.5hrs	53.7 hrs

Table 5.1: Mesh characteristics of simulated microstructures (Element size is indicated as a fraction the simulation box edge length)*

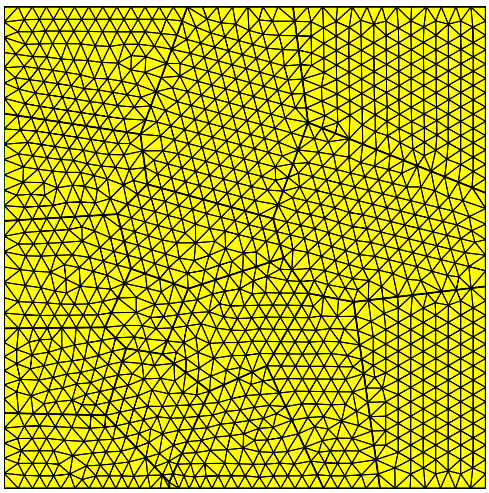

(a) Mesh-1

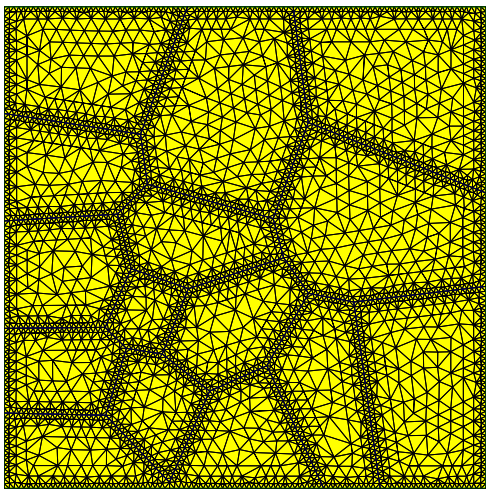

(b) Mesh-2

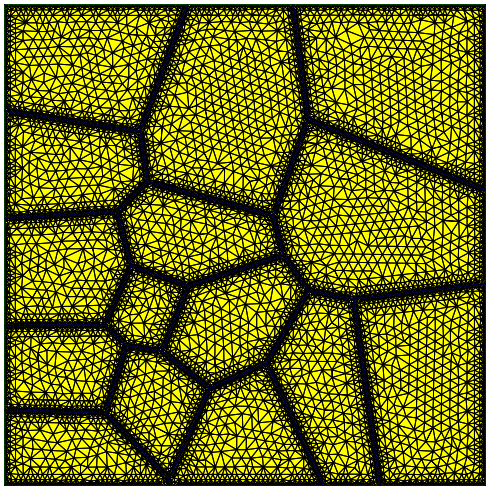

(c) Mesh-3

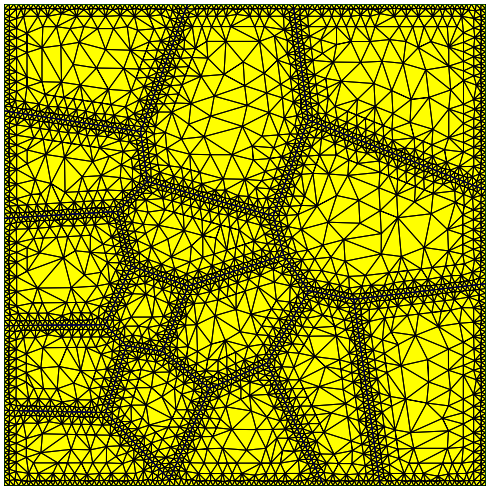

(d) Mesh-4

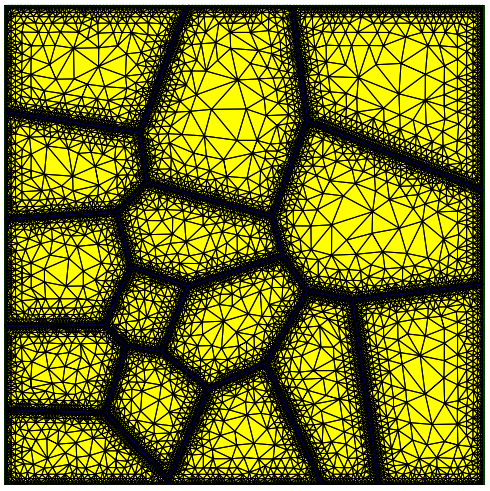

(e) Mesh-5

Figure 5.21: Meshes used for the convergence study with mesh refinement

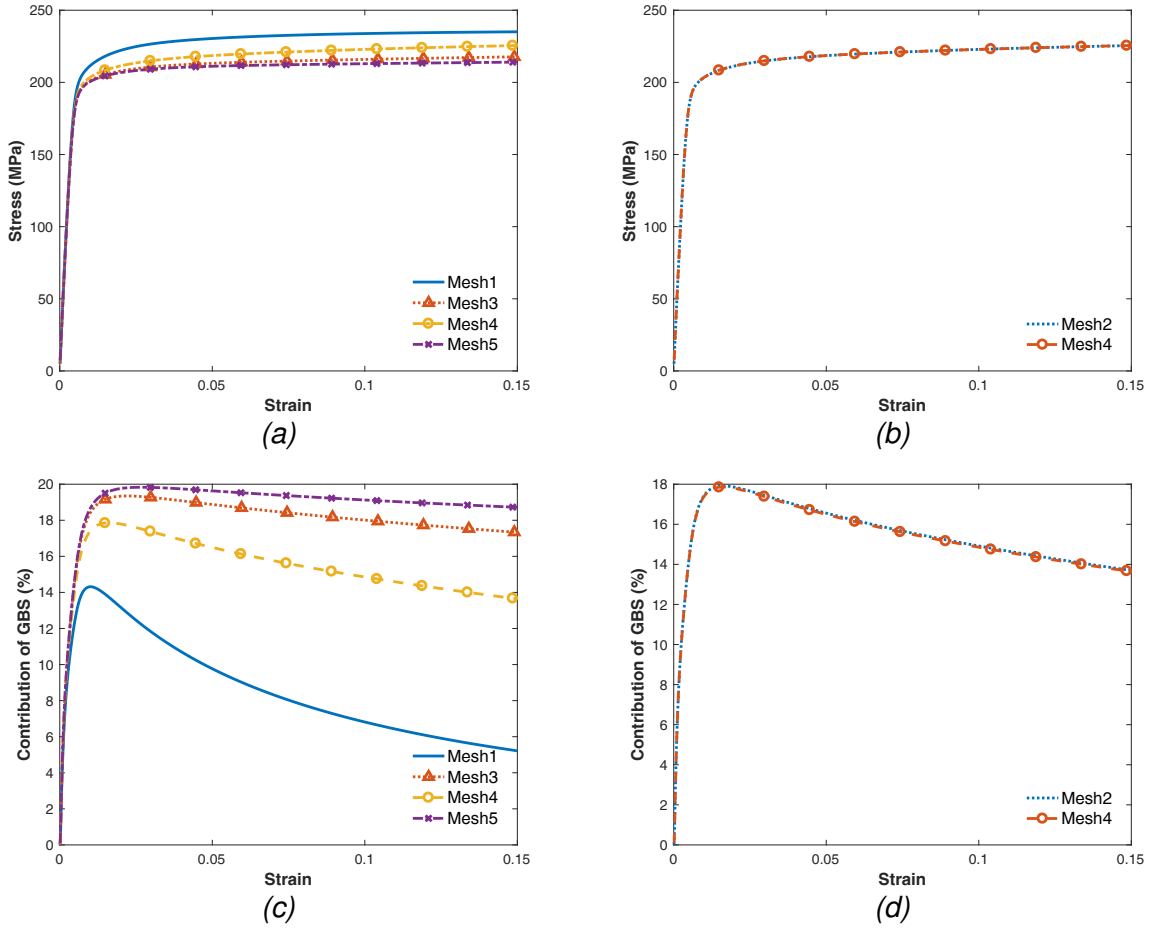

Figure 5.22: Macro and micro scale convergence with mesh refinement at GBs (a, c) and grain interior (b, d)

5.3.4 Determination of a representative volume element (RVE)

The question of the ideal size of the RVE remains a very tricky but central question when dealing with mechanics of any polycrystaline material whose microstructure is characterised by a variety of parameters such as the grain size, shape, orientation of the longest axis.

To determine the optimum number of grains required in the simulation box, so as to get rid of the scatter from one randomly-generated microstructure to the other in terms of global stress-strain behaviour, keeping the computation time reasonable, 5 different microstructures each with 15, 22 and 30 grains of similar grain size ($\sim 270nm$) are generated (Fig. 5.23). The cumulated GB length projected on the planes of maximum shear ($\pm 45^{\circ}$ to the tensile axis), their surface density and their fraction of the total GB length is described in table 5.2.

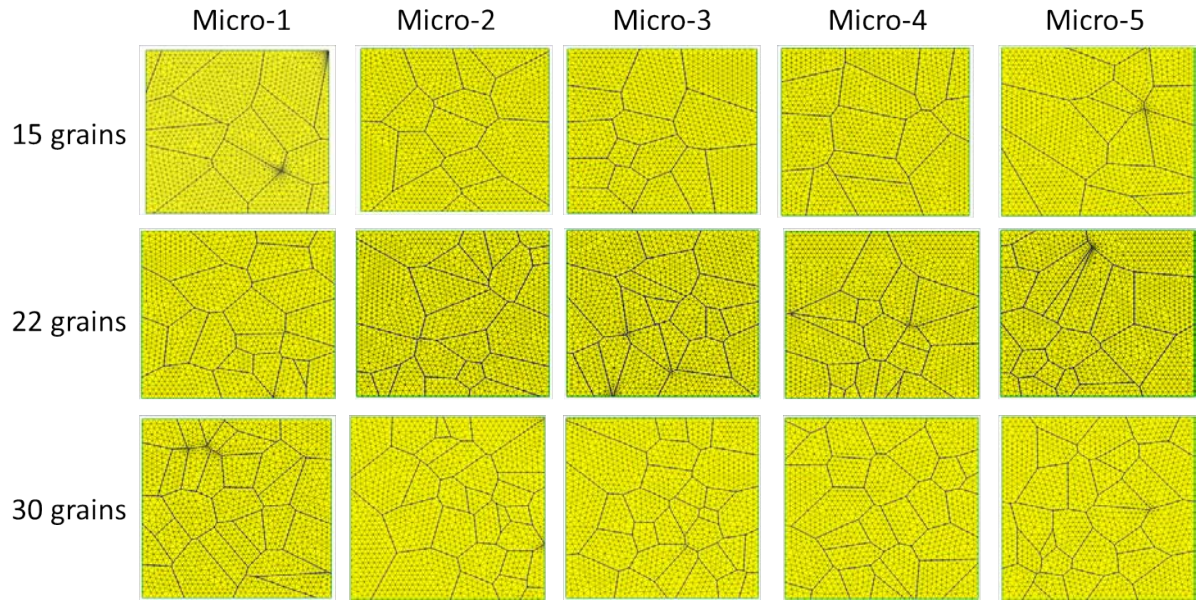

Figure 5.23: Simulated microstructures with 15 (top), 22 (middle) and 30 (bottom) grains.

Model	Number of grains	Surface line density of GBs along max. shear dir^n (μm^{-1})	Fraction of total GB length along max shear dir^n (%)
1	15	4.34	71
2	15	4.15	72
3	15	2.83	52
4	15	3.02	52
5	15	3.68	62
6	22	3.52	59
7	22	3.78	64
8	22	3.84	62
9	22	3.46	61
10	22	4.03	66
11	30	4.13	62
12	30	3.66	61
13	30	3.66	61
14	30	4.13	67
15	30	4.03	65

Table 5.2: Characteristics of simulated microstructures

A tensile test until 15% strain at $5 \times 10^{-3} s^{-1}$ is simulated for all the generated microstructures using the same parameters provided in table 5.3. The simulated stress-strain curves of the set of 5 different microstructures for the same number of grains, as well as the evolution of the contribution of GB sliding to the global strain are compared in fig. 5.24.

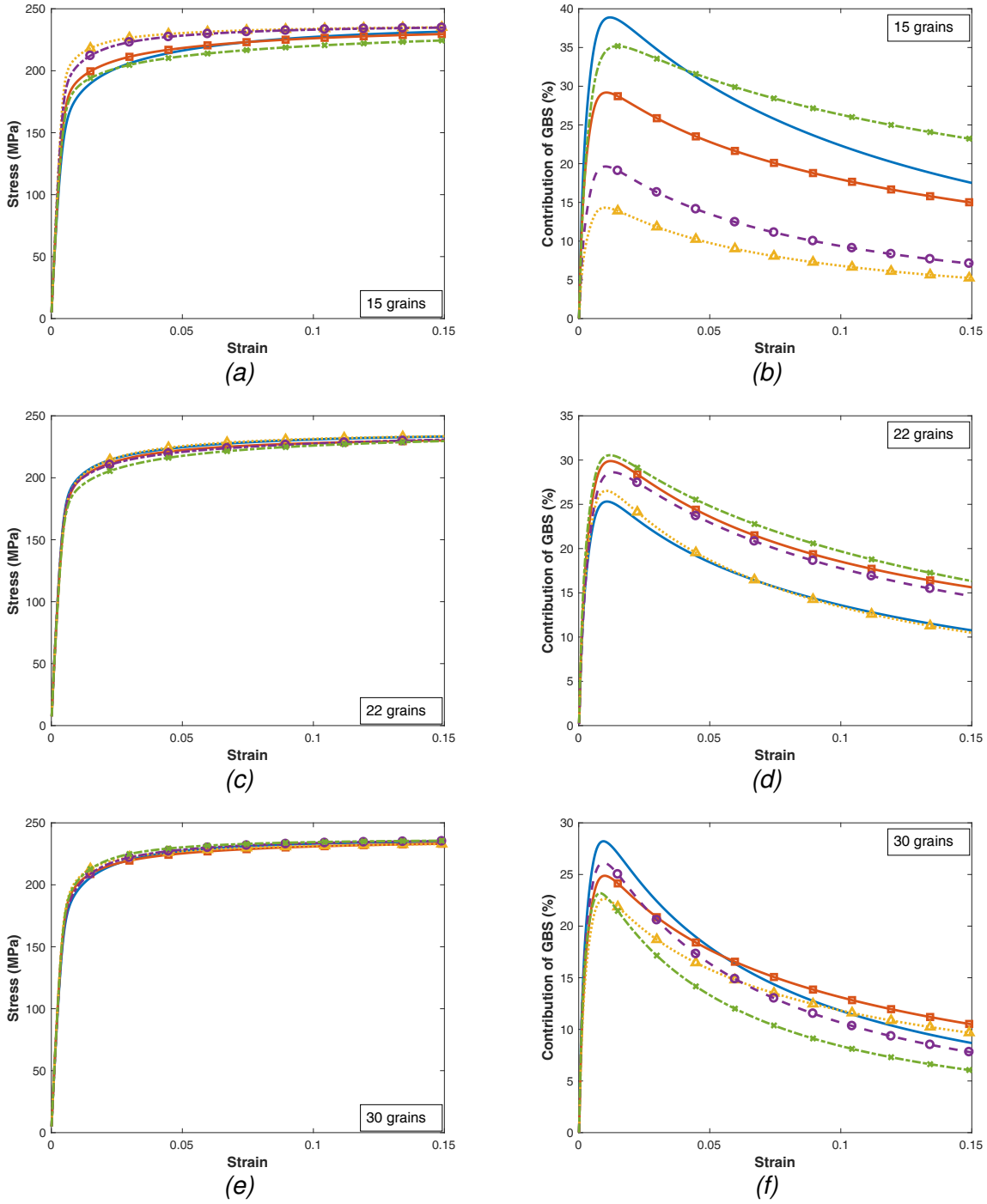

Figure 5.24: Macro (a, c, e) and micro (b, d, f) scale convergence with increasing number of grains for a strain-rate ($5 \times 10^{-3} s^{-1}$)

E	51700 MPa
ν	0.3
R_0	225 MPa
Q	90 MPa
b	45
a	$8 \cdot 10^{-3} s^{-1} MPa^{-4.16}$
n	4.16
σ_c	10 MPa
K_n	$1.8 \cdot 10^9 MPa/mm$
K_t	$4.7 \cdot 10^9 MPa/mm$
e	$2.9 \cdot 10^{-5} mm$
b_t	$5 \cdot 10^{-8} mms^{-1} MPa^{-1}$
τ_c	2 MPa

Table 5.3: List of parameters used for RVE determination

Macroscale convergence is achieved as the number of grains is increased to 22. This can be seen from the stress-strain curves for microstructures with 15, 22 and 30 grains grains (Fig. 5.24a, c, e). However, at microscale, a large scatter is observed in the contribution of GB sliding to the global strain (Fig. 5.24b, d, f). The difference between maximum and minimum GBS contribution is as high as 25% for the model with 15 grains. Model #1 and model# 3 respectively show the highest and lowest contribution for GBS. This correlates well with their respective high and low surface density of GBs aligned with maximum shear stress directions, and with the presence of well oriented GBs cutting free surfaces in model#1. Note that the highest contribution of GBs also corresponds to the softest macro-scale response, and vice versa. The scatter in GBS contribution i.e. the difference between maximum and minimum GBS contribution (and the artefact due to free side surfaces) is reduced to approximately 5% as the number of grains increases to 22. But microscale convergence is never fully achieved, even with 30 grains, as can be seen in fig. 5.24f. Since a change in strain rate can effect local phenomena like GB sliding, a similar set of simulations was run at a 100 times lower strain rate, 5×10^{-5}s^{-1} (much lower than our experimental range). The results of these simulations are presented in Fig. 5.25.

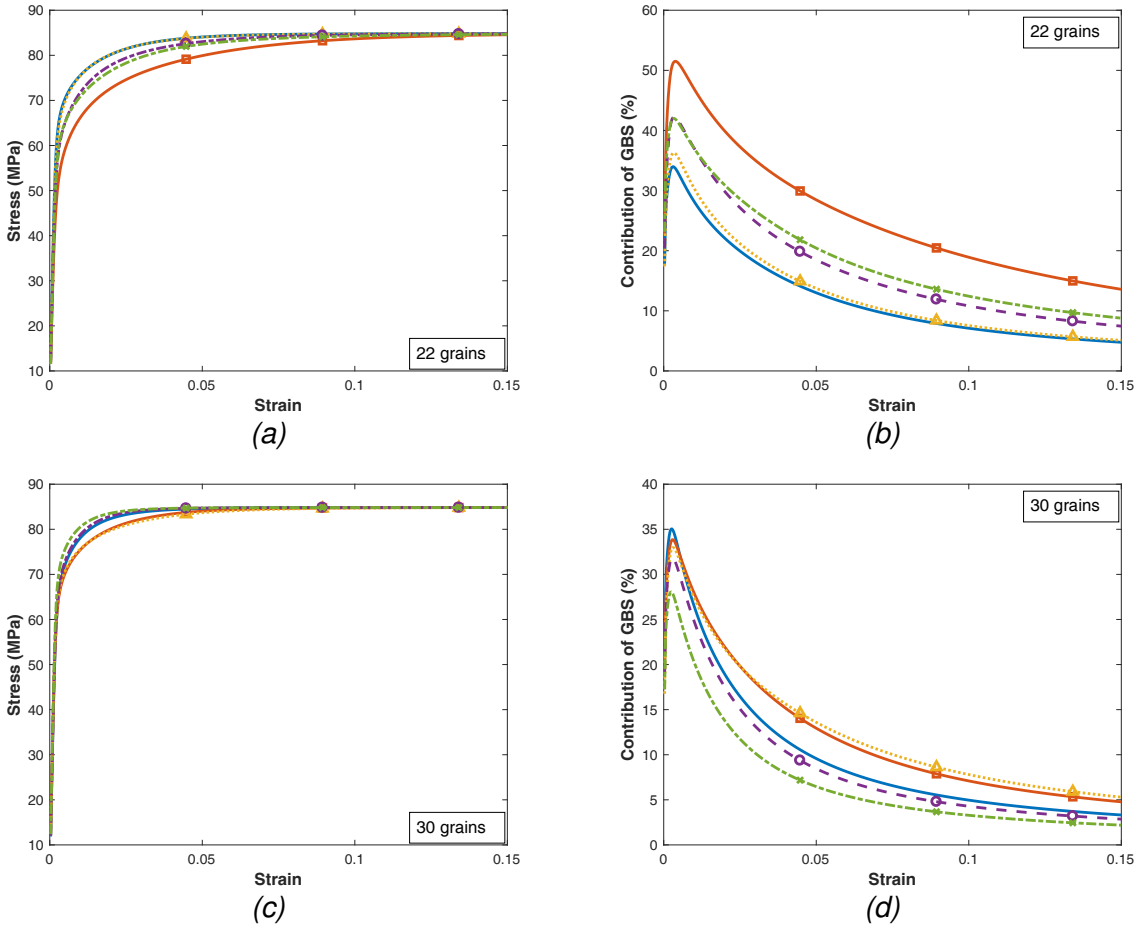

Figure 5.25: Macro (a, c) and micro (b, d) scale convergence with increasing number of grains for a 100 times lower strain-rate ($5 \times 10^{-5} s^{-1}$)

Due to an increased GBS activity, the scatter in GBS contribution is increased. More grains are required to capture the local response of the material. The microstructure with 30 grains has the least scatter and hence is chosen to run the final simulations. In order to save computation time, the microstructure with 22 grains is however chosen for the identification of the model parameters from the macroscale response.

5.3.5 Identification of the parameters

In total, 12 parameters (Table 5.4) some of which are temperature dependent have to be identified. Actually only 10 are independent, since K_0 and K_t are deduced from the global elastic moduli. Since in CG material, GBS has a negligible effect on the macroscopic stress-strain response, Young's modulus for the grains, $E(T)$ was identified from the tensile tests on CG material at each temperature, while Poisson's ratio μ was assumed to remain constant and equal to 0.3.

The hardening parameters Q and b for both CG and UFG materials were identified from the respective tensile tests at the highest strain rate at each temperature to min-

Elastic Grains	Plastic Grains	Viscous Grains	Elastic GB	Viscous GB
E(T)	$R_0(T,d)$	$a(T,d)$	$K_0(T,d) = E(T)/e(d)$	$b_t(T)$
ν	Q	$n(T,d)$	$K_t(T,d) = \mu(T)/e(d)$	$\tau_c(T)$
	b	$\sigma_c(T,d)$		

Table 5.4: 12 parameters of the model (only 10 independent)

imise the effects of viscosity. $R_0(T)$ was taken equal to the yield stress at the onset of plasticity during the fastest tensile test in CG material (see appendix 3.B), while for UFG material, a first guess was calculated from the Hall-Petch equation assuming a temperature-independent coefficient.

At high temperatures, the deformation mechanisms in CG and UFG differ significantly, as reflected by their different SRS. The three viscous parameters of the grains, $a(T)$, $n(T)$ and threshold stress $\sigma_c(T)$ were thus identified independently from available tension, creep and relaxation data, for each material.

The sliding behaviour of the grain boundaries was assumed to be similar in both materials. An initial guess for the sliding proportionality constant, b_t was found by extrapolating to the medium temperature range of interest the equation provided by Agarwal et al. [9] based on tests and simulations on Al5083 at a higher temperature. Based on the high-temperature simulations of Du et al. [10], the initial value of the GB sliding threshold stress was assumed to be very low (= 2 MPa at 200°C) and was increased for lower temperatures to match the experimental curves.

No automated optimisation module was available in Disroc code and thus the identification was done by a trial and error process. Different strategies were adopted to fit the curves, i.e. fitting tensile curves and using the identified parameters as a starting point for relaxation curves or vice versa. The former strategy was much more difficult owing to the difficulty in identifying the viscous parameters from the available tensile curves (maximum 2 at each temperature for each material). Thus, relaxation curves were fitted and the identified parameters were used as the starting points for tensile curves. Since the set of coefficients is identified by trial and error, it is not unique. The proposed best-fit sets of parameters are gathered in Table 5.5 and their evolutions with the temperature are plotted on figure 5.26.

	100°C		150°C		200°C	
	CG	UFG	CG	UFG	CG	UFG
E (MPa)	62000	62000	56900	56900	51700	51700
ν	0.3	0.3	0.3	0.3	0.3	0.3
R_0 (MPa)	119	325	114	292	105	225
Q (MPa)	122	125	115	75	90	50
b	42	45	42	45	42	45
a ($s^{-1}MPa^{-n}$)	$1.0{\cdot}10^{-19}$	$5.5{\cdot}10^{-20}$	$6.0{\cdot}10^{-15}$	$3.0{\cdot}10^{-14}$	$9.0{\cdot}10^{-12}$	$1.4{\cdot}10^{-12}$
n	7	6	4.8	4.05	2.85	4.02
σ_c (MPa)	141	89	97	48	51	15
K_n (MPa/mm)	$1.66{\cdot}10^{7}$	$4.26{\cdot}10^{9}$	$1.52{\cdot}10^{7}$	$3.91{\cdot}10^{9}$	$1.38{\cdot}10^{7}$	$3.55{\cdot}10^{9}$
K_t (MPa/mm)	$6.38{\cdot}10^{6}$	$1.64{\cdot}10^{9}$	$5.86{\cdot}10^{6}$	$1.50{\cdot}10^{9}$	$5.32{\cdot}10^{6}$	$1.37{\cdot}10^{9}$
e (mm)	$3.74{\cdot}10^{-3}$	$1.46{\cdot}10^{-5}$	$3.74{\cdot}10^{-3}$	$1.46{\cdot}10^{-5}$	$3.74{\cdot}10^{-3}$	$1.46{\cdot}10^{-5}$
b_t ($mm{\cdot}s^{-1}MPa^{-1}$)	$2.0{\cdot}10^{-10}$	$2.0{\cdot}10^{-10}$	$4.5{\cdot}10^{-9}$	$4.5{\cdot}10^{-9}$	$5.0{\cdot}10^{-8}$	$5.0{\cdot}10^{-8}$
τ_c (MPa)	42	42	10	10	2	2

Table 5.5: Identified set of parameters

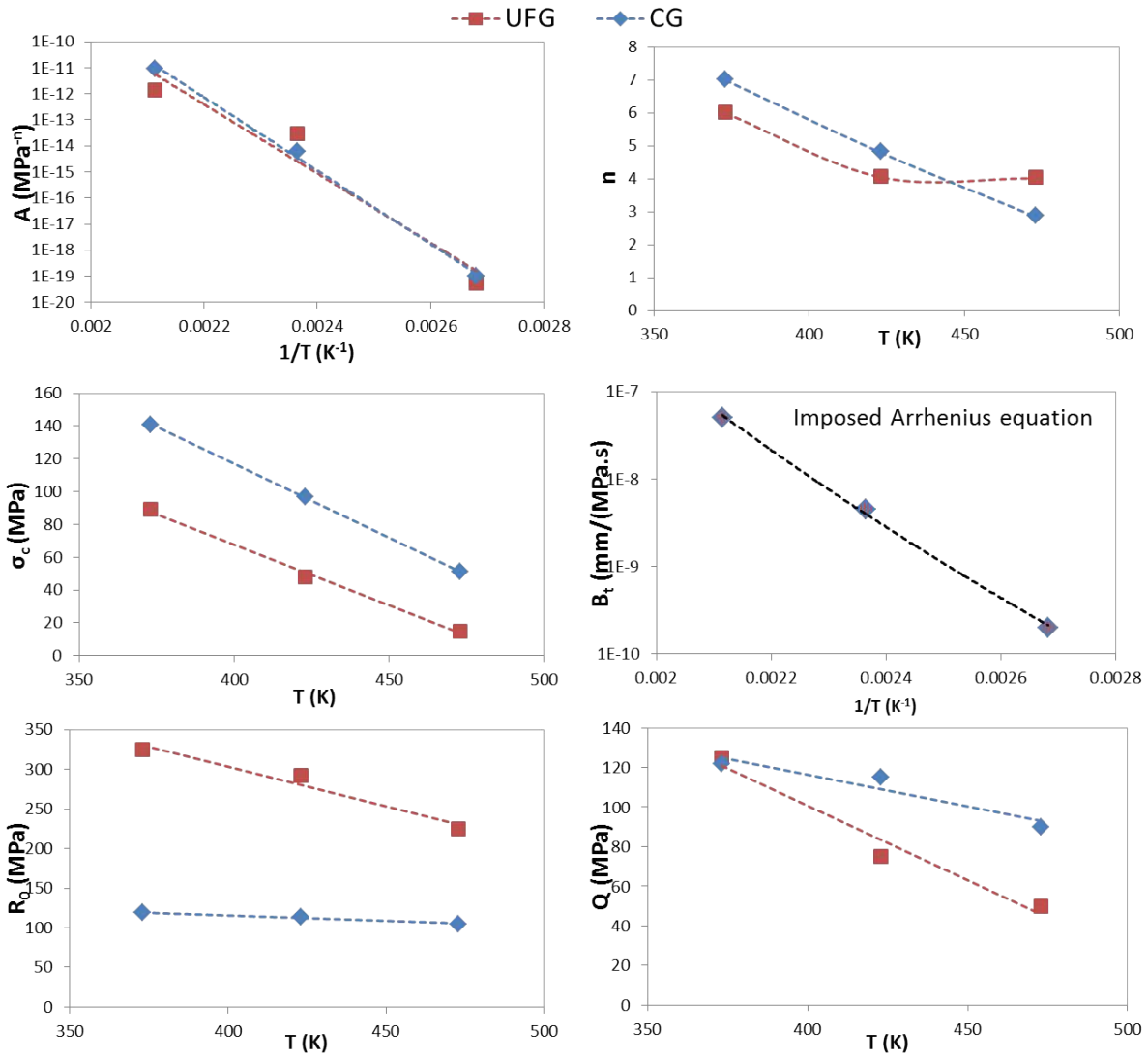

Figure 5.26: Evolution of various identified parameters with temperature

5.4 Results & Discussion

A comparison of experimental and simulated stress-strain or strain rate-stress curves is shown, for both materials and at each temperature on figures 5.27-5.29. The simulations capture the large change in tensile strength with strain rate for UFG material as well as the curvature of the relaxation curves i.e. the change in SRS. However, the relaxation tests were performed in compression and the initial yield stress was higher as compared to the tensile yield stress, especially at low temperatures. This tension-compression asymmetry is not taken into account in the model, which might explain the observed shift in the simulated relaxation curves towards lower stresses at 100 and 150°C.

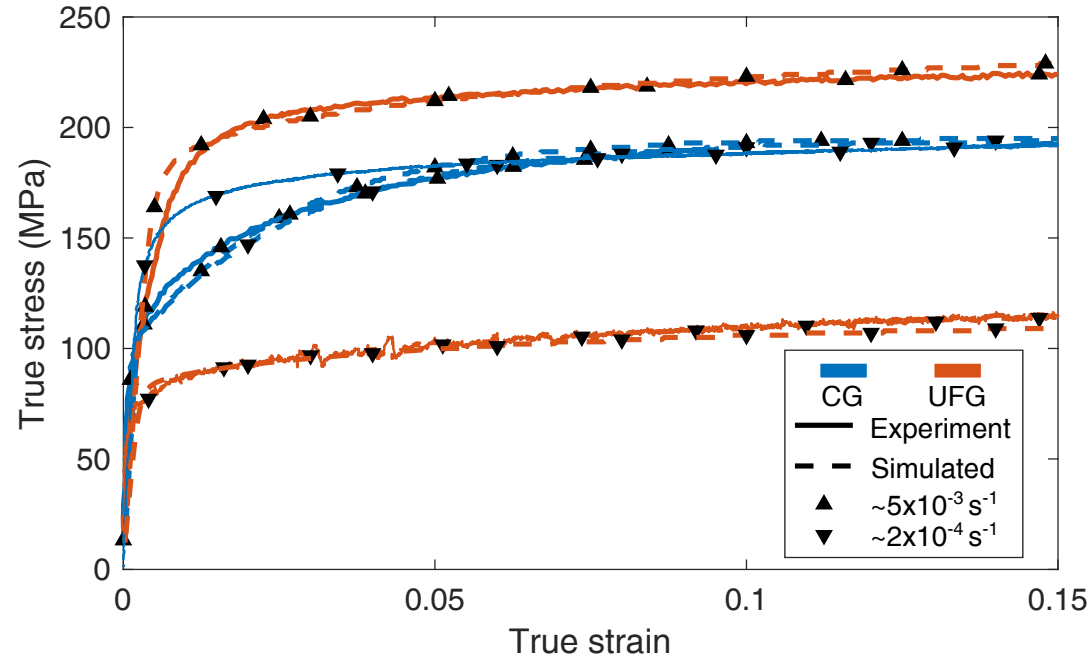

(a)

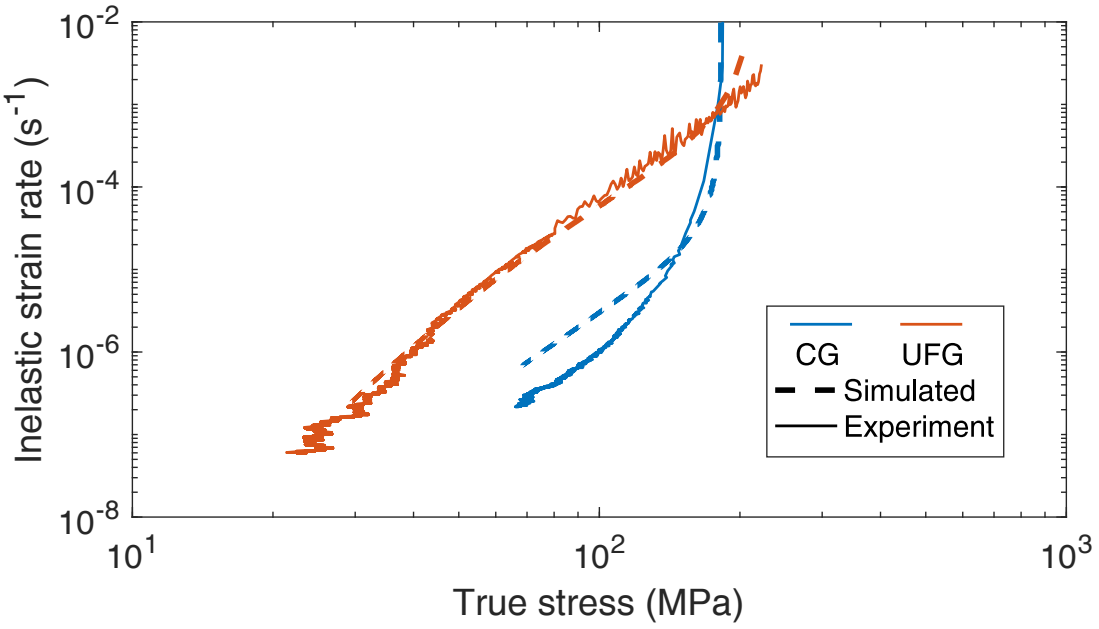

(b)

Figure 5.27: Experimental and simulated (a) tensile curves and (b) relaxation curves, for both CG and UFG material at 200° C.

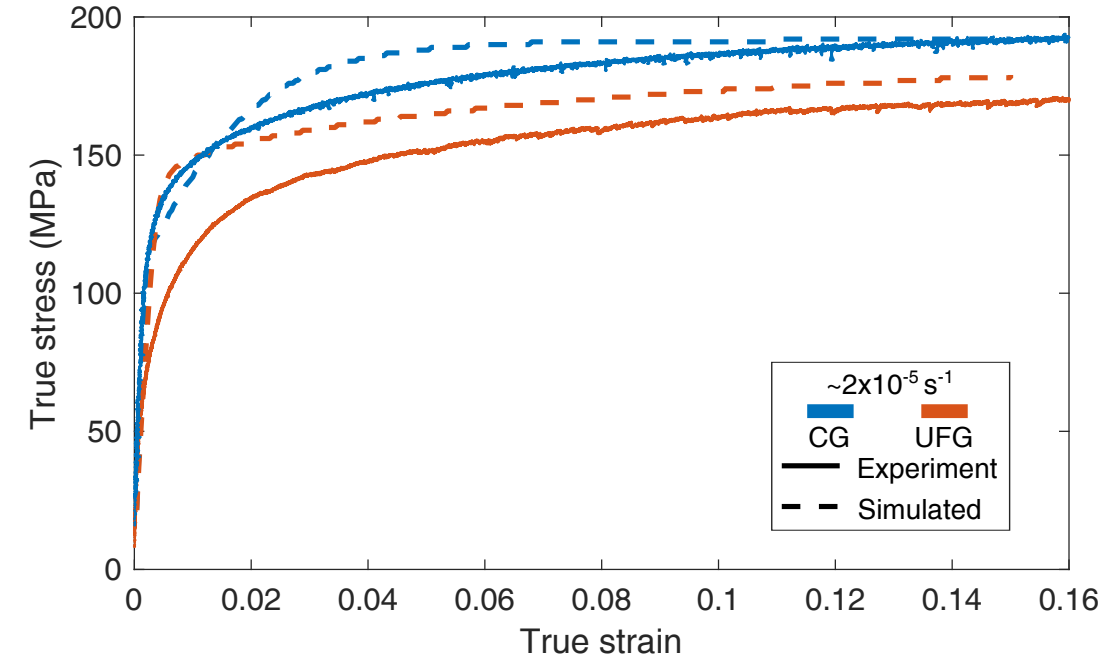

(a)

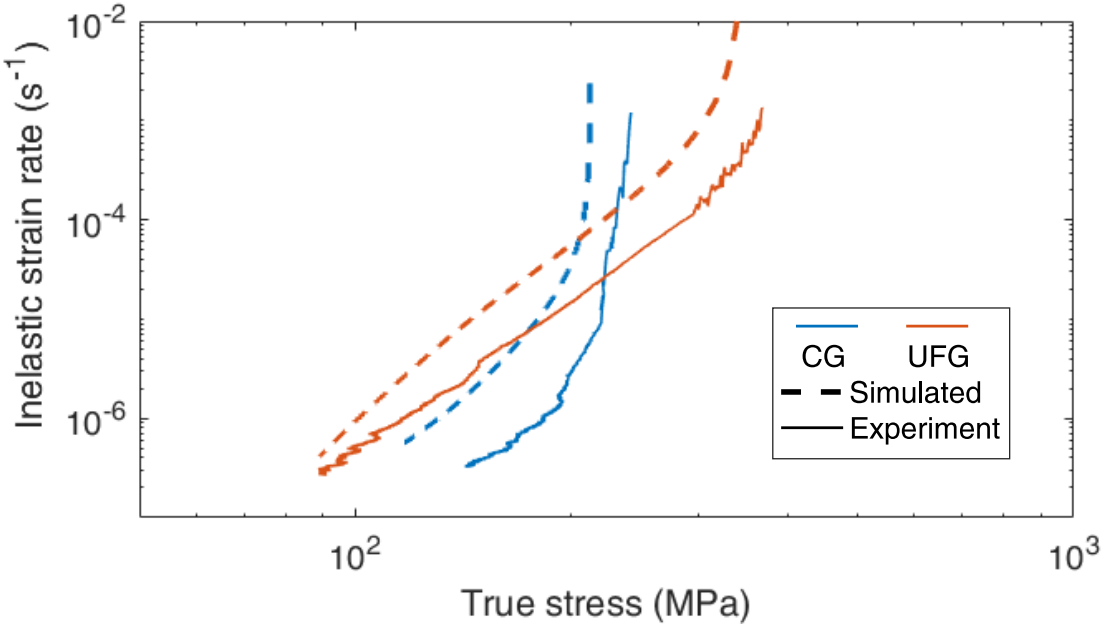

(b)

Figure 5.28: Experimental and simulated (a) tensile curves and (b) relaxation curves, for both CG and UFG material at 150° C.

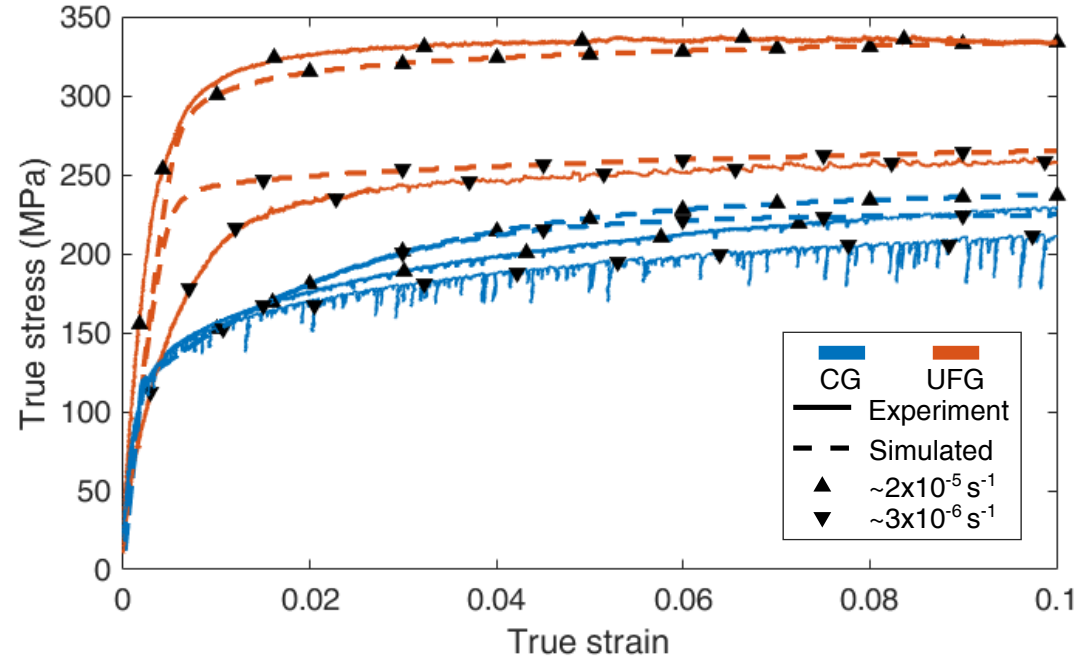

(a)

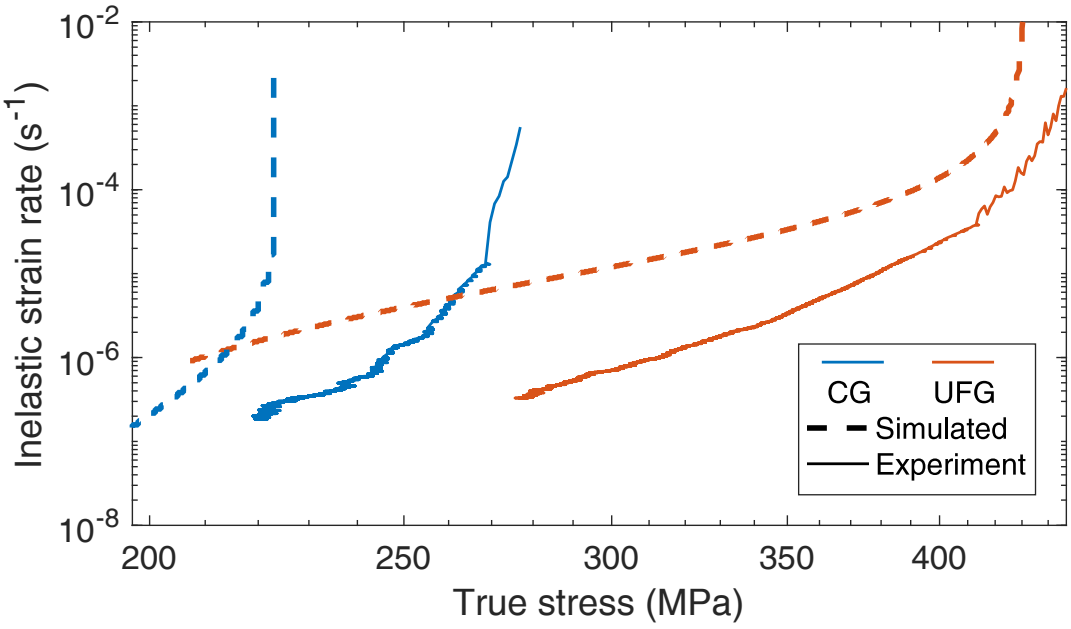

(b)

Figure 5.29: Experimental and simulated (a), (b) tensile curves and (b) relaxation curves, for both CG and UFG material at 100° C.

The contribution of grain boundary sliding was calculated by dividing the inelastic strain from GBs by the global inelastic strain. Its variation with inelastic strain (plastic + viscous) for tensile tests is plotted in figures 5.30 and 5.31.

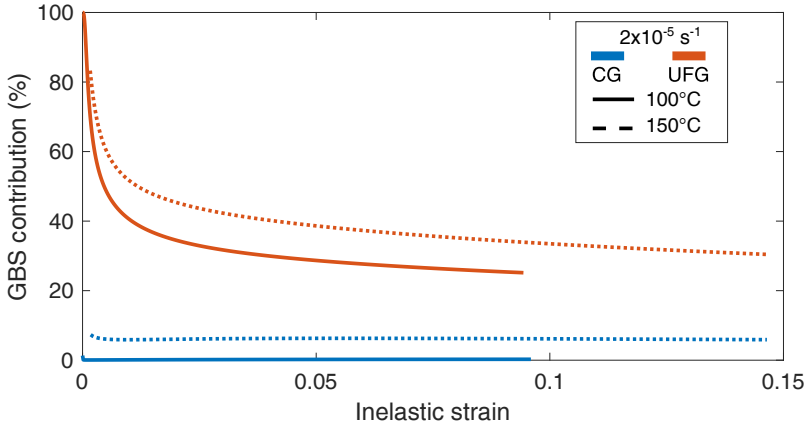

Figure 5.30: Effect of temperature and strain on the contribution of GBS to the global inelastic strain during the simulated tensile tests at $2 \times 10^{-5}\ s^{-1}$

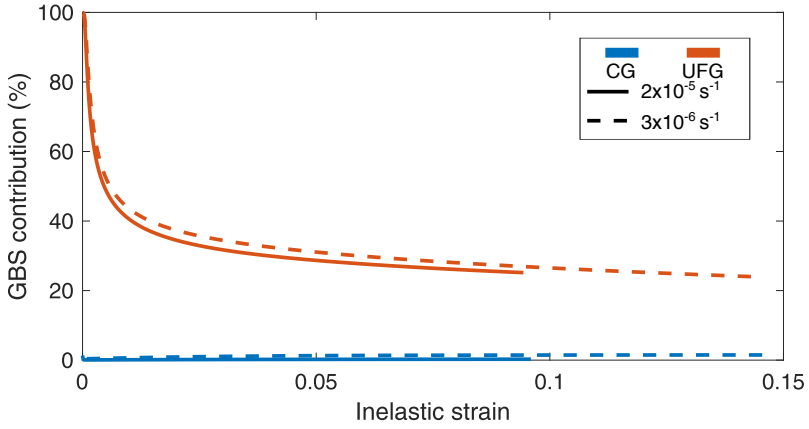

(a)

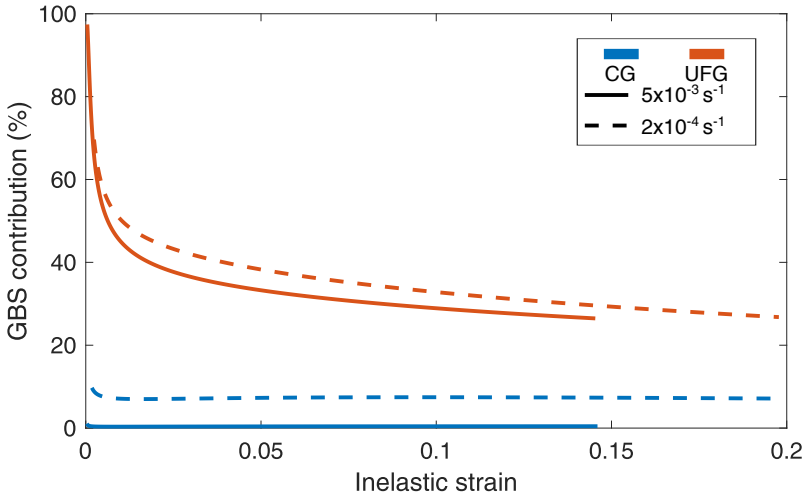

(b)

Figure 5.31: Effect of the strain and the strain rate on the contribution of GBS to the global inelastic strain during the simulated tensile tests at (a) 100° C and (b) 200° C

Because the threshold stress for GB sliding was always lower than the threshold stresses for plastic and viscous flow inside the grains (R_0 and σ_c, respectively), 100% of the inelastic strain was initially accommodated by GB sliding. This fraction then decreases as intragranular inelastic deformation develops and tends towards a steady-state value, which is always much larger in the UFG material.

This "pre-yielding" GBS is responsible for the apparently non-linear "elastic" regime leading to a decrease in apparent Young's modulus with decreasing strain rate observed during high temperature tests and well captured by the simulations as shown in figure 5.32 on which the contribution of GBS to total strain is superimposed. The Young's modulus of CG material at 200°C is almost independent from the strain rate because of the limited contribution of GBS, while for UFG material it decreases by a factor of $\sim$2.

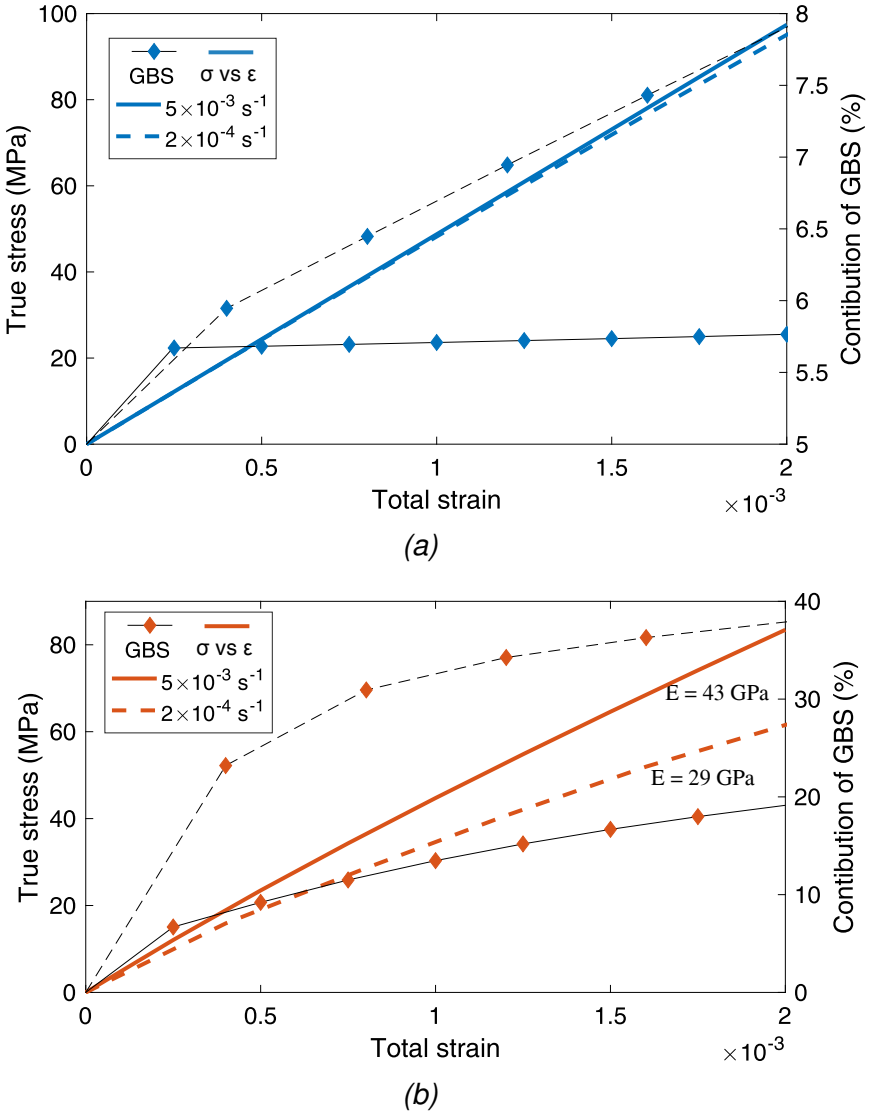

Figure 5.32: Variation in apparent elastic modulus due to GBS for (a) CG and (b) UFG materials at 200° C

The contribution of GBS is predicted to increase with decreasing strain rate and increasing temperature. This increase is non-linear as can be seen from the evolution of the contribution of GBS vs. strain rate during relaxation tests simulations (Figure 5.33).

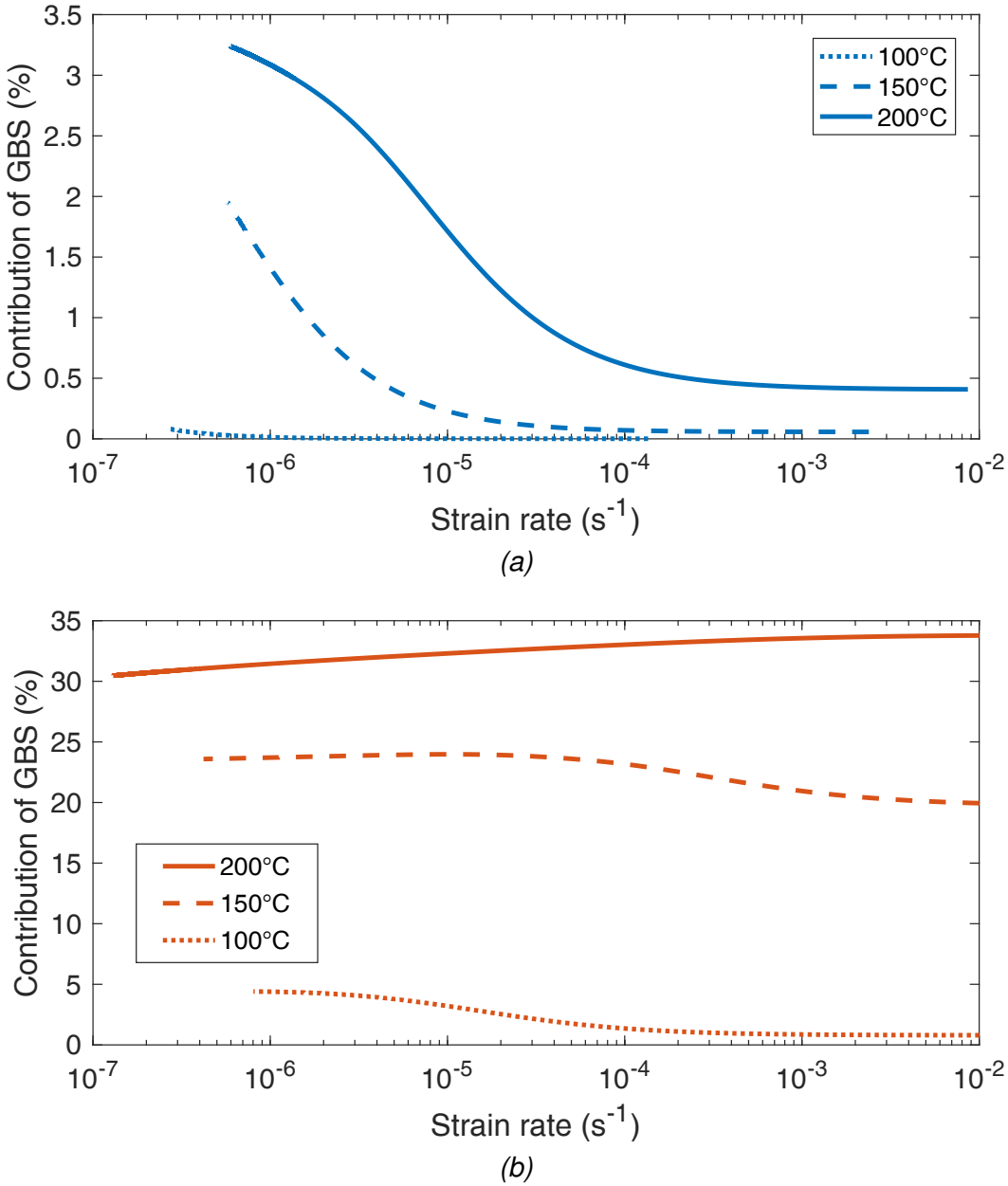

Figure 5.33: Contribution of GBS as a function of strain rate during simulated relaxation tests for (a) CG and (b) UFG materials

The predicted contribution of GBS to the global inelastic strain at 10% strain is compared with the experimental values reported in chapter 4 and are plotted against SRS in figure 5.34. It is under–predicted for UFG materials, however its relationship with SRS has a positive slope similar to the experimentally observed trends.

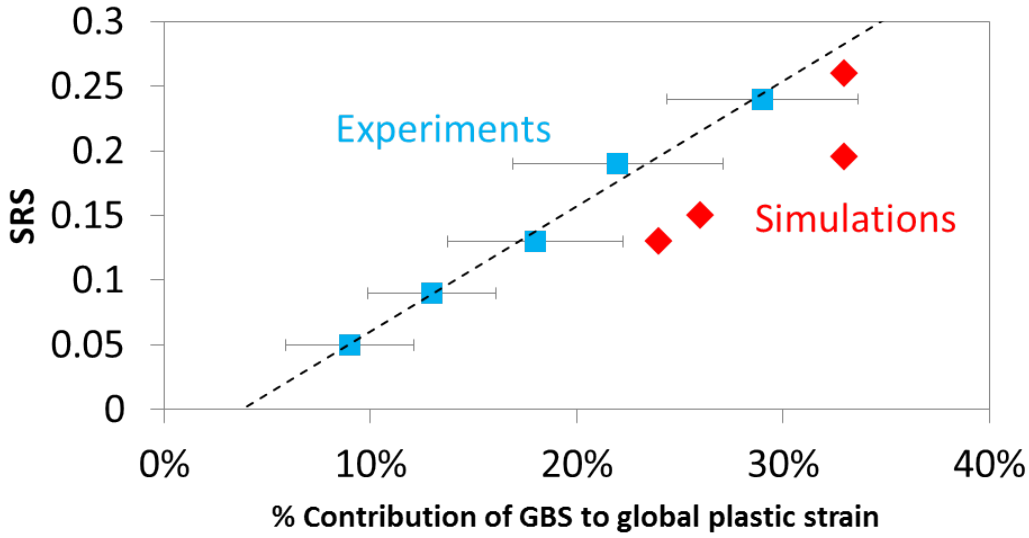

Figure 5.34: SRS vs. percentage contribution of GBS to global inelastic strain for UFG materials

The transition from GB-strengthening to GB softening with changing strain rate and temperature is well captured, as shown in figure 5.35. This shows that the increasing ability of GBs to slide with increase in temperature and decrease in strain rate, relaxes the stresses at the grain boundaries and promotes softening.

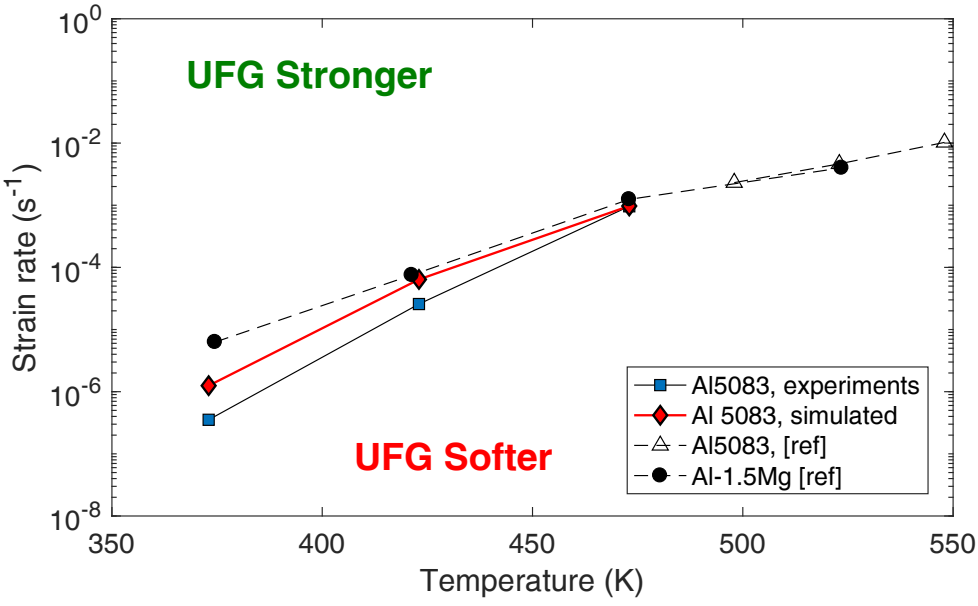

Figure 5.35: Domains of GB-induced strengthening or softening obtained from simulations or experiments [34], [35]

Figure 5.36 compares the deformed CG and UFG microstructures after 8% strain for a simulation run at $2 \times 10^{-4}\ s^{-1}$, at 200°C and figure 5.37 shows a map of inelastic sliding

displacements at GBs in the CG material. In CG material, the steps left by sliding GBs on the free surfaces are barely visible (see the 2.5 times zoomed image of a step). However, in UFG material, GBS is much more frequent and large steps are made by sliding GBs on the free surfaces. Grain rotation (marked by curved arrows) associated with GBS is also seen for UFG material.

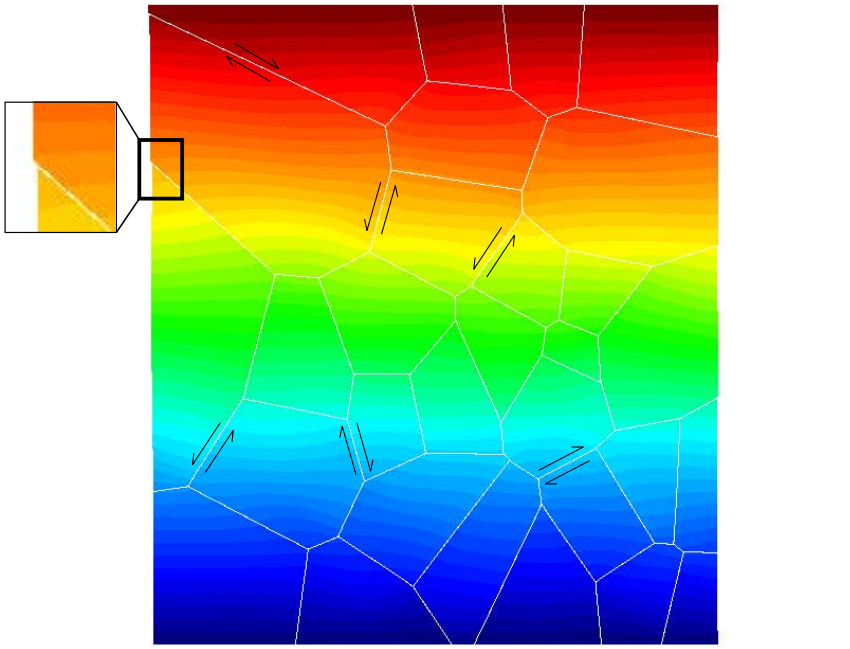

(a)

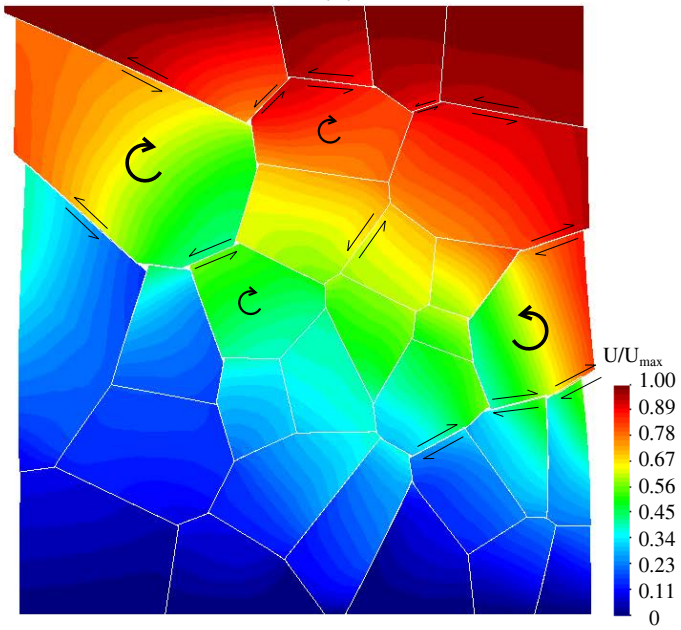

(b)

Figure 5.36: Normalised axial displacement maps after 8% deformation at $2 \times 10^{-4}\ s^{-1}$, at 200°C in (a) CG and (b) UFG materials

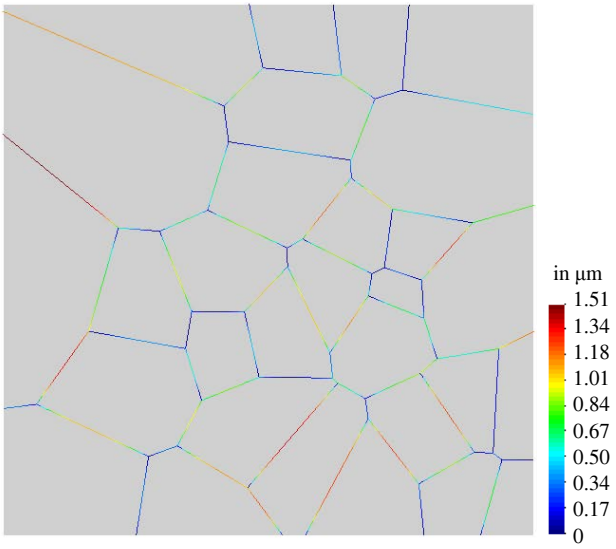

Figure 5.37: Inelastic sliding displacements at GBs after 8% deformation at $2 \times 10^{-4}\ s^{-1}$*, at 200° C in CG material*

Series of images were recorded after every 0.002% total strain for above mentioned simulation in UFG microstructure. Figure 5.38 shows the distribution of inelastic sliding displacements at the onset of GBS (= 0.01% strain). Initially, GB sliding is triggered by the far field, and thus occurs along GBs which are oriented close to the maximum shear direction ($\pm 45°$) and often for surface-cutting GBs that are less constrained. However, with increase in strain, a secondary sliding phenomenon is triggered by the local stress field along GBs not well aligned with far-field shear stress, but which are pushed by the gliding neighbouring GBs. In other words, this leads to cooperative GBS along "percolation paths" (Figure 5.39) that sometimes cross the gage width as also observed during the experiments.

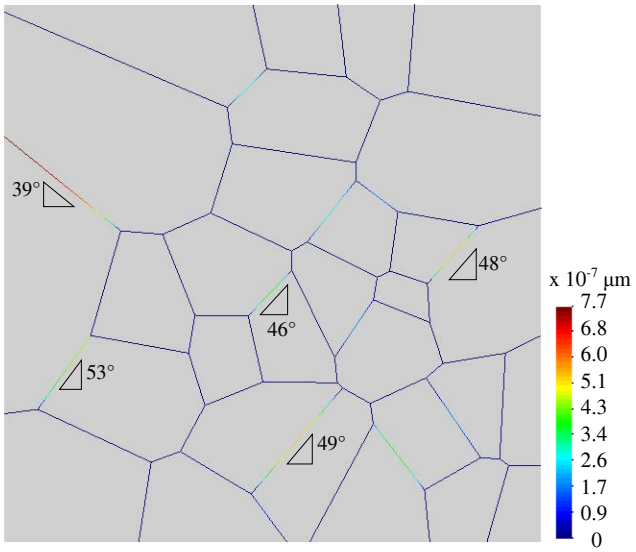

Figure 5.38: Inelastic sliding displacement along GBs after 0.01% deformation at $2 \times 10^{-4}\ s^{-1}$*, at 200° C in UFG material*

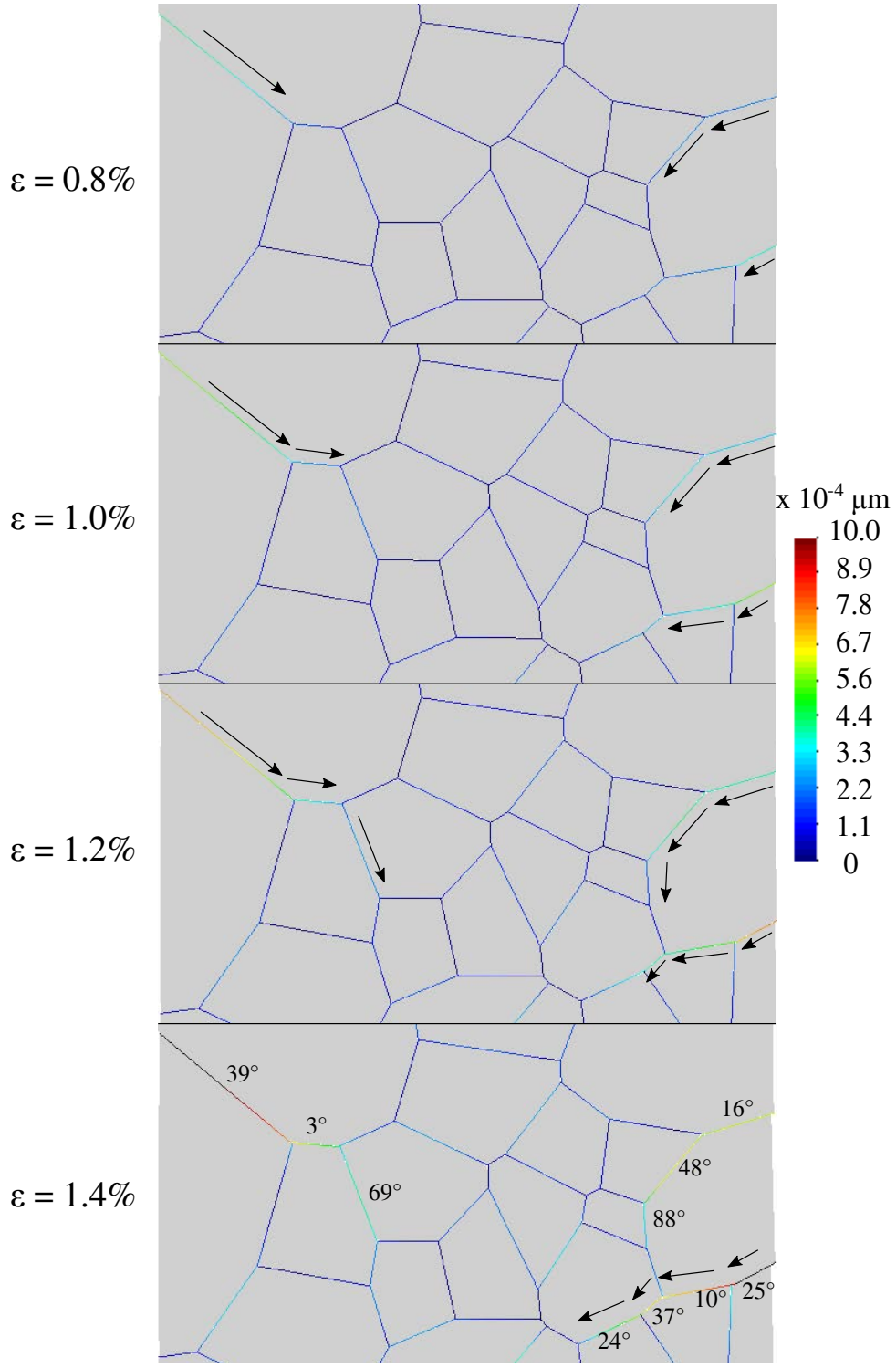

Figure 5.39: Inelastic strain from GBs at various steps for a simulation run at $2 \times 10^{-4}\ s^{-1}$*, 200° C in UFG material*

Images of the deformed microstructure of UFG material at various steps of a simulation run at $5 \times 10^{-3}\ s^{-1}$, at 200°C are shown in figure 5.40. The percolation paths sometimes connect the two free surfaces as marked by the black line. This phenomenon is similar to intense shear bands crossing the whole gauge length observed in UFG material at 200°C.

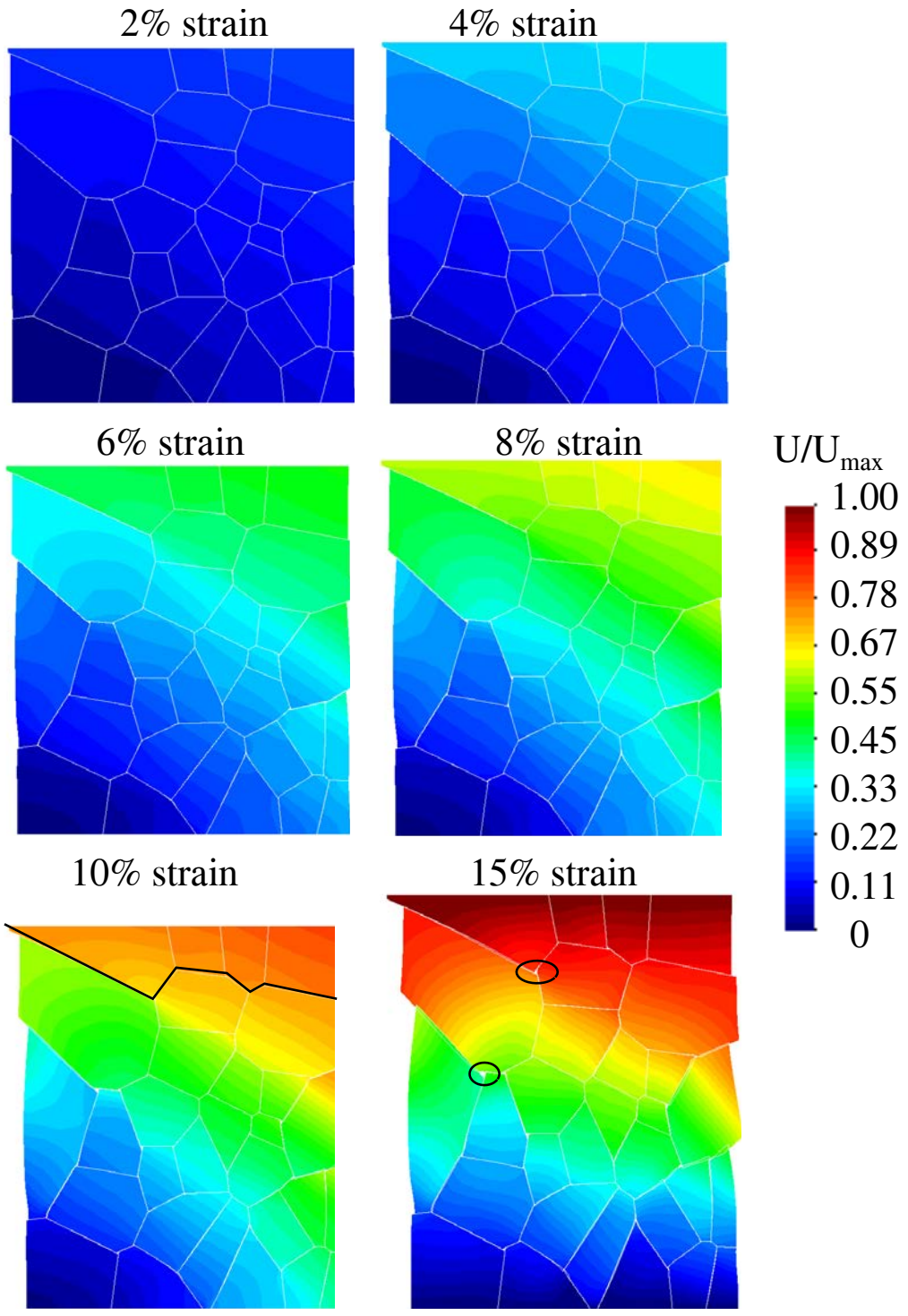

Figure 5.40: Axial displacement maps for a simulation run at $5 \times 10^{-3}\ s^{-1}$, at 200°C in UFG microstructure. Cavities are circled and a percolation path is underlined in black.

Because the model does not take diffusive accommodation processes into account, small cavities are predicted to form at triple points due to GBS and their number and size increase progressively. The area of these triple point cavities was measured and plotted as a function of total strain at 200°C for a UFG microstructure in figure 5.41. It increases with increase in strain and with decrease in strain rate. No such cavitation was observed in the simulations for CG microstructure, even at the lowest strain rate.

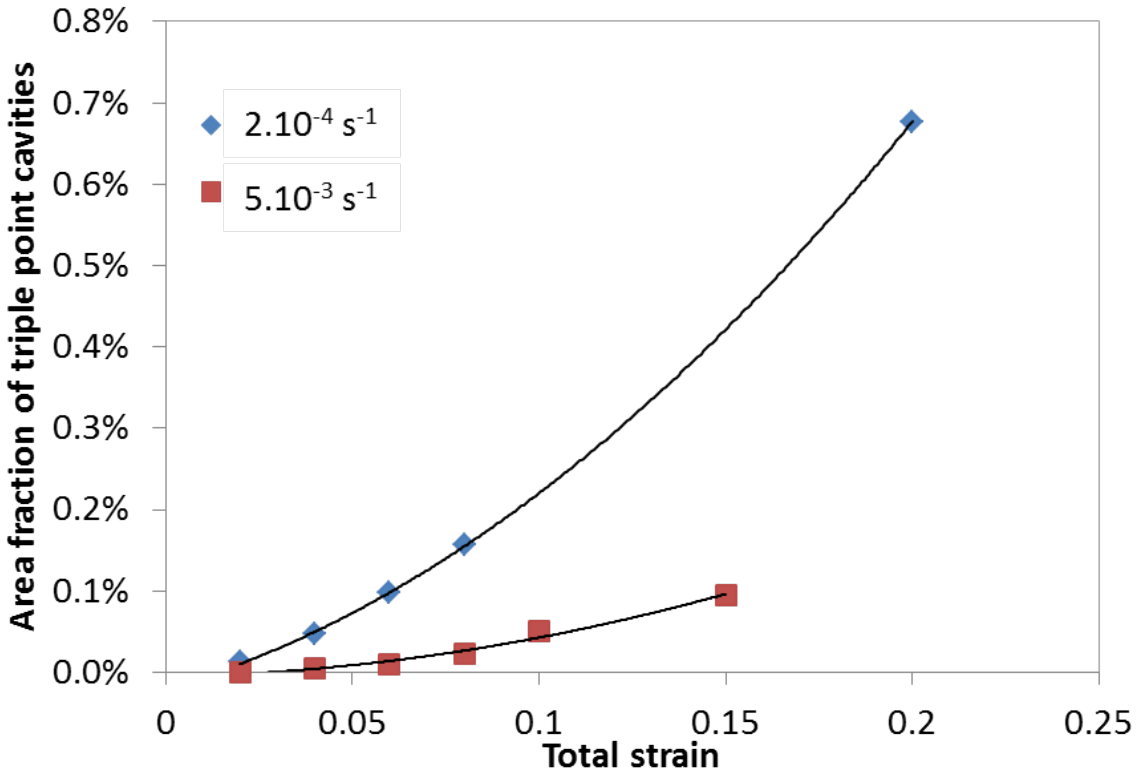

Figure 5.41: Area fraction of cavities at triple points as a function of total strain for simulations run at 200°C in UFG microstructure

5.5 Summary

In the present chapter, a 2D finite element model with viscoplastic equiaxed "grains" generated by Voronoi tessellation and elastic-viscous sliding "grain boundaries" was proposed to model the effect of grain boundary sliding in CG and UFG materials. A temperature-dependent threshold shear stress for GB sliding was introduced and above that threshold, the sliding rate of a boundary was assumed to be proportional to the resolved shear stress minus the threshold stress. The same threshold stress and proportionality constant were taken to describe GBS in both CG and UFG materials. A total of 10 independent parameters were identified from the experimental data.

- The model was able to capture the tensile and relaxation curves at different temperatures for both CG and UFG materials, as well as the boundary of the temperature and rate domains in which UFG material is stronger or softer than its CG counterpart.
- GB sliding was predicted to occur before the onset of viscoplastic flow inside the grains and to be responsible for the non-linear and rate dependent pseudo-elastic regime of the stress-strain curves in UFG material at high temperature.
- The thermally activated nature of grain boundary sliding was well captured. The contribution of GBS to the global inelastic strain increased with increase in temperature and decrease in strain rate. The predicted contributions of GBS to the global plastic strain are not so far from the experimental values. A correlation between SRS and this contribution, where there is an increase in contribution of GBS with increase in SRS, is found, as in the experiments.
- The model was also able to capture the cooperative nature of grain boundary sliding in UFG material, and the formation of percolation paths from one free surface to the other allowing unconstrained and thus very high deformations at GBs.
- Due to the lack of diffusion based accommodation processes in the model, cavities were observed to nucleate at triple points due to geometric incompatibilities associated with GBS in UFG material.

References

[1] R. Raj and M. F. Ashby, "On grain boundary sliding and diffusional creep," *Metallurgical Transactions*, vol. 2, no. 4, pp. 1113–1127, 1971.

[2] M. F. Ashby and R. A. Verrall, "Diffusion-accommodated flow and superplasticity," *Acta Metallurgica*, vol. 21, 1973.

[3] F. Crossman and M. Ashby, "The non-uniform flow of polycrystals by grain-boundary sliding accommodated by power-law creep," *Acta Metallurgica*, vol. 23, pp. 425–440, 1975.

[4] V. Tvergaard, "Effect of grain boundary sliding on creep constrained diffusive cavitation," *Journal of the Mechanics and Physics of Solids*, vol. 33, no. 5, pp. 447–469, 1985.

[5] V. Tvergaard, "Mechanical models of the effect of grain boundary sliding on creep and creep rupture.," *Rev. Phys. Appl. Rev. Phys. Appl.*, vol. 23, pp. 595–604, 1988.

[6] K. J. Hsia, D. M. Parks, and A. S. Argon, "Effects of grain boundary sliding on creep-constrained boundary cavitation and creep deformation," *Mechanics of Materials*, vol. 11, no. 1, pp. 43–62, 1991.

[7] P. Onck and E. V. D. Giessen, "Influence of microstructural variations of steady state creep and facet stresses in 2-D Freely sliding polycrytals," *International Journal of Solids and Structures*, vol. 34, no. 6, pp. 703–726, 1997.

[8] A. F. Bower and E. Wininger, "A two-dimensional finite element method for simulating the constitutive response and microstructure of polycrystals during high temperature plastic deformation," *Journal of the Mechanics and Physics of Solids*, vol. 52, no. 6, pp. 1289–1317, 2004.

[9] S. Agarwal, C. L. Briant, P. E. Krajewski, A. F. Bower, and E. M. Taleff, "Experimental validation of two-dimensional finite element method for simulating constitutive response of polycrystals during high temperature plastic deformation," *Journal of Materials Engineering and Performance*, vol. 16, pp. 170–178, 2007.

[10] N. Du, A. F. Bower, P. E. Krajewski, and E. M. Taleff, "The influence of a threshold stress for grain boundary sliding on constitutive response of polycrystalline Al during high temperature deformation," *Materials Science and Engineering A*, vol. 494, pp. 86–91, 2008.

[11] E. M. Taleff, L. G. Hector, J. R. Bradley, R. Verma, and P. E. Krajewski, "The effect of stress state on high-temperature deformation of fine-grained aluminum – magnesium alloy AA5083 sheet," *Acta Materialia*, vol. 57, pp. 2812–2822, 2009.

[12] C. Duhamel, Y. Brechet, and Y. Champion, "Activation volume and deviation from Cottrell-Stokes law at small grain size," *International Journal of Plasticity*, vol. 26, no. 5, pp. 747–757, 2010.

[13] O. Bouaziz, Y. Estrin, Y. Bréchet, and J. D. Embury, "Critical grain size for dislocation storage and consequences for strain hardening of nanocrystalline materials," *Scripta Materialia*, vol. 63, no. 5, pp. 477–479, 2010.

[14] N. Ahmed and A. Hartmaier, "Mechanisms of grain boundary softening and strain-rate sensitivity in deformation of ultrafine-grained metals at high temperatures," *Acta Materialia*, vol. 59, no. 11, pp. 4323–4334, 2011.

[15] K. Cheng, L. Zhang, C. Lu, and K. Tieu, "Coupled grain boundary motion in aluminium : the effect of structural multiplicity," *Nature Publishing Group*, no. April, pp. 1–11, 2016.

[16] L. Li, S. Van Petegem, H. Van Swygenhoven, and P. M. Anderson, "Slip-induced intergranular stress redistribution in nanocrystalline Ni," *Acta Materialia*, vol. 60, no. 20, pp. 7001–7010, 2012.

[17] J. Shi and M. A. Zikry, "Grain size, grain boundary sliding, and grain boundary interaction effects on nanocrystalline behavior," *Materials Science and Engineering A*, vol. 520, no. 1-2, pp. 121–133, 2009.

[18] Y. Qi and P. E. Krajewski, "Molecular dynamics simulations of grain boundary sliding: The effect of stress and boundary misorientation," *Acta Materialia*, vol. 55, no. 5, pp. 1555–1563, 2007.

[19] N. Du, Y. Qi, P. E. Krajewski, and A. F. Bower, "The effect of solute atoms on aluminum grain boundary sliding at elevated temperature," *Metallurgical and Materials Transactions A: Physical Metallurgy and Materials Science*, vol. 42, no. 3, pp. 651–659, 2011.

[20] D. H. Warner, F. Sansoz, and J. F. Molinari, "Atomistic based continuum investigation of plastic deformation in nanocrystalline copper," *International Journal of Plasticity*, vol. 22, no. 4, pp. 754–774, 2006.

[21] B. Jiang and G. J. Weng, "A generalized self-consistent polycrystal model for the yield strength of nanocrystalline materials," *Journal of the Mechanics and Physics of Solids*, vol. 52, no. 5, pp. 1125–1149, 2004.

[22] S. Benkassem, L. Capolungo, and M. Cherkaoui, "Mechanical properties and multi-scale modeling of nanocrystalline materials," *Acta Materialia*, vol. 55, no. 10, pp. 3563–3572, 2007.

[23] L. Capolungo, S. Benkassem, M. Cherkaoui, and J. Qu, "Self-consistent scale transition with imperfect interfaces: Application to nanocrystalline materials," *Acta Materialia*, vol. 56, no. 7, pp. 1546–1554, 2008.

[24] S. Ramtani, G. Dirras, and H. Q. Bui, "A bimodal bulk ultra-fine-grained nickel: Experimental and micromechanical investigations," *Mechanics of Materials*, vol. 42, no. 5, pp. 522–536, 2010.

[25] A. Musienko and G. Cailletaud, "Simulation of inter- and transgranular crack propagation in polycrystalline aggregates due to stress corrosion cracking," *Acta Materialia*, vol. 57, no. 13, pp. 3840–3855, 2009.

[26] Y. J. Wei and L. Anand, "Grain-boundary sliding and separation in polycrystalline metals: Application to nanocrystalline fcc metals," *Journal of the Mechanics and Physics of Solids*, vol. 52, no. 11, pp. 2587–2616, 2004.

[27] A. Barut, I. Guven, and E. Madenci, "A meshless grain element for micromechanical analysis with crystal plasticity," *International Journal for Numerical Methods in Engineering*, vol. 67, no. 1, pp. 17–65, 2006.

[28] I. Benedetti and M. H. Aliabadi, "A three-dimensional cohesive-frictional grain-boundary micromechanical model for intergranular degradation and failure in polycrystalline materials," *Computer Methods in Applied Mechanics and Engineering*, vol. 265, pp. 36–62, 2013.

[29] I. Benedetti, V. Gulizzi, and V. Mallardo, "A grain boundary formulation for crystal plasticity," *International Journal of Plasticity*, vol. 83, pp. 202–224, 2016.

[30] S. E. Shawish, L. Cizelj, and I. Simonovski, "Modeling grain boundaries in polycrystals using cohesive elements: Qualitative and quantitative analysis," *Nuclear Engineering and Design*, vol. 261, pp. 371–381, 2013.

[31] A. Pouya and M. Chalhoub, "Numerical Homogenization of Elastic Behavior of Fractured Rock Masses and Micro-cracked Materials by FEM," *The 12th international conference of IACMAG*, pp. 1–6, 2008.

[32] A. Gouissem, R. Sarangi, Q. Deng, and P. Sharma, "Bridging time-scales: Grain boundary sliding constitutive law from atomistics," *Computational Materials Science*, vol. 104, pp. 200–204, 2015.

[33] X. Sauvage, N. Enikeev, R. Valiev, Y. Nasedkina, and M. Murashkin, "Atomic-scale analysis of the segregation and precipitation mechanisms in a severely deformed Al-Mg alloy," *Acta Materialia*, vol. 72, pp. 125–136, 2014.

[34] R. Kapoor and J. K. Chakravartty, "Deformation behavior of an ultrafine-grained Al-Mg alloy produced by equal-channel angular pressing," *Acta Materialia*, vol. 55, no. 16, pp. 5408–5418, 2007.

[35] Y. G. Ko, D. H. Shin, K. T. Park, and C. S. Lee, "Superplastic deformation behavior of ultra-fine-grained 5083 Al alloy using load-relaxation tests," *Materials Science and Engineering A*, vol. 448-451, pp. 756–760, 2007.

Chapter 6

Cyclic plasticity and fatigue mechanisms

This chapter presents a comparative experimental analysis of the cyclic behaviour and fatigue performance of the CG-B and UFG-B materials in low-cycle fatigue (LCF) and high-cycle fatigue (HCF) regime. The deformation and damage mechanisms were analysed through TEM and SEM observations, as well as EBSD analysis of micro-cracks paths. The first section details the experimental procedures, and the second one the results and observations. Last section presents a discussion based on microstructural features and quantitative data about fatigue damage. The author would like to acknowledge the contribution of a chinese intern, Li Meng, from Shanghai Jiao Tong University, China for the qualitative and quantitative analysis of the fatigue damage and the preparation of thin foils.

6.1 Experimental procedures

90 mm long cylindrical specimens, 8 mm in diameter and 16 mm in gage length (Figure 2.21 chapter 2) were machined from the CG-B and UFG-B materials, with the tensile axis parallel to the bar axis for CG samples, or to the die exit direction for UFG samples. All the specimens were mechanically polished and electropolished.

A servohydraulic testing machine was used for fully reversed push-pull tests, which were plastic strain-controlled, thanks to an extensometer (Figure 6.1), in LCF and run at a fixed strain rate of $10^{-3}\ s^{-1}$), or stress-controlled in HCF (with a frequency between 5 and 10 Hz). The tests were run until complete failure of the samples. If failure did not occur within 1.2 million cycles, the stress amplitude was raised and the test resumed.

Figure 6.1: Mounted specimen with an extensometer for push-pull LCF tests.

The extensometer was not used during the HCF tests, because 1) a fast elastic shakedown occurred and made the measurement of strain useless, 2) the frequency is too high for a correct recording of the stress-strain loops, and 3) the knives of the extensometer might be responsible for premature crack initiation. However, to characterize the effect of transient cyclic plasticity, Vickers hardness measurements were made after the tests on transverse cross sections, far away from the fracture surface, using a load of 100 g.

Optical microscopy was used for a statistical analysis of micro-cracks density, lengths and orientations on the outer surface of LCF samples. Fractographic observations were made using scanning electron microscopy (SEM).

Transmission electron microscopy (TEM) was used to analyse and compare the dislocation structures induced by cyclic plasticity in CG and UFG materials. For that purpose, slices were cut normal to the tensile axis of fatigued samples, as far away from the fracture surface as possible, mechanically ground down to 100 microns, punched into 3 mm discs, and finally electropolished in a double jet Tenupol apparatus, using a solution of 25% nitric acid in 75% methanol kept at -26°C, under 12 Volts (Figure 6.2). Observations were carried out on a JEOL 2000EX microscope, under bright-field and/or weak-beam conditions by Dr. Jean-Philippe Couzinié from ICMPE, in Thiais.

(a) Foil extraction

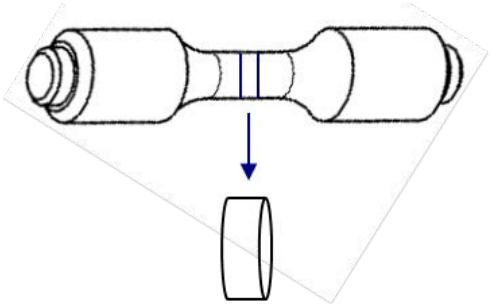

Polishing down to 100 mm

(b)

Punching of a 3mm disc

(c)

Double jet electrolytic polishing

(d)

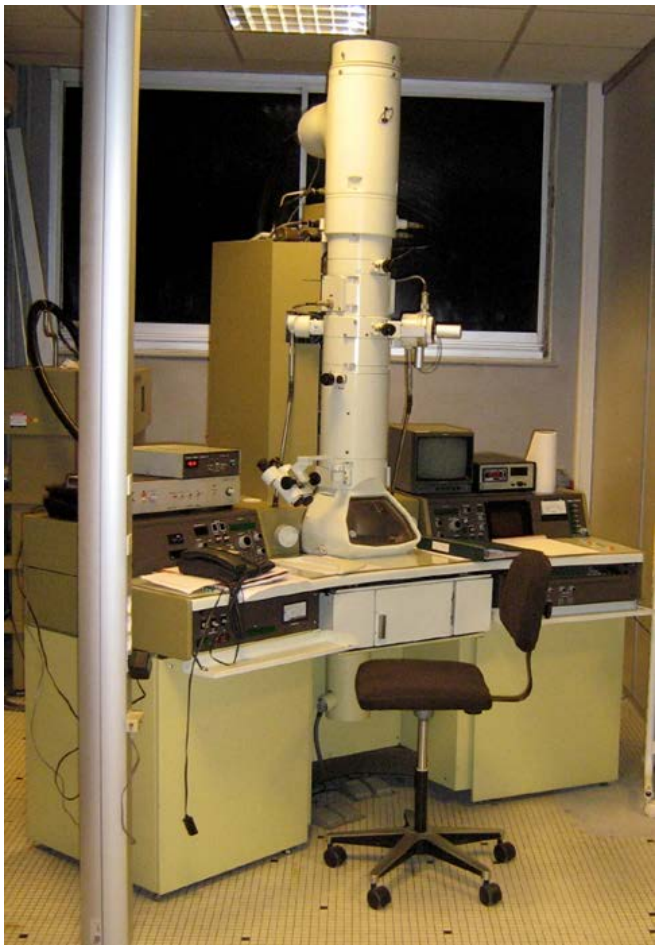

JEOL 2000EX TEM

Figure 6.2: (a-c) Foil preparation for TEM and (d) a JEOL 2000EX microscope used for TEM observations

Figure 6.3 shows the TEM micrographs of the undeformed UFG material. The largest grains contain relatively regular dislocations structures that evoke sub-boundaries.

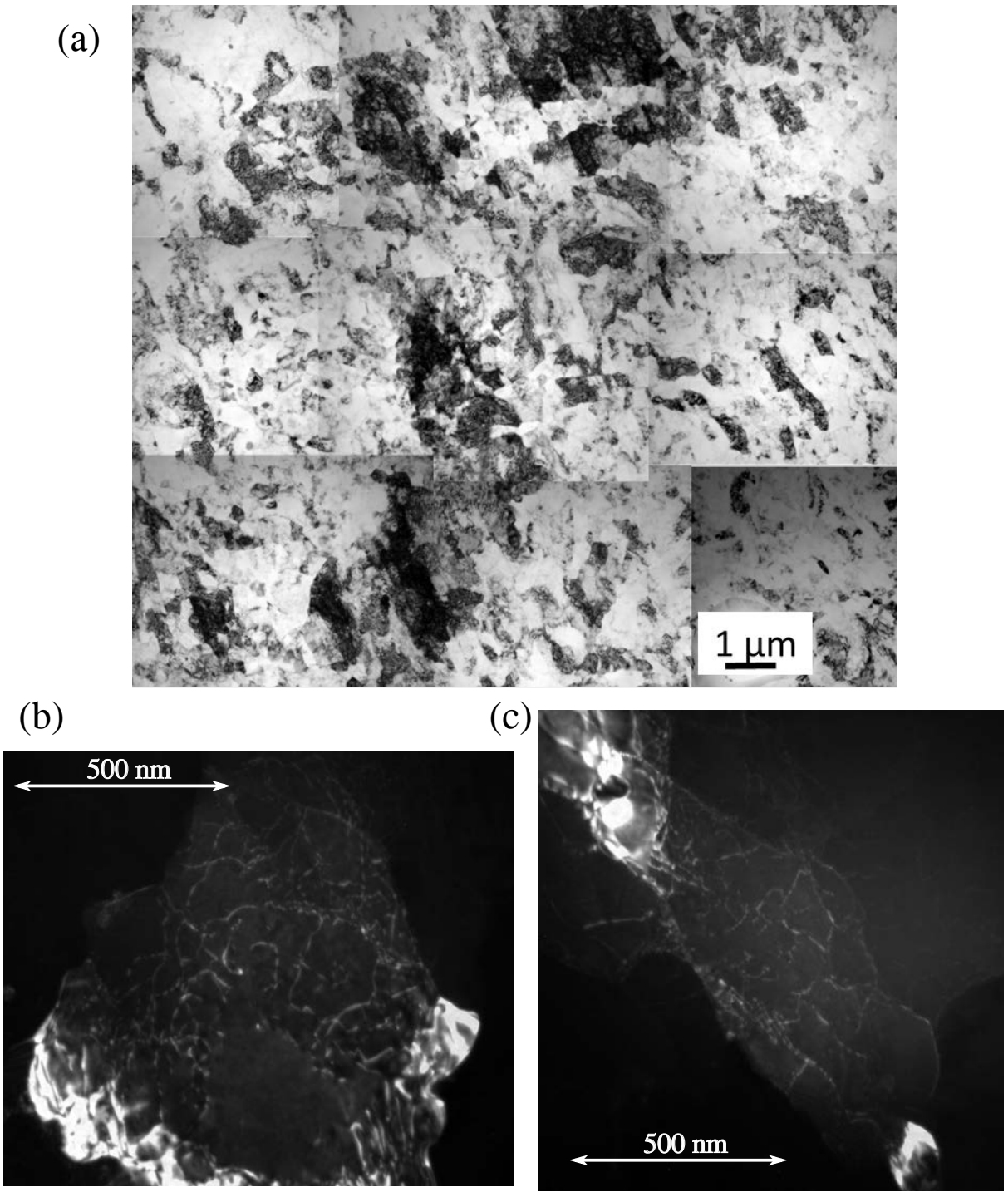

Figure 6.3: TEM micrograph of the transverse section for undeformed UFG material

Table 6.1 gathers the experimental conditions for all the tests.

CG				UFG			
$\Delta\sigma/2$ (MPa)	$\Delta\varepsilon_p/2$	control-mode	N_f	$\Delta\sigma/2$ (MPa)	$\Delta\varepsilon_p/2$	control-mode	N_f
329.0	8.1×10^{-3}	plastic-strain	102	429.5	8.2×10^{-3}	plastic-strain	200
317.6	4.0×10^{-3}	plastic-strain	1200	428.7	4.0×10^{-3}	plastic-strain	359
315.2	1.9×10^{-3}	plastic-strain	2784	402.0	1.8×10^{-3}	plastic-strain	1259
256.0	5.2×10^{-4}	total-strain	13310	319.6	-	stress	8482
198.5	-	stress	40775	253.4	-	stress	27039
149.3	-	stress	346417	204.1	-	stress	45438
120.0	-	stress	1499666*	180.0	-	stress	280000
				170.0	-	stress	>1347500*
				160.0	-	stress	394179
				150.0	-	stress	>1500000*
				140.0	-	stress	>1817800*
				120.0	-	stress	>3420000*

*Table 6.1: Experimental conditions for all the fatigue tests. * Unbroken samples.*

6.2 Observations and results

6.2.1 Cyclic plasticity

Figure 6.4a compares the evolutions of the stress amplitude versus the number of cycles, in CG and UFG materials during plastic-strain controlled tests. Both materials exhibit cyclic hardening, but this hardening is more moderate in the UFG material, as also visible from the compared monotonic and cyclic stress-strain curves (Figure 6.4b).

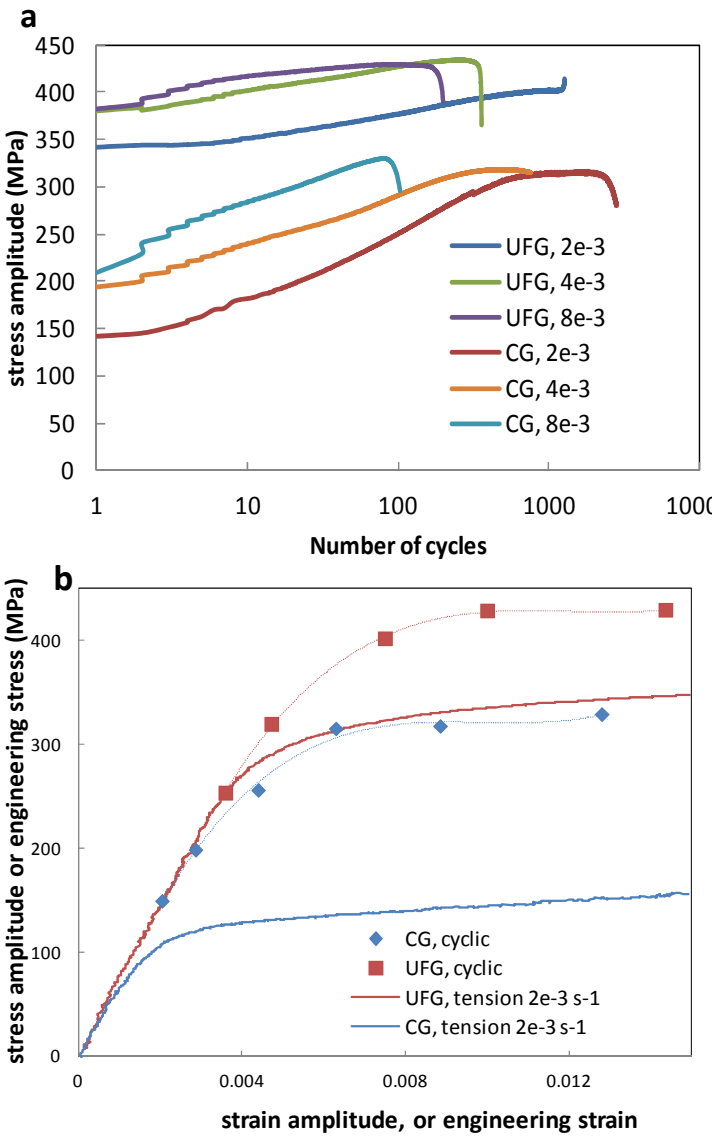

Figure 6.4: a) Evolutions of the stress amplitude and b) monotonic and cyclic stress-stress curves.

The nature of this hardening is also different, as evident from the compared steady-state stress-strain loops CG/UFG at the same amplitude, shown in figure 6.5: the loops are more elongated, with a steeper slope in the plastic regime in the UFG material,

which suggests a more pronounced kinematic hardening (in other words: stronger Bauschinger effect).

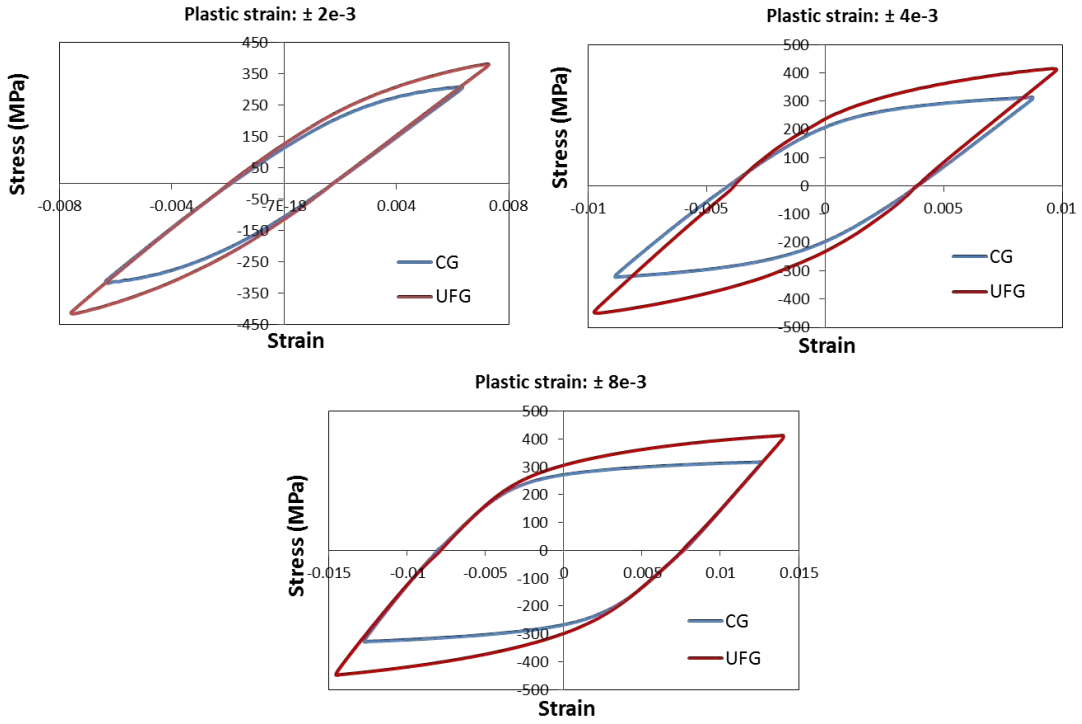

Figure 6.5: Compared steady-state stress-strain loops for CG and UFG materials

The recorded stress-strain loops were fed to a Levenberg-Marquardt algorithm (optimisation module of the Z-set FE code) in order to fit constitutive equations using isotropic and non-linear kinematic hardening variables, according to Lemaitre and Chaboche's model [1]. A Von Mises yield criterion was used, since the aim is not to describe the plastic anisotropy of the UFG material, but just the nature of its uniaxial cyclic hardening.

$$J_2(\sigma - X) - R = 0 \tag{6.1}$$

where J_2 denotes the second invariant of the stress tensor. R denotes the isotropic hardening variable:

$$R = R_0 + Q(1 - e^{-b.p}) \tag{6.2}$$

X denotes the non-linear kinematic hardening variable:

$$dX = C.\delta\varepsilon_p - D.X.\delta p \tag{6.3}$$

p denotes the cumulated plastic strain defined as follows:

$$p = \int |\dot{\varepsilon_p}|.dt \tag{6.4}$$

R0, Q, b, C and D are material parameters.

The best sets of parameters for CG and UFG materials are reported in Table 6.2. Figure 6 compares the measured and simulated stress-strain loops. The importance of kinematic hardening can be estimated by the ratio C/D, which corresponds to the asymptotic value of the kinematic variable at high tensile strain, while the importance of isotropic hardening is indicated by parameter Q. In UFG material, C/D is equal to 121.2 MPa, and is 3.3 times higher than Q (which is only 36.2MPa), while in CG material, C/D is equal to 94.6 MPa, which is smaller than Q (132 MPa).

	E (GPa)	ν	R_0 (MPa)	Q (MPa)	b	C (MPa)	D (MPa)
CG	67	0.3	102.5	132	2.6	54467	575.7
UFG	66.5	0.3	276	36.2	9.86	29523	243.5

Table 6.2: Best fit parameters for the constitutive equations of CG and UFG materials

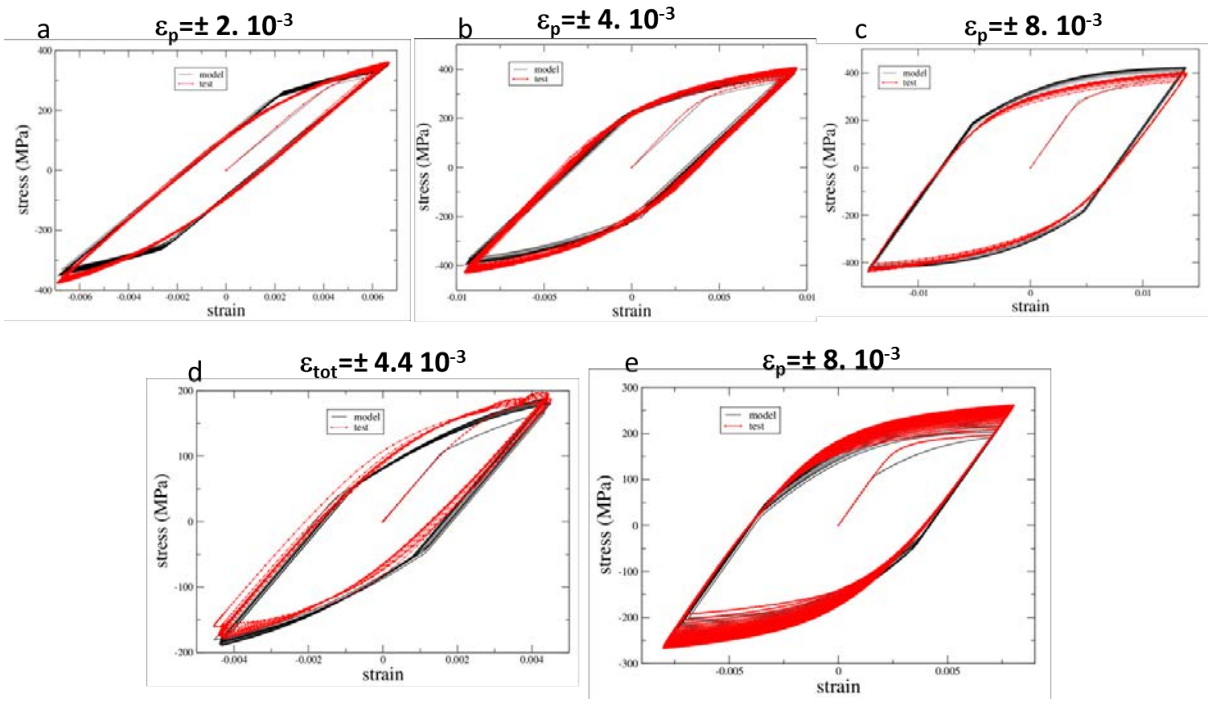

Figure 6.6: Comparison of measured and simulated stress-strain loops for UFG (a,b,c) and CG (d,e) materials

Figure 6.7 presents the evolution of hardness during the stress-controlled HCF tests for both CG and UFG materials. Both the materials exhibit significant increase in hardness with increase in the stress amplitude which is consistent with the increase in cyclic hardening. Although limited, this increased hardness in UFG material also confirms that there was no grain growth during the HCF tests.

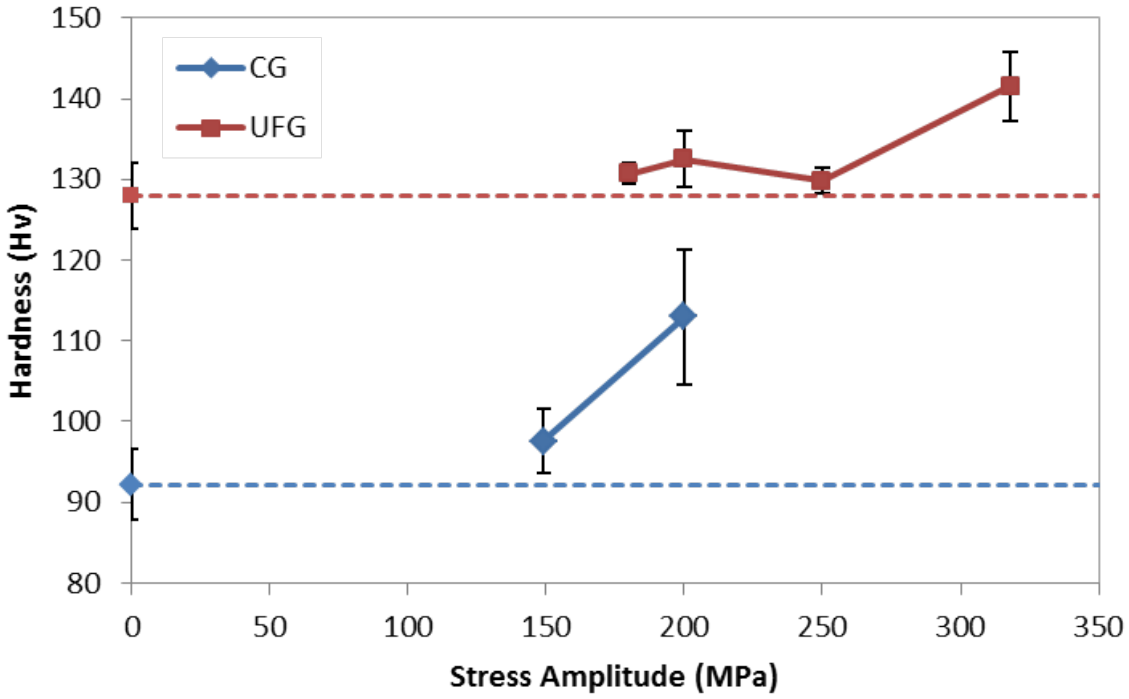

Figure 6.7: Evolution in hardness of CG and UFG materials after stress-controlled HCF tests

Figures 6.8-6.12 show TEM micrographs of dislocation arrangements for the CG and UFG materials for plastic strain amplitude of $\pm 2 \times 10^{-3}$ and $\pm 8 \times 10^{-3}$. For the lower amplitude (Figure 6.8), a relatively uniform and dense distribution of tangled and jogged dislocations, with multiple pinning points, plus tiny dislocations loops -probably formed by the dipole bypassing mechanism after jog dragging [2], [3], as described by figure 6.9 were observed in the CG material (Figure 6.8a). The presence of curved dislocations near the incoherent second phase particles suggests the Orowan-type bypassing mechanism (Figure 6.8b). No organized features like veins, cells, labyrinths or ladders were found.

In the UFG material, for the same amplitude (Figure 6.10), the microstructure was more heterogeneous from one grain (or sub-grain) to the other: while the smallest grains exhibit a very low dislocation density (Figure 6.10b), the larger grains contain loops and numerous tangled dislocations, not so different from those observed in the CG material (Figure 6.10c). The strong curvature of the dislocations suggests high internal stresses and probable pinning. Dislocation loops bowing out of low-angle grain boundaries (LAGBs) could be observed. Sub-grain boundaries were clearly visible (Figures 6.10d,e) and could be possible sources of dislocation loops.

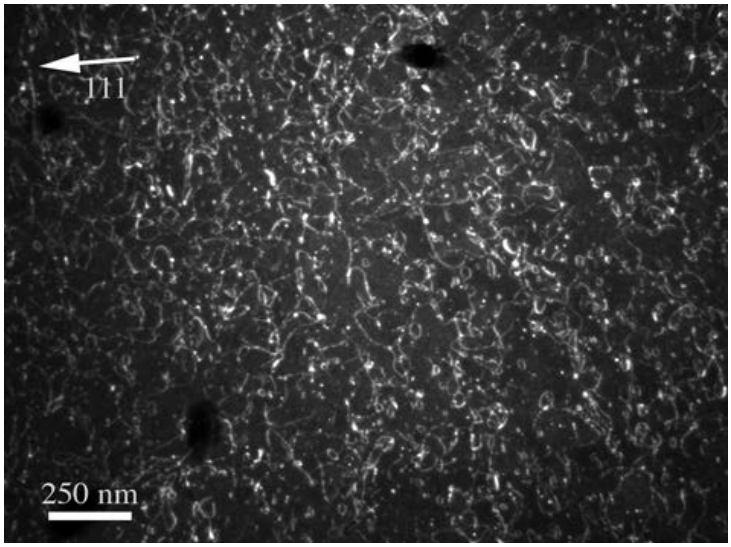

(a)

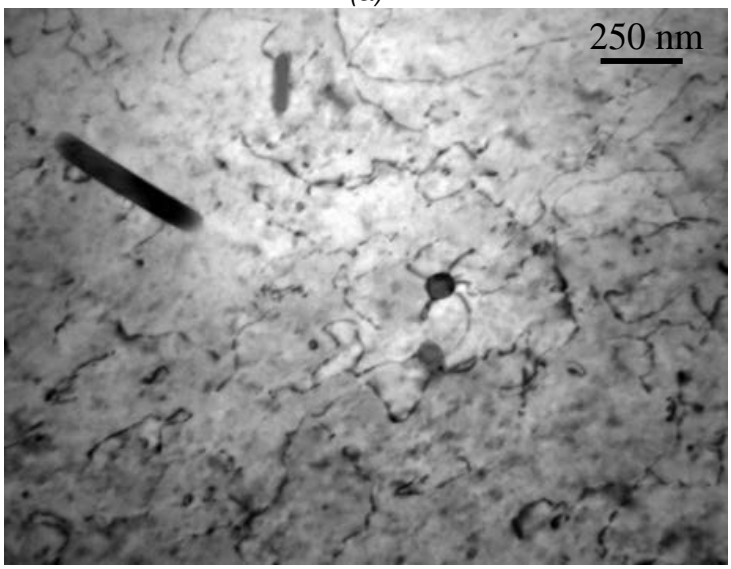

(b)

Figure 6.8: TEM observations of coarse grained LCF samples at $\varepsilon_p = \pm 2 \times 10^{-3}$

Figure 6.9: Schematics of dipole bypassing mechanism after jog dragging

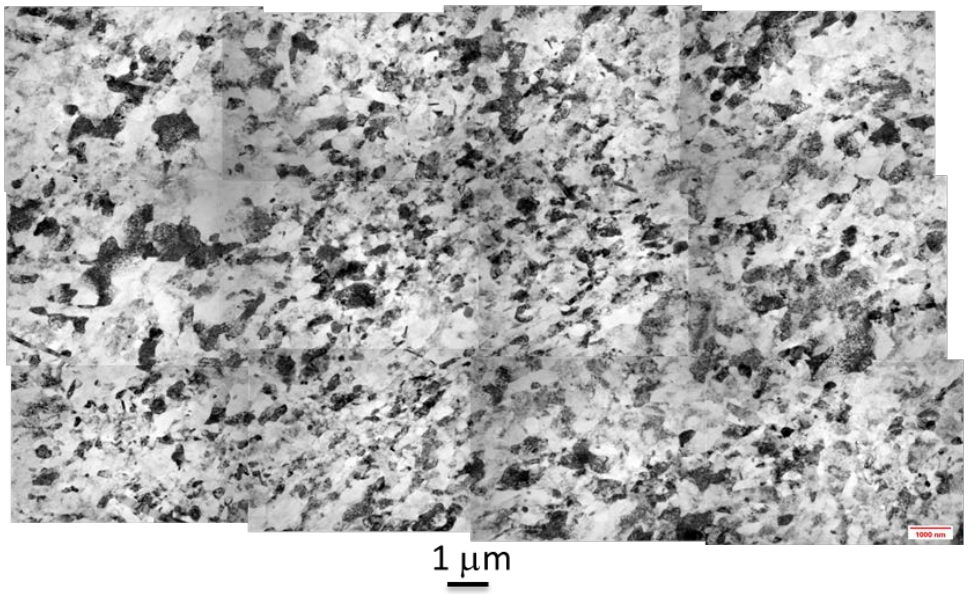

(a)

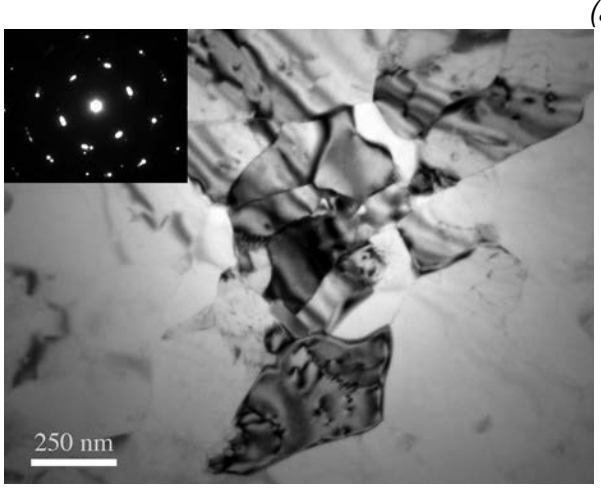

(b)

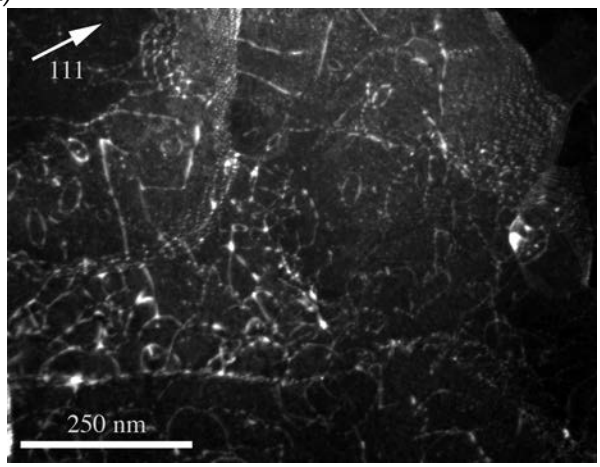

(c)

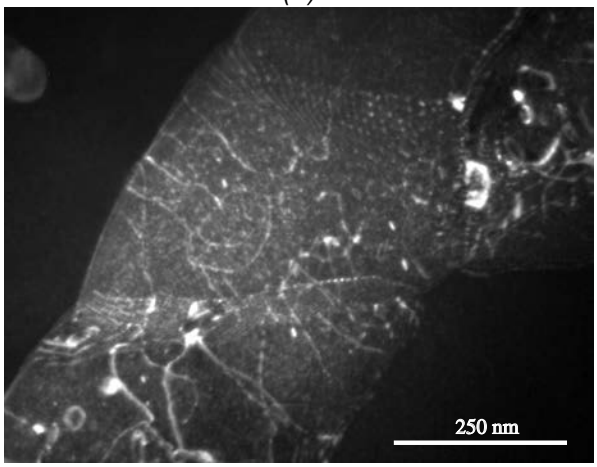

(d)

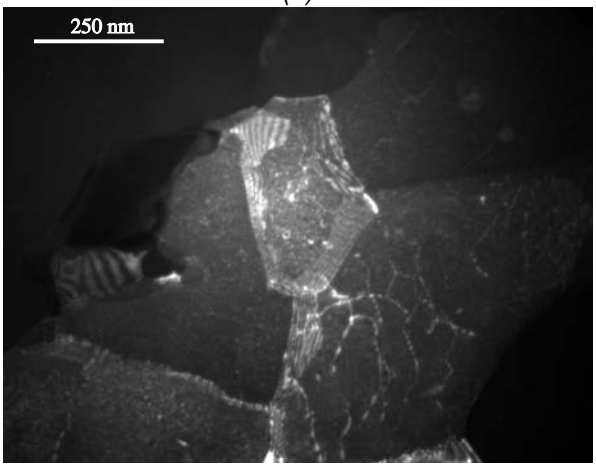

(e)

Figure 6.10: TEM observations of UFG LCF samples at $\varepsilon_p = \pm 2 \times 10^{-3}$

For the larger amplitude, a very high density of tangled dislocations with multiple pinning points was observed in most grains of the CG material (Figure 6.11a,b), and occasionally, some long and narrow band-like structures (Figure 6.11c).

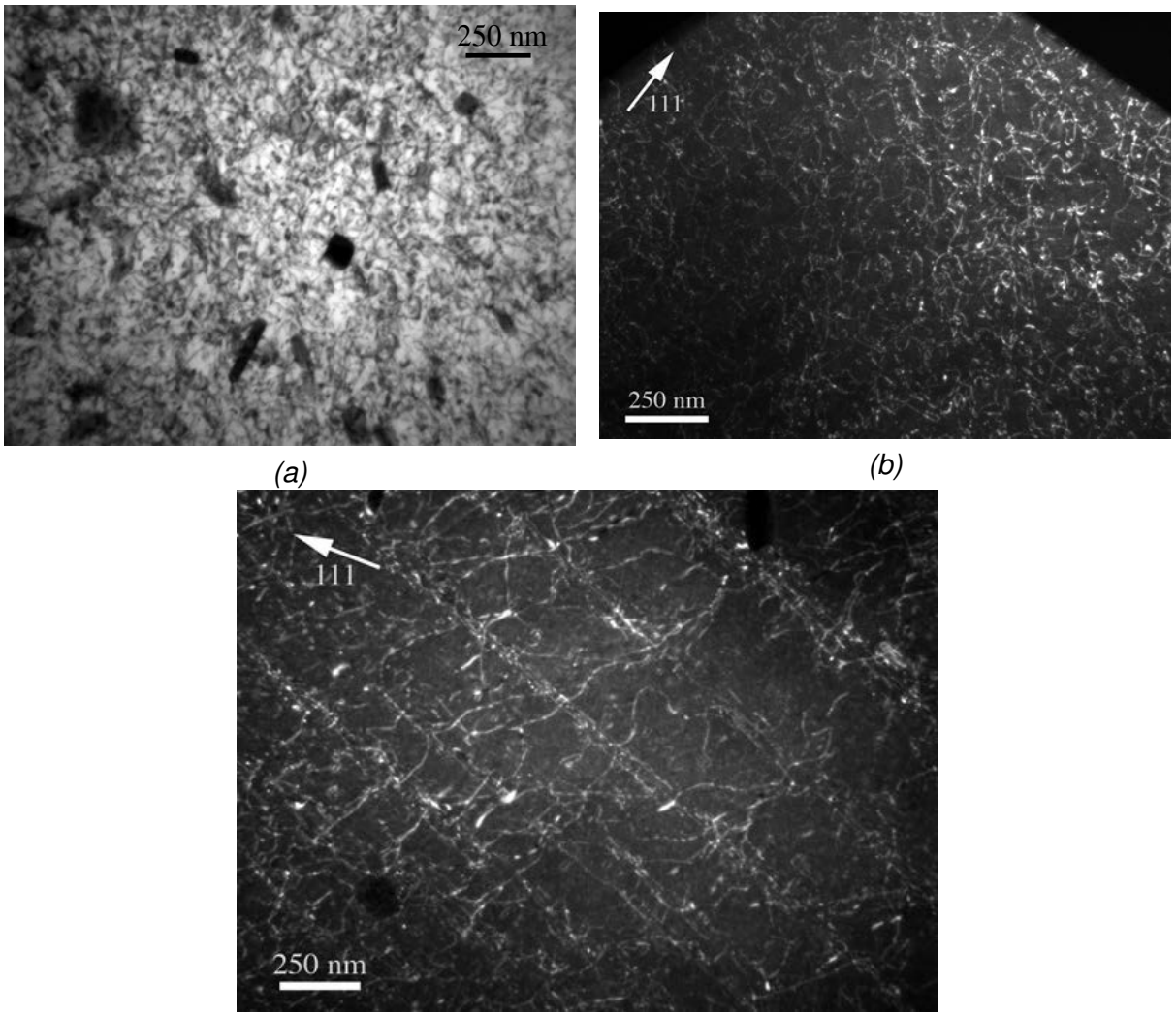

Figure 6.11: TEM observations of coarse grained LCF samples at $\varepsilon_p = \pm 8 \times 10^{-3}$

In the UFG material, very dense and non-structured network of tangled dislocations and loops was observed, without any obvious difference with the microstructure found at the lower amplitude(Figure 6.12b). The grain-to grain heterogeneity in dislocations content previously observed was still present. Although it is difficult to interpret figure 6.12c, a dislocation pile-up seem to be observed at a HAGB , as well as dislocation loops around the second phase particles. The post-treatment of EBSD mappings made on the outer surface of fatigued samples did not reveal any evolution in the mean grain size.

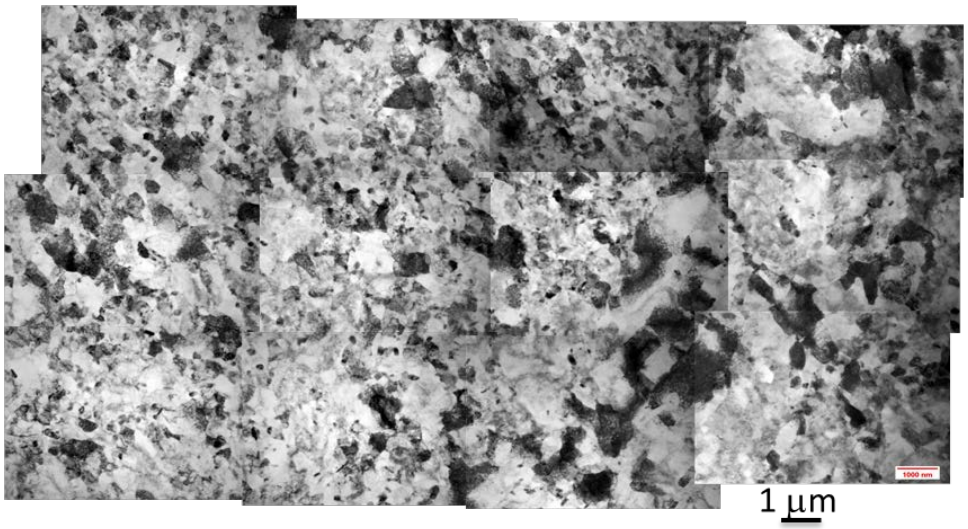

(a)

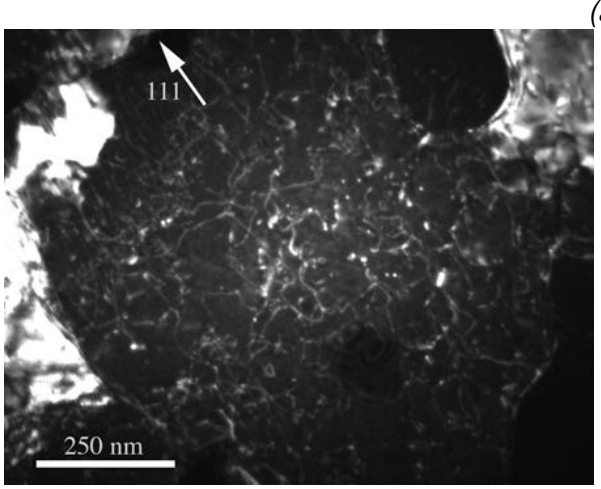

(b)

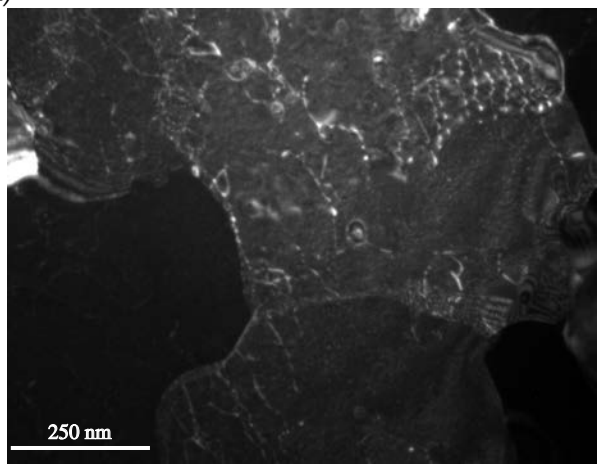

(c)

Figure 6.12: TEM observations of UFG LCF samples at $\varepsilon_p = \pm 8 \times 10^{-3}$

6.2.2 Fatigue lives

Figure 6.13 shows the fatigue lives versus plastic strain amplitudes in the LCF regime. Except for the highest amplitude, for a given plastic strain range, the UFG material exhibits a lower fatigue life than its CG counterpart, and the difference tends to rise as the plastic strain range decreases.

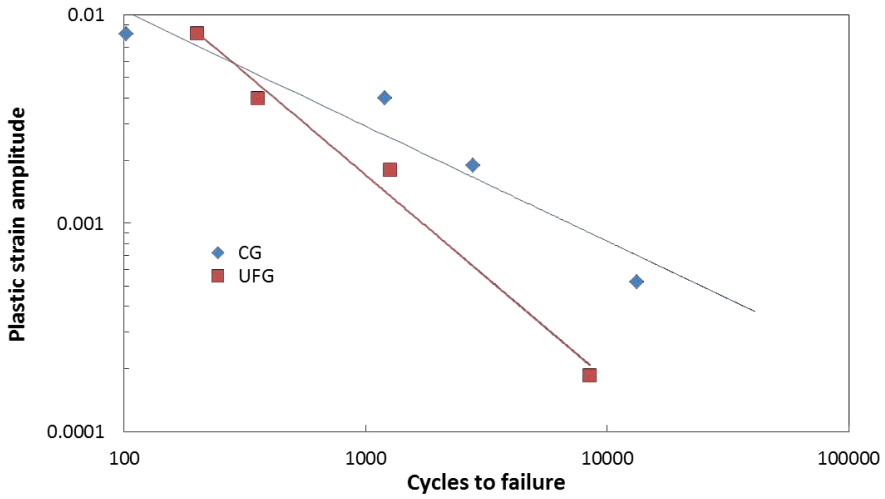

Figure 6.13: Compared fatigue lives of CG and UFG materials in the LCF regime

The S-N curves for CG and UFG materials are compared on Figure 6.14. The LCF and HCF domains can be clearly distinguished. In the LCF range (N < 10^4 cycles) the S-N curve of the UFG material lies clearly above that for the CG material. In HCF regime (N ranging from 10^4 to $2{\times}10^6$ cycles) the two curves nearly overlap, with a slightly better resistance of the UFG material. This superiority became much more apparent in the VHCF regime (from 2×10^6 to 5×10^8 cycles), as shown by tests run at 20 kHz on a piezoelectric testing machine, in parallel to this thesis [4].

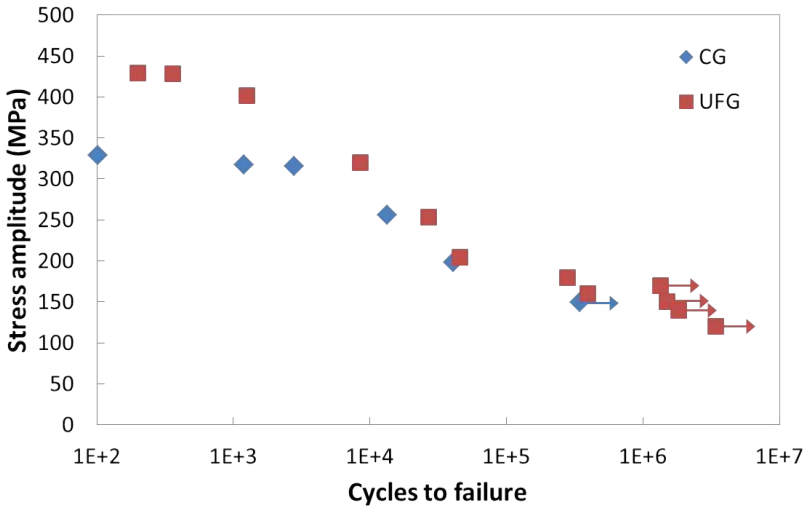

Figure 6.14: Compared S-N curves for CG and UFG materials

6.2.3 Damage mechanisms

In CG material, crack initiation always occurred at the surface, mostly from persistent slip bands (Figure 6.15a), and marginally from broken intermetallic particles (Figure 6.15b).

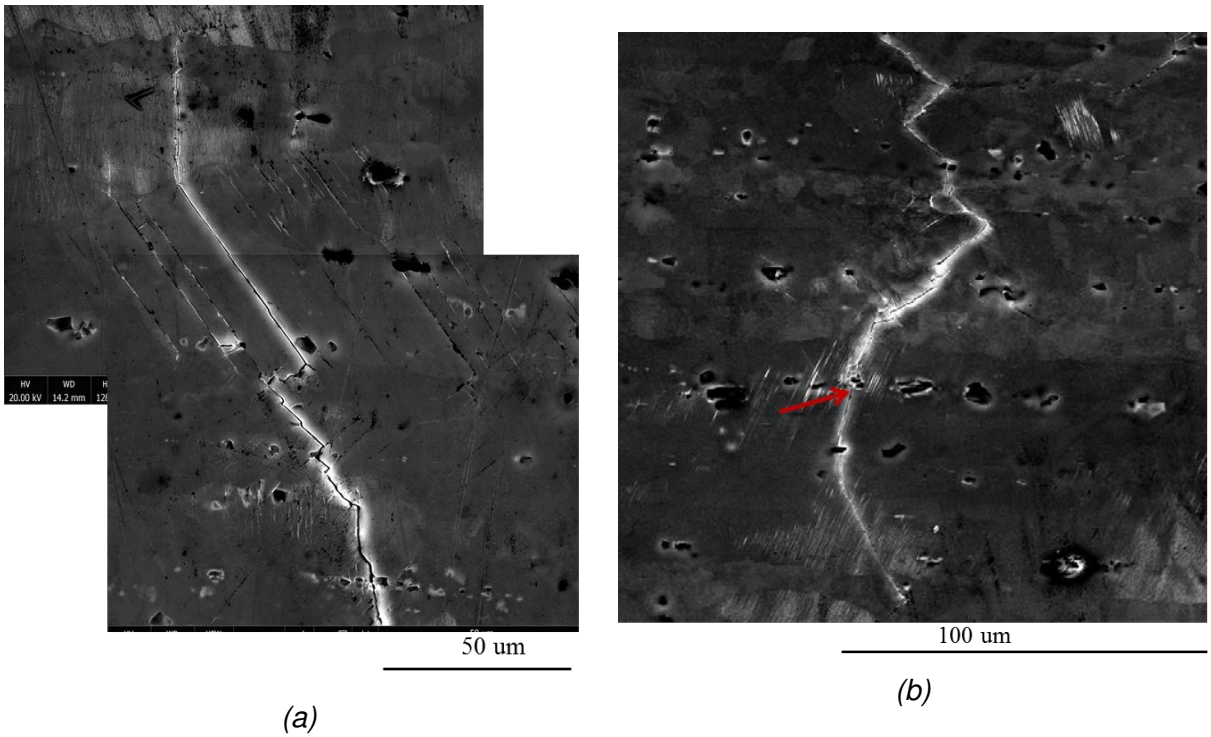

Figure 6.15: Damage mechanisms in the CG material. a) crack initiation from localized slip bands, and b) crack initiation from broken intermetallic particles. The tensile axis is horizontal.

More than one crack initiation was often observed on the fracture surfaces. These surfaces, quite classically, were characterized by a crystallographic faceted area around the crack initiation(s) site(s), corresponding to stage I growth, followed by a striated area (stage II), and finally a more or less slanted area covered with dimples corresponding to ductile fracture (Figure 6.16). No significant difference was noticed between the fracture surfaces corresponding to LCF and HCF, except the decreasing size of the shear lips when the loading range was decreased.

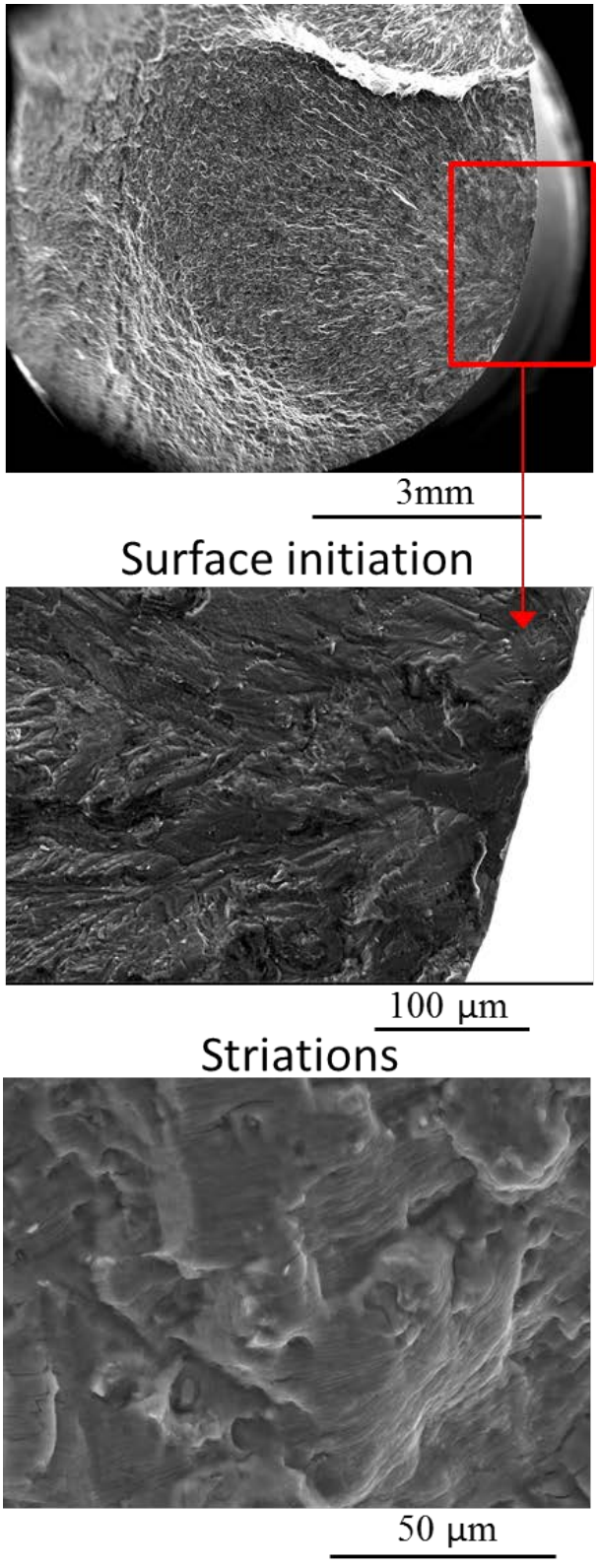

Figure 6.16: Fracture surface of broken CG sample after 2784 cycles

In UFG material, extrusions-intrusions and crack initiation from persistent slip bands was observed as in CG material (Figure 6.17a,b), but was much less frequent than crack initiation from broken intermetallic particles (Figure 6.17c), not always normal to the tensile axis, as might be expected in this case, but most often along a direction inclined by 50-60°.

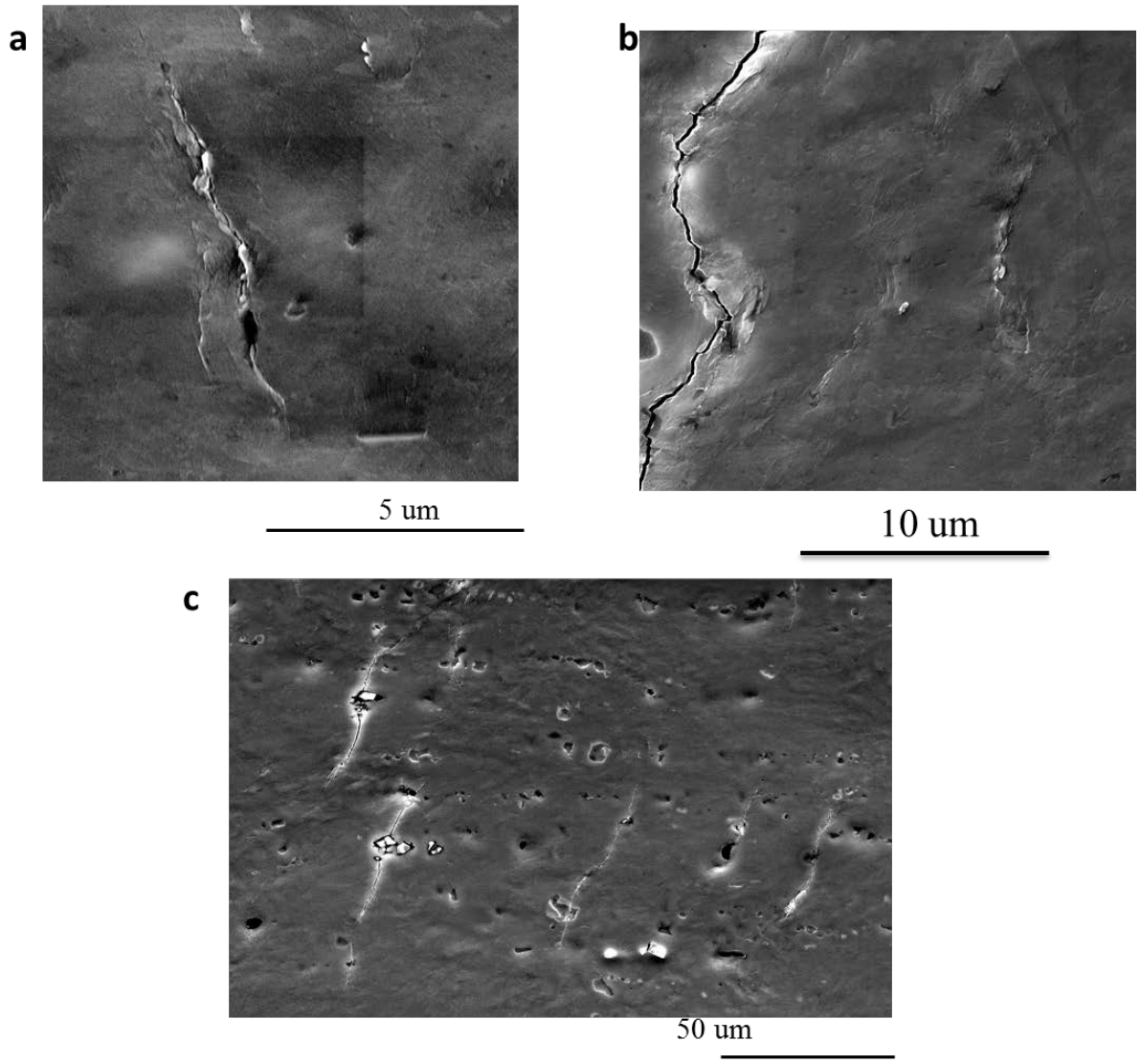

Figure 6.17: Damage mechanisms in UFG material. a-b) crack initiation from persistent slip bands, and c) crack initiation from broken intermetalic particles . The tensile axis is horizontal

Two microcracks paths are superimposed on EBSD maps on figure 6.18. It appears that the cracks grow straight across relatively large grains, but exhibit a zigzag path in areas of finer grains. In the first case, crack growth is transgranular, while it seems to be intergranular in the latter case (see the arrows (or squares) on the images).

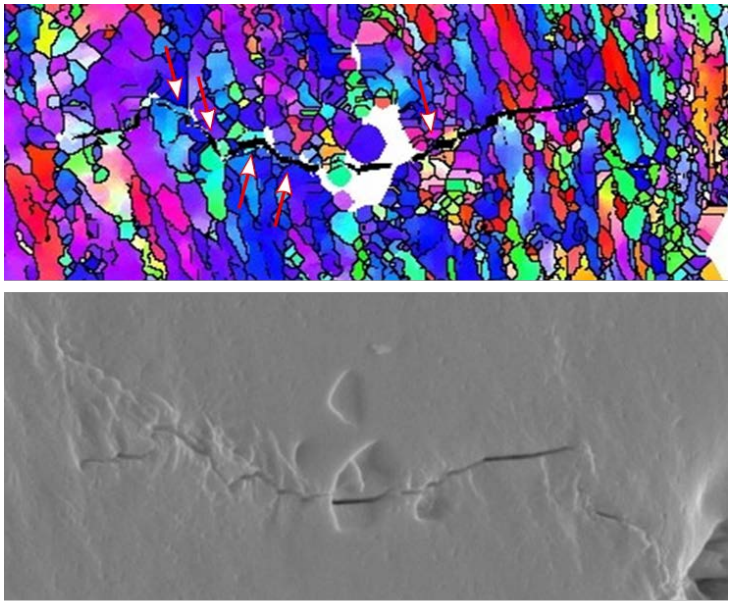

10 µm

(a)

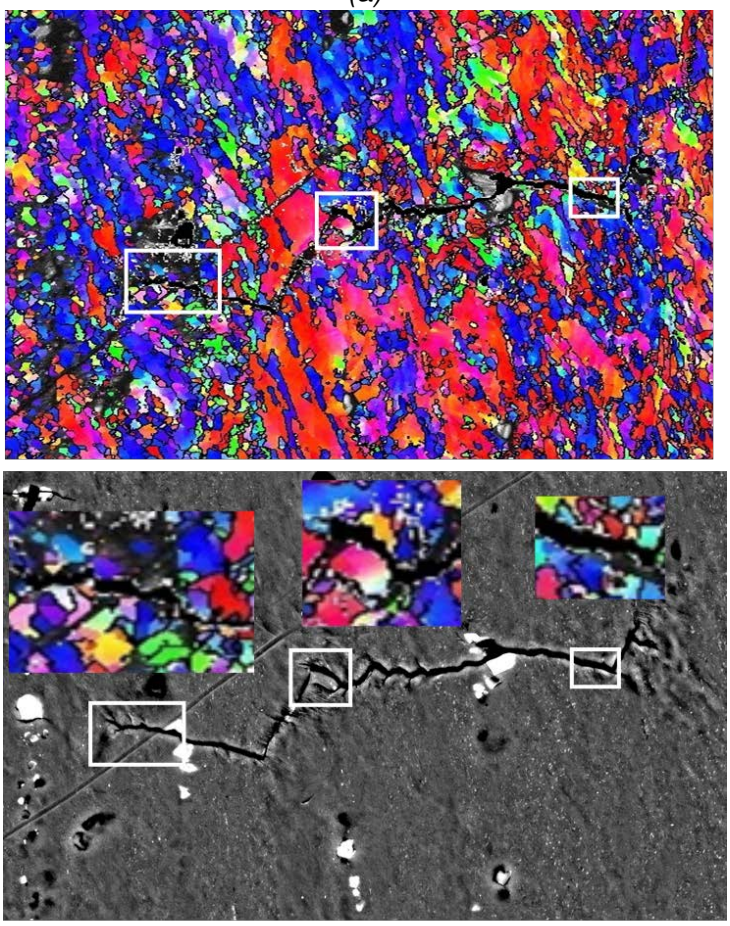

50 µm

(b)

Figure 6.18: EBSD analysis of two microcracks paths relative to the microstructure of a UFG sample $\varepsilon = \pm 4 \times 10^{-3}$. The tensile axis is vertical.

Figure 6.19 shows a fracture surface typical of the LCF regime (45,000 cycles to fracture). Several semi-circular microcracks, like the one shown on figure 6.19a initiated from the surface, and the fracture surface looked relatively smooth, with radial markings, until these cracks reached approximately 150 μm in depth (which for the stress level of 200 MPa corresponds to ΔK_I close to 3 MPa$\sqrt{m}$). Then striation-like features, up to 60 μm long, (which is nearly 100 times the mean grain size) appeared (Figure 6.19b) as if a transition from stage I to stage II occurred, but contrary to what usually happens in CG materials during such a transition, the roughness increased substantially. In the final slanted area, heavy friction marks and spalling due to the repeated contact between the crack lips were observed (Figure 6.19c).

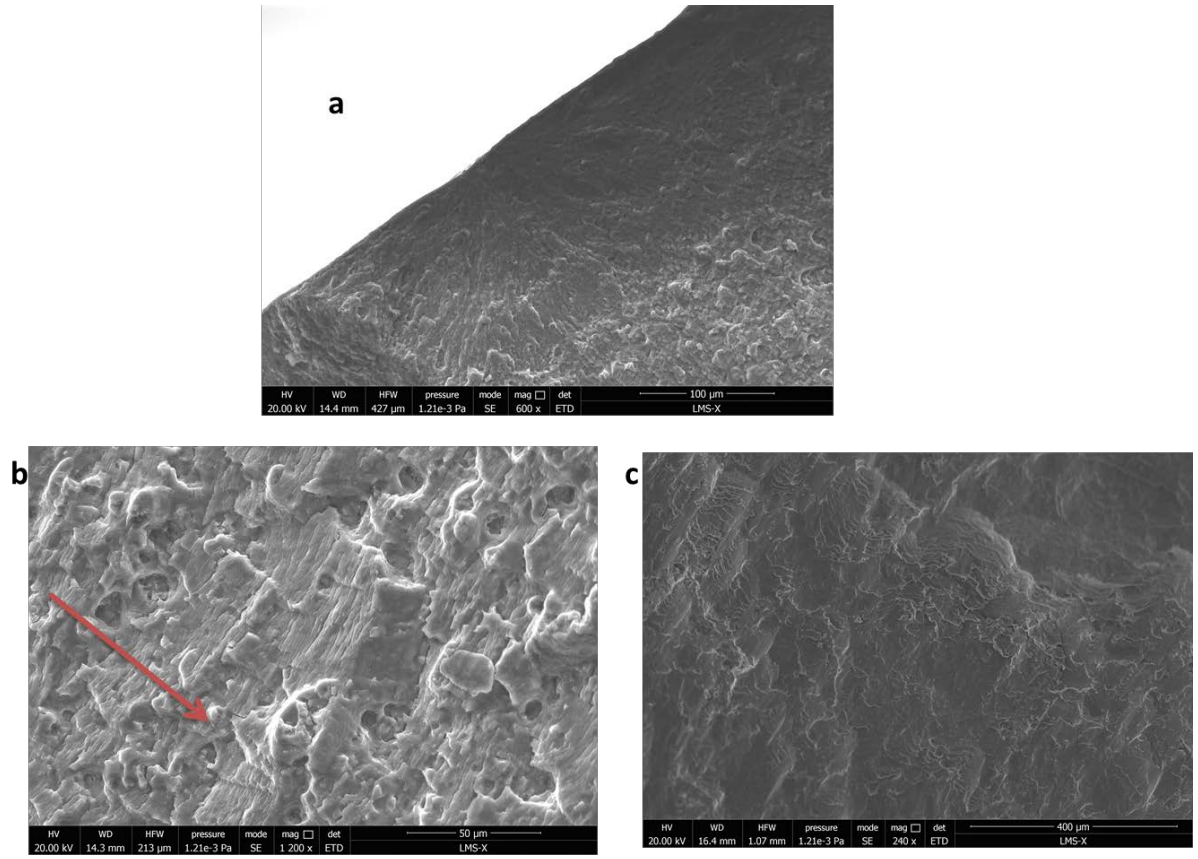

Figure 6.19: Fracture surface of a UFG sample submitted to a stress-controlled push-pull test at $\pm$200MPa (N_f=45438 cycles). a) one of the semi-circular cracks initiated from the surface, b) striation-like features (the arrow indicates the crack growth direction) and c) heavily mated slanted zone

Figure 6.20a shows the AFM scan of a secondary crack which is probably inclined into the depth and thus loaded in mixed-mode. Out of-plane sliding of the crack faces is significant. Fretting debris are clearly seen in figure 6.20b which is consistent with the wear marks shown on Figure 6.19c. Energy dissipation by friction might contribute to slow down the cracks.

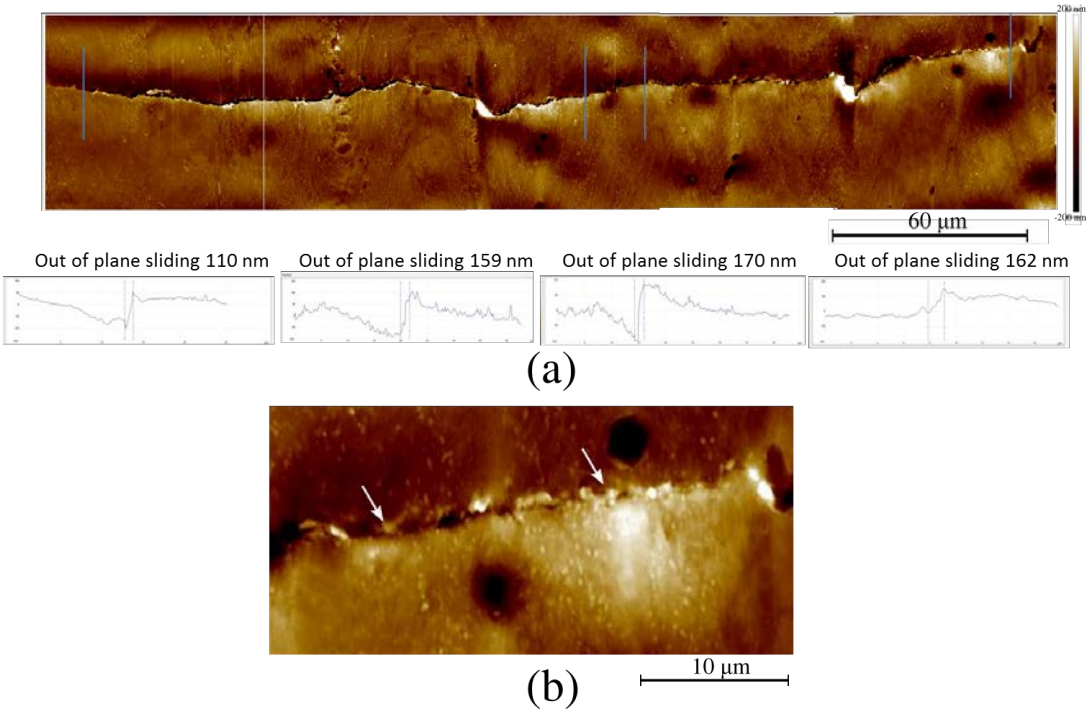

Figure 6.20: AFM image of a secondary crack in a UFG sample submitted to a stress-controlled push-pull test at 200 MPa. The vertical lines on the top image indicate where the out-of-plane displacement profiles were measured.

Statistical analysis of damage

Secondary cracks were counted and their lengths were measured after fracture on the outer surface of CG and UFG specimens submitted to similar strain or stress amplitudes, as shown in figure 6.21.

Figure 6.21: Counting and measurement of secondary crack along the gage-length of a UFG specimen subjected to a stress amplitude of 318 MPa.

Figures 6.22a and b compare the distributions of the measured secondary cracks lengths of CG and UFG samples submitted to the same plastic amplitude: ε_p=$\pm 2 \times 10^{-3}$. In CG material, the steady-state stress amplitude was 315 MPa and the fatigue life 2876 cycles, while in UFG material, the steady-state stress amplitude was 402 MPa and the fatigue life 1259 cycles. In spite of this smaller number of cycles, the density of micro-cracks was much higher (82 per mm^2) in the latter than in the former (8.8 per mm^2). This means that for this plastic strain range, crack initiation is easier and faster in the UFG material. While the angular distribution of the micro-cracks on the outer surface is relatively wide for the CG material, it is quite narrow and asymmetrical in the UFG material, with a preferential inclination around 60 degrees.

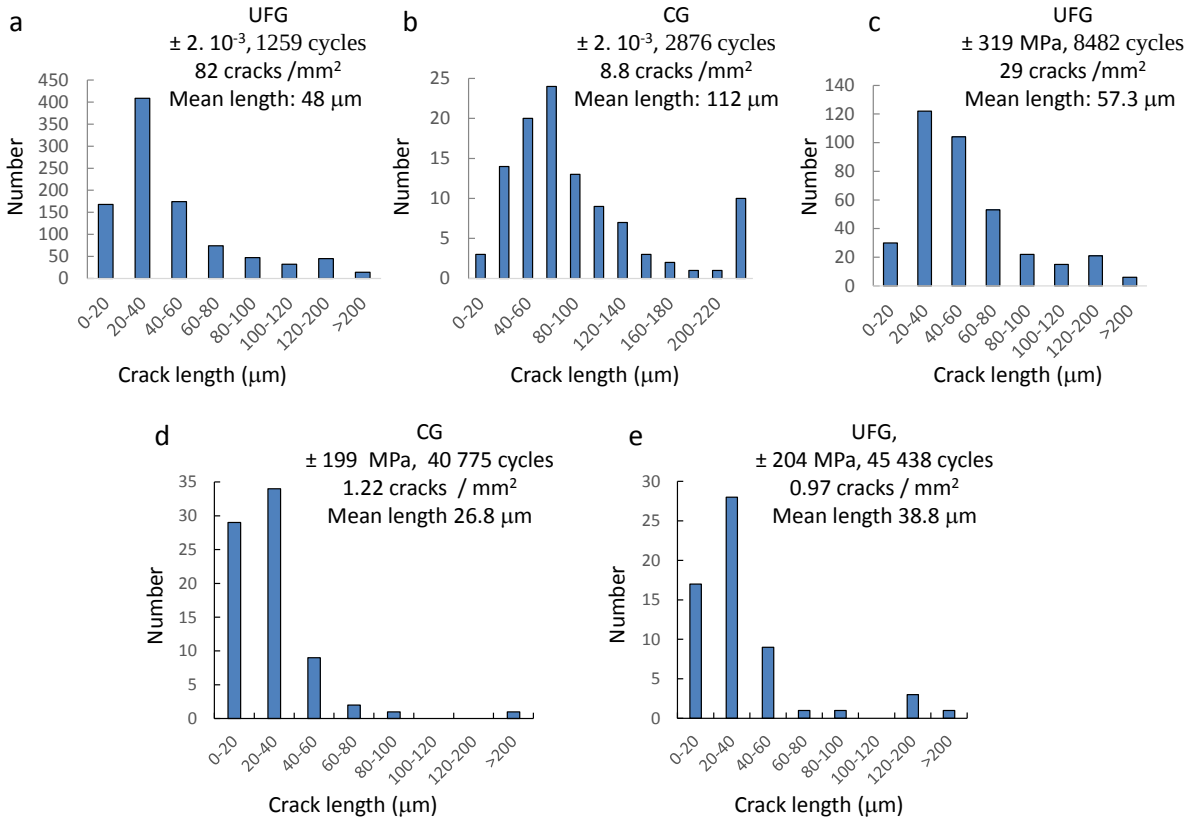

Figure 6.22: Distributions of secondary cracks lengths

Fig 6.22c shows the distributions of secondary cracks lengths on the outer surface of a UFG sample submitted nearly to the same stress amplitude ($\pm$ 319 MPa) as the sample analysed in figure 6.22b. In the UFG sample, the mean cracks length is only 57.3 μm, compared to 112 μm in the CG sample, in spite of a much larger number of cycles (8482 cycles, as compared to 2876). This indicates that for this high stress amplitude, micro-cracks growth was slower in the UFG material.

By contrast, at a lower amplitude ($\pm$200 MPa, figure 6.22d-e), the density of micro-cracks in the UFG alloy (0.97 per m^2) becomes lower than in the CG alloy (1.22 per mm^2) and the mean crack length is 40% larger (38.8 μm instead of 26.8 μm), while the number of cycles is only 11% larger, which suggests a faster growth.

The mean crack nucleation rates (final crack density divided by the number of cycles to failure) in CG and UFG samples are plotted as a function of the strain amplitude on figure 6.23. It is much higher in the UFG alloy at high strain range, but the difference with the CG alloy decreases as the strain rate decreases, and a crossing of the curves might exist (more tests would be necessary to check that point).

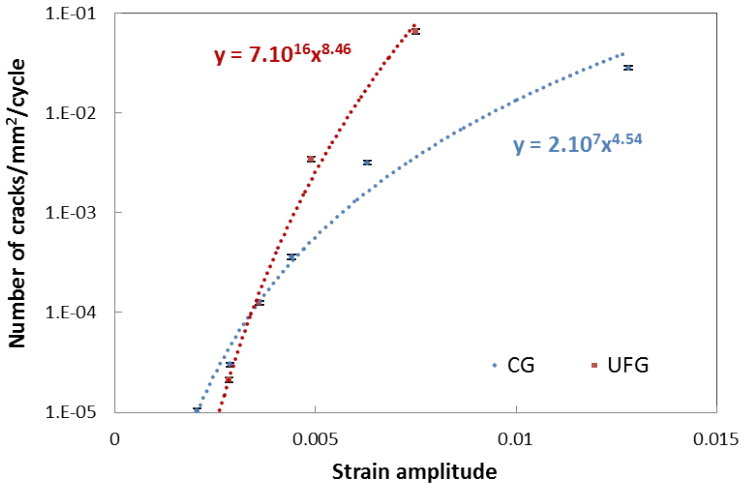

Figure 6.23: Crack nucleation rate in CG and UFG alloys

6.3 Discussion

Considering the large number of dislocation loops and jogs on the dislocations revealed by TEM in CG material after plastic-strain controlled tests, its large isotropic hardening is not surprising, since the loops constitute obstacles, and the jogs exert a drag force on gliding dislocations [2]. The non negligible kinematic hardening can be related to the interaction of dislocations with incoherent intermetallic particles. The dislocation loops left around the particles after Orowan's bypassing process is known to induce a back stress on gliding dislocations, that assists their backward glide upon load reversal and thus a Bauschinger effect.

The absence of cyclic softening of the UFG material is consistent with the results from Canadinc et al [5] about the stabilizing effect of solute Mg in Al-Mg alloys, which restricts dislocations mobility and thus hinders recovery and grain growth. The high fraction of HAGB in the material (more than 80%) probably contributes to its stability as well.

Since the dislocation density is already very high after ECAP (9×10^{14} m^{-2}) and the capacity for a further increase is limited, which explains the more modest isotropic hardening compared to the CG material. The heterogeneity in deformation from one grain to the other, and especially between the "large" and ultrafine grains in the UFG material contribute to its high kinematic hardening. A higher Bauschinger effect in the UFG microstructure was also reported (based on the pointer shape of the stress-strain loops) for ECAPed copper by Vinogradov et al [6], and this effect was even more pronounced after a short annealing treatment.

In LCF, the reduction in life of the UFG material compared to its CG counterpart decreases as the plastic strain amplitude increases, up to the point that the two curves seem to cross at the highest amplitude which should not be considered as a definitive result, owing to the limited number of data-points and the scatter often found, even in this regime [7]. This result is opposite to the trend reported in several papers (for example [8]). However, these papers mostly concern microstructurally unstable, cyclically softening UFG materials in which softening and grain coarsening, associated with strain localization tend to increase with the strain amplitude, leading to a more pronounced reduction in life than at lower amplitudes. In the present study, no such cyclic softening is observed, but at the contrary, a significant hardening. There is thus no reason to observe the same trend. Walley et al [9] who performed plastic-strain controlled LCF tests on cryomilled 5083 Al alloy (that exhibited cyclic hardening as well, after a slight transient softening attributed to the relaxation of residual stresses) also report very little difference in life with the CG material at high plastic strain amplitude, or even slightly better life for the UFG alloy, as in the present case.

The easier crack nucleation and the slower growth of micro-cracks observed here in the UFG alloy at high plastic strain amplitude are also contrary to what is usually reported, but these two results are consistent with one another and with the divergence of the Manson-Coffin curves when the plastic strain amplitude decreases. A large micro-cracks density might produce a shielding effect that would slow down micro-cracks growth. Diffuse energy dissipation by (slow) growth of many cracks would occur, instead of a more localized dissipation by (fast) growth of a smaller number of cracks. The inclination of the micro-cracks relative to the tensile axis, as well as the presence of many branches in LCF might also reduce their growth rate. When the plastic strain amplitude decreases, so does the micro-cracks density, and without a shielding effect, the usual tendency for faster crack growth in UFG materials found for macroscopic cracks in fracture mechanics samples [10] reappears.

On the other hand, the large density of micro-cracks that form in the UFG alloy in LCF also promotes the coalescence of those initiated in the same cross section, and indeed, up to six different crack initiation sites are sometimes observed on a given fracture surfaces in this regime. Such a crack coalescence phenomenon might be the main cause for its earlier fracture (with a minor contribution of the reduced crack initiation stage, which does not constitute a large part of the life in LCF).

While the micro-cracks exhibit a wide variety in their orientations relative to the tensile axis in the CG material, a preferential orientation around 60° was found in the UFG material. This direction corresponds more or less to the shear-induced elongation direction of the grains during ECAP, and it was shown by Niendorf et al. [11] or Arzaghi et al. [12] that ECAP-processed UFG materials have a preference for fatigue crack growth along the grain elongation direction. In addition, the grains with a high SF in the UFG material were all found to have a (001) direction nearly parallel to the tensile axis, so that the 111 plane with the highest SF on one of its slip systems would have a trace on the surface inclined by 50 to 60°, which corresponds to the preferential

micro-cracking direction.

6.4 Summary

In the present chapter, experimental analysis of cyclic behaviour through the determination of isotropic and kinematic hardening contributions and an interpretation of these contributions based on TEM observations was made. Fully reversed plastic-strain controlled (in LCF regime) and stress controlled (in HCF regime) push-pull tests were performed.

- The UFG Al 5083 produced by ECAP at 150°C investigated here exhibits cyclic hardening when submitted to plastic-strain controlled push-pull tests up to an amplitude of 8×10^{-3}, although in smaller proportions than its CG counterpart.
- In the UFG alloy, kinematic hardening predominates over isotropic hardening, which is attributed to a limited capacity to store more dislocations than those already present after ECAP, and to a high grain-to-grain heterogeneity in plastic deformation.
- For the same plastic strain range, the fatigue life of the UFG material is lower than that of the CG material and the density of secondary microcracks, mostly initiated from intermetallic particles previously fragmented or debonded by ECAP, is much higher. However, the shielding effect of this large micro-cracks density as well as the presence of branches slow down micro-cracks growth.
- When the amplitude decreases, the difference in crack nucleation rate between CG and UFG alloys decreases, and micro-crack growth becomes faster in UFG material. Between 10^4 to 2×10^6 cycles, the S-N curves of both materials nearly overlap.
- In the UFG material, the microcracks exhibit transgranular growth across the largest grains, but intergranular in the small grains areas.

References

[1] J. Lemaitre and J. L. Chaboche, "Mechanics of solid materials," *Cambridge university press*, 1994.

[2] U. Messerschmidt, "Dislocation dynamics during plastic deformation," *Springer series in Materials Science*, vol. 129, 2010.

[3] K. U. Snowden, "Dislocation arrangements during cyclic hardening and softening in Al crystals," *Acta metallurgica*, vol. 11, 1963.

[4] L. Meng, A. Goyal, V. Doquet, N. Ranc, and J.-P. Couzinié, "Ultrafine versus coarse grained al 5083 alloys: From low-cycle to very-high-cycle fatigue," *International Journal of Fatigue*, vol. 121, pp. 84–97, 2019.

[5] D. Canadinc, T. Niendorf, and H. Maier, "A comprehensive evaluation of parameters governing the cyclic stability of ultrafine-grained fcc alloys," *Materials Science and Engineering: A*, vol. 528, no. 21, pp. 6345–6355, 2011.

[6] A. Vinogradov, S. Hashimoto, V. Patlan, and K. Kitagawa, "Atomic force microscopic study on surface morphology of ultra-fine grained materials after tensile testing," vol. 321, pp. 862–866, 2001.

[7] K. Hockauf, T. Niendorf, S. Wagner, T. Halle, and L. Meyer, "Cyclic behavior and microstructural stability of ultrafine-grained aa6060 under strain-controlled fatigue," *Procedia Engineering*, vol. 2, no. 1, pp. 2199–2208, 2010.

[8] A. Böhner, H. Höppel, J. May, and M. Göken, "Influence of the ecap processing parameters on the cyclic deformation behavior on ultrafine-grained cubic face centered metals," *Advanced Engineering Materials*, vol. 14, Oct. 2012.

[9] J. L. Walley, E. J. Lavernia, and J. C. Gibeling, "Low-Cycle Fatigue of Ultra-Fine-Grained Cryomilled 5083 Aluminum Alloy," *Metallurgical and Materials Transactions A*, vol. 40A, 2009.

[10] P. Cavaliere, "Fatigue properties and crack behavior of ultra-fine and nanocrystalline pure metals," *International Journal of Fatigue*, vol. 31, pp. 1476–1489, 2009.

[11] T. Niendorf, F. Rubitschek, H. J. Maier, D. Canadinc, and I. Karaman, "On the fatigue crack growth-microstructure relationship in ultrafine-grained interstitial-free steel," *Journal of Materials Science*, vol. 45, no. 17, pp. 4813–4821, 2010.

[12] M. Arzaghi, C. Sarrazin-Baudoux, and J. Petit, "Fatigue Crack Growth in Ultrafine-Grained Copper Obtained by ECAP," *Advanced Materials Research*, vol. 891-892, pp. 1099–1104, 2014.

Conclusions and Perspectives

The aim of this study was to analyse the influence of grain refinement into the UFG regime on the monotonic and cyclic behaviour, deformation and damage mechanisms in tension and fatigue of an Al-Mg alloy. A special emphasis was laid on the role of grain boundary sliding which was more difficult to assess in a UFG than in a CG microstructure.

For that purpose, UFG Al 5083 alloy, was produced, initially using the ECAP facility of the LEM3 laboratory, and later, an in-house heated ECAP facility developed during the course of the thesis. A mean grain size around 700 nm was obtained by this process.

Tensile tests at various rates and relaxation tests were performed on CG and UFG materials between 20 and 200°C. The yield stress, hardening and ductility of both materials were highly strain rate and temperature-dependent. The temperature and strain rate domains where UFG Al5083 alloy is stronger and less ductile or softer and more ductile than the CG alloy were defined. The ductility of both materials was found to rise with the temperature and when the strain rate was reduced, at fixed temperature. It correlated linearly with the SRS, which exhibited the same trends. To explain these trends, SEM observations, EBSD mappings and measurement of the strain fields by DIC during *in situ* tensile tests or after *ex situ* tests at high temperature were performed.

The grain refinement after ECAP not only reduced the grain size but also changed the grain morphology (which become elongated in the shearing direction of ECAP), the texture, the nature of grain boundaries (HAGB/LAGB) and the distribution of second phase particles (that got fragmented and aligned in the shearing direction).

As a result, even though the strain fields were heterogeneous in both the materials at RT, the cause of this heterogeneity was different, and governed by their initial microstructure. In CG material, it was due to the fracture of large, intergranular second phase particles, while in UFG material, it was due to the inhomogeneous grain refinement from ECAP, and occurred mostly at the interfaces between coarse and fine grains and to a lesser extent, along rows of broken second phase particles.

Such a strain localisation pattern also explains why irrespective of the testing temperature and strain rate, fracture was always slanted in the UFG material, even outside the temperature and strain rate range for DSA. By contrast, the CG material only exhibited

slanted fracture in the PLC regime.

GBS was observed in both materials, and became more and more active as the temperature increased and as the strain rate decreased. In the UFG material, GB sliding was cooperative and at 200°C, it accommodated up to 300% strain without apparent damage inside intense shear bands. GBS was present very early during the deformation and was responsible for a rate dependence of the apparent Young's modulus. Shear banding and GBS both intensified with increase in temperature and decrease in strain rate. A linear relationship was obtained between the contribution of GBS to global plastic strain and the SRS indicating that the rise in ductility at high temperature and low strain rates is, to a large extent, a consequence of GBS. In CG material, GBS was mostly uncorrelated and accounted for at most 10% of the global strain. It was probably not responsible for the rise in SRS at high temperature/low strain rate.

Evidences of non-octahedral slip on {110}<1$\bar{1}$0> slip systems were observed at 200°C. In CG material, the volume fraction of grains in which such slip is likely to occur was too low to induce a significant rise in SRS, however in UFG material, due to a different texture, this volume fraction was larger and might partly explain, together with GBS, the rise in SRS at high temperature/low strain rate. In both materials, this additional deformation mechanism certainly contributed to the rise in ductility observed with rising temperature.

The cyclic behaviour of the two materials was analysed by performing plastic-strain controlled push-pull tests. A more modest isotropic hardening and a high kinematic hardening were observed in UFG material, which was attributed to a limited capacity to store more dislocations than those already present after ECAP, and to a higher grain-to-grain heterogeneity in plastic deformation.

At high plastic strain amplitude, the crack nucleation rate is much higher in the UFG alloy, and crack coalescence phenomena might be responsible for its reduced fatigue life, in spite of a lower crack growth rate attributed to shielding effects, as well as to the presence of many branches. The micro-cracks exhibit transgranular growth across the largest grains, but intergranular growth in the small grained areas. As the loading range decreases, the difference in crack nucleation rate between CG and UGH alloys however decreases, and this rate becomes lower in the latter. On the other hand, the microcrack growth rate in the UFG alloy becomes higher than in the CG alloy in the HCF regime, which might explain why between 10^4 and 2×10^6 cycles, its fatigue performance is just slightly better. A clear superiority of the UFG material was only shown in the VHCF regime (from 2×10^6 to 5×10^8 cycles), by tests run at 20 kHz on a piezoelectric testing machine, in parallel to this thesis.

A simple, yet efficient 2D finite element model with viscoplastic "grains" and viscous sliding "GBs" was shown to capture the temperature and rate-dependent behaviour of the CG and UFG alloys. It also gave some insights into the percolation phenomenon associated with cooperative GBS, which might lead to very intense shear bands crossing the whole gage width, with a reduced constraint at high temperature. However,

since it does not take diffusive accommodation phenomena into account, it predicts early cavitation at triple points, and thus cannot be used to model the superplastic regime.

Perspectives

One of the main limitations of this work is that only post-fracture information was available for the tests done at high temperature. The kinetics of GBS could thus not be monitored during plastic flow as it was during *in situ* tests at RT. In addition, the strain after fracture was very high, leading to errors in the measurement of the strain fields because of manual placement of correlation points. An experimental set-up has recently been developed to perform *in situ* tests at high temperature, and additional experiments might be done in the forth-coming months.

Although a successful meso-scale patterning method was developed to measure the local strain fields in UFG materials, it was not sufficient to allow a measurement of the contribution of GBS to global strain using DIC. Finally, an intercept method was used as usually done in the literature, but it is too local and lacks representativity. Better results could be obtained by the use of EBSD (which was difficult in the UFG material ECAPed at RT due to high dislocation density, but easier after ECAP at 150°C) coupled with DIC as done for CG material at 200°C. Alternatively, pre- and post-deformation AFM scans might be used, to measure the out-of-plane sliding displacements over large areas. Again, the analysed areas would need to be mapped using EBSD to locate the grains boundaries in order to correctly estimate out-of-plane GBS.

The proposed constitutive model currently employs an equiaxed microstructure, easy to obtain by Voronoi tessellation, which is not a representative of the elongated grains in the UFG material. Several simple modifications can be made to have a better representation of the actual UFG microstructure. The effect of grain shape can be introduced by changing the orientation and aspect ratio of the grains. Furthermore, instead of choosing the same threshold stress for sliding for all the GBs, the threshold stress can be introduced as a random variable to capture the difference in GB character (HAGB/LAGBs) or the presence of 2nd phase particles which restrict GBS.

université PARIS-SACLAY

ÉCOLE DOCTORALE
Sciences mécaniques et énergétiques, matériaux et géosciences (SMEMAG)

Titre : Comportement mécanique d'un alliage d'aluminium à grains ultrafins : Analyse et modélisation du rôle exacerbé des joints de grains.

Mots clés : Grains ultrafins, Plasticité, Joints de grains, Aluminium

Résumé : Ce travail compare le comportement et les mécanismes de déformation et d'endommagement en traction et fatigue d'un alliage Al-Mg classique et à grains ultrafins obtenu par déformation plastique sévère. On montre que le raffinement microstructural accroît la sensibilité à la vitesse, qui augmente avec la vitesse et contrôle la ductilité. Les domaines de vitesse et température dans lesquels le raffinement microstructural accroît la résistance en traction ont été délimités. Des essais de traction sous MEB accompagnés de mesures des champs de déformation ont montré que le glissement aux joints est d'autant plus actif que la température augmente et que la vitesse diminue et que la déformation est plus hétérogène dans le matériau à grains ultrafins. Un modèle numérique intégrant le glissement des joints rend compte des comportements observés. les deux matériaux manifestent un durcissement cyclique en fatigue, plus modeste dans l'alliage à grains ultrafins. Ce matériau a une durée de vie plus faible en fatigue oligocyclique, en raison d'un amorçage plus précoce des fissures, mais légèrement supérieure en fatigue polycyclique, grâce à une propagation plus lente.

Title : Mechanical behaviour of ultra-fine grain Al 5083 alloy: Analysis and modelling of the role of grain boundaries to overall plastic deformation.

Keywords : Ultrafine grains, Plasticity, Grain boundary sliding, Aluminium

Abstract : This work compares the viscoplastic behaviour, and the deformation and damage mechanisms in tension and fatigue of an ultra-fine grained (UFG) Al-Mg alloy obtained by severe plastic deformation with that of its coarse-grained (CG) counterpart. Microstructural refinement increases the strain rate sensitivity, which rises as the strain rate decreases, and controls the ductility. The temperature and strain rate domain for which the UFG alloy is stronger has been determined. Tensile tests run in a SEM with measurements of strain fields have shown that grain boundary sliding is more and more active in both materials as the temperature rises and as the strain rate decreases, and that the strain field is more heterogeneous in the UFG alloy. A model taking into account viscoplasticity inside the grains, and viscous sliding at the boundaries captures well the observed behaviours. Both materials exhibit cyclic hardening, although it is more modest in the UFG alloy. For a given strain range, the UFG alloy has a shorter fatigue life, because of a much easier crack initiation. For a given stress range, it has a slightly higher life, due to a slower development of microcracks.